Rosetta's daring dance with a comet *p. 502*

A Turing network that acts in limb development *pp. 516 & 566*

Unexpected particle acceleration in novae *p. 554*

Science

$10
1 AUGUST 2014
sciencemag.org

AAAS

How worms weaken immunity

Intestinal parasites compromise host antiviral defenses. *pp. 517, 573, & 578*

CONTENTS

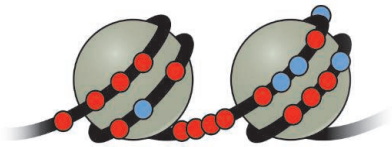

511
Toward whole-genome methylation maps for ancient DNA

1 AUGUST 2014 • VOLUME 345 • ISSUE 6196

NEWS

IN BRIEF

492 Roundup of the week's news

IN DEPTH

495 CURE SETBACKS FORCE HIV RESEARCHERS TO RESET SIGHTS
Remission seen as more realistic goal
By J. Cohen

496 WARMING MAY NOT SWAMP ISLANDS
Studies suggest that atoll islands will rise in step with a rising sea *By C. Pala*

498 KEY NARCOLEPSY–INFLUENZA VACCINE FINDINGS RETRACTED
Stanford researchers unable to replicate results *By E. Underwood*

499 VENEZUELA'S PUBLIC HEALTH PAIN
Lacking vital medical supplies, doctors struggle to treat resurgent diseases
By L. Wade

500 DECISION LOOMS ON FUTURE OF E.U. SCIENCE ADVICE
Green groups criticize adviser—and her office *By K. Kupferschmidt*

501 ITALY QUAKES DIVIDE EXPERTS
Industry report dismisses link to oil production *By E. Cartlidge*

FEATURES

502 COMET CATCHER
The Rosetta spacecraft encounters one of the solar system's most mysterious objects *By E. Hand*

504 Touch and go
By E. Hand

506 CENTRAL COMMAND
More capable than once thought, the nucleolus may be a target for treating diseases *By M. Leslie*

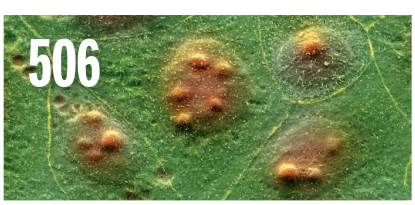

INSIGHTS

PERSPECTIVES

508 HOW BIRDS BECAME BIRDS
Sustained size reduction was essential for the origin of birds and avian flight
By M. J. Benton
▸ REPORT P. 562

510 A GEM OF A QUANTUM TELEPORTER
Diamond-based quantum teleportation works every time
By M. Atatüre and J. J. L. Morton
▸ RESEARCH ARTICLE P. 532

511 AN EPIGENETIC WINDOW INTO THE PAST?
DNA damage in ancient genomes may provide insight into past regulatory changes in humans and other species
By L. Orlando and E. Willerslev

513 MORE PAIN; LESS GAIN
Persistent pain changes a neural circuit and reduces willingness to work for food *By H. L. Fields*
▸ RESEARCH ARTICLE P. 535

514 THE BEAT OF YOUNG STARS
Pulsations from young stars provide a new chronometer for stellar evolution
By S. Stahler and F. Palla
▸ REPORT P. 550

516 IN TURING'S HANDS–THE MAKING OF DIGITS
A Turing network controls the periodic pattern of fingers and toes during development *By A. Zuniga and R. Zeller*
▸ REPORT P. 566

517 HOW HELMINTHS GO VIRAL
Cellular signals during helminth infections can skew the immune response to favor viral spreading
By R. M. Maizels and W. C. Gause
▸ REPORTS PP. 573 & 578

519 GLOBAL MANUFACTURING AND THE FUTURE OF TECHNOLOGY
Where you manufacture changes what you get *By E. R. H. Fuchs*

BOOKS *ET AL.*

521 BIOHACKERS
By A. Delfanti, reviewed by S. Golinelli and L. Henry

522 CONNECTED
By S. Cassedy, reviewed by B. C. Keegan

LETTERS

523 CHINA'S ROBOTICS SUCCESSES ABOUND
By Y. Gao and J. Liu

523 SEMANTIC PRIMING WELL ESTABLISHED
By D. E. Meyer

524 EYEING VISUAL PATHWAYS IN DYSLEXIA
By T. R. Vidyasagar

524 RESPONSE
By B. Boets

524 TECHINCAL COMMENT ABSTRACTS

DEPARTMENTS

491 EDITORIAL
Zero hunger
By M. S. Swaminathan

594 WORKING LIFE
The stressed-out postdoc
By Carrie Arnold

Science Staff 488
New Products 583
Science Careers 584

Published by AAAS

CONTENTS

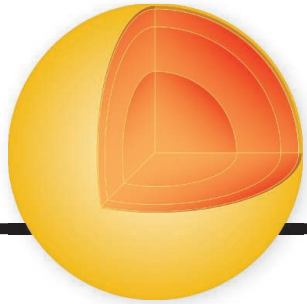

514 & 550
A glimpse into the development of young stars

1 AUGUST 2014 • VOLUME 345 • ISSUE 6196

RESEARCH

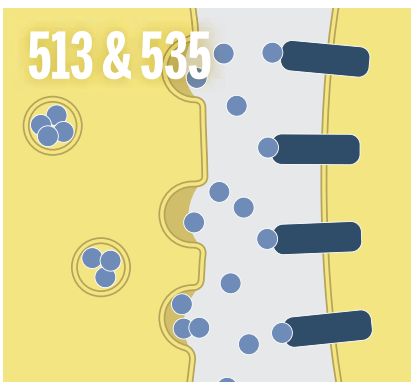

IN BRIEF

526 From *Science* and other journals

REVIEW

529 **INTERNEURONS**
Fast-spiking, parvalbumin$^+$ GABAergic interneurons: From cellular design to microcircuit function *H. Hu* et al.
REVIEW SUMMARY; FOR FULL TEXT:
dx.doi.org/10.1126/science.1255263

RESEARCH ARTICLES

531 **MOBILE DNA IN CANCER**
Extensive transduction of nonrepetitive DNA mediated by L1 retrotransposition in cancer genomes *J. M. C. Tubio* et al.
RESEARCH ARTICLE SUMMARY; FOR FULL TEXT:
dx.doi.org/10.1126/science.1251343

532 **QUANTUM INFORMATION**
Unconditional quantum teleportation between distant solid-state quantum bits *W. Pfaff* et al.
▸ PERSPECTIVE P. 510

535 **CHRONIC PAIN**
Decreased motivation during chronic pain requires long-term depression in the nucleus accumbens *N. Schwartz* et al.
▸ PERSPECTIVE P. 513

REPORTS

542 **PHOTOVOLTAICS**
Interface engineering of highly efficient perovskite solar cells *H. Zhou* et al.

546 **CATALYSIS**
Highly active copper-ceria and copper-ceria-titania catalysts for methanol synthesis from CO_2 *J. Graciani* et al.

550 **ASTEROSEISMOLOGY**
Echography of young stars reveals their evolution *K. Zwintz* et al.
▸ PERSPECTIVE P. 514

554 **NOVAE**
Fermi establishes classical novae as a distinct class of gamma-ray sources
The Fermi-LAT Collaboration
▸ PODCAST

558 **QUANTITATIVE SOCIAL SCIENCE**
A network framework of cultural history *M. Schich* et al.

562 **DINOSAUR EVOLUTION**
Sustained miniaturization and anatomical innovation in the dinosaurian ancestors of birds
M. S. Y. Lee et al.
▸ PERSPECTIVE P. 508

566 **MODELING DIGITS**
Digit patterning is controlled by a Bmp-Sox9-Wnt Turing network modulated by morphogen gradients *J. Raspopovic* et al.
▸ PERSPECTIVE P. 516

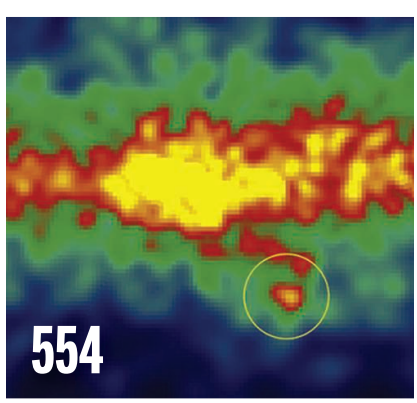

570 **HIV LATENCY**
Proliferation of cells with HIV integrated into cancer genes contributes to persistent infection *T. A. Wagner* et al.

COINFECTION

573 Helminth infection reactivates latent γ-herpesvirus via cytokine competition at a viral promoter
T. A. Reese et al.

578 Virus-helminth coinfection reveals a microbiota-independent mechanism of immunomodulation
L. C. Osborne et al.
▸ PERSPECTIVE P. 517

ON THE COVER

Colorized scanning electron micrograph of a dog roundworm (*Toxocara canis*). Intestinal parasites infect more than 1 billion people worldwide and cause serious morbidity, particularly in the developing world. In mice, intestinal parasites also dampen their host's immunity to viruses, causing latent viruses to reactivate and impeding antiviral defenses. See pages 517, 573, and 578.
Image: © Eye of Science/Science Source

PHOTO: (BOTTOM RIGHT) MAXIMILIAN SCHICH/MAURO MARTINO

SCIENCE (ISSN 0036-8075) is published weekly on Friday, except the last week in December, by the American Association for the Advancement of Science, 1200 New York Avenue, NW, Washington, DC 20005. Periodicals mail postage (publication No. 484460) paid at Washington, DC, and additional mailing offices. Copyright © 2014 by the American Association for the Advancement of Science. The title SCIENCE is a registered trademark of the AAAS. Domestic individual membership and subscription (51 issues): $153 ($74 allocated to subscription). Domestic institutional subscription (51 issues): $1282; Foreign postage extra: Mexico, Caribbean (surface mail) $55; other countries (air assist delivery) $85. First class, airmail, student, and emeritus rates on request. Canadian rates with GST available upon request, GST #1254 88122. Publications Mail Agreement Number 1069624. **Printed in the U.S.A.**
Change of address: Allow 4 weeks, giving old and new addresses and 8-digit account number. **Postmaster:** Send change of address to AAAS, P.O. Box 96178, Washington, DC 20090–6178. **Single-copy sales:** $10.00 current issue, $15.00 back issue prepaid includes surface postage; bulk rates on request. **Authorization to photocopy** material for internal or personal use under circumstances not falling within the fair use provisions of the Copyright Act is granted by AAAS to libraries and other users registered with the Copyright Clearance Center (CCC) Transactional Reporting Service, provided that $30.00 per article is paid directly to CCC, 222 Rosewood Drive, Danvers, MA 01923. The identification code for *Science* is 0036-8075. *Science* is indexed in the *Reader's Guide to Periodical Literature* and in several specialized indexes.

Published by AAAS

EDITORIAL

Zero hunger

The United Nations (UN) designated 2014 as the International Year of Family Farming, recognizing that an estimated 500 million family farms, involving over 2 billion people, play a key role in food production and consumption worldwide. It is thus an opportune time to encourage a shift in tackling global hunger—from a "food security" focus to an agenda that promotes "nutrition security" instead. The drive to reduce hunger in the world has largely relied on crops such as wheat and rice that provide calories. But an increase in calories alone is not good enough. Improved diets and good health require bolstering nutrition.

Food security programs begun since World War II, both by national governments and international agencies such as the UN Food and Agriculture Organization and the UN World Food Programme, were generally designed to address undernutrition. Ironically, this approach has led to malnutrition in some cases. For example, support for the growth and distribution of high-yielding cereals has led to predominantly cereal-based diets with deficiencies in proteins and micronutrients. Consequential health problems have been seen in several parts of India and South Asia. Such hidden hunger is ample reason to pursue crop planning that fulfills the macro- and micronutrient needs of populations in an integrated manner. Diet deficiencies of iron, zinc, iodine, vitamin A, and vitamin B12 deny nearly two billion people a healthy life. Commercial farming tends to promote market-driven monoculture of food crops, in which prioritizing nutrient need is generally absent. Without mainstreaming nutritional criteria in large-scale agricultural cropping and farming systems, the prospect for meeting the UN's Zero Hunger Challenge by 2025 will be dim.

"Family farming offers an effective and economic solution to...making sure that each person has access...to nutritious food."

Family farming is characterized by diversified crops and hence can be harnessed to support nutrition-sensitive agriculture. The steps needed to achieve such a change include survey and identification of the major nutritional problems prevailing in an area. Appropriate changes in crops to address the deficiencies can then be made on family farms. Also needed is the standardization of measurement tools to estimate the impact of the nutritional interventions on human health. This can be done by using internationally accepted measurement criteria, such as stunting among children below 2 years of age. Members of elected local bodies could be educated in the nutritional deficiencies that can be overcome through a food-based approach. These efforts are being implemented in several hunger hotspots in India such as the tribal areas of Odisha, Kerala, and Maharashtra.

In March, encouraging examples of how to enrich staple crops with desired micronutrients were presented at the Second Global Conference on Biofortification held in Kigali, Rwanda, reflecting a growing interest in biofortification among scientists and public health professionals. Many plants such as sweet potato, breadfruit, moringa, and various berries are rich in micronutrients such as iron, zinc, vitamin A, and vitamin C. Such naturally biofortified plants should find a larger place in family farming. In addition, food crops can be enriched with specific nutrients through plant breeding, as has been done with rice, wheat, cassava, beans, and pearl millet under the Harvest Plus program of the CGIAR Consortium of International Agricultural Research Centers. CGIAR works with partners to distribute technologies and resources, including to small farms, and is a model for the development of similar efforts. In the meantime, our knowledge of how to assess risks and benefits regarding genetically modified crops will hopefully grow. Golden rice, genetically enriched in vitamin A, demonstrates the potential of this approach. But regulatory mechanisms are needed to assess the biosafety of such varieties in a scientific and transparent manner.

Family farming offers an effective and economic solution to help meet the challenge of making sure that each person has access not just to calories but to nutritious food. With an estimated 8 billion mouths to feed by 2025, we must think much more precisely about the best solutions for reaching zero hunger.

– M. S. Swaminathan

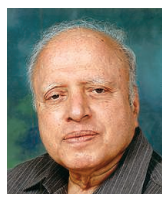

M. S. Swaminathan is the Founder Chairman of the M S Swaminathan Research Foundation, Chennai, India. E-mail: swami@mssrf.res.in

10.1126/science.1258820

PHOTOS: (INSET) FERTNIG/ISTOCKPHOTO.COM; (RIGHT) PUNJAB AGRICULTURE UNIVERSITY, LUDHIANA

Downloaded from www.sciencemag.org on August 11, 2014

Published by AAAS

NEWS

> “They’re just buying Putin enough time to run to a pet store, get five geckos, and parade them in front of us. Well, we don’t want those geckos. We want the space geckos!”
>
> Comedian **John Oliver**, dismissing Russia’s claim to have regained control of a satellite carrying a gecko mating experiment.

IN BRIEF

Western U.S. using up ground water

Arizona’s Lake Mead, in July 2007 (*left*) and July 2014 (*right*).

Over the past 14 years, drought has afflicted the Colorado River Basin. But there is also an invisible bathtub being emptied belowground: Ground water in the basin was depleted at a rate of 5.6 cubic kilometers per year from December 2004 to November 2013—six times faster than surface water, according to a study published online last week in *Geophysical Research Letters*. To detect groundwater depletion, James Famiglietti, a hydrologist at the University of California, Irvine, and his colleagues relied on a pair of NASA satellites called the Gravity Recovery and Climate Experiment. The instruments are sensitive to tiny variations in Earth’s gravity; when a mass of water disappears, gravity in that area drops. The groundwater losses, which take thousands of years to be recharged naturally, point to the unsustainability of exploding population centers and water-intensive agriculture in the basin, which includes most of Arizona and parts of Colorado, California, Nevada, Utah, New Mexico, and Wyoming. http://scim.ag/westernGW

AROUND THE WORLD

Google X to define health

MOUNTAIN VIEW, CALIFORNIA | Google X, the secretive research arm of Google Inc., intends to pin down what it means to be healthy. The company revealed last week that its new “Baseline Study” will follow thousands of people and identify patterns of biochemicals, proteins, genetic mutations, and physiological measurements that determine who gets sick. The study will be led by Google X life sciences chief Andrew Conrad, collaborating with Stanford University in Palo Alto, California, and Duke University in Durham, North Carolina. After a pilot study with 175 people this summer, the project hopes to recruit 10,000 volunteers over 2 to 3 years, says Duke cardiologist Robert Califf. Volunteers will donate blood and saliva for testing and may sport wearable medical devices, such as a glucose-sensing contact lens developed by Google X.
http://scim.ag/googlehuman

Dueling analyses of landslide

OSO, WASHINGTON | Two analyses are competing to explain one of the deadliest landslides in U.S. history. On 22 July, the Geotechnical Extreme Events Reconnaissance (GEER) Association released the first published analysis of the 22 March Oso slide, which killed 43. In GEER’s analysis, the slope began to slide, and the combination of movement and ample water turned the ground into a fast-flowing semiliquid. Four minutes later, a second part of the mountain fell after losing support from below. But an

The massive Oso landslide, in April 2014.

PHOTOS: (LEFT TO RIGHT) ETHAN MILLER/GETTY IMAGES (2); JONATHAN GODT/USGS

Downloaded from www.sciencemag.org on August 11, 2014

Published by AAAS

Grapple over the gold

Who owns this jeweled torque? That's the thorny question that an archaeological museum at the University of Amsterdam is facing. In February, the Allard Pierson Museum opened an exhibition of top archaeological treasures on loan from five Ukrainian museums—including four in Crimea, the peninsula that was annexed by Russia a month later. Now, the Crimean museums want their pieces back, a claim backed by the Russian government. But Ukraine says it's the rightful owner, because the museums were state-owned before the annexation, and wants the items sent to Kiev. Among the objects are precious jewels and gold from Chersonesus, a Greek colony in what is now Sevastopol, and from the Scythians, an ancient horse-riding people. The university is studying the legal issues and hopes to make a decision before the exhibition ends on 31 August, a spokesman says. The 17 July crash of Malaysia Airlines Flight 17, in which 195 Dutch citizens were killed, won't play a role, he adds, even though many believe Russia bears at least partial responsibility and Russian-Dutch relations have soured.

Russia and Ukraine both claim ownership over Crimean artifacts.

unpublished analysis by scientists with the U.S. Geological Survey and the University of Washington, based on a new way of analyzing low-speed seismic data, finds instead that just 50 seconds after the lower slope began to slide slowly, an upper part of the mountain broke loose. The violence of that impact, they suggest, could have caused the soil to rapidly liquefy and shoot across the valley, like a foot slamming into a mud puddle. **http://scim.ag/Osolandslide**

Fukushima's lessons for the U.S.

WASHINGTON, D.C. | To avoid the safety complacency that led to the 2011 disaster at the Fukushima Daiichi Nuclear Power Station in Japan, U.S. nuclear plant operators and regulators must keep safety features upgraded, states a report written by a committee of the National Academy of Sciences and released on 24 July. The report drew on Japanese and international investigations into the disaster, precipitated by the magnitude-9 earthquake and tsunami of 11 March 2011. The academy's report cites failures to protect safety equipment from flooding, despite evidence that the design for tsunamis was inadequate. "The overarching lesson learned from the Fukushima Daiichi accident is that nuclear plant licensees and their regulators must actively seek out and act on new information about hazards that have the potential to affect the safety of nuclear plants," the report concludes. **http://scim.ag/Fukushimareport**

Brazil's big eyes on the sky

SÃO PAULO, BRAZIL | Sometime in the 2020s, astronomers in Brazil may have access to two giant telescopes. The São Paulo Research Foundation is paying $40 million to participate in the Giant Magellan Telescope (GMT). This U.S.-led instrument, to be built in Chile, will sport seven 8.4-meter mirrors (three have already been cast) that operate as a single 21.4-meter instrument. Meanwhile, European Southern Observatory (ESO) Director General Tim de Zeeuw expects the Brazilian government to ratify Brazil's pending ESO membership. ESO needs Brazil's €132 million entrance fee, spread over 10 years, to complete its even more

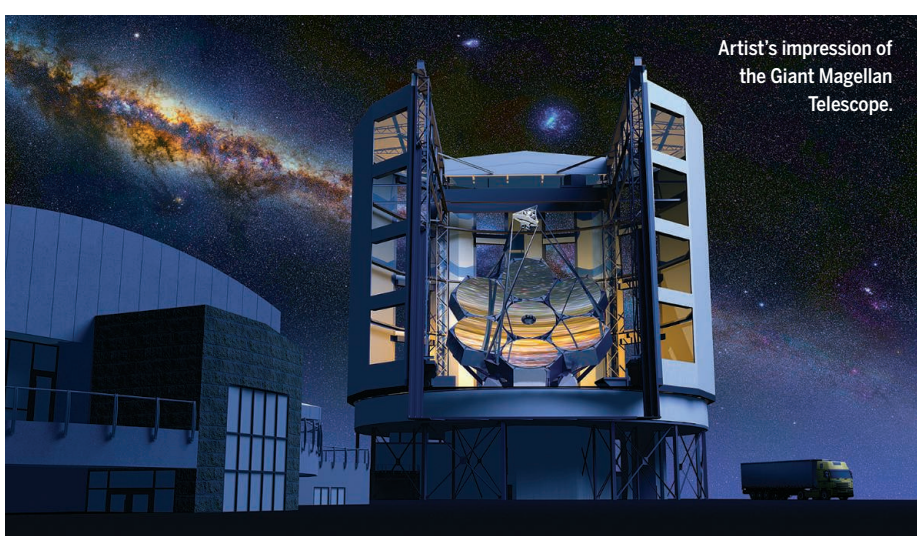

Artist's impression of the Giant Magellan Telescope.

CREDITS: (TOP TO BOTTOM) ALLARD PIERSON MUSEUM; GIANT MAGELLAN TELESCOPE/GMTO CORPORATION

Published by AAAS

Plastic *Dryas* flowers, equipped with glue, trap insects.

Fake flowers fool Arctic insects

Twenty teams of local volunteers—including some citizen scientists—are participating this summer in a coordinated experiment to study how bugs, wind, and the Arctic's iconic *Dryas* flower (right) interact. Volunteers from Alaska to Finland began the Global Dryas Project—organized by the University of Helsinki, which also provided materials to the teams—in May and June, using screens to cover 1-square-meter-sized plots where the small shrub is growing naturally. That will help them quantify how much insect pollinators increase the flower's seed production. Now *Dryas* is in flower, and the teams are moving to the next step: planting plastic "flowers" equipped with trap glue near each plot to see which insects do the pollination. The goal is to eventually predict how the pollination of *Dryas*, an important food for insects and small mammals, might change as the Arctic warms. "Sending people across the Arctic would be too resource-intensive," says ecologist Tomas Roslin of the University of Helsinki. "So we take advantage of people who are already there."

powerful 39.2-meter European Extremely Large Telescope on schedule. "I'm not worried [about Brazil's GMT participation]," De Zeeuw says. "Many ESO member states are also involved in other big astronomy projects."

New energy targets disappoint

BRUSSELS | To lower Europe's carbon emissions and its dependence on fuel imports, the European Commission proposed cutting energy use by 30% in 2030, up from the current 20% goal for 2020 (compared with 2007 projections). But to the dismay of environmental groups that had pushed for a higher, binding target, last week's proposal falls short of saying that the target should be binding on member states, which are expected to endorse the plan in October. "[T]he proposed 30% target is reducing the original ambition," but it can help boost energy efficiency innovation if the right tools—including public procurement and standardization policies—are in place, says Stefano Carosio, R&D manager of engineering consulting company D'Appolonia in Genova, Italy, and a board member of the Brussels-based nonprofit Energy Efficient Buildings Association.

BY THE NUMBERS

25

Years between the Voyager 2 spacecraft's crossing of Neptune's orbit on 25 August 1989 and the Pluto-bound New Horizons' transit across the orbit this August.

2923

Liters of fuel required, on average, to land a metric ton of shrimp and lobster, according to a study in *Fish and Fisheries*—placing those foods among the highest gas-guzzlers.

$650 million

Amount donated by philanthropist and businessman Ted Stanley to the Cambridge, Massachusetts–based Broad Institute to study the biological basis of diseases such as schizophrenia and bipolar disorder.

Spanish science needs overhaul

BARCELONA, SPAIN | More cash and profound structural changes—that is what Spain's national science and innovation system needs to become more competitive, according to a report by a peer-review panel of the European Research Area and Innovation Committee. On 24 July, the panel released a six-page document stating the Spanish government should raise its contribution to science and innovation to 0.7% from 0.61% of the gross domestic product. The report, put together at the request of the Spanish government, also argues for the creation of a national funding agency that gives out merit-based grants, more autonomy for the universities, and a major overhaul of Spain's national research centers. Above all, what is needed is a stronger culture of evaluation and accountability, even if it means increasing inequality between universities, the document says. **http://scim.ag/Spainchange**

PHOTOS: MALIN EK/GLOBAL DRYAS PROJECT (2)

Published by AAAS

A sign on Melbourne's Princes Bridge welcomed meeting delegates.

PHOTO: COURTESY OF AIDS2014.ORG

AIDS CONFERENCE

Cure setbacks force HIV researchers to reset sights

Remission is seen as a more realistic goal

By **Jon Cohen**, *in Melbourne, Australia*

A year ago it likely would have been heralded as a stunning advance. An Australian man who became infected with HIV by a blood transfusion in 1981 may have naturally "cleared" the virus, researchers reported here last week at the 20th International AIDS Conference. If so, he would be just the second person to be cured of an HIV infection.

But recent setbacks have made other researchers extra cautious. Over the past year, three HIV-infected people who received widespread attention for apparently clearing their infections had the virus come roaring back—in one case more than 2 years after it seemed to have disappeared. And so, at the end of the presentation by immunologist John Zaunders of the Sydney, Australia–based Kirby Institute for Infection and Immunity in Society, Daniel Kuritzkes of Brigham and Women's Hospital in Boston jumped to the microphone to question why Zaunders spoke of "possible clearance" of the virus. "It's certainly an intriguing case," Kuritzkes said. But he cautioned Zaunders and everyone else at the session that a major shift in thinking was under way. "No question that this patient is in sustained remission, but you can't ever discern that there's not virus there," Kuritzkes said.

At the weeklong conference here, where the 13,600 attendees collectively mourned the six delegates killed in the Malaysia Airlines crash in Ukraine, cure research still dominated the scientific agenda. But the recent failures—a child in Mississippi and two bone marrow transplantation patients, whom Kuritzkes helped analyze—highlighted the huge challenges that remain and triggered a heightened sensitivity to words like "clearance" and "cure." Kuritzkes and several others urged their colleagues to take a page from the cancer field, which typically reserves the word "cure" for patients who have remained in remission for at least 5 years.

The only person researchers widely agree has been cured is Timothy Ray Brown, known as the "Berlin patient," who stopped taking antiretroviral (ARV) drugs in February 2007 (*Science*, 13 May 2011, p. 784) and has remained virus-free until today. But Brown was unusual: He developed leukemia and twice had his own immune system destroyed so that he could receive two bone marrow transplants, both from a rare donor who had cells resistant to HIV.

Ordinarily, cocktails of potent ARVs reduce the virus to such low levels that it becomes undetectable in the blood on standard tests. But it lurks in small reservoirs of cells that harbor latent HIV DNA in their chromosomes. When these "fully suppressed" people stop taking the drugs, the virus usually returns to high levels in a few weeks. Researchers had hoped that the Mississippi child, infected by her mother in utero or at birth and started on aggressive treatment before she was 2 days old, had a reservoir so small her body could clear it while on ARVs. But the virus returned 27 months after she stopped taking her drugs. Similarly, investigators suspected that when doctors prepared the two Boston patients for their bone marrow transplants by destroying their existing immune systems, they eliminated so many infected cells that ARVs could clear the rest. Within 8 months of stopping ARVs, however, HIV came back in both men.

"We've learned now that the virus can be there but under control for a very long time," said Sharon Lewin, an HIV cure researcher at the Burnet Institute here and co-chair of the conference. "But prolonged remission is only the short-term goal. I do think a cure has to be the aspirational goal."

To outright cure an infection, many researchers have promoted a "shock and kill" strategy that aims to flush the virus out of hiding by forcing the sleeping HIV DNA inside of chromosomes to wake up and produce new viruses. Theoretically, that would lead to the destruction of the infected cells, and ARVs would keep the virus from infecting new ones. At the meeting, Ole Schmeltz Søgaard of Aarhus University in Denmark reported that a cancer drug on the market, romidepsin, could lead to such robust bursts of virus in people suppressed by ARVs for years that HIV became detectable on standard blood tests. The study involved just six participants and did not claim to reduce the reservoirs in any of them. But it's

Downloaded from www.sciencemag.org on August 11, 2014

Published by AAAS

"actually a big step," Lewin said. Søgaard and co-workers now plan to repeat the clinical experiment with both the drug and an HIV vaccine that, they hope, will boost the immune response against the virus and help deplete reservoirs.

A major hurdle facing shock and kill: Available tests can't reliably determine whether an intervention has actually reduced the reservoir's size. "Right now, the assays we have are pretty expensive, they require a lot of blood, and we're not exactly sure what they measure," said immunologist Nicolas Chomont of the Vaccine & Gene Therapy Institute of Florida in Port St. Lucie. Chomont presented a novel assay his team has developed that is relatively cheap, requires only 10 milliliters of blood, and, he contends, more meaningfully quantifies small amounts of virus than anything available. He designed it to overcome problems with the two most commonly used tests to measure reservoir size. One, which cultures blood from an infected person with uninfected cells and measures production of new viruses, vastly underestimates the reservoir. The second one grossly overestimates the size because it uses the polymerase chain reaction (PCR) to detect HIV genetic material—including hordes of mutated viral DNA that produces "dead-end" viruses, which are not viable and thus of little concern.

Chomont's new assay, dubbed TILDA, also relies on PCR but selects critical HIV genetic signatures needed for replication that often are missing in the DNA that codes for dead-end viruses.

Steven Deeks, an HIV cure researcher at the University of California, San Francisco, says if TILDA proves its worth in rigorous studies, it could spur investment in the field from wary pharmaceutical companies. "Industry is not engaged because there's no validated way to measure the reservoir," Deeks said. "How are we going to define cure, and how are the regulators going to define cure?"

Measuring the reservoir in blood isn't enough, however, because virus can often lurk in harder to access tissues like the lymph nodes, gut, and spinal fluid. (Timothy Ray Brown had each of these assessed, and the Boston patients and the Australian transfusion recipient had gut biopsies, but none of these tissues was tested in the Mississippi child.) It's possible that remote sites offer reservoirs safe harbor from ARVs or immune attack. With that in mind, virologist Brandon Keele of the National Cancer Institute in Frederick, Maryland, described a new strategy to track reservoirs in different parts of the body. Working in a monkey model, Keele and his co-workers engineered thousands of nearly identical versions of SIV, the monkey AIDS virus, which they can distinguish by means of small genetic differences that serve as unique barcodes.

The researchers have injected swarms of these SIVs into monkeys, which they plan to treat with ARVs to reduce the viruses to undetectable levels. After several months, they'll stop treatment and perform blood tests, biopsies, and, ultimately, necropsies on the animals to see if the barcodes can reveal the source of the rebounding virus.

Just where the virus hid during the Mississippi child's 27 months of remission is one of the case's baffling mysteries. In the wake of the setback, the National Institute of Allergy and Infectious Diseases (NIAID) is redesigning a study of HIV-infected newborns that would use a similarly aggressive ARV regimen shortly after birth and then, at some point, take them off drugs and see whether the virus rebounds. Trial designers have heatedly debated whether to add tissue sampling to the protocol, but sensitivities about subjecting children to the procedures have nixed it for now. "We've got to rethink that," says NIAID Director Anthony Fauci, who is not on the trial design team. The field needs answers, not more anecdotes of cures, he says. "I'm maintaining a deep degree of humility." ■

ARVs stopped, HIV rebounds

Only one person has been "cured" of HIV.

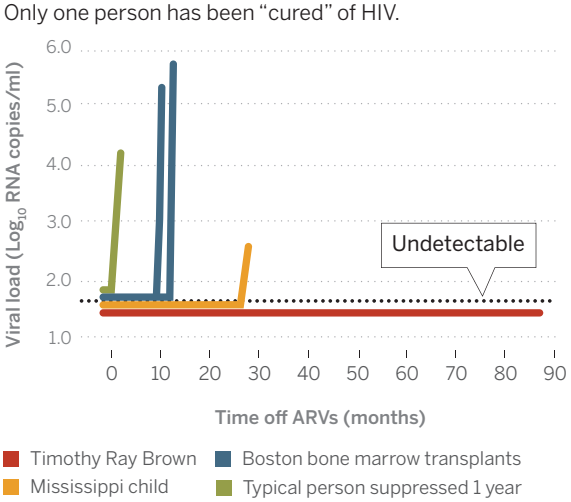

Source: Adapted from Diana Finzi, U.S. National Institute of Allergy and Infectious Diseases

CLIMATE CHANGE

Warming may not swamp islands

PHOTO: DAVID GRAY/REUTERS/CORBIS

Studies suggest that atoll islands will rise in step with a rising sea

By **Christopher Pala**, *on South Tarawa*

As the minibus wobbles over the dusty, pothole-filled road that runs the length of South Tarawa island, a song blasting over Kiribati's state radio envisions an apocalypse for this fishhook-shaped atoll halfway between Honolulu and Fiji: "The angry sea will kill us all."

The song, which won a competition organized by Kiribati's government, reflects the views of President Anote Tong, who has been warning for years of a knockout punch from climate change. In an interview with CNN in June, Tong insisted that rising sea levels due to global warming will mean "total annihilation" for this nation of 33 coral islands spread over a swath of the Central Pacific the size of India, and for other atoll island nations like Tuvalu and the Maldives. In May, Tong announced that Kiribati had spent $8.7 million to buy 22 square kilometers of land on Vanua Levu in Fiji as a haven for displaced citizens, cementing his nation's global reputation as an early victim of climate change.

Many scientists quietly demur.

No doubt, the sea is coming: In a 2013 report, the U.N. Intergovernmental Panel on Climate Change predicted that global sea levels will rise up to 1 meter by 2100. But recent geologic studies suggest that the coral reefs supporting sandy atoll islands will grow and rise in tandem with the sea. The only islanders who will have to move must do so for the same reason as millions of people on the continents: because they live too close to shore.

Paul Kench, a geomorphologist who now heads the University of Auckland's School of

Published by AAAS

Although Bikeman islet has disappeared beneath the waves, other Kiribati islands are expected to remain habitable as sea levels rise.

Environment in New Zealand, was the first to question the dire forecasts for Kiribati and similar island nations. In 1999, the World Bank asked him to evaluate the economic costs of sea-level rise and climate change to Pacific island nations. Kench, who had been studying how atoll islands evolve over time, says he had assumed that a rising ocean would engulf the islands, which consist of sand perched on reefs. "That's what everyone thought, and nobody questioned it," he says. But when he scoured the literature, he could not find a single study to support that scenario.

So Kench teamed up with Peter Cowell, a geomorphologist at the University of Sydney in Australia, to model what might happen. They found that during episodes of high seas—at high tide during El Niño events, which raise sea level in the Central Pacific, for example—storm waves would wash over higher and higher sections of atoll islands. But instead of eroding land, the waves would raise island elevation by depositing sand produced from broken coral, coralline algae, mollusks, and foraminifera. Kench notes that reefs can grow 10 to 15 millimeters a year—faster than the sea-level rise expected to occur later this century. "As long as the reef is healthy and generates an abundant supply of sand, there's no reason a reef island can't grow and keep up," he argues.

This equilibrium may not mean that all areas of atolls will remain habitable, says Scott Smithers, a geomorphologist at James Cook University, Townsville, in Australia. "The changes might happen at a rate that exceeds the recovery," he says. But the geologic record is reassuring, Kench and others found when they drilled deep cores into reef islands to probe how they responded to past sea-level changes. In a February report in *Geophysical Research Letters*, the researchers found that the island of Jabat in the Marshall Islands emerged on a reef 4800 to 4000 years ago, when sea levels were rising as fast as they are expected to rise over the next century. Other support for the model has come from monitoring how shorelines respond to seasonal changes in wave and wind patterns, investigating how extreme events like tsunamis reshape islands, and analyzing aerial photos and satellite images from the past 60 years, which have shown that the 15-centimeter sea-level rise over the past half-century has had no discernible effect on atolls.

Tong has drawn worldwide attention to evidence of his own: Bikeman islet off South Tarawa, which is already submerged; the washed-away village of Tebunginako on Abaiang island; and ubiquitous broken seawalls. But scientists blame these woes on human activity: causeways, sand removal, and poorly designed seawalls. "Pictures of flooding you see on the news have more to do with poor shoreline management and people settling on marginal land than with sea-level rise," says Simon Donner, a climate scientist at the University of British Columbia, Vancouver, in Canada who has examined sea-level variability in South Tarawa.

Some Kiribati officials agree: "[E]vidence shows that widespread erosion along the ocean and lagoon shorelines is primarily due to [local] human activities," wrote Naomi Biribo, permanent secretary in the fisheries ministry, and her Ph.D. adviser, geomorphologist Colin Woodroffe of the University of Wollongong in Australia, in the July 2013 issue of *Sustainability Science*. "[F]urther encroachment onto the active beach will … increas[e] erosion and susceptibility of the reef islands to anticipated sea-level rise."

Still, people living on lower lying and narrower sections of islands are unquestionably vulnerable to rising seas, especially on islands like South Tarawa, where 50,000 people live elbow-to-elbow in 15 square kilometers. Washover events dump salt water onto freshwater lenses—pockets of rainwater trapped in porous coral below the sand—rendering it undrinkable for weeks, until fresh water floats back to the surface. Areas already prone to flooding during storms will have to be abandoned.

Shore huggers on South Tarawa will be able to find safer land elsewhere in Kiribati, such as Kiritimati, also known as Christmas Island, which at about five times the size of Manhattan is the largest atoll in the world. Most of its residents live in a leeward part of the island that's 7 meters above sea level.

Vanua Levu in Fiji is a less appealing refuge. The purchase was "a publicity stunt," scoffs Teburoro Tito, a former president of Kiribati and member of the opposition party Protect the Maneaba. Already home to 270 farmers from the Solomon Islands, the steep, hilly tract may accommodate only a few hundred more people. If the optimists are right, no one from Kiribati will have to leave their country anyway. ■

Christopher Pala is a writer in Washington, D.C.

No need to redraw the map

The coral reefs underlying many Pacific atolls can catch sediment and grow.

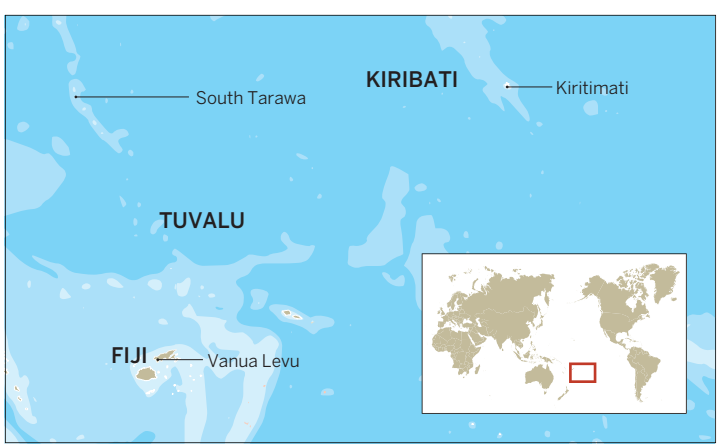

Published by AAAS

Narcolepsy-vaccine link remains mysterious.

IMMUNOLOGY

Key narcolepsy–influenza vaccine findings retracted

Stanford researchers unable to replicate findings linking immune response to sleep disorder

By **Emily Underwood**

Since swine flu swept the globe in 2009, scientists have scrambled to determine why a small percentage of children in Europe who received the flu vaccine Pandemrix developed narcolepsy, an incurable brain disorder that causes irresistible sleepiness. This week, a promising explanation was dealt a setback when prominent sleep scientist Emmanuel Mignot of Stanford University in Palo Alto, California, and colleagues retracted their influential study reporting a potential link between the H1N1 virus used to make the vaccine and narcolepsy.

Some researchers were taken aback. "This was one of the most important pieces of work on narcolepsy that has come out," says neuroimmunologist Lawrence Steinman, a close friend and colleague of Mignot's, who is also at Stanford. The retraction, announced in *Science Translational Medicine* (*STM*), "really caught me by surprise," he says. Others say that journal editors should have detected problems with the study's methodology.

The work provided the first substantiation of an autoimmune mechanism for narcolepsy, which could explain the Pandemrix side effect, researchers say. The vaccine, used only in Europe, seems to have triggered the disease in roughly one out of 15,000 children who received it. The affected children carried a gene variant for a particular human leukocyte antigen (HLA) type—a molecule that presents foreign proteins to immune cells—considered necessary for developing narcolepsy.

In the 18 December 2013 issue of *STM*, Mignot and colleagues reported that T cells from people with narcolepsy, but not from healthy controls, are primed to attack by hypocretin, a hormone that regulates wakefulness. They also showed molecular similarities between fragments of the H1N1 virus and the hypocretin molecule and suggested that these fragments might fool the immune system into attacking hypocretin-producing cells.

Up to 95% of the neurons that produce hypocretin are missing in people with narcolepsy, and many researchers believe that they're destroyed by a highly targeted autoimmune reaction, says Thomas Scammell, a neurologist at Harvard Medical School in Boston. The Mignot paper was the first "seemingly nice, objective piece of evidence" to support that hypothesis.

The retraction states that Mignot and his colleagues were unable to replicate the results of the ELISpot assay, a widely used method for measuring how immune system cells such as T cells respond to fragments of foreign proteins, called antigens. Mignot told *Science* that while attempting to develop a diagnostic test for narcolepsy based on the assay, "my lab could not make the ELISpot test work."

T cell assays in general are notoriously difficult to reproduce, says immunologist Outi Vaarala of the National Institute for Health and Welfare (THL) in Helsinki, who spent several weeks earlier this summer in Mignot's lab hoping to follow up on their finding. She's tried to replicate it herself in several ways, with no success.

Vaarala and others note several red flags about the research: For example, Mignot's group studied cells from a small number of people with narcolepsy and controls and focused on only one aspect of T cell response to hypocretin.

Katrina Kelner, editor of *STM*, says that "the paper was reviewed according to our usual rigorous standards of in-depth peer review, and in fact reported replication of the finding in three independent groups of patients."

Like Mignot and many other researchers, Vaarala still believes that some part of the influenza virus used to make Pandemrix likely mimics a native protein in the brain and triggered an autoimmune reaction that led to the destruction of hypocretin neurons in susceptible children. She is now looking for differences between Pandemrix and other flu vaccines and says she has already identified another promising protein candidate.

The retraction "does not undermine the fundamental hypothesis" that narcolepsy is caused by an autoimmune reaction "all that dramatically," Scammell says. He and others may consider different causes of narcolepsy, however. "Maybe there's a very selective virus that's very fond of targeting and then killing" hypocretin neurons, he says.

Had Mignot's results held, they could have led to the first proven example of a vaccine triggering an autoimmune response by mimicking the body's own proteins, says vaccinologist Hanna Nohynek, who is working with Vaarala at THL. The retraction "sets us back to kind of a zero point." ■

PHOTO: ASSOCIATED PRESS

Downloaded from www.sciencemag.org on August 11, 2014

Published by AAAS

PUBLIC HEALTH

Money woes cripple Venezuela's health system

Lacking vital medical supplies, doctors struggle to treat resurgent diseases

By **Lizzie Wade**

In the early morning on Sunday, 29 June, armed men stormed into an operating room at University Hospital in Caracas and killed a man being prepped for surgery. The patient, a gunshot victim, had been rushed to the country's leading hospital, and the four assailants, who got away, were presumably finishing the job. The attack, during which two staff members were injured, unnerved physicians and researchers. Before her shift 3 days later, Isabel García Fleury, a breast pathologist, posted a picture of herself on Facebook wearing a bulletproof vest over her scrubs. "Is this how we'll have to come to work at the hospitals in my country?" she wrote. "SOS Venezuela."

Lack of security in hospitals is one of the myriad woes plaguing Venezuela's public health system. "Old ghosts from our past are returning," says Gustavo Villasmil, health minister of the opposition-led state of Miranda. Malaria, eradicated from much of Venezuela by the 1960s, is surging. Nearly 45,000 cases have been reported so far in 2014, compared with 32,000 in all of 2008. Dengue is spiking and the country is bracing for a wave of the newly arrived chikungunya, a debilitating virus that's spread by the same mosquito that transmits dengue. In the meantime, maternal mortality rates have increased from 59 deaths per 100,000 births in 1990 to nearly 71 in 2011 (see graph).

The resurgence of what Villasmil calls "diseases of shame" and poverty is particularly painful for the Venezuelan medical community because for many decades, the country led Latin America in public health efforts such as malaria control and medical training. "It's like we're telling the story in reverse," says José Oletta, an internist who served as the country's health minister from 1997 to 1999, before Hugo Chávez became president. Venezuela's porous borders with Guyana and Brazil, which are frequently crossed by illegal miners, increase the risk of infectious diseases spreading in the region, Oletta says.

Venezuela's reeling public health system has been brought to its knees by a one-two economic punch. In addition to having the highest inflation rate in the world in 2013, the country is hard up for dollars, explains Marino González, a specialist on health policy at Simón Bolívar University in Caracas. The hard currency crunch makes it nearly impossible to import medical supplies. Oletta, who teaches at the Central University of Venezuela (UCV) and works with the nonprofits the Venezuelan Public Health Society and the Epidemiology Defense Network, says it recently took him 3 weeks of scouring pharmacies across the country to find penicillin. "Sometimes there aren't even gloves" in University Hospital, García Fleury adds. "Patients have to bring their own" and provide them to the staff. She points out that the hospital's director is a supporter of Nicolás Maduro's government. "It's not like they've cut us off because we're part of [the opposition]," she says.

The lack of medicines is confounding efforts to control chronic diseases like diabetes and hypertension. On 16 July, UCV's Hematology and Oncology Institute closed due to a lack of resources. The health care system, Castro says, has become "regressive, inefficient, extremely expensive, and profoundly unjust." Even as the poverty rate rises, out-of-pocket medical expenses have ballooned to nearly 60% of Venezuela's total health care spending, the highest percentage in South America, according to data from the World Health Organization.

As a result, many Venezuelans are turning to a network of free clinics called Barrio Adentro. Founded by Chávez's government in 2003 to increase access to health care in underserved and rural areas, Barrio Adentro "wasn't a bad idea," says Anabelle Bonvecchio, a Venezuelan nutritionist and public health researcher in Mexico City. But the Chávez government brought in doctors from Cuba to staff the new centers, which were never integrated into existing public health networks. Many of the Cuban doctors have since left, leaving the system in the hands of dangerously underqualified practitioners, Oletta says. García Fleury says she regularly sees patients who were misdiagnosed or given inappropriate treatments at Barrio Adentro facilities. And that's when the centers continue to operate at all. Julio Castro, the health minister of poverty-riddled Sucre, says that at least 30% of Barrio Adentro facilities in his municipality have closed their doors, in keeping with a nationwide trend.

Some states and municipalities have organized stopgaps. In Miranda, Villasmil and his colleagues have set up a network of urgent care facilities modeled after the field hospitals of oil companies. And in Sucre, Castro has organized a system of medical centers that focus on preventive care—an area neglected by Barrio Adentro, he says.

These local initiatives, like the national hospitals, suffer from acute shortages of medicines and supplies. And every day, there are fewer qualified doctors left in Venezuela to work in them, says Castro, who teaches at UCV's celebrated medical school. He estimates that up to 40% of the university's recent medical graduates leave the country every year. It's a "loss to the state," Castro says, especially because medical education in Venezuela is free for students. But he doesn't blame them for wanting to practice medicine in countries where doctors don't have to consider wearing bulletproof vests to work. ■

"Diseases of shame"

Malaria, dengue, and maternal mortality are all on the rise.

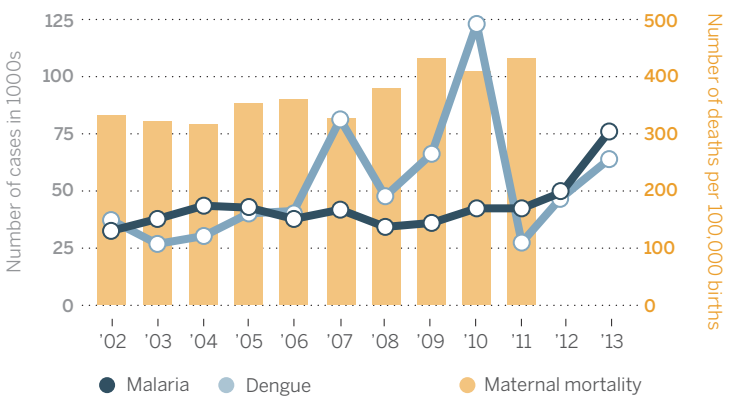

Source: Ministry of People's Power for Health/Epidemiological Bulletins 2002–2013/Annual Mortality Reports 2002–2011

Downloaded from www.sciencemag.org on August 11, 2014

Published by AAAS

EUROPE

Decision looms on future of E.U. science advice

Green groups criticize current adviser—and her office

By **Kai Kupferschmidt**

A war of words has erupted over the job of chief science adviser to the European Commission—a post created only in 2012 that hangs in the balance now that a new commission is being formed. Nine nongovernmental organizations (NGOs) have called on Jean-Claude Juncker, the commission's president-elect, to scrap the position; they are angered by the support of the current science adviser, Anne Glover, for genetically modified organisms (GMOs). Their letter has triggered a wave of support for the position from scientists and scientific organizations.

As always when GMOs are involved, the debate quickly got heated. Even Glover's supporters, however, agree that the science adviser's position has problems—including a tiny budget and an ill-defined mandate—that the new commission, set to take office in November, needs to fix.

The United States, the United Kingdom, and some other countries have long had senior scientists advising the government, and the idea is catching on elsewhere. José Manuel Barroso, the outgoing president of the European Commission, tapped Glover, until then Scotland's chief science adviser, to "provide independent expert advice on any aspect of science, technology and innovation" 2 years ago. But Glover's contract expires with Barroso's at the end of October; Juncker, a political veteran from Luxembourg, must decide whether to continue the position, and, if he does, whether to renew Glover's contract.

Just end it and eliminate the post, is the NGOs' advice. In an open letter published on 22 July, they argue that Glover has misrepresented science, for instance by saying that genetically modified plants carry no more risks than conventionally bred plants. "She sounded more like a GMO lobbyist," says Jorgo Riss, director of the Greenpeace European Unit. Riss says the problem goes beyond genetic modification. "I think there is a fundamental flaw in thinking you can place one person close to the president [to help] decide how to interpret certain data," he says. Relying on just a single scientist also makes it easier for industry to lobby, Riss argues.

Roger Pielke of the Center for Science and Technology Policy Research at the University of Colorado, Boulder, dismisses the GMO criticism. "It's a very common tendency: If you don't like the advice, get rid of the adviser," he says. James Wilsdon, an expert on science advice at the University of Sussex in the United Kingdom, says everybody benefits in the long run if policies are based on better evidence, including NGOs; he calls the NGOs' letter "utterly counterproductive and a politically dumb move."

But both agree that the row does highlight a problem: Glover's role is not well-defined. She gives speeches across Europe but it's unclear on what authority; she has a monthly chat with Barroso (*Science*, 8 March 2013, p. 1144), but her advice remains confidential. "It was inevitable that there would be this sort of conflict with interest groups that do not like her advice because it is not clear to anyone what role the office actually plays," Pielke says. That needs to change, he argues. "If Barroso had asked her for a report on GMOs," he says, "she could have produced a report and the focus would have been on the substance, and not on the science advisory process itself."

Anne Glover during a visit to CERN in Geneva, Switzerland.

PHOTO: CERN/FLICKR

Glover declined a request to discuss the letters, but says she agrees that transparency is "fundamental to building trust." "My website indicates my wish to be open and of course I respond to access-to-document requests and have been proactive in seeking meetings with a very broad range of stakeholders," she writes in an e-mail.

In a wide-ranging interview with *Science* last month, Glover said she had frustrations with the policy process in Brussels of her own. Politicians tend to look only for evidence supporting the position they already hold, she argued, although declining to give examples. "At the moment … nobody is going in there and saying: 'Why are you using that evidence, that is rather out of date, or that is rather biased,' " she said. Glover acknowledged that her limited budget—she has a staff of six—has hampered her. "At the moment we are really limited, too many ideas and not enough hands to man the deck and deliver," she said.

Glover has tried to make up for that by forging alliances. She has set up a network of delegates from 14 E.U. member states to discuss how best to include scientific evidence in policymaking, as well as a new Science & Technology Advisory Council that reports to the commission's president. Given the circumstances, "I think Anne has done well and arguably better than could be expected," Wilsdon says.

Glover wants to stay on as chief science adviser, but with the position strengthened. One option under discussion is to tie the post more closely to the European Union's Joint Research Centre, which has 3000 staff members at seven institutes in five countries, Wilsdon says. That would put Glover at the center of the evidence-gathering process for E.U. policies.

Pielke feels confident that Juncker will keep the post of chief science adviser, with or without Glover; terminating the position now would send a strong antiscientific message that the commission will avoid, he predicts. He just hopes the debate will become more sophisticated than it now is. "We concentrate on the politics, the horse race, should we keep her, should she go? I think what is far more important is: What should she be doing?" ■

Downloaded from www.sciencemag.org on August 11, 2014

Published by AAAS

Aftermath of a 29 May 2012 earthquake in the town of Concordia sulla Secchia.

PHOTO: ASSOCIATED PRESS

ITALY

Deadly quakes divide experts

New industry-sponsored study rules out any link between Italian earthquakes and oil production

By **Edwin Cartlidge**

Two deadly earthquakes that struck the Emilia-Romagna region in the north of Italy in 2012 continue to generate political aftershocks. According to the Italian government, a report by six U.S. scientists puts to rest the suggestion that the quakes, which killed 27 people, could have been triggered by increasing production at a nearby oil field, known as Cavone. But some researchers are unconvinced, while experts and the public alike question the origins of the study, which the government requested from the oil field's owner.

The possibility that activities at Cavone might have triggered the two quakes, a magnitude-5.9 event on 20 May 2012 and a magnitude-5.8 event 9 days later, was raised earlier this year in a different report, from a panel known as ICHESE. That panel was set up in December 2012 at the request of the Emilia-Romagna regional government, following local rumors that exploratory drilling for a gas storage facility had set off the tremors.

In its report, ICHESE—made up of two Italian and three foreign geoscientists as well as engineer Franco Terlizzese, director of mineral and energetic resources at Italy's Ministry of Economic Development—dismissed that link. The panel did, however, find that increased petroleum extraction and wastewater injection at nearby Cavone correlated with a rise in seismic activity in the year leading up to the quakes. The panel concluded that a humanmade triggering of the 20 May event "cannot be excluded" but added that physics-based modeling of the oil field was needed to be sure.

ICHESE's report generated controversy, in part because the regional government received it in mid-February but only made it public on 15 April, just 4 days after *Science* reported the study's main conclusions (11 April, p. 141). Regional President Vasco Errani explained that he needed time to carry out "further studies" in order "not to cause alarm." His administration also suspended all new hydrocarbon exploration in the region.

Both the Ministry of Economic Development and the regional government say that the latest report, written by leading U.S. geoscientists, resolves the controversy. The U.S. researchers developed a mathematical model to simulate the mechanical effects of fluid flow on the rocks in and around the Cavone oil field. The model also draws on measurements of fluid pressure at the bottom of the wastewater injection well carried out by the field's operator, Padana Energia, in May and June this year. The experts conclude that activities at Cavone could not have altered pressure and stress within the crust enough to have triggered the two quakes.

In a press release, the ministry cites an analysis by Italy's National Institute of Geophysics and Volcanology (INGV) that "attests to the validity" of the new report. Some scientists also give the American report the thumbs up. Marco Mucciarelli, a seismologist at Italy's National Institute of Oceanography and Experimental Geophysics in Trieste, says the study provides an "unequivocal" response to the uncertainties surrounding Cavone.

Others, however, challenge the work. In their model, the American researchers simulated how the changing output at Cavone would have affected the fault nearest the oil field—the Mirandola fault—but not the more distant Middle Ferrara fault, which lies about 20 km away. But one expert in induced seismicity who wishes to remain anonymous points out that it was on the Middle Ferrara fault that the 20 May quake occurred. None of the U.S. experts responded to repeated requests for a reaction.

Meanwhile, Franco Ortolani, a retired geologist at the University of Naples Federico II, has publicly attacked what he calls "a game played between the interested parties," complaining that Padana Energia was given the task of commissioning the new research and taking the pressure measurements. He argues that only the judiciary has the independence to shed light on the controversy. Indeed, last week a number of environmental groups filed a complaint in several local courts calling for an investigation of both the ICHESE and U.S. studies.

Science has learned that Padana Energia entrusted the commissioning of the modeling research to energy and mineral trade body Assomineraria, which worked on the task together with the ministry. But instead of commissioning a brand new study, the trade body and the ministry simply released an expanded version of the American group's research, which had been commissioned and funded by ENI in late 2012 or early 2013. (ENI sold Padana Energia to the company Gas Plus in 2010.) One of the study's authors, James Dieterich of the University of California, Riverside, told *Science* that the modeling and pressure tests "confirmed our initial conclusions concerning the origins of the 2012 earthquakes."

Terlizzese defends the decision to use the American research, arguing that the six scientists are internationally renowned and were already well-versed in the subject matter, adding that "we also needed the study done quickly." He acknowledges that commissioning the report via Padana Energia "seems like a conflict of interest" but says that the review by INGV "attenuated" that conflict. The modeling required oil field data that only the ministry, the regional government, and Padana Energia possessed, he adds. ■

Edwin Cartlidge is a science writer in Rome.

Downloaded from www.sciencemag.org on August 11, 2014

Published by AAAS

FEATURES

Comet catcher

Europe's Rosetta spacecraft is about to orbit and then land on one of the solar system's most mysterious objects

By **Eric Hand**

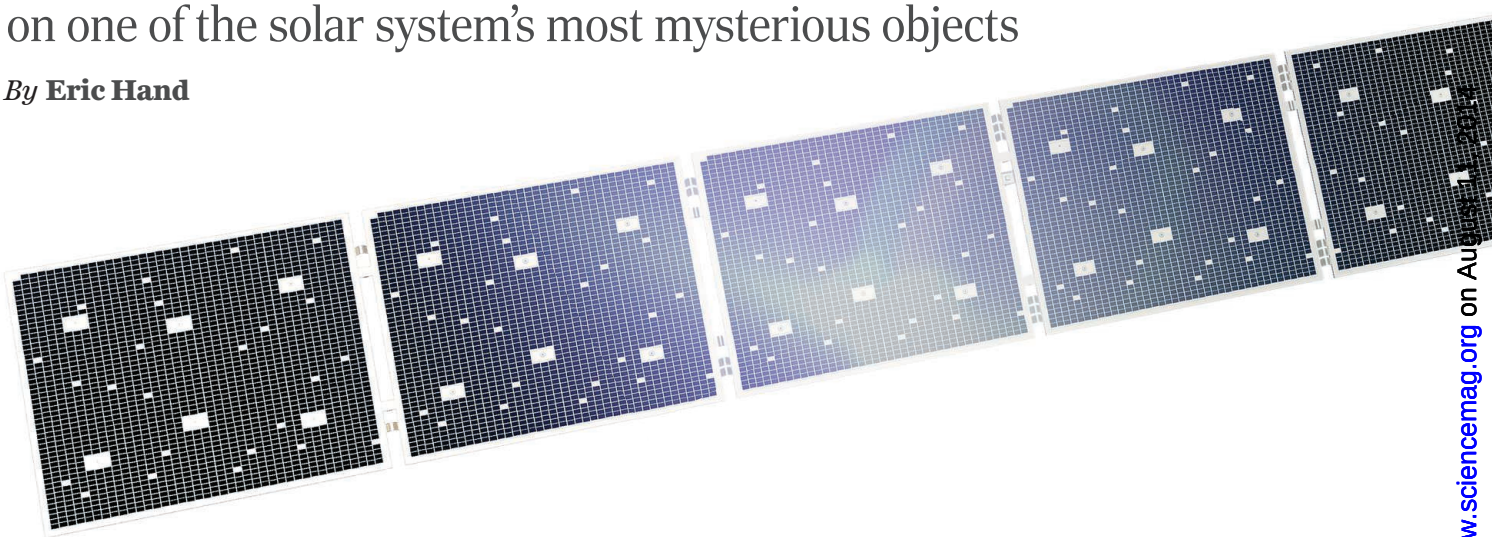

Downloaded from www.sciencemag.org on August 1, 2014

The lump of ice and dust tumbled into view as little more than a dot. Then it grew to a smudge. It was sputtering fitfully in a halo of expelled gas and dust, a sign that its internal engine was revving up but had not yet been stoked by the sun to full throttle.

As the spacecraft drew closer, the dot became a pixelated blob. A few weeks ago, its true shape began to emerge: The object is 4 kilometers long and lopsided, with two lobes. From certain angles, it looks like a rubber duck. It rotates, languidly, every 12 hours. Now, the spacecraft is just 1000 kilometers away from the object, called 67P/Churyumov-Gerasimenko, and closing in. Each day brings new terrain into focus, all encrusted in organic dust blacker than asphalt.

67P is a comet: that most eccentric of solar system species, in orbit and behavior. The great amateur comet hunter David Levy once said: "Comets are like cats. They have tails, and they do precisely what they want." Yet comets are also time capsules. Formed in the cold of the outer solar system 4.5 billion years ago, they have stayed cold—and, the thinking goes, chemically inert—but for their occasional dalliances with the sun. For this reason, researchers think they hold valuable information about the solar system's formation and about their own possible role in delivering water and organics to Earth early in its history.

67P's pursuer is Rosetta, a €1.3 billion flagship mission of the European Space Agency. Launched in 2004, the spacecraft spent a decade chasing down the comet, looping once around Mars and three times around Earth in gravity slingshots. On 6 August, Rosetta will finally intercept the comet at a point 3.5 times Earth's distance from the sun—between the orbits of Mars and Jupiter—and the entwined couple will begin a dance around the sun, one that should get ever hotter and more intimate. There have been just a handful of comet missions, beginning in 1985 with Giotto's voyage to Halley's Comet, and each achieved its 15 minutes of fame through whipsaw flybys that lasted about that long. Rosetta, by contrast, will be the first to orbit a comet—no mean feat, given 67P's jumpy behavior and feeble, irregular gravity field.

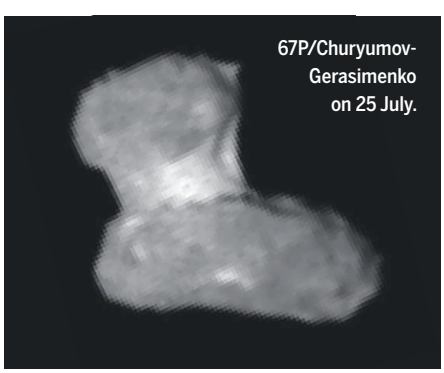

67P/Churyumov-Gerasimenko on 25 July.

Rosetta is also the first spacecraft to accompany a comet during a full trip around the sun. Below the thin, dirty skin of 67P are stores of ice—predominantly water ice, but also ices of carbon dioxide, methane, and ammonia. As the heat of the sun penetrates the surface, the ices will thaw and sublimate, creating diffuse jets of gas that also blow out dust. The comet's coma, or atmosphere, will expand to thousands or even millions of times the size of its nucleus. In August 2015, 67P will make its closest approach to the sun, between the orbits of Earth and Mars, and the comet's dual tails—one of dust, one of

CREDITS: (TOP TO BOTTOM) ESA/ATG MEDIALAB; ESA/ROSETTA/MPS FOR OSIRIS TEAM MPS/UPD/LAM/IAA/SSO/INTA/UPM/DASP/IDA

Published by AAAS

ionized gas, both pointing away from the sun like windsocks—will reach their peak.

Perhaps the most daring moment of the mission will come on 11 November, when mission leaders plan to drop the Philae lander to the surface (see sidebar, p. 504). Whereas landings on the moon or Mars are preceded by years of reconnaissance, Rosetta will have just 6 weeks to map the comet's surface and find a suitable landing site for Philae. During those weeks, the atmosphere at the European Space Operations Centre in Darmstadt, Germany, will be frenzied and intense, says Andrea Accomazzo, Rosetta's flight director. "We know everything when we fly to Mars," he says. "We don't know anything when we fly to the comet."

Scientists are expecting the unexpected. Contrary to what they used to think, comets are not simply dirty snowballs. Rosetta, watching from afar in 2005 as the Deep Impact mission sent a penetrator 25 meters into the comet 9P/Tempel 1, found that the explosion kicked up more dust than water vapor—proof that, in some cases at least, comets are icy dirtballs. And their range

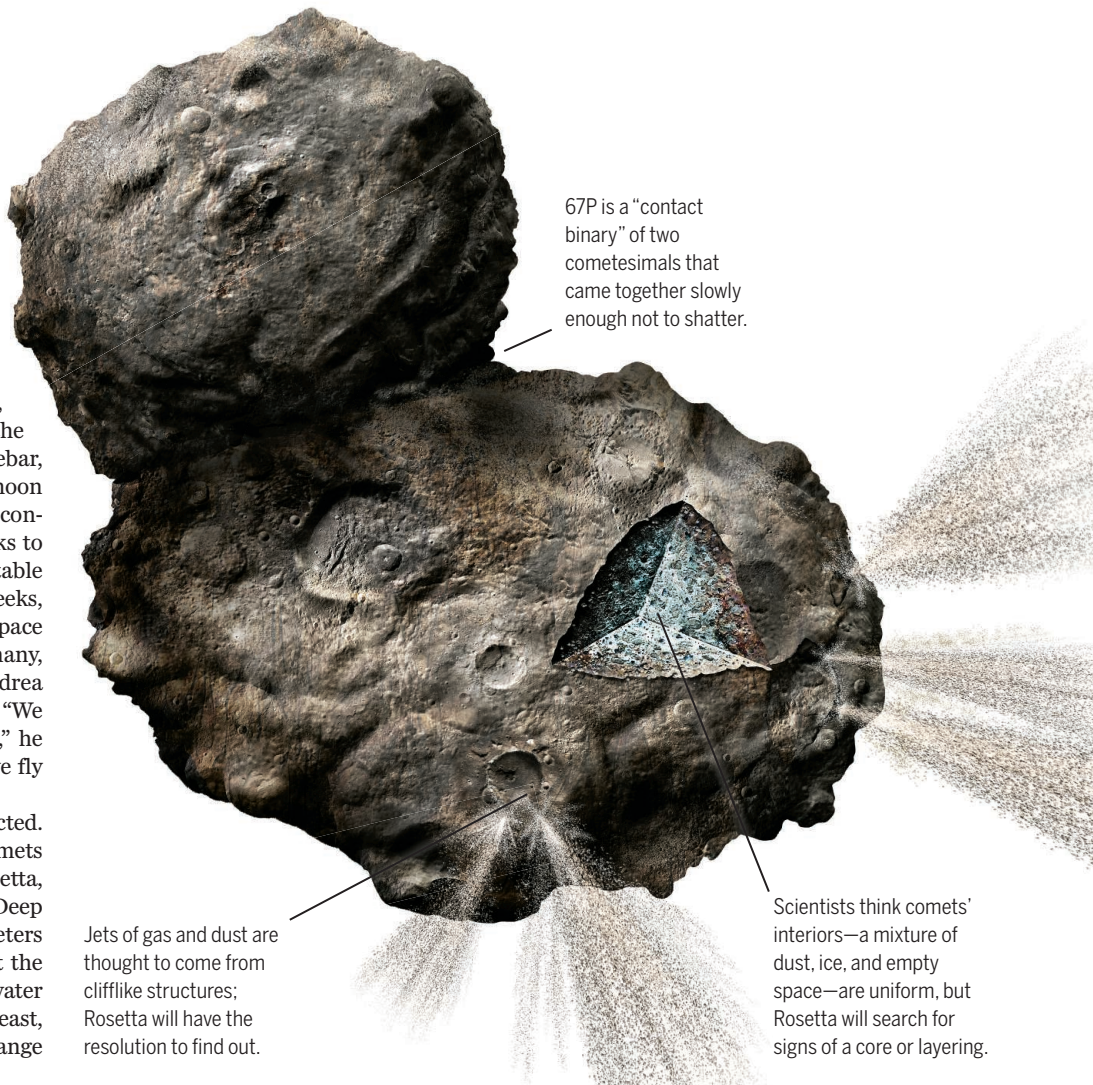

ILLUSTRATION: NICOLLE R. FULLER

Published by AAAS

of shapes and sizes is staggering. In 2010, Deep Impact went on to explore the peanut-shaped comet 103P/Hartley 2 and found that its two lobes have significantly different compositions—evidence that they started out as separate cometesimals.

Even the surfaces of individual comets are surprisingly varied. "You have cliffs, you have smooth flows, you have material moving from one side of the comet to the other and redepositing," says Jessica Sunshine, a planetary scientist at the University of Maryland (UMD), College Park, and the principal investigator for a proposed NASA Comet Hopper mission. "None of those things were on the table in the snowball days." One of Rosetta's major tasks will be to distinguish which aspects of the comet's composition and terrain were present when it formed and which ones have accumulated during its passages around the sun, which it orbits every 6.45 years. "Is the heterogeneity an evolutionary effect, or is it from when you made the solar system? My personal opinion is that there are examples of both," says Michael A'Hearn, a planetary scientist at UMD and the principal investigator of the Deep Impact mission. "It's the kind of thing that Rosetta is well positioned to study."

Rosetta will arrive in time to watch 67P's jets turn on. In the comet's previous orbits, telescopes spotted three active jet areas. Scientists don't understand the precise nature of those jets or how they might be shaping cometary surface features, but they found valuable clues when NASA's Stardust-NExT mission flew past Tempel 1 in 2011. Viewing that comet's active areas from a distance of 181 kilometers, Stardust-NExT found gas and dust emanating from what appeared to be cliffs surrounding craterlike outgassing scars. Orbiting at 30 kilometers or less, Rosetta should be able to see with better than 60-centimeter resolution—sharp enough to observe the way that jet activity constructs or destroys these landforms, says Matt Taylor, the mission's project scientist. "We'll see that evolution," he says.

But getting into orbit is no easy task. Next week, when Rosetta arrives at the comet, it will still be 100 kilometers away. It will make its first shape and gravity models of the comet while flying a triangular pattern out in front of it, on the sunward side. By 24 August, Rosetta will have moved to within 50 kilometers but will still not be in orbit. Finally, on 10 September, mission managers plan to put it into a 30-kilometer orbit. At that point, the spacecraft will begin to feel the gentle pressure of the jets on its 64 square meters of solar panels, which will act like giant sails. "It's pushing us away all the time," Taylor says. Mission controllers will try to keep the panels pointed edge-on to the comet surface to minimize both dust collection and gas pressure.

Another complication is the 40-minute

ILLUSTRATION: ADAPTED FROM ESA/ATG MEDIALAB

Touch and go

By **Eric Hand**

When you really have to stick the landing, it helps to carry a couple of harpoons. On 11 November, Rosetta will swoop down to just several kilometers above the rugged surface of comet 67P/Churyumov-Gerasimenko and will eject the Philae lander, a box the size of a dishwasher. There will be no parachute or retrorockets. The lander will simply unfold its three legs and, over anywhere from 100 minutes to several hours, drift unpowered to the surface at walking speeds. That is the benefit of a gravitational field hundreds of thousands of times weaker than Earth's. But the weak field also carries a risk: A bounce could send the lander flying into the abyss.

Sensors in the toes of each lander leg will signal touchdown. Seconds later, the harpoons will burst from the belly of Philae. A thruster on the lander's back will fire simultaneously, keeping the lander pressed down during the harpooning. Meanwhile, screws in the three toes will spin furiously to find purchase, especially if the surface material is soft. The tense hours of descent and landing will surpass the "7 minutes of terror" of the Curiosity rover's descent to Mars, says Hermann Böhnhardt, one of the

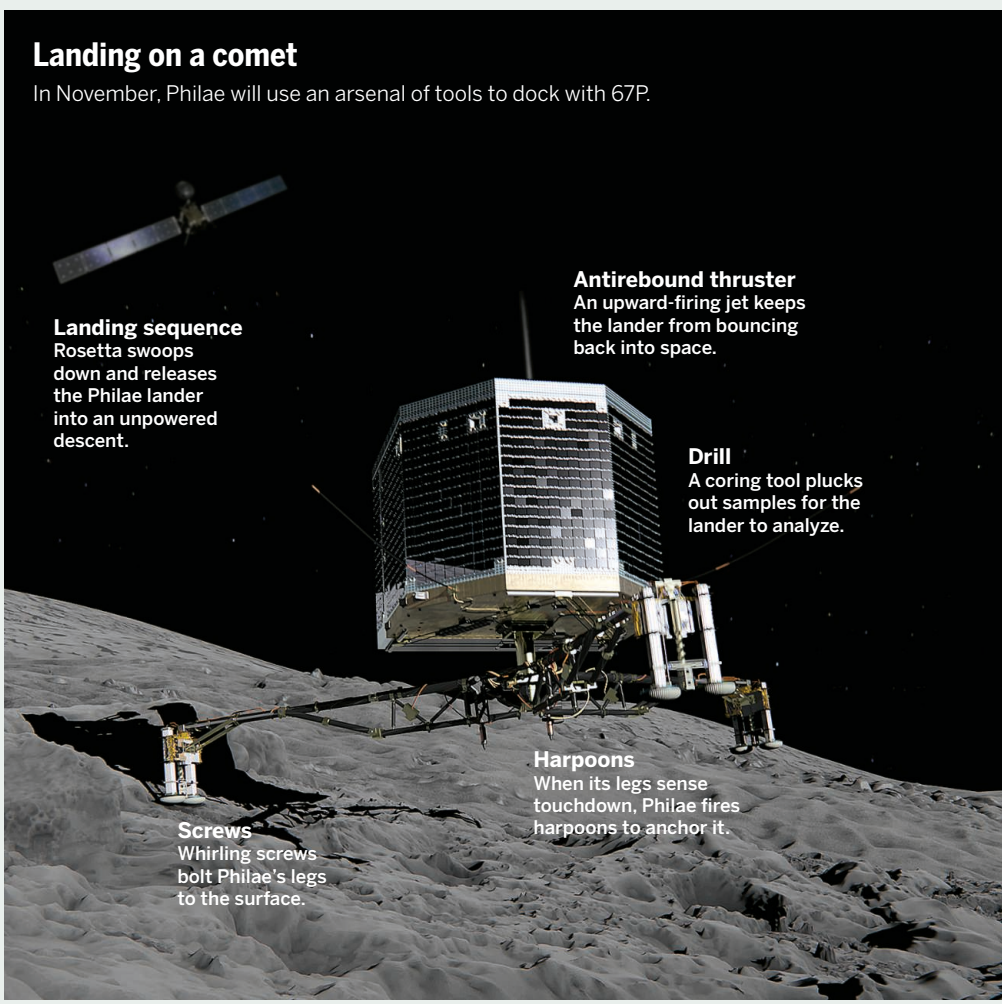

Published by AAAS

A long, looping chase

Rosetta used Earth and Mars flybys to catch its quarry.

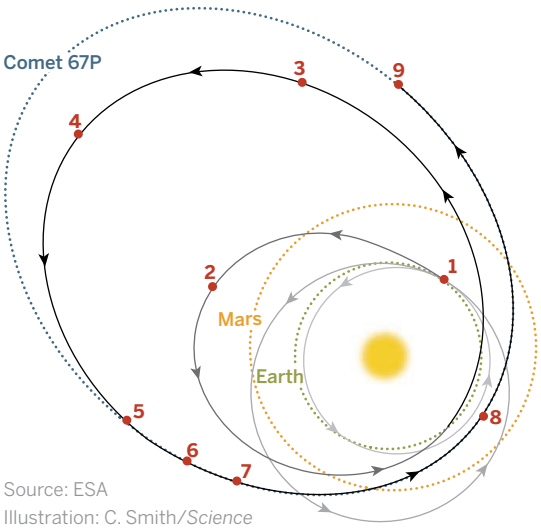

Source: ESA
Illustration: C. Smith/*Science*

1. **2 March 2004**
   Launch
2. **5 September 2008**
   Asteroid Steins flyby
3. **10 July 2010**
   Asteroid Lutetia flyby
4. **8 June 2011**
   Enter deep space hibernation
5. **20 January 2014**
   Exit deep space hibernation
6. **August 2014**
   Arrive at comet
7. **November 2014**
   Lander delivery
8. **13 August 2015**
   Closest approach to sun
9. **31 December 2015**
   Nominal end of mission

travel time for commands to arrive from Earth. Except for twice-a-week course corrections, the spacecraft will operate autonomously, keeping its camera pointed at 67P and backing off to a higher orbit to regain its bearings anytime the comet slips out of the viewfinder. The team will not attempt to lower the spacecraft into a 20- or 10-kilometer orbit until it gauges the stability of the orbit.

Still, after a journey of a decade and more than 6 billion kilometers, mission scientists are happy that they are no longer chasing a will-o'-the-wisp. Holger Sierks, principal investigator for the OSIRIS camera at the Max Planck Institute for Solar System Research in Göttingen, Germany, was overjoyed when he saw some of his first multipixel images a few weeks ago. "It's overwhelming to see it has a shape," he said. Now, the team faces a tougher, more thrilling job, as the distant shape gives way to an intimate encounter. ■

two lead scientists for Philae. "It is for us a very stressful and dramatic period of time," says Böhnhardt, a comet scientist at the Max Planck Institute for Solar System Research in Göttingen, Germany.

Mission scientists hope to improve the odds by identifying a safe landing site. When Philae was designed and built in the 1990s, little was known about the surface strength of comets. So the lander is designed to handle all manner of terrains, from a surface as tough as solid ice to one as soft as cigarette ash, Böhnhardt says. "Something in between would be good," he says. Some scientists want to land near the plumes of gas and dust erupting from the comet—assumed to come from ice-rich regions—in order to sample them. Others say it would be safer to avoid the jets; they would target a pristine area that may harbor organic dust that has been unaltered by outgassing. The emerging picture of 67P as a contact binary—with two lobes barely attached to each other—adds to the challenge: Some areas may be dangerously unstable. And with a landing footprint nearly a kilometer across—on a comet with just 50 square kilometers of area—mission scientists may not get to be so choosy.

Assuming Philae lands safely—and mission manager Fred Jansen can be coaxed only into a gut estimate of 70% landing success—it will launch into a preprogrammed science routine that could last months. One key experiment is CONSERT, which will detect radio waves beamed from the mother spacecraft when it is on the opposite side of the comet. By measuring their travel time, researchers will build a 3D model of the nucleus. "We have no idea if anything is concentrated at the center," says Michael A'Hearn, a planetary scientist at the University of Maryland, College Park. Some theorists speculate that at the birth of the solar system, the comet-forming region could have harbored enough of the short-lived and hot radioactive isotope aluminum-26 to melt ice. If Philae finds evidence for hydrated minerals, or increasing concentrations of ice with depth, it would support the notion that a hot, watery chemistry altered comets soon after their formation—and that maybe comets aren't as pristine as thought.

Philae will also sample the comet with a coring tool that will drill to depths of about 20 centimeters and supply thimblefuls of material to a carousel of 26 ovens that can vaporize dust at temperatures up to 800°C. Gas from the ovens will be routed to gas chromatographs and mass spectrometers for analysis. One experiment, Ptolemy, will assess the abundance of lightweight molecules such as water and heavy water, which contains an atom of hydrogen that has an extra neutron. In 2011, researchers using the Herschel space telescope found that comet 103P/Hartley 2 contained almost the same fraction of heavy hydrogen as Earth's oceans—a result that revived the long-standing debate over whether a rain of comets, rather than icy asteroids, delivered Earth's water.

Another experiment, COSAC, will look for heavier molecules—in particular long-chain organic ones. Ground-based telescopes have identified many rudimentary organic molecules in comets, but they are hampered by atmospheric interference and are limited to studying molecules that end up suspended in a comet's halolike coma. The Stardust probe, which swept through the coma of comet Wild 2 (*Science*, 9 January 2004, p. 151) collecting dust and gas, also found organic molecules, including the amino acid glycine. COSAC, by sampling the nucleus itself, will compile a much longer list of organics that may include many more amino acids. The longer the list delivered to Earth, the easier it is to explain how life could have begun, says Scott Sandford, a planetary scientist at NASA Ames Research Center in Moffett Field, California, and a principal investigator on a proposed comet sample return mission. "It wouldn't hurt to start with as wide a mix of chemicals as possible so you can play with your Lego blocks," he says.

COSAC will also be able to detect the chirality, or handedness, of these molecules. On Earth, all amino acids used in biology are left-handed, even though life based on right-handed molecules would have worked just fine. If COSAC finds any left-handed bias in comets, it would be a clue that life didn't need to select for left-handedness—it could have simply picked up what asteroids and comets dropped off. ■

Published by AAAS

Nucleoli (raised, orange ovals) stand out in these colon cancer cells.

PHOTO: STEVE GSCHMEISSNER/SCIENCE SOURCE

Central command

More capable than once thought, the cellular structure known as the nucleolus may be a target for treating diseases

By **Mitch Leslie**

Hit cancer cells where they're unique: the mutated genes and deranged molecular pathways that drive rampant growth. That's the strategy most researchers have adopted to kill cancer cells without massacring healthy ones, but it's backward, says cell biologist Ross Hannan of the Peter MacCallum Cancer Centre in East Melbourne, Australia. The way to take down tumor cells, he says, is to disturb the normal cellular "housekeeping processes," which are even more crucial to fast-growing cancer cells. And a focal point of those mundane processes is a dark spot in the cell nucleus called the nucleolus.

Hannan and his colleagues, who are running a clinical trial of an experimental cancer drug targeting the nucleolus, are capitalizing on a new understanding of this obscure organelle. For more than 30 years, researchers thought that the nucleolus performed a vital but circumscribed role in the nucleus—manufacturing a specific type of RNA, dubbed rRNA, that assembles into ribosomes, the organelles that make proteins. But scientists have come to realize that, as molecular cell biologist Robert Tsai of the Texas A&M Health Science Center in Houston puts it, "the nucleolus is much more complex than rRNA synthesis."

Besides serving as a ribosome factory, the organelle also functions as a command center that monitors a cell's condition and orchestrates responses when it's under stress. By storing certain proteins and doling them out when they are required, the nucleolus "endows cells with an accurate way to regulate distribution of proteins," says Michal Hetman, a molecular and cellular neurobiologist at the University of Louisville in Kentucky. Ultimately, the nucleolus helps determine whether cells reproduce and when they die.

All of that makes it a tempting target for treating diseases, starting with cancer. Researchers have known for more than 200 years that cancer cells often sport extra nucleoli, which balloon as they attempt to help the rapidly dividing cells meet their insatiable need for proteins. In recent years, hints have emerged that the nucleolus's activities also contribute to heart disease, neurological illnesses, and other diseases.

Downloaded from www.sciencemag.org on August 11, 2014

Published by AAAS

DESCRIBED BY MICROSCOPISTS in the 1830s officially, the nucleolus isn't enveloped by a membrane, unlike other cellular organelles. But nucleoli—even normal mammalian cells can have more than one—are distinct from the surrounding nuclear material. They are about twice as dense and, according to estimates by biophysicist Clifford Brangwynne of Princeton University and colleagues, roughly 100,000 times more viscous, like thick honey. In a 2011 paper in the *Proceedings of the National Academy of Sciences*, Brangwynne and his co-workers provided evidence that nucleoli in frog eggs are a distinct phase of matter. "They behave like liquid droplets," he says, perhaps because of the unique combination of proteins—more than 4000 different kinds spend time there—and RNA molecules they harbor.

The recipe for these organelles resides in chromosome stretches called nucleolar organizing regions, or NORs, which contain numerous copies of genes encoding rRNAs. NORs prompt a nucleolus to form around them, as cell and molecular biologist Brian McStay of the National University of Ireland, Galway, demonstrated for the first time in vertebrate cells this year. His team crafted synthetic NORs that contain mouse ribosome genes and repeated DNA segments that bind to a nucleolar protein. When the researchers inserted these "neo-NORs" at different chromosome locations in cultured human cells, functional nucleoli sprang up around them, the team reported in the 1 February issue of *Genes & Development*.

The best-known function of the nucleolus came to light in the 1960s: making ribosomes. An enzyme called RNA polymerase I reads the ribosomal RNA genes in NORs and fashions rRNA molecules. After processing, these rRNAs combine in the nucleolus with proteins and other RNAs made elsewhere in the cell. The final assembly of ribosomes occurs in the cytoplasm, where they get to work making proteins.

These days, however, researchers refer to the "plurifunctional nucleolus." Cell biologist Thoru Pederson of the University of Massachusetts Medical School in Worcester, who coined the term in the 1990s, says he chose "plurifunctional" over "multifunctional" because it would be correct even if the nucleolus had only two functions. "I was being cautious," he says.

He didn't need to worry. The nucleolus has turned out to be a busy cellular housekeeper. It helps manage the cell cycle, the series of events that culminates in cell division. It stimulates DNA repair and organizes a molecular complex necessary for sorting proteins in the cytoplasm. Pederson and colleagues recently identified a hint of yet another function. "We've discovered a small number of microRNAs in the nucleolus," he says. These diminutive RNAs usually operate in the cytoplasm, fine-tuning protein production. What microRNAs are doing in the nucleolus "is a development we need to pin down," Pederson says.

The most important job for the nucleolus might be reining in p53, the protein known as the guardian of the genome because it protects against cancer. p53 is so potent—it can trigger cellular suicide—that cells continually make and then destroy the protein, thus keeping its levels low. But myriad stimuli, ranging from DNA damage to heat, can slow the destruction and allow the protein to accumulate. In 2003, a finding by biochemist Carlos Rubbi, now at the University of Liverpool in the United Kingdom, and his colleague Jo Milner suggested that the nucleolus is a key sensor for such stresses. The pair showed that even if cells carried injured DNA, they didn't begin to amass p53 unless their nucleolus was zapped with radiation. Moreover, Rubbi and Milner revealed that breaking up the nucleolus could liberate p53.

> ***"We've hardly scratched the surface of what the nucleolus has evolved to do in mammalian cells."***
>
> **Ross Hannan**, Peter MacCallum Cancer Centre

Nucleoli "are very sensitive to physical and chemical conditions," Rubbi says. When all cellular readings are normal, the nucleolus keeps p53 under wraps. If the nucleolus is injured or the cell is under duress, it stops performing this function and unleashes p53, which can kill the cell.

THAT LIFE-AND-DEATH POWER makes the nucleolus a bull's-eye for cancer therapy. Hannan and colleagues are now testing a drug called CX-5461, which was designed to thwart RNA polymerase I, the enzyme that makes rRNAs. When rRNA synthesis slows drastically, the nucleolus allows p53 levels to rise. Two years ago, Hannan and colleagues demonstrated that administering CX-5461 to mice cranked up p53 to lethal levels in cancer cells and preferentially killed them, presumably because they are more sensitive than are normal cells to reductions in rRNA synthesis. "We've shown that a housekeeping process that's in every cell can be a good target," Hannan says. The current trial of CX-5461 is largely to evaluate its safety in people, but the researchers will also monitor if it slows or stops the blood cancers the subjects suffer from.

The compound might just be the start. Cancer biologist Marikki Laiho of the Johns Hopkins University School of Medicine in Baltimore, Maryland, and colleagues have found another compound that targets RNA polymerase I in the nucleolus, called BMH-21. Earlier this year, they revealed that it kills cancer cells in culture and curbs tumor growth in mice, and they are now looking for a biotech or pharmaceutical company that will help develop it further.

Researchers are also starting to uncover evidence for a nucleolar role in other diseases. In 2008, molecular biologist Mark Sussman of San Diego State University in California and colleagues stumbled on a link to heart disease while studying the heart's ability to renew itself after injury. When Sussman's team probed cells from damaged hearts for nucleostemin—a nucleolus protein thought to be made mainly by stem cells—they found a surprising pattern. "It's expressed in adult heart muscle cells, and they are generally thought not to be cells that renew," he says.

To tease out the protein's role in the organ, the researchers disrupted blood flow to the hearts of mice to simulate a heart attack. Bloated, deformed nucleoli appeared in some cells in the damaged areas of the animals' hearts, the team revealed in the *Proceedings of the National Academy of Sciences* in 2011. That's a signal the organelles are under stress. In response, the nucleoli released nucleostemin and another protein called nucleophosmin. Sussman thinks the proteins may be the nucleolus's way of turning back the clock, reactivating a mechanism found in stem cells that would protect the organelle.

In other diseases, a stressed nucleolus may hasten damage rather than heal it. Dopamine-producing neurons die off in Parkinson's disease (PD), and in 2011 researchers reported injured nucleoli in samples of these cells from the brains of PD patients. They also showed that inducing nucleolar stress in mice with a PD-like illness leads to the death of these neurons. Findings such as these suggest that compounds to soothe the nucleolus might stem neurodegenerative diseases—although such drugs are still far off.

These days, says Texas A&M Health Science Center's Tsai, "more and more people are thinking about the nucleolus," as they realize how many cellular processes it touches. The spotlight on this small dark spot will likely illuminate more surprises, Hannan says. "We've hardly scratched the surface of what the nucleolus has evolved to do in mammalian cells." ■

Published by AAAS

Reading the past in ancient genomes *p. 511*

Neural circuits of pain and motivation *p. 513*

PERSPECTIVES

EVOLUTION

How birds became birds

Sustained size reduction was essential for the origin of birds and avian flight

By **Michael J. Benton**

Birds evolved from dinosaurs, but how long did this evolutionary transition take? Twenty years ago, it was widely assumed that the first bird—*Archaeopteryx*, which lived in the Late Jurassic (see the photo)—evolved its feathers, wings, and ability to fly within just 10 million years or so. Since then, it has become clear that most of the 30 or more characteristics that distinguished the small, flying *Archaeopteryx* from ground-dwelling, carnivorous dinosaurs (theropods) emerged much earlier. On page 562 of this issue, Lee *et al.* (*1*) provide evidence for sustained miniaturization for 50 million years before *Archaeopteryx* evolved (see the graph).

The story of this revolution begins in 1994, when paleontologists from China brought photographs of amazing new fossils to the Annual Meeting of the Society of Vertebrate Paleontology in New York. The photos showed a small dinosaur without wings or other bird characters, but covered with a fuzz of feathers. This was the beginning of a flood of Chinese theropod fossils with feathers of all kinds, from simple bristles through branched down feathers to fully elaborated flight-type feathers (*2*, *3*). Some theropod dinosaurs even had extended forearms and quill-like feathers arranged as wings. The dromaeosaurid *Microraptor* also had distinct wings on its legs, resurrecting the old "tetrapteryx," a supposed four-winged precursor of modern two-winged birds (*4*). The fossils showed that from about 170 to 120 million years ago, all these dinosaurs—the Paraves—were experimenting with flight in various modes, including parachuting, gliding, and leaping from tree to tree. One clade,

School of Earth Sciences, University of Bristol, Bristol BS8 1RJ, UK. E-mail: mike.benton@bristol.ac.uk

Early bird. Fossils of *Archaeopteryx*, which lived around 150 million years ago, provide important clues to how birds evolved from their theropod ancestors.

PHOTO: CHRIS HELLIER/SCIENCE SOURCE

Published by AAAS

represented by *Archaeopteryx*, made the crucial leap to powered flight, and so birds were born.

Feathers are so typically avian today that they are often seen as the key character of birds. However, feathers arose at least 50 million years before *Archaeopteryx*, and perhaps much earlier (*5*). They presumably arose first for insulation and display, as witnessed by the colorful, patterned feathers of dinosaurs (*6*, *7*), and were then co-opted in expanded gliding surfaces and increasingly in substantial, aerodynamic wing structures among Paraves (*8*).

So, what makes a bird a bird and not a flying dinosaur? As Lee *et al.* show, the key seems to be miniaturization.

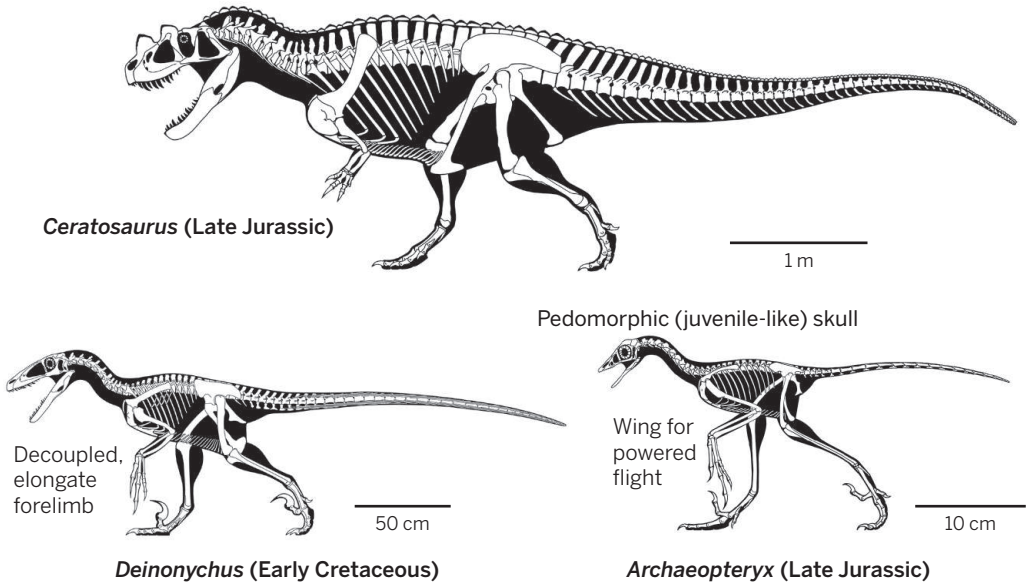

Making a bird from a dinosaur. Key characteristics of birds that distinguish them from their theropod ancestors include quill-like feathers, forelimbs that are decoupled from hindlimbs, a pedomorphic skull, and small size.

The trend to miniaturization in Paraves had already been noted in size comparisons across all theropods (*9*). Macroevolutionary analysis has confirmed that this size reduction happened at evolutionary rates 150 times faster than normal (*10*). Lee *et al.* now show that miniaturization was a long-term trend over 50 million years (see the graph). The study is based on analysis of an enormous data set and uses sophisticated analytical tools. The authors looked at 120 species of theropod dinosaurs and early birds, coded for 1549 skeletal characters (a data matrix comprising 185,880 cells), and calculated the best-fitting phylogenetic tree while also exploring evolutionary rates.

Until recently, paleontologists relied on qualitative approaches to establish narratives of change through geologic time. They used cladistic methods to discover best-fitting or most likely phylogenetic trees; evolutionary change was then mapped loosely over the tree. Now, phylogenetic comparative methods (*11*) make it possible to calculate ancestral states of any character, and to establish points of unusually fast or slow rates of change. Such "diversification shifts" help in determining the most likely evolutionary models for a tree or part of a tree.

Earlier studies (*9*, *10*) used three steps: build the tree, date the branching points, and then map the characters. Lee *et al.* ran all three calculations simultaneously, working with phylogenetic information, geologic dates for branching points, and character state reconstructions at the same time. All methods are well established, and it is not clear which approach is most reliable. They all give similar results in this case.

The authors find that theropod body size decreased 12 times, from an initial mean mass of 163 kg to 0.8 kg in *Archaeopteryx*. How could such a long-term trend be maintained? Lee *et al.* note that miniaturization brought numerous changes, because it shortened normal developmental patterns. For example, bird heads can be seen as dinosaur heads that retain juvenile features in the adult (pedomorphic) (*12*), with short snouts, large brains, and large eyes (see the figure). Smaller size might also have been facilitated by co-option of feathers for insulation. In addition, birds have decoupled hindlimbs and forelimbs (*13*), allowing each limb set to function independently, unlike in most other tetrapods (see the figure). What might have triggered these changes?

The crucial driver may have been a move to the trees, perhaps to escape from predation or to exploit new food resources. Tree living requires small bodies, and reduced body size enables other characteristics that enhance success in the trees, such as enlarged eyes for three-dimensional vision (so avoiding collisions when leaping from branch to branch); enlarged brains to cope with diverse arboreal habitats; insulating feathers to enable nocturnal activity (many insects are nocturnal to evade cold-blooded predators); and elongated forelimbs, distinct from the hindlimbs in their function, and with expanded flight surfaces to enable ever more daring leaps from tree to tree. The physical changes are reminiscent of those that later occurred in our own clade, the Primates, also interpreted as driven by tree living. ■

Body size miniaturization

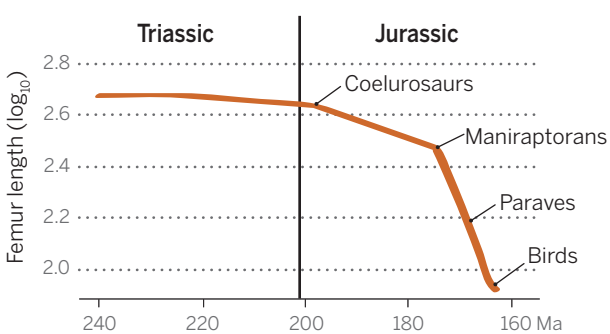

Getting smaller. Lee *et al.* show that between 210 and 160 million years ago (Ma), the ancestors of today's birds shrank at a rapid evolutionary rate, as captured by the length of the femur (thigh bone). This was crucial to enable flight.

ILLUSTRATION: (TOP) SCOTT HARTMAN

REFERENCES

1. M. S. Y. Lee *et al.*, *Science* **345**, 562 (2014).
2. P. Chen, Z. Dong, S. Zhen, *Nature* **391**, 147 (1998).
3. J. Qiang *et al.*, *Nature* **393**, 753 (1998).
4. X. Xu, Z. Zhou, X. Wang, *Nature* **408**, 705 (2000).
5. P. Godefroit *et al.*, *Science* **345**, 451 (2014).
6. F. Zhang *et al.*, *Nature* **463**, 1075 (2010).
7. Q. Li *et al.*, *Science* **327**, 1369 (2010).
8. J. Clarke, *Science* **340**, 690 (2013).
9. A. H. Turner *et al.*, *Science* **317**, 1378 (2007).
10. M. N. Puttick *et al.*, *Evolution* **68**, 1497 (2014).
11. J. S. Felsenstein, *Am. Nat.* **125**, 1 (1985).
12. B.-A. S. Bhullar *et al.*, *Nature* **487**, 223 (2012).
13. V. Allen *et al.*, *Nature* **497**, 104 (2013).

10.1126/science.1257633

Published by AAAS

QUANTUM INFORMATION

A gem of a quantum teleporter

Diamond-based quantum teleportation works every time

By **Mete Atatüre**[1] and **John J. L. Morton**[2]

The television series "Star Trek" owes its longevity to the fact that when Captain Kirk was in danger on the surface of a planet, his chief engineer, Montgomery Scott, could teleport him back to the Enterprise each and every time, not just once every thousand episodes. The quantum-mechanical realization of teleportation—where a quantum state can be teleported to a distant location—has taken a while to reach this level of reliability. On page 532 of this issue, Pfaff *et al.* (*1*) report on the first deterministic and unconditional quantum teleportation using matter-based systems.

Quantum teleportation addresses the basic question of how to transmit information about the state of a quantum system without sending the physical system itself. It is the quantum equivalent of the fax machine. Heisenberg's uncertainty principle states that it is impossible to obtain all of the information about a quantum system by measuring it and equally impossible to make an accurate copy. However, this task is not hopeless. In 1993, Bennett *et al.* (*2*) devised a method based on quantum entanglement and a basic classical communication channel, by which a quantum state could cease to exist in one location and then reappear at another. In this protocol, two parties ("Alice" and "Bob") each possess a quantum bit (or qubit), having first established quantum entanglement between them—more or less the way Einstein, Podolsky, and Rosen (*3*) first described nonlocal quantum correlations.

Alice then has a quantum system in some unknown state $|\phi\rangle$ that she would like to send to Bob. She first interacts this system with her qubit and then measures both. At this point, the state $|\phi\rangle$ is neither with Alice nor with Bob. Bob's qubit is one simple transformation away from becoming $|\phi\rangle$, but Alice must tell Bob the result of her measurements (using a classical channel; a phone line would do) for Bob to know what this transformation needs to be. As Bennett *et al.* observed, "The net result of teleportation is completely prosaic: the removal of $|\phi\rangle$ from Alice's hands and its appearance in Bob's hands a suitable time later." So, the quantum fax machine shreds the input state as it sends it.

Implementing this protocol in practice is challenging, because it requires bringing together a number of elements of the quantum practitioner's toolbox—creating entanglement, storing quantum states, and feeding forward the results of Alice's measurement to determine operations applied on Bob's system. Proof-of-concept demonstrations were performed by three different groups of researchers based on single photons and squeezed light (*4*–*6*). Without the resources to allow Alice and Bob to store quantum-correlated light (this requires a quantum memory, which is still under development), such methods enable state teleportation only in an a posteriori probabilistic manner or require a continuously running bright optical link between Alice and Bob. Nevertheless, teleportation using photons has been demonstrated over distances of almost 150 km (*7*). Space (e.g., satellite links) is the next, if not final, frontier.

The problem with probabilistic teleportation. Previous demonstrations of quantum teleportation between matter-based systems were probabilistic, leading to mostly unsuccessful attempts and therefore corrupting the final teleported state. The approach of Pfaff *et al*. verifies entanglement before performing the teleportation steps, so every attempt is successful in the end

Demonstrating quantum teleportation with matter systems is arguably even more intriguing, because light already does a good job of transmitting quantum states without any help from physicists. The obvious way for Alice and Bob to possess entangled matter qubits is to entangle two qubits through local interactions and then separate them, giving one each to Alice and Bob. Performing such a separation of qubits within their lifetime is challenging in practice. A more elegant scheme is to entangle remote qubits by causing each to emit a photon that is correlated with its state and then interfering those two photons and measuring them (*8*).

This act can project the two matter qubits into an entangled state, even though they never interacted directly. However, practical implementations of this are not deterministic and have a very low probability of success (see the figure). Remote entanglement has been performed with both trapped ions and cavity-coupled atoms separated by a few meters, enabling quantum teleportation between them (*9*, *10*). Currently, atoms in cavities are the state-of-the-art and can clock 10 successful teleportation events per second, based on 10,000 attempts per second. The "post-selected" data answers the question "when Alice and Bob did share entanglement, were they able to teleport their state?"

The next step is to be able to wait until entanglement is successfully created and only then attempt teleportation—the quantum equivalent of waiting for a dial tone. Entangled qubits must be stored long enough to verify their entanglement before commencing the teleportation protocol. Pfaff *et al.* have turned this approach into reality using the spins of impurity atoms in diamond. Diamond impurities, such as the negatively charged nitrogen vacancy (NV), are nature's cost-effective trapped ions. Strong confinement of electrons by an impurity atom automatically provides discrete energy levels for preparation, control, and measurement of the electronic spin qubit. Essential properties of the NV center in diamond include long spin coherence lifetimes (approaching 1 s), optical transitions that allow readout of the spin state and spin-photon entanglement, and a neighborhood of nuclear spins interacting with the NV electron spin that form a small quantum register.

Pfaff *et al.* have harnessed each of these capabilities into one quantum teleportation protocol that follows the original

[1]Cavendish Laboratory, University of Cambridge, Cambridge CB3 0HE, UK. [2]London Centre for Nanotechnology, University College London, London WC1H 0AH, UK. E-mail: ma424@cam.ac.uk; jjl.morton@ucl.ac.uk

ILLUSTRATION: PETER AND MARIA HOEY/WWW.PETERHOEY.COM

Published by AAAS

proposal almost verbatim. They used two cryogenically cooled NV centers (belonging to Alice and Bob, respectively) separated by 3 m and defined a nitrogen spin near Alice's NV center to be the input qubit. As in the case of the atomic counterparts, the remote entanglement is formed probabilistically (with a rather modest rate of once every 250 s) and heralded by a successful measurement outcome of interfering photons from the two NVs (*11*). The heralding places the two NV electron spins into an entangled singlet state that lasts as long as the electronic spin coherence time (a few milliseconds, with the help of active error protection known as dynamical decoupling) (*12*). This time is sufficient for Alice to couple the nearby nitrogen spin qubit with her half of the entangled pair, measure both spins through optical readout, and then feed forward this information to determine the operation to be performed on Bob's qubit. In contrast to previous demonstrations, this work distinguished all four of the different measurement outcomes of Alice's qubits in a single shot, a prerequisite for the success rate to exceed 50%. Bringing all of these elements together, Pfaff *et al.* demonstrated deterministic quantum teleportation between distant matter qubits.

As usual with cutting-edge research, there is sufficient room for improvement. The actual teleportation fidelity was 86%, caused by the combined effect of practical imperfections at each stage. The initial step of generating entangled spins is the current bottleneck on the operation bandwidth of 1/250 Hz. Better photon collection efficiency, possibly through optical cavities, could result in this step being reduced to milliseconds. Another area of focus is improving the millisecond storage time scale of the initial singlet state, perhaps using nuclear spins on both sites as the storage qubits, so that there is time for entangling a larger number of qubits in a concatenated computation protocol. With some if not all of these improvements, a fundamentally secure and feasible quantum communications network with diamond-based quantum nodes is within reach. ■

REFERENCES

1. W. Pfaff *et al.*, *Science* **345**, 532 (2014).
2. C. H. Bennett *et al.*, *Phys. Rev. Lett.* **70**, 1895 (1993).
3. A. Einstein, B. Podolsky, N. Rosen, *Phys. Rev.* **47**, 777 (1935).
4. D. Bouwmeester *et al.*, *Nature* **390**, 575 (1997).
5. A. Furusawa *et al.*, *Science* **282**, 706 (1998).
6. D. Boschi, S. Branca, F. De Martini, L. Hardy, S. Popescu, *Phys. Rev. Lett.* **80**, 1121 (1998).
7. X.-S. Ma *et al.*, *Nature* **489**, 269 (2012).
8. C. Simon, W. T. M. Irvine, *Phys. Rev. Lett.* **91**, 110405 (2003).
9. S. Olmschenk *et al.*, *Science* **323**, 486 (2009).
10. C. Nölleke *et al.*, *Phys. Rev. Lett.* **110**, 140403 (2013).
11. H. Bernien *et al.*, *Nature* **497**, 86 (2013).
12. G. de Lange *et al.*, *Science* **330**, 60 (2010).

10.1126/science.1256698

EVOLUTION

An epigenetic window into the past?

DNA damage in ancient genomes may provide insight into past regulatory changes in humans and other species

By **Ludovic Orlando** *and* **Eske Willerslev**

Over the past 30 years, ancient DNA has helped to track past population dynamics, environmental changes, and historical epidemics. Studies of ancient genomes have provided insights into the evolution of humans (*1*, *2*) and other mammals (*3*). Going beyond sequences, epigenetic changes, such as methylation patterns, can also be detected in ancient genomes (*4*, *5*). This epigenetic information has the potential to elucidate regulatory changes underlying species divergence and population adaptation.

Epigenetic information regulates the accessibility of chromatin to transcription factors and thereby coordinates gene expression. Consequently, epigenetic changes influence various biological processes, including cell differentiation, aging, and cancer (*6*). Cytosine methylation (^{m}C), one of the best-known epigenetic markers, is often associated with gene silencing and is generally found at CpG dinucleotide sites in vertebrate genomes (*6*). The best method for reconstructing high-resolution methylation maps is bisulphite sequencing, which converts unmethylated cytosines into uracils (U) and therefore CpG sites into UpG sites. At ^{m}CpG sites, where methylation precludes bisulphite conversion, no mutation is observed. Applied to 26,000-year-old bison bones, this method revealed methylation patterns at four candidate loci (*7*). However, bisulphite conversion is associated with severe DNA degradation and is thus poorly suited for ancient DNA, which is only available in trace amounts.

DNA conversion reactions similar to those caused by bisulfite treatment take place naturally after an organism dies. The most common such reaction mostly occurs at single-stranded overhangs, converting CpG into UpG sites and ^{m}CpG into TpG sites. Current approaches for reconstructing ancient methylation maps exploit this pattern by disabling the sequencing of UpGs on high-throughput platforms (*4*, *5*). The location of CpG→TpG mutations in the genome reveals places where cytosines were methylated (*8*) (see the figure).

Pedersen *et al.* have applied this approach to the genome sequence of a 4000-year-old paleo-Eskimo (called Inuk), revealing methylation patterns closely matching those from modern hair (*4*). The DNA had been extracted from hair. Thus, methylation data could help to identify the source of ancient DNA molecules and rule out contamination from modern human DNA, a major problem in past studies. The methylation state at clock CpG sites, where methylation levels change with age in a predictable manner (*9*), revealed that Inuk probably died in his fifties. The methylation map was then used to attempt to predict gene expression in Inuk's hair. Genes coding for key hair proteins appeared to be highly expressed, and predicted levels of gene expression were significantly correlated with transcription levels in living hair follicles.

These studies provide hope that it may be possible to identify the epigenetic contribution to past evolutionary transitions.

Using a similar approach, Gokhman *et al.* have shown that the bone methylation maps from two archaic hominins that lived 50,000 to 130,000 years ago in the Altai mountains strongly resemble those from human osteoblast cells (*5*), except for ~2000 regions where at least one archaic hominin showed differential methylation. These regions include the *HOXD* cluster, a key regulator of limb development. If confirmed for more individuals, these findings could identify key regulatory sites that contribute to the anatomical differences between modern humans and archaic hominins.

Centre for GeoGenetics, Natural History Museum of Denmark, University of Copenhagen, Øster Voldgade 5-7, 1350K Copenhagen, Denmark. E-mail: lorlando@snm.ku.dk

Published by AAAS

The long-term epigenetic reprogramming observed in people born right after the Dutch Hunger Winter of 1944–1945 (*10*) suggests that epigenetic changes have accompanied past environmental, climatic, and social crises. Smith *et al.* have detected genome-wide hypermethylation of pre-Islamic (600–900 B.P.) barley following viral infection (*11*), revealing how epigenetic signals can be used to monitor past exposure to biotic stresses. The recent change in lifestyle of many indigenous peoples, the transition from hunting-gathering to farming, and the industrial revolution could thus have affected human epigenomes and ultimately human health. Epigenetic changes in animals and plants might also have accompanied their extinction or their domestication. The above studies provide hope that it may be possible to identify the epigenetic contribution to such evolutionary transitions. The same approaches may even benefit studies related to the more recent past, such as age determination of victims in forensics or in repatriation cases, if the DNA is highly degraded.

In living cells, a range of epigenetic modifications can complement DNA methylation to modulate DNA packaging (*12*). DNA segments are wrapped around histones to form nucleosomes. In certain environments, packaging into nucleosomes can persist after an organism dies, offering a shelter to DNA. As a result, nucleosome-rich regions can be overrepresented after shotgun sequencing of ancient DNA. This pattern was seen in the sequences underlying Inuk's genome and was used to reconstruct a full nucleosome map, which helped to refine which genes were likely expressed in Inuk's hair (*4*). A number of factors, including the overrepresentation of GC-rich templates during library amplification or differences in mappability along the genome, can affect patterns of coverage variation. These factors must be corrected before being translated into nucleosome occupancy maps.

Deamination of ^{m}CpG sites after death is central to current approaches used to reconstruct ancient methylation maps. However, a substantial fraction of the ^{m}CpG sites in ancient DNA fragments can be left intact, particularly in double-stranded regions, where deamination is much slower than in overhanging ends. Current approaches can therefore only achieve reliable methylation maps from highly deaminated sites. High-coverage data, which enhance the statistical chance of observing ancient deamination events, also appears essential.

In the future, enrichment approaches using methyl-binding domains that directly target intact ^{m}CpG sites (*11*) should facilitate identification of hypermethylated regions. In such regions, the number of sequences available post-enrichment will be higher, which will improve our ability to detect ancient polymorphisms and therefore to reconstruct the demographic and migration history of past populations. In addition, such approaches may reduce sequencing costs, because direct enrichment for vertebrate-specific methylations should help to filter out microbial environmental DNA. The efficiency of such approaches will, however, decrease with the age of the specimen and vary with abiotic parameters that influence DNA degradation (*11*); it will not be suitable if deamination reactions have eliminated all (or most) ^{m}CpG sites.

In the longer term, technologies that directly record epigenetic modifications while sequencing (*13*) should open access to other types of methylation marks, such as those affecting adenines that are often found in bacterial genomes. However, base modifications introduced postmortem might prove problematic and confuse native epigenetic signals.

The biological interpretation of ancient epigenomic results is challenging. The epigenome of a given cell type is complex (*14*), and understanding of how environmental factors, epigenetic markers, and genetic variants interact to drive subtle differences in expression remains limited. Ancient DNA extracts often derive from bones and teeth, which can hardly inform about regulatory changes in the brain and other important organs. They also consist of a mixture of different cell types that are averaged in the epigenetic signal. And unlike the genome, the epigenome is highly variable with age, sex, health, and the environment (*15*). Nevertheless, the potential to obtain information that is not coded and thus not directly available in genome sequences makes ancient epigenomes worth investigating. ■

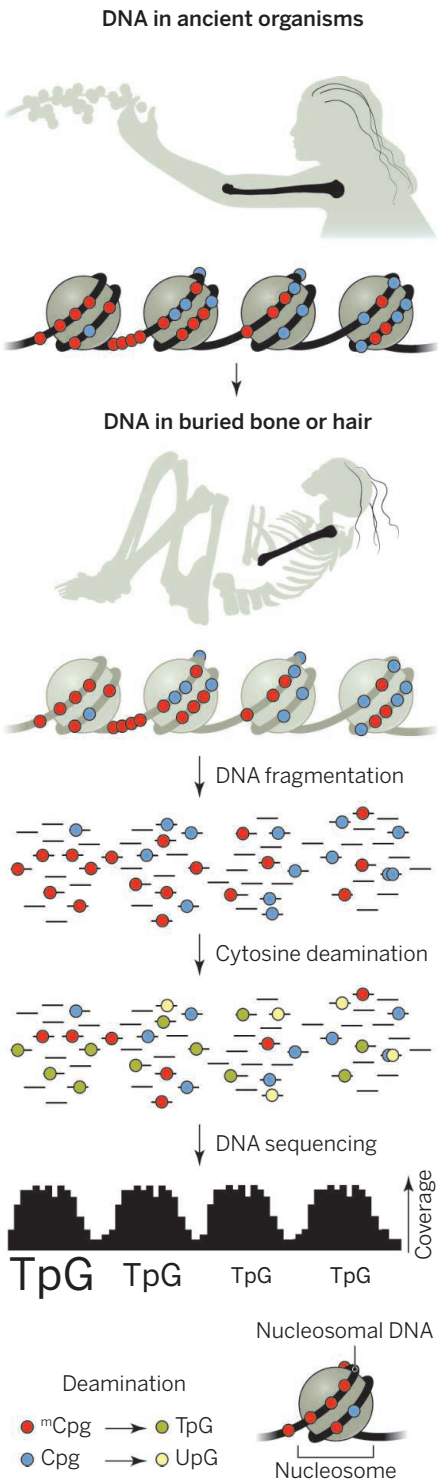

Ancient epigenomics. Postmortem DNA decay leads to specific sequence patterns in ancient DNA data, making it possible to identify genes that are epigenetically reprogrammed during evolution. One such patterns results from deamination reactions that convert CpGs and ^{m}CpGs into UpGs and TpGs. Use of molecular tools that detect only the latter reveal regions that were methylated in ancient genomes. Patterns of coverage variation along the genome can also help to track ancient nucleosome occupancy.

REFERENCES AND NOTES

1. K. Prüfer *et al.*, *Nature* **505**, 43 (2014).
2. M. Raghavan *et al.*, *Nature* **505**, 87 (2014).
3. L. Orlando *et al.*, *Nature* **499**, 74 (2013).
4. J. S. Pedersen *et al.*, *Genome Res.* **24**, 454 (2014).
5. D. Gokhman *et al.*, *Science* **344**, 523 (2014).
6. M. M. Suzuki, A. Bird, *Nat. Genet. Rev* **9**, 465 (2008).
7. B. Llamas *et al.*, *PLOS ONE* **7**, e30226 (2012).
8. A. W. Briggs *et al.*, *Nucleic Acids Res.* **38**, e87 (2010).
9. S. Horvath, *Genome Biol.* **14**, R115 (2013).
10. E. W. Tobi *et al.*, *Hum. Mol. Genet.* **18**, 4046 (2009).
11. O. Smith *et al.*, *Sci. Report* **4**, 5559 (2014).
12. O. Bell, V. K. Tiwari, N. H. Thomä, D. Schübeler, *Nat. Rev. Genet.* **12**, 554 (2011).
13. J. Shim *et al.*, *Sci. Rep* **3**, 1389 (2013).
14. ENCODE Project Consortium, B. E. Bernstein *et al.*, *Nature* **489**, 57 (2012).
15. R. Feil, M. F. Fraga, *Nat. Genet. Rev* **13**, 97 (2012).

ACKNOWLEDGMENTS

This work was supported by the Danish Council for Independent Research, Natural Sciences (FNU), and the Danish National Research Foundation (DNRF94).

10.1126/science.1256515

ILLUSTRATION: P. HUEY/*SCIENCE*

Published by AAAS

NEUROSCIENCE

More pain; less gain

Persistent pain changes a neural circuit and reduces willingness to work for food

By **Howard L. Fields**

Pain is arguably the most completely understood of all sensations at the molecular and neural circuit level (*1*–*3*). Noxious stimuli elicit a variety of rapid tissue-protective responses. Pain also has an unpleasant affective-motivational dimension that, when persistent, can dominate behavior. When chronic, pain produces fatigue and mood changes that diminish many of life's pleasures. In contrast to our detailed understanding of acute pain, we know much less about how persistent pain alters behaviors at the molecular and neural circuit levels. On page 535 of this issue, Schwartz *et al.* (*4*) advance our understanding of how persistent noxious stimuli affect reward-seeking behavior.

From an evolutionary perspective, animals with more complex behavioral repertoires have greater flexibility in their responses to environmental challenges. This flexibility presents an animal with the challenge of choosing the best option among concurrent conflicting goals that require different actions. Selecting requires a cost-benefit computation in which the weight assigned to the net benefit or loss of each action is determined by genetic predispositions, past experiences, and the current context. It also requires choosing the optimal actions to meet motivational drives, and then implementing the selected choice while inhibiting competing options. Schwartz *et al.* demonstrate, using mouse models, that persistent painful input produces robust synaptic changes in a specific brain circuit, resulting in reduced motivation to work for a reward (in this case, food).

The stage for the study by Schwartz *et al.* was set by recent changes in our understanding of the neural circuits underlying appetitive motivation. Links in this so-called "reward circuit" include the midbrain ventral tegmental area and its projection targets in the cortex, amygdala, and nucleus accumbens (*5*). This circuit was originally discovered through the finding that rodents would work to receive electrical stimulation in these brain regions (*6*). These regions were found to overlap with the distribution of dopaminergic neurons and their projections to the prefrontal cortex and nucleus accumbens (*7*). The status of this circuit as a "pleasure center" was affirmed by studies showing that injection of nicotine or opiates into the ventral tegmental area, or of psychostimulants (which block removal of synaptic dopamine) into the nucleus accumbens, led to positive reinforcement (*5*).

Although initially considered to be largely separate from the pain circuit, these so-called reward centers include parallel opposing circuits that can elicit either reward or punishment. Thus, although most midbrain dopamine neurons respond to either unexpected or predicted rewards, a substantial subset of midbrain dopamine neurons is activated by noxious stimuli (*8*, *9*). Furthermore, when different subgroups of dopamine neurons are activated optogenetically (i.e., genetically programmed to be activated by light), they can produce either positive reinforcement or punishment (*10*). Human functional imaging studies also show extensive overlap between brain regions (including the nucleus accumbens) that are activated by reward and pain cues (*11*, *12*) and have revealed connectivity changes between the cortex and nucleus accumbens that precede and predict the transition from acute to chronic lower back pain (*13*).

Consistent with this idea of dual opposing mesolimbic circuits, there are two functionally distinct subpopulations of neurons in the nucleus accumbens that release the neurotransmitter γ-aminobutyric acid (GABA): ones that express the dopamine D1 receptor (DADR1) and others that express the dopamine D2 receptor (DADR2). DADR1 neurons promote reward seeking and positive reinforcement, whereas DADR2 neurons inhibit reward seeking and have an aversive or punishing effect (*14*). One intriguing possibility is that these two neuronal subsets interact to produce their opposing effects on behavior. Nucleus accumbens DADR1 neurons have branches that contact ventral pallidum neurons that presumably receive DADR2 neuron input, and both ventral pallidum and DADR1 neurons project directly to the midbrain (*15*).

Using two different rodent models of chronic pain—nerve injury and inflammation—Schwartz *et al.* noted that after a week of nociceptive input, there was a robust reduction of the mouse's motivation to work for a food reward. Although the mice showed no reduction in the consumption of easily available food, they were unwilling to exert extra effort to obtain food. The main excitatory inputs to the nucleus accumbens from the amygdala and cortex are glutamatergic. In nucleus accumbens brain slices, Schwartz *et al.* compared the function of DADR1 and DADR2 neurons in response to glutamate and observed an early increase in *N*-methyl-D-aspartate (NMDA) receptor function and a later reduction in the function of the α-amino-3-hydroxy-5-methyl-4-isoxazolepropionic acid (AMPA) receptor (the NMDA and AMPA receptors are both receptors for glutamate). Surprisingly, this change only occurred in the DADR2

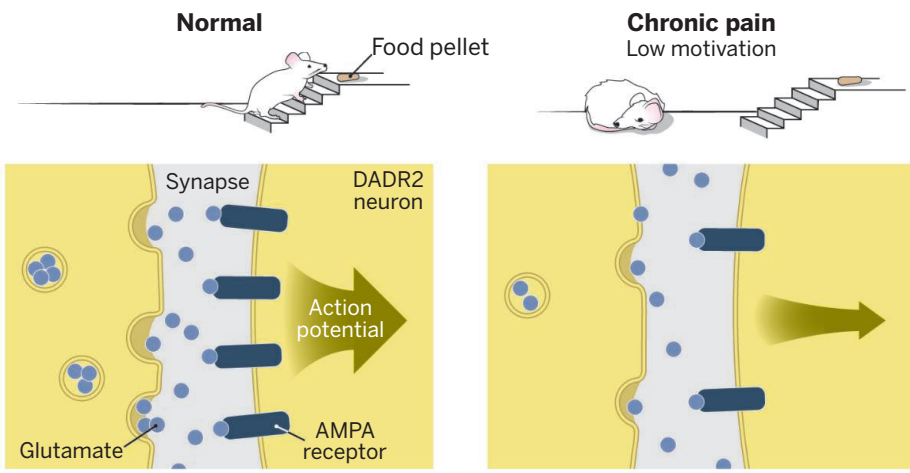

Excitability and motivation. Glutamate inputs excite nucleus accumbens medium spiny neurons. Chronic pain reduces AMPA receptor function in the DADR2-expressing class of these neurons, thereby reducing their activation by glutamate input. This decreases the motivation to work for a food reward.

ILLUSTRATION: V. ALTOUNIAN/*SCIENCE*

Department of Neurology and Wheeler Center for the Neurobiology of Addiction, University of California School of Medicine, San Francisco, CA 94143, USA. E-mail: howard.fields@ucsf.edu

Published by AAAS

neurons. Furthermore, long-term depression (weakening of specific glutamate synapses) was lost in DADR2 neurons.

Schwartz *et al.* identified the neuropeptide galanin as the link between the selective changes in glutamate receptor function in the nucleus accumbens and the reduced motivation to work for a palatable taste reward. Decreasing galanin 1 receptor expression in the nucleus accumbens with RNA interference prevented both the behavioral and glutamate receptor changes induced by persistent pain. Furthermore, preventing NMDA-dependent long-term depression both blocked the pain-induced reduction in AMPA receptor function in DADR2 neurons and blocked the reduction in motivation to work for food. This supports a causal link between the reduction in the excitability of DADR2 neurons and the reduced motivation to work for a reward.

By identifying a critical circuit element, Schwartz *et al.* have taken a vital step toward solving the fundamental neurobiological problem of action selection in the presence of conflicting motivations. It will be informative to relate the activity of DADR2 neurons to the effort expended to obtain food in awake behaving animals and to determine how the presence of ongoing pain changes this activity. Further work is also needed to define the behavior-relevant circuit, first by identifying the input pathway to the galanin-releasing neurons in the nucleus accumbens that mediate the change in glutamate receptor function in DADR2 neurons. To understand why reduced excitability in DADR2 neurons reduces the motivation to work for palatable food, it will be essential to determine how they act on their downstream targets. ■

REFERENCES

1. *Wall and Melzack's Textbook of Pain* (Elsevier/Saunders, Philadelphia, ed. 6, 2013).
2. A. I. Basbaum, D. M. Bautista, G. Scherrer, D. Julius, *Cell* **139**, 267 (2009).
3. J. J. Balcita-Pedicino, N. Omelchenko, R. Bell, S. R. Sesack, *J. Comp. Neurol.* **519**, 1143 (2011).
4. N. Schwartz *et al.*, *Science* **345**, 535 (2014).
5. G. F. Koob, M. Le Moal, *Neurobiology of Addiction* (Academic Press, London, 2006).
6. J. Olds, P. Milner, *J. Comp. Physiol. Psychol.* **47**, 419 (1954).
7. A. Dahlström, K. Fuxe, L. Olson, U. Ungerstedt, *Acta Physiol. Scand.* **62**, 485 (1964).
8. E. S. Bromberg-Martin, M. Matsumoto, O. Hikosaka, *Neuron* **68**, 815 (2010).
9. F. Brischoux, S. Chakraborty, D. I. Brierley, M. A. Ungless, *Proc. Natl. Acad. Sci. U.S.A.* **106**, 4894 (2009).
10. S. Lammel *et al.*, *Nature* **491**, 212 (2012).
11. J. Jensen *et al.*, *Neuron* **40**, 1251 (2003).
12. B. Knutson, C. M. Adams, G. W. Fong, D. Hommer, *J. Neurosci.* **21**, RC159 (2001).
13. M. N. Baliki *et al.*, *Nat. Neurosci.* **15**, 1117 (2012).
14. A. V. Kravitz, L. D. Tye, A. C. Kreitzer, *Nat. Neurosci.* **15**, 816 (2012).
15. A. Tripathi, L. Prensa, C. Cebrián, E. Mengual, *J. Comp. Neurol.* **518**, 4649 (2010).

10.1126/science.1258477

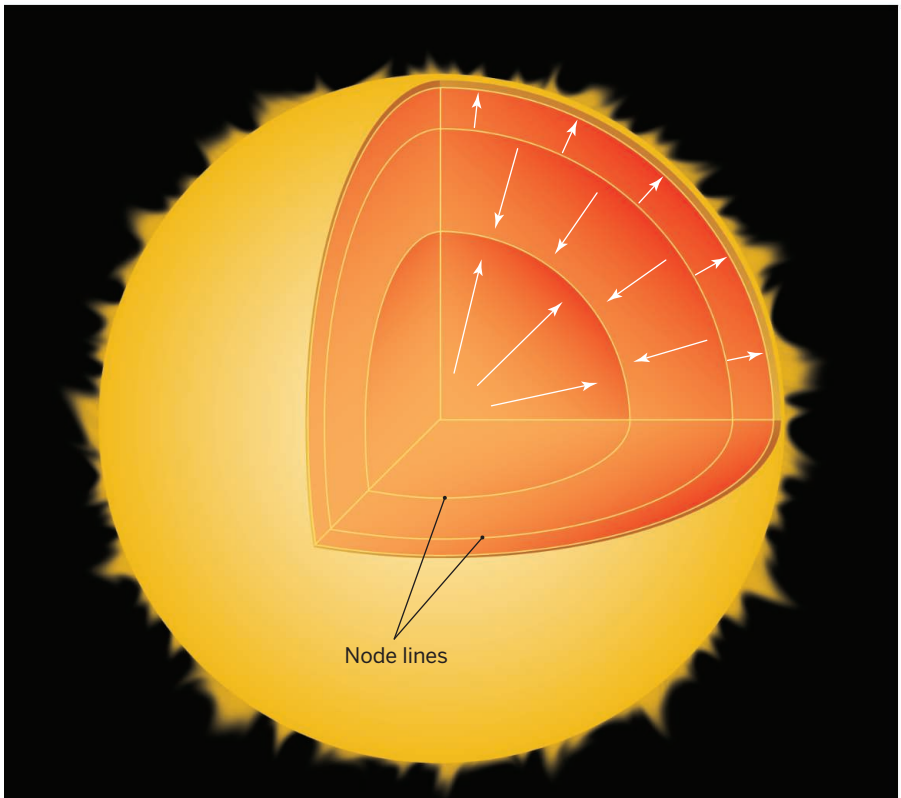

Oscillations inside a young star. Adjacent layers contract and expand periodically. At the node lines, gas remains stationary.

ILLUSTRATION: FIGURE COURTESY OF M. MARCONI; ADAPTED BY P. HUEY/*SCIENCE*

ASTRONOMY

The beat of young stars

Pulsations from young stars provide a new chronometer for stellar evolution

By **Steven Stahler**[1] *and* **Francesco Palla**[2]

A star is a ball of gas held together by the compressive force of self-gravity and supported from within by thermal pressure. For most of a star's life, this dynamical balance is stable; perturbing the star does not lead to explosion or collapse, but to oscillation about its equilibrium configuration. Such perturbations arise constantly from small motions within the star itself. Consequently, stars of many evolutionary phases exhibit periodic fluctuations in their luminosity (see the first figure). On page 550 of this issue, Zwintz *et al.* (*1*) report on oscillations of stars so young that they are not yet fusing hydrogen into helium. Expanding on earlier studies of such pre–main-sequence stars (*2*), Zwintz *et al.* find that the observed frequencies of oscillation of a star vary with its age, and do so in the way that theory predicts. Thus, the oscillations potentially provide a new chronometer—something greatly needed in the field of early stellar evolution.

The standard way to assess the age of a star is to measure two quantities: its luminosity, L, and its effective (or surface) temperature, $T_{\rm eff}$. L is a measure of the total power emitted by the star, which is inferred from the measured flux on Earth, together with the distance to the star. $T_{\rm eff}$ is determined from a high-resolution spectrum of the starlight. The pattern of absorption lines reflects specific wavelengths where the flux is diminished because of absorption by atoms in the stellar surface. Given L and $T_{\rm eff}$, the star can then be placed in the Hertzsprung-Russell (HR) diagram (see the second figure). The

[1]*Department of Astronomy, University of California, Berkeley, CA 94720, USA.* [2]*Arcetri Observatory, Largo E. Fermi 5, Florence 50125, Italy. E-mail: stahler@berkeley.edu*

Published by AAAS

star's position in the diagram is the indicator of both its age and evolutionary phase.

As stars evolve, both L and T_{eff} change. Thus, the point representing a star will move within the diagram. These paths are predicted by theory and are called pre–main-sequence tracks (*3*). Physically, the young star is contracting, and its diminishing surface area changes its energy output, which comes from the contraction itself. All tracks eventually land on a curve known as the main sequence, where hydrogen ignites and halts contraction. Note that stars of higher mass contract to the main sequence relatively quickly because of their stronger self-gravity.

In principle, assigning an age to a pre–main-sequence star should be relatively straightforward. After using observations to place the object in the HR diagram, the evolutionary track is identified that passes through that point. The star's age—that is, how long it has been contracting—and its mass can then be read off. Applying this procedure not just to one star but to a whole cluster, the resulting collection of ages and masses yields the star formation history of that group.

In reality, however, the situation is more complicated. Young stars are surrounded by copious amounts of dusty cloud gas, which both dims and reddens their light before it reaches us. Discerning the star's true intrinsic luminosity and surface temperature can thus be difficult. In addition, many of these stars have circumstellar disks that may periodically dump matter onto the stellar surface. This accretion process releases energy, which could be misinterpeted as part of the underlying stellar luminosity (*4*). Both problems are ameliorated with stars that either have quickly dissipated their disks or have expelled much of the nearby cloud gas.

In 1998, Marconi and Palla discovered that a subset of pre–main-sequence stars, with masses between 1 and 4 times that of the Sun, can sustain self-excited pulsations (*5*). These pulsations are driven by variations in the opacity of the star's outer layers, where hydrogen and helium are partially ionized. If the star contracts, the opacity increases. As a result, energy emanating from the deep interior is dammed up, causing the star to inflate. The opacity then falls, and the release of excess energy causes the star to shrink, thus restarting the cycle. Whether or not the mechanism operates depends sensitively on the star's effective temperature. If T_{eff} is too low, the ionization region is so deep that it cannot move overlying gas. Conversely, in a star with too high a T_{eff}, the layer is at such a shallow depth that only a small amount of the outgoing luminosity can be absorbed.

Pursuing this line of reasoning, Marconi and Palla showed that there is an "instability strip" in the HR diagram (see the figure). Pre–main-sequence stars that pass through this area are susceptible to the oscillations. Following their prediction, several dozen young pulsating stars have been found. Gratifyingly, the stars indeed all lie within the instability strip. The actual pulsation amplitudes are small, and satellite observations have greatly increased the precision of the measurements in recent years.

Any star lying within the instability strip can oscillate not just at a single frequency, but at many, just as a taut string can vibrate in many normal modes. There is an upper limit to the oscillation frequency, called the acoustic cutoff. At higher frequencies, internal pressure disturbances (that is, sound waves) do not reflect at the star's surface, as is necessary to sustain the oscillation. Instead, these high-frequency waves pass through the surface to the sparser external medium (*6*). In their sample of 34 stars, Zwintz *et al.* focused on the acoustic cutoff frequency, and found that it increases with stellar age, where the latter was gauged from a modified form of the HR diagram.

This observed trend is just what theory predicts. For any star in balance between self-gravity and pressure, a sound wave crosses it in about the same time it would take the object to freely collapse in the absence of pressure. This hypothetical free-fall time is inversely proportional to the square root of the star's mean density. It follows that the frequency of any oscillation mode is directly proportional to the square root of the density. The frequency thus should increase as the star contracts and its density rises, and this is exactly what Zwintz *et al.* found.

Although a reliable measurement of these stellar frequencies requires the precision and sensitivity of a space-based telescope, the resulting age is not fraught with the uncertainties that have plagued the traditional determination of L and T_{eff}. Thus, the path lies open to a new determination of stellar age. Of course, the new chronometer must first be calibrated, through observations of stars that both oscillate and are relatively free of circumstellar matter. The chronometer will be most useful for young clusters populous enough to contain several stars in the proper mass range. Zwintz *et al.* have already started down this road, observing nine members of the NGC 2264 cluster and finding evidence for a substantial age spread in this group.

The finding of Zwintz *et al.* already suggests the utility of the new chronometer. If there is indeed an age spread in NGC 2264, then the parent cloud forming the cluster did so over an extended time. Other clouds presumably spawn stars in a similarly protracted manner. Over the past 15 years, it has been argued that the clouds actually collapse quickly (in a free-fall time) and form their stars in a single burst. Any apparent spread in stellar ages is illusory, an artifact of the various uncertainties mentioned earlier (*7*). A new and more precise chronometer should settle the issue, and thus advance our knowledge of early stellar evolution. ■

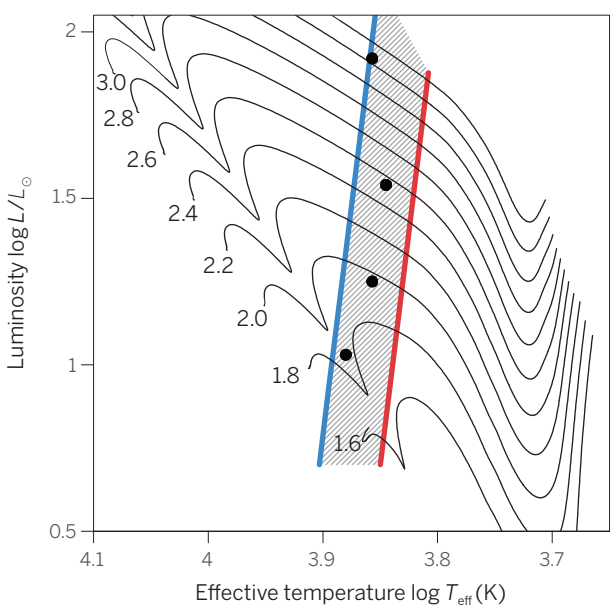

Pulsating young stars in the Hertzsprung-Russell diagram. The solid curves are pre–main-sequence tracks for stars of different masses, here indicated in solar units. The shaded area is the instability strip, as found by Marconi and Palla (*5*). Solid circles represent some of the known pulsators. From top to bottom, the stars range in age from about 1 to 10 million years.

REFERENCES

1. K. Zwintz *et al.*, *Science* **345**, 550 (2014).
2. K. Zwintz, W. W. Weiss, *Astron. Astrophys.* **457**, 237 (2006).
3. S. Stahler, F. Palla, *The Formation of Stars* (Wiley, Weinheim, Germany, 2004), chap. 16.
4. I. Baraffe, G. Chabrier, J. Gallardo, *Astrophys. J.* **702**, L27 (2009).
5. M. Marconi, F. Palla, *Astrophys. J.* **507**, L141 (1998).
6. C. Aerts, J. Christensen-Dalsgaard, D. W. Kurtz, *Asteroseismology* (Springer, New York, 2010), chap. 3.
7. R. D. Jeffries, S. P. Littlefair, T. Naylor, N. J. Mayne, *Mon. Not. R. Astron. Soc.* **418**, 1948 (2011).

10.1126/science.1257301

Published by AAAS

DEVELOPMENT

In Turing's hands—the making of digits

A Turing network controls the periodic pattern of fingers and toes during development

By **Aimée Zuniga** *and* **Rolf Zeller**

Alan Turing is best known as the father of theoretical computer sciences and for his role in cracking the Enigma encryption codes during World War II. He was also interested in mathematical biology and published (*1*) a theoretical rationale for the self-regulation and patterning of tissues in embryos. The so-called reaction-diffusion model allows mathematical simulation of diverse types of embryonic patterns with astonishing accuracy (*1*–*3*). During the past two decades, the existence of Turing-type mechanisms has been experimentally explored and is now well established in developmental systems such as skin pigmentation patterning in fishes, and hair and feather follicle patterning in mouse and chicken embryos (*3*). However, the extent to which Turing-type mechanisms control patterning of vertebrate organs is less clear. Often, the relevant signaling interactions are not fully understood and/or Turing-like features have not been thoroughly verified by experimentation and/or genetic analysis (*3*). Raspopovic *et al.*, on page 566 in this issue, now make a good case for Turing-like features in the periodic pattern of digits by identifying the molecular architecture of what appears to be a Turing network functioning in positioning the digit primordia within mouse limb buds (*4*).

The patterning of digits during vertebrate limb development (i.e., formation of fingers and toes) is a paradigm of vertebrate organogenesis (*5*). Experimental and genetic analysis suggests that graded sonic hedgehog (SHH) signaling—that is, a spatiotemporally morphogen gradient rather than a Turing-type reaction-diffusion mechanism—patterns digit progenitors (see the figure, left) (*5*). However, the periodic nature of the cartilage condensations of the future digits has long hinted that a Turing-type mechanism provides the necessary positional information during autopod (hand and foot) development. Newman and colleagues first proposed that the digit-forming territories are determined by a reaction-diffusion mechanism as defined by Turing (*1*, *6*). There is evidence that Hoxd transcription factors, which are targets of SHH and essential for specifying digit identities, might modulate the periodicity and wavelength of a Turing network (*7*), but the molecular nature of the two postulated Turing morphogens has been a mystery until now.

Raspopovic *et al.* use an elegant combination of transcriptome analysis, functional manipulation of mouse limb buds, and mathematical simulations to show that ligands of the bone morphogenetic protein (BMP) and WNT signaling pathways act as Turing morphogens during digit patterning (see the figure, right). They show that the Turing network consist of these two signaling pathways that act in concert with the *Sox9* transcription factor. The periodic expression of *Sox9* in the autopod territory slightly precedes the appearance of morphologically distinct digit primordia. In addition, the ligand *Bmp2* is expressed in a periodic pattern by the interdigit mesenchyme, and BMP signaling from the interdigit mesenchyme positively regulates the periodicity of *Sox9* expression in the limb bud mesenchymal cells that form the digit ray primordia (*8*). In contrast, WNT signal transduction is highest in the interdigit mesenchyme (i.e., "out-of-phase" with Sox9) and inhibits both *Sox9* expression and cartilage formation (*9*).

These initial results allowed the authors to construct a simple and robust three-node BMP-Sox9-WNT (BSW) Turing network for mathematical simulation of digit formation in growing limb bud domains (see the figure, lower schemes). Including the modulatory effects of fibroblast growth factor (FGF) signaling and Hoxd transcription factors (*7*) in the Turing network topology resulted in accurate simulation of the sequence by which the Sox9-positive digit primordia formed in developing autopods of mouse embryos. Experimental inhibition of either BMP or WNT signal transduction disrupted this periodicity, resulting either in loss of *Sox9* expression (inhibiting BMP), or homogeneous (inhibiting WNT) rather than periodic *Sox9* expression, exactly as predicted by the simulations. Gain- and loss-of-function experiments further supported the striking similarities of the

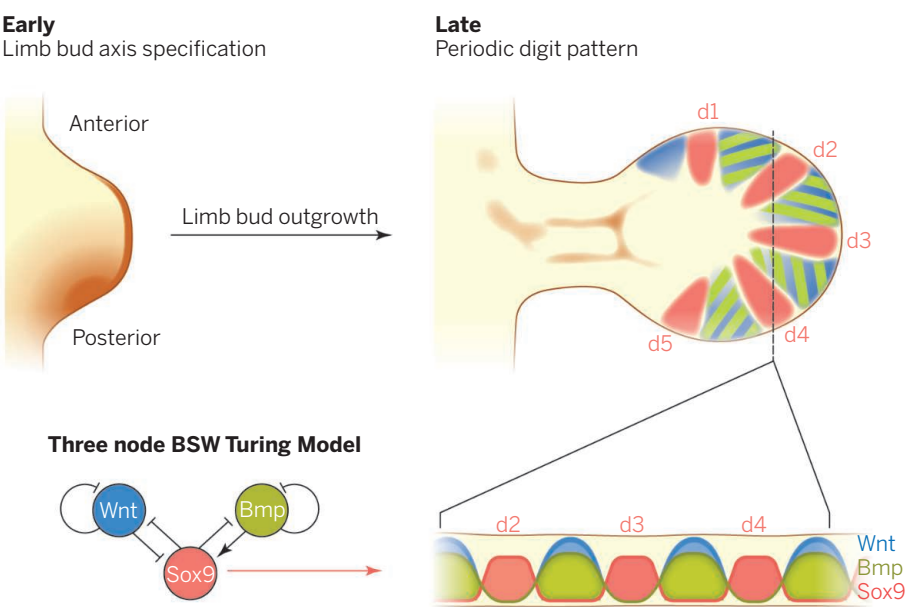

How to make a hand. The antero-posterior limb bud axis is specified early in development by posterior SHH signaling (upper left scheme, graded SHH signaling indicated in orange-brown). A three-node Turing network composed of the WNT and BMP signaling pathways and the Sox9 transcriptional regulator expressed by digit progenitors interact to determine the periodic digit pattern (lower schemes). WNT signal transduction (blue) inhibits *Sox9* in the prospective interdigit, while the periodic *Bmp2* expression (green) in the interdigit tissue stimulates *Sox9* expression in the mesenchymal cells that form the digit primordia (red, upper right scheme). The periodic Sox9-positive domains that give rise to digits are indicated as d1 to d5 with anterior to posterior sequence (thumb to little finger).

Developmental Genetics, Department of Biomedicine, University of Basel, Mattenstrasse 28, CH-4058 Basel, Switzerland. E-mail: rolf.zeller@unibas.ch; aimee.zuniga@unibas.ch

Published by AAAS

mathematical simulations with the experimentally observed changes in Sox9 periodicity and digit patterns.

Together with the previous study by Sheth *et al.* (*7*), the analysis by Raspopovic *et al.* provides strong experimental support for a Turing-type mechanism controlling the emergence of the periodic pattern of the Sox9-positive digit primordia in mouse limb buds. Identification of the BMP and WNT signaling pathways suggests that it may be possible to genetically manipulate the BSW Turing network. As the antero-posterior (AP) polarity of the limb bud mesenchyme and digit progenitors are specified much earlier by graded SHH signaling (see the figure, left) (*10*), it will be important to understand which mechanism links this early AP axis polarization to the BSW Turing network that controls the stereotypic pattern of the digit condensations during autopod development. These early and late patterning systems can be genetically uncoupled, as digit condensations can occur in the absence of the SHH signaling system and disruption of the Turing network results in loss of all digit primordia without effects on early AP patterning (*4*, *11*, *12*). During evolution of tetrapod limbs, the two mechanisms must have become interlinked as digit numbers were reduced from rudimentary polydactyly (six or more digits) to pentadactyly (five digits with distinct AP identities). One likely link involves the SHH-mediated regulation of *Hoxd* expression in limb buds. This in turn modulates the BSW Turing network and, in concert with FGF signaling, confers robustness on the periodic expression pattern of *Sox9* (*4*, *7*).

Now that we know that a Turing-type mechanism controls the periodicity of digits, the next challenge will be to determine if Turing-type mechanisms are involved in coordinating the formation of digits with the patterning of other limb tissues such as tendons, ligaments, and the musculoskeletal anatomy. ■

PHOTO: JANICE MURRAY AND MAIZELS LABORATORY/UNIVERSITY OF EDINBURGH

REFERENCES

1. A. M. Turing, *Philos. Trans. R. Soc. Lond. B Biol. Sci.* **237**, 37 (1952).
2. A. Gierer, H. Meinhardt, *Kybernetik* **12**, 30 (1972).
3. S. Kondo, T. Miura, *Science* **329**, 1616 (2010).
4. J. Raspopovic, L. Marcon, L. Russo, J. Sharpe, *Science* **345**, 566 (2014).
5. R. Zeller, J. López-Ríos, A. Zuniga, *Nat. Rev. Genet.* **10**, 845 (2009).
6. S. A. Newman, H. L. Frisch, *Science* **205**, 662 (1979).
7. R. Sheth *et al.*, *Science* **338**, 1476 (2012).
8. R. D. Dahn, J. F. Fallon, *Science* **289**, 438 (2000).
9. D. ten Berge, S. A. Brugmann, J. A. Helms, R. Nusse, *Development* **135**, 3247 (2008).
10. J. Zhu *et al.*, *Dev. Cell* **14**, 624 (2008).
11. J. D. Bénazet *et al.*, *Development* **139**, 4250 (2012).
12. P. te Welscher *et al.*, *Science* **298**, 827 (2002).

10.1126/science.1257501

IMMUNOLOGY

How helminths go viral

Cellular signals during helminth infections can skew the immune response to favor viral spreading

By **Rick M Maizels**[1] *and* **William C Gause**[2]

Research into infectious diseases is generally highly reductionist, focusing on the disease-causing agent while meticulously excluding extraneous factors, such as unrelated pathogens. But the real world is quite different, with multiple concurrent microorganisms (viruses, bacteria) and macro-organisms (parasites), each with differing dynamics and impacts on the host (*1*). Many of these agents are relatively neglected, especially those such as the helminth worms (see the photo). They also predominantly affect people in low-income tropical environments and influence susceptibility to a range of other infectious diseases (*2*). On pages 573 and 578 of this issue, Reese *et al.* (*3*) and Osborne *et al.* (*4*), respectively, provide fine detail on how helminth worms can substantially enhance and reactivate viral infection, with major health implications for tropical medicine.

Heligmosomoides polygyrus

Reese *et al.* found that a latent murine herpesvirus infection in macrophages was reactivated by either of two helminth worm species. Because helminths are strong activators of T helper cell 2 (T_H2) (*5*), the authors propose a skewing of immunity toward the key T_H2 cytokines interleukin-4 (IL-4) and IL-13, and away from the antiviral cytokine interferon-γ (IFN-γ). T_H2 environments also stimulate the "alternative activation" of macrophages through the IL-4 receptor toward an "M2" state (*5*, *6*). Notably, in helminth-infected mice, many virally infected macrophages expressed the enzyme arginase, a marker of M2 macrophages that is expressed in response to IL-4 receptor activation. Exposure to IL-4 greatly increased viral replication in macrophages in vitro. In addition, either IL-4 or IL-13 (both bind to the IL-4 receptor) replicated the effects of worm infection, but not in mice lacking signal transducer and activator of transcription 6 (STAT6), a signaling molecule that is activated by the IL-4 receptor. Moreover, IL-5, a cytokine that is released by T_H2 cells during helminth infection but does not activate STAT6, failed to reawaken the virus from latency. The ability of IL-4 to promote viral growth was directly antagonized by IFN-γ, however.

How does herpesvirus break out of latency in response to IL-4? Reese *et al.* show that in infected macrophages, STAT6 binds to the promoter of *gene50*, a viral gene associated with exit from latency (see the figure). This was the case both for murine γ-herpesvirus and for the related human Kaposi's sarcoma–associated herpesvirus. This surprising degree of evolutionary conservation presumably reflects an adaptation that permits the viruses to sense the immunological status of their host. Thus, when the cytokine environment is dominated by IFN-γ (which activates a spectrum of antiviral mechanisms), the virus remains latent; but if the coast is clear and IL-4 prevails, the virus exits the latent state.

[1]*Institute for Immunology and Infection Research and Centre for Immunity, Infection and Evolution, University of Edinburgh, Edinburgh, UK.* [2]*Center for Immunity and Inflammation, Department of Medicine, New Jersey Medical School, Rutgers–the State University of New Jersey, Newark, NJ, USA. E-mail: r.maizels@ed.ac.uk*

Published by AAAS

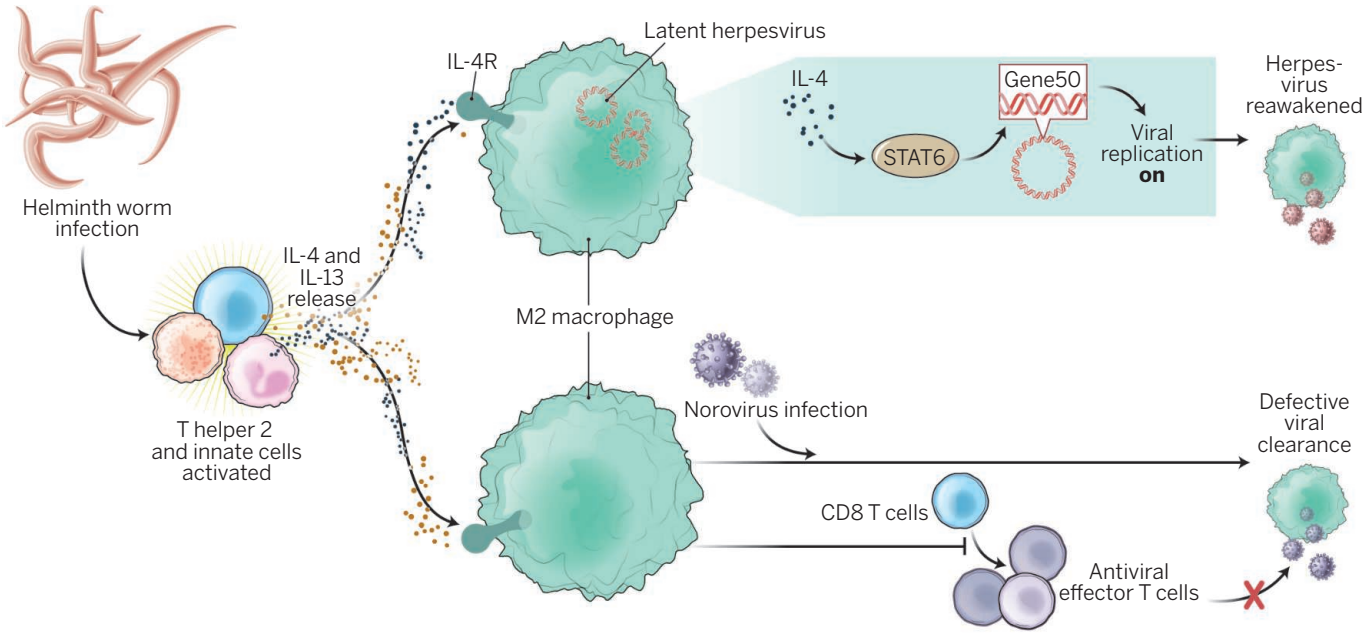

Altered immunity. Helminth infection activates T_H2 cells to release IL-4 and IL-13, both of which ligate the IL-4 receptor (IL-4R) on M2 macrophages. In M2 macrophages harboring latent herpesvirus, the IL-4R activates host cell STAT6, which then acts directly on the key viral gene that initiates viral replication. In another scenario, M2 macrophages activated by IL-4 and/or IL-14 directly inhibit the production of virus-specific T cells. Thus, subsequent infection by a virus (norovirus shown) is not controlled.

The study of Osborne *et al.* follows a similar storyline of helminth exacerbation of infections, but with a quite different plot. The authors also linked greater viral growth to the alternatively activated M2 phenotype of the host macrophage. Moreover, during helminth infections, a range of T cell responses to viral infection are severely down-regulated. Although helminth-associated T cell hyporesponsiveness develops through multiple routes (*7*), in the setting of a viral infection (in this case, by norovirus), Osborne *et al.* connect the M2 macrophages to inhibition of the T cell proliferation. In the absence of STAT6, T cell functions were rescued and viral loads diminished, whereas exposing macrophages to IL-4 increased viral production in the cells. Mice receiving IL-4–treated macrophages showed reduced T cell responses alongside higher viral titers. This regulatory function of M2 macrophages in this setting was further linked to a prominent secreted product, Ym-1, whereas inhibition of other macrophage products, including arginase, were not found to differ in helminth promotion of infection.

Osborne *et al.* also addressed the question of whether the effect of helminths on virus load was mediated by direct modulation of the host immune system, or was acting indirectly through changes to the commensal intestinal bacterial load. Changes in microbiota populations in mice following helminth infections have been observed (*8*, *9*), but Osborne *et al.* found that even in germ-free mice, the introduction of a helminth infection exerted the same depressive effect on immunity to the virus. It will be of interest to examine the extent to which helminth-induced changes in the intestinal microbiome may affect host responses to other viruses and other types of pathogens.

Beyond the similarities, the studies of Reese *et al.* and Osborne *et al.* have fascinating contrasts. In the herpesvirus system, an exquisite adaptation of the viral genome is a promoter sequence that recognizes STAT6 as well as the prevailing T_H2 environment of a helminth-infected host. Although evolutionarily conserved, this mechanism is operative only in this set of related viruses. However, helminth infections also drive alternative activation of macrophages through STAT6, generating virus-nonspecific pathways that inhibit the generic T cell response—a mechanism that would impede immunity to all viral challenges. These quite different effects of helminth infection on viral immunity are likely the tip of the iceberg in terms of the range of mechanisms through which helminths influence immune responses to microbial pathogens. Increasing evidence suggests that these dynamic interactions resulting from helminth coinfections may have substantial effects on susceptibility to global microbial pathogens. In particular, recent studies suggest that urogenital schistosomiasis may increase susceptibility of African women to HIV (*10*). However, it should be kept in mind that the type 2 immune response stimulated by helminths may also mitigate tissue damage during microbial infections by reducing harmful inflammation and directly enhancing wound repair (*11*).

The findings of Reese *et al.* and Osborne *et al.* deepen our perspective of the complexity of infectious diseases, given that multiple colonization is ubiquitous in nature and the interactions between pathogens, commensals, and immunity operate at every level, from genes to tissues and systemic cell populations. Learning more about each of the players and their molecular and cellular interactions will be essential if we are to avoid any unintended consequences of antihelminth drug treatment or of live helminth therapy in humans (*12*). ■

REFERENCES

1. E. C. Griffiths, A. B. Pedersen, A. Fenton, O. L. Petchey, *Proc. Biol. Sci.* **281**, 20132286 (2014).
2. P. Salgame, G. S. Yap, W. C. Gause, *Nat. Immunol.* **14**, 1118 (2013).
3. T. A. Reese *et al.*, *Science* **345**, 573 (2014).
4. L. C. Osborne *et al.*, *Science* **345**, 578 (2014).
5. J. E. Allen, R. M. Maizels, *Nat. Rev. Immunol.* **11**, 375 (2011).
6. T. Kreider, R. M. Anthony, J. F. Urban Jr., W. C. Gause, *Curr. Opin. Immunol.* **19**, 448 (2007).
7. M. D. Taylor, N. van der Werf, R. M. Maizels, *Trends Immunol.* **33**, 181 (2012).
8. S. T. Walk, A. M. Blum, S. A. Ewing, J. V. Weinstock, V. B. Young, *Inflamm. Bowel Dis.* **16**, 1841 (2010).
9. S. Rausch *et al.*, *PLOS ONE* **8**, e74026 (2013).
10. E. F. Kjetland *et al.*, *Int. J. STD AIDS* 10.1177/0956462414523743 (2014).
11. W. C. Gause, T. A. Wynn, J. E. Allen, *Nat. Rev. Immunol.* **13**, 607 (2013).
12. J. V. Weinstock, D. E. Elliott, *Int. J. Parasitol.* **43**, 245 (2013).

10.1126/science.1258443

ILLUSTRATION: V. ALTOUNIAN/*SCIENCE*

Published by AAAS

ECONOMICS

Global manufacturing and the future of technology

Where you manufacture changes what you get

By **Erica R. H. Fuchs**

The global locus of manufacturing has been changing dramatically over the last three decades, driven by industrializing nations, most prominently China. Classical economics suggests that global productivity gains achieved by shifting the location of manufacturing will outweigh the losses (*1*). But shifts in the global locus of manufacturing may affect not just production costs, but the nature and pace of technological change.

Moving manufacturing to a different nation might hinder innovation at home: increased distance, electronic dependence, time zone changes, and national differences reduce knowledge flows (*2*, *3*). Firms can benefit by locating near one another (*4*), and this "commons" can be industry specific. Once a critical mass of supplier and producer firms in an industry moves overseas, domestic manufacture is less likely to be competitive (*5*).

POLICY

When manufacturing moves offshore, will research and development (R&D) follow? Evidence suggests that, although some middle-stage innovation may move, to date, the leading edge of innovation in most industries has remained in the United States (*6*, *7*). Further, economic theory suggests that shifts in manufacturing may hurt wages in nations that lose manufacturing, but global innovation and productivity gains will not suffer (*8*).

However, recent work shows that moving the locus of manufacturing overseas, in particular to developing countries, may reduce innovation, domestically and globally, at least in the short to medium term (*9*–*11*). Production characteristics (wages, yields, downtimes, materials, and organization of production) can differ greatly across nations (and in particular between developed and developing ones), changing which product developments are profitable for firms to pursue. In two cases—automobile bodies and high-end optoelectronic components for communications—when U.S. firms shifted production to developing East Asia, products developed in the U.S. based on the most advanced technologies were no longer immediately profitable. The overseas firms stopped producing these advanced products and, in optoelectronics, also stopped innovation in the most advanced products overseas and in the United States (*9*–*11*).

NOT ALL TECHNOLOGIES ARE CREATED EQUAL. The impact of manufacturing location on global technology development is shaped by three constraints: (i) the largest number of manufacturing facilities economically sustainable for a firm; (ii) the location of design expertise and whether the designers need to experiment regularly on and be physically present at the production line; and (iii) the importance, security, and enforcement of intellectual property rights.

The manufacture of high-end optoelectronic components for communications shows how policy can shape cutting-edge technologies for firms facing the most constraints. First, manufacturing and product innovation are bound together. Production yields are low, and the process is more an art than a science, with engineers regularly called to the shop floor. Second, the market is small relative to the production volumes required to achieve economies of scale. Firms can afford only one manufacturing facility, and there are not enough engineers in developing East Asia with capabilities to support local production of the new technology. Therefore, firms must choose between producing the most advanced technology in the United States or older technology in developing East Asia (see the chart). Expected changes in technology and production in the two regions over the short to medium term have typically increased the cost advantage of the old technology produced in developing East Asia over all other options (*9*).

Challenges from low yields and separating design from manufacturing are common for early-stage products in such industries as semiconductors (*12*), specialty chemicals, and pharmaceuticals, in which product innovations are fundamentally linked to advances in manufacturing. A small market compared with the production required for economies of scale is also common for such firms. These constraints affect a subset of early-stage high-technology start-ups.

The United States continues to lead innovation in many technologies. However, with the decline of U.S. corporate R&D laboratories and large firms' increased reliance on innovations of small- and medium-sized firms, long-term research faces new challenges. In the case of high-end components, the majority of manufacturers have gone offshore and abandoned production of the most advanced technology products, despite their promise for accessing new, larger markets. All public firms that remained active in the industry moved offshore. The firms that stayed onshore and pursued the most advanced technology were privately owned and venture- or government-backed (*11*). These findings complement evidence that private equity may have positive effects on firms' innovation (*13*); public firms may be less innovative (*14*).

Certain factors—such as the ability to separate design from manufacturing, minimum efficient plant size, and transportation costs—are largely technically determined. Other factors—such as market size, number of competitors, and the heterogeneity of consumer markets—are shaped by other social, political, and economic forces. Governments' levers to influence constraints faced by firms include funding of early-stage start-ups (shaping market forces within the industry), procurement (shaping market size), workforce education (shaping the locus of knowledge), and funding

ILLUSTRATION: ESENKARTAL/ISTOCK VECTORS/GETTY IMAGES

Department of Engineering and Public Policy, Carnegie Mellon University, Pittsburgh, PA 15213, USA. erhf@andrew.cmu.edu

Published by AAAS

Downloaded from www.sciencemag.org on August 11, 2014

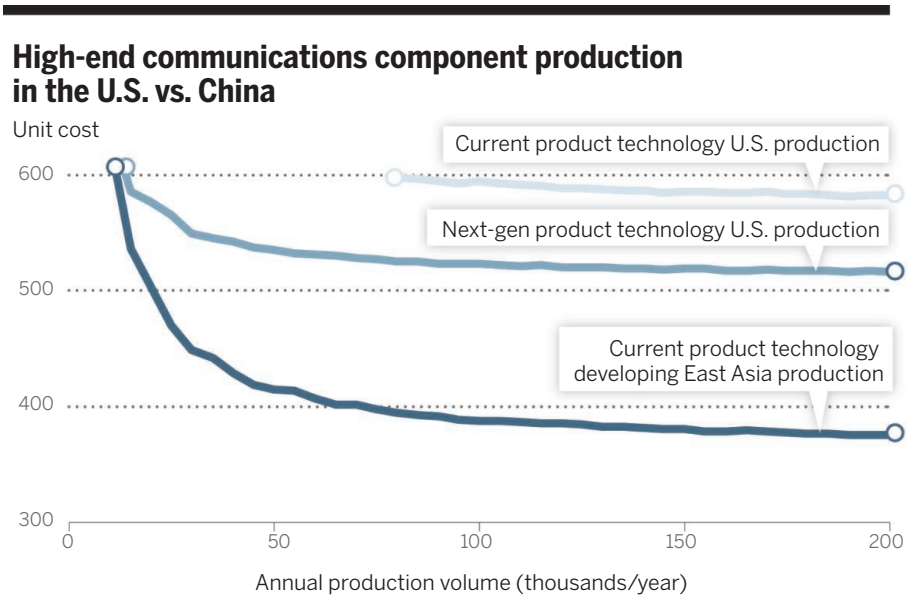

Lines shown represent average capabilities across firms in the industry. [Adapted from (*9*)]

of R&D (shaping those constraints that are technologically determined). The time scale by which these levers can affect change varies substantially.

Some government actions, such as those related to the market, can have immediate ramifications. Government funding of highly constrained start-ups can help alleviate market pressures. For example, because of needs within the Department of Defense, the U.S. Defense Advanced Research and Development Agency (DARPA) funded companies to develop and, it was hoped, subsequently to produce the most advanced optoelectronic communication technologies.

Government funding of workforce education and technological advancement takes longer to have an effect, and outcomes are uncertain. There are, however, historical precedents. DARPA, the National Science Foundation, and the Office of Naval Research played critical roles (*15*) in facilitating the separation of central processing unit (CPU) design and manufacturing in the semiconductor industry, which enabled university researchers to develop new designs without having an expensive fabrication facility. It eventually enabled production to move overseas to emerging markets. However, even in semiconductors, design and manufacturing are integrated when changes are introduced in the nanoscale "devices" (e.g., transistors) that comprise the CPUs or when changes require coordination between device or material improvements and CPU architecture.

Increased global participation in manufacturing need not be universally detrimental for innovation. In less-constrained cases, global manufacturing can increase opportunities and incentives to innovate. For example, automotive manufacturers have found production sufficiently standardized to separate design of advanced automobile bodies from manufacturing, and composite-materials expertise is available outside the United States. The plant size required for economies of scale allows automobile manufacturers to efficiently produce for regional markets. Automobile bodies' high transportation costs and global market heterogeneity build on these incentives to produce regionally for regional markets. Policies that constrain choices of body manufacturing locations would reduce opportunities and incentives for innovation.

To take advantage of economies of scale in both production and R&D, companies with multiple product offerings develop "platforms" consisting of a series of parts shared across larger families of products. For example, one-quarter of the world's vehicles are made in China (*16*) where, since 2009, automobile sales have exceeded those in the United States. Chinese consumers may have a greater willingness to pay for electrified vehicles than consumers in the United States, given regulatory and physical infrastructure in both countries (*17*). Technologies designed for sale in China are unlikely to be used only in China. Because of these platform economies, the global shift in the locus of production and demand for personal vehicles may lead to greater economic incentives and opportunities for electric vehicles globally. This has potential to enhance economic growth, increase national energy security (through reduced oil use), and (depending on efforts to reduce air emissions from electricity generation) improve the global environment.

TECHNOLOGICALLY NUANCED POLICY. It will be critical to avoid a "one-size-fits-all" policy approach, both across technologies and across nations, because policies that enhance one sector can undermine another. One important issue, especially for advanced technologies, is integrating technical and industry expertise into government decision-making. DARPA, for example, brings technical experts from academia and industry into limited, 3- to 5-year positions as program managers, from which they fund new technology directions in academia and industry (*18*). In the Semiconductor Research Corporation (a U.S. public-private partnership), industry articulates its performance needs, finds supporting government funding, and funds academics to develop new technologies to achieve these goals (*19*). With manufacturing continuing to shift to developing nations, and with the global future of technology at stake, nations have reason to act for themselves and multilaterally. ■

REFERENCES AND NOTES

1. D. Ricardo, in *The Works and Correspondence of David Ricardo*, P. Sraffa, Ed. (Univ. of Cambridge Press, Cambridge, 1953).
2. C. Gibson, J. Gibbs, *Adm. Sci. Q.* **51**, 451 (2006).
3. J. N. Cummings *et al.*, *Inf. Syst. Res.* **20**, 420 (2009).
4. A. Marshall, *Principles of Economics* (Macmillan, London, 1890).
5. G. Pisano, W. Shih, *Producing Prosperity* (Harvard Business Review Press, Cambridge, MA, 2012).
6. J. Macher, D. Mowery, *Innovation in Global Industries* (National Academies Press, Washington, DC, 2008).
7. L. Branstetter, G. Li, F. Veloso, in *The Changing Frontier: Rethinking Science and Innovation Policy*, A. Jaffe and B. Jones, Eds. (forthcoming Univ. of Chicago Press, Chicago, n.d.), chap. 1; http://papers.nber.org/books/jaff13-1.
8. P. Samuelson, *J. Econ. Perspect.* **18**, 135 (2004).
9. E. R. H. Fuchs, R. E. Kirchain, *Manage. Sci.* **56**, 2323 (2010).
10. E. R. H. Fuchs *et al.*, *Int. J. Prod. Econ.* **132**, 79 (2011).
11. C. Yang, R. Nugent, E. Fuchs, *Gains from Others' Losses* (Carnegie Mellon Univ. working paper, Pittsburgh, PA, 2013); http://papers.ssrn.com/sol3/papers.cfm?abstract_id=2080595.
12. C. Lecuyer, *Making Silcon Valley* (MIT Press, Cambridge, MA, 2005).
13. J. Lerner *et al.*, *J. Finance* **66**, 445 (2011).
14. S. Bernstein, Does going public affect innovation? (Research paper no. 2126, Stanford Graduate School of Business, Stanford, CA, 2012).
15. National Research Council, *Funding a Revolution: Government Support for Computing Research* (National Academies Press, Washington, DC, 1999).
16. International Organization of Motor Vehicle Manufacturers (OICA), World Motor Vehicle Production by Country and Type (2013); www.oica.net/category/production-statistics/.
17. J. Helveston *et al.*, "Will subsidies drive electric vehicle adoption in China and the United States?" (Carnegie Mellon Univ. working paper, Pittsburgh, PA, 2013); www.cmu.edu/me/ddl/publications/2014-WP-Helveston-etal-EVs-in-China.pdf.
18. E. Fuchs, *Res. Policy* **39**, 1133 (2010).
19. R. Burger, *Cooperative Research: The New Paradigm* (Semiconductor Research Corporation, Research Triangle Park, NC, 2014); www.src.org/about/p001960.pdf.

ACKNOWLEDGMENTS

E.R.H.F. is funded by the NSF Science of Science and Innovation Policy Program, DARPA, and the National Institute of Standards and Technology. E.R.H.F. thanks D. Andersen, D. Hounshell, G. Morgan, and anonymous reviewers for feedback.

10.1126/science.1250193

Published by AAAS

OPEN BIOLOGY

Rebels or profiteers?

Biohackers
The Politics of Open Science
Alessandro Delfanti
Pluto Press, 2013. 168 pp.

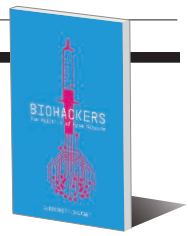

By **Stefano Golinelli**[1] *and* **Luc Henry**[2]

"Open," the new black of political controversy, has become ubiquitous in contemporary debates surrounding scientific practices. Just as software activists managed to free information technologies from the realms of academia and industry, today some biologists believe their science would have a larger impact if carried out in the open. However, most scientists still have a narrow conception of where the "open revolution" comes from and what it means.

What does "open science" have in common with, for example, "open access," "open-source," "open data," or "open innovation"? Probably less than what billionaire scientist-entrepreneur Craig Venter shares with Italian virologist Ilaria Capua or do-it-yourself (DIY) hobbyists who carry out biotech experimentations in their garage. In *Biohackers*, Alessandro Delfanti considers the activities of hobbyists, Venter, and Capua to explore the transformations that postgenomic biology has brought to scientific practices and the impact of information technologies on the life sciences.

Besides offering numerous tools for analyzing the ever-growing amounts of data, the digital universe and Internet have inspired new approaches to conducting research and disseminating scientific discoveries as well as spread competition and rebellion at an unprecedented scale and pace. It is in this context that biohacking was born. Biohackers may be "rebels" or "profiteers," but they do not simply hack DNA to crack and manipulate the code of life. Delfanti, a sociologist and open-science advocate at McGill University, describes biohacking as a set of heterogeneous attempts to free biology from its closed contemporary socio-institutional context.

In their own ways, each of the three examples Delfanti chose personifies the figure of the biohacker: Capua, a rebel, challenged the World Health Organization policy on access to avian flu data and won her battle against this international institution. Venter,

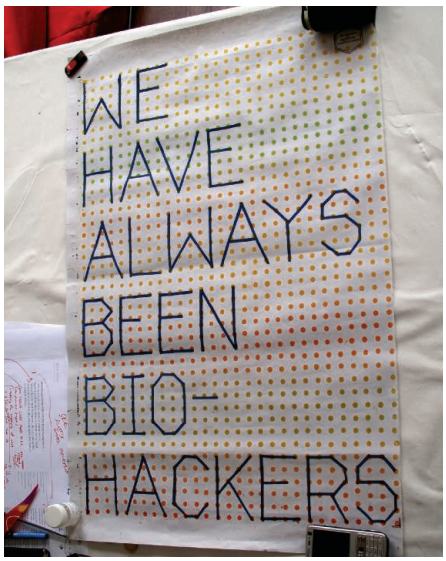

a profiteer, financed spectacular open-access genomic initiatives while filing controversial patents for potential applications in synthetic biology. Members of the DIY biology movement, however, certainly provide the most interesting case. Half-rebel, half-profiteers, these self-identified biohackers participate in a highly diverse set of activities, all of which are aimed at translating open-source principles into the life sciences.

From his consideration of these examples, and in spite of his personal political commitment to openness, Delfanti elegantly dismisses dominant narratives that portray open science (in particular, open biology) as an up-to-date version of the traditional Mertonian norms now endangered by corporate neoliberalism. He suggests instead that the changes he discusses are actually a complex pollination of the life sciences by information technologies, emerging from what he calls a "cultural feedback."

In other words, biohackers' openness is much more than freely sharing information to challenge the tragedy of the anticommons induced by the increasing scope of intellectual property rights (*1*). These elements are further remixed with other distinctive, and sometimes conflicting, features of the hacker's ethos, such as intense relations with the media, hedonism, creativity, entrepreneurial drive, communitarian spirit, and radical resistance to external interference (be that from public regulations, corporate interests, or academic institutions).

Although in political terms, open science is often portrayed as a rebellion against neoliberal ideologies, Delfanti invites readers to think of it as an "a-capitalist" project (*2*), which may even extend the scope of capitalist exploitation. He warns us that "in a world in which openness, flexibility and freedom from bureaucracies and cooperation are elements that belong to a capitalistic mode of organising labour and production, we must rethink any easy commitment to open science as good per se." Just as entrepreneurs of the sharing economy have amputated the reciprocity bonds of the Internet-based gift economy (*3*), companies such as 23andMe are recycling open practices to create value based on an asymmetric relationship with their customers (*4*).

Recent years have witnessed the emergence of many more important bottom-up life science initiatives, such as PatientsLikeMe, that would have surely enriched Delfanti's portrait, which sometimes appears to excessively rely on interpretative frameworks developed with respect to the software hackers (*5*). Nonetheless, the book offers an insightful sociological account of recent scientific transformations and a compelling invitation to think of biology as a social system, in which technical issues are mediated by cultural paradigms and social, economic, and institutional interests.

By carefully avoiding making predictions about the future impact of open biology, Delfanti brings fresh air to an overpoliticized debate. *Biohackers* will likely be a source of disappointment for some naïve activists. But as an early account and interpretation of open-biology phenomena, the book certainly presents a neutral, dynamic, and convincing perspective. Their motivations may well be diverse and potentially conflicting, but it cannot be denied that Delfanti's biohackers are playing constitutive roles in the ways science will be produced, disseminated, rewarded, and perceived in the 21st century.

[1]*Rural Sociology Group, School of Social Sciences, Wageningen University, Netherlands.* [2]*Institute of Chemical Sciences and Engineering, École Polytechnique Fédérale de Lausanne, 1015 Lausanne, Switzerland. E-mail: luc.henry@epfl.ch*

REFERENCES AND NOTES

1. M. A. Heller, R. S. Eisenberg, *Science* **280**, 698–701 (1998).
2. www.choike.org/nuevo_eng/informes/2623.html.
3. www.salon.com/2014/03/14/sharing_economy_shams_deception_at_the_core_of_the_internets_hottest_businesses.
4. M. Levina, *J. Clin. Outcomes Manag.* **9**, A06 (2010); http://jcom.sissa.it/archive/09/01/Jcom0901(2010)A06.
5. G. Coleman, *Coding Freedom: The Ethics and Aesthetics of Hacking* (Princeton Univ. Press, Princeton, NJ, 2012).

10.1126/science.1257253

PHOTO: COURTESY THE CENTER FOR GENOMIC GASTRONOMY

Downloaded from www.sciencemag.org on August 11, 2014

Published by AAAS

SOCIAL SCIENCES

Links in our past

By **Brian C. Keegan**

Steven Cassedy's *Connected* covers an age of profound technological change when "social" prefixed every buzzword on the lips of journalists and scholars and old institutions struggled against highly networked organizations. Neither a hagiography of early 21st-century startup culture nor a manifesto for 21st-century science, the book offers a wide-ranging review of converging technological, cultural, and even theological developments in the United States at the turn of the 20th century. Lest we put too much stock in bromides about the recent flatness of the world, this history contextualizes the developments that created a vastly more interconnected social world more than a century ago.

Cassedy argues that 19th-century Americans increasingly lived within interconnected networks that offered both promise and constraint. These not only included transportation and telecommunication systems that we recognize today as complex sociotechnical assemblies; Cassedy also identifies more subtle changes that embedded individuals within networks of interacting biological elements, complex technical standards, and sweeping new social ideas. He holds that the conveniences of modernity have cost us a loss of individual autonomy as we have become embedded in ever more pervasive networks. Although the book offers an anthology of rich and diverse case studies, few social scientists will be surprised by Cassedy's conclusion that social structures such as networks simultaneously enable and constrain individual agency.

The first of the book's sections, "Body and Mind," considers how scientific and medical advancements led to a popular reimagination of the self as networks of interconnected cells, the mind became a network of both physical neurons and psychological desires, and the public health movement made one responsible for the health of others. Cassedy then discusses the "new physical world" composed of individuals networked through standardized time, houses networked through municipal infrastructures, and consumers networked through globalized supply chains. The final section, "The Secular, Ecumenical Collective," covers individuals networked by their genes to new transnational racial concepts, by their religion to care for collective justice rather than individual salvation, and by the state through new regulations and national identities. Throughout, Cassedy narrates each episode using books, lectures, and newspapers of the era while sprinkling in literary Easter eggs and surprising historical coincidences. These texts reflect the popular consensus among scholars, journalists, and activists of the time, who viewed their social world as increasingly resembling a network, organism, or other evocative analogy of interconnected complex systems migrating out from contemporaries' scientific discoveries and technological advancements.

Although the concept of networks should be foundational to the book's argument, there is little for network scientists to digest here. Cassedy offers perfunctory definitions in the preface and alludes to terms such as nodes, links, and hubs throughout, but his concept of networks implies a ubiquitous and homogeneous connectivity rather than the complex structures observed in social networks. There are no references to social network theories, nor does the book provide historical network data or integrate biological relationships, technical infrastructures, and group associations into something more than a paradox of autonomy. Somewhat ironically, the book never connects to social network theory's pedigrees from turn-of-the century sociology, psychology, and graph theory (*1*). And the author's account would have been strengthened had he tapped the rich scholarship on the networked nature of contemporary life [e.g., (*2*)] and historical studies that illuminate the emergence and influence of what we now term social networks in political alliances and trade [e.g., (*3*, *4*)].

Despite its faults, *Connected* shines in the chapter "The Network of Spatialized Time." Whereas textbooks teach that standardized time arose from the need for railroads to coordinate schedules, Cassedy identifies additional factors such as political demands for reform in response to railroads' horrific safety records, technological changes that allowed mass-produced mobile timepieces, and the needs for coordinating social and economic life: "The pocket watch links you through your jeweler, through the synchronized clocks in your place of business, through the clock above the Broadway entrance to Macy's..., to the Naval Observatory in Washington. ... [Time] spoke through the millions of [watches], linking the individual owners of these devices with one another." This remarkable accomplishment serves as an important benchmark against which we should evaluate the effectiveness of contemporary mobile devices at providing affordable, widely available, and accurate products for coordinating our social lives. While Cassedy's book unfortunately does not connect to social network concepts or contemporary networked aspirations and anxieties, it may prove a useful source of succinct social histories about our highly networked ancestors.

The reviewer is at the College of Social Sciences and Humanities, Northeastern University, 360 Huntington Avenue, Boston, MA 02115, USA. E-mail: b.keegan@neu.edu

Connected
How Trains, Genes, Pineapples, Piano Keys, and a Few Disasters Transformed Americans at the Dawn of the Twentieth Century
Steven Cassedy
Stanford University Press, 2014. 339 pp.

REFERENCES

1. L. C. Freeman, *The Development of Social Network Analysis: A Study in the Sociology of Science* (Empirical, Vancouver, 2004).
2. L. Raine, B. Wellman, *Networked: The New Social Operating System* (MIT Press, Cambridge, MA, 2012).
3. J. F. Padgett, C. K. Ansell, *Am. J. Sociol.* **98**, 1259 (1993).
4. C. Wetherell, *Int. Rev. Soc. Hist.* **43** (suppl. S6), 125 (1998).

10.1126/science.1255973

PHOTO: UNDERWOOD & UNDERWOOD/CORBIS

Downloaded from www.sciencemag.org on August 11, 2014

Published by AAAS

LETTERS

Edited by **Jennifer Sills**

China's robotics successes abound

THE IN BRIEF NEWS STORY "China's lunar rover languishes" (6 June, p. 1067) should be put in the context of China's ambitious robotics development, which began more than 40 years ago. Recent advances in robotics have allowed China to explore extreme environments such as space, natural disaster areas, the deep sea, and the North and South Poles. The lunar rover Yutu ("Jade rabbit"), discussed in the News

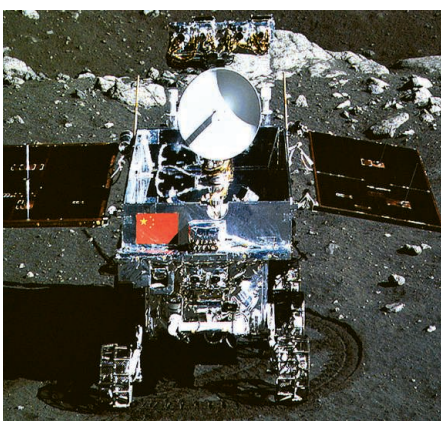

Yutu, China's lunar rover.

PHOTO: CHINA STRINGER NETWORK/REUTERS

story, landed successfully on the Moon in December 2013. Robotic manipulators and mobile robots are envisaged to play an important role in the ongoing Chinese Space Station project and future missions to the Moon and Mars. Three different types of robots were deployed to assist the search and rescues after the Ya'an earthquake in 2013 (*1*). In deep-sea exploration, Chinese manned submersible vessel Jiaolong reached a record depth of 7062 m in 2012 (*2*). China also applied robotic technologies during various expeditions to the Poles, including to the Arctic in 2008 and 2010 and to Antarctica in 2007 and 2012 (*3*, *4*).

Recent events, such as Yutu's locomotion problem and the absence of underwater robots during the search for the missing flight MH370, reveal the limitations of existing robotic technologies and highlight directions for potential improvement. Chinese roboticists acknowledge the technical challenges in achieving robust, reliable, and autonomous operations in space and the deep sea. Their approach has been to adopt state-of-the-art solutions proposed by the international robotics community rather than relying on home-grown innovations. This has worked particularly well with developing software-based techniques such as control and computing algorithms. The biggest weakness in advanced robotics in China is in high-performance mechatronics. This is because China lacks high-precision, industrial manufacturing capabilities, and as a result, depends on expensive imports of components from the United States, Europe, and Japan. The robotics community in China is striving to improve their influence in large national R&D programs as well as to foster concrete international collaborations to help enhance their capabilities in both theoretical research and hardware development.

Yang Gao[1]* and Jinguo Liu[2]

[1]STAR Lab, Surrey Space Centre, University of Surrey, Guildford, Surrey, GU2 7XH, UK. [2]State Key Laboratory of Robotics, Shenyang Institute of Automation, Chinese Academy of Science, Shenyang, Liaoning, 110016, China.

*Corresponding author. E-mail: yang.gao@surrey.ac.uk

REFERENCES

1. "Robots join rescue in quake zone" (21 April 2013); http://news.xinhuanet.com/english/china/2013-04/21/c_132328009.htm.
2. R. Monastersky, *Nature* **489**, 194 (2012).
3. Y. C. Wang, *Chin. Sci. Bull. (Chin. Ver.)* **58** (suppl. II), 1 (2013).
4. C. Chen, C. G. Bu, Y. Q. He, J. D. Han, *Chin. Sci. Bull. (Chin. Ver.)*, **58** (suppl. II), 75 (2013).

Semantic priming well established

AMIDST THE RECENT furor over failures to replicate some empirical results on behavior priming by social psychologists ("Fresh misconduct charges hit Dutch social psychology," F. v. Kolfschooten, News & Analysis, 9 May, p. 566; "Replication effort provokes praise—and 'bullying' charges," J. Bohannon, In Depth, 23 May, p. 788; "Psychologist's defense challenged," F. v. Kolfschooten, In Depth, 30 May, p. 957), it is important to emphasize that some basic behavior-priming effects are real, robust, and easily replicable even if others are much more problematic.

For example, if an English reader is presented with a printed word like "dog," then on average, s/he will be at least 10 to 20% faster at recognizing and responding to a subsequent associated word like "cat" when it is presented within a few seconds after the previous word. This psychological phenomenon, called "semantic priming," has been demonstrated many times during past decades; the mental processes and brain mechanisms that mediate it are at least moderately well understood (*1*–*3*). Many other highly reliable priming phenomena like this have been found in human perception, memory, and language processing (*4*). Consequently, in his 23 May In Depth story, J. Bohannon's statement that "…for behavior priming…the results [of recent replication attempts] are particularly grim" should have been much more carefully qualified.

To be specific, the recent failed replication attempts concern much more exotic types of putative behavior priming [e.g., the ones reported originally in (*5*–*8*); see (*9*)]. Viewed from a metaphorical perspective, what some social psychologists have done is essentially like trying to show that presenting the printed word "dog" may incline English-reading adult male humans more toward visiting remote "cathouses" (slang for brothels) even after substantial amounts of time (several minutes or more) have elapsed since the original exposure to "dog." Much further research is needed for assessing to what extent such behavior-priming effects are real. Meanwhile, until the necessary research has been completed, journalists in the public news media [e.g., (*10*)] and scientist authors of popular best-selling books [e.g., (*11*)] that prominently tout these less-substantiated, albeit intriguing, phenomena should treat them with considerable caution, uncertainty, and skepticism.

David E. Meyer

Department of Psychology, University of Michigan, Ann Arbor, MI 48109, USA. E-mail: demeyer@umich.edu

REFERENCES AND NOTES

1. D. E. Meyer, R. W. Schvaneveldt, *J. Exp. Psychol.* **90**, 227 (1971).
2. D. E. Meyer, R. W. Schvaneveldt, *Science* **192**, 27 (1976).
3. J. H. Neely, in *Basic Processes in Reading: Visual Word Recognition*, D. Besner, G. W. Humphreys, Eds. (Erlbaum, Hillsdale, NJ, 1991).
4. T. McNamara, *Semantic Priming: Perspectives from Memory and Word Recognition* (Psychology Press, New York, 2005).
5. J. A. Bargh, M. Chen, L. Burrows, *J. Person. Soc. Psychol.* **71**, 230 (1996).
6. J. A. Bargh *et al.*, *J. Person. Soc. Psychol.* **81**, 1014 (2001).
7. T. J. Carter, M. J. Ferguson, R. R. Hassin, *Psychol. Sci.* **22**, 1011 (2011).
8. E. M. Caruso *et al.*, *J. Exp. Psychol. Gen.* **142**, 301 (2013).
9. For example, Bargh *et al.* (*5*) claimed that surreptitiously exposing college students to printed words like "bingo," "gray," and "Florida," which may be related to old age in the United States, primed them to walk more slowly as they later exited the laboratory. However, multiple failures to replicate this specific behavior-priming effect have been subsequently reported (*12*,*13*).
10. M. Gladwell, *Blink: The Power of Thinking without Thinking* (Back Bay Books, Little, Brown, New York, 2007).
11. D. Kahneman, *Thinking: Fast and Slow* (Farrar, Straus, and Giroux, New York, 2011).
12. S. Doyen *et al.*, *PLOS One* **7**, 1 (2012).
13. H. Pashler, C. Harris, N. Coburn, "Elderly-related words prime slow walking" (2011); http://psychfiledrawer.org/replication.php?attempt=MTU%3D.

Published by AAAS

Downloaded from www.sciencemag.org on August 11, 2014

Eyeing visual pathways in dyslexia

IN THEIR REPORT "Intact but less accessible phonetic representations in adults with dyslexia" (6 December 2013, p. 1251), B. Boets *et al.* show convincingly that adults with dyslexia exhibit normal neural representations of speech phonemes. They suggest that the core problem in dyslexia is defective access to normal phonetic representations. Poor access is supported by the finding of weaker connectivity between the Wernicke's and Broca's areas in their dyslexic subjects. However, their conclusion overlooks the possibility of defects in the visual system before the signals from reading a text reach the phonological realm; with certain words, signals never even enter the phonological route. Although most people with reading impairments have severe phonological deficits, mere correlation cannot establish causality (*1*).

People who are illiterate have poorer phonological skills than those who can read, perhaps because reading helps the development of phonemic awareness (*2*). The huge difference in time spent on reading may also explain the connectivity differences found by Boets *et al.* between good and bad readers.

Reading, being a recent historical development, is unlikely to be associated with the evolution of any specific brain area devoted to it, so it probably uses brain functions evolved for other purposes. One such function is postulated to be a top-down attentional mechanism essential for visual search, but co-opted for sequential processing of letters in a text (*3*). There is now substantial evidence demonstrating significant deficits in visuospatial attention in dyslexia (*3*, *4*). Longitudinal studies also predict reading proficiency from performance on visual attention tasks (*5*), and remediation programs involving visual attention rapidly improve reading scores (*6*).

Reading difficulties of dyslexics and their poor access to phonological representations may be independent outcomes of a single underlying deficit. A temporal sampling disorder in speech recognition, recently suggested as a neural explanation for the phonological problems in dyslexia (*7*), may in fact be part of a more general sampling problem that causes parallel deficits in sampling visual stimuli as well (*8*). Thus, phonological difficulties may show correlation with, but not cause, a reading impairment.

T. R. Vidyasagar

Department of Optometry and Vision Sciences and Melbourne Neuroscience Institute, University of Melbourne, Parkville, VIC, 3010, Australia. E-mail: trv@unimelb.edu.au

REFERENCES

1. A. Castles, M. Coltheart, *Cognition* **91**, 77 (2004).
2. S. Dehaene *et al.*, *Science* **330**, 1359 (2010).
3. T. R. Vidyasagar, K. Pammer, *Trends Cognit. Sci.* **14**, 57 (2010).
4. A. Facoetti, P. Paganoni, M. Turatto, V. Marzola, G. G. Mascetti, *Cortex* **36**, 109 (2000).
5. A. Kevan, K. Pammer, *Neuropsychologia* **47**, 3174 (2009).
6. S. Franceschini *et al.*, *Curr. Biol.* **23**, 462 (2013).
7. U. Goswami, *Trends Cognit. Sci.*, **15**, 3 (2011).
8. T. R. Vidyasagar, *Front Human Neurosci.* **7**, 811 (2013).

Response

I APPRECIATE VIDYASAGAR'S attempt to point to the important role of visual processing in reading and dyslexia. My colleagues and I have also been investigating visual impairments in (preschool children at risk of) dyslexia (*1*–*3*). However, I don't think that the possible importance of visual skills discredits our findings in any manner.

Vidyasagar emphasizes the importance of excluding deficits in the visual system before identifying one of the downstream stages as the site of the main deficit. However, visual performance is completely irrelevant to our neuroimaging study. Subjects did not have to read at all; they just had to listen to speech sounds and were even instructed to close their eyes. Despite this lack of visual input, the observed pattern of functional and structural brain connectivity related to individual differences in phonology, reading, and spelling.

I agree that problems in visual processing may also result in literacy impairment and that a certain proportion of individuals with dyslexia may indeed present visual processing problems. However, I disagree that this is the primary impairment causing subsequent phonological deficits. There is abundant evidence that individuals with dyslexia do show early phonological impairments, even before going to school or before receiving any reading instruction. Thus, this certainly is not simply a secondary consequence of less print exposure or orthographic skill (*4*, *5*).

B. Boets

Child and Adolescent Psychiatry, KU Leuven, 3000, Leuven, Belgium and McGovern Institute for Brain Research, Massachusetts Institute of Technology, Cambridge, MA 02139, USA. E-mail: bart.boets@ppw.kuleuven.be

REFERENCES

1. B. Boets, J. Wouters, A. van Wieringen, P. Ghesquiere, *Vision Res.* **46**, 527 (2006).
2. B. Boets, J. Wouters, A. van Wieringen, B. De Smedt, P. Ghesquiere, *Brain Lang.* **106**, 29 (2008).
3. B. Boets, M. Vandermosten, P. Cornelissen, J. Wouters, P. Ghesquiere, *Child Dev.* **82**, 854 (2011).
4. B. Boets *et al.*, *Br. J. Dev. Psychol.* **28**, 5 (2010).
5. H. S. Scarborough, *J. Educ. Psychol.* **81**, 101 (1989).

TECHNICAL COMMENT ABSTRACTS

Comment on "Mechanism of eukaryotic RNA polymerase III transcription termination"

Aneeshkumar G. Arimbasseri, George A. Kassavetis, Richard J. Maraia

Nielsen *et al.* (Reports, 28 June 2013, p. 1577) characterized their RNA polymerase III (Pol III) preparation and concluded that it requires an RNA hairpin/duplex structure for terminating transcription. We could not corroborate their findings using bona fide Pol III from two laboratory sources. We show that Pol III efficiently terminates transcription in the absence of a hairpin/duplex in vitro and in vivo.
Full text at http://dx.doi.org/10.1126/science.1253783

Response to Comment on "Mechanism of eukaryotic RNA polymerase III transcription termination"

Soren Nielsen and Nikolay Zenkin

Arimbasseri *et al.*, in their Comment, suggest that to terminate transcription in vivo, RNA polymerase III uses a mechanism other than hairpin-dependent termination and that properties of purified polymerase may depend on preparation procedure. Evidence suggests that our preparation is indeed different from that of other methods. Our new data suggest that, apart from hairpin-dependent termination, one or more "fail-safe" termination mechanisms may exist in the cell.
Full text at http://dx.doi.org/10.1126/science.1254246

PHOTO: LISA VALDER/ISTOCKPHOTO

Published by AAAS

TECHNICAL COMMENT

TRANSCRIPTION

Comment on "Mechanism of eukaryotic RNA polymerase III transcription termination"

Aneeshkumar G. Arimbasseri,[1] George A. Kassavetis,[2] Richard J. Maraia*[1,3]

Nielsen *et al*. (Reports, 28 June 2013, p. 1577) characterized their RNA polymerase III (Pol III) preparation and concluded that it requires an RNA hairpin/duplex structure for terminating transcription. We could not corroborate their findings using bona fide Pol III from two laboratory sources. We show that Pol III efficiently terminates transcription in the absence of a hairpin/duplex in vitro and in vivo.

A biochemical analysis of *Saccharomyces cerevisiae*–derived RNA polymerase III (Pol III) by Nielsen *et al*. (*1*) showed that although a fraction of the enzyme paused at the known termination signal, oligo(T), it failed to release the transcript in the absence of a terminator-proximal RNA hairpin or other RNA duplex structure. This work contrasts with that of others that concluded that no hairpin or dyad structure is required for termination by Pol III (*2*, *3*). Soren Nielsen and Nikolay Zenkin graciously provided us with a sample of their Pol III. Our analyses reveal that the Nielsen Pol III fails to terminate in the absence of a terminator-proximal RNA hairpin or other RNA duplex structure, as they reported, but this polymerase preparation differs substantially from Pol III purified independently by A. Arimbasseri and G. Kassavetis using different methods in different laboratories.

Using the template specified by Nielsen *et al*. to produce a transcript lacking secondary structure, we found that our *S. cerevisiae* Pol III efficiently released transcripts at oligo(T). Further analyses indicated that the disparity must lie in the polymerases rather than variables of the assays. This was confirmed by direct comparisons of the two polymerases, the Nielsen Pol III (NP) and ours (AP) (*4*), using two different templates and two immobilization methods: (i) through the

[1]Intramural Research Program of the *Eunice Kennedy Shriver* National Institute of Child Health and Human Development, National Institutes of Health, Bethesda, MD, USA. [2]Division of Biological Sciences, University of California, San Diego, CA, USA. [3]Commissioned Corps, U.S. Public Health Service.
*Corresponding author. E-mail: maraiar@mail.nih.gov

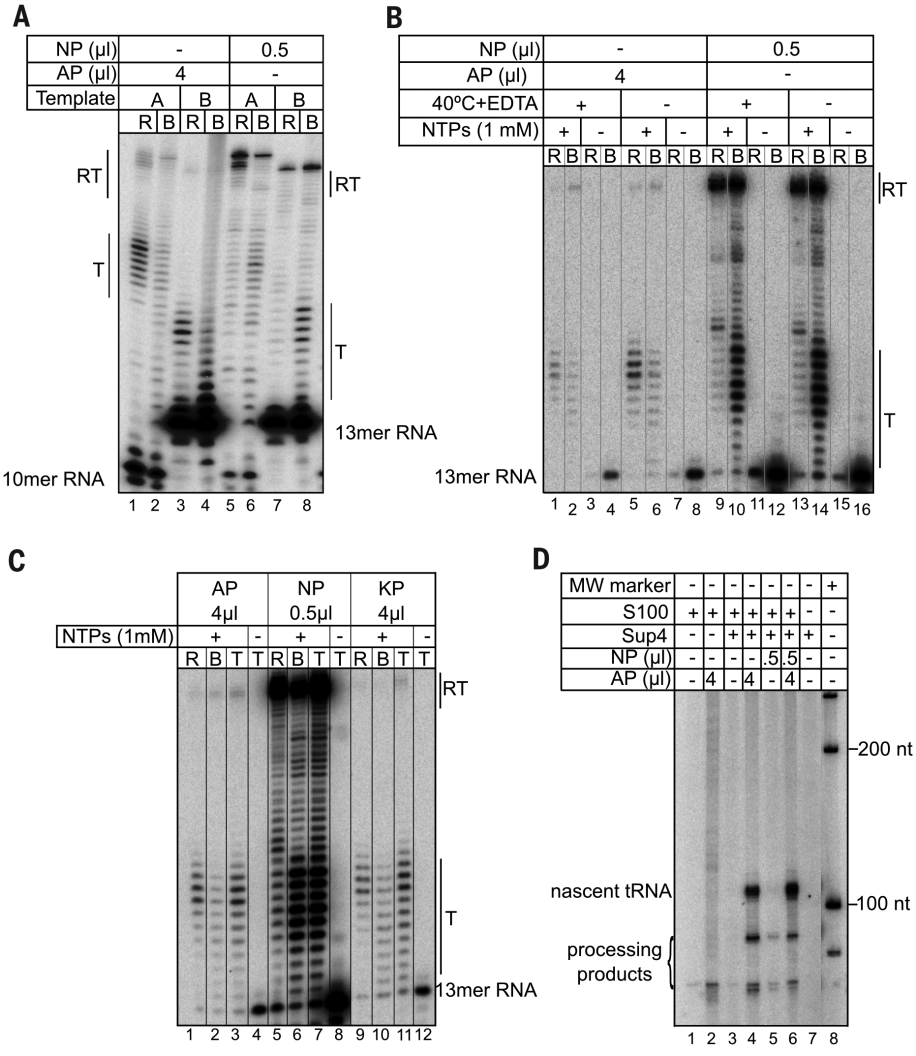

Fig. 1. Direct comparisons of NP polymerase and AP Pol III for termination and transcription factor TFIIIB+TFIIIC–dependent initiation. (**A**) Elongation complexes (EC) were assembled on templates A and B and immobilized, through the RNA polymerase His_6 tag, on Ni-NTA (nitrilotriacetic acid) agarose. NTPs were added, incubated for 10 min, and the released (R) and bound (B) transcripts separated, as indicated above each lane. (**B**) Comparison of elongation complex formation and transcription by AP and NP on immobilized template B. The quantities of AP and NP used are the same as in (A); reactions were for 1 min. Lanes 1 to 4 and 9 to 12 were done as described (*4*), whereas lanes 5 to 8 and 13 to 16 were done in the absence of EDTA and 40°C incubation. (**C**) Comparison of transcript release by three different preparations of Pol III. AP was purified on NiNTA agarose (*4*) (used in other figures), whereas untagged KP was highly purified by sequential ion-exchange chromatography (*6*). The quantities of AP and NP used are the same as in (A) and (B). Released, bound, and total (T) transcripts are indicated. (**D**) Pol III–specific transcription assay. Pre-initiation complexes were formed by incubating a *SUP4* tRNA gene plasmid with *S. cerevisiae* S100 extract deficient in endogenous Pol III activity, followed by the addition of AP or NP, as indicated above the lanes. Reactions were started by the addition of NTPs (with α-[^{32}P] GTP) and $MgCl_2$ and incubated for 20 min.

polymerase His_6 tag (*4*) (Fig. 1A) or (ii) through the 5′-biotin–tagged nontemplate strand DNA (Fig. 1B) (*1*). For the experiment shown in Fig. 1A, templates A and B contain differently positioned 9T and 10T terminators, respectively, producing 5′-^{32}P–labeled RNA primer-directed transcripts predicted to lack secondary structure; AP efficiently released transcripts at the T tracts of both templates (lanes 1 and 3). In contrast, NP produced more read-through transcripts (RT), and most of the transcripts with 3′ ends at the T tract were in the bound fractions (lanes 6 and 8). For the experiment shown in Fig. 1B, we used immobilized DNA, unlabeled RNA primer and α-[^{32}P]GTP (guanosine triphosphate) incorporation (*1*), and the same amounts of polymerases as in Fig. 1A. In this assay, NP was far more active than AP and also produced more RT. Transcripts paused at oligo(T) were not released by NP but were efficiently released by AP (Fig. 1B). It is noteworthy that substantial RT was also produced by NP for transcripts with a hairpin and on even longer T tracts [Fig. 2C in (*1*)], reflecting unexpectedly low termination efficiency relative to what would result with other preparations of Pol III [with comparable nucleoside triphosphate (NTP) concentrations; see (*3*–*5*)]. We also compared NP and AP with an untagged preparation of Pol III, KP (*6*), using immobilized DNA (Fig. 1C). KP was nearly indistinguishable from AP, whereas NP again produced mostly bound transcripts, arrested at oligo(T). It is likely important that NP was substantially more active than AP in the immobilized DNA assay relative to the immobilized polymerase assay. NP also differed in read-through beyond its oligo(T) elongation-arrest site compared with read-through beyond the oligo(dT) pause/release site by AP and KP. Thus, NP is very different from AP and KP. Its activity also differs from Pol IIIΔ, a form that lacks its C53/C37 subcomplex, because Pol IIIΔ efficiently releases transcripts at long, 9T terminators (*4*).

We also compared AP and NP for factor-dependent initiation of transcription of the *SUP4* tRNA gene by assembling initiation complexes with an *S. cerevisiae* S100 extract deficient in Pol III activity (from Pol IIIΔ–expressing cells (*4*)). Addition of AP produced the expected 104-nucleotide (nt) transcript (*6*) and smaller products consistent with pre-tRNA processing in cellular extracts (*7*), whereas NP produced substantially less (Fig. 1D, lanes 4 and 5). Mixing AP and NP yielded levels similar to AP alone (lane 6). Because NP terminates efficiently on the *SUP4* gene (*1*), the low ratio of specific to nonspecific transcription observed with NP indicates an additional difference between the Pol III preparations.

Examining the 280 Pol III transcribed genes in the *S. cerevisiae* genome for potential RNA secondary structure within 12 nt upstream of their terminators, Nielsen *et al.* proposed that their RNA structure model is relevant to Pol III termination in vivo (*1*). We employed an *Schizosaccharomyces pombe* suppressor-tRNA reporter system to examine this issue directly (*8*, *9*). Figure 2A depicts pSer7T, which has a short 3′ trailer between the end of the tRNA module and the 7T terminator. The nearest RNA duplex structure for pSer7T has its 3′ end 9 nt upstream from the terminator. Construct pSer7T-US contains a 26-nt CA-repeat unstructured spacer (US) in the 3′ trailer, and pSer7T-HP contains a 26-nt spacer containing a G+C–rich dyad sequence forming an 8-bp hairpin (HP). Structure prediction of the full-length sequences (*10*) confirmed that the US would be single-stranded, whereas HP would form an independent hairpin. The control constructs pSer3T-US and pSer3T-HP have only 3 Ts in the terminator region and should produce RT transcripts only; the downstream complementary read-through (cRT) region is complementary to, and can base pair with, the tRNA sequence, thereby blocking normal processing (*8*). The three 7T constructs produced high levels of suppression, reflected by white colony/patch color (Fig. 2B, top row). The 3T constructs demonstrated that suppression is not achieved in the absence of termination. Northern blot analysis shown in Fig. 2C using an intron-based probe of the suppressor-tRNA pSer constructs in Fig. 2B displayed the expected primary nascent RNAs of different lengths reflected in Fig. 2A (Fig. 2C). Previous characterizations indicate that the major—i.e., lowest—band designated by the arrow in Fig. 2C is an intron-containing intermediate substrate for mature tRNA production (*11*). Comparable levels of this band in lanes 1 to 3 reflect the comparable suppression activities in Fig. 2B. These findings provide strong evidence that a terminator-proximal hairpin is largely inconsequential to suppressor tRNA production by Pol III in vivo.

A mechanistic link between termination and reinitiation is widely believed to underlie the high productivity of Pol III, which is important

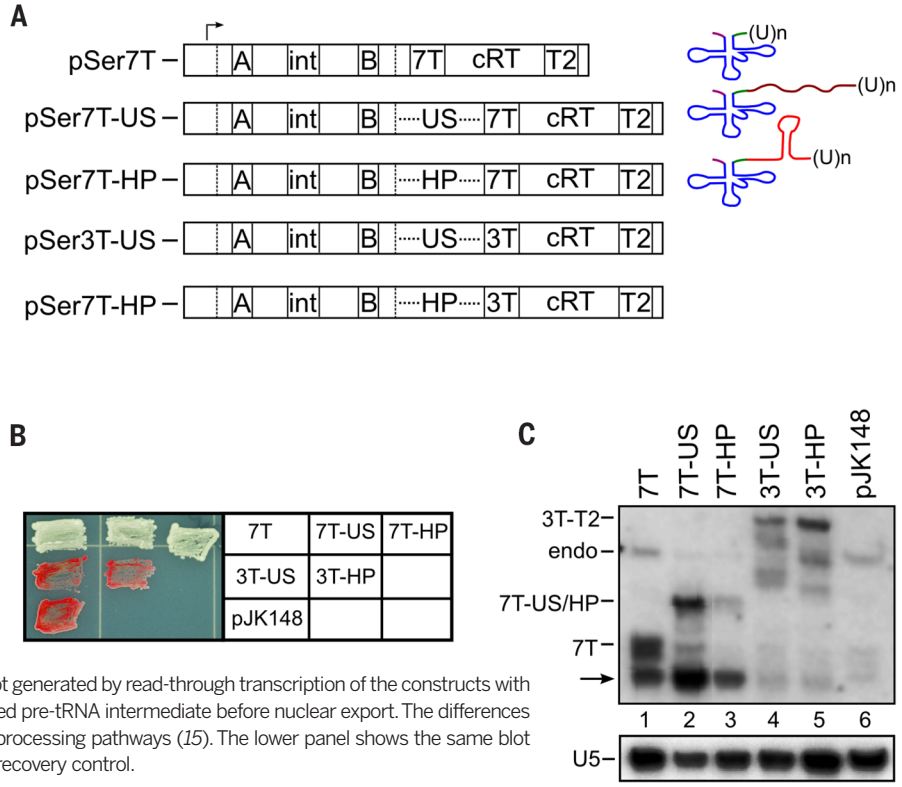

Fig. 2. Pol III termination is independent of transcript terminator–proximal RNA structure in vivo. (**A**) Schematic of the different suppressor tRNA constructs used. pSer7T is the parent construct (*8*). Promoter elements and other features are indicated (arrow, start site; box A; intron; box B; 7T or 3T terminators; T2, read-through terminator). The dashed vertical lines delineate the 5′ and 3′ matured/processed ends of the tRNA. An unstructured spacer (US) or a spacer that forms a stable hairpin (HP) was introduced within the 3′ trailer, immediately upstream of the terminator. On the right side is a schematic of the resultant predicted pre-tRNA products. (**B**) Patch suppression assay analysis of *S. pombe* colonies carrying the different suppressor constructs. Red color indicates lack of suppression, and white color indicates efficient suppression. (**C**) Northern blot analysis of the nascent tRNAs produced by the different suppressor constructs using an intron-specific probe. 7T- and 7T-US/HP designations to the left side indicate the position of the nascent 7T-terminated pre-tRNAs of pSer7T and pSer7T-US/HP constructs, respectively. "Endo" indicates the nascent transcript of the endogenous dimeric tRNAser-tRNAi-met gene. 3T-T2 indicates the 3′ extended transcript generated by read-through transcription of the constructs with the 3T terminator. The arrow indicates a partially processed pre-tRNA intermediate before nuclear export. The differences in the profiles in lanes 2 and 3 likely reflect alternative 3′ processing pathways (*15*). The lower panel shows the same blot probed for the pol II-transcribed U5 snRNA as a sample recovery control.

for proliferation, growth, and development (*12*, *13*). High productivity and additional features also make Pol III a compelling choice for therapeutic expression of small interfering RNAs for RNA interference (RNAi) and other purposes (*14*). In this regard, our data indicate that a terminator-proximal hairpin is not essential for termination, either in vivo or in vitro.

REFERENCES AND NOTES

1. S. Nielsen, Y. Yuzenkova, N. Zenkin, *Science* **340**, 1577–1580 (2013).
2. D. F. Bogenhagen, D. D. Brown, *Cell* **24**, 261–270 (1981).
3. X. Wang, W. R. Folk, *J. Biol. Chem.* **269**, 4993–5004 (1994).
4. A. G. Arimbasseri, R. J. Maraia, *Mol. Cell. Biol.* **33**, 1571–1581 (2013).
5. H. Matsuzaki, G. A. Kassavetis, E. P. Geiduschek, *J. Mol. Biol.* **235**, 1173–1192 (1994).
6. G. A. Kassavetis, B. R. Braun, L. H. Nguyen, E. P. Geiduschek, *Cell* **60**, 235–245 (1990).
7. D. R. Engelke, P. Gegenheimer, J. Abelson, *J. Biol. Chem.* **260**, 1271–1279 (1985).
8. M. Hamada, A. L. Sakulich, S. B. Koduru, R. J. Maraia, *J. Biol. Chem.* **275**, 29076–29081 (2000).
9. Y. Huang, R. V. Intine, A. Mozlin, S. Hasson, R. J. Maraia, *Mol. Cell. Biol.* **25**, 621–636 (2005).
10. M. Zuker, *Science* **244**, 48–52 (1989).
11. V. Cherkasova, J. Bahler, D. Bacikova, K. Pridham, R. J. Maraia, *Mol. Biol. Cell* **23**, 480 (2011).
12. A. G. Arimbasseri, K. Rijal, R. J. Maraia, *Transcription* **4**, (2013).
13. L. Marshall, S. J. Goodfellow, R. J. White, *PLOS Biol.* **5**, e286 (2007).
14. M. C. Yen *et al*., *Cancer Gene Ther.* **20**, 351–357 (2013).
15. R. J. Maraia, T. N. Lamichhane, *WIRES RNA* **2**, 362–375 (2011).

ACKNOWLEDGMENTS

We thank N. Zenkin and S. Nielsen for NP3, and E. P. Geiduschek, M. Kashlev, R. Landick, and A. Vannini for discussion and comments. This work was supported by direct funding from the Intramural Research Program of the Eunice Kennedy Shriver National Institute of Child Health and Human Development.

24 March 2014; accepted 25 June 2014
10.1126/science.1253783

RESEARCH

Seismic analysis checks the age of adolescent stars
Zwintz et al. *p. 550*

IN *SCIENCE* JOURNALS

Edited by **Melissa McCartney** *and* **Margaret Moerchen**

Limbs self-organize in development

MODELING DIGITS

How do fingers know where to grow?

Most researchers today believe that each finger forms because of its unique position within the early limb bud. However, 30 years ago, developmental biologists proposed that the arrangement of fingers followed the Turing pattern, a self-organizing process during early embryo development. Raspopovic *et al.* provide evidence to support a Turing mechanism (see the Perspective by Zuniga and Zeller). They reveal that Bmp and Wnt signaling pathways, together with the gene Sox9, form a Turing network. The authors used this network to generate a computer model capable of accurately reproducing the patterns that cells follow as the embryo grows fingers. — BAP

Science, this issue p. 566; see also p. 516

DINOSAUR EVOLUTION

Turning large dinosaurs into small birds

Most paleontologists agree that birds are descended from dinosaurs. How did such large terrestrial or aquatic animals evolve into small feathered fliers? Lee *et al.* used two large databases of theropod morphology to explore possible evolutionary patterns that may have driven this dramatic transformation (see the Perspective by Benton). They found no clear pattern of miniaturization across the entire clade of Theropoda. However, several lines of evidence suggested that the lineage leading to birds underwent sustained miniaturization. Within that lineage, body sizes decreased and species evolved faster. They also developed ecological and morphological innovations linked to smaller body sizes. — SNV

Science, this issue p. 562; see also p. 508

CO-INFECTION

Parasites make it hard to fight viruses

Microbial co-infections challenge the immune system—different pathogens often require different flavors of immune responses for their elimination or containment (see the Perspective by Maizels and Gause). Two teams studied what happens when parasitic worms and viruses infect mice at the same time. Reese *et al.* found that parasite co-infection woke up a dormant virus. Osborne *et al.* found that mice already infected with parasitic worms were worse at fighting off viruses. In both cases, worms skewed the immune response so that the immune cells and the molecules they secreted created an environment favorable for the worm at the expense of antiviral immunity. — KLM

Science, this issue p. 573 and p. 578; see also p. 517

CHRONIC PAIN

A neuropeptide kills patients' motivation

Chronic pain is not only extremely disturbing and unpleasant; it can also make people depressed and demotivated. What causes these effects? Schwartz *et al.* discovered that chronic pain causes changes in the way a neuropeptide called galanin affects certain neurons in a brain region called the nucleus accumbens (see the Perspective by Fields). Galanin influences a variety of behaviors, including feeding and certain aspects of pain. In this case, it depresses synaptic transmission at specific excitatory synapses. It does so, in part, by changing the ratio of subunits of an important receptor protein. — PRS

Science, this issue p. 535; see also p. 513

CATALYSIS

Converting CO_2 into methanol by catalysis

By hydrogenating CO_2, scientists can transform a greenhouse gas into methanol, a desirable fuel. Graciani *et al.* cast copper in the role of the highly active catalyst for this reaction by putting copper particles on cerium oxide. The interface between the cerium oxide and the copper enables the reverse water-gas shift reaction

PHOTOS: (TOP TO BOTTOM) NASA/ESA, J. MUZEROLLE/STSCI, E. FURLAN/NOAO AND CALTECH, K. FLAHERTY/UNIVERSITY OF ARIZONA/STEWARD OBSERVATORY, Z. BALOG/MAX PLANCK INSTITUTE FOR ASTRONOMY, R. GUTERMUTH/UNIVERSITY OF MASSACHUSETTS, AMHERST; MARC C. PERKINS PHOTOGRAPHY, COSTA MESA, CA

Downloaded from www.sciencemag.org on August 11, 2014

Published by AAAS

that converts CO_2 into CO, which reacts more readily with hydrogen to make methanol. This result takes a step forward in innovating catalysts for this environmentally friendly process. — PDS

Science, this issue p. 546

QUANTUM INFORMATION

Toward quantum teleportation on demand

Quantum information processing relies on the ability to store, manipulate, and propagate information encoded in quantum states of matter. Doing so, however, may destroy or compromise these delicate quantum states. Pfaff *et al.* present a quantum teleportation protocol that uses two defects in diamond 3 m apart (see the Perspective by Atatüre and Morton). They then map the quantum state of one of the diamond defects onto the other. The work presents a key building block for the successful development of larger quantum networks. — ISO

Science, this issue p. 532; see also p. 510

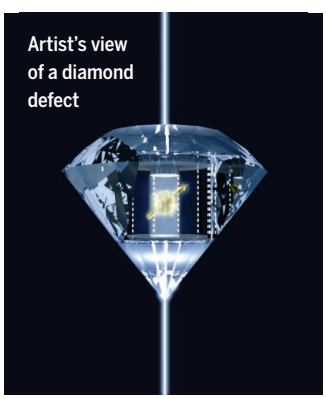

Artist's view of a diamond defect

CANCER

Preventing drug resistance in breast cancer

Some patients with breast cancer respond to therapy with trastuzumab, but many later develop resistance. Breast tumors often lack SIRT6, which encodes an enzyme that is a tumor suppressor. Thirumurthi *et al.* found that the kinase AKT phosphorylated SIRT6, triggering a chain of events that breaks it down. Patients whose breast tumors had high SIRT6 levels and low AKT levels had higher survival rates. Preventing SIRT6 from being degraded or phosphorylated made resistant breast cancer cells less resistant to trastuzumab, suggesting that high SIRT6 may improve therapeutic responses in patients. — LKF

Sci. Signal. **7**, ra71 (2014).

CELL BIOLOGY

New tools for sorting good and bad fat cells

There's "good fat" and there's "bad fat." Brown adipose tissue is considered "good" because it burns calories and could thus be harnessed to combat obesity. When brown fat cells develop within "bad" white fat, the tissue is called "beige." Ussar *et al*. developed tools for imaging these cell subtypes or targeting drugs to them. The authors identified three protein markers of white, beige, and brown fat cells—ASC-1, PAT2, and P2RX5—which they selected using computational methods, confirmed in mice, and then verified in human adipose tissue. The proteins sit on the cell surface, making them especially useful for imaging tissue and guiding drugs. — MLF

Sci. Transl. Med. **6**, 247ra103 (2014)

NOVAE

Gamma-ray novas may be garden variety

When astronomers detected gamma rays from the nova V407 Cyg, an explosive mass transfer from a red giant onto a white dwarf, they found it surprising enough. They blamed the rays on strong stellar winds enabling particle acceleration. Now, the Fermi-LAT Collaboration has observed gamma rays from three more novas, all lacking the strong winds. Although the three sources vary slightly in nature, none is particularly unusual. If all novas emit gamma rays, then astronomers would expect to see the same number of novas that they did in fact see within a 5-kpc distance over 5 years. — MMM

Science, this issue p. 554

IN OTHER JOURNALS

Edited by **Kristen Mueller** *and* **Jesse Smith**

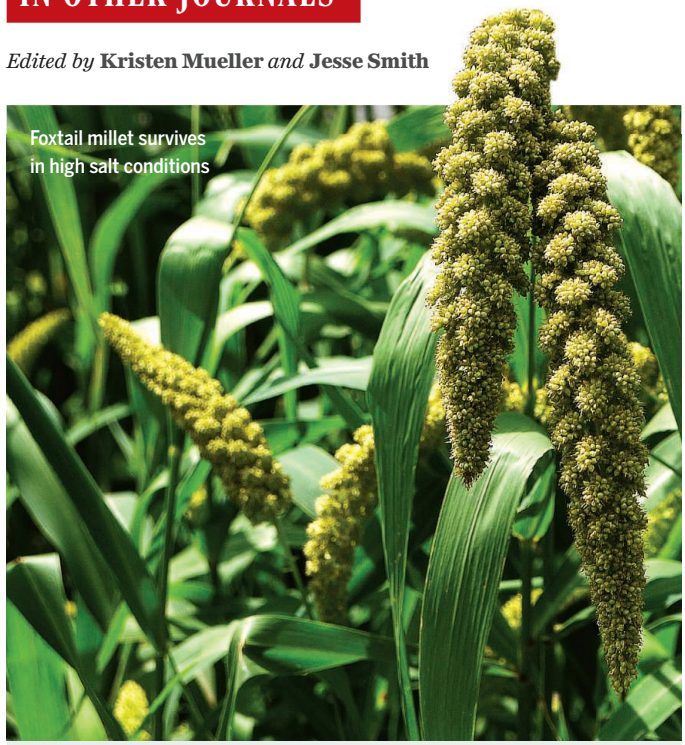

Foxtail millet survives in high salt conditions

ABIOTIC STRESS

How plants survive (salt) stress

Foxtail millet, a grain crop cultivated in China since the sixth century BC, tolerates high salt concentrations well. All land plants produce proteins called remorins, several of which help plants respond to abiotic (environmental) stress. To determine whether foxtail millet uses remorins to help protect it from excess salt, Yue *et al*. first identified 11 remorin genes in this plant. When the plants grew in salty soil, they produced a remorin called *SiREM6*. Engineering *Arabidopsis* plants to express *SiREM6* allowed the plants to survive better in salty conditions. Their advantage increased with the salinity: While brackish water killed normal *Arabidopsis* plants, *SiREM6*-expressing plants survived. — PJH

PLOS ONE **9**, e100772 (2014).

COGNITIVE PSYCHOLOGY

Developing a judgment of confidence

When you place a bet, you need to estimate your chance of winning, and you also need to know the accuracy of your estimate. That is, when the odds appear to be in your favor, but you're not entirely sure, you'll make a smaller wager than when you're rock-solid certain. Adults who are good judges of their own accuracy tend to be better at problem-solving, regulating their emotions, and thinking critically, among other skills. Vo *et al.* wondered whether this also holds true for children. The authors found that 5- to 8-year-old children are pretty good at making judgments about their accuracy when it comes to estimating quantities, but they don't evaluate themselves as well when comparing facial emotions. — GJC

Psychol. Sci. **25**, 10.1177/0956797614538458 (2014).

PHOTOS: (LEFT TO RIGHT) WOLFGANG PFAFF; STRONGLK7/WIKIMEDIA COMMONS

Published by AAAS

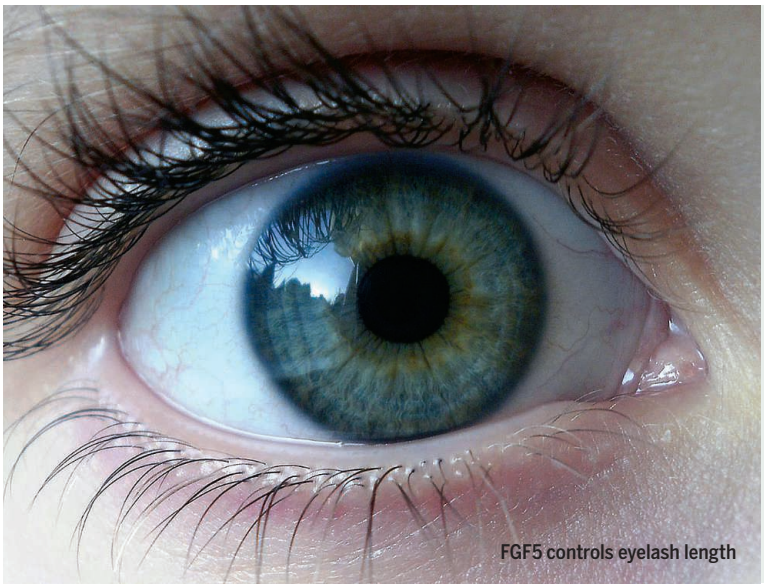

FGF5 controls eyelash length

DEVELOPMENT

The long and short of hair growth

The length of your eyelashes probably differs from the length of the hair on your head—and unlike your hair, your eyelashes can never reach your shoulders. What controls how long hair can get? To find out, Higgins *et al*. studied people with a rare disorder called familial trichomegaly, who have very long eyelashes and longer hair on the arms. They found that these people had a mutation in the gene that encodes fibroblast growth factor 5 (FGF5). When human hair follicles produce FGF5, they stop growing hair. Targeting FGF5 could potentially control the growth and rest phases of hair follicles, preventing unwanted hair from sprouting or growing longer lashes and locks. — LC

Proc. Natl. Acad. Sci. U.S.A. 10.1073/pnas.1402862111 (2014).

EDUCATION

Promoting evidence-based teaching

Empirical studies of science educational methods illuminate the best practices for getting students to learn. But why don't more science educators use such evidence-based teaching methods in their classrooms? They might not have access to the studies, DeChenne *et al.* report. The authors examined the role of practitioner-focused, discipline-based education research (DBER) journals in promoting and encouraging postsecondary teachers to adopt laboratory exercises supported by education research. Results showed a missed opportunity: DBER journals publish only a limited number of evidence-based instructional practices. — MM

J. Coll. Sci. Teach. **43**, 89 (2014).

ELECTRON TRANSFER

Electron tunneling or flickering resonance?

When electrons move from one site to another in biological molecules and the transfer drops off exponentially with distance, physicists usually assume they're seeing the electrons quantum-tunneling through energy barriers. A theoretical study by Zhang *et al.* provides a different interpretation. Molecules with the right combination of sites, with energy levels that align fleetingly during structural fluctuations, can produce the same decay signature. These "flickering resonances" temporarily create a band-like state for the electron, and as more sites are involved (corresponding to longer distances), the probability of creating the resonance drops exponentially. This mechanism operates over scale lengths of up to about 15 angstroms and could explain the short-distance electron transfer between bases in DNA. — PDS

Proc. Natl. Acad. Sci. U.S.A. 10.1073 pnas.1316519111 (2014).

MARINE BIOLOGY

Ship strikes threaten blue whale numbers

Whale-ship collisions may be behind low blue whale population counts despite international protections. Irvine *et al*. used satellites to track 171 blue whales off California over 15 years. The whales, part of the eastern North Pacific population, returned each summer to krill-rich upwelling zones off Santa Barbara and San Francisco—areas also crossed by major shipping lanes. At least three blue whales were killed by ship strike during 2 weeks in 2007. But a similar problem in Canada's Bay of Fundy offers hope: Eleven years ago, its maritime industry moved a shipping lane and reduced speed limits, reducing the likelihood of vessels striking right whales by 80%. — VM

A blue whale killed by a ship strike

PLOS ONE 10.1371/journal.pone.0102959(2014).

MICROBIAL PATHOGENS

How to make a not-so-painful ulcer

Buruli ulcer disease causes extensive skin lesions and can be deadly, but the lesions themselves don't hurt, which can stop patients from seeking the appropriate care. The pathogen *Mycobacterium ulcerans* causes Buruli ulcers and also alleviates the pain. Although many scientists studying this disease thought the pathogen caused nerve damage that blocked the pain, Marion *et al.* now show that the mycobacteria produce the mycolactone toxin, which causes analgesia by blocking the function of pain-responsive nerves. The findings could potentially help researchers develop a whole new class of painkillers. — SMH

Cell **157**, 1565 (2014).

GEOPHYSICS

Ample explanation for seismic variation

Geophysicists use seismic waves to make images of Earth's interior, but how they interpret those pictures depends on the properties of the minerals that make up the mantle. Wu and Wentzcovitch show that when the electron configuration of the iron in one of the most abundant minerals in the mantle, ferropericlase, changes at depths of 1000 km and greater, so does the way seismic waves propagate. The authors discuss several seismic features of the mantle previously thought to reflect different arrangements of minerals, such as compressional wave speed variations at depths of around 1750 km. Such features could be due not to mineralogy but to this electronic spin effect. — BG

Proc. Nat. Acad. Sci. U.S.A. 10.1073 pnas.1322427111 (2014).

PHOTOS: (TOP TO BOTTOM) KAREN ROE/FLICKR; FLIP NICKLIN/MINDEN PICTURES

Published by AAAS

ALSO IN *SCIENCE* JOURNALS

Edited by **Melissa McCartney** *and* **Margaret Moerchen**

INTERNEURONS

A central player in brain computation

A small subgroup of nerve cells plays a central role in information processing in the brain. Hu *et al.* review our present knowledge about the specific makeup of these neurons. Specifically, the individual properties of the molecules, their distribution within the cell, and the anatomy of the cells themselves are described. This information helps to explain why these neurons are so important for the function of microcircuits in the brain, as well as the behavior of the organism. This detailed level of understanding will become relevant as these cells become future targets for the treatment of neurological diseases. — PRS

Science, this issue p. 529

COMPUTATIONAL SOCIOLOGY

A macroscopic view of cultural history

Sociologists and anthropologists study the growth and evolution of human culture, but it is hard to measure cultural interactions on a historical time scale. Schich *et al.* developed a tool for extracting information about cultural history from simple but large sets of birth and death records. A network of cultural centers connected via the birth and death of more than 150,000 notable individuals revealed human mobility patterns and cultural attraction dynamics. Patterns of city growth over a period of 2000 years differed between countries, but the distribution of birth-to-death distances remained unchanged over more than eight centuries. — BJ

Science, this issue p. 558

PHOTOVOLTAICS

A layered approach improves solar cells

Perovskite films received a boost in photovoltaic efficiency through controlled formation of charge-generating films and improved current transfer to the electrodes. Zhou *et al.* lowered the defect density of the film by controlling humidity while the perovskite film formed from lead chloride and methylammonium iodide. Low-temperature processing steps allowed the use of materials that draw current out of the perovskite layer more efficiently. These and other modifications enabled a maximum cell efficiency of just over 19% and an average of 16.6%. — PDS

Science, this issue p. 542

MOBILE DNA IN CANCER

Hitchhiking through the tumor genome

Retrotransposons are DNA repeat sequences that are constantly on the move. By poaching certain cellular enzymes, they copy and insert themselves at new sites in the genome. Sometimes they carry along adjacent DNA sequences, a process called 3′ transduction. Tubio *et al*. found that 3′ transduction is a common event in human tumors. Because this process can scatter genes and regulatory sequences across the genome, it may represent yet another mechanism by which tumor cells acquire new mutations that help them survive and grow. — PAK

Science, this issue p. 531

HIV LATENCY

A not-so-random integration for HIV

Even in the face of a cocktail of antiretroviral drugs, HIV manages to hang on. It does so by integrating its own genome into those of host cells, where it persists in a latent state. To better understand this process, Wagner *et al*. determined the sites where HIV integrated into three HIV-infected patients treated with antiretroviral drugs for more than a decade. They found an overrepresentation of sites where HIV integrated into genes associated with cancer and cell proliferation. Also, multiple cells in the same individual harbored the same integration sites. This suggests that integration into specific genes may drive cell proliferation and viral persistence. — KLM

Science, this issue p. 570

ASTEROSEISMOLOGY

A finger on the pulse of young stars

Adolescent stars quiver and quake before the onset of nuclear fusion in their cores. Zwintz *et al.* confirm theoretical predictions that the frequency of the seismic oscillations in a given star is tied to its evolutionary status (see the Perspective by Stahler and Palla). As the protostar evolves and contracts, growing hotter and denser, it pulsates faster. Though previously applied only to aging stars, asteroseismology now offers a powerful tool for discerning the ages of very young stars. The relative timing of star formation within young clusters especially benefits from this refinement, as stars there are often tagged with one blanket age. — MMM

Science, this issue p. 550; see also p. 514

EPIGENOMICS

Ancient patterns reveal species divergence

Modifications to DNA, termed epigenetic changes, regulate the expression of genes. Scientists have recently detected such epigenetic changes in the remains of human ancestors that have been preserved for thousands of years. In a Perspective, Orlando and Willerslev explain that differences between the ancient epigenetic patterns and those in living humans can shed light on how humans have adapted to changing environments and how species have diverged from each other. Epigenetic patterns are complicated and vary with cell type, age, gender, health, and the environment. Further experimental advances are needed to fully unlock the epigenetic information in ancient DNA. — JFU

Science, this issue p. 511

Published by AAAS

REVIEW SUMMARY

INTERNEURONS

Fast-spiking, parvalbumin$^+$ GABAergic interneurons: From cellular design to microcircuit function

Hua Hu, Jian Gan, Peter Jonas*

BACKGROUND: Neuronal networks in the brain include glutamatergic principal neurons and GABAergic interneurons (GABA, γ-aminobutyric acid). The latter may be a minority cell type, but they are vital for normal brain function because they regulate the activity of principal neurons. If interneuron function is impaired, higher brain function can be damaged and seizures may result. The fast-spiking, parvalbumin-positive interneurons (PV$^+$ interneurons) are readily characterized and, consequently, have been adopted as a research model for systematic and quantitative investigations. These cells contribute to feedback and feedforward inhibition and are critically involved in the generation of network oscillations. They can convert an excitatory input signal into an inhibitory output signal within a millisecond, but it is unclear how these signaling properties are implemented at the molecular and cellular levels, nor how PV$^+$ interneurons shape complex network functions.

ADVANCES: Recent work sheds light on the subcellular signaling properties of PV$^+$ interneurons. PV$^+$ cells show a high degree of polarity. The weakly excitable dendrites allow PV$^+$ interneurons to sample activity in the surrounding network, whereas the highly excitable axons enable analog-to-digital conversion and fast propagation of the digital signal to a large number of target cells. Additionally, tight coupling of Ca^{2+} channels and release sensors at GABAergic output synapses increases the efficacy and speed of the inhibitory output.

Recent results also provide a better understanding of how PV$^+$ interneurons operate in neuronal networks. Not only are PV$^+$ interneurons involved in basic microcircuit functions, such as feedforward and feedback inhibition or gamma-frequency oscillations, but they also play a role in complex network operations, including expansion of dynamic activity range, pattern separation, modulation of place and grid field shapes, phase precession, and gain modulation of sensory responses. Thus, PV$^+$ interneurons are critically involved in advanced computations in microcircuits and neuronal networks.

OUTLOOK: Parvalbumin-expressing interneurons may also play a key role in numerous brain diseases. These include epilepsy, but also complex psychiatric diseases such as schizophrenia. Thus, PV$^+$ interneurons may become important therapeutic targets in the future. However, much needs to be learned about the basic function of these interneurons before clinical neuroscientists will have a chance to successfully use PV$^+$ interneurons for therapeutic purposes. ■

ON OUR WEBSITE

Read the full article at http://dx.doi.org/10.1126/science.1255263

IST Austria (Institute of Science and Technology Austria), Am Campus 1, A-3400 Klosterneuburg, Austria.
*Corresponding author. E-mail: peter.jonas@ist.ac.at
Cite this article as H. Hu *et al.*, *Science* 345, 1255263 (2014).
DOI: 10.1126/science.1255263

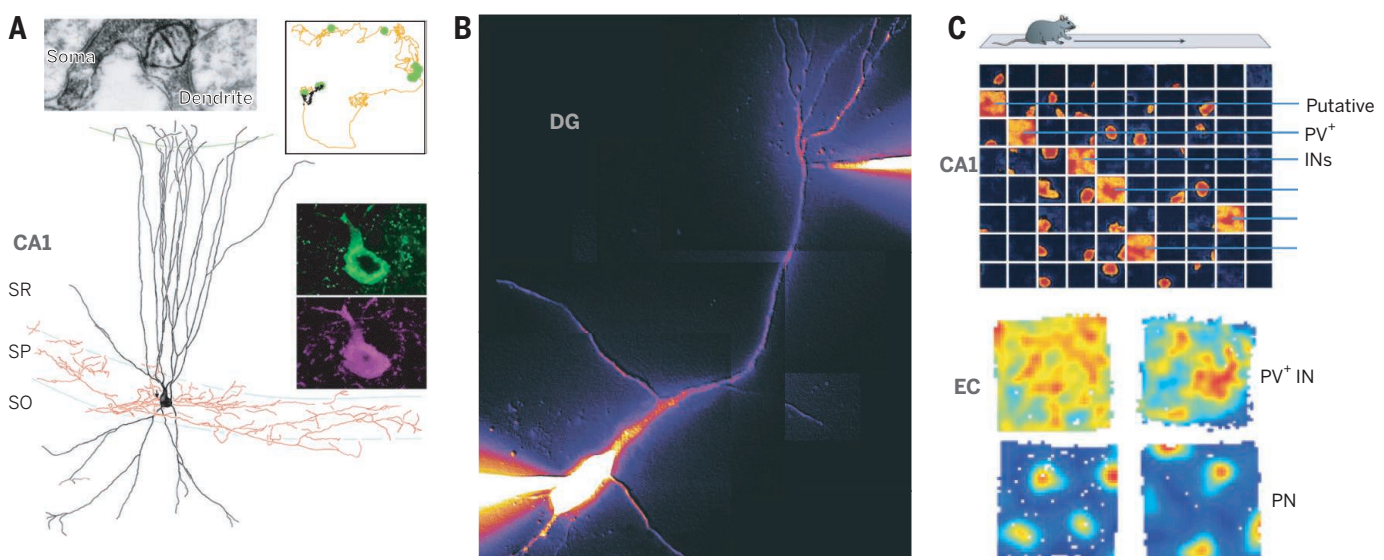

PV$^+$ interneurons: from cellular design to microcircuit function. (**A**) Morphological properties of PV$^+$ interneurons. Reconstruction of a PV$^+$ basket cell in the CA1 region of the hippocampus previously recorded in a freely moving rat. Soma and dendrites are shown in black; axon is depicted in red. CA1, cornu ammonis region 1; SR, stratum radiatum; SP, stratum pyramidale; SO, stratum oriens. For details, see Fig. 1B. (**B**) Subcellular physiology of PV$^+$ interneurons. Simultaneous recording from the soma and dendrite of a PV$^+$ interneuron in the dentate gyrus (DG) in vitro. (Bottom left) Somatic recording pipette (used for fluorescent dye labeling); (top right) dendritic recording pipette. For details, see Fig. 2A. (**C**) Network function of PV$^+$ interneurons. (Top) Place cell firing of hippocampal neurons; (bottom) grid cell firing of entorhinal cortex (EC) neurons in vivo. Warm colors indicate high action potential frequency. Putative PV$^+$ interneurons (PV$^+$ INs) have broader spatial fields than principal neurons (PNs). For details, see Fig. 6B.

SOURCE (LEFT TO RIGHT): DATA FROM LAPRAY *ET AL.* (2012). WITH PERMISSION FROM THE PUBLISHER; DATA FROM HU *ET AL.* (2010); DATA FROM WILSON AND MCNAUGHTON (1993) AND BUETFERING *ET AL.* (2014). WITH PERMISSION FROM THE PUBLISHER

Published by AAAS

REVIEW

INTERNEURONS

Fast-spiking, parvalbumin$^+$ GABAergic interneurons: From cellular design to microcircuit function

Hua Hu, Jian Gan, Peter Jonas*

The success story of fast-spiking, parvalbumin-positive (PV$^+$) GABAergic interneurons (GABA, γ-aminobutyric acid) in the mammalian central nervous system is noteworthy. In 1995, the properties of these interneurons were completely unknown. Twenty years later, thanks to the massive use of subcellular patch-clamp techniques, simultaneous multiple-cell recording, optogenetics, in vivo measurements, and computational approaches, our knowledge about PV$^+$ interneurons became more extensive than for several types of pyramidal neurons. These findings have implications beyond the "small world" of basic research on GABAergic cells. For example, the results provide a first proof of principle that neuroscientists might be able to close the gaps between the molecular, cellular, network, and behavioral levels, representing one of the main challenges at the present time. Furthermore, the results may form the basis for PV$^+$ interneurons as therapeutic targets for brain disease in the future. However, much needs to be learned about the basic function of these interneurons before clinical neuroscientists will be able to use PV$^+$ interneurons for therapeutic purposes.

In a reductionist's view of the brain, neuronal networks are composed of two types of neurons: glutamatergic principal neurons and GABAergic interneurons (GABA, γ-aminobutyric acid). Across all cortical circuits, glutamatergic neurons form ~80 to 90% of the neuronal population, whereas GABAergic neurons constitute the remaining 10 to 20% (*1*–*3*). Thus, in terms of neuron numbers, GABAergic cells represent only a minority. Nevertheless, these GABAergic neurons serve important functions. Most notably, they control the activity level of principal neurons in the entire brain. If GABAergic interneuron function breaks down, excitation takes over, leading to seizures and failure of higher brain functions (*4*).

A hallmark of interneurons is their structural and functional diversity (Fig. 1A). Twenty-one different classes of interneurons have been distinguished in the CA1 region of the hippocampus (*5*), and it is likely that an even larger number of types can be dissected in the neocortex (*6*). These interneurons can be distinguished on the basis of three sets of criteria: (i) morphological properties, particularly the target selectivity of the axon; (ii) expression of molecular markers, such as neuropeptides (somatostatin, cholecystokinin, vasoactive intestinal peptide, and neuropeptide-Y) and Ca^{2+}-binding proteins (parvalbumin, calretinin, and calbindin); and (iii) functional characteristics—most importantly, the action potential phenotype (*7*).

IST Austria (Institute of Science and Technology Austria), Am Campus 1, A-3400 Klosterneuburg, Austria.
*Corresponding author. E-mail: peter.jonas@ist.ac.at

How can we systematically and quantitatively study the function of such an enormously diverse population of cells? One approach is to focus on models, identifiable on the basis of standardized criteria. That is why, around 1990, several laboratories started to work on one particular type of GABAergic interneuron: the fast-spiking, parvalbumin-positive (PV$^+$) interneuron (Box 1). In the hippocampal CA1 region, 11% of neurons are GABAergic, and 24% of those are PV$^+$; thus, PV$^+$ interneurons represent only 2.6% of the total neuronal population (*8*). Accordingly, PV$^+$ interneurons appear to be somewhat exotic. However, numerous technical advantages outweigh this potential disadvantage (Fig. 1). The selective expression of the Ca^{2+}-binding protein PV allows unequivocal post hoc labeling by highly specific antibodies (*9*, *10*) (Fig. 1B). Both the short action potential duration and the fast-spiking action potential phenotype make it easy to identify these cells under experimental conditions (Fig. 1D). The high selectivity of the promoter of the PV gene can be used to genetically target these cells by enhanced green fluorescent protein and optogenetic methods (*11*, *12*) (Fig. 1, E and F). The specific developmental trajectory of cortical PV$^+$ interneurons, which are born in the medial ganglionic eminence and depend on specific sets of transcription factors (i.e., Nkx2-1 and Lhx6), may be exploited for labeling (*13*–*15*).

In this Review, we summarize current knowledge about fast-spiking, PV$^+$ interneurons at the molecular, cellular, and network levels. We concentrate on basket cells (the classical PV$^+$ interneurons) but include information about axo-axonic cells or other types of GABAergic interneurons also expressing PV (*5*) (Box 2). Furthermore, we focus on the hippocampus and the neocortex. For in vitro analysis of PV$^+$ interneurons, the advantages of the hippocampus are evident, especially the clearly defined layering and the availability of elaborate classification schemes (*5*). For in vivo analysis, the advantages of the neocortex become apparent, including the superficial localization of cells in the brain and the opportunity to easily define adequate behavioral stimuli.

Morphological properties and connectomics of PV$^+$ interneurons

How can we understand the function of PV$^+$ interneurons at the molecular, cellular, and network levels? Following Francis Crick's statement "If you want to understand function, study structure" (*16*), let us first take a look at the structure of PV$^+$ interneurons, particularly their input domains, the dendrites, and their output domains, the axons.

The morphological properties of the dendrites of PV$^+$ interneurons are notable in several ways (*1*). PV$^+$ interneurons have multiple dendrites that often cross layers (*17*–*20*), which permits the interneurons to receive input from different afferent pathways, such as feedforward and feedback pathways. The cumulative dendritic length of a single PV$^+$ interneuron ranges from 3.1 to 9 mm (*17*–*20*). Long dendrites allow PV$^+$ interneurons to sample input from a large population of principal cells. Finally, the somata and dendrites of PV$^+$ interneurons are densely covered with synapses. PV$^+$ interneurons in the hippocampal CA3 or CA1 region have ~16,000 to 34,000 synapses, 94% of which are excitatory and 6% are inhibitory (*17*, *20*). A large proportion of inhibitory synapses is PV$^+$ (*17*), but inhibitory inputs from vasoactive intestinal peptide- and somatostatin-expressing interneurons are also present (*21*, *22*). Thus, PV$^+$ interneurons receive convergent excitatory input from principal neurons, and inhibitory input primarily from other PV$^+$ interneurons. Because the dendrites of PV$^+$ interneurons are largely aspiny, excitatory synapses are formed on dendritic shafts. This may facilitate the generation of fast excitatory postsynaptic potentials (EPSPs) (*23*).

The morphological properties of the axon of PV$^+$ interneurons are also intriguing (*1*). In the classical anatomical literature, GABAergic interneurons were sometimes referred to as "short axon" cells. However, for many PV$^+$ interneurons, this seems entirely incorrect. The axon shows extensive arborization, and the cumulative axonal length of a single PV$^+$ interneuron is 30 to 50 mm [33 mm in the dentate gyrus (*18*), 46 mm in the hippocampal CA1 region (*24*), 20 and 24 mm in the frontal cortex (*25*)]. A huge number of "en passant" ("in passing," upon literal translation) terminals emerge from the extensive axonal arbor [10400 in CA1 (*24*), 3200 and 3800 in the frontal cortex (*25*)]. Thus, PV$^+$ interneurons generate a massively divergent inhibitory output (*8*). PV$^+$ interneurons innervate postsynaptic target cells in

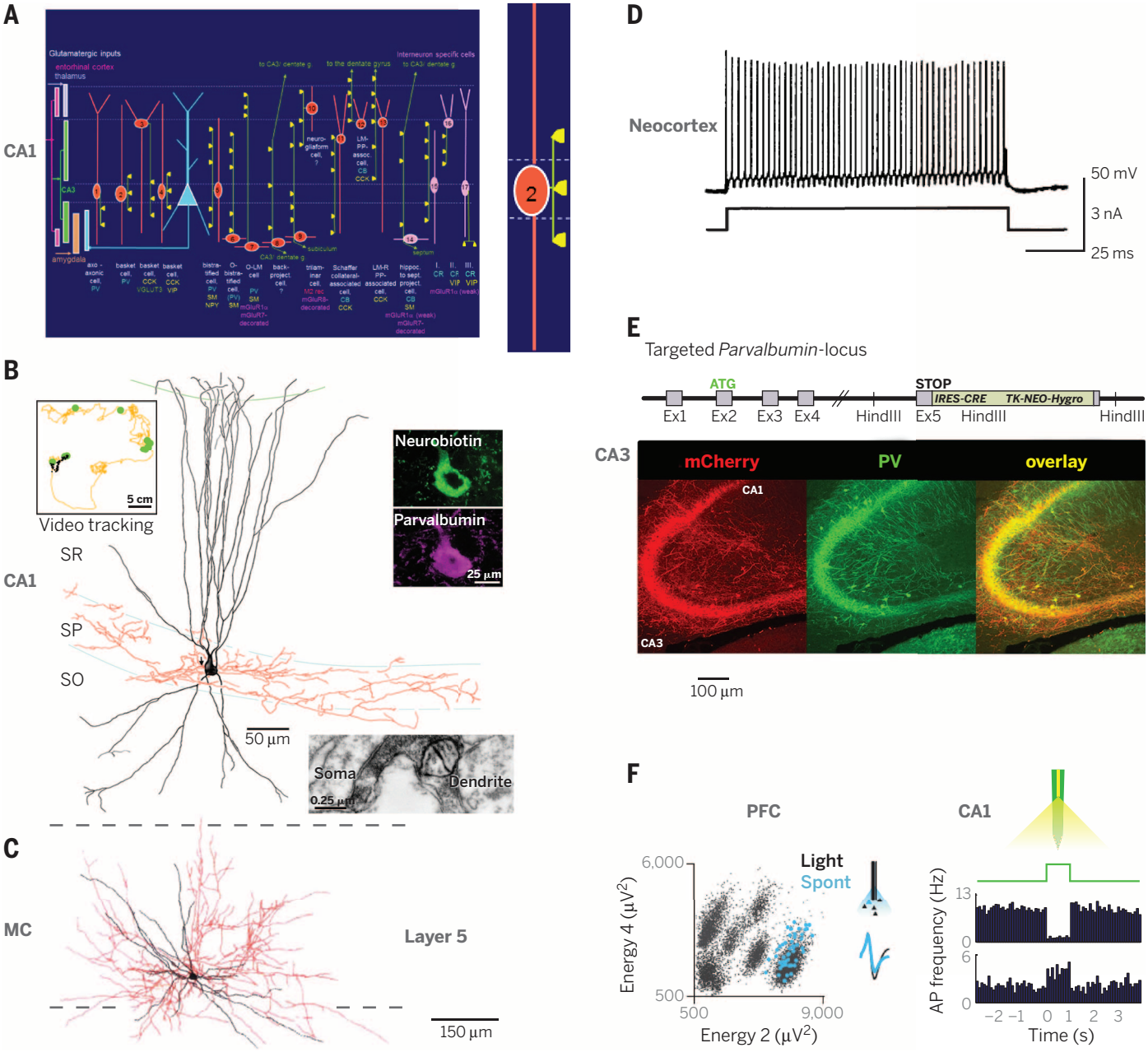

Fig. 1. The PV$^+$ interneuron: An interneuron subtype with salient properties and distinct experimental identifiability. (**A**) The placement of PV$^+$ interneurons in interneuron diversity schemes (*122*). (Left) Scheme showing a subset of the 21 types of GABAergic interneurons currently known in the hippocampal CA1 region. PV$^+$ axo-axonic cells and basket cells are located on the left side. (Right) A PV$^+$ basket cell (probably the most abundant type of PV$^+$ interneuron). Soma and dendrites are shown in orange; axons are depicted in yellow. (**B**) A PV$^+$ basket cell in the CA1 region of the hippocampus recorded in a freely moving rat. SR, stratum radiatum; SP, stratum pyramidale; SO, stratum oriens. (Upper left inset) Movement trajectory of the animal. (Upper right inset) PV immunoreactivity. (Lower right inset) Electron micrograph of output synapses. Data are from (*87*). (**C**) A basket cell in layer five of the motor cortex (MC). Data are from (*123*). Color code in (B) and (C): Soma and dendrites are shown in black; axon is depicted in red. (**D**) Fast-spiking action potential phenotype of a putative PV$^+$ interneuron in the neocortex in vitro. A long somatic current pulse evoked a high-frequency train of action potentials in the intracellularly recorded neuron. Data are from (*124*). (**E**) Genetic fluorescent protein labeling of PV$^+$ interneurons, using mice expressing Cre recombinase under the control of the PV promoter. (Left) mCherry labeling after adenoassociated virus infection; (center) PV immunoreactivity; (right), overlay. Inset on top shows targeted PV gene. Scheme on top is from (*125*). (**F**) Functional labeling of PV$^+$ interneurons, using mice expressing Cre recombinase and channelrhodopsin or halorhodopsin under the control of the PV promoter in vivo. (Left) Identification of unit activity in PV$^+$ interneurons expressing channelrhodopsin in an awake, freely moving mouse recorded with "optrodes." Data are from (*126*). (Right) Activity of a PV$^+$ interneuron expressing halorhodopsin in an awake mouse moving on a linear track. Note that the light pulse abolishes action potential (AP) initiation in the PV$^+$ interneuron (top) but increases the action potential frequency in a simultaneously recorded pyramidal neuron (bottom). Data are from (*92*). CA1, cornu ammonis region 1; CA3, cornu ammonis region 3; PFC, prefrontal cortex.

the perisomatic domain. In basket cells, the axon forms basket-like arrangements around principal cell somata and proximal dendrites. In axo-axonic cells, the axon of the interneuron follows the axon initial segment of the principal cell, resulting in a chandelier-like configuration (*5*). These morphological characteristics suggest that PV^+ interneurons generate a particularly powerful inhibition, because they innervate a large number of target cells near the site of action potential initiation. However, these properties also raise new questions: For example, one may wonder how reliable action potential propagation is achieved in the highly branching interneuron axon (*26*) and how the functions of signal propagation and transmitter release are integrated into a single structure. To address these questions, we must examine the function of PV^+ interneurons directly at the subcellular level with micrometer spatial and microsecond temporal resolution. Subcellular patch-clamp recording now allows researchers to obtain such measurements in both dendrites and axons of PV^+ interneurons.

The subcellular physiology of PV^+ interneurons: Dendrites

Direct dendritic recordings have provided a detailed quantitative picture of the electrical events in PV^+ interneuron dendrites (Fig. 2, A and B). First, action potentials backpropagate into the dendrites in a highly decremental manner (*27*), confirming findings of previous Ca^{2+} imaging experiments (*28*–*31*) (Fig. 2C). Similar results were obtained in both basket and axo-axonic cells (*27*). These properties differ from those of pyramidal neurons, where backpropagation is active (*32*). Second, dendritic spikes cannot be initiated, neither by dendritic current injection nor by synaptic stimulation (*27*), although a recent study suggested that dendritic spikes may be evoked by massive glutamate uncaging (*31*). Again, these properties differ from those of pyramidal neurons, where dendritic spikes are abundant (*33*). Third, the dendrites of PV^+ interneurons contain only a low density of voltage-gated Na^+ channels; Na^+ channels are almost absent at distances >100 μm from the soma (*27*). Fourth, the dendrites of hippocampal PV^+ interneurons contain a high density of voltage-gated K^+ channels, consistent with the results of previous Ca^{2+} imaging experiments with K^+ channel blockers (*28*). The high dendritic ratio of K^+ to Na^+ channels distinguishes PV^+ interneurons from pyramidal cells and also from other interneuron subtypes (*32*–*35*). Lastly, analysis of gating and pharmacological properties revealed that these channels are primarily of the Kv3 type, one of the four main subfamilies of voltage-gated K^+ channels (*7*). These channels show high activation threshold, fast activation, and fast deactivation (*7*).

Why should PV^+ interneurons express high-threshold K^+ channels in the dendrites if the amplitude of backpropagated action potentials is too small to activate them? As it turns out, dendritic Kv3 channels work synergistically with the small diameter of dendrites and the large amplitude and fast time course of the AMPA receptor–mediated postsynaptic conductance at excitatory input synapses (*23*, *36*, *37*). In the thin dendrites of PV^+ interneurons, AMPA receptor–mediated conductances generate local EPSPs with large peak amplitude (*18*), resulting in efficient activation of dendritic Kv3 channels (*7*, *27*) (Fig. 2D). This has profound functional consequences: Dendritic K^+ channel activation accelerates the decay time course of the EPSP, shortening the time period of temporal summation and promoting action potential initiation with high speed and temporal precision (*27*, *38*) (Fig. 2E) (Table 1). K^+ channel activation conveys sublinear integration (*27*), which may allow PV^+ interneurons to accurately sample principal neuron activity over a wide range. Additionally, K^+ channel activation makes PV^+ cells less sensitive to clustered excitatory input, which activates K^+ channels efficiently, but relatively more sensitive to distributed

Box 1. The steep scientific career of PV^+ interneurons.

1986: Celio (*9*) suggests that PV is expressed in the majority of GABAergic neurons in the cortex.
1987: Kawaguchi *et al*. (*132*) suggest that PV is selectively expressed in fast-spiking interneurons.
1995: Geiger *et al*. (*36*) demonstrate that fast-spiking, PV^+ interneurons express AMPA-type glutamate receptors with high Ca^{2+} permeability and fast gating, caused by a low relative abundance of GluA2 subunit mRNA.
1996: Du *et al*. (*133*) demonstrate that Kv3 K^+ channel subunits are selectively expressed in PV^+ cells, providing the first suggestion of a molecular mechanism underlying the fast-spiking action potential phenotype.
1997: Geiger *et al*. (*23*) show that fast-spiking PV^+ interneurons in the dentate gyrus receive fast excitatory synaptic inputs.
2001: Pouille and Scanziani (*72*) demonstrate that feedforward inhibition, presumably provided by PV^+ interneurons, shortens the coincidence detection window in pyramidal neurons.
2005: Hippenmeyer *et al*. (*125*) generate a PV-Cre mouse line that specifically expresses Cre recombinase in PV^+ interneurons. This opened the door for both selective labeling and manipulation.
2009: Cardin *et al*. and Sohal *et al*. (*11*, *12*) show that rhythmic optogenetic stimulation of PV^+ interneurons results in the generation of gamma oscillations, whereas inhibition of PV^+ interneurons reduces gamma power.
2010: Hu *et al*. (*27*) provide the first recordings from subcellular processes of PV^+ interneurons (dendrites and, later, axons). This now results in a complete mapping of the functional properties of these cells along the dendrite-soma-axon axis.
2012: Wilson *et al*., Atallah *et al*., and Lee *et al*. (*94*, *95*, *102*) show that PV^+ interneurons control gain of sensory responses. This is probably the first demonstration that a specific aspect of signal processing in neuronal networks can be attributed to a distinct cell type.
June 2014: A PubMed search for "parvalbumin interneuron" returns 1644 hits, with many recent papers published in *Science* and *Nature*.

Box 2. The several caveats of PV^+ interneuron identification.

How can we identify the fast-spiking, PV-expressing basket cell? Ideally, for rigorous interneuron identification, one would like to see complete morphological visualization, expression analysis for the most important interneuron markers, and functional characterization. In practice, identification often relies on a subset of parameters. In the past, identification was often based on the action potential phenotype (*124*) (fast spiking; action potential frequency > 50 Hz at 22°C and > 150 Hz at 34°C) and the morphology of the axon (basket cells; ~90% of collaterals in the cell body layer) (*5*). However, cholecystokinin- and vasoactive intestinal peptide-expressing basket cells have maximal action potential frequencies that are less than a factor of 2 lower than those of PV^+ neurons (*57*). More recently, identification increasingly exploited PV expression, for example, in optogenetic experiments (*11*, *12*). However, PV is expressed not only in basket cells, but also in a subset of axo-axonic cells, bistratified cells, and even in oriens-alveus–lacunosum-moleculare (OLM) interneurons (*5*). Furthermore, one needs to consider regional differences. In the prefrontal cortex, only a subset of axo-axonic cells may express PV (*14*); in the dentate gyrus, analogs of bistratified cells may not be present. Finally, PV expression levels matter because OLM interneurons express PV at lower concentrations than basket or axo-axonic cells (*10*). More work is needed to elucidate the functional differences between PV^+ cell types, mainly basket versus axo-axonic cells. This distinction is particularly important because basket cells have inhibitory effects on their postsynaptic target cells, whereas axo-axonic cells may be excitatory (*134*).

input, which activates these channels only minimally (27) (Fig. 2E).

Dendrites of PV$^+$ interneurons in both the hippocampus and the neocortex are highly interconnected by gap junctions (39–42). Such a syncytial organization of dendritic trees will also affect synaptic integration. Gap junctions will lead to speeding of the EPSP time course, because excitatory charge can escape into adjacent dendrites. Furthermore, gap junctions may widen the spatial range of detection of principal neuron activity, including input synapses that are unconnected to a given PV$^+$ interneuron but are connected to adjacent interneurons (37). Finally, gap junctions may boost the efficacy of distal inputs and increase the average action potential frequency after repetitive synaptic stimulation of distal synapses (35).

The subcellular physiology of PV$^+$ interneurons: Axons

Direct recordings also revealed several surprising properties of axons of hippocampal PV$^+$ interneurons (43) (Fig. 3, A and B): (i) The action potential is initiated very proximally, ~20 μm from the soma (43) (Fig. 3A). This is different from pyramidal neurons, where the initiation site is more remote, sometimes even beyond the axon initial segment (44). (ii) Action potentials propagate with high reliability; propagation failures occur only rarely. (iii) The orthodromic action potential propagation velocity is ~1.5 m s^{-1} at near-physiological temperature, notable for a thin, largely unmyelinated axon (43). The propagation velocity is faster than that of principal neuron axons under comparable conditions (45, 46). (iv) PV$^+$ interneurons exhibit a distinct Na$^+$ channel distribution: a stepwise density increase from the soma to the proximal axon, followed by a

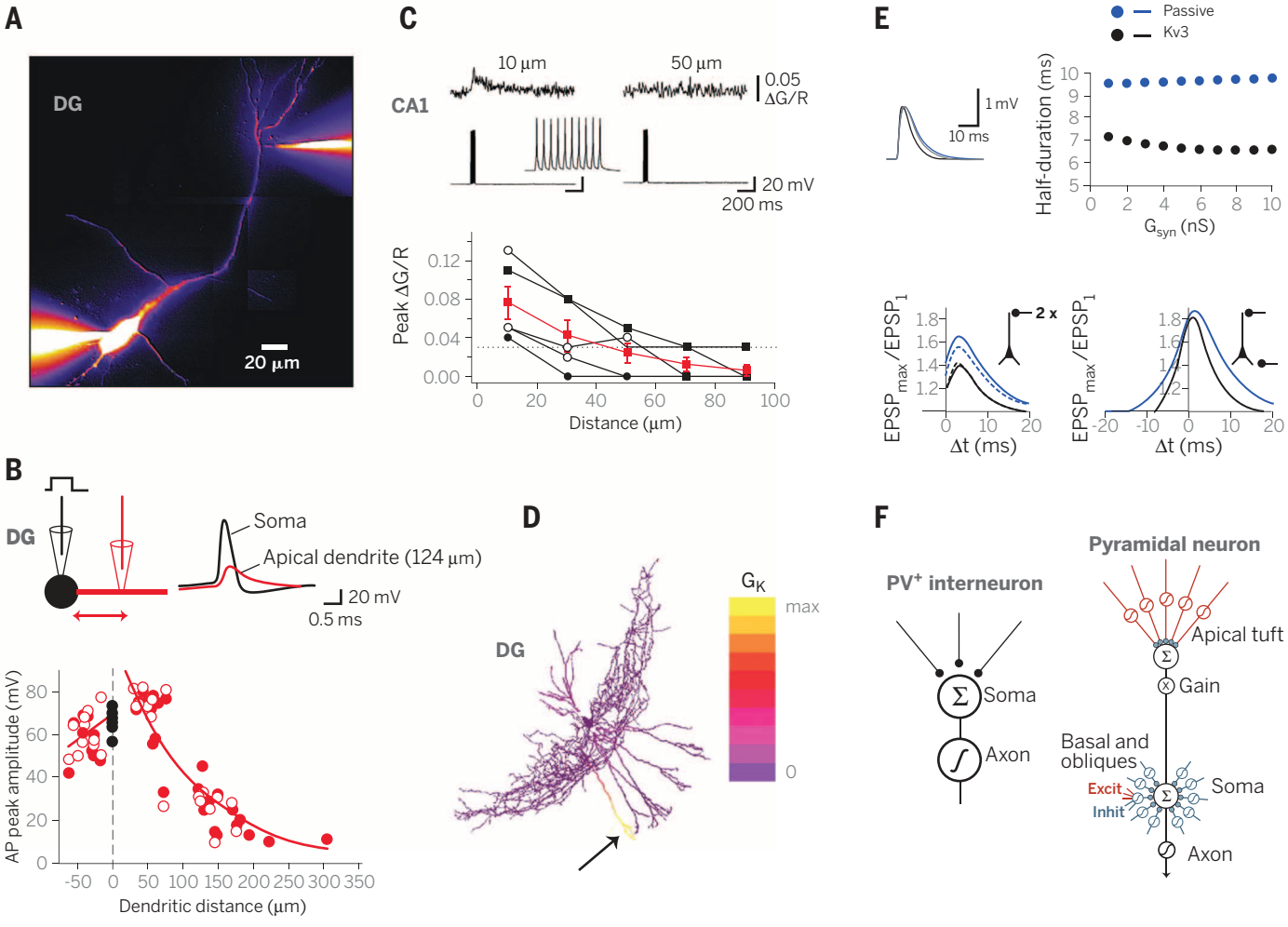

Fig. 2. The "in" and "out" of PV$^+$ interneurons: dendrites. (**A**) Direct patch-clamp recording from subcellular processes of PV$^+$ interneurons in the dentate gyrus (DG), using confocally targeted patch-clamp recording in a brain slice in vitro. The cell was first loaded with fluorescent dye (Alexa Fluor 488) via a somatic recording pipette. A dendritic recording was subsequently obtained on the distal dendrite. (**B**) Decremental action potential back-propagation into dendrites. Peak amplitude of the action potential at the dendrite was plotted against distance, with recording sites at basal dendrites (negative distance) and apical dendrites (positive distance). Solid circles, somatic current injection; open circles, dendritic current injection. Inset on top shows action potentials at the soma (black) and dendrite (red), with the current pulse applied to the soma. (**C**) Dendritic Ca^{2+} transients in PV$^+$ interneurons in the hippocampal CA1 region in vitro. (Top) Dendritic Ca^{2+} transients at 10 and 50 μm distance from the soma. (Bottom) Decline of amplitude of dendritic Ca^{2+} transients as a function of distance from the soma. Error bars indicate SEM. R, red; G, green fluorescent signal. Data are from (30). (**D**) Dendritic Kv3-type K$^+$ channels in a PV$^+$ interneuron model are locally activated by synaptic input (apical dendrite, arrow). Pseudocolor code indicates the activated K$^+$ conductance (G_K). (**E**) Dendritic Kv3-type K$^+$ channels in PV$^+$ interneurons accelerate the EPSP time course (top) and enhance the ability of the neuron to detect temporally coincident, but spatially distributed inputs (bottom). Blue, passive dendrites; black, K$^+$ channels in synapse-containing dendrites. G_{syn}, synaptic peak conductance. Data in (A), (B), (D), and (E) are from (27). (**F**) Schematic illustration of the different rules of dendritic integration in PV$^+$ interneurons (left) and pyramidal neurons (right). In PV$^+$ interneurons, the high ratio of K$^+$ channels to Na$^+$ channels in dendrites confers linear or sublinear integration (Σ, linear summation mechanism). In pyramidal neurons, the high ratio of Na$^+$ channels to K$^+$ channels in dendrites enriches the repertoire of single-neuron computations [∫, sigmoidal threshold mechanism (127)].

further gradual increase to the distal axon (*43*, *47*) (Fig. 3B). In the distal axon, the Na^+ conductance density is ~600 pS μm^{-2}, which is comparable to values in invertebrate axons (*43*). Thus, PV^+ interneurons show a weakly excitable "analog" somatodendritic domain (with graded synaptic potentials) and a highly excitable "digital" axonal domain (with all-or-none action potentials), separated by a steep transition zone. Assuming that the axon represents ~74% of the surface area (*18*), ~99% of the Na^+ channels would be located in the axon. Hence, the excitability mechanism of PV^+ cells is almost entirely axonal. (v) The axon of PV^+ interneurons contains voltage-gated K^+ channels with properties similar to those in the dendrites of PV^+ cells (*43*, *48*).

Why should PV^+ interneurons express an excessively high density of Na^+ channels in the axon? The first guess was that the high density guarantees reliability of action potential propagation (*26*). However, experiments and simulations indicate that Na^+ channels are expressed at higher density values than the critical value required for reliability (*43*). The "supercritical" Na^+ channel density has two additional advantages: It increases the speed of action potential propagation and the maximal action potential frequency during sustained somatic current injection (*43*). Hence, the high Na^+ channel density in the axon contributes to rapid signaling in PV^+ interneurons (Table 1). In relation to propagation speed, the high channel density compensates for the unfavorable morphological properties of interneuron axons (small segmental diameter, extensive branching, and high bouton density).

What is the molecular identity of Na^+ and K^+ channels in the axon of PV^+ interneurons? For voltage-gated Na^+ channels, $Na_V1.1$ and $Na_V1.6$ immunoreactivity is abundantly present in the axons (*49*, *50*). However, the contribution of other subunits cannot be excluded, because $Na_V1.2$, -1.4, and -1.7 mRNAs are also detectable in PV^+ interneurons (*51*). For voltage-gated K^+ channels, Kv3 subunits are heavily expressed in PV^+ interneurons, and Kv3 immunoreactivity has been localized to axons (*7*, *52*). Furthermore, the pharmacological and gating properties of axonal K^+ channels imply that they are primarily of the Kv3 subtype (*48*). The high activation threshold and the fast deactivation of these channels may ensure fast action potential repolarization in the axon. Finally, Kv1 channels are present in the axon initial segment of hippocampal and neocortical PV^+ interneurons (*50*, *53*, *54*). The low activation threshold and the slower gating of these channels may define characteristic input-output conversion properties in PV^+ cells. Long current pulses will activate these channels, suppressing the initiation of action potentials (*53*). In contrast, fast EPSPs will bypass Kv1 channel activation, leading to action potential initiation with short delay (*53*). Thus, Kv1 channels may implement a fast coincidence detection mechanism in PV^+ interneurons (Table 1). In addition, the profound inactivation of these channels may explain delayed spiking during long-lasting depolarizations (*53*).

From axons to presynaptic terminals: Fast GABA release

Multiple properties of dendrites and axons of PV^+ interneurons are specialized for rapid signaling. But how is the electrical signal in the axon converted into GABA release (*55*)? Several factors are important for this conversion, including the duration of the presynaptic action potential, the gating of the presynaptic Ca^{2+} channels, the coupling between Ca^{2+} channels and release sensors, and the Ca^{2+} binding and unbinding rates of the release sensor. Collectively, these factors will determine the "synaptic delay," that is, the time interval between the action potential in the presynaptic terminal and the event of exocytosis.

Many of these factors in PV^+ interneuron output synapses are optimized for speed (Fig. 3C). Direct recordings revealed that axonal action potentials are brief, comparable to those at the soma (*43*). Because presynaptic terminals are of the en passant type, this will directly translate into fast and synchronous transmitter release. Consistent with this hypothesis, broadening of the presynaptic action potential by K^+ channel blockers enhances both presynaptic Ca^{2+} transients and peak amplitudes of postsynaptic currents (*48*).

Whereas several types of synapses use mixtures of P/Q-, N-, and R-type Ca^{2+} channels for transmitter release (*56*), the output synapses of PV^+ cells in both the hippocampus and the neocortex exclusively rely on P/Q-type channels (*57*–*60*). As P/Q-type Ca^{2+} channels show the fastest gating among all Ca^{2+} channel subtypes (*56*), the specific usage of these channels will contribute to both the shortening of the synaptic delay and the increase in the temporal precision of transmitter release.

Another specific property of transmission is the tight ("nanodomain") coupling between Ca^{2+}

Table 1. Fast signaling properties of PV^+ interneurons.

Property	Functional consequence	Molecular mechanism	Reference(s)
Fast EPSCs	Fast EPSP time course; coincidence detection	GluA1 and GluA4 AMPA receptor subunits	(*23*, *37*)
Fast IPSCs	High-frequency network oscillations	GABRA1 $GABA_A$ receptor subunits	(*129*, *130*)
Dendritic K^+ channels (high activation threshold, fast deactivation)	Sublinear summation; sensitivity to distributed inputs	Kv3	(*27*, *28*)
Perisomatic K^+ channels (high activation threshold, fast deactivation)	Short action potentials; fast-spiking AP phenotype	Kv3	(*7*, *131*)
D-type K^+ channels in axon initial segment	Coincidence detection; delayed spiking during long current pulses	Kv1	(*50*, *53*, *54*)
Supercritical Na^+ channel density in axon	Fast axonal action potential propagation; fast-spiking AP phenotype	$Na_V1.1$ $Na_V1.6$	(*43*, *49*, *50*)
Fast presynaptic Ca^{2+} channels	Speed and temporal precision of GABA release	$Ca_V2.1$, P/Q-type Ca^{2+} channel	(*57*–*60*)
Tight coupling between presynaptic Ca^{2+} channels and release sensors	Speed and temporal precision of synaptic transmission	Unknown	(*57*, *59*)
Fast release sensors	Speed and temporal precision of synaptic transmission	Synaptotagmin 2	(*63*, *64*, *66*, *67*)

channels and release sensors of exocytosis (61, 62) (Fig. 3C). Tight coupling increases the efficacy of release, shortens the synaptic delay, and increases the temporal precision of release (61). Furthermore, GABA release at presynaptic terminals of PV^+ interneurons is initiated by a small number of Ca^{2+} channels, probably only two or three per release site (59). The usage of a small number of Ca^{2+} channels could help avoid the broadening of presynaptic action potentials or, in extreme cases, the generation of Ca^{2+} spikes in presynaptic terminals. Thus, the small number of Ca^{2+} channels per release site at PV^+ interneuron output synapses contributes to fast and temporally precise transmitter release.

Finally, a subset of PV^+ interneurons in the hippocampus and the neocortex uses synaptotagmin 2 (1 out of the 15 members of the synaptotagmin family) as a release sensor for synaptic transmission; in contrast, principal neurons primarily rely on synaptotagmin 1 (63–65). Recent studies have used synaptotagmin 2 immunolabeling to selectively visualize PV^+ boutons in the visual cortex (66). As synaptotagmin 2 has the fastest Ca^{2+}-binding kinetics throughout the synaptotagmin family (67), the expression of this synaptotagmin isoform may also contribute to rapid signaling. Direct measurement of Ca^{2+}-binding rates of different synaptotagmin isoforms will be needed to quantitatively test this hypothesis.

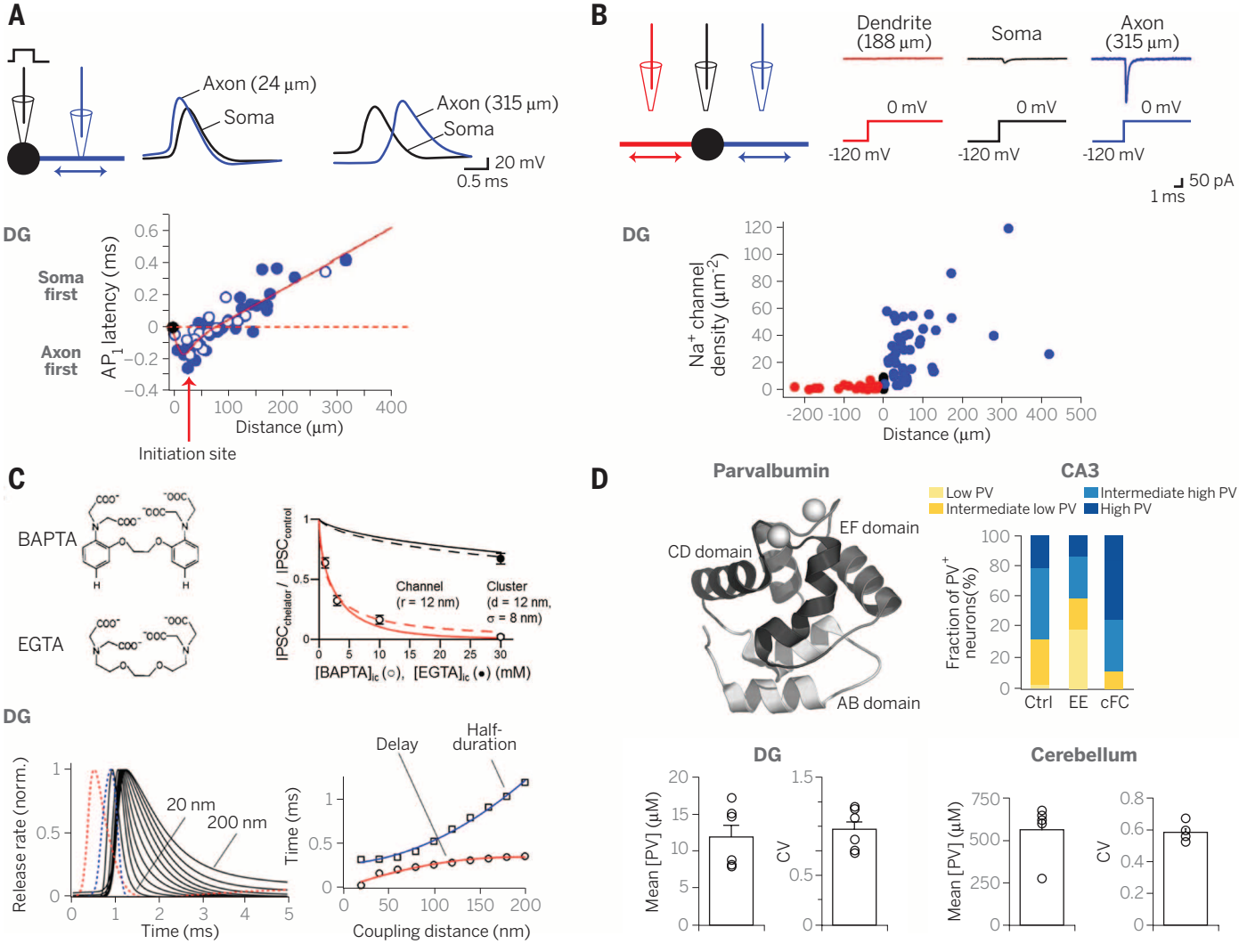

Fig. 3. The "in" and "out" of PV^+ interneurons: axons and presynaptic terminals. (**A**) Proximal initiation of action potentials. (Top) Action potentials at the soma (black) and axon (blue) in two different soma-axon recordings with different axonal distance. (Bottom) Latency between action potentials in axon and soma was plotted against distance, with negative values indicating "axon-first" behavior and positive values representing "soma-first" behavior. Note the sharp initiation site in the axon ~20 µm from the soma. (**B**) Voltage-gated Na^+ channel spatial distribution profile. Channel density measured in the outside-out patch configuration is plotted against distance, with negative values indicating dendritic location and positive values indicating axonal location. Note the stepwise increase of Na^+ channel density from the soma to the proximal axon, followed by a gradual increase to the distal axon. Data in (A) and (B) are from (43). (**C**) Tight coupling between Ca^{2+} channels and release sensors at the output synapses of PV^+ interneurons. (Top left) Chemical structure of the fast Ca^{2+} chelator BAPTA and the slow Ca^{2+} chelator EGTA used to probe the coupling configuration. (Top right) Concentration dependence of the effects of the two chelators on GABA release. Curves represent linearized models fit to the experimental data, revealing a coupling distance of 12 nm. IPSC, inhibitory postsynaptic current; r, coupling distance; d, mean coupling distance; σ, SD. (Bottom left) Dependence of simulated time course of release on coupling distance in a source-sensor model. (Bottom right) Simulated synaptic delay and half-duration of the time course of release as a function of coupling distance. Data are from (61). (**D**) Action of the endogenous Ca^{2+} binding protein PV on transmitter release. (Top left) Secondary structure of PV, with the spheres indicating bound Ca^{2+} ions. Data are from (128). (Top right) Activity-dependent regulation of PV concentration in interneurons of the hippocampal CA3 region. EE, enriched environment; cFC, contextual fear conditioning. Data are from (69). (Bottom) Estimation of absolute PV concentration in the soma of different types of inhibitory interneurons by calibrated immunocytochemistry. Data are from (10).

What are the effects of PV on GABA release at PV^+ interneuron output synapses? The EF-hand domains of PV bind both Ca^{2+} and Mg^{2+} ions (Fig. 3D). Therefore, it is generally thought that Mg^{2+} must leave before Ca^{2+} can bind, conferring slow Ca^{2+} binding properties to this protein (*68*). How can such a Ca^{2+} buffer act in nanodomain coupling regimes? The high PV concentration may provide an answer to this question. If the PV concentration is at millimolar levels, as found in cerebellar basket cells (*10*), or if the PV concentration is up-regulated during behavior (e.g., contextual fear conditioning or learning completion), as observed in the hippocampal PV^+ interneurons (*69*), the free "apo" form of PV may become functionally relevant (Fig. 3D). Under these conditions, PV may modulate transmitter release, for example, by acting as an antifacilitation factor (*10*).

The role of PV^+ interneurons in microcircuits: Beyond simple inhibition

GABAergic interneurons are involved in both feedforward and feedback inhibition (*70*–*73*) (Box 3). But what is the specific contribution of PV^+ cells, and what is the functional relevance of their fast signaling mechanisms? Experimental evidence indicates that PV^+ interneurons in the hippocampus are involved in feedforward inhibition (Fig. 4). In the hippocampal CA1 region, feedforward inhibition initiated by stimulation of Schaffer collaterals is primarily mediated by perisomatic inhibitory interneurons, because somatodendritic recordings from CA1 pyramidal neurons reveal a distance-dependent decline of inhibition (*72*). Furthermore, this inhibition is primarily mediated by fast-spiking PV^+ cells, because these interneurons fire early after stimulation, before pyramidal cells and regularly spiking interneurons (*74*) (Fig. 4C).

Feedforward microcircuits incorporating PV^+ cells may have several functions beyond simple inhibition. For example, feedforward inhibition by PV^+ interneurons narrows the window for temporal summation of EPSPs and action potential initiation in principal neurons (*72*) (Fig. 4D). Feedforward inhibition by PV^+ interneurons will expand the dynamic range of activity in large principal neuron ensembles (*74*) (Fig. 4E). For both functions, the fast signaling of PV^+ interneurons is critically important. PV^+ interneuron-mediated

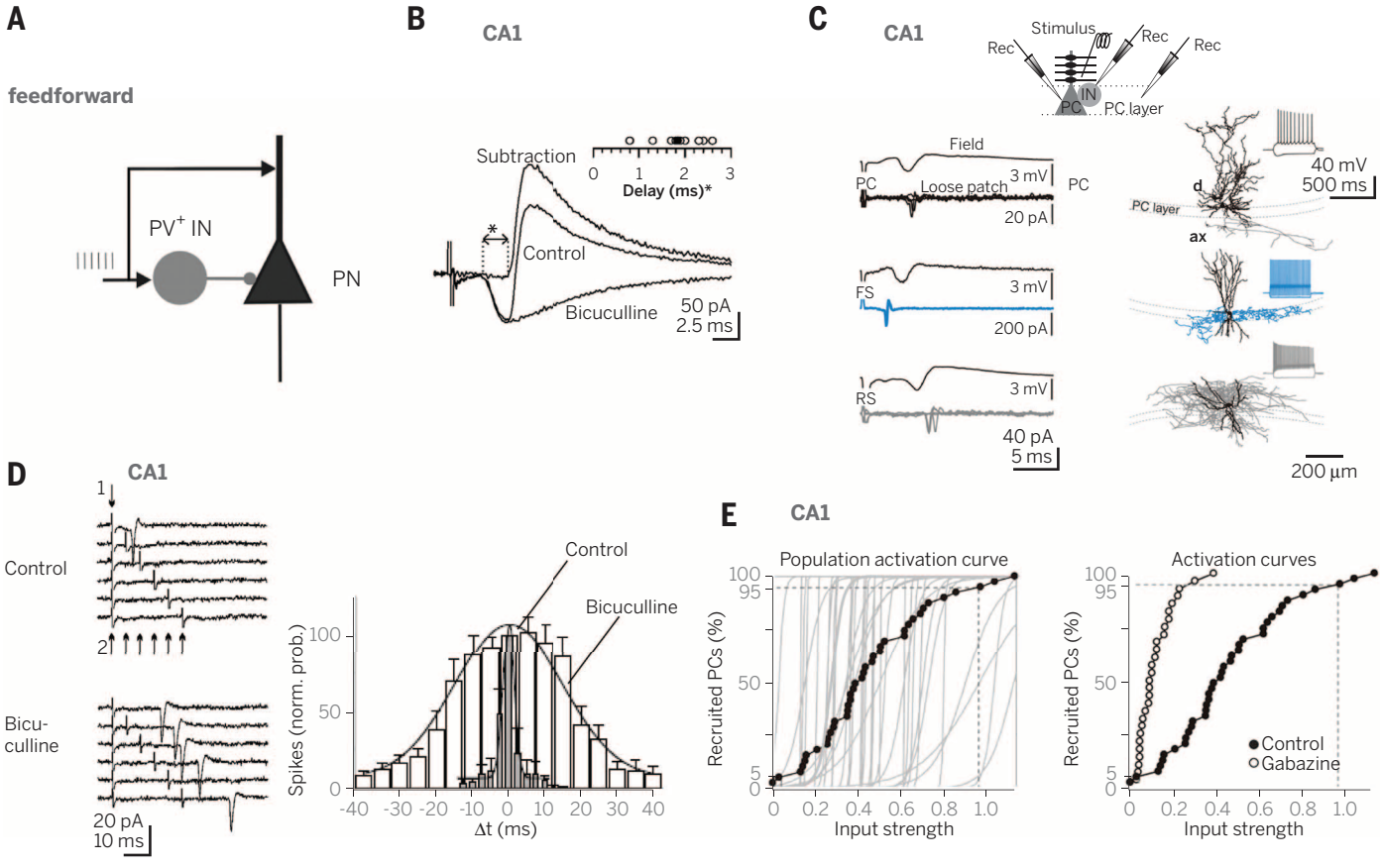

Fig. 4. The role of PV^+ interneurons in feedforward inhibitory microcircuits. (**A**) Schematic illustration of the feedforward inhibitory microcircuit. IN, interneuron; PN, principal neuron. [Scheme courtesy of G. Buzsáki.] (**B**) Time course of disynaptic feedforward inhibition in the hippocampal CA1 region. Traces indicate control signal (monosynaptic EPSC and disynaptic IPSC), pharmacologically isolated EPSC, and analog subtraction. Note the short latency of the disynaptic IPSCs (inset). The asterisk indicates delay. Data are from (*72*). (**C**) Activation of pyramidal neurons (top), fast-spiking interneurons (center), and regularly spiking interneurons (bottom) during feedforward inhibition. Upper traces show local field potentials; lower traces illustrate loose-patch recordings. Right panels show corresponding morphological properties of the recorded cells. Inset on top schematically illustrates stimulation procedure. Data are from (*74*). (**D**) Feedforward inhibition shortens the coincidence detection window in CA1 pyramidal neurons. (Left) Traces indicate action potentials recorded in the cell-attached configuration after stimulation of two Schaffer collateral inputs at different time intervals under control conditions (top) and after a block of inhibition (bottom). Arrows indicate time points of first and second stimulus. (Right) Spike probability after stimulation of two excitatory inputs with time interval Δt in the presence of inhibition (gray bars) and after a block of inhibition (white bars). Error bars denote SEM. Data are from (*72*). (**E**) Feedforward inhibition expands the dynamic range of principal neuron population activity. (Left) Plot of proportion of recruited CA1 pyramidal cells (PCs) against synaptic input strength. Filled data points and the black curve show the results for the entire population of CA1 pyramidal neurons; gray curves show the results for individual cells. (Right) Comparison of population input-output curves in the presence of inhibition (solid circles) and after a block of inhibition (open circles). Although PV^+ interneurons are likely to play an important role, other interneuron types may also be involved. Data are from (*74*).

inhibition has to be fast enough to ensure that a substantial inhibitory conductance is generated before action potentials are initiated in principal neurons.

PV^+ interneurons are also involved in feedback (recurrent and lateral) inhibition (Fig. 5). Reciprocal coupling between principal neurons and fast-spiking interneurons has been demonstrated in several circuits, including the hippocampus and the entorhinal cortex (*23*, *75*) (Fig. 5, B and C). Antidromic activation of hippocampal CA1 pyramidal neurons by alveus stimulation generates substantial inhibition after both single stimuli and high-frequency trains (*73*) (Fig. 5D). Early inhibition is primarily mediated by perisomatic inhibitory interneurons, whereas late inhibition during trains is primarily mediated by dendritic inhibitory interneurons, as shown by the different slope of the IPSP at somatic and dendritic recording sites (*73*) (Fig. 5D). Quadruple recording in the entorhinal cortex also suggests a substantial contribution of PV^+ interneurons to both recurrent and lateral inhibition (*75*).

Feedback and lateral microcircuits involving PV^+ cells may have several functions beyond simple inhibition. Feedback inhibition implements a "winner-takes-all" mechanism (*76*, *77*) (Fig. 5E): Once the principal cells with the strongest input fire, action potential initiation in the remaining cells is inhibited. This computation could be particularly important in the dentate gyrus, where it may contribute to sparsification of activity (*78*), pattern separation (*79*), and grid-to-place code conversion (*77*, *80*). Under certain conditions, network models with recurrent inhibitory connectivity are also able to generate grid cell response patterns (*75*, *81*) (Fig. 5F), which may suggest that PV^+ interneurons contribute to the grid cell activity of stellate cells in the entorhinal cortex [but see (*82*)].

In the winner-takes-all feedback inhibitory microcircuit (*76*, *77*), it has been suggested that the cells that receive excitation within a certain percentage of the maximum excitation fire (independently of the distribution of excitation), and this percentage is determined by the ratio of the delay of disynaptic inhibition over the membrane time constant of the principal cells (*76*) (Fig. 5E). Thus, the fast signaling properties of PV^+ interneurons, which define the delay of disynaptic inhibition, are critically important for the winner-takes-all mechanism.

It is often assumed that connectivity in feedforward or feedback inhibitory microcircuits is random and that the properties of inhibitory synaptic transmission are uniform (*83*). However, this may not be the case. PV^+ basket cells in the hippocampal CA1 region receive stronger excitatory input from superficial pyramidal neurons but provide more powerful output to deep pyramidal neurons (*84*). Inhibition at the output synapses of PV^+ interneurons in the dentate gyrus has distance-dependent properties, with stronger and faster inhibition at short distances and weaker and slower inhibition at long distances (*85*). In addition, inhibition at the output synapses on PV^+ interneurons is stronger in target cells with strong synaptic excitation and high activity levels (*86*). Thus, PV^+ interneurons are substantially more than simple network stabilizers. They contribute to advanced computations in microcircuits and neuronal networks. Furthermore, they are not randomly and uniformly connected but are embedded in microcircuits according to specific rules.

Activity of PV^+ interneurons in vivo

A central question in neuroscience is how specific neuron types shape higher brain functions, up to the level of animal behavior. The distinct experimental accessibility and the detailed knowledge about the cellular properties of PV^+ interneurons may give us a chance, for the first time, to rigorously address this question.

One way to approach the problem is to examine the activity of PV^+ interneurons in vivo in awake, behaving animals during ongoing network activity (Fig. 6, A to C). The activity of PV^+ interneurons in the hippocampus substantially changes during network oscillations, such as theta (4 to 10 Hz), gamma (40 to 100 Hz), and ripple activity (140 to 200 Hz). In the absence of oscillatory activity, action potential frequency is low (6.5 Hz) (*87*). During theta oscillations, action potential frequency markedly increases (21 Hz). During sharp wave ripples (SWRs), the firing frequency increases by more than one order of magnitude to 122 Hz [(*87*, *88*), see (*89*) for similar in vitro data] (Fig. 6A). The massive activation of PV^+ interneurons during SWRs (*87*) may be explained by the ability of these cells to efficiently respond to synchronous distributed input, which will be generated by pyramidal cell activity during SWRs (*90*). Further, the high action potential frequency in PV^+ interneurons in this network state (*87*) demonstrates that PV^+ interneurons make use of their fast-spiking phenotype (*7*) under in vivo conditions.

An alternative way to approach the question is to examine the activity of PV^+ interneurons following adequate stimuli. In the hippocampus, a substantial proportion of neurons are place cells, so the location of the animal appears to be the adequate stimulus. Whereas pyramidal neurons show narrow place fields, PV^+ interneurons have much broader place fields (*91*, *92*) (Fig. 6B). Similarly, whereas a large proportion of stellate cells in the entorhinal cortex are grid cells (*80*), PV^+ interneurons show substantially broader spatial tuning (*81*, *82*) (Fig. 6B). In the primary visual cortex, neurons are often sensitive to both orientation and contrast of the stimulus, for example, when animals are exposed to drifting gratings. However, PV^+ interneurons exhibit broader orientation tuning and weaker contrast specificity than pyramidal neurons [(*93*–*95*), but see (*96*)] (Fig. 6C). In all of these cases, the broad tuning of PV^+ interneurons may be explained by the convergent input from a large number of principal neurons with a wide range of spatial or orientation preferences. The action potential frequency of PV^+ interneurons in both hippocampal and neocortical circuits increases with running (*88*, *97*). Thus, PV^+ interneurons may receive a velocity-modulated input that could be used for path integration, for instance.

The role of PV^+ interneurons in network function and animal behavior in vivo

A more direct approach to bridge the gap between cellular and network level is to interfere with the activity of PV^+ interneurons in vivo and to examine the behavioral consequences in awake animals (Fig. 6, D to F). In principle, optogenetics [e.g., channelrhodopsin (*11*), halorhodopsin (*12*), or archaerhodopsin] or pharmacogenetics [e.g., pharmacologically selective effector molecules in combination with chimeric ligand-gated ion channels (*98*)] allow researchers to interfere with the function of PV^+ interneurons in either the positive or negative direction.

Such experiments are beginning to provide insight into the function of PV^+ interneurons at both network and behavioral levels. Optogenetic manipulation of PV^+ interneuron activity showed

Box 3. Feedforward and feedback microcircuits.

In feedforward inhibition, afferent glutamatergic axons activate principal cells and interneurons in parallel (Fig. 4A). In feedback (recurrent and lateral) inhibition, afferent glutamatergic axons activate principal cells, which then activate interneurons in series (Fig. 5A).

Feedback inhibition must be further subdivided into recurrent and lateral inhibition. However, the distinction between these two forms often remains fuzzy. Multiple cell recording provides an elegant way to quantitatively distinguish the two forms. Recurrent inhibition in a network can be defined as the proportion of principal cells that provide excitation to and receive inhibition from a given PV^+ interneuron, whereas lateral inhibition is the proportion of principal cells that do not provide excitation to but receive inhibition from a given PV^+ interneuron (*75*) (Fig. 5C).

The speed of both feedforward and feedback inhibition is impressive; the latency of disynaptic inhibition under physiological conditions is only 2 ms or less (*71*, *72*). This high speed may be unexpected, because inhibition is composed of several steps (IN excitation via PN-IN synapses → propagation of EPSPs to the soma → action potential initiation in the axon initial segment → action potential propagation into the IN axon → GABA release → PN inhibition via GABAergic output synapses). The fast signaling properties of PV^+ interneurons (Table 1) play a key role in minimizing the delay.

that they are necessary and sufficient for the generation of network oscillations in both the hippocampus and neocortex. Stimulation of PV^+ cells at theta frequency induces theta spike resonance in CA1 pyramidal cells (*99*), and stimulation of PV^+ cells at gamma frequency leads to gamma oscillations in the local field potential in the somatosensory cortex (*11*, *12*). Conversely, suppression of PV^+ cells reduces gamma oscillations (*12*). This confirms a major role of PV^+ interneurons in network oscillations, as previously inferred from in vitro data (*100*).

Experimental manipulation of PV^+ interneuron activity in the hippocampus demonstrated that PV^+ interneurons regulate both the precise shape of place fields and the phenomenon of phase precession in CA1 pyramidal neurons (*92*) (Fig. 6D). As an animal moves from the periphery toward the center of a place field, the action potentials in pyramidal neurons shift to earlier phases of the theta cycle (*101*). When PV^+ interneurons are inhibited, the steepness of the phase-position relation becomes reduced (*92*) (Fig. 6D). Thus, PV^+ interneurons regulate the precise timing of action potential initiation in a pyramidal neuron ensemble, probably making use of their fast signaling properties.

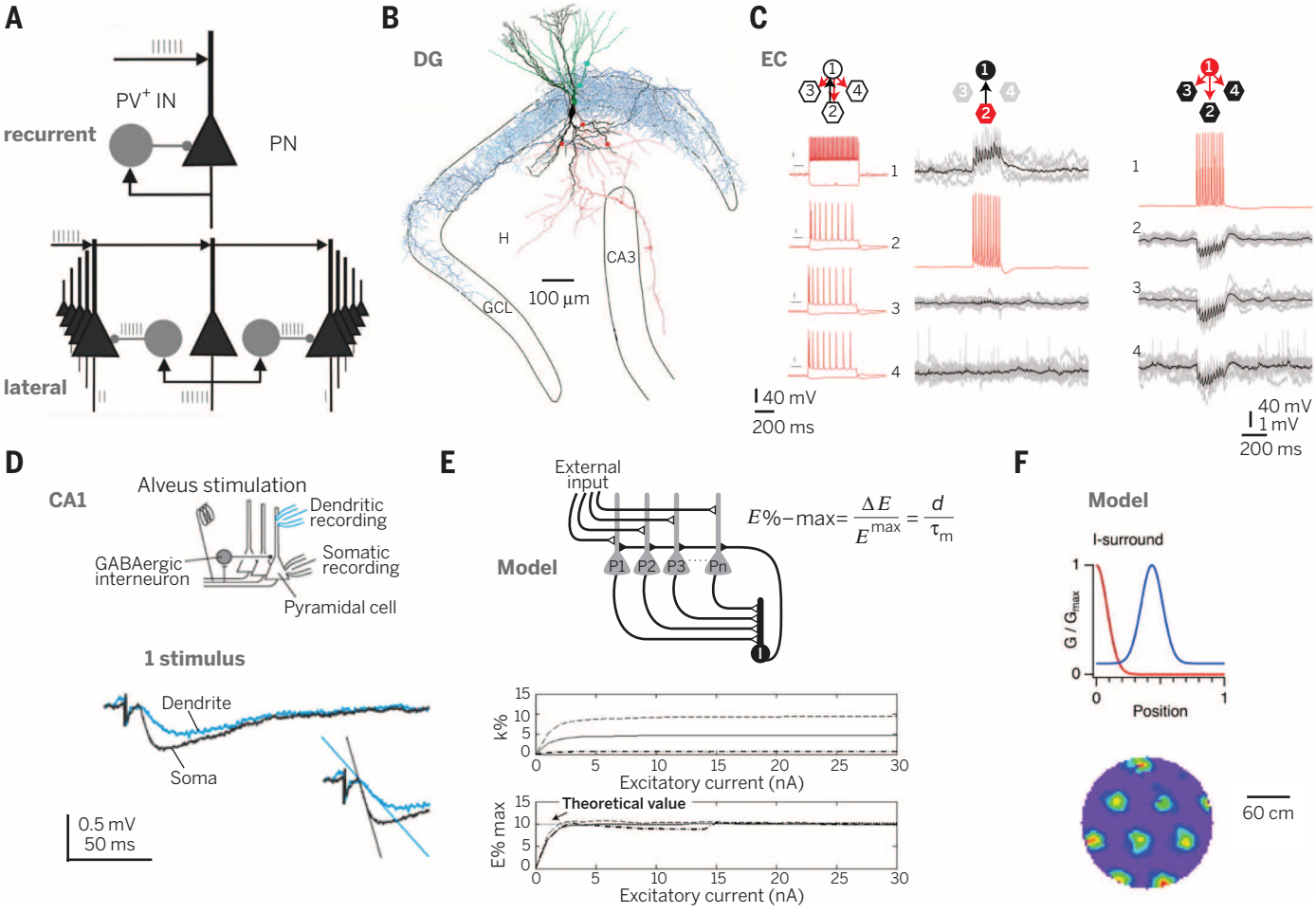

Fig. 5. The role of PV^+ interneurons in feedback inhibitory microcircuits. (**A**) Schematic illustration of the feedback inhibitory microcircuit. (Top) Recurrent inhibition; (bottom) lateral inhibition. [Scheme courtesy of G. Buzsáki.] (**B**) Feedback inhibition in the dentate gyrus. Reciprocal coupling between a fast-spiking (putative PV^+) interneuron and a granule cell. Neurons were filled with biocytin during recording and subsequently reconstructed. Black, soma and dendrites of PV^+ interneuron; blue, axon of PV^+ interneuron; green, soma and dendrites of granule cell; red, granule cell axon. Red dots, putative excitatory synapses on interneurons; green dots, inhibitory synapses on granule cells. H, hilus; GCL, granule cell layer. Data are from (*23*). (**C**) Feedback inhibition in the entorhinal cortex (EC). Simultaneous recording from one fast-spiking (putative PV^+) interneuron and three layer-two stellate cells. (Left) Action potential phenotype of the four neurons. (Center) Action potentials in a stellate cell evoked EPSPs in the putative PV^+ interneuron. (Right) Action potentials in the interneuron evoked IPSPs in all three stellate cells. (Top) Schematic illustration of connectivity (circle, putative PV^+ interneuron; hexagons, stellate cells). Data are from (*75*). (**D**) Recurrent inhibition in the hippocampal CA1 region. (Top) Schematic illustration of the stimulation procedure. (Bottom) Traces illustrating IPSPs simultaneously recorded in the soma and the dendrite of a CA1 pyramidal neuron. The slope of rise is higher at the somatic versus the dendritic recording site (inset), indicating that inhibition is generated perisomatically. Data are from (*73*). (**E**) Feedback inhibition implements a winner-takes-all mechanism. (Top) Scheme of the neuronal network with external input and feedback inhibition. (Bottom) Plot of the proportion of firing cells (k%) and the proportion of cells that receive excitation within E% of the maximal excitation (E% max). Line styles indicate different distributions of inputs. Note that E% max is relatively independent of the stimulus current. Also note that E% max is d/τ_m, where d is the delay of disynaptic inhibition and τ_m is the membrane time constant of the pyramidal cell. Thus, fast signaling in inhibitory interneurons is critically important for the computational properties of the winner-takes-all mechanism. Data are from (*76*). (**F**) A continuous attractor network model based on feedback inhibition may produce grid cell activity patterns in excitatory neurons. (Top) Distribution of E-I and I-E synaptic conductances in the model (E, excitatory; I, inhibitory). (Bottom) Pseudocolor representation of simulated activity of E cells in two-dimensional space. Cells receive background activation, theta-modulated input, velocity-modulated input, and place-cell input from the hippocampus. Synaptic output is shifted according to the direction of preferred movement. Data are from (*81*).

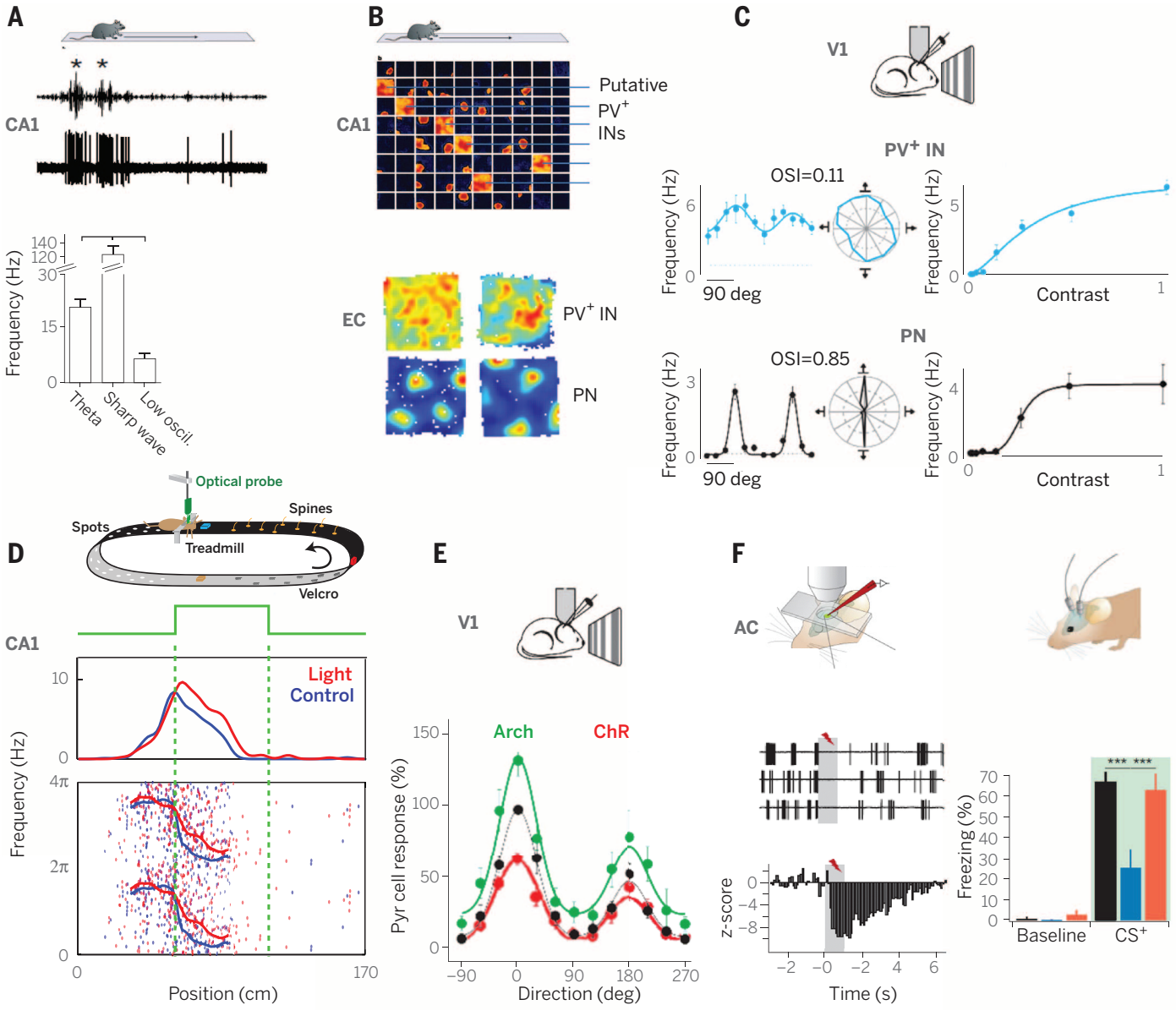

Fig. 6. The role of PV$^+$ interneurons in complex animal behavior. (**A**) Activity of PV$^+$ interneurons in the hippocampal CA1 region of freely moving rats. (Top) Firing of a PV$^+$ interneuron during SWRs. Upper trace, local field potential (filtered 130–230 Hz); lower trace, unit activity from a PV$^+$ interneuron. Asterisks indicate ripples. (Bottom) Summary bar graph indicating the mean action potential frequency. Note that the action potential frequency of PV$^+$ interneurons is >100 Hz during SWRs. Error bars denote SEM. Data are from (*87*). (**B**) Spatial firing of PV$^+$ interneurons and principal neurons. (Top) Place cell firing of hippocampal neurons; (bottom) grid cell firing of entorhinal cortex neurons. Warm colors indicate high action potential frequency. Note that putative PV$^+$ interneurons (PV$^+$ INs) have broader spatial fields than principal neurons (PNs). Data are from (*82*, *91*). (**C**) Orientation selectivity (left) and contrast sensitivity (right) of layer two and three pyramidal neurons in the primary visual cortex. Top graphs, PV$^+$ interneuron; bottom graphs, principal neuron. Note the broad orientation specificity and shallow contrast sensitivity of PV$^+$ interneurons in comparison to pyramidal neurons. V1, primary visual cortex; OSI, orientation selectivity index. Error bars indicate SEM. Data are from (*95*). (**D**) PV$^+$ interneuron activity regulates place field shape and phase precession in headfixed mice running on a treadmill belt. (Top) Spike frequency of CA1 pyramidal neurons versus location. (Bottom) Theta phase of action potentials versus location. Blue, control data; red, data after light pulses, leading to halorhodopsin-mediated inhibition of PV$^+$ interneurons. Data are from (*92*). (**E**) PV$^+$ interneuron activity regulates the gain of orientation-selective visual responses. Tuning curves of pyramidal neuron activity in the primary visual cortex during a visual stimulus (drifting grating) are shown. Black, control conditions; red, after activation of PV$^+$ interneurons with channelrhodopsin; green, after suppression of PV$^+$ interneurons with archaerhodopsin. Error bars indicate bootstrapped 95% confidence intervals. Data are from (*95*). (**F**) Role of PV$^+$ interneurons in associative auditory fear conditioning. (Left, top) Activity of PV$^+$ interneuron in the auditory cortex during unconditional stimuli (foot shocks, cell-attached recording). (Left, bottom) Summary of activity changes of PV$^+$ interneurons during foot shocks (*z* score). (Right) Behavioral freezing of the animal in baseline conditions and in the presence of the conditioned stimulus (CS$^+$, tone). Black, sham control; blue, with optogenetic stimulation of PV$^+$ interneurons; red, after reconditioning without optogenetic stimulation. Data are from (*104*). AC, auditory cortex. Error bars, SEM; asterisks, significance ($P < 0.001$).

Manipulation of PV^+ interneuron activity revealed that PV^+ interneurons regulate the gain of sensory responses (*94*, *95*, *102*) (Fig. 6E). In the primary visual cortex, activation or inactivation of PV^+ interneurons changes the gain of orientation tuning curves in pyramidal neurons, whereas the width of these curves remains largely unchanged [(*94*, *95*), but see (*102*)]. Such a gain modulation would be consistent with an underlying feedback inhibition mechanism (*76*). Similarly, in the barrel cortex, activation of PV^+ interneurons changes the amplitude of sensory responses evoked by whisker stimulation (*11*). However, the changes are more complex in this system because the number of spikes, latency, and spike precision are affected (*11*).

Finally, PV^+ interneurons are involved in the regulation of plasticity and learning (*69*, *103*–*106*) (Fig. 6F). PV^+ interneurons in the visual cortex are transiently inhibited after monocular deprivation; this down-regulation appears to be necessary to enable ocular dominance plasticity in the critical period (*103*, *106*). Furthermore, PV^+ interneurons in the auditory cortex are inhibited by aversive foot shocks in an auditory fear-conditioning paradigm, and this inhibition plays a critical role for associative fear learning (*104*, *105*) (Fig. 6F). Additionally, stimulation of PV^+ interneurons in the prefrontal cortex accelerates extinction of reward seeking behavior (*107*). In summary, suppression of PV^+ interneurons (i.e., disinhibition of pyramidal neurons) is necessary for certain forms of learning, whereas activation of PV^+ cells may promote extinction. Recent results further suggest that not only do PV^+ interneurons regulate learning, but learning also induces plastic changes in PV^+ interneurons (*69*). Thus, the involvement of PV^+ interneurons in learning is bidirectional.

The role of PV^+ interneurons in neurological and psychiatric diseases

Another major challenge in neuroscience is to understand how specific neuron types are involved in neurological or psychiatric diseases. What are the links between PV^+ interneurons and brain diseases? The problem is not in finding the links, but instead that there are too many! In several neurological and psychiatric diseases, the function of PV^+ interneurons appears to be altered. These include epilepsy, schizophrenia, depression, autism, and Alzheimer's disease (*108*). The detailed knowledge about PV^+ interneurons at the molecular, cellular, and network levels may now help us to focus on the most important relations, where the disease gene is selectively expressed in PV^+ cells and the phenotype can be replicated by restricted disease gene expression in PV^+ interneurons.

One recently identified link leads from the axonal $Na_V1.1$ channel in PV^+ interneurons to Dravet syndrome [severe myoclonic epilepsy of infancy (SMEI)] and GEFS+ (generalized epilepsy with febrile seizures plus) (*109*). Truncation mutations in the $Na_V1.1$/*SCN1A* gene have been identified in SMEI patients, and mouse models with general or PV^+ interneuron-selective deletion of the *SCN1A* gene replicate the disease phenotype (*110*–*113*). Thus, haploinsufficiency of the *SCN1A* gene in PV^+ interneurons appears to be the cause of the disease. As $Na_V1.1$ mRNA is highly expressed in PV^+ interneurons (*51*), and $Na_V1.1$ immunoreactivity is primarily present in the axons of these cells (*49*), both fast-spiking action potential phenotype and fast signal propagation in the axon will be affected. Furthermore, missense mutations in the $Na_V1.1$/*SCN1A* gene have been identified in GEFS+ patients. In one of the most common mutations, the Na^+ channel inactivation curve is left-shifted, which will reduce the number of available Na^+ channels (*114*). Thus, we increasingly understand the relations between the fast signaling properties of PV^+ interneurons and a neurological disease phenotype.

Another link leads from the receptor tyrosine kinase ErbB4 (epidermal growth factor receptor 4)—a protein selectively expressed in PV^+ interneurons (basket cells and axo-axonic cells) of several brain regions (*115*)—to schizophrenia (*116*). Mutations in both the *ErbB4* gene and the gene of neuregulin 1, the putative ErbB4 ligand, are frequently found in schizophrenic patients. Furthermore, mouse models with general or PV^+ interneuron-specific genetic elimination of ErbB4 replicate aspects of the disease phenotype (*117*). However, even in such a clearly defined case, the underlying mechanisms are highly complex. Genetic elimination of ErbB4 impairs both the excitatory synaptic input (*115*, *118*, *119*) and the inhibitory synaptic output of PV^+ interneurons (*115*, *119*). Consistent with the hypothesis of deficient PV^+ interneuron excitation, ErbB4 immunoreactivity is located in postsynaptic densities of glutamatergic input synapses on dendrites of PV^+ interneurons (*87*, *115*). Finally, neuregulin 1 application impairs the fast-spiking action potential phenotype by regulating Na^+ and Kv1 K^+ channels (*120*, *121*). Thus, we are beginning to understand the relations between the fast signaling properties of PV^+ interneurons and the extremely complex phenotype of a psychiatric disease.

REFERENCES AND NOTES

1. T. F. Freund, G. Buzsáki, Interneurons of the hippocampus. *Hippocampus* **6**, 347–470 (1996). doi: 10.1002/(SICI)1098-1063(1996)6:4<347::AID-HIPO1>3.0.CO;2-I; pmid: 8915675
2. Y. Aika, J. Q. Ren, K. Kosaka, T. Kosaka, Quantitative analysis of GABA-like-immunoreactive and parvalbumin-containing neurons in the CA1 region of the rat hippocampus using a stereological method, the disector. *Exp. Brain Res.* **99**, 267–276 (1994). doi: 10.1007/BF00239593; pmid: 7925807
3. K. Halasy, P. Somogyi, Distribution of GABAergic synapses and their targets in the dentate gyrus of rat: A quantitative immunoelectron microscopic analysis. *J. Hirnforsch.* **34**, 299–308 (1993). pmid: 8270784
4. G. Westbrook, "Seizures and epilepsy," in *Principles of Neural Science*, E. Kandel, J. H. Schwartz, T. M. Jessell, S. Siegelbaum, A. J. Hudspeth, Eds. (McGraw-Hill, New York, 2013), pp. 1116–1139.
5. T. Klausberger, P. Somogyi, Neuronal diversity and temporal dynamics: The unity of hippocampal circuit operations. *Science* **321**, 53–57 (2008). doi: 10.1126/science.1149381; pmid: 18599766
6. J. DeFelipe *et al*., New insights into the classification and nomenclature of cortical GABAergic interneurons. *Nat. Rev. Neurosci.* **14**, 202–216 (2013). doi: 10.1038/nrn3444; pmid: 23385869
7. B. Rudy, C. J. McBain, Kv3 channels: Voltage-gated K^+ channels designed for high-frequency repetitive firing. *Trends Neurosci.* **24**, 517–526 (2001). doi: 10.1016/S0166-2236(00)01892-0; pmid: 11506885
8. M. J. Bezaire, I. Soltesz, Quantitative assessment of CA1 local circuits: Knowledge base for interneuron-pyramidal cell connectivity. *Hippocampus* **23**, 751–785 (2013). doi: 10.1002/hipo.22141; pmid: 23674373
9. M. R. Celio, Parvalbumin in most γ-aminobutyric acid–containing neurons of the rat cerebral cortex. *Science* **231**, 995–997 (1986). doi: 10.1126/science.3945815; pmid: 3945815
10. E. Eggermann, P. Jonas, How the 'slow' Ca^{2+} buffer parvalbumin affects transmitter release in nanodomain-coupling regimes. *Nat. Neurosci.* **15**, 20–22 (2012). doi: 10.1038/nn.3002; pmid: 22138646
11. J. A. Cardin *et al*., Driving fast-spiking cells induces gamma rhythm and controls sensory responses. *Nature* **459**, 663–667 (2009). doi: 10.1038/nature08002; pmid: 19396156
12. V. S. Sohal, F. Zhang, O. Yizhar, K. Deisseroth, Parvalbumin neurons and gamma rhythms enhance cortical circuit performance. *Nature* **459**, 698–702 (2009). doi: 10.1038/nature07991; pmid: 19396159
13. L. Tricoire *et al*., A blueprint for the spatiotemporal origins of mouse hippocampal interneuron diversity. *J. Neurosci.* **31**, 10948–10970 (2011). doi: 10.1523/JNEUROSCI.0323-11.2011; pmid: 21795545
14. H. Taniguchi, J. Lu, Z. J. Huang, The spatial and temporal origin of chandelier cells in mouse neocortex. *Science* **339**, 70–74 (2013). doi: 10.1126/science.1227622; pmid: 23180771
15. G. Bartolini, G. Ciceri, O. Marín, Integration of GABAergic interneurons into cortical cell assemblies: Lessons from embryos and adults. *Neuron* **79**, 849–864 (2013). doi: 10.1016/j.neuron.2013.08.014; pmid: 24012001
16. F. Crick, in *What Mad Pursuit: A Personal View of Scientific Discovery* (Basic Books, New York, 1988), p. 150.
17. A. I. Gulyás, M. Megías, Z. Emri, T. F. Freund, Total number and ratio of excitatory and inhibitory synapses converging onto single interneurons of different types in the CA1 area of the rat hippocampus. *J. Neurosci.* **19**, 10082–10097 (1999). pmid: 10559416
18. A. Nörenberg, H. Hu, I. Vida, M. Bartos, P. Jonas, Distinct nonuniform cable properties optimize rapid and efficient activation of fast-spiking GABAergic interneurons. *Proc. Natl. Acad. Sci. U.S.A.* **107**, 894–899 (2010). doi: 10.1073/pnas.0910716107; pmid: 20080772
19. Y. Kubota *et al*., Conserved properties of dendritic trees in four cortical interneuron subtypes. *Sci. Rep.* **1**, 89 (2011). doi: 10.1038/srep00089; pmid: 22355608
20. J. J. Tukker *et al*., Distinct dendritic arborization and *in vivo* firing patterns of parvalbumin-expressing basket cells in the hippocampal area CA3. *J. Neurosci.* **33**, 6809–6825 (2013). doi: 10.1523/JNEUROSCI.5052-12.2013; pmid: 23595740
21. H. Hioki *et al*., Cell type-specific inhibitory inputs to dendritic and somatic compartments of parvalbumin-expressing neocortical interneuron. *J. Neurosci.* **33**, 544–555 (2013). doi: 10.1523/JNEUROSCI.2255-12.2013; pmid: 23303934
22. C. K. Pfeffer, M. Xue, M. He, Z. J. Huang, M. Scanziani, Inhibition of inhibition in visual cortex: The logic of connections between molecularly distinct interneurons. *Nat. Neurosci.* **16**, 1068–1076 (2013). doi: 10.1038/nn.3446; pmid: 23817549
23. J. R. P. Geiger, J. Lübke, A. Roth, M. Frotscher, P. Jonas, Submillisecond AMPA receptor-mediated signaling at a principal neuron-interneuron synapse. *Neuron* **18**, 1009–1023 (1997). doi: 10.1016/S0896-6273(00)80339-6; pmid: 9208867
24. A. Sik, M. Penttonen, A. Ylinen, G. Buzsáki, Hippocampal CA1 interneurons: An in vivo intracellular labeling study. *J. Neurosci.* **15**, 6651–6665 (1995). pmid: 7472426
25. F. Karube, Y. Kubota, Y. Kawaguchi, Axon branching and synaptic bouton phenotypes in GABAergic nonpyramidal cell subtypes. *J. Neurosci.* **24**, 2853–2865 (2004). doi: 10.1523/JNEUROSCI.4814-03.2004; pmid: 15044524
26. I. Parnas, I. Segev, A mathematical model for conduction of action potentials along bifurcating axons. *J. Physiol.* **295**, 323–343 (1979). pmid: 521942
27. H. Hu, M. Martina, P. Jonas, Dendritic mechanisms underlying rapid synaptic activation of fast-spiking hippocampal interneurons. *Science* **327**, 52–58 (2010). doi: 10.1126/science.1177876; pmid: 19965717

28. J. H. Goldberg, G. Tamas, R. Yuste, Ca^{2+} imaging of mouse neocortical interneurone dendrites: Ia-type K^+ channels control action potential backpropagation. *J. Physiol.* **551**, 49–65 (2003). doi: 10.1113/jphysiol.2003.042580; pmid: 12844506
29. Y. Aponte, J. Bischofberger, P. Jonas, Efficient Ca^{2+} buffering in fast-spiking basket cells of rat hippocampus. *J. Physiol.* **586**, 2061–2075 (2008). doi: 10.1113/jphysiol.2007.147298; pmid: 18276734
30. O. Camiré, L. Topolnik, Dendritic calcium nonlinearities switch the direction of synaptic plasticity in fast-spiking interneurons. *J. Neurosci.* **34**, 3864–3877 (2014). doi: 10.1523/JNEUROSCI.2253-13.2014; pmid: 24623765
31. B. Chiovini *et al*., Dendritic spikes induce ripples in parvalbumin interneurons during hippocampal sharp waves. *Neuron* **82**, 908–924 (2014). doi: 10.1016/j.neuron.2014.04.004; pmid: 24853946
32. G. J. Stuart, B. Sakmann, Active propagation of somatic action potentials into neocortical pyramidal cell dendrites. *Nature* **367**, 69–72 (1994). doi: 10.1038/367069a0; pmid: 8107777
33. N. L. Golding, N. Spruston, Dendritic sodium spikes are variable triggers of axonal action potentials in hippocampal CA1 pyramidal neurons. *Neuron* **21**, 1189–1200 (1998). doi: 10.1016/S0896-6273(00)80635-2; pmid: 9856473
34. M. Martina, I. Vida, P. Jonas, Distal initiation and active propagation of action potentials in interneuron dendrites. *Science* **287**, 295–300 (2000). doi: 10.1126/science.287.5451.295; pmid: 10634782
35. K. Vervaeke, A. Lorincz, Z. Nusser, R. A. Silver, Gap junctions compensate for sublinear dendritic integration in an inhibitory network. *Science* **335**, 1624–1628 (2012). doi: 10.1126/science.1215101; pmid: 22403180
36. J. R. P. Geiger *et al*., Relative abundance of subunit mRNAs determines gating and Ca^{2+} permeability of AMPA receptors in principal neurons and interneurons in rat CNS. *Neuron* **15**, 193–204 (1995). doi: 10.1016/0896-6273(95)90076-4; pmid: 7619522
37. M. Galarreta, S. Hestrin, Spike transmission and synchrony detection in networks of GABAergic interneurons. *Science* **292**, 2295–2299 (2001). doi: 10.1126/science.1061395; pmid: 11423653
38. D. Fricker, R. Miles, EPSP amplification and the precision of spike timing in hippocampal neurons. *Neuron* **28**, 559–569 (2000). doi: 10.1016/S0896-6273(00)00133-1; pmid: 11144364
39. M. Galarreta, S. Hestrin, A network of fast-spiking cells in the neocortex connected by electrical synapses. *Nature* **402**, 72–75 (1999). doi: 10.1038/47029; pmid: 10573418
40. J. R. Gibson, M. Beierlein, B. W. Connors, Two networks of electrically coupled inhibitory neurons in neocortex. *Nature* **402**, 75–79 (1999). doi: 10.1038/47035; pmid: 10573419
41. G. Tamás, E. H. Buhl, A. Lörincz, P. Somogyi, Proximally targeted GABAergic synapses and gap junctions synchronize cortical interneurons. *Nat. Neurosci.* **3**, 366–371 (2000). doi: 10.1038/73936; pmid: 10725926
42. M. Bartos, I. Vida, M. Frotscher, J. R. P. Geiger, P. Jonas, Rapid signaling at inhibitory synapses in a dentate gyrus interneuron network. *J. Neurosci.* **21**, 2687–2698 (2001). pmid: 11306622
43. H. Hu, P. Jonas, A supercritical density of Na^+ channels ensures fast signaling in GABAergic interneuron axons. *Nat. Neurosci.* **17**, 686–693 (2014). doi: 10.1038/nn.3678; pmid: 24657965
44. M. H. Kole *et al*., Action potential generation requires a high sodium channel density in the axon initial segment. *Nat. Neurosci.* **11**, 178–186 (2008). doi: 10.1038/nn2040; pmid: 18204443
45. J. P. Meeks, S. Mennerick, Action potential initiation and propagation in CA3 pyramidal axons. *J. Neurophysiol.* **97**, 3460–3472 (2007). doi: 10.1152/jn.01288.2006; pmid: 17314237
46. C. Schmidt-Hieber, P. Jonas, J. Bischofberger, Action potential initiation and propagation in hippocampal mossy fibre axons. *J. Physiol.* **586**, 1849–1857 (2008). doi: 10.1113/jphysiol.2007.150151; pmid: 18258662
47. M. Martina, P. Jonas, Functional differences in Na^+ channel gating between fast-spiking interneurones and principal neurones of rat hippocampus. *J. Physiol.* **505**, 593–603 (1997). doi: 10.1111/j.1469-7793.1997.593ba.x; pmid: 9457638
48. E. M. Goldberg *et al*., Specific functions of synaptically localized potassium channels in synaptic transmission at the neocortical GABAergic fast-spiking cell synapse. *J. Neurosci.* **25**, 5230–5235 (2005). doi: 10.1523/JNEUROSCI.0722-05.2005; pmid: 15917463
49. I. Ogiwara *et al*., $Na_V1.1$ localizes to axons of parvalbumin-positive inhibitory interneurons: A circuit basis for epileptic seizures in mice carrying an *Scn1a* gene mutation. *J. Neurosci.* **27**, 5903–5914 (2007). doi: 10.1523/JNEUROSCI.5270-06.2007; pmid: 17537961
50. A. Lorincz, Z. Nusser, Cell-type-dependent molecular composition of the axon initial segment. *J. Neurosci.* **28**, 14329–14340 (2008). doi: 10.1523/JNEUROSCI.4833-08.2008; pmid: 19118165
51. B. W. Okaty, M. N. Miller, K. Sugino, C. M. Hempel, S. B. Nelson, Transcriptional and electrophysiological maturation of neocortical fast-spiking GABAergic interneurons. *J. Neurosci.* **29**, 7040–7052 (2009). doi: 10.1523/JNEUROSCI.0105-09.2009; pmid: 19474331
52. M. Weiser *et al*., The potassium channel subunit KV3.1b is localized to somatic and axonal membranes of specific populations of CNS neurons. *J. Neurosci.* **15**, 4298–4314 (1995). pmid: 7790912
53. E. M. Goldberg *et al*., K^+ channels at the axon initial segment dampen near-threshold excitability of neocortical fast-spiking GABAergic interneurons. *Neuron* **58**, 387–400 (2008). doi: 10.1016/j.neuron.2008.03.003; pmid: 18466749
54. E. Campanac *et al*., Enhanced intrinsic excitability in basket cells maintains excitatory-inhibitory balance in hippocampal circuits. *Neuron* **77**, 712–722 (2013). doi: 10.1016/j.neuron.2012.12.020; pmid: 23439123
55. U. Kraushaar, P. Jonas, Efficacy and stability of quantal GABA release at a hippocampal interneuron-principal neuron synapse. *J. Neurosci.* **20**, 5594–5607 (2000). pmid: 10908596
56. L. Li, J. Bischofberger, P. Jonas, Differential gating and recruitment of P/Q-, N-, and R-type Ca^{2+} channels in hippocampal mossy fiber boutons. *J. Neurosci.* **27**, 13420–13429 (2007). doi: 10.1523/JNEUROSCI.1709-07.2007; pmid: 18057200
57. S. Hefft, P. Jonas, Asynchronous GABA release generates long-lasting inhibition at a hippocampal interneuron-principal neuron synapse. *Nat. Neurosci.* **8**, 1319–1328 (2005). doi: 10.1038/nn1542; pmid: 16158066
58. A. V. Zaitsev, N. V. Povysheva, D. A. Lewis, L. S. Krimer, P/Q-type, but not N-type, calcium channels mediate GABA release from fast-spiking interneurons to pyramidal cells in rat prefrontal cortex. *J. Neurophysiol.* **97**, 3567–3573 (2007). doi: 10.1152/jn.01293.2006; pmid: 17329622
59. I. Bucurenciu, J. Bischofberger, P. Jonas, A small number of open Ca^{2+} channels trigger transmitter release at a central GABAergic synapse. *Nat. Neurosci.* **13**, 19–21 (2010). doi: 10.1038/nn.2461; pmid: 20010820
60. E. Rossignol, I. Kruglikov, A. M. van den Maagdenberg, B. Rudy, G. Fishell, Ca_V 2.1 ablation in cortical interneurons selectively impairs fast-spiking basket cells and causes generalized seizures. *Ann. Neurol.* **74**, 209–222 (2013). pmid: 23595603
61. I. Bucurenciu, A. Kulik, B. Schwaller, M. Frotscher, P. Jonas, Nanodomain coupling between Ca^{2+} channels and Ca^{2+} sensors promotes fast and efficient transmitter release at a cortical GABAergic synapse. *Neuron* **57**, 536–545 (2008). doi: 10.1016/j.neuron.2007.12.026; pmid: 18304483
62. E. Eggermann, I. Bucurenciu, S. P. Goswami, P. Jonas, Nanodomain coupling between Ca^{2+} channels and sensors of exocytosis at fast mammalian synapses. *Nat. Rev. Neurosci.* **13**, 7–21 (2012). doi: 10.1038/nrn3125; pmid: 22183436
63. Z. P. Pang *et al*., Synaptotagmin-2 is essential for survival and contributes to Ca^{2+} triggering of neurotransmitter release in central and neuromuscular synapses. *J. Neurosci.* **26**, 13493–13504 (2006). doi: 10.1523/JNEUROSCI.3519-06.2006; pmid: 17192432
64. A. M. Kerr, E. Reisinger, P. Jonas, Differential dependence of phasic transmitter release on synaptotagmin 1 at GABAergic and glutamatergic hippocampal synapses. *Proc. Natl. Acad. Sci. U.S.A.* **105**, 15581–15586 (2008). doi: 10.1073/pnas.0800621105; pmid: 18832148
65. M. Geppert *et al*., Synaptotagmin I: A major Ca^{2+} sensor for transmitter release at a central synapse. *Cell* **79**, 717–727 (1994). doi: 10.1016/0092-8674(94)90556-8; pmid: 7954835
66. J. P. Sommeijer, C. N. Levelt, Synaptotagmin-2 is a reliable marker for parvalbumin positive inhibitory boutons in the mouse visual cortex. *PLOS ONE* **7**, e35323 (2012). doi: 10.1371/journal.pone.0035323; pmid: 22539967
67. J. Xu, T. Mashimo, T. C. Südhof, Synaptotagmin-1, -2, and -9: Ca^{2+} sensors for fast release that specify distinct presynaptic properties in subsets of neurons. *Neuron* **54**, 567–581 (2007). doi: 10.1016/j.neuron.2007.05.004; pmid: 17521570
68. B. Schwaller, M. Meyer, S. Schiffmann, 'New' functions for 'old' proteins: The role of the calcium-binding proteins calbindin D-28k, calretinin and parvalbumin, in cerebellar physiology. Studies with knockout mice. *Cerebellum* **1**, 241–258 (2002). doi: 10.1080/14734220232088355l; pmid: 12879963
69. F. Donato, S. B. Rompani, P. Caroni, Parvalbumin-expressing basket-cell network plasticity induced by experience regulates adult learning. *Nature* **504**, 272–276 (2013). doi: 10.1038/nature12866; pmid: 24336286
70. G. Buzsàki, E. Eidelberg, Commissural projection to the dentate gyrus of the rat: Evidence for feed-forward inhibition. *Brain Res.* **230**, 346–350 (1981). doi: 10.1016/0006-8993(81)90413-3; pmid: 7317783
71. R. Miles, Synaptic excitation of inhibitory cells by single CA3 hippocampal pyramidal cells of the guinea-pig in vitro. *J. Physiol.* **428**, 61–77 (1990). pmid: 2231426
72. F. Pouille, M. Scanziani, Enforcement of temporal fidelity in pyramidal cells by somatic feed-forward inhibition. *Science* **293**, 1159–1163 (2001). doi: 10.1126/science.1060342; pmid: 11498596
73. F. Pouille, M. Scanziani, Routing of spike series by dynamic circuits in the hippocampus. *Nature* **429**, 717–723 (2004). doi: 10.1038/nature02615; pmid: 15170216
74. F. Pouille, A. Marin-Burgin, H. Adesnik, B. V. Atallah, M. Scanziani, Input normalization by global feedforward inhibition expands cortical dynamic range. *Nat. Neurosci.* **12**, 1577–1585 (2009). doi: 10.1038/nn.2441; pmid: 19881502
75. J. J. Couey *et al*., Recurrent inhibitory circuitry as a mechanism for grid formation. *Nat. Neurosci.* **16**, 318–324 (2013). doi: 10.1038/nn.3310; pmid: 23334580
76. L. de Almeida, M. Idiart, J. E. Lisman, A second function of gamma frequency oscillations: An E%-max winner-take-all mechanism selects which cells fire. *J. Neurosci.* **29**, 7497–7503 (2009). doi: 10.1523/JNEUROSCI.6044-08.2009; pmid: 19515917
77. L. de Almeida, M. Idiart, J. E. Lisman, The input-output transformation of the hippocampal granule cells: From grid cells to place fields. *J. Neurosci.* **29**, 7504–7512 (2009). doi: 10.1523/JNEUROSCI.6048-08.2009; pmid: 19515918
78. A. J. Pernía-Andrade, P. Jonas, Theta-gamma-modulated synaptic currents in hippocampal granule cells in vivo define a mechanism for network oscillations. *Neuron* **81**, 140–152 (2014). doi: 10.1016/j.neuron.2013.09.046; pmid: 24333053
79. J. K. Leutgeb, S. Leutgeb, M. B. Moser, E. I. Moser, Pattern separation in the dentate gyrus and CA3 of the hippocampus. *Science* **315**, 961–966 (2007). doi: 10.1126/science.1135801; pmid: 17303747
80. T. Hafting, M. Fyhn, S. Molden, M. B. Moser, E. I. Moser, Microstructure of a spatial map in the entorhinal cortex. *Nature* **436**, 801–806 (2005). doi: 10.1038/nature03721; pmid: 15965463
81. H. Pastoll, L. Solanka, M. C. van Rossum, M. F. Nolan, Feedback inhibition enables θ-nested γ oscillations and grid firing fields. *Neuron* **77**, 141–154 (2013). doi: 10.1016/j.neuron.2012.11.032; pmid: 23312522
82. C. Buetfering, K. Allen, H. Monyer, Parvalbumin interneurons provide grid cell-driven recurrent inhibition in the medial entorhinal cortex. *Nat. Neurosci.* **17**, 710–718 (2014). doi: 10.1038/nn.3696; pmid: 24705183
83. A. M. Packer, R. Yuste, Dense, unspecific connectivity of neocortical parvalbumin-positive interneurons: A canonical microcircuit for inhibition? *J. Neurosci.* **31**, 13260–13271 (2011). doi: 10.1523/JNEUROSCI.3131-11.2011; pmid: 21917809
84. S. H. Lee *et al*., Parvalbumin-positive basket cells differentiate among hippocampal pyramidal cells. *Neuron* **82**, 1129–1144 (2014). doi: 10.1016/j.neuron.2014.03.034; pmid: 24836505
85. M. Strueber, P. Jonas, M. Bartos, "Distance dependence of efficacy and timing of synaptic inhibition in the hippocampal network." program no. 655.10 2011, Neuroscience Meeting Planner (Society for Neuroscience, Washington, DC, 2011).
86. M. Xue, B. V. Atallah, M. Scanziani, Equalizing excitation–inhibition ratios across visual cortical neurons. *Nature* **511**, 596–600 (2014). doi: 10.1038/nature13321
87. D. Lapray *et al*., Behavior-dependent specialization of identified hippocampal interneurons. *Nat. Neurosci.* **15**, 1265–1271 (2012). doi: 10.1038/nn.3176; pmid: 22864613
88. C. Varga, P. Golshani, I. Soltesz, Frequency-invariant temporal ordering of interneuronal discharges during

hippocampal oscillations in awake mice. *Proc. Natl. Acad. Sci. U.S.A.* **109**, E2726–E2734 (2012). doi: 10.1073/pnas.1210929109; pmid: 23010933
89. N. Hájos *et al*., Input-output features of anatomically identified CA3 neurons during hippocampal sharp wave/ripple oscillation in vitro. *J. Neurosci.* **33**, 11677–11691 (2013). doi: 10.1523/JNEUROSCI.5729-12.2013; pmid: 23843535
90. J. Csicsvari, H. Hirase, A. Mamiya, G. Buzsáki, Ensemble patterns of hippocampal CA3-CA1 neurons during sharp wave-associated population events. *Neuron* **28**, 585–594 (2000). doi: 10.1016/S0896-6273(00)00135-5; pmid: 11144366
91. M. A. Wilson, B. L. McNaughton, Dynamics of the hippocampal ensemble code for space. *Science* **261**, 1055–1058 (1993). doi: 10.1126/science.8351520; pmid: 8351520
92. S. Royer *et al*., Control of timing, rate and bursts of hippocampal place cells by dendritic and somatic inhibition. *Nat. Neurosci.* **15**, 769–775 (2012). doi: 10.1038/nn.3077; pmid: 22446878
93. S. B. Hofer *et al*., Differential connectivity and response dynamics of excitatory and inhibitory neurons in visual cortex. *Nat. Neurosci.* **14**, 1045–1052 (2011). doi: 10.1038/nn.2876; pmid: 21765421
94. N. R. Wilson, C. A. Runyan, F. L. Wang, M. Sur, Division and subtraction by distinct cortical inhibitory networks *in vivo*. *Nature* **488**, 343–348 (2012). doi: 10.1038/nature11347; pmid: 22878717
95. B. V. Atallah, W. Bruns, M. Carandini, M. Scanziani, Parvalbumin-expressing interneurons linearly transform cortical responses to visual stimuli. *Neuron* **73**, 159–170 (2012). doi: 10.1016/j.neuron.2011.12.013; pmid: 22243754
96. C. A. Runyan *et al*., Response features of parvalbumin-expressing interneurons suggest precise roles for subtypes of inhibition in visual cortex. *Neuron* **67**, 847–857 (2010). doi: 10.1016/j.neuron.2010.08.006; pmid: 20826315
97. P. O. Polack, J. Friedman, P. Golshani, Cellular mechanisms of brain state-dependent gain modulation in visual cortex. *Nat. Neurosci.* **16**, 1331–1339 (2013). doi: 10.1038/nn.3464; pmid: 23872595
98. C. J. Magnus *et al*., Chemical and genetic engineering of selective ion channel-ligand interactions. *Science* **333**, 1292–1296 (2011). doi: 10.1126/science.1206606; pmid: 21885782
99. E. Stark *et al*., Inhibition-induced theta resonance in cortical circuits. *Neuron* **80**, 1263–1276 (2013). doi: 10.1016/j.neuron.2013.09.033; pmid: 24314731
100. M. Bartos, I. Vida, P. Jonas, Synaptic mechanisms of synchronized gamma oscillations in inhibitory interneuron networks. *Nat. Rev. Neurosci.* **8**, 45–56 (2007). doi: 10.1038/nrn2044; pmid: 17180162
101. J. O'Keefe, M. L. Recce, Phase relationship between hippocampal place units and the EEG theta rhythm. *Hippocampus* **3**, 317–330 (1993). doi: 10.1002/hipo.450030307; pmid: 8353611
102. S. H. Lee *et al*., Activation of specific interneurons improves V1 feature selectivity and visual perception. *Nature* **488**, 379–383 (2012). doi: 10.1038/nature11312; pmid: 22878719
103. S. J. Kuhlman *et al*., A disinhibitory microcircuit initiates critical-period plasticity in the visual cortex. *Nature* **501**, 543–546 (2013). doi: 10.1038/nature12485; pmid: 23975100
104. J. J. Letzkus *et al*., A disinhibitory microcircuit for associative fear learning in the auditory cortex. *Nature* **480**, 331–335 (2011). doi: 10.1038/nature10674; pmid: 22158104
105. S. B. Wolff *et al*., Amygdala interneuron subtypes control fear learning through disinhibition. *Nature* **509**, 453–458 (2014). doi: 10.1038/nature13258; pmid: 24814341
106. Y. Yazaki-Sugiyama, S. Kang, H. Câteau, T. Fukai, T. K. Hensch, Bidirectional plasticity in fast-spiking GABA circuits by visual experience. *Nature* **462**, 218–221 (2009). doi: 10.1038/nature08485; pmid: 19907494
107. D. R. Sparta *et al*., Activation of prefrontal cortical parvalbumin interneurons facilitates extinction of reward-seeking behavior. *J. Neurosci.* **34**, 3699–3705 (2014). doi: 10.1523/JNEUROSCI.0235-13.2014; pmid: 24599468
108. O. Marín, Interneuron dysfunction in psychiatric disorders. *Nat. Rev. Neurosci.* **13**, 107–120 (2012). pmid: 22251963
109. W. A. Catterall, F. Kalume, J. C. Oakley, $Na_v1.1$ channels and epilepsy. *J. Physiol.* **588**, 1849–1859 (2010). doi: 10.1113/jphysiol.2010.187484; pmid: 20194124
110. F. H. Yu *et al*., Reduced sodium current in GABAergic interneurons in a mouse model of severe myoclonic epilepsy in infancy. *Nat. Neurosci.* **9**, 1142–1149 (2006). doi: 10.1038/nn1754; pmid: 16921370
111. C. S. Cheah *et al*., Specific deletion of $Na_v1.1$ sodium channels in inhibitory interneurons causes seizures and premature death in a mouse model of Dravet syndrome. *Proc. Natl. Acad. Sci. U.S.A.* **109**, 14646–14651 (2012). doi: 10.1073/pnas.1211591109; pmid: 22908258
112. S. B. Dutton *et al*., Preferential inactivation of Scn1a in parvalbumin interneurons increases seizure susceptibility. *Neurobiol. Dis.* **49C**, 211–220 (2012). pmid: 22926190
113. I. Ogiwara *et al*., $Na_v1.1$ haploinsufficiency in excitatory neurons ameliorates seizure-associated sudden death in a mouse model of Dravet syndrome. *Hum. Mol. Genet.* **22**, 4784–4804 (2013). doi: 10.1093/hmg/ddt331; pmid: 23922229
114. T. Mashimo *et al*., A missense mutation of the gene encoding voltage-dependent sodium channel ($Na_v1.1$) confers susceptibility to febrile seizures in rats. *J. Neurosci.* **30**, 5744–5753 (2010). doi: 10.1523/JNEUROSCI.3360-09.2010; pmid: 20410126
115. P. Fazzari *et al*., Control of cortical GABA circuitry development by Nrg1 and ErbB4 signalling. *Nature* **464**, 1376–1380 (2010). doi: 10.1038/nature08928; pmid: 20393464
116. D. A. Lewis, T. Hashimoto, D. W. Volk, Cortical inhibitory neurons and schizophrenia. *Nat. Rev. Neurosci.* **6**, 312–324 (2005). doi: 10.1038/nrn1648; pmid: 15803162
117. L. Wen *et al*., Neuregulin 1 regulates pyramidal neuron activity via ErbB4 in parvalbumin-positive interneurons. *Proc. Natl. Acad. Sci. U.S.A.* **107**, 1211–1216 (2010). doi: 10.1073/pnas.0910302107; pmid: 20080551
118. Y. Abe, H. Namba, T. Kato, Y. Iwakura, H. Nawa, Neuregulin-1 signals from the periphery regulate AMPA receptor sensitivity and expression in GABAergic interneurons in developing neocortex. *J. Neurosci.* **31**, 5699–5709 (2011). doi: 10.1523/JNEUROSCI.3477-10.2011; pmid: 21490211
119. I. Del Pino *et al*., *Erbb4* deletion from fast-spiking interneurons causes schizophrenia-like phenotypes. *Neuron* **79**, 1152–1168 (2013). doi: 10.1016/j.neuron.2013.07.010; pmid: 24050403
120. M. J. Janssen, E. Leiva-Salcedo, A. Buonanno, Neuregulin directly decreases voltage-gated sodium current in hippocampal ErbB4-expressing interneurons. *J. Neurosci.* **32**, 13889–13895 (2012). doi: 10.1523/JNEUROSCI.1420-12.2012; pmid: 23035098
121. K. X. Li *et al*., Neuregulin 1 regulates excitability of fast-spiking neurons through Kv1.1 and acts in epilepsy. *Nat. Neurosci.* **15**, 267–273 (2012). doi: 10.1038/nn.3006; pmid: 22158511
122. P. Somogyi, T. Klausberger, Defined types of cortical interneurone structure space and spike timing in the hippocampus. *J. Physiol.* **562**, 9–26 (2005). doi: 10.1113/jphysiol.2004.078915; pmid: 15539390
123. A. M. Thomson, D. C. West, J. Hahn, J. Deuchars, Single axon IPSPs elicited in pyramidal cells by three classes of interneurones in slices of rat neocortex. *J. Physiol.* **496**, 81–102 (1996). pmid: 8910198
124. D. A. McCormick, B. W. Connors, J. W. Lighthall, D. A. Prince, Comparative electrophysiology of pyramidal and sparsely spiny stellate neurons of the neocortex. *J. Neurophysiol.* **54**, 782–806 (1985). pmid: 2999347
125. S. Hippenmeyer *et al*., A developmental switch in the response of DRG neurons to ETS transcription factor signaling. *PLOS Biol.* **3**, e159 (2005). doi: 10.1371/journal.pbio.0030159; pmid: 15836427
126. D. Kvitsiani *et al*., Distinct behavioural and network correlates of two interneuron types in prefrontal cortex. *Nature* **498**, 363–366 (2013). doi: 10.1038/nature12176; pmid: 23708967
127. P. Poirazi, B. W. Mel, Impact of active dendrites and structural plasticity on the memory capacity of neural tissue. *Neuron* **29**, 779–796 (2001). doi: 10.1016/S0896-6273(01)00252-5; pmid: 11301036
128. C. A. Bottoms, J. P. Schuermann, S. Agah, M. T. Henzl, J. J. Tanner, Crystal structure of rat α-parvalbumin at 1.05 Å resolution. *Protein Sci.* **13**, 1724–1734 (2004). doi: 10.1110/ps.03571004; pmid: 15169955
129. M. Bartos *et al*., Fast synaptic inhibition promotes synchronized gamma oscillations in hippocampal interneuron networks. *Proc. Natl. Acad. Sci. U.S.A.* **99**, 13222–13227 (2002). doi: 10.1073/pnas.192233099; pmid: 12235359
130. M. Galarreta, S. Hestrin, Electrical and chemical synapses among parvalbumin fast-spiking GABAergic interneurons in adult mouse neocortex. *Proc. Natl. Acad. Sci. U.S.A.* **99**, 12438–12443 (2002). doi: 10.1073/pnas.192159599; pmid: 12213962
131. M. Martina, J. H. Schultz, H. Ehmke, H. Monyer, P. Jonas, Functional and molecular differences between voltage-gated K^+ channels of fast-spiking interneurons and pyramidal neurons of rat hippocampus. *J. Neurosci.* **18**, 8111–8125 (1998). pmid: 9763458
132. Y. Kawaguchi, H. Katsumaru, T. Kosaka, C. W. Heizmann, K. Hama, Fast spiking cells in rat hippocampus (CA1 region) contain the calcium-binding protein parvalbumin. *Brain Res.* **416**, 369–374 (1987). doi: 10.1016/0006-8993(87)90921-8; pmid: 3304536
133. J. Du, L. Zhang, M. Weiser, B. Rudy, C. J. McBain, Developmental expression and functional characterization of the potassium-channel subunit Kv3.1b in parvalbumin-containing interneurons of the rat hippocampus. *J. Neurosci.* **16**, 506–518 (1996). pmid: 8551335
134. J. Szabadics *et al*., Excitatory effect of GABAergic axo-axonic cells in cortical microcircuits. *Science* **311**, 233–235 (2006). doi: 10.1126/science.1121325; pmid: 16410524

ACKNOWLEDGMENTS

We thank J. Csicsvari, T. Freund, S. Hippenmeyer, T. Klausberger, J. Lisman, and I. Soltesz for critically reading the manuscript; A. Solymosi for text editing; and all colleagues at IST Austria for generating a stimulating scientific environment. This work was supported by the Fond zur Förderung der Wissenschaftlichen Forschung (grant P 24909-B24 to P.J.) and the European Union (European Research Council Advanced Grant 268548 to P.J.). We apologize for the fact that, owing to space constraints, not all relevant papers could be cited.

10.1126/science.1255263

RESEARCH ARTICLE SUMMARY

MOBILE DNA IN CANCER

Extensive transduction of nonrepetitive DNA mediated by L1 retrotransposition in cancer genomes

Jose M. C. Tubio *et al.**

INTRODUCTION: The human genome is peppered with mobile repetitive elements called long interspersed nuclear element–1 (L1) retrotransposons. Propagating through RNA and cDNA intermediates, these molecular parasites copy and insert themselves throughout the genome, with potentially disruptive effects on neighboring genes or regulatory sequences. In the germ line, unique sequence downstream of L1 elements can also be retrotransposed if transcription continues beyond the repeat, a process known as 3′ transduction. There has been growing interest in retrotransposition and 3′ transduction as a possible source of somatic mutations during tumorigenesis.

RATIONALE: To explore whether 3′ transductions are frequent in cancer, we developed a bioinformatic algorithm for identifying somatically acquired retrotranspositions in cancer genomes. We applied our algorithm to 290 cancer samples from 244 patients across 12 tumor types. The unique downstream sequence mobilized with 3′ transductions effectively fingerprints the L1 source element, providing insights into the activity of individual L1 loci across the genome.

RESULTS: Across the 290 samples, we identified 2756 somatic L1 retrotranspositions. Tumors from 53% of patients had at least one such event, with colorectal and lung cancers being most frequently affected (93% and 75% of patients, respectively). Somatic 3′ transductions comprised 24% of events, half of which represented mobilizations of unique sequence alone, without any accompanying L1 sequence. Overall, 95% of 3′ transductions identified derived from only 72 germline L1 source elements, with as few as four loci accounting for 50% of events. In a given sample, the same source element could generate 50 or more somatic transductions, scattered extensively across the genome. About 5% of somatic transductions arose from L1 source elements that were themselves somatic retrotranspositions. In three of the cases in which we sequenced more than one sample from a patient's tumor, we were able to place 3′ transductions on the phylogenetic tree. We found that the activity of individual source elements fluctuated during tumor evolution, with different subclones exhibiting much variability in which elements were "on" and which were "off." The ability to identify the individual L1 source elements active in a given tumor enabled us to study the promoter methylation of those elements specifically. We found that 3′ transduction activity in a patient's tumor was always associated with hypomethylation of that element. Overall, 2.3% of transductions distributed exons or entire genes to other sites in the genome, and many more mobilized deoxyribonuclease I (DNAse-I) hypersensitive sites or transcription factor binding sites identified by the ENCODE project. Occasionally, somatic L1 insertions inserted near coding sequence and redistributed these exons elsewhere in the genome. However, we found no general effects of retrotranspositions on transcription levels of genes at the insertion points and no evidence for aberrant RNA species resulting from somatically acquired transposable elements. Indeed, as with germline retrotranspositions, somatic insertions exhibited a strong enrichment in heterochromatic, gene-poor regions of the genome.

ON OUR WEBSITE

Read the full article at http://dx.doi.org/10.1126/science.1251343

CONCLUSION: Somatic 3′ transduction occurs frequently in human tumors, and in some cases transduction events can scatter exons, genes, and regulatory elements widely across the genome. Dissemination of these sequences appears to be due to a small number of highly active L1 elements, whose activity can wax and wane during tumor evolution. The majority of the retrotransposition events are likely to be harmless "passenger" mutations. ■

Lists of authors and their affiliations are available in the full article online.
*Corresponding author: Peter J. Campbell (pc8@sanger.ac.uk)
Cite this article as J. M. C. Tubio *et al.*, *Science* **345**, 1251343 (2014). DOI: 10.1126/science.1251343

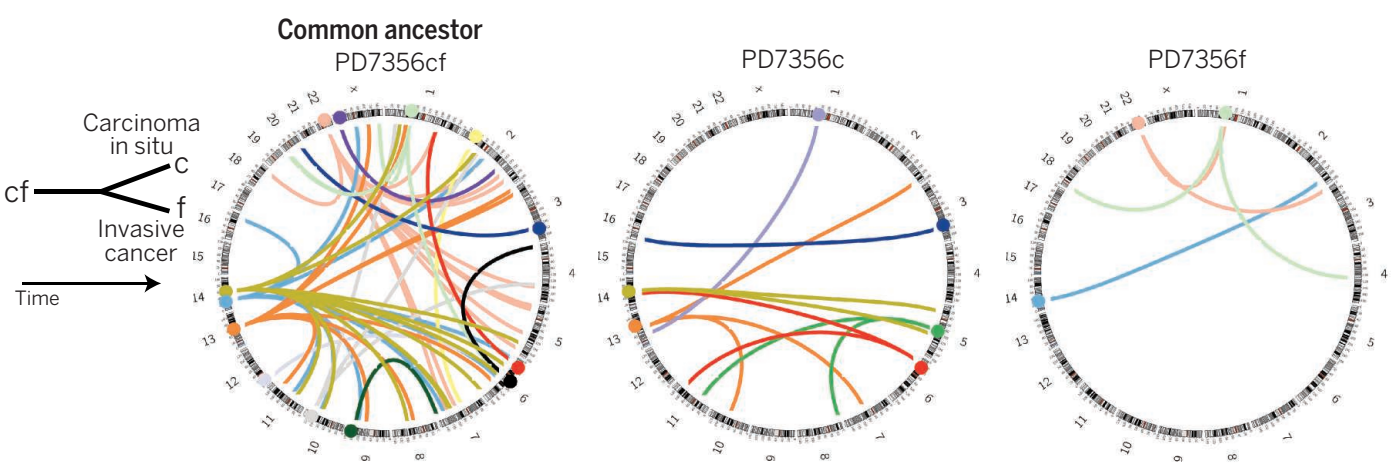

The activity of individual L1 elements fluctuates during tumor evolution. In a lung tumor, hundreds of 3′ transductions arose from a small number of active L1 source elements (colored circles on outer rim of circle). As the tumor evolved from the preinvasive common ancestor to invasive cancer, individual elements exhibited variable activity over time.

Published by AAAS

RESEARCH ARTICLE

MOBILE DNA IN CANCER

Extensive transduction of nonrepetitive DNA mediated by L1 retrotransposition in cancer genomes

Jose M. C. Tubio,[1] Yilong Li,[1*] Young Seok Ju,[1*] Inigo Martincorena,[1] Susanna L. Cooke,[1] Marta Tojo,[2] Gunes Gundem,[1] Christodoulos P. Pipinikas,[3] Jorge Zamora,[1] Keiran Raine,[1] Andrew Menzies,[1] Pablo Roman-Garcia,[1] Anthony Fullam,[1] Moritz Gerstung,[1] Adam Shlien,[1] Patrick S. Tarpey,[1] Elli Papaemmanuil,[1] Stian Knappskog,[1,4,5] Peter Van Loo,[1,6] Manasa Ramakrishna,[1] Helen R. Davies,[1] John Marshall,[1] David C. Wedge,[1] Jon W. Teague,[1] Adam P. Butler,[1] Serena Nik-Zainal,[1,10] Ludmil Alexandrov,[1] Sam Behjati,[1] Lucy R. Yates,[1] Niccolo Bolli,[1,33] Laura Mudie,[1] Claire Hardy,[1] Sancha Martin,[1] Stuart McLaren,[1] Sarah O'Meara,[1] Elizabeth Anderson,[1] Mark Maddison,[1] Stephen Gamble,[1] ICGC Breast Cancer Group,[1]† ICGC Bone Cancer Group,[1]† ICGC Prostate Cancer Group,[1,7,8]† Christopher Foster,[9] Anne Y. Warren,[10] Hayley Whitaker,[8] Daniel Brewer,[7,11] Rosalind Eeles,[7] Colin Cooper,[7,11] David Neal,[8] Andy G. Lynch,[8] Tapio Visakorpi,[12] William B. Isaacs,[13] Laura van't Veer,[14] Carlos Caldas,[8] Christine Desmedt,[15] Christos Sotiriou,[15] Sam Aparicio,[16] John A. Foekens,[17] Jórunn Erla Eyfjörd,[18] Sunil R. Lakhani,[19,20,21] Gilles Thomas,[22] Ola Myklebost,[23] Paul N. Span,[24] Anne-Lise Børresen-Dale,[23] Andrea L. Richardson,[25] Marc Van de Vijver,[26] Anne Vincent-Salomon,[27,28] Gert G. Van den Eynden,[29] Adrienne M. Flanagan,[30,31] P. Andrew Futreal,[1,32] Sam M. Janes,[3] G. Steven Bova,[12] Michael R. Stratton,[1] Ultan McDermott,[1] Peter J. Campbell[1,10,33]‡

Long interspersed nuclear element–1 (L1) retrotransposons are mobile repetitive elements that are abundant in the human genome. L1 elements propagate through RNA intermediates. In the germ line, neighboring, nonrepetitive sequences are occasionally mobilized by the L1 machinery, a process called 3′ transduction. Because 3′ transductions are potentially mutagenic, we explored the extent to which they occur somatically during tumorigenesis. Studying cancer genomes from 244 patients, we found that tumors from 53% of the patients had somatic retrotranspositions, of which 24% were 3′ transductions. Fingerprinting of donor L1s revealed that a handful of source L1 elements in a tumor can spawn from tens to hundreds of 3′ transductions, which can themselves seed further retrotranspositions. The activity of individual L1 elements fluctuated during tumor evolution and correlated with L1 promoter hypomethylation. The 3′ transductions disseminated genes, exons, and regulatory elements to new locations, most often to heterochromatic regions of the genome.

Long interspersed nuclear element (LINE)–1 (L1) retrotransposons are widespread repetitive elements in the human genome, composing about 17% of the entire DNA content (*1*). They are a remarkably successful parasitic unit, relying on the cell's transcription and translation machinery to initiate their reproduction and reinsertion, a process completed with the reverse transcriptase and integration capability of proteins encoded on the L1 transcript. In the germ line, L1s have contributed extensively to the evolution of genes and genomes by generating structural variation that can potentially affect function, shaped by ongoing mutation and natural selection across thousands of generations (*2*). Most of the repeat elements that reside in the human genome are inactive, because of inverted rearrangements or truncations introduced during retrotransposition or subsequent inactivating point mutations across human evolution. However, it is estimated, on the basis of full-length L1 elements with preserved open reading frames and activity in in vitro retrotransposition assays, that there are 50 to 120 currently active L1 repeats in the human genome, of which a small number are highly active, earning the moniker "hot-L1s" (*3*–*5*).

Among the many ways in which L1 retrotranspositions have shaped the human genome is the mobilization of unique DNA downstream of the LINE (*6*). This process, known as 3′ transduction, is likely the consequence of a weak transcription termination signal at the end of the L1, causing the transcription machinery to bypass the L1 polyadenylation signal and use another polyadenylation site downstream. The unique genomic sequence picked up in the hybrid transcript can then be reverse transcribed and reinserted by the L1 machinery, causing mobilization of up to several thousand nucleotides of nonrepetitive DNA (*7*). These 3′ transductions can drive the mobilization of adjacent coding regions, increasing the potential of this process to exert functional effects (*6*). The mobilization of unique downstream sequence effectively barcodes the source element from which a transduction arose, a property that has been exploited in germline genome analyses to track the lineages of active L1 elements (*8*) and that we exploit here for cancer genomes.

In somatic cells, there is increasing evidence that spontaneous L1 mobilizations occur during normal neurogenesis (*9*–*12*) and during cancer development (*13*–*17*). Similar to the germ line, this mutational process has considerable potential to restructure the cancer genome. As with all mutational processes, individual mutational events occur randomly and are then subjected to selective forces. Those events that generate functional consequences of advantage to the cell help that clone to expand over its competitors. The potential functional repertoire of somatic retrotransposition is extensive. Genes can be disrupted

[1]Wellcome Trust Sanger Institute, Hinxton, Cambridgeshire, UK. [2]Department of Physiology, School of Medicine–Center for Resesarch in Molecular Medicine and Chronic Diseases, Instituto de Investigaciones Sanitarias, University of Santiago de Compostela, Spain. [3]Lungs for Living Research Centre, Rayne Institute, University College London (UCL), London, UK. [4]Department of Clinical Science, University of Bergen, Bergen, Norway. [5]Department of Oncology, Haukeland University Hospital, Bergen, Norway. [6]Human Genome Laboratory, Department of Human Genetics, VIB and KU Leuven, Leuven, Belgium. [7]Institute of Cancer Research, Sutton, London, UK. [8]Cancer Research UK (CRUK) Cambridge Institute, University of Cambridge, Cambridge, UK. [9]University of Liverpool and HCA Pathology Laboratories, London, UK. [10]Cambridge University Hospitals National Health Service (NHS) Foundation Trust, Cambridge, UK. [11]University of East Anglia, Norwich, UK. [12]Institute of Biosciences and Medical Technology–BioMediTech, University of Tampere and Tampere University Hospital, Tampere, Finland. [13]Johns Hopkins University, Baltimore, MD, USA. [14]Netherlands Cancer Institute, Amsterdam, Netherlands. [15]Breast Cancer Translational Research Laboratory, Institut Jules Bordet, Université Libre de Bruxelles, Brussels, Belgium. [16]British Columbia Cancer Agency, Vancouver, Canada. [17]Department of Medical Oncology, Erasmus Medical Center Cancer Institute, Erasmus University Medical Center, Rotterdam, Netherlands. [18]Cancer Research Laboratory, University of Iceland, Reykjavik, Iceland. [19]School of Medicine, University of Queensland, Brisbane, Australia. [20]Pathology Queensland, Royal Brisbane and Women's Hospital, Brisbane, Australia. [21]UQ Centre for Clinical Research, University of Queensland, Brisbane, Australia. [22]Université Lyon 1, Institut National du Cancer (INCa)–Synergie, Lyon, France. [23]Institute for Cancer Research, Oslo University Hospital, Oslo, Norway. [24]Department of Radiation Oncology and Department of Laboratory Medicine, Radboud University Medical Center, Nijmegen, Netherlands. [25]Dana-Farber Cancer Institute, Boston, MA, USA. [26]Department of Pathology, Academic Medical Center, Meibergdreef 9, 1105 AZ Amsterdam, Netherlands. [27]Institut Bergonié, 229 cours de l'Argone, 33076 Bordeaux, France. [28]Institut Curie, Department of Tumor Biology, 26 rue d'Ulm, 75248 Paris cédex 05, France. [29]Translational Cancer Research Unit and Department of Pathology, GZA Hospitals, Antwerp, Belgium. [30]Royal National Orthopaedic Hospital, Middlesex, UK. [31]UCL Cancer Institute, University College London, London, UK. [32]MD Anderson Cancer Center, Houston, TX, USA. [33]Department of Haematology, University of Cambridge, Cambridge, UK.
*These authors contributed equally to this work. †Participants are listed in the supplementary materials. ‡Corresponding author. E-mail: pc8@sanger.ac.uk

by insertions, leading to their inactivation and, on occasion, to their activation through disruption of cis-regulatory elements (*17*). Recently, processed pseudogenes, a by-product of somatic retrotransposition occurring when mature messenger RNA transcripts are reverse transcribed and inserted in the genome by the L1 machinery, have been described in cancer genomes (*18*, *19*). One example of a 3′ transduction has been described in a colorectal tumor (*16*), but this particular variation of retrotransposition has not been systematically studied in cancer genomes.

Here, we describe extensive somatic mobilization of genetic material mediated by L1 3′ transduction in many cancers, finding examples of genes, exons, and potential regulatory elements being repeatedly copied and strewn across the genome, sometimes in their tens to hundreds. With nonrepetitive sequence to fingerprint these transductions, the evidence implicates an unexpectedly small number of source elements as culpable for the vast majority of this genome shuffling. The activity of individual L1 donors may wax and wane during tumor evolution, but their progeny can themselves aspire to source element status, leading to cascading propagation of the family line.

Somatic L1 transductions can masquerade as chromosomal translocations

In a structural variant analysis of patients with lung cancer, we identified a patient with 22 somatically acquired interchromosomal rearrangements clustered in an intronic region of ~1700 base pairs (bp) in the gene *TTC28* on chromosome 22q12 (Fig. 1A). Preliminary analysis of the paired-end mapping reads revealed two characteristics suggestive of retrotransposition mediated by L1. First, all chromosome 22q12 breakpoints were clustered immediately after the 3′ extreme of a full-length L1 element. Second, in the relevant region of the partner chromosome, there were several reads whose unmapped mates reported a polyadenylate [poly(A)] tract inserted at the breakpoint junction. Clustered rearrangements in this same region of chromosome 22q12 were identified in two additional lung cancer patients and two lung cancer cell lines.

In the original patient, a similar cluster of 50 rearrangements was found originating from a small intronic region in the *PHACTR1* gene on chromosome 6p24.1 (Fig. 1B). Validation by polymerase chain reaction (PCR) across the breakpoint confirmed that these rearrangements were somatically acquired (Fig. 1C) and that the insertion of a poly(A) sequence was real.

The clustering of rearrangement breakpoints downstream from L1 elements coupled with poly (A) insertion suggests that these events represent L1 transductions. At first pass, it would be easy to misinterpret such events as balanced translocations because read-pairs spanning either end of the insertion appear to report reciprocal interchromosomal rearrangements. Indeed, retrotransductions could explain several puzzling clusters of rearrangements published by us and by others (*20*–*24*) (table S1). For example, in a colon cancer data set, 21 somatic translocations involving gene *TTC28* were reported (*23*). We believe that these represent transductions of the same small region at chromosome 22q12 that we describe above. Similarly, in a squamous cell lung cancer data set (*24*), we identified that 80/592 (14%) of the reported rearrangements were located immediately downstream of germline hot-L1 loci. The distinction between balanced chromosomal translocations and retrotransductions matters, because the former can create oncogenic fusion genes whereas the latter cause insertions of up to a few kilobases and would predominantly drive oncogenesis through effects on transcription of the target gene (*14*, *15*).

Identification of somatic transductions and retrotranspositions

We developed a bioinformatic pipeline to explore the frequency and signatures of all classes of somatic retrotransposition in cancer [TraFiC: Transposome Finder in Cancer (supplementary text)]. The pipeline is capable of detecting three different classes of retrotranspositions: solo-L1 events, in which either partial or complete LINEs are somatically retrotransposed; partnered transductions, in which a LINE and downstream nonrepetitive sequence are retrotransposed; and orphan transductions, in which only the unique sequence downstream of an active L1 is retrotransposed without the cognate LINE. We denote the L1 element from which a somatic retrotransposition originates as the source element. The pipeline relies on the identification of genomic hallmarks of retrotransposition at both the integration point and the L1 source element locus (Fig. 1, D and E, and fig. S1).

We ran TraFiC on whole-genome sequencing data from 290 tumor and matched normal pairs (210 primary tumors, 52 metastatic tumors, and 28 cancer cell lines with matched normal cell lines) from 244 cancer patients across 12 cancer types. The analysis retrieved a total of 2756 L1 retrotranspositions that includes solo L1s and 3′ transductions (tables S2 and S3). PCR validation (fig. S2) and capillary sequencing of 308 insertions (131 solo L1s, 72 partnered transductions, 91 orphan transductions, and 14 Alu insertions from both cell lines and primary tumors) confirmed the somatic acquisition of 303 (true positive rate 98%). Mapping of at least one of the two breakpoints per insertion to base-pair resolution by capillary sequencing was obtained for 84% (259/308). To evaluate the sensitivity of TraFiC to detect somatic retrotranspositions in cancer genome sequencing data, we performed in silico simulations. We generated a mock cancer genome into which we had seeded known somatic retrotransposition events of each type at differing levels of tumor clonality ranging from 25 to 100%. We then simulated sequencing reads from this mock cancer genome to the standard levels of coverage achieved in our cohort and ran TraFiC. The results confirmed the high specificity (>99%) of the pipeline and indicated a sensitivity ranging from 73 to 83% for tumor clonalities from 25 to 100%, respectively (table S4).

TraFiC obtained a partial reconstruction of the 5′ and 3′ extremes for 89% (2458/2756) of the total L1-mediated insertions, identified putative target site duplications for many of the insertions (table S3), and estimated an average insertion length of 1.09 kb for the insertions without 5′ inversion. Where present, target site duplications were typically in the range of 10 to 20 bp, as expected for retrotransposition. We were able to unambiguously assign 86% of somatic solo-L1 transpositions to a specific L1 subfamily; in every case, the transposable element (TE) belonged to L1Hs, based on the presence of diagnostic nucleotides (*14*, *25*); in the remaining 14%, sequencing reads did not cover the diagnostic nucleotides. All these features are shown in table S3.

L1 3′ transductions are present in 25% of cancer genomes

Overall, 53% (129/244) of the patients have at least one somatic L1 retrotransposition event, most frequently colon cancers (93%) and lung cancers (75%) (Fig. 2A). L1-mediated transductions of downstream sequence comprise 24% (655/2756 insertions) of the total somatic L1 retrotranspositions that occurred (tables S2 and S3). This represents a substantial contribution to the mutational landscape of cancer genomes not previously documented and adds to the previous reports of somatic solo-L1 retrotransposition in cancer (*13*, *14*, *16*). Orphan transductions represent half (333/655) of all transductions, demonstrating that truncation during somatic integration is frequent. This corroborates earlier analyses of somatic solo-L1 insertions, which also showed a high rate of truncations (*14*). The size of the transduced regions was typically less than 1 kb (Fig. 2B), but occasional transductions were found that captured genomic sequence located up to 12 kb downstream of the L1 source element (Fig. 2C).

In numerical terms, somatic retrotransposition is an important component of the structural variation landscape in some tumors (fig. S3). In lung cancer sample PD7354k, for example, L1 activity produced 565 unique somatic events, of which 120 are transductions, compared with 142 classic genomic rearrangements. In the evolution of lung tumors PD7354 and PD7356, transductions increased the genome size by 120 and 55 kb, respectively. Somatic L1 retrotransposition activity was higher in metastatic than in primary prostate cancer (12 versus 1 retrotransposition per sample, respectively; $P = 0.001$), suggesting that in this disease it is a late-onset mutational process.

Few L1 loci drive 3′ transductions in cancer

Because partnered and orphan transductions are defined by the retrotransposition of unique genomic sequence, we can unambiguously identify the L1 source element whence they derive. We find that 95% of all transductions identified can be attributed to only 72 germline L1 loci, with considerable variability in activity among them (Fig. 3A and table S5). Just two hot-L1 loci, located at chromosomes 22q12 and 6p24.1, account for more than a third of all somatic transductions

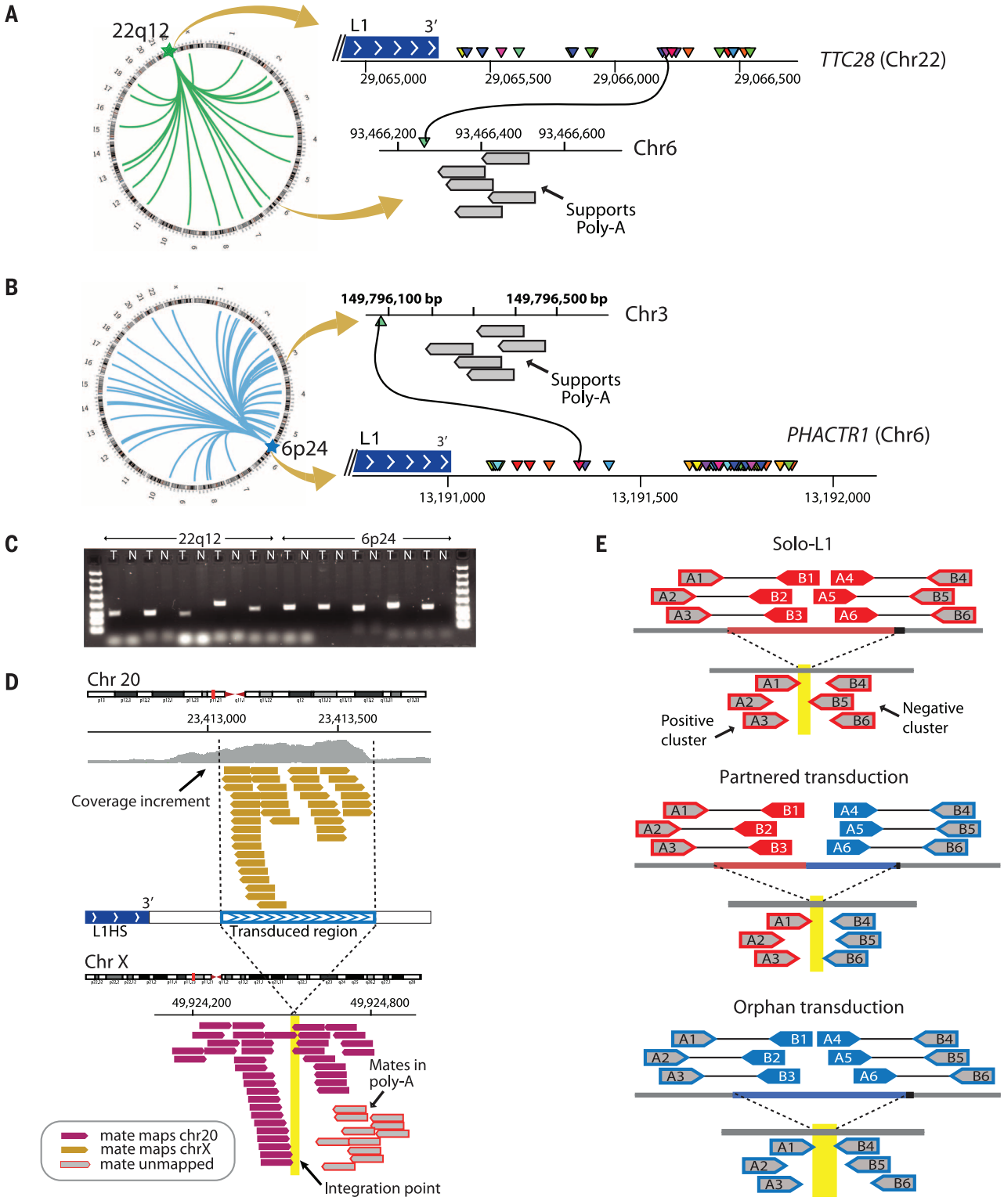

Fig. 1. Somatically acquired 3′ transductions are frequent in cancer genomes. (**A**) Putative translocations involving 22q12 (*TTC28*) show characteristics suggestive of L1-mediated 3′ transduction. Breakpoints at 22q12 (triangles of different colors) are clustered immediately after a germline full-length element. On the other side of the breakpoint, there are reads whose pairs report the presence of poly(A) tails (gray boxes). (**B**) Breakpoints clustered in *PHACTR1* just after a polymorphic L1 element not present in the reference genome. (**C**) PCR profiles showing the somatic acquisition of transductions from 22q12 and 6p24. T, tumor; N, normal. (**D**) The hallmarks of 3′ transduction. The donor-L1 locus at chromosome 20 shows coverage increment downstream of the element resulting from genome-wide amplification of the transduced material. Reads responsible for the coverage increment pair with different chromosomes (chromosome X illustrated). A cluster of reads around the breakpoint indicates the presence of a poly(A) tail. Other reads reveal the presence of target site duplication (not shown; details in table S3). (**E**) The strategy followed for somatic solo-L1 and transduction identification. The pipeline relies on the identification of two read clusters (i.e., positive and negative clusters) pointing to the same region of the genome where the somatic element is inserted.

we identify. Previous analyses of which L1 elements are likely to be active in the (germline) human genome have identified full-length L1 repeats with intact open reading frames found either in the reference genome or as polymorphisms in the population and studied their activity in in vitro retrotransposition assays (*4*, *5*). Of the 72 source elements we find to be active in somatic cells, only 18 overlap with loci documented in these previous analyses (table S5). This indicates that a more extensive repertoire of L1 elements may be competent for retrotransposition, probably a reflection of events arising from intact L1 elements that are rare polymorphisms in the human population. Unfortunately, because of the short read lengths (100 bp) and library inserts (~500 bp) generated, we were unable to attribute somatic solo-L1 retrotranspositions to their germline source element and so cannot know whether the same source elements that trigger transductions also generate isolated L1 transpositions.

The activity of individual L1 source elements varied across tumor types (Fig. 3A), with lung

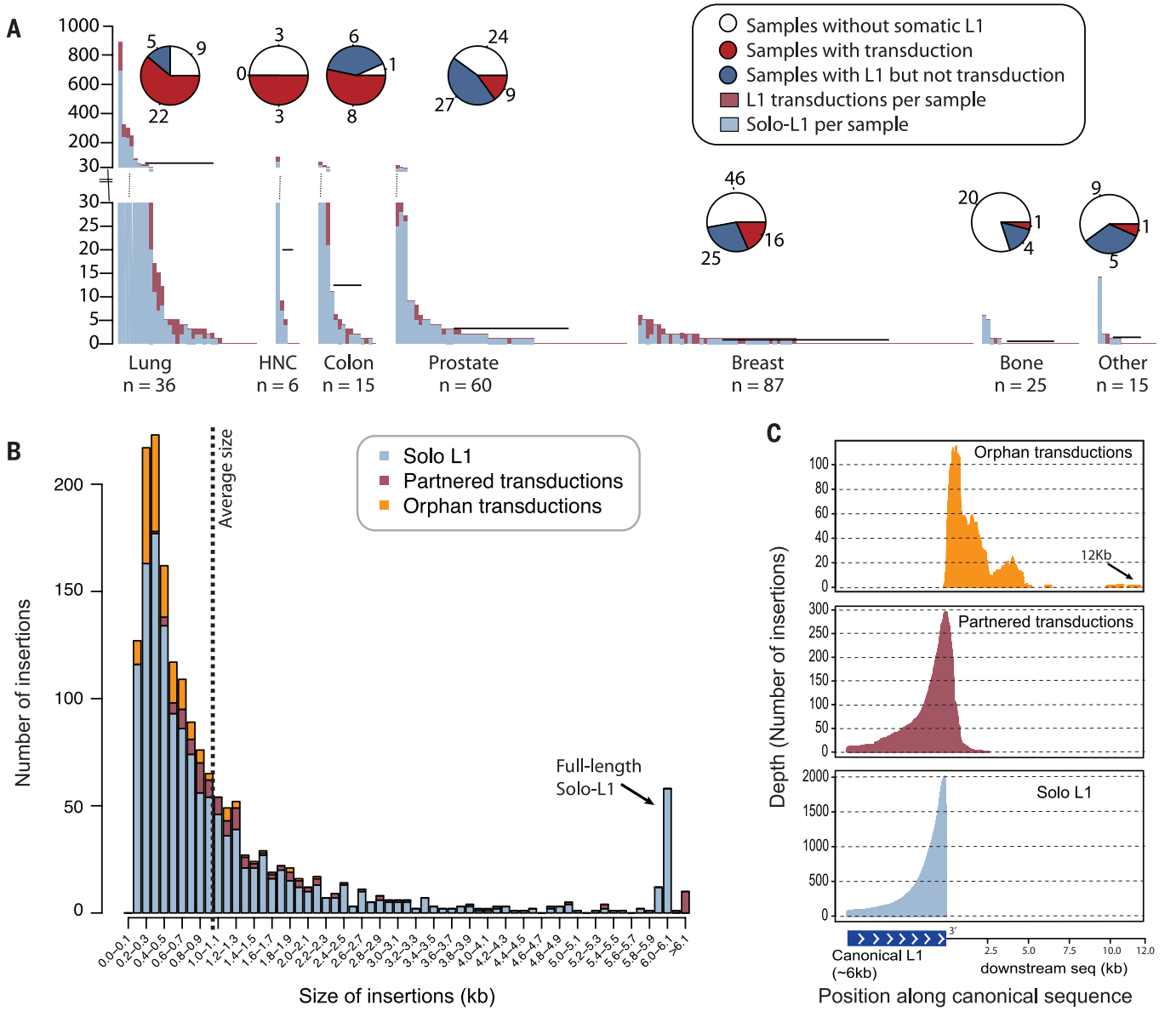

Fig. 2. The somatic L1 retrotransposition activity in 290 cancers. (**A**) Distribution of L1 retrotransposition activity in 290 cancers. Pie charts display the proportions of analyzed cancer samples with at least one transduction (blue), no transductions but at least one solo L1 (red), and no L1 retrotransposition (white). Bars represent the somatic L1 count of each cancer sample. Horizontal black lines indicate mean somatic retrotransposition counts for each cancer type. (**B**) The size distribution for L1 insertions (including solo L1s and transductions), in bins corresponding to 100-nucleotide increments in insertion lengths, shows an overrepresentation of truncated L1 insertions below 2 kb (average length of insertion is ~1.1 kb). Only insertions without 5′ inversion, or with inversion when it is lower than 500 bp, are shown. There are 81 L1 elements with estimated length >5.9 kb, of which 11 are partnered transductions. These full-length insertions represent ~5% (81/1752) of the total non–5′-inverted insertions (table S3). (**C**) The lengths of all L1 insertions (transductions included) are illustrated as a coverage plot over the schematic representation of a canonical solo-L1 sequence (~6 kb) and its downstream sequence (~12 kb). Most somatic L1 insertions (solo L1s and partnered transductions) are truncated at the 5′ end. For insertions with 5′ extreme inversion, the insertion length estimated corresponds to the minimal size that could be recognized (table S3), so it is underestimated. Full-length transductions and orphans mobilize nonrepetitive DNA sequences up to 12 kb away from the L1 source element end. Most of the transductions correspond to DNA material located within a distance of 1 kb to the end of the L1 source element.

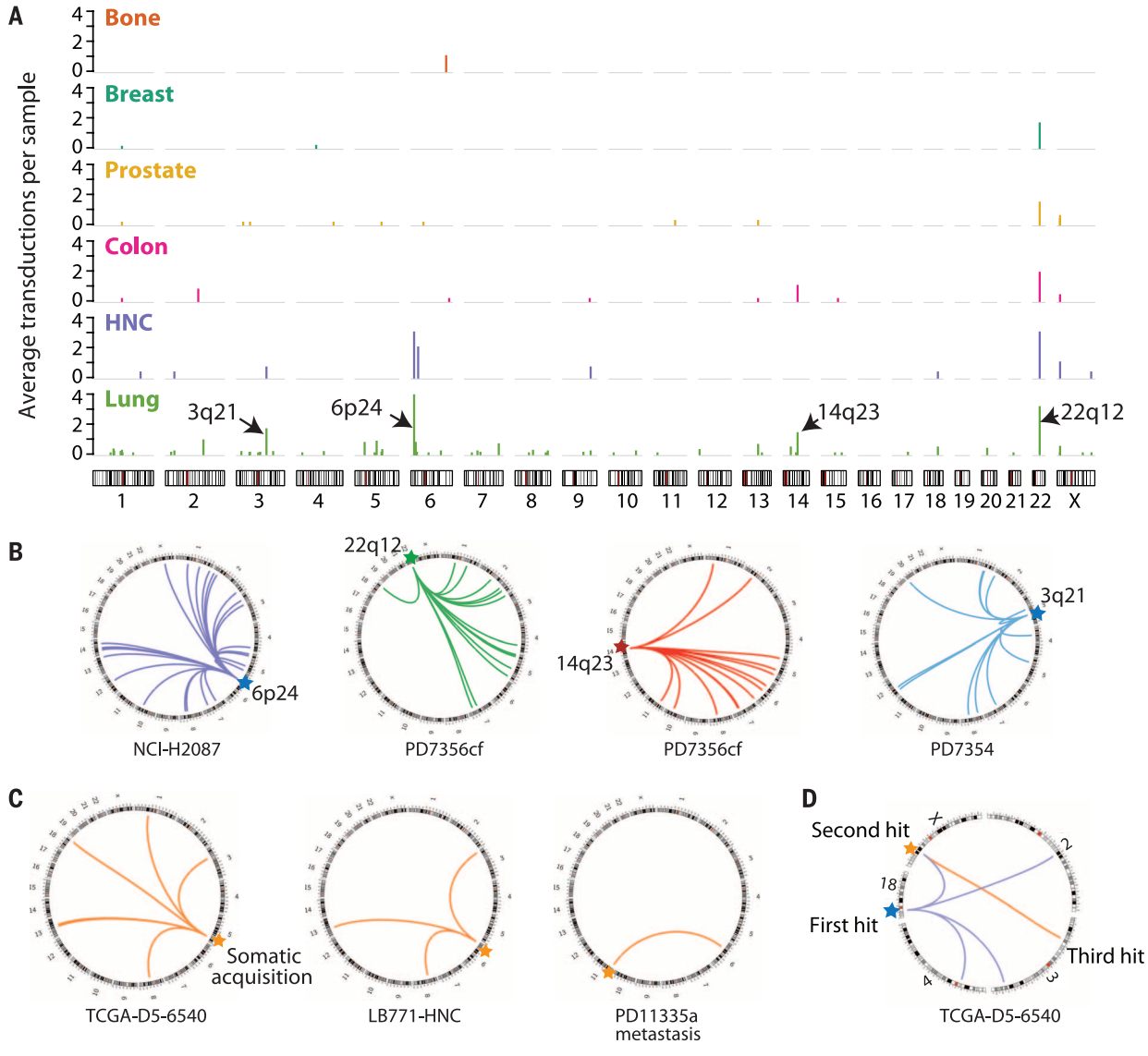

Fig. 3. Somatic 3′ transductions originate from a limited repertoire of L1 source elements. (**A**) Rate of source element activity within and among tumor types. The *y* axis denotes the average number of transductions involving the given element per sample for that tumor type. (**B**) Individual source elements show dramatic transduction activity in some lung cancer genomes. (**C**) Transductions arising from somatically acquired L1 copies in a colon cancer (TCGA-D5-6540), a head and neck cancer (LB771-HNC), and a prostate cancer (PD11335a). (**D**) Three-hit somatic retrotransposition example. A full-length L1 element acquired somatically (first hit) generated four somatic transductions, one of which (second hit) induces further mobilization, leading to a third hit. (**E**) Structural configuration of the breakpoints originated in the three-hit retrotransposition example. An intact L1 is somatically retrotransposed into *ANKRD62*, causing further transduction of 1114 bp of *ANKRD62* into *DMD*. A subsequent transduction picks up some of *DMD* together with *ANKRD62* and inserts both into *MYRIP* on chromosome 3 (third hit). (**F**) Read clusters supporting breakpoints shown in (E). Paired reads are shown as boxes connected with lines, colored by the genomic region they map to.

cancer showing the highest number of active copies (59 loci). In breast cancer, the source element at 22q12 is the only active L1 locus in 93% (15/17) of the breast cancer genomes where transductions occurred (fig. S4). Of particular note, some source elements, when active, can individually seed as many as 50 or more separate daughter copies in a single cancer. For example, the source element at 6p24.1 gave rise to 56 different somatic transductions during the evolution of the lung cancer PD7354 (Fig. 1B) and 25 transductions in the lung cancer cell line NCI-H2087 (Fig. 3B). Other hot-L1 elements, with at least 40 derived copies in a single sample, are located at 14q23 and 3q21 (Fig. 3B), and an additional nine source elements have shown at least 10 transductions each (table S5).

Somatically acquired L1 insertions are themselves transduction-competent

In theory, when a full-length L1 retrotransposition occurs, it takes with it all the machinery required to catalyze further retrotranspositions. By using the unique tags of downstream sequence as a marker of transduction competency, we searched for examples of somatically acquired L1 retrotranspositions that led to further dissemination from the new insertion site. We found 29 retrotranspositions from 17 L1 loci that were themselves somatically acquired insertions (Fig. 3C and table S5). The read-pair data confirmed that the de novo, somatically acquired source element was, as expected, a full-length L1 element in each example. Such somatic source elements were in general responsible for a low fraction of the transductions we observed (4.4%, 29/655) but would occasionally contribute the

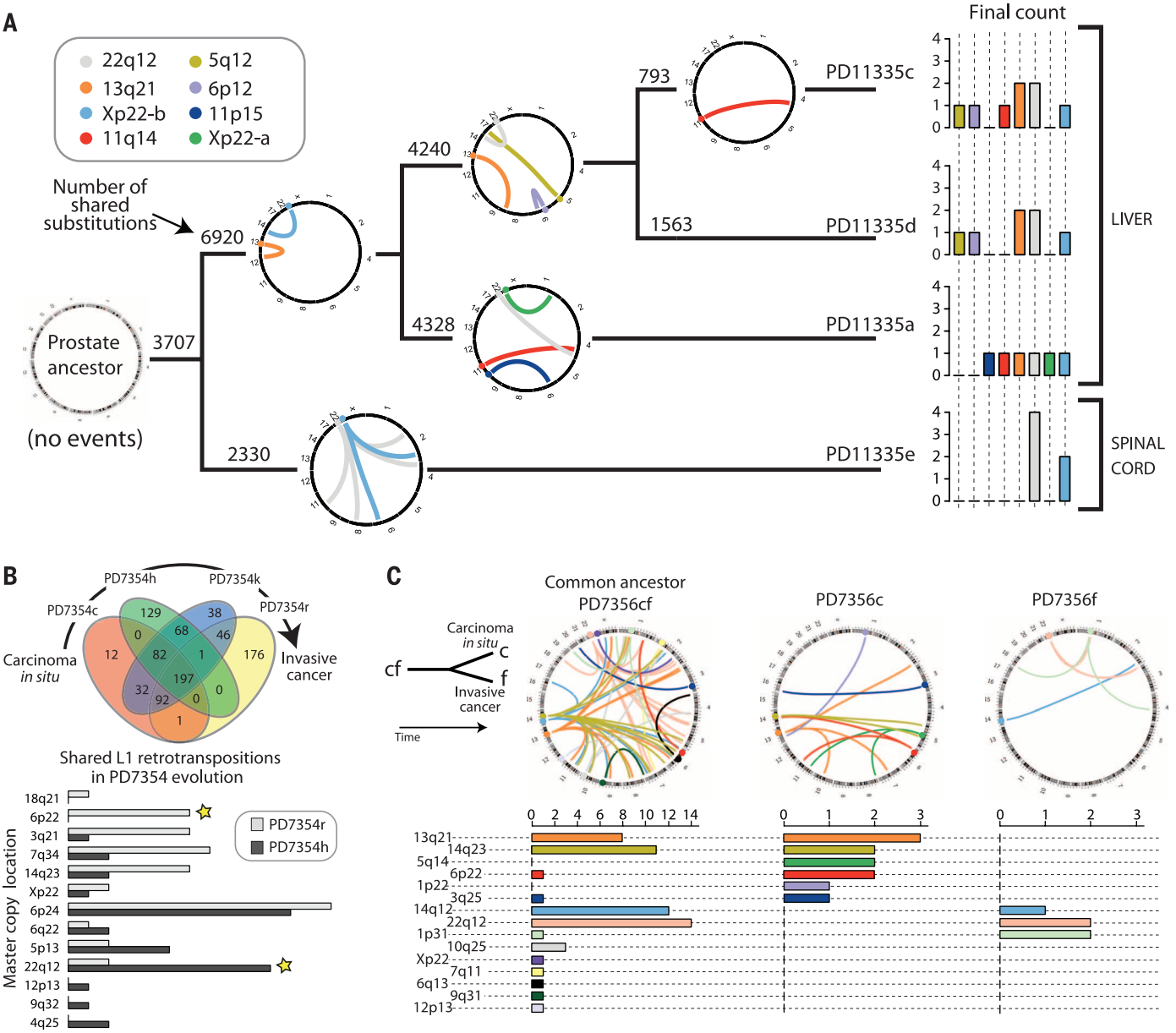

Fig. 4. L1 source element activity waxes and wanes during tumor evolution. (**A**) Evolution of prostate cancer PD11335. (Left) The phylogeny shows new somatic mobilizations in each branch of the phylogenetic tree, colored by the source element that is active on that branch. (Right) The final counts for each active source element in the sample sequenced. (**B**) Evolution of lung cancer PD7354. The Venn diagram shows the number of shared and nonshared somatic L1 retrotranspositions among the four samples sequenced. Source elements at 6p22 and 22q12 differed in activity between PD7354r and PD7354h (bar graph). (**C**) Evolution of lung cancer PD7356, sequenced at an early carcinoma in situ phase and a late invasive cancer. Somatic retrotranspositions were classified as shared between both lesions (early) or isolated to one or other lesion alone (late). Among the events isolated to only one or other lesion, there was no overlap in source elements, indicating individual activity varied during evolution of the tumor.

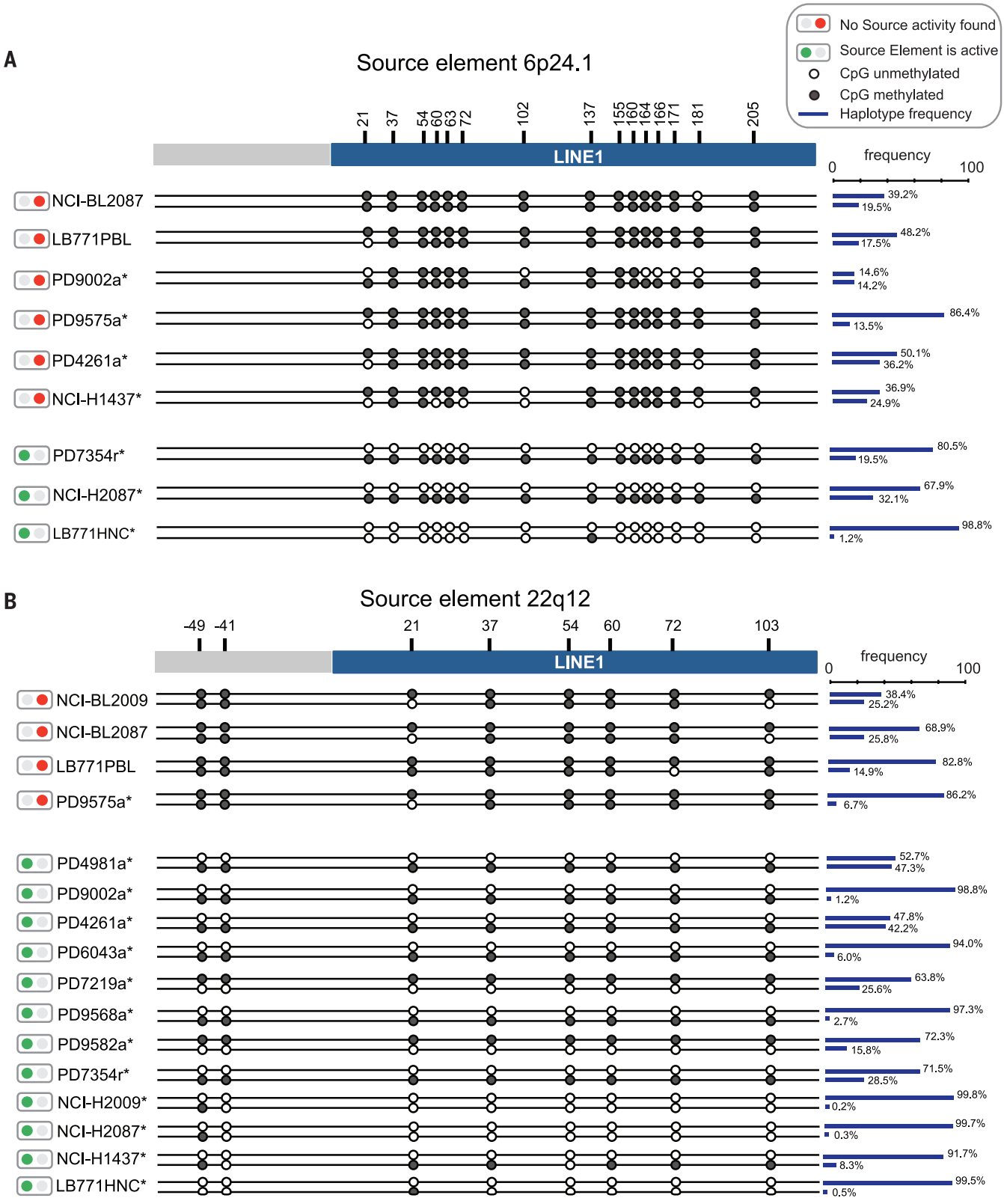

Fig. 5. Specific hypomethylation of L1 promoter of active and inactive source elements. (**A** and **B**) After bisulfite treatment of DNA and PCR amplification of L1 promoter regions composing the six most frequently active source elements, massively parallel sequencing was undertaken. The two most commonly observed haplotypes for each sample are depicted, with open circles representing CpG dinucleotides that are unmethylated and solid circles representing methylated CpG dinucleotides. The fraction of reads reporting each haplotype is shown on the right. Green circles on the left indicate which samples showed transductions derived from that source element; red circles indicate samples without activity of that source element. Asterisks after the sample name indicate tumor samples; those without asterisks are matched normal samples.

majority of transductions in a given sample. For instance, in colon cancer TCGA-D5-6540, four L1 insertions that were themselves somatic retrotranspositions gave rise to 12 somatic transductions, compared with 11 transductions originating from germline source elements.

In one notable colon cancer, we found a chain of three consecutive somatic retrotranspositions (Fig. 3, D to F). The first hit corresponds to the somatically acquired integration of a full-length L1 element within *ANKRD62* on chromosome 18. This new somatic element itself then transduces the full-length L1 element, together with a 1114-bp region of *ANKRD62*, into the *DMD* gene on chromosome X (second hit). Last, this new element at chromosome X transduces a region of 147 bp of *DMD* together with the 1114 bp of *ANKRD62* that was previously inserted there, integrating this

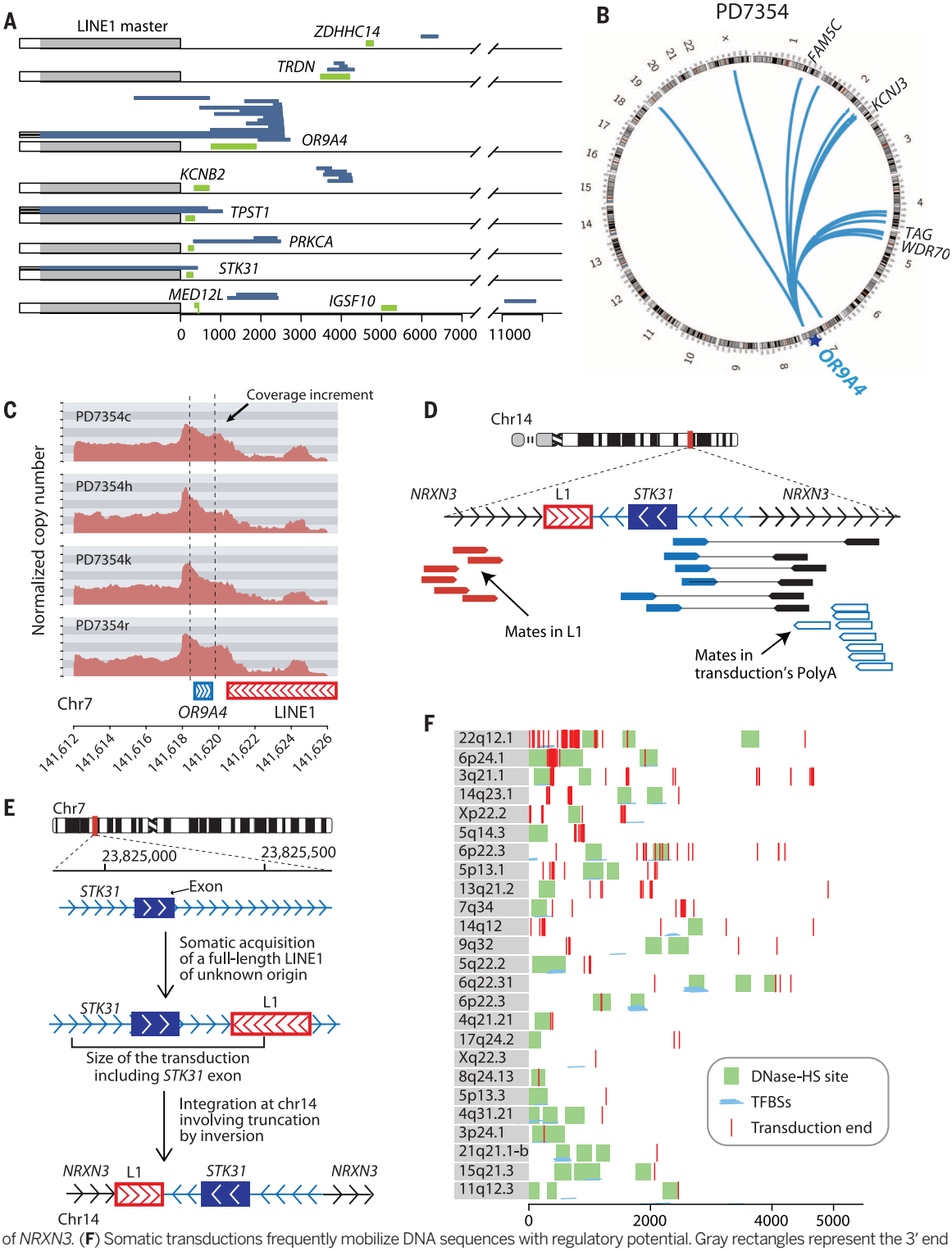

Fig. 6. Somatic shuffling of coding and regulatory regions mediated by L1 transductions. (**A**) Somatic transductions can mobilize coding sequences. Gray rectangles represent each L1 source element (LINE1 master), and white boxes at 5′ represent the L1 promoter. The *x* axis shows the distance downstream of the source element. Exons are represented by green rectangles. Blue lines represent the region transduced elsewhere in the genome. (**B**) In PD7354, the Circos (http://circos.ca) plot shows transductions mediated by the source element at chromosome 7q34 involved in the somatic amplification of *OR9A4*. (**C**) Coverage increment demonstrating amplification of *OR9A4* in different samples of tumor PD7354. (**D**) Read clusters supporting the integration of *STK31* exon into chromosome 14, with the sequence of events shown in (E). (**E**) Structural configuration of breakpoints involved in the *STK31* exon shuffling mediated by a somatic L1 element. An intact, transduction-competent L1 element inserts somatically immediately downstream of an exon of *STK31*. A further partnered transduction event occurs in which the exon of *STK31* and a portion of the somatic L1 element retrotranspose to an intron of *NRXN3*. (**F**) Somatic transductions frequently mobilize DNA sequences with regulatory potential. Gray rectangles represent the 3′ end of the L1 source elements. The *x* axis shows the distance downstream of each source element. Green rectangles represent DNAse-I–hypersensitive sites, and horizontal blue lines represent transcription factor binding sites. Every vertical red line represents the end point of a somatic transduction event.

new material into *MYRIP* on chromosome 3 (third hit). In this final transduction, the L1 element suffers an internal inversion, rendering it transduction-incompetent. This succession of events leads to the juxtaposition of intronic sequences from three different genes (*MYRIP*, *DMD*, and *ANKRD62*) in the final rearrangement.

Fluctuating activity of source elements during tumor evolution

To evaluate the timing of retrotransposition during cancer evolution, we analyzed eight patients with prostate cancer in whom we had sequenced multiple metastases, three patients with prostate cancer in whom we had sequenced multiple foci of the primary tumor, and three patients with squamous lung cancer in whom we had sequenced samples from two or more time points during progression from carcinoma in situ to invasive cancer. Three patients had sufficient numbers of somatic transductions for us to evaluate source element activity across the cancer's development, although we acknowledge that our sensitivity to detect early shared events is greater than for late events found in only one sample.

For one prostate cancer (Fig. 4A), we reconstructed the phylogenetic tree from 23,881 somatic substitutions across a spinal cord metastasis and three liver deposits. We mapped somatic transductions onto this phylogenetic tree. Transductions were distributed across all internal branches and all but one of the terminal branches of the tree. Four source elements (Xp22-b, 22q12, 11q14, and 13q21) gave rise to transductions on more than one branch of the phylogenetic tree, suggesting that they were repeatedly active in different clonal lineages during tumor evolution. Nonetheless, they were not universally active, nor were the activity profiles among source elements correlated.

Similar patterns were observed during the evolution of carcinoma in situ to invasive squamous cell lung cancer for patient PD7354. In this case, the four lesions sequenced are each complex admixtures of subclones, making reconstruction of a complete evolutionary history challenging. However, we do see differences in the activity rate of individual source elements across this time series (Fig. 4B). For example, comparing events exclusive to either PD7354h or PD7354r, the locus at 6p22 spawned six transductions in PD7354r but none in PD7354h, whereas the source element at 22q12 initiated 10 transductions in PD7354h but only two specific to PD7354r. The differences in activity across source elements between the two lesions were statistically significant (P = 0.01). Similarly, for a second patient (PD7356) in whom we sequenced a squamous carcinoma in situ and its related invasive cancer, we found no overlap in source element activity after divergence of the two clonal populations from the common ancestor (Fig. 4C).

Taken together, these data indicate that activity of individual source elements waxes and wanes during tumor evolution. We cannot know whether transposition events can occur in normal cells before oncogenic transformation—this would require single normal cell cloning and sequencing (*26*). These examples do show that somatic retrotransposition persists into the late stages of tumor development.

Hypomethylation activates L1 source elements in cancer genomes

DNA methylation of the L1 promoter is an important inhibitor of L1 activity (*27*–*30*). In previous analyses of methylation profiles, it had been shown that there might be genome-wide variation in methylation correlated with somatic retrotranspositions in cancer (*13*) and that global methylation of L1 promoters is about 20% lower in hepatocellular cancers than in normal liver (*17*). These assays essentially report methylation status at a global level. With transductions, because we know the individual L1 source elements that are active in any given sample, we are able to directly measure the methylation status of the given element in that sample. To do this, we combined bisulfite DNA treatment with massively parallel sequencing of the promoter region, assaying six loci in 16 samples.

We found a remarkably consistent correlation between CpG hypomethylation on the promoter of a source element and its retrotransposition activity in that sample. In every sample in which the source element had been active, the most common haplotype observed was fully unmethylated across the promoter. In contrast, samples without transductions arising from the given source element generally showed high levels of promoter methylation at that locus (Fig. 5 and fig. S5). In the source element 6p24.1, for example, in a lung cancer cell line (NCI-H2087), we found fully unmethylated CpG dinucleotides in the repeat, whereas the matched transformed lymphoblastoid cell line from the same patient (NCI-BL2087) is methylated (Fig. 5A). These correlations were also observed in primary tumors. For instance, for primary breast cancer samples encompassing the range of retrotransposition activity at source L1 locus 22q12, methylation patterns revealed by massively parallel sequencing showed a fully unmethylated haplotype (usually the most frequent one) in samples where the

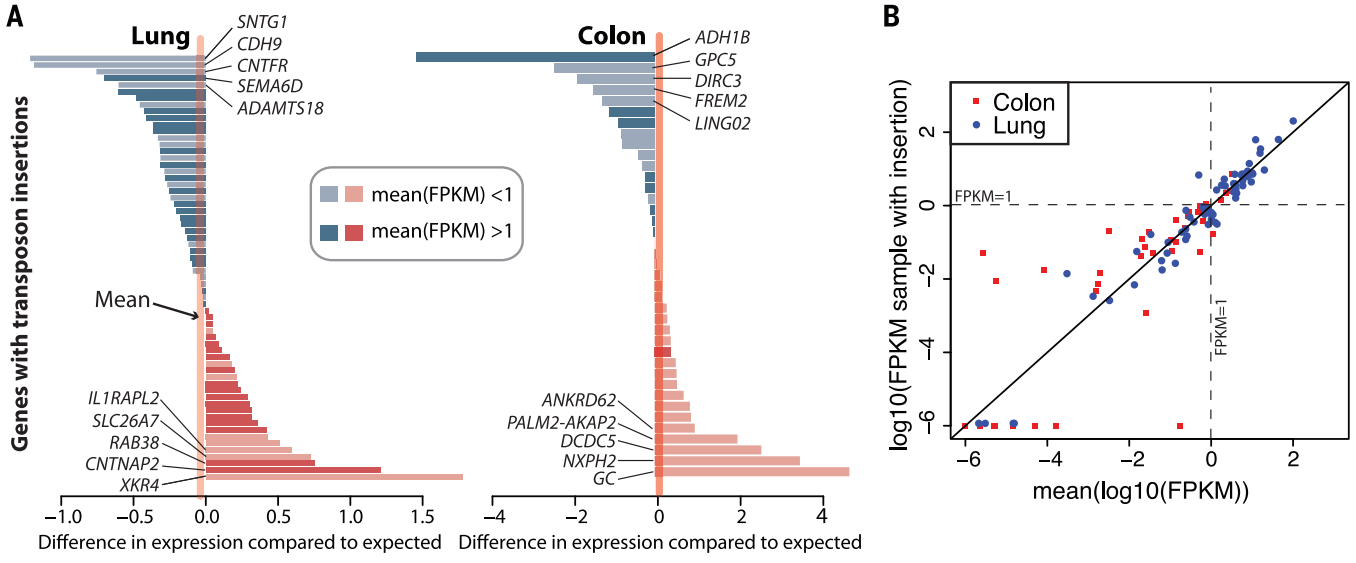

Fig. 7. Gene expression effects associated with L1 insertions. (**A**) For lung and colon cancers, each bar represents the difference between the $\log_{10}$(FPKM) for the target gene in the relevant sample compared to the average $\log_{10}$(FPKM) for other samples of that tumor type. FPKM, fragments per kilobase of transcript per million mapped reads. Genes with FPKM > 1 average expression have darker bars. (**B**) Scatter plot showing the data in (A). The *y* axis shows the $\log_{10}$(FPKM) for the target gene in the relevant sample, and the *x* axis shows the average $\log_{10}$(FPKM) for that gene for other samples of that tumor type. In expressed genes [mean $\log_{10}$(FPKM) > 0], the expression level in the affected sample is very close to the overall expression level of the gene in the corresponding tissue. Most large expression level differences occur at unexpressed genes [mean $\log_{10}$(FPKM) < 0].

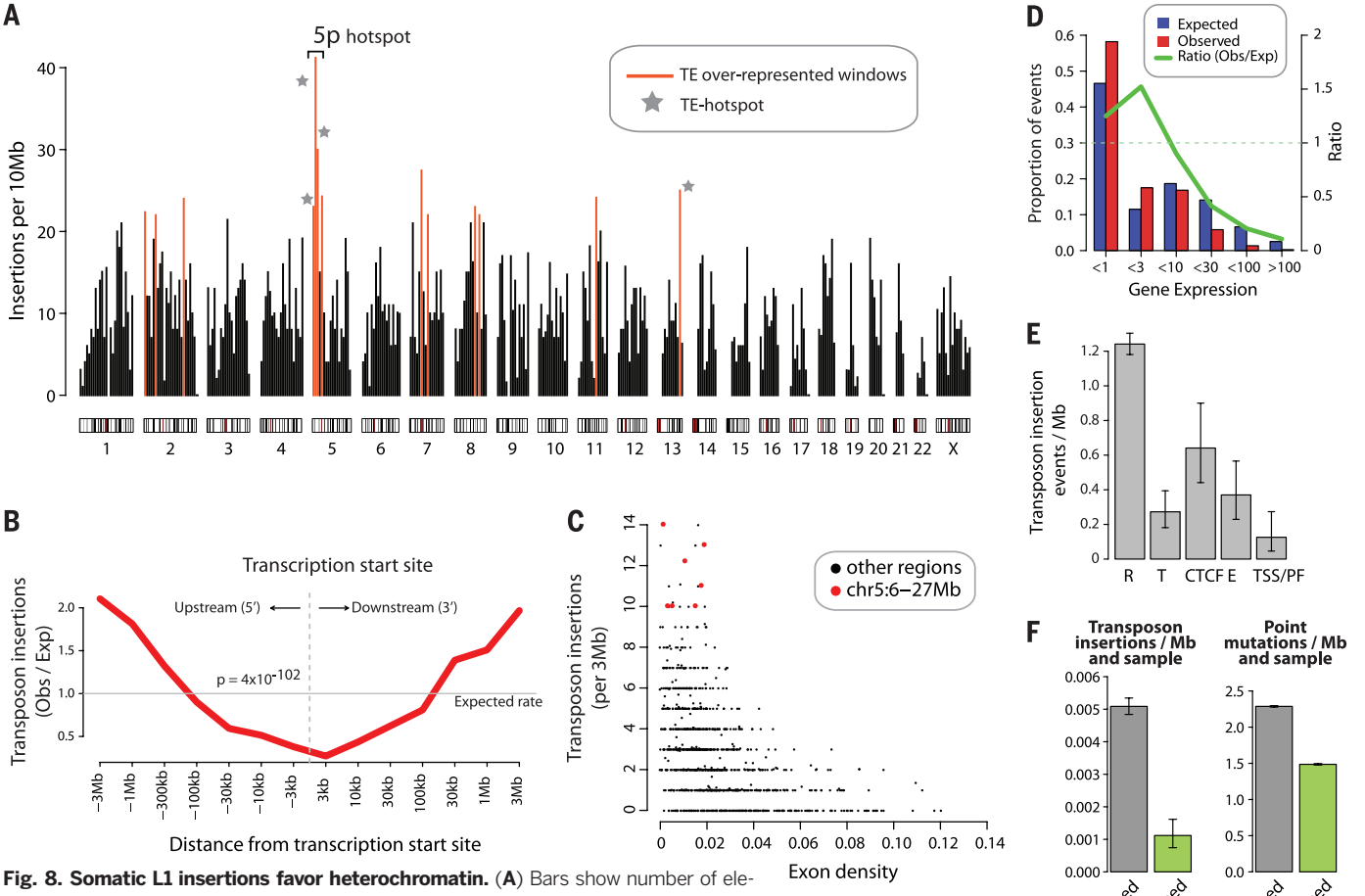

Fig. 8. Somatic L1 insertions favor heterochromatin. (**A**) Bars show number of elements per 10-Mb window. Red bars represent the 13 regions with overrepresentation of elements. Asterisk represents hotspots of TEs in the cancer genome (i.e., 10 or more elements are clustered together within a region of 1 to 1.5 Mb). (**B**) Somatic integrations of TEs are more abundant far away from the transcription start site of the nearest gene. The *x* axis shows the rate of observed versus expected somatic insertions. The *y* axis shows the distance to the transcription start site of the nearest gene. (**C**) Somatic integrations of TEs are more frequently associated with exon-poor regions of the cancer genome. The *x* axis shows the number of somatic TEs in windows of 3 Mb of the genome, whereas the *y* axis shows the density of exons. Windows at chromosome 5p, which showed the highest somatic TE insertion rates in the cancer genome, are highlighted. (**D**) TEs are enriched in lowly expressed genes (<3 FPKM) relative to highly expressed genes. (**E**) Overall, TEs are overrepresented in transcriptionally repressed regions of the genome (most likely heterochromatic), similar to previous observations of point mutations in cancer (*37*). The relative abundance of insertions in repressed chromatin is 4.55 times higher than in transcriptionally active regions of the genome. R, repressed; T, transcriptionally active; CTCF, CCCTC binding factor–enriched element; E/WE, enhancer or weak enhancer regions; TSS/PF, promoters and flanking regions. Error bars reflect Poisson confidence intervals. (**F**) Average rate of TE insertions and synonymous point mutations in repressed and active chromatin. The difference in mutation rate between repressed and active chromatin is much larger in TE insertions relative to point mutations.

source element shows activity (Fig. 5B). Results were similar for the other four source elements (fig. S5) and were confirmed by capillary sequencing (fig. S6). There were occasional exceptions to this pattern; although activity was always associated with hypomethylation, sometimes hypomethylation did not indicate activity. In three samples of 66 scenarios analyzed, we found a fully unmethylated promoter at a source element from which we detected no transductions (Fig. 5 and fig. S5).

To determine how far the hypomethylation at active L1 elements extended, we analyzed Illumina (Illumina, Incorporated, San Diego, California) methylation array data available for 19 colon cancer samples from the Cancer Genome Atlas (TCGA) (*23*). We did not find any correlation between source element activity and hypomethylation in the 5 Mb surrounding the L1 locus (*P* values ranging from 0.4 to 0.9, *t* test) (fig. S7). This suggests that L1 activation in cancer genomes is more likely the consequence of the hypomethylation of a highly localized DNA region surrounding the source element (or restricted to each specific L1 locus) rather than hypomethylation of larger chromosomal regions. These results reveal that, although global hypomethylation is a factor predisposing to L1 activation (*13*) in cancer, individual L1 source elements become active only when hypomethylation occurs in the promoter region of that element.

Transduction of genes, exons, and regulatory elements in cancer genomes

When an L1 source element is located near a coding region, transductions can cause mobilization of exons (*6*, *31*). We found capture of adjacent coding regions to be relatively common in somatic transductions (Fig. 6A), with about 2.3% of events (15/655) distributing a proximal exon or complete gene elsewhere in the genome.

One lung carcinoma in situ, PD7354, demonstrates recurrent transduction of the single-exon gene *OR9A4*, an olfactory receptor, originating from a germline L1 element just 862 bp downstream of the gene (Fig. 6, B and C). Among 14 different somatic transductions, we found four complete copies of the *OR9A4* gene and five partial copies distributed across the genome, often inserted into footprints of other genes. Similarly, we identified duplication of the third exon of the *TPST1* gene in two primary lung cancers, TCGA-60-2722 and PD7356 (fig. S8). There, the exon is mobilized by the action of a germline L1 element located 145 bp upstream.

Somatic retrotranspositions can mobilize coding sequence when they themselves propagate.

In one lung cancer cell line, NCI-H2087, a full-length L1 element had integrated into the kinase gene *STK31* as a somatically acquired retrotransposition (Fig. 6, D and E, and fig. S9). This new somatic L1 insertion was transduction-competent: In one event, it picked up the whole of exon 18 of *STK31* located 169 bp downstream, catalyzing its insertion into the footprint of another gene, *NRXN3*. Such secondary transductions mean that the range of genomic elements that could potentially be targeted by transduction is considerably larger than just those near germline transduction-competent L1 elements.

Transductions could also potentially mediate distribution of sequences with regulatory potential around the genome (Fig. 6F). We screened the somatic transductions identified in our cohort for mobilization of deoxyribonuclease I (DNAse-I) hypersensitive sites or transcription factor binding sites defined by the Encyclopedia of DNA Elements (ENCODE) project (*32*). We found 43 transductions that mobilized a total of 54 full-length DNAse-I hypersensitive sites. Similarly, 86 transductions led to 251 transcription factor binding sites being copied and inserted elsewhere in the genome, although we recognize that ENCODE used a variety of normal cell types to define these sites. In the absence of tumor-specific epigenetic profiling data, it is difficult to know what the effects of mobilizing any one of these putative regulatory elements would be, but our data do show that somatic transductions would theoretically have the potential to shuffle such elements around the genome and near key genes.

Chromatin organization influences regional rates of L1 retrotransposon insertion

Recent work has provided evidence that a small, but important, fraction of the L1 insertions in a cancer genome may influence gene function (*14*). To assess this, we analyzed RNA-sequencing data available from TCGA samples of 13 lung and 11 colon cancers. We did not find any strong evidence that retrotransposon insertion altered expression levels generally for the 66 and 39 genes, respectively, with somatic L1 insertions (Fig. 7). This finding differs from a previous analysis that suggested L1 insertions caused frequent down-regulation of gene expression (*14*), a discrepancy we believe to be due to skewness in the distribution of gene expression levels (discussed extensively in the materials and methods and figs. S10 and S11). In addition, we did not find any evidence for aberrant fusion transcripts arising from inclusion of transduced sequence in the target gene. In total, 16 insertions occurred in footprints of genes identified as recurrently mutated (*33*), mostly intronic, and probably of minimal importance (table S6). There was one somatic insertion, of an Alu element into the promoter of *NFE2L2* in a squamous lung cancer, of uncertain importance.

To understand the properties of the insertion points of retrotranspositions, we analyzed the genome-wide distribution of 2850 somatic TEs (including 2756 L1 and 94 non-L1 insertions). At a macroscopic scale, we found significant heterogeneity across the genome in the density of insertion points (Fig. 8A). This is particularly evident in the first 30 Mb of chromosome 5p, where we identified no fewer than 93 separate insertions. Beyond this, we also found evidence for more-localized clusters of integration sites, identifying four particular hotspots, three of which are located in the subtelomeric region of 5p. Each of these hotspots is 1 to 1.5 Mb in size and contains 10 insertions from our data set (Fig. 8A).

Somatic retrotranspositions are more likely to insert in intergenic or heterochromatic regions of the cancer genome than expected by chance. First, higher frequency of TE integration correlates with greater distance to the transcription start site of the nearest gene (Fig. 8B), indicating that most of the integration events occur at intergenic regions. Second, somatic insertions are more frequently observed in regions of the genome where exon density is lower (Fig. 8C). Third, TEs more frequently insert into lowly expressed genes compared with those that are highly expressed ($P = 2 \times 10^{-24}$), even after correction for the length of the gene ($P = 5 \times 10^{-4}$) (Fig. 8D). Fourth, the rate of somatic insertion is five times higher in repressed or low-activity regions of the genome predicted by ENCODE than in transcribed regions (Fig. 8E). This difference in mutation rates between heterochromatin and euchromatin is much larger for retrotransposon insertions (4.55 times higher rate in heterochromatin) than for somatic substitutions (1.54 times higher) (Fig. 8F). When we repeated this analysis for polymorphic germline retrotranspositions (that must have occurred recently in evolutionary time) identified from three different databases, we find a very similar enrichment for heterochromatin insertion as for somatic events ($P = 0.6$; fig. S12).

Two possible explanations, not necessarily mutually exclusive, could underpin the apparent enrichment of somatic retrotransposition into heterochromatin. First, insertions into gene footprints could be deleterious to the cancer clone and therefore subject to negative selection, or, second, the insertion machinery could preferentially target heterochromatin. We cannot formally distinguish between these possibilities on the basis of our data but believe the latter to be the more dominant because most of the insertions in active chromatin do not have an impact on gene expression and because negative selection is less powerful in somatic cells than in the germ line.

The majority of these retrotransposition events are likely to be passenger mutations. This is no different from any other mutational process—kataegis, the *POLE* hypermutator phenotype in endometrial cancer, and the tandem duplicator phenotype in breast and ovarian cancer (*34*–*36*), for example. Nonetheless, generation of genomic variability is the first stage of Darwinian evolution, and it is a key aim of cancer genomics to describe mutational processes in full, multidimensional detail. This includes information about the patterns and frequency of the mutational process, its genome-wide distribution, its distribution across tumor types, its timing during cancer evolution, and its correlation with other processes generating genomic instability. To understand how 3′ transductions can generate functional and tumorigenic consequences, we will need to survey the topography of somatic retrotransposition on a considerably larger scale, across thousands of cancer genomes, integrated with other mutational processes and transcriptional data.

REFERENCES AND NOTES

1. E. S. Lander *et al.*, Initial sequencing and analysis of the human genome. *Nature* **409**, 860–921 (2001). doi: 10.1038/35057062; pmid: 11237011
2. H. H. Kazazian Jr., Mobile elements: Drivers of genome evolution. *Science* **303**, 1626–1632 (2004). doi: 10.1126/science.1089670; pmid: 15016989
3. D. M. Sassaman *et al.*, Many human L1 elements are capable of retrotransposition. *Nat. Genet.* **16**, 37–43 (1997). doi: 10.1038/ng0597-37; pmid: 9140393
4. B. Brouha *et al.*, Hot L1s account for the bulk of retrotransposition in the human population. *Proc. Natl. Acad. Sci. U.S.A.* **100**, 5280–5285 (2003). doi: 10.1073/pnas.0831042100; pmid: 12682288
5. C. R. Beck *et al.*, LINE-1 retrotransposition activity in human genomes. *Cell* **141**, 1159–1170 (2010). doi: 10.1016/j.cell.2010.05.021; pmid: 20602998
6. J. V. Moran, R. J. DeBerardinis, H. H. Kazazian Jr., Exon shuffling by L1 retrotransposition. *Science* **283**, 1530–1534 (1999). doi: 10.1126/science.283.5407.1530; pmid: 10066175
7. S. T. Szak, O. K. Pickeral, D. Landsman, J. D. Boeke, Identifying related L1 retrotransposons by analyzing 3′ transduced sequences. *Genome Biol.* **4**, R30 (2003). doi: 10.1186/gb-2003-4-5-r30; pmid: 12734010
8. C. M. Macfarlane *et al.*, Transduction-specific ATLAS reveals a cohort of highly active L1 retrotransposons in human populations. *Hum. Mutat.* **34**, 974–985 (2013). doi: 10.1002/humu.22327; pmid: 23553801
9. N. G. Coufal *et al.*, L1 retrotransposition in human neural progenitor cells. *Nature* **460**, 1127–1131 (2009). doi: 10.1038/nature08248; pmid: 19657334
10. A. R. Muotri *et al.*, L1 retrotransposition in neurons is modulated by MeCP2. *Nature* **468**, 443–446 (2010). doi: 10.1038/nature09544; pmid: 21085180
11. G. D. Evrony *et al.*, Single-neuron sequencing analysis of L1 retrotransposition and somatic mutation in the human brain. *Cell* **151**, 483–496 (2012). doi: 10.1016/j.cell.2012.09.035; pmid: 23101622
12. J. K. Baillie *et al.*, Somatic retrotransposition alters the genetic landscape of the human brain. *Nature* **479**, 534–537 (2011). doi: 10.1038/nature10531; pmid: 22037309
13. R. C. Iskow *et al.*, Natural mutagenesis of human genomes by endogenous retrotransposons. *Cell* **141**, 1253–1261 (2010). doi: 10.1016/j.cell.2010.05.020; pmid: 20603005
14. E. Lee *et al.*, Landscape of somatic retrotransposition in human cancers. *Science* **337**, 967–971 (2012). doi: 10.1126/science.1222077; pmid: 22745252
15. Y. Miki *et al.*, Disruption of the APC gene by a retrotransposal insertion of L1 sequence in a colon cancer. *Cancer Res.* **52**, 643–645 (1992). pmid: 1310068
16. S. Solyom *et al.*, Extensive somatic L1 retrotransposition in colorectal tumors. *Genome Res.* **22**, 2328–2338 (2012). doi: 10.1101/gr.145235.112; pmid: 22968929
17. R. Shukla *et al.*, Endogenous retrotransposition activates oncogenic pathways in hepatocellular carcinoma. *Cell* **153**, 101–111 (2013). doi: 10.1016/j.cell.2013.02.032; pmid: 23540693
18. S. L. Cooke *et al.*, Processed pseudogenes acquired somatically during cancer development. *Nat. Commun.* **5**, 3644 (2014). doi: 10.1038/ncomms4644; pmid: 24714652
19. A. D. Ewing *et al.*, Retrotransposition of gene transcripts leads to structural variation in mammalian genomes. *Genome Biol.* **14**, R22 (2013). doi: 10.1186/gb-2013-14-3-r22; pmid: 23497673
20. S. C. Baca *et al.*, Punctuated evolution of prostate cancer genomes. *Cell* **153**, 666–677 (2013). doi: 10.1016/j.cell.2013.03.021; pmid: 23622249
21. S. Banerji *et al.*, Sequence analysis of mutations and translocations across breast cancer subtypes. *Nature* **486**, 405–409 (2012). doi: 10.1038/nature11154; pmid: 22722202
22. P. J. Campbell *et al.*, The patterns and dynamics of genomic instability in metastatic pancreatic cancer. *Nature*

467, 1109–1113 (2010). doi: 10.1038/nature09460; pmid: 20981101
23. D. M. Muzny *et al*., Comprehensive molecular characterization of human colon and rectal cancer. *Nature* **487**, 330–337 (2012). doi: 10.1038/nature11252; pmid: 22810696
24. P. S. Hammerman *et al*., Comprehensive genomic characterization of squamous cell lung cancers. *Nature* **489**, 519–525 (2012). doi: 10.1038/nature11404; pmid: 22960745
25. A. D. Ewing, H. H. Kazazian Jr., High-throughput sequencing reveals extensive variation in human-specific L1 content in individual human genomes. *Genome Res.* **20**, 1262–1270 (2010). doi: 10.1101/gr.106419.110; pmid: 20488934
26. J. S. Welch *et al*., The origin and evolution of mutations in acute myeloid leukemia. *Cell* **150**, 264–278 (2012). doi: 10.1016/j.cell.2012.06.023; pmid: 22817890
27. D. Bourc'his, T. H. Bestor, Meiotic catastrophe and retrotransposon reactivation in male germ cells lacking Dnmt3L. *Nature* **431**, 96–99 (2004). doi: 10.1038/nature02886; pmid: 15318244
28. L. Menendez, B. B. Benigno, J. F. McDonald, L1 and HERV-W retrotransposons are hypomethylated in human ovarian carcinomas. *Mol. Cancer* **3**, 12 (2004). doi: 10.1186/1476-4598-3-12; pmid: 15109395
29. J. A. Yoder, C. P. Walsh, T. H. Bestor, Cytosine methylation and the ecology of intragenomic parasites. *Trends Genet.* **13**, 335–340 (1997). doi: 10.1016/S0168-9525(97)01181-5; pmid: 9260521
30. K. Hur *et al*., Hypomethylation of long interspersed nuclear element-1 (LINE-1) leads to activation of proto-oncogenes in human colorectal cancer metastasis. *Gut* **63**, 635–646 (2014). doi: 10.1136/gutjnl-2012-304219; pmid: 23704319
31. Y. Ejima, L. Yang, *Trans* mobilization of genomic DNA as a mechanism for retrotransposon-mediated exon shuffling. *Hum. Mol. Genet.* **12**, 1321–1328 (2003). doi: 10.1093/hmg/ddg138; pmid: 12761047
32. ENCODE Project Consortium, An integrated encyclopedia of DNA elements in the human genome. *Nature* **489**, 57–74 (2012). doi: 10.1038/nature11247; pmid: 22955616
33. M. S. Lawrence *et al*., Discovery and saturation analysis of cancer genes across 21 tumour types. *Nature* **505**, 495–501 (2014). doi: 10.1038/nature12912; pmid: 24390350
34. S. Nik-Zainal *et al*., Mutational processes molding the genomes of 21 breast cancers. *Cell* **149**, 979–993 (2012). doi: 10.1016/j.cell.2012.04.024; pmid: 22608084
35. D. J. McBride *et al*., Tandem duplication of chromosomal segments is common in ovarian and breast cancer genomes. *J. Pathol.* **227**, 446–455 (2012). doi: 10.1002/path.4042; pmid: 22514011
36. C. Palles *et al*., Germline mutations affecting the proofreading domains of POLE and POLD1 predispose to colorectal adenomas and carcinomas. *Nat. Genet.* **45**, 136–144 (2013). doi: 10.1038/ng.2503; pmid: 23263490

ACKNOWLEDGMENTS

J.M.C.T. is supported by a Marie Curie Fellowship FP7-PEOPLE-2012-IEF (project number 328264) and thanks H. Kazazian and S. Solyom for providing with L1Hs specific oligonucleotide primer sequences. We thank the TCGA project team and their specimen donors for providing sequencing data. This work was supported by the Wellcome Trust, the Chordoma Foundation, and the Skeletal Cancer Action Trust. Y.S.J. and I.M. are supported by European Molecular Biology Organization long-term fellowships (LTF 1203-2012 and 1287-2012). P.J.C. and S.M.J. are Wellcome Trust Senior Clinical Fellows. P.V.L. is a postdoctoral researcher of the Research Foundation Flanders (FWO). S.N.-Z. is funded by a Wellcome Trust Intermediate Clinical Research Fellowship (WT100183MA). U.M. is supported by a CRUK Clinician Scientist fellowship. Support was provided to A.M.F. by the National Institute for Health Research, the University College London Hospitals Biomedical Research Centre, and the Cancer Research UK University College London Experimental Cancer Centre. C.D. is supported by a grant from the Brussels Region–Impulse Programme Life Sciences. Samples from Addenbrooke's Hospital were collected with support from the NIHR Cambridge Biomedical Resource Centre. The ICGC Breast Cancer Consortium was supported by a grant from the European Union (BASIS) and the Wellcome Trust. The ICGC Prostate UK Cancer Consortium is funded by CRUK grant C5047/A14835, by the Dallaglio Foundation, and the Wellcome Trust. We also acknowledge support from the Bob Champion Trust, the Orchid Cancer appeal, the RoseTrees Trust, the North West Cancer Research Fund, Big C, the Grand Charity of Freemasons, and the Research Foundation Flanders (FWO). We acknowledge the Biomedical Research Centre at the Institute of Cancer Research and the Royal Marsden NHS Foundation Trust. We thank the NIHR, Hutchison Whampoa Limited, Human Research Tissue Bank (Addenbrookes Hospital), CRUK Cambridge Research Institute Histopathology, In-situ Hybridisation Core Facility, Genomics Core Facility Cambridge, and Cambridge University Hospitals Media Studio. P.J.C. holds equity in, and is a paid consultant for, 14M Genomics Limited.

SUPPLEMENTARY MATERIALS

www.sciencemag.org/content/345/6196/1251343/suppl/DC1
Materials and Methods
Supplementary Text
Figs. S1 to S14
Tables S1 to S8
References (*37*–*46*)

27 January 2014; accepted 26 June 2014
10.1126/science.1251343

RESEARCH ARTICLES

QUANTUM INFORMATION

Unconditional quantum teleportation between distant solid-state quantum bits

W. Pfaff,[1*] B. J. Hensen,[1] H. Bernien,[1] S. B. van Dam,[1] M. S. Blok,[1] T. H. Taminiau,[1] M. J. Tiggelman,[1] R. N. Schouten,[1] M. Markham,[2] D. J. Twitchen,[2] R. Hanson[1†]

Realizing robust quantum information transfer between long-lived qubit registers is a key challenge for quantum information science and technology. Here we demonstrate unconditional teleportation of arbitrary quantum states between diamond spin qubits separated by 3 meters. We prepare the teleporter through photon-mediated heralded entanglement between two distant electron spins and subsequently encode the source qubit in a single nuclear spin. By realizing a fully deterministic Bell-state measurement combined with real-time feed-forward, quantum teleportation is achieved upon each attempt with an average state fidelity exceeding the classical limit. These results establish diamond spin qubits as a prime candidate for the realization of quantum networks for quantum communication and network-based quantum computing.

The reliable transmission of quantum states between remote locations is a major open challenge in quantum science. Quantum state transfer between nodes containing long-lived qubits (*1*–*3*) can extend quantum key distribution to long distances (*4*), enable blind quantum computing in the cloud (*5*), and serve as a critical primitive for a future quantum network (*6*). When provided with a single copy of an unknown quantum state, directly sending the state in a carrier such as a photon is unreliable due to inevitable losses. Creating and sending several copies of the state to counteract such transmission losses is impossible by the no-cloning theorem (*7*). Nevertheless, quantum information can be faithfully transmitted over arbitrary distances through quantum teleportation provided the network parties (named "Alice" and "Bob") have previously established a shared entangled state and can communicate classically (*8*–*11*).

[1]Kavli Institute of Nanoscience Delft, Delft University of Technology, Post Office Box 5046, 2600 GA Delft, Netherlands. [2]Element Six, Ltd., Kings Ride Park, Ascot, Berkshire SL5 8BP, UK.
*Present address: Department of Applied Physics, Yale University, New Haven, CT 06511, USA. †Corresponding author. E-mail: r.hanson@tudelft.nl

Unconditional quantum teleportation

In the teleportation protocol (Fig. 1A), Alice is initially in possession of the state to be teleported (qubit 1), which is most generally given by $|\psi\rangle = \alpha|0\rangle + \beta|1\rangle$. Alice and Bob each have one qubit of an entangled pair (qubits 2 and 3) in the joint state $|\Psi^-\rangle_{23} = (|01\rangle_{23} - |10\rangle_{23})/\sqrt{2}$. The combined state of all three qubits can be rewritten as

$$|\psi_1\rangle|\Psi^-\rangle_{23} = \frac{1}{2}[|\Phi^+\rangle_{12}(\alpha|1\rangle_3 - \beta|0\rangle_3) + |\Phi^-\rangle_{12}(\alpha|1\rangle_3 + \beta|0\rangle_3) + |\Psi^+\rangle_{12}(-\alpha|0\rangle_3 + \beta|1\rangle_3) - |\Psi^-\rangle_{12}(\alpha|0\rangle_3 + \beta|1\rangle_3)]$$

where $|\Phi^\pm\rangle = (|00\rangle \pm |11\rangle)/\sqrt{2}$, $|\Psi^\pm\rangle = (|01\rangle \pm |10\rangle)/\sqrt{2}$ are the four Bell states. To teleport the quantum state, Alice performs a joint measurement on her qubits (qubits 1 and 2) in the Bell basis, projecting Bob's qubit into a state that is equal to $|\psi\rangle$ up to a unitary operation that depends on the outcome of Alice's measurement. Alice sends the outcome via a classical communication channel to Bob, who can then recover the original state by applying the corresponding local transformation.

Because the source qubit state always disappears on Alice's side, it is irrevocably lost whenever the protocol fails. Therefore, to ensure that each qubit state inserted into the teleporter unconditionally reappears on Bob's side, Alice must be able to distinguish between all four Bell states in a single shot, and Bob has to preserve the coherence of the target qubit during the communication of the outcome and the final conditional transformation. Several pioneering experiments have explored teleportation between remote nodes (*12*–*14*), but unconditional teleportation between long-lived qubits (*1*–*3*) has so far only been demonstrated within a local qubit register (*15*–*17*).

We demonstrate unconditional teleportation between diamond spin qubits residing in independent setups separated by 3 m. This result is

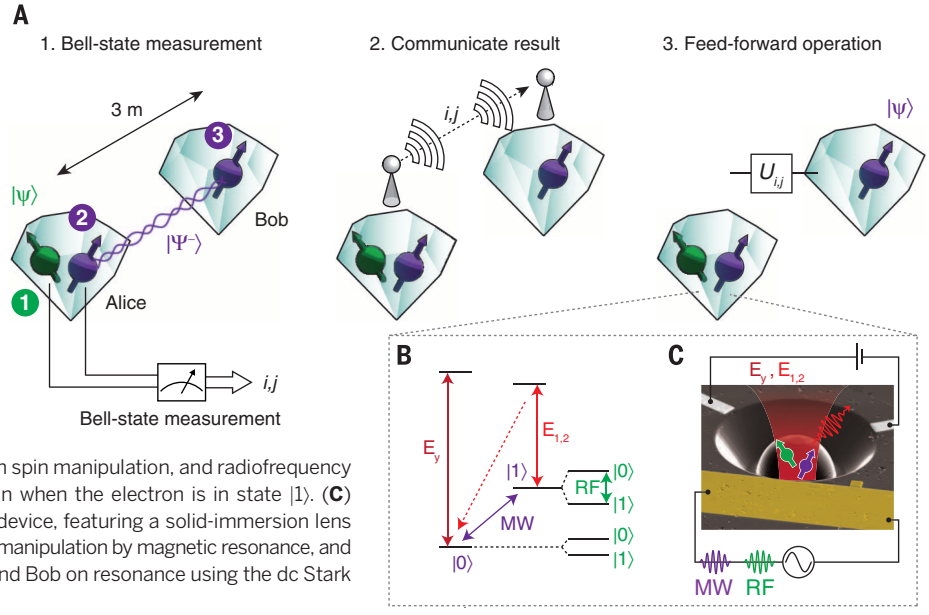

Fig. 1. Teleportation scheme and system description. (**A**) General scheme for teleportation. In our experiment, Alice and Bob each control a single NV center in a single-crystal chemical vapor deposition–grown diamond by operating an independent cryogenic confocal microscope setup (T = 8 K for Alice and T = 4 K for Bob). (**B**) Energy-level scheme and qubit control methods. The source state is encoded in Alice's nitrogen-14 spin (green) with basis states $|0\rangle \equiv m_I = 0$, $|1\rangle \equiv m_I = -1$. Two distant NV electronic spins (purple), with basis states encoded as $|0\rangle \equiv m_s = 0, |1\rangle \equiv m_s = -1$, form the remote entangled pair shared by Alice and Bob. The electron spin is initialized by optical spin pumping on the NV center's $E_{1,2}$ transitions (bright red arrows), and read out by spin-selective optical excitation via the E_y transition (dark red arrow) (*18*). Microwave (MW) pulses allow for electron spin manipulation, and radiofrequency (RF) pulses are used to manipulate the nuclear spin when the electron is in state $|1\rangle$. (**C**) Scanning electron microscope image of a diamond device, featuring a solid-immersion lens for enhanced collection efficiency, a stripline for spin manipulation by magnetic resonance, and electrodes for bringing the optical transitions of Alice and Bob on resonance using the dc Stark effect. See supplementary methods for details (*23*).

achieved by fully separating the generation of remote entanglement (the preparation of the teleporter) from the two-qubit Bell state measurement and feed-forward (the actual teleportation action). In particular, a photonic channel is used to generate heralded remote entanglement between two nitrogen-vacancy (NV) center electronic spins, whereas the teleportation protocol solely exploits matter qubits that—unlike photonic qubits—allow for a deterministic Bell state measurement with current technology. The source state is encoded in a nuclear spin close to one of the NV electron spins after preparation of the teleporter. We preserve the target qubit's coherence by dynamical decoupling while the measurement outcome is forwarded and the final correction pulse is applied. This protocol ensures that the source state is successfully teleported in each of the experimental runs.

Experimental implementation: Preparing the teleporter

Alice and Bob each operate an independent low-temperature confocal microscope setup that addresses a single NV center. The two NV electronic spins (labeled as qubits 2 and 3) are used as the distributed entangled pair that is the medium for teleportation. These spins can be initialized and read out in a single shot by spin-resolved optical excitation (*18*) and coherently manipulated using microwave (MW) pulses (*19*) (Fig. 1B).

To prepare the teleporter, the electrons are initialized in the nonlocal entangled state $|\Psi^-\rangle_{23} = (|01\rangle_{23} - |10\rangle_{23})/\sqrt{2}$ through a recently demonstrated protocol (*20*, *21*) that is based on local entanglement between electron spin and photon number and subsequent joint measurement of the photons (Fig. 2A). Because successful entanglement generation is heralded by photon detection events, the protocol is robust against photon loss. Compared to the initial demonstration of this entangling protocol (*21*), we have further enhanced the efficiency of photon collection from our device through an antireflection coating. Also, we have improved both the spectral stability of the NV center's optical transition and the charge state initialization by resonant repumping on the neutral-charge state zero-phonon line (*22*, *23*). As a result, the generation rate of the entangled state $|\Psi^-\rangle_{23}$ is increased fivefold to 1/250 s^{-1} and the entangled state fidelity is improved from 0.73 to an estimated 0.87.

The additional qubit in Alice's node—essential for making the teleportation unconditional—is provided by the nitrogen-14 nuclear spin of Alice's NV (qubit 1). Before establishing the entanglement link, this nuclear spin is initialized into state $|1\rangle$ by a projective measurement via the electron spin (*18*, *24*). We reinitialize the nuclear spin after each 250 entanglement attempts in order to preserve its purity (*23*) (Fig. 2, C and D). The source state is prepared after establishing remote entanglement, thus avoiding possible dephasing of the source state by repeated optical excitation of the nearby electron (*25*, *26*) during entanglement generation. We use a decoherence-protected gate (*27*) on Alice's side to set the nuclear spin to the source state $|\psi\rangle = \alpha|0\rangle + \beta|1\rangle$. This gate combines two nuclear spin rotations with a refocusing pulse on the electron spin such that the entangled state is efficiently preserved for the duration of the gate (Fig. 3, A and B). This operation concludes the preparation of the teleporter and the insertion of the source qubit, with the three-qubit system left in the state $|\psi\rangle_1|\Psi^-\rangle_{23} = (\alpha|0\rangle_1 + \beta|1\rangle_1)(|01\rangle_{23} - |10\rangle_{23})/\sqrt{2}$ (*23*).

Experimental implementation: Teleportation

At the heart of unconditional qubit teleportation is a deterministic Bell-state measurement (BSM) by Alice on qubits 1 and 2 that generally involves two steps. First, the four Bell states are mapped onto the four different qubit eigenstates $|i\rangle_1|j\rangle_2$ by quantum gate operations. In the second step, each of the two qubits is read out in a single shot, and the two measurement outcomes are sent to Bob. In our scheme (Fig. 3, A and B), we implement the Bell-state mapping by applying a two-qubit controlled-NOT gate (CNOT) followed by a $\pi/2$ rotation on the nuclear spin using another decoherence-protected gate (*23*). Then we read out the electron spin in a single shot (average fidelity 0.963 ± 0.005). Finally, we read out the nuclear

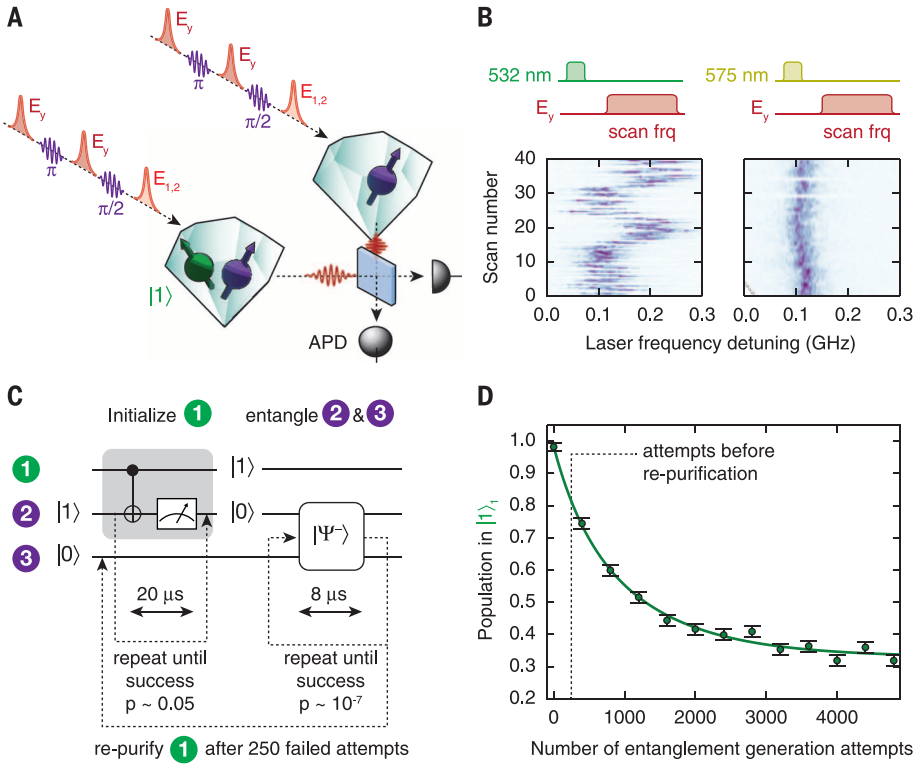

Fig. 2. Preparation of the teleporter. (**A**) Schematic showing generation of remote entanglement. After initializing qubit 1 in $|1\rangle$, the following sequence is applied. First, both qubits 2 and 3 are initialized in $|0\rangle$ by optical pumping. Then a combination of spin rotations and spin-selective optical excitation on E_y creates local entanglement between spin and photon number at each node, followed by two-photon quantum interference and photon detection (for projecting qubits 2 and 3 onto an entangled state) using avalanche photo detectors (APDs) (*20*, *21*, *23*). This sequence is repeated until successful. In the experiment, the photons are guided through fibers to the beamsplitter and the APDs. (**B**) Measurement of the frequency stability of the optical transition labeled E_y. We repeatedly apply a charge repump pulse and then scan a red laser (5 nW) over the E_y resonance. Spectral diffusion is strongly slowed down for the charge repump laser (50 nW) on resonance with the NV^0 zero-phonon line at 575 nm (right) compared to conventional off-resonant charge repumping using laser light (150 μW) at 532 nm (left) (*22*). For the scans using a 575-nm repump laser, we apply a strong laser pulse on resonance with NV^- (50 nW) before each scan to enforce ionization to NV^0. The red laser frequency shown is relative to 470.4636 THz. Color encodes the photon count rate during the scan; darker color indicates higher intensity. (**C**) Circuit diagram for the periodic measurement-based reinitialization of the nuclear spin (qubit 1) in between remote entanglement-generation attempts. Both the probability for success per attempt and the time duration of a single attempt are indicated for the initialization by measurement of qubit 1 and the generation of entanglement between qubits 2 and 3. (**D**) Measured probability $P(|1\rangle)$ to preserve the initialized nuclear spin state $|1\rangle$ as a function of number of entanglement generation attempts N_{ent}. A fit (solid line) to a rate-equations model yields a probability of $(0.85 \pm 0.05) \times 10^{-3}$ per entanglement-generation attempt that the nuclear spin flips (*23*). The dashed line marks the maximum number of attempts before the nuclear spin is reinitialized ($N_{ent} = 250$).

spin by mapping its state onto the electron spin, followed by electron spin readout. The two single-shot readout results give the outcome of the BSM.

We benchmark the BSM by preparing each of the four Bell states as input states in Alice's register (Fig. 3C). This procedure yields an uncorrected mean fidelity, given by the probability to obtain the measurement result corresponding to the prepared Bell state, of 0.89 ± 0.02. To gain more insight into the sources of imperfections, we compare the data with numerical simulations that use the independently determined infidelities of the nuclear spin initialization, CNOT gate, and electron single-shot readout as input. These simulations predict an average fidelity of 0.9 (Fig. 3C) (*23*), in excellent agreement with the data. Taking known errors in the preparation of the input states into account, we infer a BSM fidelity of 0.93 ± 0.02.

The final challenge for successful unconditional teleportation is to maintain the coherence of Bob's target qubit (qubit 3) during the BSM and feed-forward. In our experiment, Bob's qubit is mostly affected by interactions with the surrounding nuclear spin bath. We counteract this

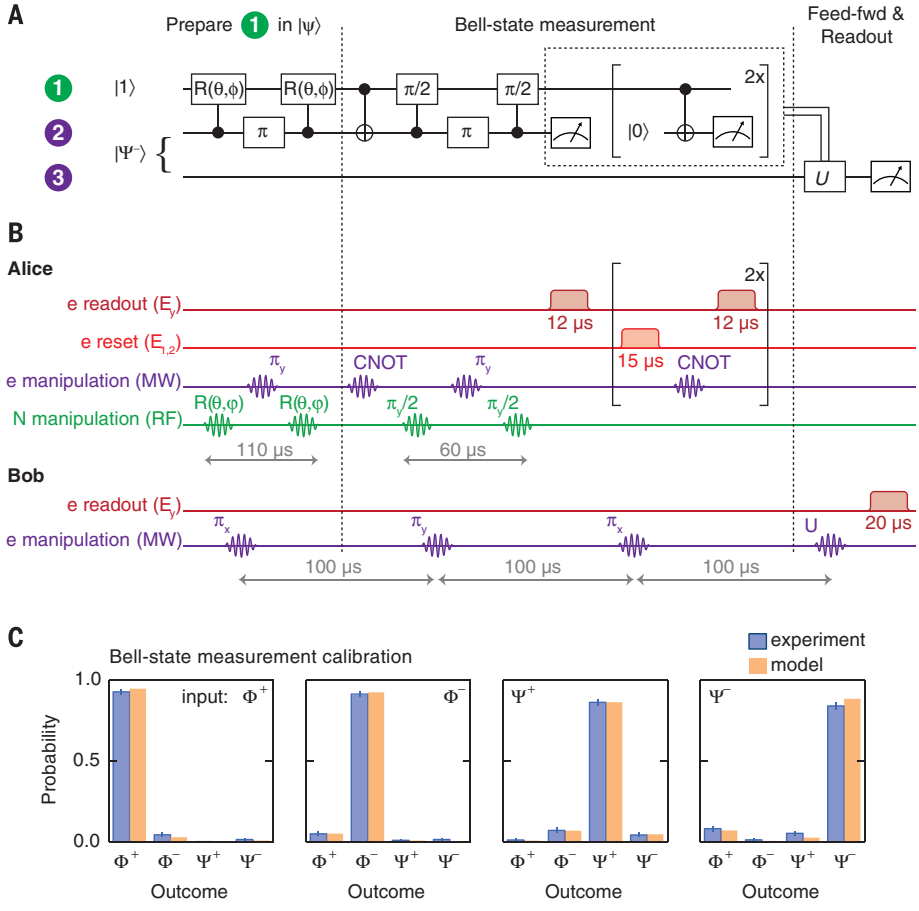

Fig. 3. Deterministic Bell-state measurement (BSM) and real-time feed-forward. (**A**) Circuit diagram and (**B**) pulse scheme of our implementation. The label "e" ("N") indicates operations acting on the electron spin (nitrogen nuclear spin). To enhance the readout fidelity for the nuclear spin, we perform the mapping to the electron spin via a CNOT and the subsequent electron readout twice. While Alice is performing her BSM, Bob applies an XY4 decoupling sequence on his electron qubit. After receiving the BSM outcome from Alice, Bob applies the feed-forward operation *U* and reads out his qubit. $\pi_{x,y}$ denote rotations around the *x* axis and *y* axis, respectively. (**C**) Characterization of the BSM by inserting the four different Bell states on Alice's side and determining the probability with which the ideal outcome is observed (blue bars). Data are not corrected for imperfect preparation of the input states. Expectations based on independently determined experimental imperfections are shown in orange. Error bars are two statistical SDs.

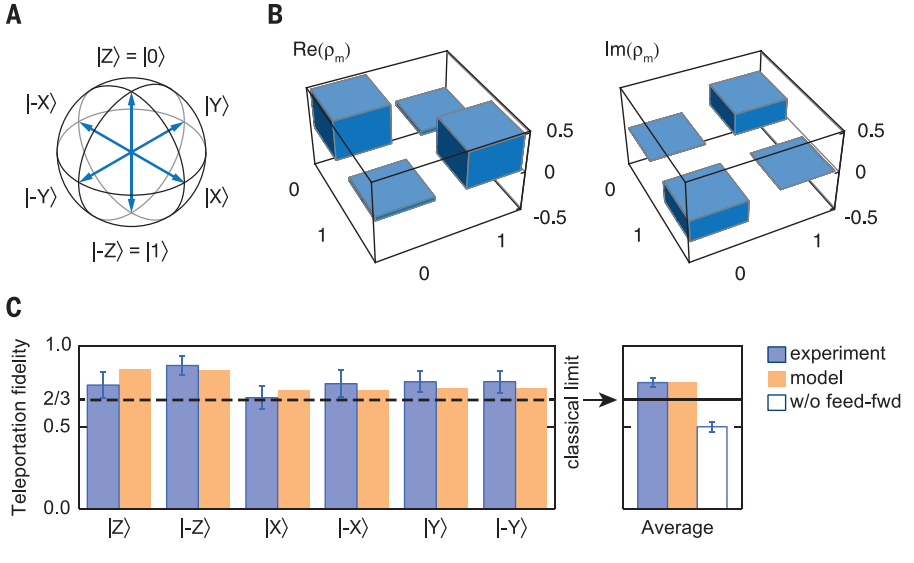

Fig. 4. Demonstration of unconditional quantum teleportation between remote qubits. (**A**) Bloch sphere with the six mutually unbiased basis states that we teleport. $|\pm X\rangle = (|0\rangle \pm |1\rangle)/\sqrt{2}$, $|\pm Y\rangle = (|0\rangle \pm i|1\rangle)/\sqrt{2}$. (**B**) State tomography after teleportation of the input state $|Y\rangle$. We determine the density matrix ρ_m by measuring the expectation values of the Pauli spin operators, $\langle\sigma_x\rangle$, $\langle\sigma_y\rangle$, $\langle\sigma_z\rangle$, where the required qubit rotations before readout are performed conditional on the BSM outcome. The measured (ideal) entries of the density matrix are $\rho_{00} = 1 - \rho_{11} = 0.52 \pm 0.08$ (0.5) and $\rho_{01} = (\rho_{10})^* = [0.05 \pm 0.08] - i[0.28 \pm 0.07]$ ($-i0.5$), respectively. (**C**) Average teleportation fidelity from the measured fidelities of the six states (blue bars). Sample sizes are (left to right) 54, 89, 73, 49, 52, and 47. Predictions from simulations are shown in orange. Without feed-forward, the target state is completely mixed (white bar). The horizontal line marks the classical limit of 2/3 (*30*). Data are not corrected for source state initialization errors. Uncertainties are 1 statistical SD.

decoherence by applying an XY4 dynamical decoupling sequence (*19*, *28*, *29*). The time between entanglement generation and the triggering of the feed-forward operation based on the BSM outcome is 300 μs. For this duration, the decoupling protocol preserves the qubit state, with an average fidelity of 0.96 ± 0.02.

Verifying quantum teleportation

We first verify that the teleporter is calibrated correctly by applying it to the nominal input state $|Y\rangle = (|0\rangle + i|1\rangle)/\sqrt{2}$ and performing tomography on the state that appears on Bob's side. The reconstructed density matrix (Fig. 4B) shows that the target state vector is aligned well with Y and therefore that the reference frames of Alice and Bob are correctly set.

To prove that our quantum teleporter outperforms any classical communication strategy, we teleport an unbiased set of six basis states $|\psi\rangle$ (Fig. 4A) and determine the fidelity of the teleported state on Bob's side with respect to the ideal input state. In these experiments, we use a feed-forward operation that maps the ideal state of qubit 3 onto a qubit eigenstate such that the readout directly yields the teleportation fidelity (*23*). Because the feed-forward operation is conditional on the BSM outcome, ignoring the BSM outcome yields a completely mixed state and random outcomes, ensuring that no information is transmitted. Without feed-forward, we indeed observe a mean teleportation fidelity, averaged over all six input states, of $\langle F\rangle = 0.50 \pm 0.03$ (Fig. 4C). In contrast, including the feed-forward loop, we find that $\langle F\rangle = 0.77 \pm 0.03$. This value exceeds the classical limit of 2/3 by more than 3 standard deviations, thus proving the quantum nature of our teleporter (*30*). We note that this fidelity presents a lower bound on the actual teleportation fidelity because it does not take into account initialization errors of the source state. Notably, this result is obtained without any postselection: Each teleportation attempt is included in the data presented here.

We also simulate the outcomes by using independently determined infidelities in the protocol. The only unknown parameter is the fidelity of the entangled state shared by Alice and Bob. We find that our data are well reproduced by the simulations if we assume a fidelity to the ideal Bell state $|\Psi^-\rangle_{23}$ of 0.87 (Fig. 4C). The simulations also enable us to quantify the effect of imperfect initialization of the source qubit on the measured fidelities. In this way, we estimate the teleportation fidelity to be ~0.86 (*23*).

Conclusions and outlook

The ability to generate remote entanglement and to control and read out multiple qubits per node, as shown in the present teleportation experiment, makes NV centers a leading candidate for realizing a quantum network (*6*, *31*). Our teleportation scheme is both unconditional and scalable to large distances, as it can mitigate photon loss by heralding and purification of the distributed entangled state (*4*). Our current capabilities could be supplemented with quantum memories that are robust against optical excitation of the electrons, enabling remote entanglement purification (*4*, *32*) and the connection of multiple nodes into the network. A promising route is the use of weakly coupled nuclear spins (*33*–*35*) on which multi-qubit quantum control has very recently been demonstrated (*36*). For such nuclear spins, coherence times of >1 s under optical excitation have been reported (*37*), while the incorporation of NV centers into optical cavities may enable remote entanglement generation on millisecond time scales (*38*). Furthermore, the entanglement and readout fidelities reported here are sufficient for a violation of a Bell inequality with the detection loophole closed, making NV centers a promising system for realizing a loophole-free Bell test and device-independent quantum key distribution (*39*).

REFERENCES AND NOTES

1. D. D. Awschalom, L. C. Bassett, A. S. Dzurak, E. L. Hu, J. R. Petta, *Science* **339**, 1174–1179 (2013).
2. M. H. Devoret, R. J. Schoelkopf, *Science* **339**, 1169–1174 (2013).
3. C. Monroe, J. Kim, *Science* **339**, 1164–1169 (2013).
4. H. J. Briegel, W. Dür, J. I. Cirac, P. Zoller, *Phys. Rev. Lett.* **81**, 5932–5935 (1998).
5. S. Barz *et al.*, *Science* **335**, 303–308 (2012).
6. H. J. Kimble, *Nature* **453**, 1023–1030 (2008).
7. W. K. Wootters, W. H. Zurek, *Nature* **299**, 802–803 (1982).
8. C. H. Bennett *et al.*, *Phys. Rev. Lett.* **70**, 1895–1899 (1993).
9. D. Bouwmeester *et al.*, *Nature* **390**, 575–579 (1997).
10. A. Furusawa *et al.*, *Science* **282**, 706–709 (1998).
11. S. Takeda, T. Mizuta, M. Fuwa, P. van Loock, A. Furusawa, *Nature* **500**, 315–318 (2013).
12. S. Olmschenk *et al.*, *Science* **323**, 486–489 (2009).
13. C. Nölleke *et al.*, *Phys. Rev. Lett.* **110**, 140403 (2013).
14. H. Krauter *et al.*, *Nat. Phys.* **9**, 400–404 (2013).
15. M. Riebe *et al.*, *Nature* **429**, 734–737 (2004).
16. M. D. Barrett *et al.*, *Nature* **429**, 737–739 (2004).
17. L. Steffen *et al.*, *Nature* **500**, 319–322 (2013).
18. L. Robledo *et al.*, *Nature* **477**, 574–578 (2011).
19. G. de Lange, Z. H. Wang, D. Ristè, V. V. Dobrovitski, R. Hanson, *Science* **330**, 60–63 (2010).
20. S. D. Barrett, P. Kok, *Phys. Rev. A* **71**, 060310 (2005).
21. H. Bernien *et al.*, *Nature* **497**, 86–90 (2013).
22. P. Siyushev *et al.*, *Phys. Rev. Lett.* **110**, 167402 (2013).
23. Materials and methods are available at *Science* Online.
24. P. Neumann *et al.*, *Science* **329**, 542–544 (2010).
25. L. Jiang *et al.*, *Phys. Rev. Lett.* **100**, 073001 (2008).
26. M. S. Blok *et al.*, *Nat. Phys.* **10**, 189–193 (2014).
27. T. van der Sar *et al.*, *Nature* **484**, 82–86 (2012).
28. C. A. Ryan, J. S. Hodges, D. G. Cory, *Phys. Rev. Lett.* **105**, 200402 (2010).
29. B. Naydenov *et al.*, *Phys. Rev. B* **83**, 081201 (2011).
30. S. Massar, S. Popescu, *Phys. Rev. Lett.* **74**, 1259–1263 (1995).
31. N. H. Nickerson, Y. Li, S. C. Benjamin, *Nat. Commun.* **4**, 1756 (2013).
32. L. Childress, J. M. Taylor, A. S. Sørensen, M. D. Lukin, *Phys. Rev. Lett.* **96**, 070504 (2006).
33. T. H. Taminiau *et al.*, *Phys. Rev. Lett.* **109**, 137602 (2012).
34. S. Kolkowitz, Q. P. Unterreithmeier, S. D. Bennett, M. D. Lukin, *Phys. Rev. Lett.* **109**, 137601 (2012).
35. N. Zhao *et al.*, *Nat. Nanotechnol.* **7**, 657–662 (2012).
36. T. H. Taminiau, J. Cramer, T. van der Sar, V. V. Dobrovitski, R. Hanson, *Nat. Nanotechnol.* **9**, 171–176 (2014).
37. P. C. Maurer *et al.*, *Science* **336**, 1283–1286 (2012).
38. M. Lončar, A. Faraon, *MRS Bull.* **38**, 144–148 (2013).
39. N. Brunner, D. Cavalcanti, S. Pironio, V. Scarani, S. Wehner, *Rev. Mod. Phys.* **86**, 419–478 (2014).

ACKNOWLEDGMENTS

We thank L. Childress, L. DiCarlo, M. Hatridge, J. J. L. Morton, A. Reiserer, L. M. K. Vandersypen, and P. Walther for valuable discussions. We acknowledge support from the Dutch Organization for Fundamental Research on Matter (FOM), the Defense Advanced Research Projects Agency QuASAR program, the European Union DIAMANT and S3NANO programs, a Marie Curie Intra-European Fellowship, and the European Research Council through a Starting Grant.

SUPPLEMENTARY MATERIALS

www.sciencemag.org/content/345/6196/532/suppl/DC1
Materials and Methods
Figs. S1 to S6
Table S1
References (*40*–*44*)

18 March 2014; accepted 19 May 2014
Published online 29 May 2014;
10.1126/science.1253512

CHRONIC PAIN

Decreased motivation during chronic pain requires long-term depression in the nucleus accumbens

Neil Schwartz,[1] Paul Temkin,[1] Sandra Jurado,[1,2] Byung Kook Lim,[1,3] Boris D. Heifets,[1] Jai S. Polepalli,[1] Robert C. Malenka[1]*

Several symptoms associated with chronic pain, including fatigue and depression, are characterized by reduced motivation to initiate or complete goal-directed tasks. However, it is unknown whether maladaptive modifications in neural circuits that regulate motivation occur during chronic pain. Here, we demonstrate that the decreased motivation elicited in mice by two different models of chronic pain requires a galanin receptor 1–triggered depression of excitatory synaptic transmission in indirect pathway nucleus accumbens medium spiny neurons. These results demonstrate a previously unknown pathological adaption in a key node of motivational neural circuitry that is required for one of the major sequela of chronic pain states and syndromes.

Symptoms that profoundly affect the quality of life of patients with chronic pain include fatigue, reductions in pre-pain activities, and depression (*1*–*4*). A common feature of these symptoms is a decrease in the motivation to undertake and to successfully complete goal-directed actions. Although in the setting of acute pain these features may be adaptive by limiting activity during the healing process and reducing the likelihood of future injury by motivating

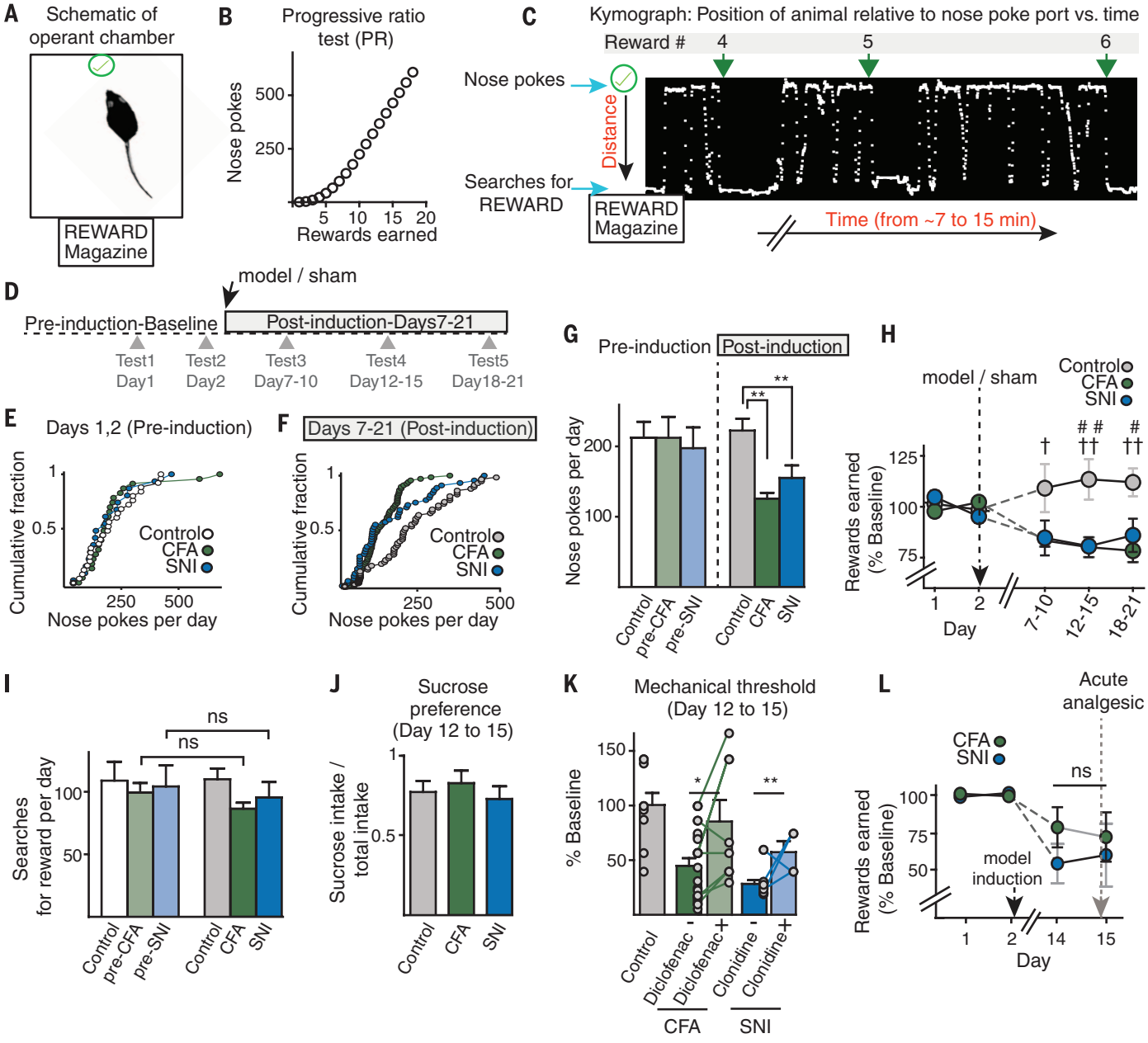

Fig. 1. Motivation is impaired in models of chronic pain. (**A**) Schematic of mouse in the operant chamber. (**B**) Sum of nose pokes required to earn rewards on PR schedule. (**C**) Kymograph illustrating distance from nose poke port (*y* axis) versus time (*x* axis). Green arrows indicate times at which rewards 4 to 6 were earned. (**D**) Time line of experiments. Results from 2 PR tests before induction of pain models were compared with results from 6 PR tests at three time points after induction. (**E**) Nose pokes per animal during 2 days of baseline testing. (**F** to **H**) Both CFA and SNI induction reduced number of nose pokes, resulting in a drop in the rewards earned at the respective time points (control, $n = 12$ mice, includes SNI sham surgery $n = 4$, CFA sham injections $n = 5$, untreated $n = 3$; CFA $n = 10$ mice; SNI $n = 8$ mice). (G) $^{**}P < 0.01$ versus control. (H) CFA $^{\dagger}P < 0.05$, $^{\dagger\dagger}P < 0.01$; SNI $^{\#}P < 0.05$, $^{\#\#}P < 0.01$; post hoc *t* tests. (**I** and **J**) During PR tests, there was no difference in searches for rewards before or after induction nor differences in the sucrose preference test (control $n = 6$ mice, CFA $n = 6$ mice, SNI $n = 5$ mice). (**K**) Both pain models reduce mechanical threshold, and this is ameliorated by analgesic administration (diclofenac, subcutaneous, $n = 8$ mice, $^{*}P < 0.05$; clonidine, intrathecal, $n = 5$ mice, $^{**}P < 0.01$; Student's *t* tests). (**L**) Neither acute analgesic affects the reduction in rewards earned after model induction. For all figures, error bars are SEM.

[1]Nancy Pritzker Laboratory, Department of Psychiatry and Behavioral Sciences, Stanford University School of Medicine, 265 Campus Drive, Stanford, CA 94305, USA. [2]Department of Pharmacology, School of Medicine, University of Maryland, 655 West Baltimore Street, Baltimore, MD 21201, USA. [3]Neurobiology Section, Division of Biological Sciences, University of California, San Diego, La Jolla, CA 92093, USA.
*Corresponding author. E-mail: malenka@stanford.edu

hypothesize that like the maladaptive neural plasticity that contributes to somatosensory symptoms of chronic pain (*7*, *8*), concurrent maladaptive plasticity occurs in neural circuits that regulate motivation. Therefore, we focused on the nucleus accumbens core (NAc) because it is a key node of the neural circuits mediating motivated behaviors (*9*–*11*), and activity within the human NAc correlates with both the subjective experience of pain as well as the transition to chronic pain (*12*, *13*).

Chronic pain reduces motivation in two mouse models

We used two mouse models of chronic pain (*14*, *15*); chronic inflammatory pain induced by

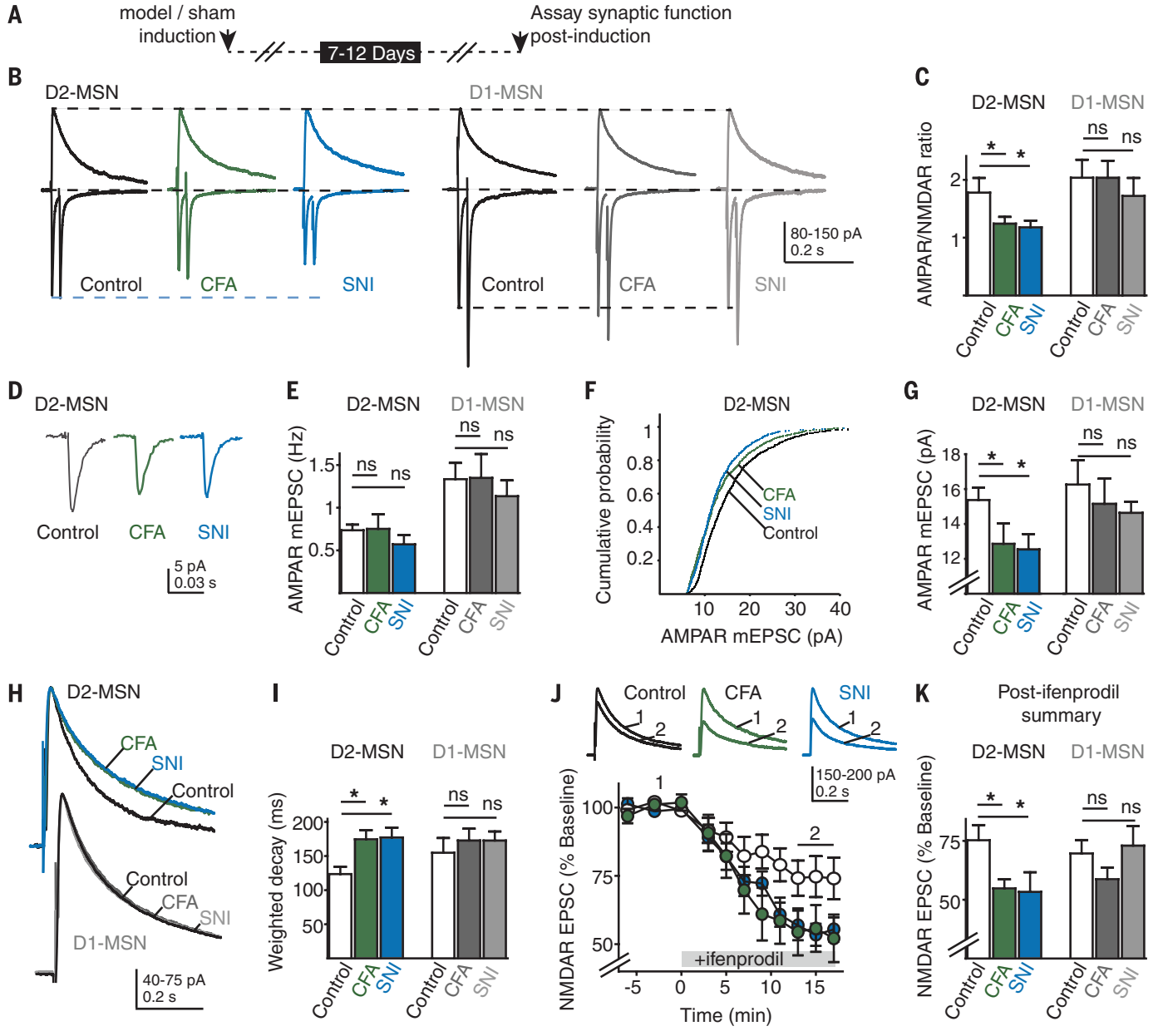

Fig. 2. Excitatory synapses are modified 7 to 12 days after induction of chronic pain. (**A**) Time course of experiments in (B) to (K). (**B**) Sample EPSCs recorded at +40 mV (top traces) and two EPSCs evoked with a 50-ms interval recorded at –70 mV (bottom traces) from NAc D2-MSNs and D1-MSNs at 7 to 12 days after sham procedures or after model induction. EPSC amplitudes are normalized to peaks at +40 mV. (**C**) Summary showing AMPAR/NMDAR ratios in D2-MSNs and D1-MSNs in both pain models (D2, control n = 15 cells, CFA n = 13 cells, SNI n = 12 cells, $^*P < 0.05$ post hoc t test; D1, control n = 12 cells, CFA n = 7 cells, SNI n = 11 cells). (**D**) Average traces of 100 mEPSCs from representative D2-MSNs. (**E**) mEPSC frequency was unaffected by CFA and SNI treatments. (**F** and **G**) Cumulative distribution of mEPSC amplitudes (F) and averages (G) in D2-MSNs and D1-MSNs in both pain models (D2, control n = 14 cells, CFA n = 10 cells, SNI n = 12 cells, $^*P < 0.05$ Student's t test; D1, control n = 13 cells, CFA n = 14 cells, SNI n = 13 cells). (**H**) Sample normalized average traces of pharmacologically isolated NMDAR EPSCs. (**I**) Summary data of NMDAR EPSC decay kinetics from D2-MSNs and D1-MSNs in both pain models (D2, control n = 12 cells, CFA n = 9 cells, SNI n = 6 cells, $^*P < 0.05$ post hoc t tests; D1, control n = 9 cells, CFA n = 7 cells, SNI n = 12 cells). (**J** and **K**) In both models, ifenprodil (3 μM) caused a larger depression of NMDAR EPSCs in D2-MSNs versus D1-MSNs (D2, control n = 8 cells, CFA n = 8 cells, SNI n = 6 cells; D1, control n = 9 cells, CFA n = 7 cells, SNI n = 5 cells; $^*P < 0.05$ post hoc t tests).

means of injection of complete Freund's adjuvant (CFA) into the hind paw and neuropathic pain induced by means of selective injury of the sciatic nerve (SNI). To measure motivation, we used a progressive ratio (PR) operant test in which it becomes progressively more difficult to earn each subsequent reward (*16*, *17*). The point at which the subject gives up provides a measure of motivation to work for reward (Fig. 1, A to C). Before inducing the models, all animals made a similar number of nose pokes and earned a comparable number of rewards (over the course of the 2-day baseline period) (Fig. 1, D and E, and fig. S1A). In contrast, 7 to 21 days after induction of chronic pain, animals exhibited a ~40% drop in the number of nose pokes to earn rewards, resulting in a stable reduction in the rewards earned over the 3-week testing period (Fig. 1, F to H). There was no change in the number of searches for reward (Fig. 1I), implying that animals exhibited no change in their ability to cross the chamber to

search for the reward and no change in their perceived value of the reward.

To further test the animals' valuation of rewards, on day 22 after pain induction, animals were tested on a fixed ratio 1 (FR1) schedule of reward, during which each nose poke earns a reward. Under this schedule, all groups earned the maximum number of rewards (30) at the same rate and searched for rewards a comparable number of times (fig. S1B). Similarly, neither model affected sucrose preference (Fig. 1J) or food consumption (fig. S1C).

Last, although the mechanical threshold of the animal did not predict its level of impairment on the PR task (fig. S2), we asked whether acutely suppressing the somatosensory symptoms of the models would ameliorate the observed reduction in motivation. In two subsets of animals after CFA and after SNI induction, the analgesics diclofenac and clonidine, respectively, were administered before testing on day 15. Despite an increase in paw withdrawal thresholds in both pain models (Fig. 1K), neither acute analgesic ameliorated performance on the PR task (Fig. 1L).

Chronic pain elicits synaptic modifications in nucleus accumbens

To determine whether chronic pain elicits synaptic changes in NAc circuitry, we prepared brain slices from bacterial artificial chromosome (BAC) transgenic animals and made targeted whole-cell recordings from visually identified medium spiny neurons (MSNs) belonging to either the direct pathway, D1 dopamine receptor expressing MSNs (D1-MSNs), or the indirect pathway, D2 dopamine receptor expressing MSNs (D2-MSNs) (*18*). We first calculated the ratio of α-amino-3-hydroxy-5-methyl-4-isoxazolepropionic acid receptor (AMPAR)–mediated excitatory postsynaptic currents (EPSCs) to *N*-methyl-D-aspartate receptor (NMDAR)–mediated EPSCs (AMPAR/NMDAR ratio). Seven to 12 days after either CFA injection or SNI surgery, this ratio was significantly lower in NAc D2-MSNs but was unchanged in NAc D1-MSNs (Fig. 2, A to C). This decrease in the two models was at least in part due to a decrease in the number and/or function of AMPARs because the amplitude of miniature EPSCs (mEPSCs) was decreased in D2-MSNs but not in D1-MSNs (Fig. 2, D, F, and G). In contrast, assays of presynaptic function were not affected in either model (Fig. 2E and fig. S3).

The fractional decrease for D2-MSN mEPSC amplitudes in both models was less than the fractional decrease in the AMPAR/NMDAR ratios, suggesting that chronic pain may have also affected NMDAR-mediated synaptic transmission. We therefore recorded pharmacologically isolated NMDAR EPSCs and found that their time constant of decay was prolonged in D2-MSNs, but not D1-MSNs, in NAc slices prepared 7 to 12 days after model induction (Fig. 2, H and I). Prolonged NMDAR EPSC decay kinetics are normally due to an increase in the proportion of synaptic NMDARs containing the GluN2B subunit (*19*). We confirmed this possibility; the GluN2B antagonist ifenprodil caused a larger depression of NMDAR EPSCs in D2-MSNs 7 to 12 days after induction as compared with that of controls (Fig. 2, J and K). This difference was not observed in D1-MSNs (Fig. 2K).

In the early stages of withdrawal from drugs of abuse, a change in the stoichiometry of synaptic NMDARs in MSNs can be observed, and this is followed at later time points by modulation of AMPAR-mediated transmission (*20*). To determine whether similar changes occur at the onset of the pain experience, we repeated the assays of synaptic function at 12 hours after injection of CFA (CFA12hrs). At this early time point, AMPAR-mediated synaptic transmission was unchanged compared with controls (Fig. 3, A to E), yet NMDAR EPSCs exhibited prolonged decay kinetics in D2-MSNs (Fig. 3, F and G).

Galanin is required for pain-induced synaptic modifications in NAc

In several brain regions, activation of G protein–coupled receptors (GPCRs) by different neuromodulators causes changes in synaptic NMDAR stoichiometry (*19*). We investigated the possible role of the neuropeptide galanin (Gal) in the pain-induced changes in NMDAR stoichiometry in NAc D2-MSNs for several reasons. In patients, polymorphisms affecting Gal signaling predict the development of comorbidities during chronic pain, increased reactivity in the NAc to rewards, and poor resilience to long-term stress (*21*–*24*). In rodents, intraventricular infusion of Gal reduces performance on a PR task (*25*), and in several pain models, Gal is up-regulated in brain regions that project to NAc (*26*–*29*). We observed Gal-positive neurons, which were retrogradely labeled by a rabies virus injected into the NAc (*30*), in several brain regions (Fig. 4A). Also consistent with previous studies (*31*, *32*), in both D1-MSNs and D2-MSNs Gal (1 μM) caused

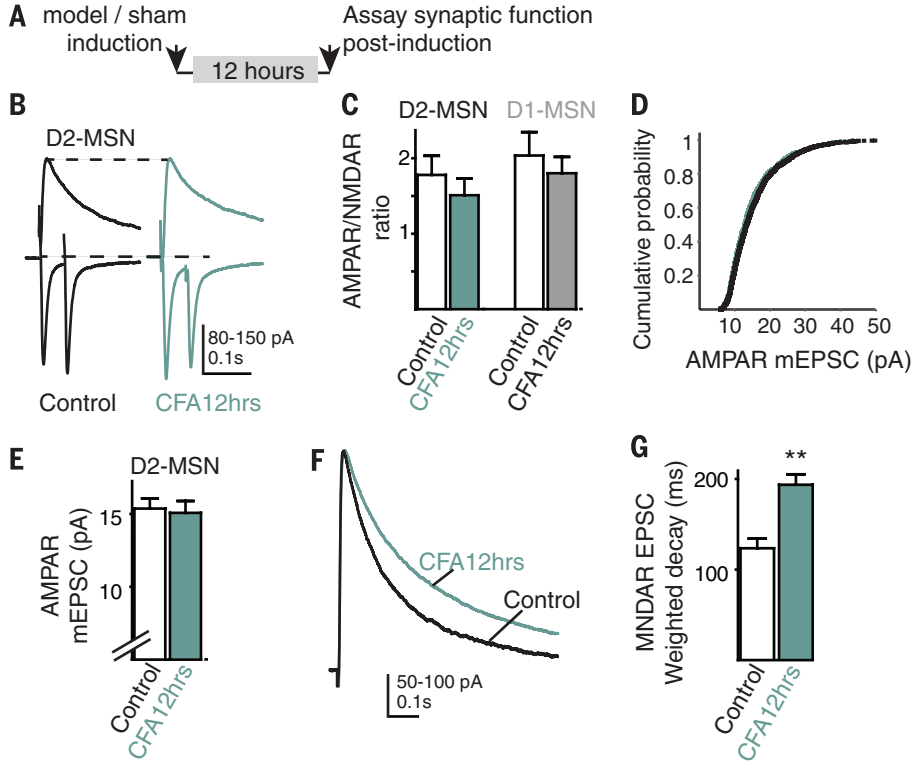

Fig. 3. NMDAR EPSCs are slower in D2-MSNs 12 hours after induction of chronic pain. (**A**) Experimental protocol. (**B**) Sample EPSCs from D2-MSNs recorded 12 hours after saline (control) or CFA injection (CFA12hrs). Traces are normalized to peak at +40 mV. (**C**) Summary of AMPAR/NMDAR ratios in D2-MSNs and D1-MSNs at this time point (D2, control, $n = 15$ cells, CFA12hrs $n = 12$ cells; D1, control $n = 12$ cells, CFA12hrs $n = 9$ cells). (**D** and **E**) Cumulative distribution and average of mEPSC amplitudes from D2-MSNs at this time point (control $n = 14$ cells, CFA12hrs $n = 10$ cells). (**F**) Sample normalized average NMDAR EPSCs from D2-MSN neurons. (**G**) Summary of NMDAR EPSC weighted decay time constants 12 hours after CFA (control $n = 12$ cells; CFA12hrs $n = 16$ cells; $^{**}P < 0.01$ Student's t test).

a transient, presynaptic decrease in excitatory transmission, which was unaffected by loading MSNs with guanosine 5′-*O*-(2′-thiodiphosphate) (GDP-β-S) to inhibit GPCR signaling in postsynaptic compartments (Fig. 4B and figs. S4 and S5) (*31*). In contrast to this transient change, the decay kinetics of NMDAR EPSCs in D2-MSNs but not D1-MSNs were prolonged after Gal application (Fig. 4C and fig. S5). This change in NMDAR EPSC decay kinetics was blocked by postsynaptic GDP-β-S (fig. S5) and was accompanied by an increase in the magnitude of the NMDAR EPSC depression caused by ifenprodil in D2-MSNs only (Fig. 4D).

To directly test whether Gal signaling within the NAc is required for the change in NMDAR EPSC kinetics in D2-MSNs, we used two complementary approaches. In one set of animals, we infused the galanin receptor 1,2 (GalR1,2) antagonist M40 (0.4 μg μL^{-1}) into the NAc preceding and during the 12-hour period after CFA treatment. In another set of animals, before CFA treatment we expressed an effective short hairpin RNA (shRNA) to GalR1 in the NAc bilaterally because GalR1, but not GalR2, has been implicated in regulating motivation (Fig. 4E) (*25*). We chose CFA injections because the symptoms develop and plateau rapidly, producing a temporally more well-defined model of chronic pain (*14*, *33*). Both manipulations prevented the increase in NMDAR EPSC decay kinetics in D2-MSNs normally caused by CFA treatments, whereas intra-NAc injection of vehicle alone did not (Fig. 4, F to H). Furthermore, knockdown of GalR1 prevented the increased sensitivity to ifenprodil caused by CFA injection (Fig. 4I).

The results thus far suggest that during the onset of chronic pain, Gal in the NAc signals through GalR1 to increase the synaptic fraction of GluN2B in D2-MSNs. Then over the ensuing 1 to 2 weeks, AMPAR-mediated synaptic transmission progressively decreases. In other brain regions, a similar change in NMDAR stoichiometry has been suggested to reduce the threshold for induction of long-term depression (LTD) of AMPAR-mediated transmission (*34*). Consistent with this hypothesis, preincubating NAc slices in Gal increased the magnitude of LTD elicited in D2-MSNs (fig. S6, A to C). NMDAR-dependent LTD in control slices was blocked by D-AP5 (fig. S6, D and E) but was unaffected by ifenprodil, whereas in Gal-treated slices, ifenprodil strongly inhibited LTD (fig. S7). Three findings suggest that similar events occur in vivo in the NAc in the pain models. First, in both models knockdown of GalR1 in vivo prevented the decrease in AMPAR/NMDAR ratios in NAc D2-MSNs (Fig. 5, A and B). Second, NMDAR-dependent LTD in D2-MSNs was reduced—presumably occluded—in slices prepared from animals 7 to 12 days after model

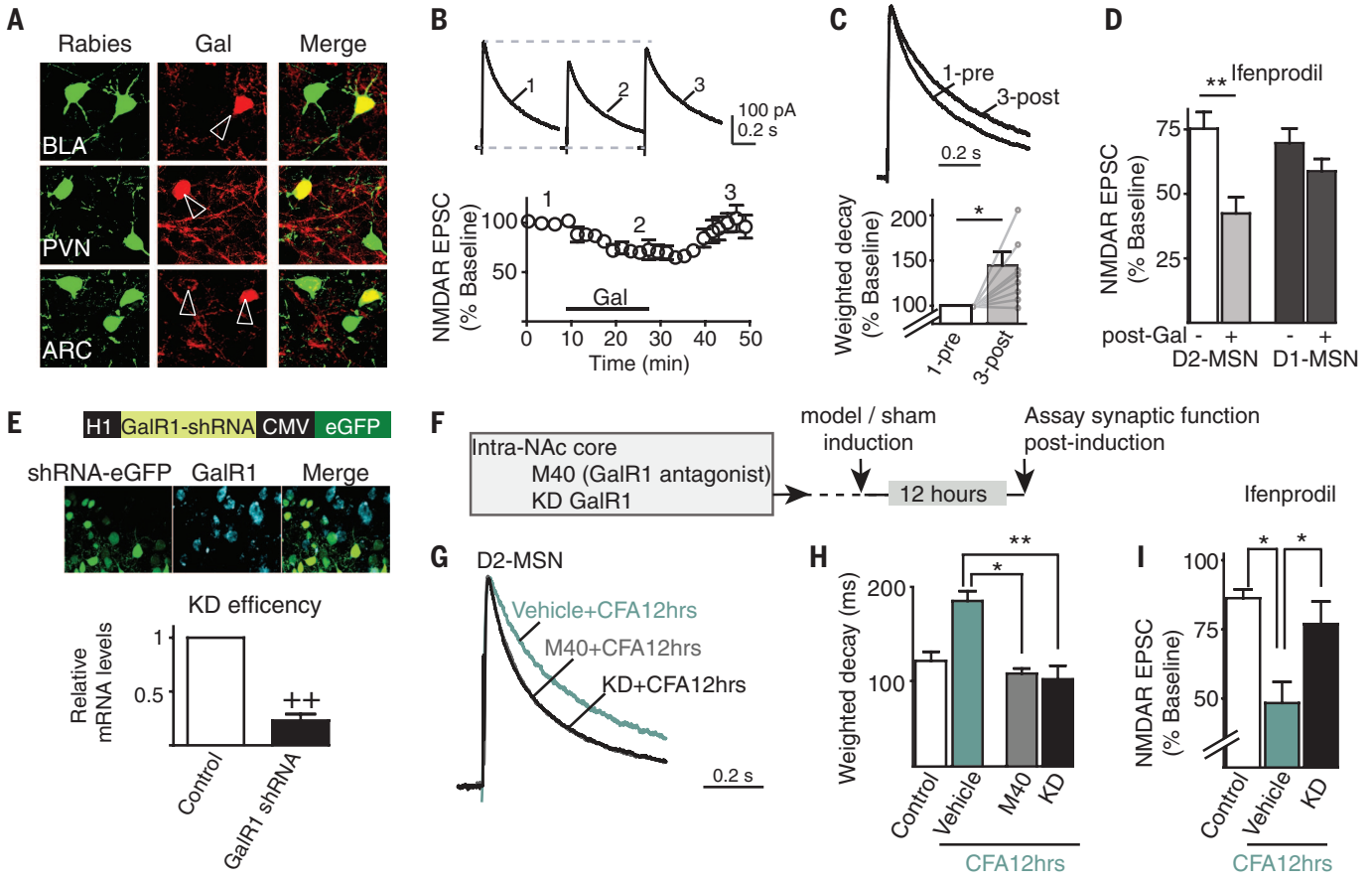

Fig. 4. Increase in NMDAR EPSC decay 12 hours after induction of chronic pain requires GalR1. (**A**) Images of neurons retrogradely labeled by rabies virus expressing eGFP (green) injected into NAc overlaid with Gal-antibody labeling (red) from basoateral amygdala (BLA), paraventricular nucleus of thalamus (PVN), and arcuate nucleus of hypothalamus (ARC). (**B**) Sample NMDAR EPSCs from D2-MSN taken at time points indicated on summary graph showing transient effects of Gal (1 μM). (**C**) Summary of change in NMDAR EPSC decay kinetics after wash-out of Gal (n = 8 cells; $^*P < 0.05$ repeated measure t test). (**D**) Ifenprodil causes larger depression of NMDAR EPSCs in D2-MSNs versus D1-MSNs from slices preincubated in Gal (D2, nontreated from Fig. 2K, post-Gal+ n = 6 cells; D1, nontreated from Fig. 2K, post-Gal+ n = 6 cells; $^{**}P < 0.01$ Student's t test). (**E**) Schematic of adeno-associated virus vector expressing GalR1 shRNA and eGPF, with images showing eGFP expression and GalR1 staining 1 month after infection of NAc. Graph shows relative mRNA levels from sister hippocampal cultures infected with eGFP and GalR1 shRNA, respectively (n = 3 experiments; $^{++}P = 0.006$ Student's t test). (**F**) Time line of experiments in (G) to (I). (**G**) Sample normalized NMDAR EPSCs from D2-MSNs. (**H**) Summary graph of NMDAR EPSC decay kinetics 12 hours after CFA. KD, knockdown. (D2, control taken from Fig. 3, vehicle+CFA12hrs n = 9 cells, M40 +CFA12hrs n = 12 cells, KD+CFA12hrs n = 8 cells; $^{**}P < 0.01$, $^*P < 0.05$ post hoc t tests). (**I**) Effects of ifenprodil on NMDAR EPSCs 12 hours after CFA (control n = 8 cells, Vehicle+CFA12hrs n = 5 cells, KD+CFA12hrs n = 5 cells; $^*P < 0.05$ post hoc t test).

induction (Fig. 5, C to E). Third, the reduction in LTD that occurs in the chronic-pain models was reversed in D2-MSNs in which knockdown of GalR1 occurred (Fig. 5, D and E).

NAc synaptic modifications required for decreased motivation during chronic pain

To determine whether GalR1-dependent synaptic changes in NAc are necessary for the decreased motivation accompanying the chronic pain models, we performed behavioral assays in animals that had been injected bilaterally into the NAc with viruses expressing enhanced green fluorescent protein (eGFP) alone, the GalR1 shRNA, or the GalR1 shRNA along with a GalR1-eGFP replacement construct (Rep.GalR1 KD) (Fig. 5, F and G). Behavior during baseline PR testing was similar between groups (Fig. 5H), and after model induction, a new set of control animals (uninjected or expressing eGFP alone) showed comparable decreases in motivation to nose poke for rewards (Fig. 5, I and J). Therefore, these groups were combined. Knockdown of GalR1 bilaterally in the NAc ameliorated the decrease in motivation normally caused by both pain models (Fig. 5, I and J), whereas expression of the Rep. GalR1 knockdown in CFA-treated animals returned their behavior to that resembling control animals: They exhibited a decrease in nose pokes after model induction (Fig. 5I). To limit the expression of the replacement GalR1 construct to indirect pathway NAc MSNs, we injected a CRE-dependent Rep.GalR1 KD construct into the NAc of Adenosine A2a CRE mice, in which CRE expression is limited to D2-MSNs (*35*). These animals exhibited a decrease in nose pokes after SNI comparable with the decrease observed in controls after SNI (fig S8). Somatosensory symptoms and other measures of operant behavior were not affected by the knockdown of GalR1 in either model (fig. S9).

To determine whether the depression of AMPAR-mediated transmission and reduction/occlusion of LTD were required for the pain-induced behavioral changes, we took advantage of the finding that NMDAR-dependent LTD depends on the appropriate synaptic positioning of the critical phosphatase calcineurin (PP2B) by the scaffolding protein A-kinase anchoring protein 79/150 (AKAP) (*36*). Thus, we knocked down AKAP in the NAc and replaced it with a mutant AKAP that does not bind PP2B (AKAPΔPP2B), a manipulation that blocks LTD in the hippocampus (*36*). This manipulation inhibited LTD in NAc MSNs, whereas replacement of AKAP with a shRNA-resistant wild-type AKAP (AKAPWT) did not (Fig. 6, A to C). Although the basal AMPAR/NMDAR ratio in D2-MSNs was not affected by AKAPΔPP2B, the decrease in this ratio elicited by the CFA model was inhibited (Fig. 6D).

Next, we repeated the behavioral experiments in animals expressing the AKAP replacement constructs in the NAc bilaterally (Fig. 6E). These manipulations did not affect the behavioral responses during baseline PR testing (Fig. 6F and fig. S10). However, whereas animals expressing control constructs (AKAPWT and eGFP) exhibited the expected decrease in nose pokes after model induction, animals expressing AKAPΔPP2B showed no deficits in performance (Fig. 6, G and H). Thus, in two different pain models, two different molecular manipulations (GalR1 knockdown and AKAPΔPP2B), which prevented chronic pain–induced modifications of excitatory synapses on NAc D2-MSNs via completely independent mechanisms, prevented pain-induced motivational impairments (Fig. 6I) while having no effect on mechanical thresholds or other measures of operant goal-directed behaviors (figs. S9 and S10).

Discussion

The NAc is a key node of the neural circuitry that regulates motivation (*10*). Manipulations that disrupt its activity appear to impair performance on

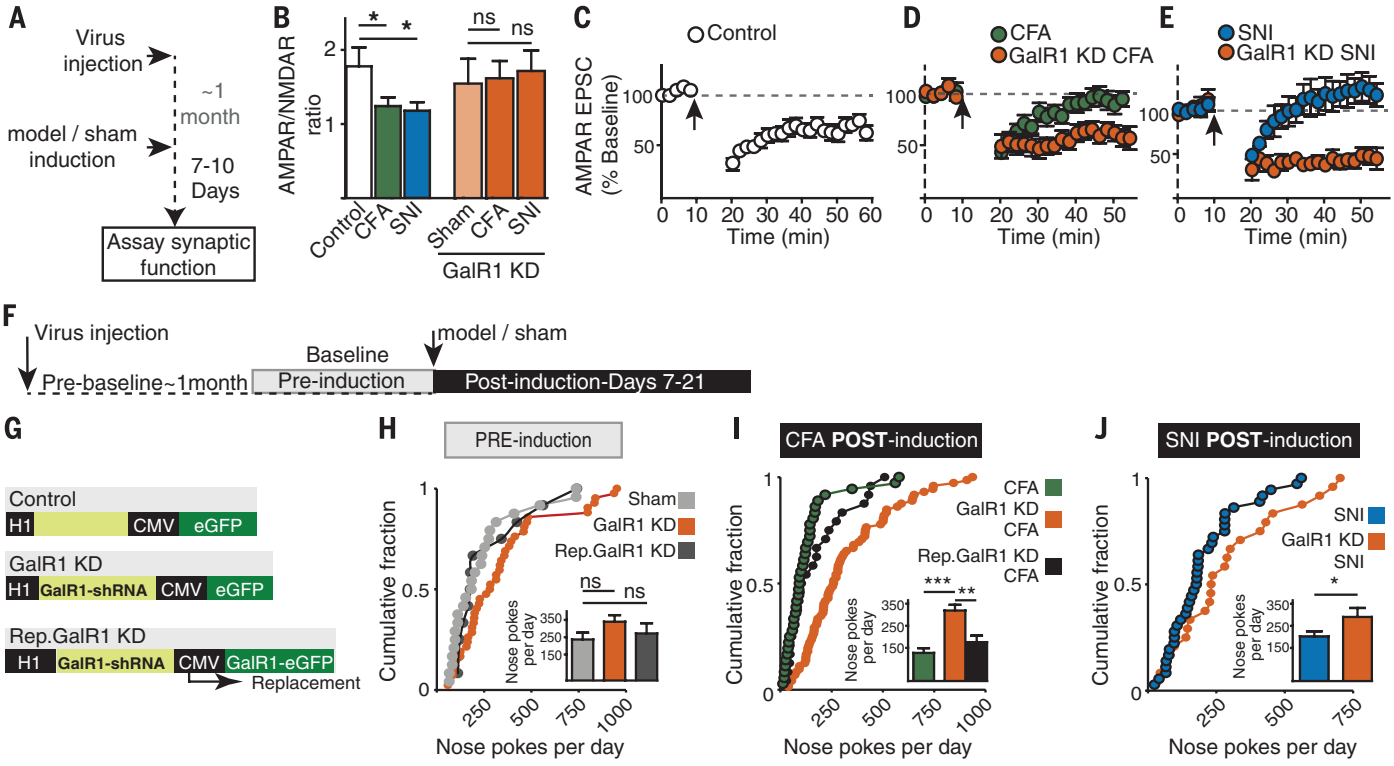

Fig. 5. GalR1 in NAc is required for pain-induced synaptic depression in D2-MSNs and reduction in motivation. (**A**) Time line of acute slice experiments in (B) to (E). (**B**) Decrease in AMPAR/NMDAR ratios in D2-MSNs in both pain models is prevented by GalR1 KD [control, CFA and SNI (left group) taken from Fig. 2; GalR1 KD, sham $n = 5$ cells, CFA $n = 11$ cells, SNI $n = 8$ cells). (**C** to **E**) Summary graphs of LTD in D2-MSNs in both pain models and effects of GalR1 KD (control, $n = 11$ cells, CFA $n = 10$ cells, GalR1 KD+CFA $n = 7$ cells, SNI $n = 6$ cells, GalR1 KD+SNI $n = 6$ cells). (**F**) Timeline of behavior experiments in (H) to (J). (**G**) Schematics of virus constructs. (**H**) Cumulative distribution of nose pokes per session and average nose pokes per day during before-induction baseline period (PRE). (sham $n = 12$ mice includes eGFP $n = 5$ mice, naive $n = 7$ mice; GalR1 KD $n = 18$ mice, Rep. GalR1 KD $n = 6$ mice). (**I** and **J**) Effects of GalR1 KD in NAc on nose pokes after model induction and rescue by coexpression of shRNA-resistant GalR1 (Rep.GalR1 KD) in CFA model. (I) CFA $n = 6$ mice includes eGFP $n = 3$ mice, naive $n = 3$ mice; GalR1 KD+CFA $n = 12$ mice, Rep. GalR1 KD+CFA $n = 6$ mice, $^{**}P < 0.01$, $^{***}P < 0.001$ Tukey's post hoc t test. (J) SNI $n = 6$ mice includes eGFP $n = 2$ mice, naïve $n = 4$ mice; GalR1 KD +SNI $n = 6$ mice, $^{*}P < 0.05$ Student's t test.

more difficult operant tasks but have little effect on the performance of easy operant tasks, perhaps because impairments of NAc function bias behavioral choices to those that require less effort (*9*, *37*–*39*). Here, we demonstrate that two different chronic pain models cause a selective impairment in performance on a difficult PR task but have no detectable effects on easier tasks or the value of rewards. This chronic pain–induced decrease in motivation requires a decreased excitatory drive onto indirect pathway NAc MSNs downstream of activation of the neuropeptide receptor GalR1 via a cascade of synaptic modifications (Fig. 6J).

Simple models proposing a dichotomous role for striatal indirect and direct pathways have been useful in generating hypotheses with which to describe the circuit adaptations underlying behaviors associated with models of addiction and depression (*30*, *40*). However, they are inadequate to account for the diverse actions of neuropeptides on NAc synaptic and circuit function (*30*, *41*–*44*) as well as the neuronal activity observed during operant behaviors (*45*, *46*). Nonetheless, the present findings—along with the observations that reductions in effortful behavior are caused by blocking D2 receptors in NAc and that these effects can be reversed by A2a receptor antagonists (*38*, *39*)—support a key role of NAc D2-MSNs in regulating performance during more difficult tasks. Because the NAc integrates inputs from multiple structures, future studies will need to address the critical question of whether the

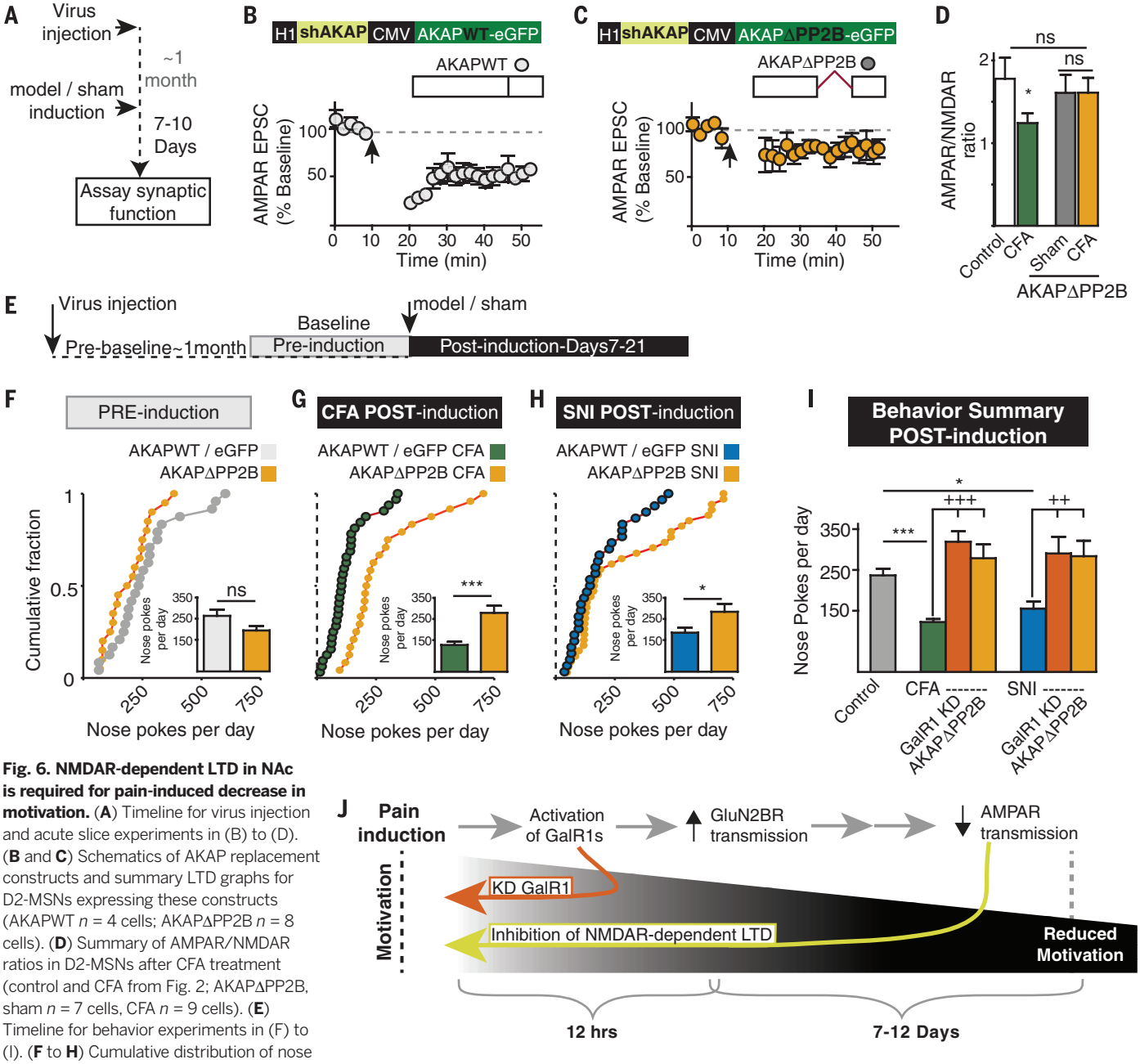

Fig. 6. NMDAR-dependent LTD in NAc is required for pain-induced decrease in motivation. (**A**) Timeline for virus injection and acute slice experiments in (B) to (D). (**B** and **C**) Schematics of AKAP replacement constructs and summary LTD graphs for D2-MSNs expressing these constructs (AKAPWT $n = 4$ cells; AKAPΔPP2B $n = 8$ cells). (**D**) Summary of AMPAR/NMDAR ratios in D2-MSNs after CFA treatment (control and CFA from Fig. 2; AKAPΔPP2B, sham $n = 7$ cells, CFA $n = 9$ cells). (**E**) Timeline for behavior experiments in (F) to (I). (**F** to **H**) Cumulative distribution of nose pokes per session and average nose pokes per day during before-induction baseline (PRE) and after model induction (POST). (F) AKAPWT/eGFP $n = 13$ mice includes eGFP $n = 5$ mice, AKAPWT $n = 8$ mice; AKAPΔPP2B $n = 10$ mice. (G) AKAPWT/eGFP CFA $n = 7$ mice includes eGFP $n = 3$ mice, AKAPWT, $n = 4$ mice; AKAPΔPP2B+CFA $n = 4$. (H) AKAPWT/eGFP SNI $n = 6$ mice includes eGFP $n = 2$ mice, AKAPWT $n = 4$ mice; AKAPΔPP2B+SNI $n = 6$ mice; $^{*}P < 0.05$, $^{***}P < 0.001$ Student's t test. (**I**) Summary of effects of GalR1 KD and AKAPΔPP2B expression on nose pokes per day after model induction (data pooled from Figs. 1, 5, and 6) ($^{*}P < 0.05$,$^{***}P < 0.001$ post hoc t test versus control; $^{++}P < 0.01$, $^{+++}P < 0.001$ Tukey's post hoc t test versus respective pain model). (**J**) Schematic summarizing temporal order of synaptic and behavioral changes after pain induction.

chronic pain–induced synaptic changes are global, affecting all excitatory inputs onto MSNs, or rather are input-specific.

Previous studies on mouse models of chronic pain report no change in home cage behaviors or measures of affective behaviors during the first month of the pathology (*14*, *15*). Within a similar time frame, by focusing on a more subtle aspect of goal-directed operant behavior—the motivation to work for natural reward—we found that motivation was impaired. Our results suggest that pain-induced synaptic adaptations within the NAc contribute to a subjective impairment in the ability to initiate or sustain physical or mental tasks (*47*, *48*), or to the symptom of central fatigue commonly reported by chronic pain patients (*1*, *2*). These results also suggest specific synaptic targets that may be susceptible to therapeutic interventions.

REFERENCE AND NOTES

1. B. Nicholson, S. Verma, *Pain Med.* **5**, S9–S27 (2004).
2. D. C. Turk, J. Audette, R. M. Levy, S. C. Mackey, S. Stanos, *Mayo Clin. Proc.* **85**, S42–S50 (2010).
3. J. Dersh, P. B. Polatin, R. J. Gatchel, *Psychosom. Med.* **64**, 773–786 (2002).
4. T. Jonsson *et al.*, *Acta Anaesthesiol. Scand.* **55**, 69–74 (2011).
5. J. P. Johansen, H. L. Fields, B. H. Manning, *Proc. Natl. Acad. Sci. U.S.A.* **98**, 8077–8082 (2001).
6. D. Borsook *et al.*, *Eur. J. Pain* **11**, 7–20 (2007).
7. C. A. von Hehn, R. Baron, C. J. Woolf, *Neuron* **73**, 638–652 (2012).
8. A. I. Basbaum, D. M. Bautista, G. Scherrer, D. Julius, *Cell* **139**, 267–284 (2009).
9. J. D. Salamone, M. Correa, *Neuron* **76**, 470–485 (2012).
10. G. J. Mogenson, D. L. Jones, C. Y. Yim, *Prog. Neurobiol.* **14**, 69–97 (1980).
11. B. W. Balleine, J. P. O'Doherty, *Neuropsychopharmacology* **35**, 48–69 (2010).
12. D. J. Scott, M. M. Heitzeg, R. A. Koeppe, C. S. Stohler, J.-K. Zubieta, *J. Neurosci.* **26**, 10789–10795 (2006).
13. M. N. Baliki *et al.*, *Nat. Neurosci.* **15**, 1117–1119 (2012).
14. R. Urban, G. Scherrer, E. H. Goulding, L. H. Tecott, A. I. Basbaum, *Pain* **152**, 990–1000 (2011).
15. I. Yalcin *et al.*, *Biol. Psychiatry* **70**, 946–953 (2011).
16. H. S. Roane, *J. Appl. Behav. Anal.* **41**, 155–161 (2008).
17. C. P. O'Brien, E. L. Gardner, *Pharmacol. Ther.* **108**, 18–58 (2005).
18. J. A. Shuen, M. Chen, B. Gloss, N. Calakos, *J. Neurosci.* **28**, 2681–2685 (2008).
19. A. Sanz-Clemente, R. A. Nicoll, K. W. Roche, *Neuroscientist* **19**, 62–75 (2013).
20. B. R. Lee, Y. Dong, *Neuropharmacology* **61**, 1060–1069 (2011).
21. M. B. Max *et al.*, *Mol. Pain* **2**, 14 (2006).
22. P. G. Unschuld *et al.*, *J. Affect. Disord.* **105**, 177–184 (2008).
23. N. R. Wray *et al.*, *Mol. Psychiatry* **17**, 36–48 (2012).
24. Y. S. Nikolova, E. K. Singhi, E. M. Drabant, A. R. Hariri, *Genes Brain Behav.* **12**, 516–524 (2013).
25. M. E. Anderson, J. Runesson, I. Saar, U. Langel, J. K. Robinson, *Behav. Brain Res.* **239**, 90–93 (2013).
26. V. Sergeyev, C. Broberger, T. Hökfelt, *Brain Res. Mol. Brain Res.* **90**, 93–100 (2001).
27. H. Imbe *et al.*, *Neurosci. Lett.* **368**, 102–106 (2004).
28. H. Nishii, M. Nomura, H. Aono, N. Fujimoto, T. Matsumoto, *Regul. Pept.* **141**, 105–112 (2007).
29. X.-L. Gu, Y.-G. Sun, L.-C. Yu, *Behav. Brain Res.* **179**, 331–335 (2007).
30. B. K. Lim, K. W. Huang, B. A. Grueter, P. E. Rothwell, R. C. Malenka, *Nature* **487**, 183–189 (2012).
31. Y. Dong, J. P. Tyszkiewicz, T. M. Fong, *J. Neurophysiol.* **95**, 3228–3234 (2006).
32. E. B. Einstein, Y. Asaka, M. F. Yeckel, M. J. Higley, M. R. Picciotto, *Eur. J. Neurosci.* **37**, 1541–1549 (2013).
33. E. J. Cobos *et al.*, *Pain* **153**, 876–884 (2012).
34. K. Yashiro, B. D. Philpot, *Neuropharmacology* **55**, 1081–1094 (2008).
35. P. F. Durieux *et al.*, *Nat. Neurosci.* **12**, 393–395 (2009).
36. S. Jurado, V. Biou, R. C. Malenka, *Nat. Neurosci.* **13**, 1053–1055 (2010).
37. S. M. Nicola, *J. Neurosci.* **30**, 16585–16600 (2010).
38. A. M. Farrar *et al.*, *Neuroscience* **166**, 1056–1067 (2010).
39. J. L. Santerre *et al.*, *Pharmacol. Biochem. Behav.* **102**, 477–487 (2012).
40. M. K. Lobo, E. J. Nestler, *Front. Neuroanat.* **5**, 41 (2011).
41. J. C. Lemos *et al.*, *Nature* **490**, 402–406 (2012).
42. B. B. Land *et al.*, *J. Neurosci.* **28**, 407–414 (2008).
43. G. Dölen, A. Darvishzadeh, K. W. Huang, R. C. Malenka, *Nature* **501**, 179–184 (2013).
44. M. Marinelli, P. V. Piazza, *Eur. J. Neurosci.* **16**, 387–394 (2002).
45. G. Cui *et al.*, *Nature* **494**, 238–242 (2013).
46. F. Kasanetz *et al.*, *Science* **328**, 1709–1712 (2010).
47. A. Chaudhuri, P. O. Behan, *Lancet* **363**, 978–988 (2004).
48. K. B. Norheim, G. Jonsson, R. Omdal, *Rheumatology (Oxford)* **50**, 1009–1018 (2011).

ACKNOWLEDGMENTS

We thank members of the Malenka lab for helpful feedback and comments during the study. We thank S. Fang and A. Darvishzadeh for help with stereotaxic injections and P. Rothwell for setting up the operant behavior chambers and software. This work was supported by a Banting postdoctoral fellowship (N.S.) and the NIH (R.C.M.). All primary data (behavioral, electrophysiological, and immunohistochemical) are archived in the Department of Psychiatry and Behavioral Sciences, Stanford University School of Medicine.

SUPPLEMENTARY MATERIALS

www.sciencemag.org/content/345/6196/535/suppl/DC1
Materials and Methods
Figs. S1 to S10
References (*49*–*54*)

27 March 2014; accepted 12 June 2014
10.1126/science.1253994

REPORTS

PHOTOVOLTAICS

Interface engineering of highly efficient perovskite solar cells

Huanping Zhou,[1,2]* Qi Chen,[1,2]* Gang Li,[1] Song Luo,[1,2] Tze-bing Song,[1,2] Hsin-Sheng Duan,[1,2] Ziruo Hong,[1] Jingbi You,[1] Yongsheng Liu,[1,2] Yang Yang[1,2]†

Advancing perovskite solar cell technologies toward their theoretical power conversion efficiency (PCE) requires delicate control over the carrier dynamics throughout the entire device. By controlling the formation of the perovskite layer and careful choices of other materials, we suppressed carrier recombination in the absorber, facilitated carrier injection into the carrier transport layers, and maintained good carrier extraction at the electrodes. When measured via reverse bias scan, cell PCE is typically boosted to 16.6% on average, with the highest efficiency of ~19.3% in a planar geometry without antireflective coating. The fabrication of our perovskite solar cells was conducted in air and from solution at low temperatures, which should simplify manufacturing of large-area perovskite devices that are inexpensive and perform at high levels.

Organic-inorganic hybrid materials, particularly the perovskite family, have shown great promise for use in field-effect transistors, light-emitting diodes, sensors, and photodetectors for more than a decade (*1*). Recently, the power conversion efficiency (PCE) of lead halide perovskite ($CH_3NH_3PbX_3$, X = Cl, Br, I)–based thin film photovoltaic devices has skyrocketed from 3.8% to more than 17% in just 4 years (*2*–*6*). In a typical perovskite solar cell, a several-hundred-nanometer-thick absorber layer, either with or without mesoporous scaffold, is sandwiched between the electron and hole transport layers (ETLs and HTLs, respectively). Upon the absorption of incident photons, carriers are created in the absorber that travel through a transport pathway including the ETL or HTL, the electrodes, and each interface in between. To increase the PCE, it is essential to precisely manipulate carriers along the entire pathway from the absorber to both electrodes.

To date, rapid progress has been made on each isolated layer, with major emphasis on perovskite film processing and relevant material design. As a result, various processing approaches have been reported that focus on the absorber properties and consequent device performance (*7*–*15*). These include one-step and sequential solution deposition (*7*–*10*), vacuum deposition (*11*), and vapor-assisted solution processing (*12*), which clearly show a strong relation between the structure, composition, and corresponding properties of the perovskite absorber. Based on a deep understanding of its hybrid nature, a delicate control over the carrier behavior in the perovskite film is expected. Despite our comparatively nascent understanding of this class of absorber

[1]Department of Materials Science and Engineering, University of California, Los Angeles, CA 90095, USA. [2]California NanoSystems Institute, University of California, Los Angeles, CA 90095, USA.
*These authors contributed equally to this work. †**Corresponding author. E-mail: yangy@ucla.edu**

materials, much success has been achieved by optimizing the device architecture and introducing new materials as carrier transport layers (*16*–*30*), especially ETL materials such as TiO_2, ZnO, and TiO_2-graphene composites (*20*–*26*). Although the improved electronic properties of these materials could offer device performance advantages, interface barriers between the absorber, transport layer, and electrode are often treated as secondary concerns compared with the generation and preservation of carrier populations in the absorber itself. In pursuit of high PCE, cells will inevitably require an optimized carrier transport pathway that leverages all of the device layers and their corresponding interfaces.

We have manipulated carrier behavior in an efficient carrier pathway across solution-processed planar heterojunction perovskite solar cells through the exploration of the perovskite film, the ETL, and their relevant interfaces. We demonstrate perovskite film deposition through an enhanced reconstruction process in controlled humidity conditions. This process leads to perovskite films with substantially decreased carrier recombination. We also improved the electron transport channel in the device by doping the TiO_2 ETL to enhance its carrier concentration and modifying the ITO electrode to reduce its work function. These changes produced a PCE of 19.3% [see (*31*) for measurement details]. These findings can be further used in perovskite-based devices across a variety of applications, such as light-emitting diodes, field-effect transistors, nonlinear optical elements, photoconductive devices, chemical sensors, and radiation detectors.

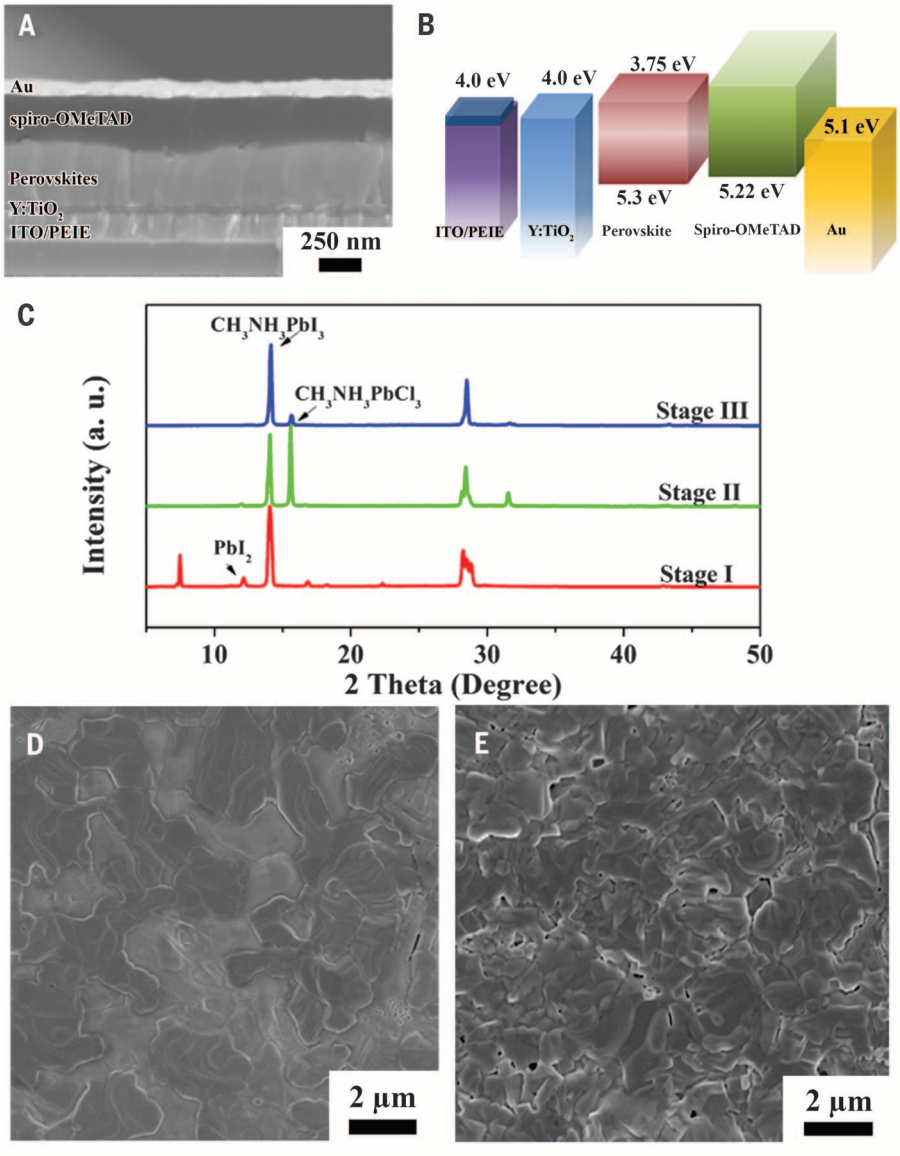

Fig. 1. Structure and energy-level alignment of the perovskite solar cell. (**A**) SEM cross-sectional image of the device. The layers from the bottom are: (i) ITO/PEIE, (ii) Y-TiO_2, (iii) perovskite, (iv spiro-OMeTAD, and (v) Au. (**B**) Diagram of energy levels (relative to the vacuum level) of each functional layer in the device. (**C**) XRD patterns corresponding to perovskite film evolution with annealing time (stage I: 20 min, stage II: 60 min, stage III: 85 min). (**D** and **E**) Top-view SEM images of perovskite films at stage II (D) and stage III (E).

We fabricated perovskite solar cells with a device architecture similar to the commonly used planar configuration, but with some modifications. The entire device fabrication procedure was carried out at low temperature (<150°C). A scanning electron microscopy (SEM) image of its structure is shown in Fig. 1A. In contrast to the majority of perovskite solar cells, which are based on FTO electrodes, ITO was used as the electrode, which was further modified with polyethyleneimine ethoxylated (PEIE) (*32*), a polymer containing simple aliphatic amine groups to reduce the work function of ITO. Yttrium-doped TiO_2 (Y-TiO_2) was used as the ETL to enhance electron extraction and transport. For hole extraction, cobalt and lithium co-doped spiro-OMeTAD [2,2′,7,7′-tetrakis-(*N*,*N*-di-4-methoxyphenylamino)-9,9′-spirobifluorene] (*8*) and gold were used as the HTL and electrode, respectively. The energy levels of relevant functional layers, as determined by ultraviolet (UV) photoelectron spectroscopy (UPS) and UV-visible absorption spectroscopy measurements, are shown in Fig. 1B. With PEIE modification, the work function of ITO was reduced to 4.0 eV from its original 4.6 eV (fig. S1) (*31*), which facilitates efficient electron transport between the ETL and ITO layers. The Y-TiO_2 layer exhibited a conduction band minimum (CBM) of 4.0 eV (fig. S2) (*31*). The valence band maximum (VBM) and CBM for the $CH_3NH_3PbI_{3-x}Cl_x$ are reported as 5.3 and 3.75 eV, respectively (*18*), and the highest occupied molecular orbital (HOMO) of spiro-OMeTAD was located at 5.22 eV (*16*). The favorable alignment between the CBM of the Y-TiO_2 and the HOMO of spiro-OMeTAD with the CBM and VBM of the perovskite allows for the efficient extraction of photogenerated carriers without inducing excessive interface recombination or inhibiting quasi-Fermi level splitting within the absorber material.

The characteristics of the perovskite can be optimized during film growth by careful control of the intercalation reaction between the organic and inorganic species. We investigated perovskite film growth under controlled humidity conditions (30 ± 5% relative humidity), and we propose an enhanced reconstruction mechanism to explain the observed effects of humidity on device properties. Solution deposition was conducted by directly depositing the mixture of CH_3NH_3I and $PbCl_2$ (3:1 molar ratio) in a *N*,*N*′-dimethylformamide (DMF) solution onto TiO_2-coated ITO substrates to fabricate the absorber layer (*31*).

During annealing under controlled humidity, the film transformed through three distinct stages, as evidenced by x-ray diffraction (XRD) measurements (Fig. 1C) and SEM (Fig. 1, D and E). In the first stage (20 min total annealing time), the film was transparent and light yellow and showed XRD peaks at 7.48°, 12.23°, 14.17°, and 28.51° (Fig. 1C). The peak at 7.48° could not be assigned to any perovskite or lead halide phase

and is presumably associated with the intermediate of the Pb halide–DMF complex (*33*). The peak centered at 12.23° was attributed to PbI_2, and the peaks at 14.17° and 28.51° were assigned to the $CH_3NH_3PbI_3$ phase. The absence of any $PbCl_2$ phase is possibly a result of ion exchange between I^- and Cl^- in the solution or the rapid intercalation reaction that forms the perovskite phase during deposition. In the second stage (60 min total annealing time), the films gradually turned black and opaque and showed two prevalent XRD peaks at 14.17° and 15.57° that we attributed to the $CH_3NH_3PbI_3$ and $CH_3NH_3PbCl_3$ phases, respectively (Fig. 1C). In addition, the intermediate phase (with a peak at 7.48°) disappeared, probably as a result of the removal of residual DMF in the film upon sufficient heating. Excess organic species were likely intercalated into the resulting inorganic framework at this stage of the reaction. At the third stage (85 min total annealing time), the films became dark brown and transparent, and the $CH_3NH_3PbCl_3$ phase observed in the second stage was consumed, leaving $CH_3NH_3PbI_3$ as the dominant phase (Fig. 1C), which is consistent with conversion from $CH_3NH_3PbCl_3$ to $CH_3NH_3PbI_3$ in the presence of excess CH_3NH_3I during film growth. As indicated by previous results (*34*, *35*), the $CH_3NH_3PbCl_3$ phase shows relatively lower thermal stability as compared with $CH_3NH_3PbI_3$. The decomposition of the $CH_3NH_3PbCl_3$ phase may release CH_3NH_3Cl that is replaced by the excess CH_3NH_3I to form $CH_3NH_3PbI_3$ and/or $CH_3NH_3PbI_{3-x}Cl_x$. The phase transformation described in XRD measurements is in excellent agreement with the SEM images taken at each corresponding stage. Two species with distinct contrast were observed in the film in stage II (Fig. 1D). In stage III (Fig. 1E), the film shows similar contrast and grain size across the entire field of view, which is visibly different from the previous stage.

Without controlled humidity, however, the film-formation process proceeds quite differently. As a reference, films fabricated under dry air conditions were also investigated, and the detailed XRD and SEM characterizations are given in the fig. S5 (*31*). No strong $CH_3NH_3PbCl_3$ phase was observed at the representative stage, and the final $CH_3NH_3PbI_{3-x}Cl_x$ film was formed predominately through the gradual consumption of PbI_2 species. The mechanism of perovskite film formation with moisture involvement is likely to originate from the hygroscopic organic species in the $CH_3NH_3PbX_3$ phases and their nature of ionic crystal: Moisture may enhance the reconstruction process during film formation by partially dissolving the reactant species and accelerating mass transport within the film.

The $CH_3NH_3PbI_{3-x}Cl_x$ film grown at 30% relative humidity in air exhibited enhanced optoelectronic properties compared with a film grown in dry conditions. We used time-resolved photoluminescence (PL) to characterize radiative and nonradiative carrier recombination of films prepared on glass substrates (Fig. 2A). The PL decay lifetime in the film with enhanced reconstruction was 736 ns (compared with the reference lifetime of 382 ns), which was likely a result of a reduced defect density that suppressed nonradiative recombination channels.

To further address the carrier behavior in the perovskite and correlate the film properties to device performance, devices with an identical structure were fabricated based on the two films (*31*). Their corresponding current-voltage (J-V) characteristics (Fig. 2B) show that the reconstruction process increases the perovskite device PCE from 13.5 to 16.4%. Substantial improvement was simultaneously observed in open-circuit voltage from 1.02 to 1.11 V and in fill factor from 61.41 to 65.88%, which together indicate that carrier recombination has been noticeably alleviated in the film with enhanced reconstruction. These findings imply that the optoelectronic properties of perovskite are affected by the phase conversion from $CH_3NH_3PbCl_3$ to $CH_3NH_3PbI_3$ and/or $CH_3NH_3PbI_{3-x}Cl_x$, and they further emphasize that the halide in the $CH_3NH_3PbX_3$ is vital in determining the material's properties by its close involvement in the film formation.

We further manipulated carrier behavior in the ETL by using Y-TiO_2 to improve the conductivity of this layer. Although TiO_2 is commonly used as the ETL and has appropriate energy levels for transferring electrons while blocking holes, its conductivity is ~1/10 that of spiro-OMeTAD (*36*), which may result in unnecessary ohmic losses or a nonideal space charge distribution within the device. To improve the electron transport property, Y-doped TiO_2 has been successfully used as the mesoporous scaffold in dye-sensitized solar cells and perovskite solar cells; however, it still requires high-temperature sintering (*25*). Here, Y-TiO_2 nanocrystals processed at low temperature (150°C) were used as the ETL coupled in the planar heterojunction. The J-V characteristics of the solar cells with TiO_2 and Y-TiO_2 as the ETL are shown in Fig. 2C. The TiO_2-based cell produced a short-circuit current (J_{SC}) of 19.9 mA/cm^2, open-circuit voltage (V_{OC}) of 1.06 V, and fill factor (*FF*) of 65.44%, yielding a PCE of 13.8%, whereas the Y-TiO_2 based device had J_{SC} of 22.8 mA/cm^2 and a PCE of 16.5%. There was no apparent difference between the absorbance of perovskite films deposited on the two substrates. Four-point conductivity measurements revealed a higher conductivity (2×10^{-5} S/cm) for the Y-TiO_2 film versus the undoped TiO_2 film (6×10^{-6} S/cm), possibly due to the increased carrier concentration. The series resistance in the device was also reduced from 9.12 to 5.34 ohms. The improved conductivity of Y-TiO_2 matches that of spiro-OMeTAD (*26*), which balances the carrier transport to reduce nonideal space charge distribution.

A Schottky barrier at the interface between TiO_2 and the transparent conductor can cause an apparent decrease in the maximum power output when it becomes too large (*37*). The general principle to reduce the interfacial barrier at a metal-semiconductor junction on the n-type side of a device is to reduce the work function of the metal being used. Modification of the electrode to achieve a work function that is near or lower than the Fermi energy of TiO_2 will then facilitate electron collection at the interface. Here, a solution of PEIE in methoxyethanol (~0.1% by weight)

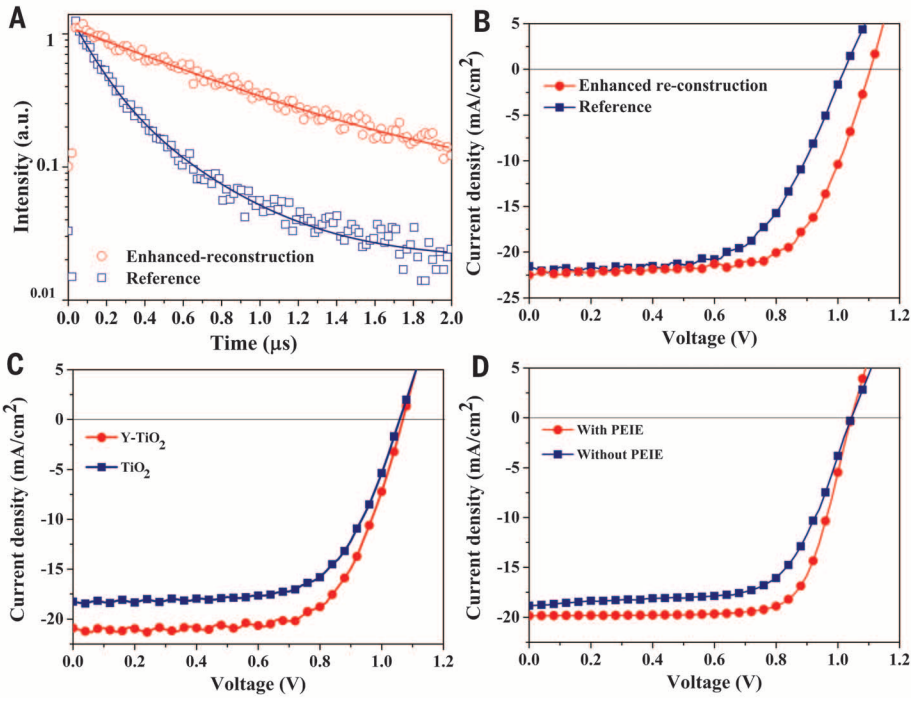

Fig. 2. Photoluminescence and photovoltaic characterization. (**A**) Photoluminescence decay curves of perovskite films prepared in controlled humidity (red circles) and dry air (blue squares). a.u., arbitrary units. (**B**) J-V curves of devices based on the corresponding films. (**C**) J-V curves of devices with Y-TiO_2 compared with undoped TiO_2. (**D**) J-V curves of devices with and without PEIE modification.

was used to form an ultrathin layer physisorbed on the ITO surface. The introduced molecular dipole interactions successfully reduced the work function of ITO from 4.6 to 4.0 eV. This shift likely helped to facilitate improved electron transport from the TiO_2 to ITO layers. As shown in Fig. 2D, an increase of fill factor in the PEIE-modified device was observed, which is consistent with the suppression of a barrier to carrier injection into the electrode. PEIE modification enables a perovskite solar cell with PCE >15%, in which V_{OC} = 1.04 V, J_{SC} = 19.9 mA/cm^2, and FF = 73.28%. As a comparison, the device without PEIE modification exhibited V_{OC} = 1.04 V, J_{SC} = 18.9 mA/cm^2, and FF = 65.25%. In addition, we observed a slightly reduced surface roughness of the perovskite films with relevant morphology change due to the employment of PEIE on the ITO substrates (fig. S6) (*31*).

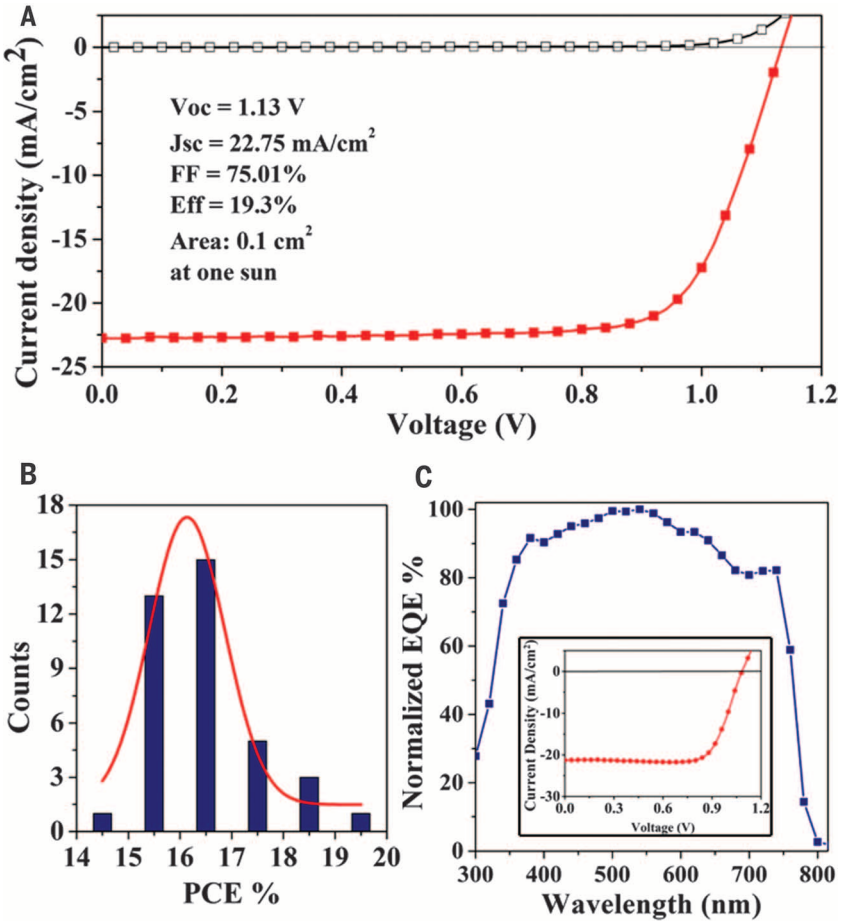

Fig. 3. Efficiency measurements. (**A**) J-V curves for the champion cell without antireflective coating. (**B**) Histogram of solar cell efficiencies for 40 devices. (**C**) Normalized EQE spectrum of a typical cell. (Inset) The corresponding J-V curve of the device.

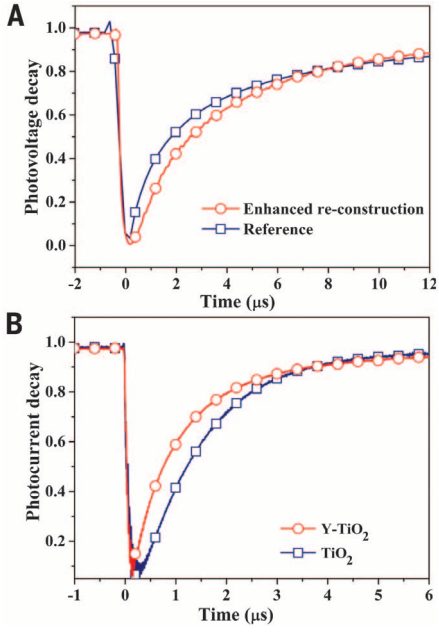

Fig. 4. Carrier lifetimes. (**A**) Transient photovoltage decay curves of devices with perovskite absorbers processed in controlled humidity (red circles) and in dry air (blue squares). (**B**) Transient photocurrent decay curves of devices based on ETL of TiO_2 (blue squares) and Y-TiO_2 (red circles).

Combined optimization of the entire carrier pathway has led to a device PCE of 19.3% under AM1.5 illumination without antireflective coating; the V_{OC}, J_{SC}, and FF are 1.13 V, 22.75 mA/cm^2, and 75.01%, respectively (Fig. 3). The error in J_{SC} measurement is within 5% by considering that light intensity, spectrum mismatch, and testing mask aperture effect (*31*). In general, the devices exhibit V_{OC} = 1.04 to 1.15 V, J_{SC} = 18.16 to 22.80 mA/cm^2, FF = 66.9 to 76.3%, and the resulting PCE = 14.5 to 19.3%. The average device efficiency is more than 16.6%, which shows the good reproducibility of the approach. The external quantum efficiency (EQE) spectrum (Fig. 3C) of a typical device (in-house measured V_{OC}, J_{SC}, FF, and PCE are 1.08 V, 21.26 mA/cm^2, 75.36%, and 17.3%, respectively, under AM1.5G, as shown in the inset of Fig. 3C) shows the onset of photocurrent at 790 nm, consistent with the reported band gap of $CH_3NH_3PbI_{3-x}Cl_x$ (*18*). The EQE reaches a peak value at ~550 nm with a gradual decrease from 600 nm, indicating a photocurrent loss due to either insufficiency in the absorption of perovskite layer or optical interference. The use of a simple planar structure and the production of such high-efficiency devices with low-temperature processing confirm the extraordinary potential of perovskite materials in photovoltaic applications. The representative device shows hysteresis in the current-voltage curves (fig. S8) (*31*), which is similar to the findings of a recent report (*38*). We also carried out a preliminary stability investigation of the perovskite solar cell by storing the devices in different environments. As shown in fig. S9 (*31*), the devices stored in either dry air or nitrogen retain 80% of the initial performance after 24 hours and 20% after 6 days, whereas the devices stored in ambient air retain less than 20% of the initial performance after 24 hours and 5% after 6 days. These results show that better stability with advanced encapsulation techniques is needed for practical use of the perovskite solar cells.

To further examine the origin of the improved device characteristics, we used transient photovoltage and photocurrent measurements to investigate the carrier dynamics along the entire pathway in the completed cells. Transient photovoltage measurements, which correlate to the electron lifetime in the absorber, provide insight into carrier recombination rates in the cell. Two devices were compared: one was based on a perovskite film with enhanced reconstruction (V_{OC} =1.13 V, J_{SC} = 22.06 mA/cm^2, FF = 71.25%,

PCE = 17.76%), and the other was the reference without enhanced reconstruction (V_{OC} = 1.02 V, J_{SC} = 20.53 mA/cm^2, FF = 61.41%, PCE = 12.85%). Based on the voltage decay time, the device with the enhanced reconstruction film showed ~50% longer electron lifetime than that of the reference cell (Fig. 4A). In both cases, the photovoltage decay constants are on the scale of microseconds. This is consistent with the observation of very slow microsecond time scale recombination at ambient solar intensities (*39*), indicating that the carrier recombination is predominately limited by the perovskites layer. This result also reveals that the photovoltage decay time benefits from substantially reduced trap densities in the perovskite material or at its interfaces by enhanced reconstruction film formation. This observation is in good agreement with both the longer carrier lifetime, as mentioned previously, and the decreased saturation current density (fig. S10) (*31*). Note that high V_{OC} value reported here is near the thermodynamic limit, which is constrained by radiative recombination in the absorber (*40*).

Transient photocurrent measurements indicate that carrier transport in the devices was improved by modification in the TiO_2 layer. The Y-TiO_2–based devices exhibited faster photocurrent decay than that of reference devices, in which the perovskite layers were deposited by the same method. This result is in accordance with the PL measurements (fig. S11) (*31*), where perovskites on Y-TiO_2 layer showed a decay time ~30% smaller than the reference. More efficient carrier extraction in the Y-TiO_2 devices probably resulted from the improved interface at the Y-TiO_2 layer. UPS characterization exhibited a slight upward shift of the Fermi level in the Y-TiO_2 layer, indicating an increased donor concentration in response to the enhanced conductivity. This is further confirmed by the capacitance-voltage measurement (fig. S12) (*31*). Increased donor concentration often reduces space charge depletion width at interfaces (*26*). Presumably, the narrower depletion region lowers the contact resistance and facilitates the charge extraction at both interfaces adjacent to the ETL.

REFERENCES AND NOTES

1. D. B. Mitzi, *Prog. Inorg. Chem.* **48**, 1–121 (2007).
2. A. Kojima, K. Teshima, Y. Shirai, T. Miyasaka, *J. Am. Chem. Soc.* **131**, 6050–6051 (2009).
3. www.nrel.gov/ncpv/images/efficiency_chart.jpg.
4. B. V. Lotsch, *Angew. Chem. Int. Ed.* **53**, 635–637 (2014).
5. N.-G. Park, *J. Phys.Chem. Lett.* **4**, 2423–2429 (2013).
6. H. J. Snaith, *J. Phys.Chem. Lett.* **4**, 3623–3630 (2013).
7. M. M. Lee, J. Teuscher, T. Miyasaka, T. N. Murakami, H. J. Snaith, *Science* **338**, 643–647 (2012).
8. J. Burschka *et al.*, *Nature* **499**, 316–319 (2013).
9. J.-Y. Jeng *et al.*, *Adv. Mater.* **25**, 3727–3732 (2013).
10. D. Liu, T. L. Kelly, *Nat. Photonics* **8**, 133–138 (2014).
11. M. Liu, M. B. Johnston, H. J. Snaith, *Nature* **501**, 395–398 (2013).
12. Q. Chen *et al.*, *J. Am. Chem. Soc.* **136**, 622–625 (2014).
13. G. E. Eperon, V. M. Burlakov, P. Docampo, A. Goriely, H. J. Snaith, *Adv. Funct. Mater.* **24**, 151–157 (2014).
14. B. Conings *et al.*, *Adv. Mater.* **26**, 2041–2046 (2014).
15. P.-W. Liang *et al.*, *Adv. Mater.* **26**, 3748–3754 (2014).
16. H. S. Kim *et al.*, *Sci. Rep.* **2**, 591 (2012).
17. O. Malinkiewicz *et al.*, *Nat. Photonics* **8**, 128–132 (2014).
18. P. Docampo, J. M. Ball, M. Darwich, G. E. Eperon, H. J. Snaith, *Nat. Commun.* **4**, 2761 (2013).
19. J. H. Heo *et al.*, *Nat. Photonics* **7**, 486–491 (2013).
20. A. Abrusci *et al.*, *Nano Lett.* **13**, 3124–3128 (2013).
21. H.-S. Kim *et al.*, *Nano Lett.* **13**, 2412–2417 (2013).
22. A. Yella, L.-P. Heiniger, P. Gao, M. K. Nazeeruddin, M. Grätzel, *Nano Lett.* **14**, 2591–2596 (2014).
23. Z. Zhu *et al.*, *J. Am. Chem. Soc.* **136**, 3760–3763 (2014).
24. D.-Y. Son, J.-H. Im, H.-S. Kim, N.-G. Park, *J. Phys. Chem. C* (2014).
25. P. Qin *et al.*, *Nanoscale* **6**, 1508–1514 (2014).
26. K. Wojciechowski, M. Saliba, T. Leijtens, A. Abate, H. Snaith, *Energy Environ. Sci.* **7**, 1142–1147 (2014).
27. J. A. Christians, R. C. M. Fung, P. V. Kamat, *J. Am. Chem. Soc.* **136**, 758–764 (2014).
28. N. J. Jeon *et al.*, *J. Am. Chem. Soc.* **135**, 19087–19090 (2013).
29. J. You *et al.*, *ACS Nano* **8**, 1674–1680 (2014).
30. W. Zhang *et al.*, *Nano Lett.* **13**, 4505–4510 (2013).
31. See supplementary materials on *Science* Online.
32. Y. Zhou *et al.*, *Science* **336**, 327–332 (2012).
33. I. Persson, K. Lyczko, D. Lundberg, L. Eriksson, A. Płaczek, *Inorg. Chem.* **50**, 1058–1072 (2011).
34. J. Błażejowski, E. Kowalewska, *Thermochim. Acta* **105**, 257–286 (1986).
35. P. Dokurno, J. Łubkowski, J. Błaejowski, *Thermochim. Acta* **165**, 31–48 (1990).
36. T. Leijtens, J. Lim, J. Teuscher, T. Park, H. J. Snaith, *Adv. Mater.* **25**, 3227–3233 (2013).
37. H. J. Snaith, M. Grätzel, *Adv. Mater.* **18**, 1910–1914 (2006).
38. H. J. Snaith *et al.*, *J. Phys.Chem. Lett.* **5**, 1511–1515 (2014).
39. C. S. Ponseca Jr. *et al.*, *J. Am. Chem. Soc.* **136**, 5189–5192 (2014).
40. R. R. King *et al.*, *Prog. Photovolt. Res. Appl.* **19**, 797–812 (2011).

ACKNOWLEDGMENTS

This work was financially supported by a grant from the NSF (grant no. ECCS-1202231, Program Director P. Werbos), a grant from the Air Force Office of Scientific Research (grant no. FA9550-12-1-0074, Program Manager C. Lee), and UCLA Internal Funds. We thank H. S. Jung and B. Kim of Sungkyunkwan University in Korea for valuable discussion in the starting stage of a perovskite solar cell, S. Lu for synthesizing Co salt, B. Bob and E. Richard for editing, W. Hsu for assistance with UPS measurements and analysis, L. Dou for TiO_2 nanocrystal synthesis, J. D. Huang for inspiring technical discussion, K. Emery (National Renewable Energy Laboratory) for calibrating UCLA's in-house KG5 Si reference cell and valuable discussion on EQE measurement, and M. O'Donnell (Newport Corporation) for helping on spectral mismatch factor calculation.

SUPPLEMENTARY MATERIALS

www.sciencemag.org/content/345/6196/542/suppl/DC1
Materials and Methods
Figs. S1 to S12
Tables S1 and S2
Reference (*41*)

28 March 2014; accepted 18 June 2014
10.1126/science.1254050

CATALYSIS

Highly active copper-ceria and copper-ceria-titania catalysts for methanol synthesis from CO_2

Jesús Graciani,[1] Kumudu Mudiyanselage,[2] Fang Xu,[2] Ashleigh E. Baber,[2] Jaime Evans,[3] Sanjaya D. Senanayake,[2] Darío J. Stacchiola,[2] Ping Liu,[2] Jan Hrbek,[2] Javier Fernández Sanz,[1] José A. Rodriguez[2]*

The transformation of CO_2 into alcohols or other hydrocarbon compounds is challenging because of the difficulties associated with the chemical activation of CO_2 by heterogeneous catalysts. Pure metals and bimetallic systems used for this task usually have low catalytic activity. Here we present experimental and theoretical evidence for a completely different type of site for CO_2 activation: a copper-ceria interface that is highly efficient for the synthesis of methanol. The combination of metal and oxide sites in the copper-ceria interface affords complementary chemical properties that lead to special reaction pathways for the CO_2→CH_3OH conversion.

Methanol is a key commodity used to produce acetic acid, formaldehyde, and a number of key chemical intermediates (*1*). It is synthesized industrially from mixtures of H_2, CO_2, and CO at elevated pressures (50 to 100 atm) and temperatures (450 to 600 K) with a Cu/ZnO/Al_2O_3 catalyst (*2*–*4*). Of particular interest is the synthesis of methanol from CO_2 (*2*, *5*–*9*), not only as a way to mitigate this greenhouse gas but also because of the potential use of CO_2 as an alternative and economical feedstock (*2*, *5*, *10*–*12*). The activation of CO_2 and its hydrogenation to alcohols or other hydrocarbon compounds is an important approach to recycle the released CO_2 (*2*, *5*, *11*, *12*). This is a challenging task because of the difficulties associated with the chemical inertness of CO_2 (*2*, *5*–*9*, *13*). A recent study has identified the active site for the activation of CO_2 and the synthesis of methanol on Cu/ZnO/Al_2O_3 industrial catalysts (*2*). The active site consists of Cu steps decorated with Zn atoms. Cu alone interacts very poorly with CO_2 (*2*, *6*–*9*), and alloying with Zn is necessary in order to bind the reactant better and accelerate its transformation into methanol (*2*). Here we present experimental and theoretical evidence for a completely different type of site for CO_2 activation: A Cu-ceria interface, which is highly active for the synthesis of

[1]Department of Physical Chemistry, University of Seville, E-41012, Seville, Spain. [2]Department of Chemistry, Brookhaven National Laboratory, Upton, NY 11973, USA. [3]Facultad de Ciencias, Universidad Central de Venezuela, Caracas, 1020-1, Venezuela.
***Corresponding author. E-mail: rodrigez@bnl.gov**

methanol. The combination of metal and oxide centers in the Cu-ceria interface provides favorable reaction pathways for the $CO_2 \rightarrow CH_3OH$ conversion not seen over a Cu-Zn alloy (*2*).

The activity for methanol synthesis of a series of catalysts that contain Cu is compared in Fig. 1A (pressure of CO_2 = 0.5 atm; pressure of H_2 = 4.5 atm; temperature = 500 to 600 K). In addition to methanol synthesis, these surfaces also catalyze the generation of CO through the reverse water-gas shift reaction (RWGS, fig. S1). The data for Cu(111) and Cu/ZnO(000$\bar{1}$) were taken from (*6*). Extended surfaces of pure Cu exhibit a very low activity for the hydrogenation of CO_2 to methanol (*6*–*8*). Clean Cu(111) does not bind CO_2, but under reaction conditions, the metal binds it via interactions with H adatoms to form a surface formate species ($HCOO^-$) (*2*, *6*). The deposition of Cu nanoparticles on ZnO(000$\bar{1}$) produces a system that is more catalytically active than Cu(111). Cu nanoparticles still do not bind CO_2 well, but catalyze subsequent steps in the $CO_2 \rightarrow CH_3OH$ conversion better than Cu(111) (*6*). At a temperature of 575 K, the turnover frequency (TOF) for methanol synthesis on Cu(111) is 6.3×10^{-3} molecules per Cu site per second. If one assumes that all of the Cu atoms in Cu/ZnO(000$\bar{1}$) participate in the reaction, the corresponding TOF for methanol synthesis is 9.3×10^{-2} molecules per second (*6*), which implies an increase of ~15 times in the rate of methanol production with respect to Cu(111).

Previous studies have enhanced the reactivity of Cu toward CO_2 through alloying Cu with Zn (*2*) or late transition metals (*8*, *9*). We decided to follow a different approach, coupling Cu to a reducible oxide. The CeO_x/Cu(111) system has been studied before as a catalyst for the WGS and CO oxidation reactions (*13*, *14*). The cations of the ceria nanoparticles in contact with Cu(111) can easily alternate between 3+ and 4+ oxidation states (fig. S2). Thus, in CeO_x/Cu(111), an active metal-oxide interface can have oxide centers with dynamic chemical properties. The CeO_2/Cu_2O/Cu(111) system was prepared by vapor-depositing Ce onto Cu(111) in an atmosphere of O_2 (*14*, *15*) to form ceria islands on the step edges of a Cu_2O surface (*13*, *15*). An in situ scanning tunneling microscope (STM) (*16*) image of one of these ceria islands is shown in Fig. 1B. The ceria islands in the as-prepared system are predominantly one layer thick, exhibiting rough surfaces that occasionally have a CeO_2(111) termination. After exposing CeO_2/Cu_2O/Cu(111) to 1.5 torr of H_2, the complete reduction of Cu_2O to Cu and the formation of clusters of O vacancies in the ceria is achieved (Fig. 1C). Reduction in H_2 increased the surface roughness of the ceria particles, creating an expanded ceria-Cu interface.

We investigated the hydrogenation of CO_2 over a CeO_x/Cu(111) surface in which ~20% of the Cu substrate was covered by ceria. Post-reaction surface analysis with x-ray photoelectron spectroscopy (XPS) indicated that the active phase of the catalyst was Ce_2O_3/Cu(111), as shown in fig. S2. The data for CeO_x/Cu(111) in Fig. 1A indicate that this system is a much better catalyst for methanol synthesis than either Cu(111) or Cu/ZnO(000$\bar{1}$). The STM image in Fig. 1C illustrates the difficulties associated with the precise quantification of the active sites at the metal-oxide interface on a CeO_x/Cu(111) surface. As a first approximation, one can assume that for the CeO_x/Cu(111) system in Fig. 1A, the concentration of active sites in the metal-oxide interface will be at the most equal to the area initially covered by ceria: ~20% of the concentration existing on a clean Cu(111) surface. Given this assumption, we estimate a minimum TOF value of 1.3 molecules per active site per second for methanol synthesis on CeO_x/Cu(111) at 575 K. Thus, the rate of methanol production on CeO_x/Cu(111) is ~200 times faster than on Cu(111) and ~14 times faster than on Cu/ZnO(000$\bar{1}$). Furthermore, the apparent activation energy for methanol synthesis decreases from 25 kcal/mol on Cu(111) to 16 kcal/mol on Cu/ZnO(000$\bar{1}$) and 12 kcal/mol on CeO_x/Cu(111).

Using ambient-pressure (AP) XPS and infrared reflection absorption spectroscopy (IRRAS), we investigated the interaction of CO_2 and CO_2/H_2 mixtures with Cu(111), CeO_2(111), and CeO_x/Cu(111) surfaces at temperatures between 300 and 500 K. Pure CO_2 did not adsorb on Cu(111) at these temperatures. On the other hand, the adsorption of CO_2 on a CeO_2(111) surface produced strongly bound carbonate (CO_3^{2-}) species (*17*). Figure 2 shows IRRAS spectra obtained at room temperature after the exposure of CeO_x/Cu(111) to CO_2 at two different pressures. At 6.5×10^{-3} torr of CO_2 (top spectrum), two peaks were observed at 1288 and 1610 cm^{-1} that indicate the presence of a carboxylate ($CO_2^{\delta-}$) species on the surface (*14*, *18*), and we conclude that a ceria-Cu interface activates CO_2. An increase in the CO_2 pressure up to 1.0 torr induced the appearance of new peaks at 1210, 1402, and 1440 cm^{-1} that correspond to carbonate (CO_3^{2-}) species (*17*). At this pressure, both carbonate and carboxylate species were stable on CeO_x/Cu(111) at 300 K. After adding 9.0 torr of H_2 at 300 K, no changes in the spectrum were observed.

To investigate temperature effects, the CeO_x/Cu(111) system was annealed in CO_2 + H_2 to 500 K, which led to the appearance of infrared (IR) peaks at 1295, 1330, 1370, 1598, and 2858 cm^{-1}. The peak at 1295 cm^{-1} we assigned to $CO_2^{\delta-}$, whereas the other features we assigned to a formate ($HCOO^-$) species (*19*). The peaks at 1330 and 1370 cm^{-1} we assigned to symmetric OCO stretches, ν_s(OCO), whereas the peak at 1598 cm^{-1} is for the asymmetric OCO stretches, ν_{as}(OCO), and the peak at 2858 cm^{-1} is for CH stretch modes, ν(CH). After evacuating the gases from the AP cell while keeping the sample at 500 K, all of the peaks disappeared, indicating that the adsorbed species formed only under reaction conditions (fig. S3). However, the surface formate species were stable after the sample was cooled down to 300 K under CO_2 + H_2 and the subsequent evacuation of gases from the AP cell (fig.

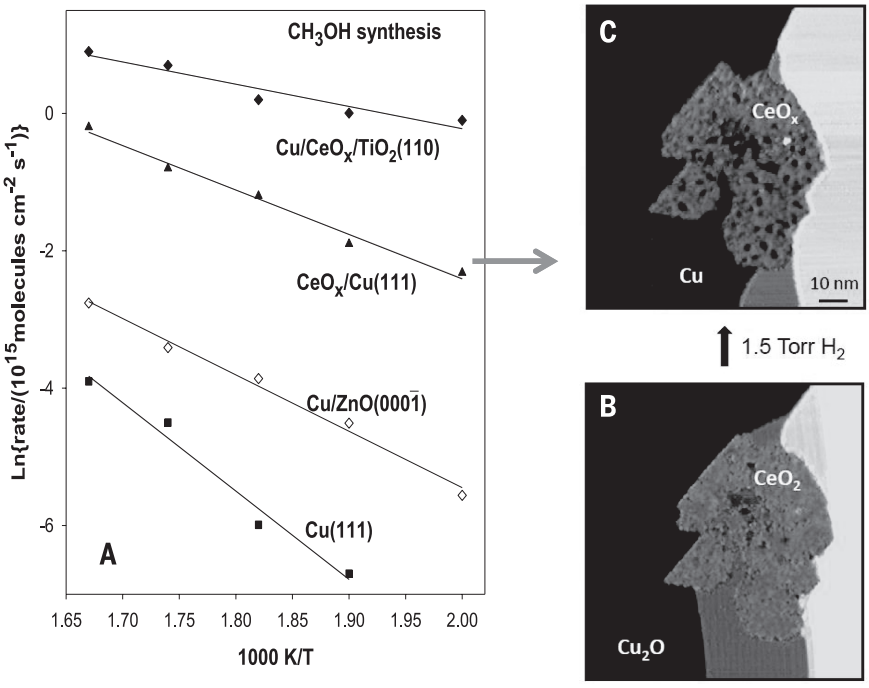

Fig. 1. Kinetics and STM studies. (**A**) Arrhenius plot for methanol synthesis on Cu(111), a 0.2 ML of Cu on ZnO(000$\bar{1}$), a Cu(111) surface covered 20% by ceria, and a 0.1 ML of Cu on a TiO_2(110) surface precovered 15% with ceria. In a batch reactor, the catalysts were exposed to 0.5 atm of CO_2 and 4.5 atm of H_2. The reported values are steady-state rates measured at 600, 575, 550, 525, and 500 K. (**B**) STM image of a CeO_x/Cu(111) surface as prepared. (**C**) In situ STM image taken during exposure to 1.5 torr of H_2 at 300 K after 26 hours of reaction. Scanning parameters: 0.3 nA, 1.0 V.

S3). Similar results were observed with the AP XPS experiments.

Figure 3 shows a C 1s AP-XPS spectrum obtained for a CeO_x/Cu(111) surface under a CO_2/H_2 mixture at 473 K. The weak features at ~284 eV denote the deposition of a very small amount of C on the surface of the catalyst as a consequence of the complete decomposition of CO_2. The main feature can be fitted with two peaks at 289.2 and 288.4 eV that we attributed to formates and carboxylates, respectively (*14*, *20*), in agreement with the IRRAS results in Fig. 2. The formates were stable under ultrahigh vacuum (UHV) at temperatures between 300 and 400 K. The carboxylate species were detected in appreciable amounts only when ceria was dispersed on the Cu substrate and were not stable in UHV. The lower stability of the $CO_2^{\delta-}$ species makes for a better intermediate for methanol synthesis than the formate species, which have high stability (*2*, *6*) and may not be efficient as transient species in the $CO_2 \rightarrow CH_3OH$ conversion (*21*). Thus, the addition of CeO_x nanoparticles to Cu(111) creates a metal-oxide interface that allows the adsorption and activation of CO_2, opening a new reaction pathway for the synthesis of methanol.

To provide a molecular description of the methanol synthesis mechanism on our system, we performed state-of-the-art density functional theory (DFT) calculations, looking for possible intermediates and screening them to build a plausible thermodynamic reaction pathway (Fig. 4). Following previous studies for CO_2 hydrogenation on clean Cu(111) (*2*, *6*, *22*), we considered reaction pathways that initially involved the formation of formate ($HCOO^-$) but abandoned them because of the high stability of this species. The experimental measurements point to the simultaneous production of methanol and CO during CO_2 hydrogenation (fig. S1). The reaction path in Fig. 4 shows the best calculated route for the RWGS and methanol synthesis. The overall reaction takes place under a H-rich atmosphere. Exothermic pre-hydrogenation of the ceria creates Ce^{3+} centers, which facilitates CO_2 adsorption (adsorption energy = –12.2 kcal/mol, "a"). On these centers, CO_2 is activated in a bent conformation ("b") and hydrogenated to yield a carboxyl OCOH species ("c"). The calculated energy barriers for these processes are in the range of 10 to 11 kcal/mol. An even lower energy barrier of 4.6 kcal/mol is associated with the OCOH → CO + OH ("d") transformation. At this point, water is formed from adsorbed H and OH species. The exothermic adsorption-dissociation of a second H_2 molecule (–9 kcal/mol) facilitates the water desorption, a process that at 0 K is still endothermic by 12.2 kcal/mol. However, taking into account the favorable entropy contribution for desorption and the reaction temperature (575 K), the calculated energy for water desorption is as low as 3 kcal/mol. Through these steps, the RWGS reaction takes place. Subsequent steps achieve the hydrogenation of CO to methanol through expected intermediates: HCO (formyl, "f"), H_2CO (formaldehyde, "g"), and H_3CO (methoxy, "h"). Our experimental data indicate that the RWGS reaction and methanol synthesis have similar apparent activation energies (table S1). This phenomenon has been seen before for CO_2 hydrogenation on Cu(111) (*7*) or Cu/ZnO(000$\bar{1}$) (*6*) and suggests that both reactions go through a common intermediate (*21*). The DFT results summarized in Fig. 4 point to OCOH as the common intermediate. The calculated reaction barriers for the transformation of CO_2 into OCOH and the first hydrogenation of CO are similar (11 to 14 kcal/mol)

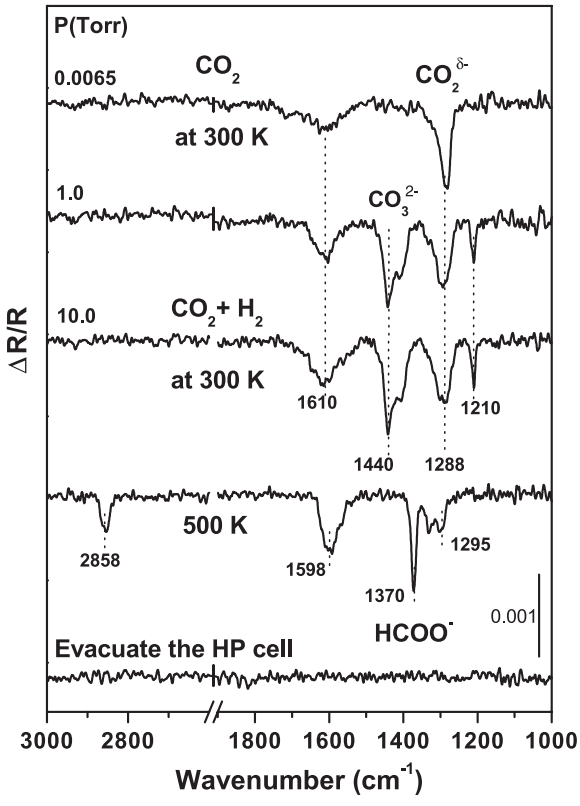

Fig. 2. IRRAS spectra at ambient pressures. The spectra were obtained after the exposure of CeO_x/Cu(111) to CO_2 and H_2 at the indicated pressures and temperatures. All the spectra except the one at the bottom were collected in the presence of CO_2 or a CO_2 + H_2 mixture at the indicated pressures. ΔR/R, normalized reflectivity change.

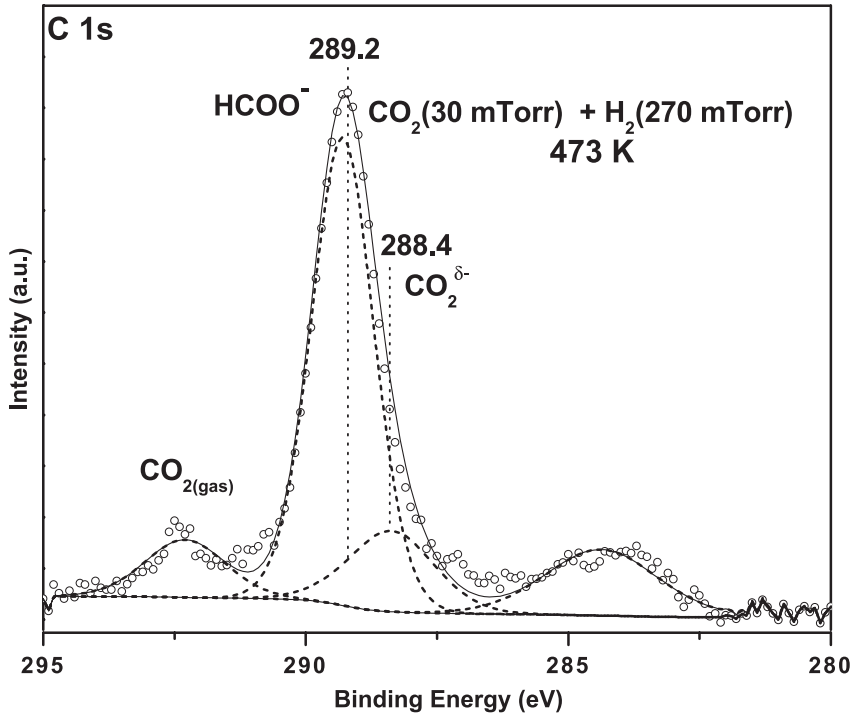

Fig. 3. XPS data. The C 1s AP-XPS data obtained for CeO_x/Cu(111) after exposure to CO_2 (30 mtorr) and H_2 (270 mtorr) at 473 K.

and close to the apparent activation energies observed in the experiments for CeO_x/Cu(111) (11 to 12 kcal/mol). The calculated energy barriers for the HCO→H_2CO, H_2CO→H_3CO, and H_3CO→H_3COH hydrogenations are quite small, 5.3, 3.5, and 5 kcal/mol, respectively. The final desorption of the methanol to complete the whole reaction ($CO_2 + 3\ H_2 \rightarrow CH_3OH + H_2O$) is highly endothermic (19.1 kcal/mol) but, again, taking into account the favorable entropy and temperature contributions, the energy for the desorption process is only 5.3 kcal/mol. The theoretical results in Fig. 4 indicate that the thermochemistry of the reaction steps associated with the formation of methanol on a ceria-Cu interface is predominantly downhill, with an overall exothermic process, which is not the case for the thermochemistry of the reaction on a CuZn alloy (*2*), the active site for Cu/ZnO/Al_2O_3.

The absence of CO, HCO, H_2CO, and H_3CO in the in situ IR and XPS spectra is probably a consequence of the low residence time of these species on the surface under reaction conditions. CO adsorbs weakly on Cu (*14*, *15*). After the addition of the first H to CO, the barriers for the subsequent hydrogenation steps are relatively small (<6 kcal/mol) and can be easily overcome by the high temperature (>450 K) necessary for the catalytic synthesis of methanol. Under reaction conditions, the only species observed in the IR and XPS spectra are $HCOO^-$ (Figs. 2 and 3), a spectator, and the active species CO_2^- and OH (Figs. 2 and 3 and fig. S4). The ceria component enhances the stability of CO_2^- and OH on the surface of the catalyst, opening efficient routes for methanol synthesis not seen on pure Cu or CuZn alloys (*2*, *6*).

A comparison of the results in Fig. 1A for Cu(111) and Cu/ZnO(000$\bar{1}$) points to an enhancement of the catalytic activity of Cu when this element is present in the form of nanoparticles. We investigated the hydrogenation of CO_2 on catalysts generated by codepositing nanoparticles of Cu and ceria on TiO_2(110). Previous studies have examined the properties of the CeO_x/TiO_2 (110) mixed-metal oxide in detail (*23*–*25*). Ceria nanoparticles in contact with titania form small wirelike structures and have Ce^{3+} and Ce^{4+} states of almost equal stability (*23*, *24*). STM images show a close contact between Cu and ceria on a TiO_2(110) substrate (*24*). Thus, the type of chemistry seen in Figs. 2 to 4 for the Cu-ceria interface of CeO_x/Cu(111) also can occur in Cu/CeO_x/TiO_2(110). Kinetics data for methanol synthesis on a catalyst generated by depositing a ~0.1 monolayer (ML) of Cu on a TiO_2(110) surface pre-covered 15% by ceria nanoparticles (Fig. 1A) show that this surface is clearly the best catalyst. At 575 K, we estimate a TOF of 8.1 molecules per active site per second. The rate of methanol production on Cu/CeO_x/TiO_2(110) is ~1280 times faster than on Cu(111) and ~87 times faster than on Cu/ZnO(000$\bar{1}$). In control experiments, we examined the synthesis of methanol on 0.1 ml of Cu supported on TiO_2(110) or CeO_2(111) surfaces and measured catalytic activities that were somewhat greater than that of Cu/ZnO(000$\bar{1}$) but much less than that of Cu/CeO_x/TiO_2(110) or even CeO_x/Cu(111). Plain CeO_x/TiO_2(110) had no activity for methanol synthesis. Thus, the extremely high activity of Cu/CeO_x/TiO_2(110) is probably a consequence of generating a metal-oxide interface involving Cu and ceria nanoparticles.

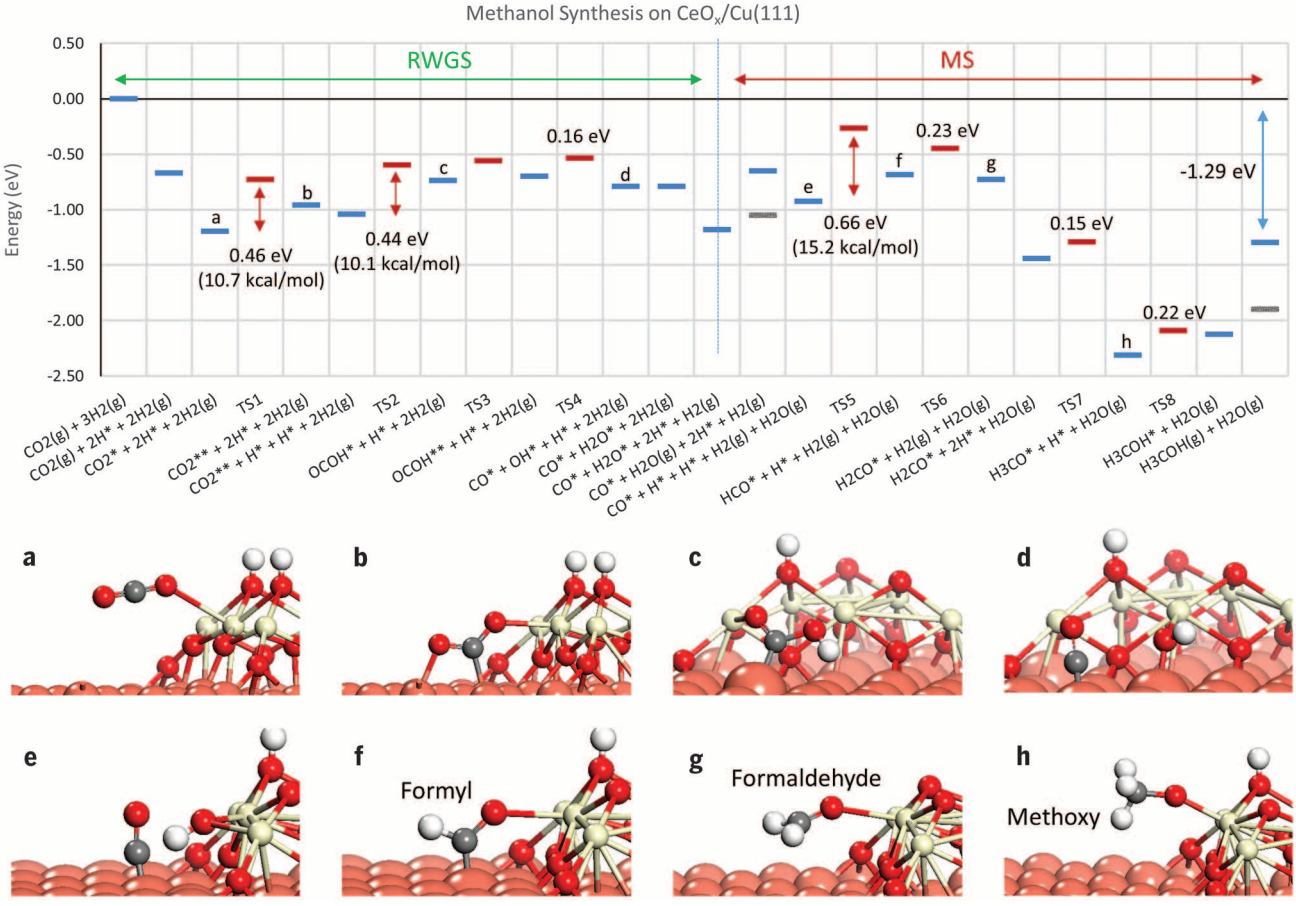

Fig. 4. DFT studies. Reaction path for methanol synthesis (MS) by CO_2 hydrogenation on the CeO_x/Cu(111) system. Step colors are as follows: local minima states (blue), transition states (TS) (red), and energies including the entropy contribution (gray). The calculated energy for the whole methanol synthesis reaction is indicated on the right side of the graph. The main transition states are pointed out by vertical red arrows, and the respective energy values are also shown under the arrows. The other energy barriers are indicated above the respective transition-state step. The whole reaction has been divided into two parts: The first one constitutes the RWGS (indicated by a green arrow on the top of the graph), and the second one consists of the steps leading to the methanol synthesis (MS) (red arrow on the top of the graph). The optimized structures for the main intermediates are included in the bottom part of the figure. Carboxylate species observed in the IRRAS experiments correspond to the structure shown in b. Colors: O (red), C (gray), H (white), cerium (light-beige), Cu (dark pink).

This study illustrates the substantial benefits that can be obtained by properly tuning the properties of a metal-oxide interface in catalysts for methanol synthesis. In a metal-oxide interface, one can have adsorption/reaction sites with complementary chemical properties (*14*, *26*), truly bifunctional sites that would be very difficult to generate on the surface of a pure metal or alloy system (*2*, *9*, *27*).

REFERENCES AND NOTES

1. G. A. Olah, A. Goeppert, G. K. Surya Prakash, *Beyond Oil and Gas: The Methanol Economy* (Wiley-VCH, Weinheim, Germany, 2011)
2. M. Behrens *et al*., *Science* **336**, 893–897 (2012).
3. G. C. Chinchen, P. J. Denny, D. G. Parker, M. S. Spencer, D. A. Whan, *Appl. Catal.* **30**, 333–338 (1987).
4. M. S. Spencer, *Top. Catal.* **8**, 259–266 (1999).
5. M. Aresta, Ed., *Carbon Dioxide as Chemical Feedstock* (Wiley-VCH, New York, 2010).
6. Y. Yang, J. Evans, J. A. Rodriguez, M. G. White, P. Liu, *Phys. Chem. Chem. Phys.* **12**, 9909–9917 (2010).
7. J. Yoshihara, C. T. Campbell, *J. Catal.* **161**, 776–782 (1996).
8. P. B. Rasmussen, M. Kazuta, I. Chorkendorff, *Surf. Sci.* **318**, 267–280 (1994).
9. Y. Yang, M. G. White, P. Liu, *J. Phys. Chem. C* **116**, 248–256 (2012).
10. D. Preti, C. Resta, S. Squarcialupi, G. Fachinetti, *Angew. Chem. Int. Ed.* **50**, 12551–12554 (2011).
11. M. B. Ansari, B.-H. Min, Y.-H. Mo, S.-E. Park, *Green Chem.* **13**, 1416 (2011).
12. A. B. Vidal *et al*., *J. Phys. Chem. Lett.* **3**, 2275–2280 (2012).
13. S. D. Senanayake, D. J. Stacchiola, J. A. Rodriguez, *Acc. Chem. Res.* **46**, 1702–1711 (2013).
14. K. Mudiyanselage *et al*., *Angew. Chem. Int. Ed.* **52**, 5101–5105 (2013).
15. J. A. Rodriguez *et al*., *Angew. Chem. Int. Ed.* **48**, 8047–8050 (2009).
16. A. E. Baber *et al*., *J. Am. Chem. Soc.* **135**, 16781–16784 (2013).
17. C. Li *et al*., *J. Chem. Soc., Faraday Trans. I* **85**, 929 (1989).
18. O. Seiferth *et al*., *Surf. Sci.* **421**, 176–190 (1999).
19. W. O. Gordon, Y. Xu, D. R. Mullins, S. H. Overbury, *Phys. Chem. Chem. Phys.* **11**, 11171–11183 (2009).
20. X. Deng *et al*., *Langmuir* **24**, 9474–9478 (2008).
21. Y. Yang, C. A. Mims, D. H. Mei, C. H. F. Peden, C. T. Campbell, *J. Catal.* **298**, 10–17 (2013).
22. Y. F. Zhao *et al*., *J. Catal.* **281**, 199–211 (2011).
23. J. B. Park *et al*., *Proc. Natl. Acad. Sci. U.S.A.* **106**, 4975–4980 (2009).
24. J.-B. Park *et al*., *J. Am. Chem. Soc.* **132**, 356–363 (2010).
25. J. Graciani, J. J. Plata, J. F. Sanz, P. Liu, J. A. Rodriguez, *J. Chem. Phys.* **132**, 104703 (2010).
26. I. X. Green, W. Tang, M. Neurock, J. T. Yates Jr., *Science* **333**, 736–739 (2011).
27. F. Studt *et al*., *Nat. Chem.* **6**, 320–324 (2014).

ACKNOWLEDGMENTS

The research carried out at Brookhaven National Laboratory was supported by the U.S. Department of Energy, Chemical Sciences Division (DE-AC02-98CH10886). J.E. is grateful to the Instituto de Tecnologia Venezolana para el Petroleo for support of the work carried out at the Universidad Central de Venezuela. The work performed at the University of Seville was funded by the Ministerio de Economía y Competitividad (Spain, grants MAT2012-31526 and CSD2008-0023) and European Regional Development Fund. Computational resources were provided by the Barcelona Supercomputing Center/Centro Nacional de Supercomputación (Spain). The AP-XPS spectra were acquired at the Advanced Light Source (beamline 9.3.2), which is supported by the U.S. Department of Energy under contract no. DE-AC02-05CH11231.

SUPPLEMENTARY MATERIALS

www.sciencemag.org/content/345/6196/546/suppl/DC1
Materials and Methods
Figs. S1 to S4
References (*28*–*37*)

7 March 2014; accepted 9 June 2014
10.1126/science.1253057

ASTEROSEISMOLOGY

Echography of young stars reveals their evolution

K. Zwintz,[1]* L. Fossati,[2] T. Ryabchikova,[3] D. Guenther,[4] C. Aerts,[1,5] T. G. Barnes,[6] N. Themeßl,[7] D. Lorenz,[7] C. Cameron,[8] R. Kuschnig,[7] S. Pollack-Drs,[7] E. Moravveji,[1] A. Baglin,[9] J. M. Matthews,[10] A. F. J. Moffat,[11] E. Poretti,[12] M. Rainer,[12] S. M. Rucinski,[13] D. Sasselov,[14] W. W. Weiss[7]

We demonstrate that a seismic analysis of stars in their earliest evolutionary phases is a powerful method with which to identify young stars and distinguish their evolutionary states. The early star that is born from the gravitational collapse of a molecular cloud reaches at some point sufficient temperature, mass, and luminosity to be detected. Accretion stops, and the pre–main sequence star that emerges is nearly fully convective and chemically homogeneous. It will continue to contract gravitationally until the density and temperature in the core are high enough to start nuclear burning of hydrogen. We show that there is a relationship for a sample of young stars between detected pulsation properties and their evolutionary status, illustrating the potential of asteroseismology for the early evolutionary phases.

The earliest phases in the lives of stars determine their future fate. For example, the production of chemical elements, which are used to trace the history of galactic evolution, depends on the initial mass and metallicity of young stars. Also, the angular momentum obtained during the birth process is vital for the further stellar life. Therefore, understanding the physical processes that occur during the earliest stages of stellar evolution is essential.

During the early evolutionary phases, after the star's appearance on the birthline (*1*–*3*), the central temperatures and densities are not yet high enough to initiate substantial nuclear burning; hence, the early star derives all of its energy (heat and radiative) from the release of gravitational potential energy. The interior structure undergoes several changes as the temperature rises, and in general, the opacities decrease (*1*). Initially, the higher opacities and the outward transportation of the released gravitational energy force the star to be nearly fully convective. But as the star heats up and the opacities drop, a radiative core develops. At this point, the star leaves the Hayashi track (*4*) and follows the Henyey track (*5*), moving leftward to hotter surface temperatures in the evolutionary diagram. Eventually, the star's central regions become hot enough for nuclear burning to occur. Models predict that for intermediate-mass stars [with 1.5 to 8 solar masses ($M_{\odot}$)], just before the star reaches this nuclear burning stage, called the main-sequence (MS) phase, there is a "bump" or brief period of nuclear burning during which carbon is "burned" by the CNO cycle (a chain of hydrogen burning reactions catalyzed by the presence of C, N, and O) until C and N reach nuclear burning equilibrium. As this happens, the star's core briefly becomes convective, and the star's luminosity increases. Shortly thereafter, the star resumes its contraction onto the zero-age main sequence (ZAMS), when nuclear burning of hydrogen reignites and remains the dominant source of energy throughout most of the rest of the star's life. The precise definition of the ZAMS is critical when comparing ages of young stars. Here, we define the ZAMS as the time after the CN equilibrium burning bump, when the nuclear burning accounts for at least 1% of the total luminosity of the star.

For pre–main sequence (pre-MS) stars with 1.5 to 4 $M_{\odot}$, the interior structure will become unstable to acoustic oscillation modes at some point during their evolution along the Henyey track. These can be observed at the surface as periodic variations in luminosity and temperature or as Doppler shifts of spectral lines. So for at least some pre-MS stars, it is possible at some evolutionary stages to use asteroseismology to explore their structure and evolution. The pre-MS stars addressed in this study show coherent self-excited low-radial-order pressure (p) modes (*6*), with periods from ~18 min up to 6 hours. Until 2008, only 36 of them were known (*7*); through

[1]Instituut voor Sterrenkunde, Katholieke Universiteit (KU) Leuven, Celestijnenlaan 200D, 3001 Leuven, Belgium. [2]Argelander Institut für Astronomie der Universität Bonn, Auf dem Hügel 71, 53121 Bonn, Germany. [3]Institute of Astronomy, Russian Academy of Sciences (RAS), Pyatnitskaya 48, 109017 Moscow, Russia. [4]Department of Astronomy and Physics, St. Mary's University, Halifax, Nova Scotia B3H 3C3, Canada. [5]Department of Astrophysics, Institute for Mathematics, Astrophysics and Particle Physics, Radboud University Nijmegen, Post Office Box 9010, 6500 GL Nijmegen, Netherlands. [6]The University of Texas at Austin, McDonald Observatory, 82 Mt. Locke Road, McDonald Observatory, TX 79734, USA. [7]Universität Wien, Institut für Astrophysik, Türkenschanzstraße 17, 1180 Vienna, Austria. [8]Department of Mathematics, Physics and Geology, Cape Breton University, 1250 Grand Lake Road, Sydney, Nova Scotia B1P 6L2, Canada. [9]Laboratoire d'Études Spatiales et d'Instrumentation en Astrophysique, Observatoire de Paris-Meudon, 5 place Jules Janssen, 92195, Meudon, France. [10]Department of Physics and Astronomy, University of British Columbia, 6224 Agricultural Road, Vancouver, British Columbia V6T 1Z1, Canada. [11]Département de Physique, Université de Montréal, C.P. 6128, Succ. Centre-Ville, Montréal, Quebec H3C 3J7, Canada. [12]Istituto Nazionale di Astrofisica–Osservatorio Astronomico di Brera, Via E. Bianchi 46, 23807 Merate, Italy. [13]Department of Astronomy and Astrophysics, University of Toronto, 50 St. George Street, Toronto, Ontario M5S 3H4, Canada. [14]Harvard-Smithsonian Center for Astrophysics, 60 Garden Street, Cambridge, MA 02138, USA.
***Corresponding author. E-mail: konstanze.zwintz@ster.kuleuven.be**

2011, the number increased substantially to more than 60 (*8*) through the use of dedicated ground-based observations and high-precision time-series photometry obtained with the Microvariability and Oscillations of Stars (MOST) (*9*) and Convection, Rotation et Transits planétaires (CoRoT) (*10*) satellites. Although the pulsations of pre-MS stars could be studied in relative detail, little information was available concerning the stars' fundamental astrophysical properties—such as effective temperature ($T_{\rm eff}$), surface gravity (log g), luminosity, mass (M), projected rotational velocity ($v\sin i$), and metallicity ([Fe/H])—due to the lack of spectroscopic measurements for this type of object.

Our sample comprises 34 stars with confirmed pre-MS evolutionary status, pulsational variability, and accurate fundamental parameters determined from detailed spectroscopic analyses. We assessed the pre-MS status of the stars in our sample in two different ways: through their membership in open clusters known to be younger than 10 million years, which ensures that 1.5 to 4 $M_\odot$ stars have not reached the ZAMS yet, or through their identification as Herbig Ae stars (*11*), which are associated with star-forming regions.

The pulsational properties of the sample stars were determined from ground- and space-based observations. For 19 stars, high-precision space photometry from the MOST (*9*) and CoRoT (*10*) satellites was used to investigate the pulsations. For eight of those (HD 261737, HD 262014, HD 262209, HD 37357, NGC 2244 45, NGC 2244 183, NGC 2244 271, and NGC 2244 399), the pulsational variability was discovered in the course of this study, whereas the seismic properties for the remaining 11 objects observed from space have been described in previous work (all references are provided in the supplementary materials). Additionally, the pulsational properties for 15 stars were taken from ground-based observing campaigns reported in the literature (all references are provided in the supplementary materials).

For the determination of the fundamental parameters, we obtained high-resolution, high-signal-to-noise ratio spectra for 27 objects of our sample to complement the variability analysis; for the other seven stars, fundamental parameters were available in the literature (supplementary materials).

To put the stars' positions in the $T_{\rm eff}$ – log g plane in context to their relative evolutionary stage, we computed pre-MS evolutionary tracks with the Yale Stellar Evolution Code (YREC) (*12*) for solar metallicity (Z = 0.02) (Figs. 1 and 2). We find that our sample includes stars that gain their energy solely from gravitational contraction (stars that are on the Henyey track just before arriving on the ZAMS); stars in which incomplete nuclear burnings have started (stars that are briefly burning CN, producing the short rise in the luminosity before the star settles onto the ZAMS, as discussed above); and stars close to the ZAMS in which hydrogen-burning in the cores has already started.

In general, the stellar lifetime strongly depends on the birth mass. In the case of pre-MS stars, this dependence is manifested by the Kelvin-Helmholtz contraction time scale (*13*) rather than the nuclear time scale that rules the evolution of MS stars. The 34 pre-MS stars of our sample have masses between 1.5 and 3.0 $M_\odot$. Although this mass range is rather narrow, the differences in stellar ages at the ZAMS are substantial: A star with 3.0 $M_\odot$ needs only ~8 million years from the birthline (the point at which the star emerges from the molecular cloud and mass

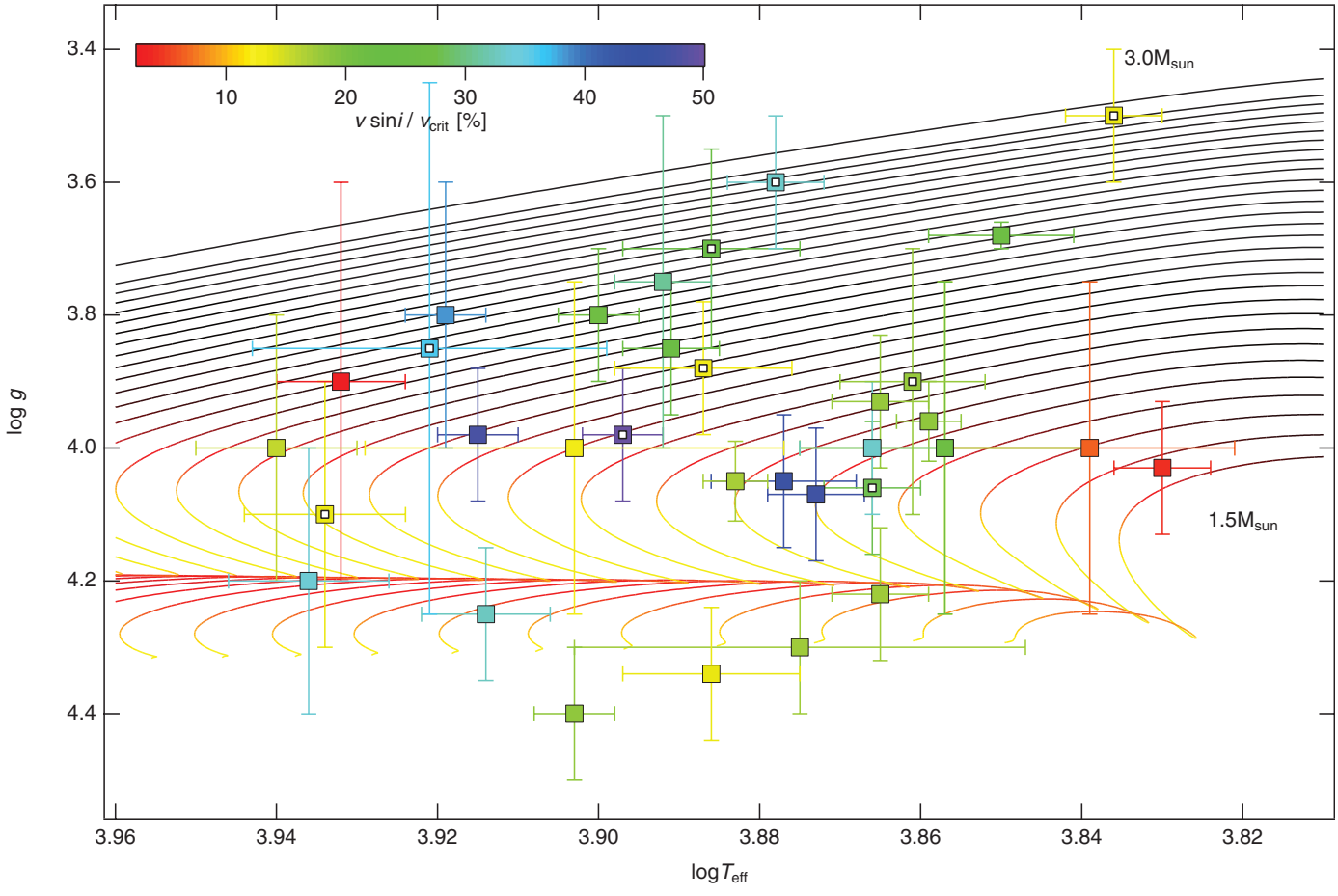

Fig. 1. Thirty-four pulsating pre-MS stars in the evolutionary diagram. Evolutionary diagram of surface gravity versus effective temperature for the 34 pulsating pre-MS stars. Symbol colors correspond to the percentage of critical breakup velocity ($v\sin i/v_{\rm crit}$) according to the scale at top left. Pre-MS evolutionary tracks (*12*) are shown from 1.5 to 3.0 $M_\odot$ in steps of 0.05 $M_\odot$ and are color-coded according to the contribution of gravitational potential energy to the total energy output: When gravitational contraction is the only energy source, the pre-MS tracks are drawn in black; the track brightness increases as the ratio of gravitational potential energy to the total energy output drops, with the onset of first nonequilibrium nuclear burnings closer to the ZAMS. The symbols marked with a white smaller square in their centers are members of the young cluster NGC 2264 labeled "A" to "I" in Figs. 2 and 3.

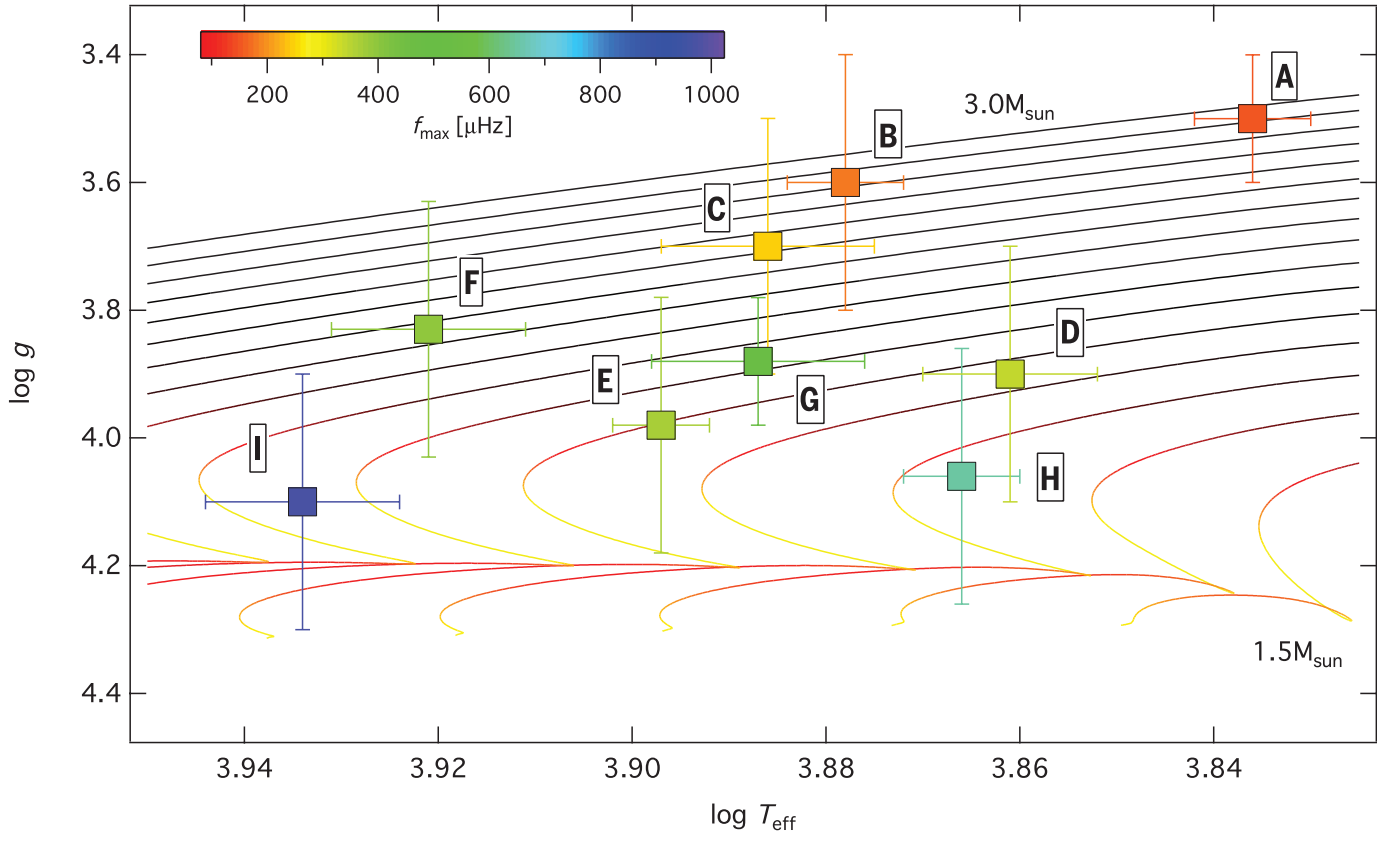

Fig. 2. NGC 2264 evolutionary diagram. Evolutionary diagram of surface gravity against effective temperature showing a subset of nine pulsating pre-MS stars in the young cluster NGC 2264: V 589 Mon, V 588 Mon, HD 261230, HD 262209, HD 261737, HD 261387, HD 262014, NGC 2264 104, and HD 261711 labeled "A" to "I." Symbol colors correspond to the highest observed p-mode frequency, f_{max}, according to the scale at top left. Pre-MS evolutionary tracks (*12*) are shown from 1.5 to 3.0 $M_{\odot}$ in steps of 0.1 $M_{\odot}$ and are color-coded according to the contribution of gravitational potential energy to the total energy output (as in Fig. 1). The amplitude spectra of these nine objects are shown in Fig. 3 using the same labels.

accretion stops) until hydrogen is ignited in its core (the arrival on the ZAMS), whereas a star with 1.5 $M_{\odot}$ has a ZAMS age of ~33 million years. The duration of the star formation process is thus strongly dependent on the mass of the pre-MS star.

The evolution of stellar rotation rates during the pre-MS phases is poorly understood. As young stars contract during their transition from the birthline to the ZAMS, stellar evolution theory predicts an increase in their rotational velocities if angular momentum is conserved (*14*). The fraction of the projected rotational velocity ($v\sin i$) over the critical breakup velocity (v_{crit}) for the 34 pre-MS stars (Fig. 1) indeed indicates the occurrence of higher rotation rates at the times of the first nuclear burning as compared with that of stars in the earlier stages. We find that the majority of the pre-MS stars in our sample rotates at a low to moderate fraction of their critical breakup velocity (fig. S3), which points to angular momentum loss by, for example, winds or star-disk coupling. Our results agree with recent results reported for Herbig Ae/Be stars in a similar mass range (*15*).

The acoustic cut-off frequency is the highest frequency of a pressure mode that can still be trapped inside the star and is therefore an important seismic characteristic. Theoretical computations for pre-MS stars predict the highest values to occur close to the ZAMS (~1000 μHz or 86.4 d^{-1}) and the lowest values (~100 μHz or 8.6 d^{-1}) close to the birthline (*16*). For high-order pressure modes, the acoustic cut-off frequency scales with the frequency of maximum power, ν_{max} (*17*). For comparison with our observational sample, we used the highest significant pressure-mode frequency, f_{max}, which is the measurable quantity in our data coming closest to the acoustic cut-off frequency computed from seismic models. Our observations indeed confirm the theoretical predictions: The coolest and least evolved stars have the lowest f_{max} values and therefore pulsate with the longest periods (fig. S4). The hottest and most evolved stars have the highest f_{max} values and pulsate with the shortest periods. A similar relation is found when we use ν_{max} derived from our data instead of f_{max}. In the present sample, f_{max} ranges from 76.47 μHz (for the star HR 5999) to 970.37 μHz (for the star HD 261711).

Our sample consists of a mixture of different types of pre-MS objects (cluster members and Herbig Ae field stars) that also have different formation histories. By taking a subsample of pulsating stars that formed from the same molecular cloud and had the same initial conditions, we reduced possible ambiguities in the interpretation. In the young open cluster NGC 2264 (*18*, *19*), nine pulsating pre-MS members were discovered with multi-epoch observations conducted with the MOST and the CoRoT space telescopes. The pulsational variability of HD 261737, HD 262014, and HD 262209 is reported for the first time in this work (supplementary materials), and the seismic properties for V 588 Mon, V 589 Mon, HD 261230, HD 261387, NGC 2264 104, and HD 261711 have been described in previous work (all references are provided in the supplementary materials). The nine pre-MS pulsators in NGC 2264 (marked as "A" through "I" in Figs. 2 and 3) have different masses and are found to be in different relative evolutionary phases. Their evolutionary tracks in conjunction with their pulsational properties (Figs. 2 and 3) illustrate that the least-evolved stars pulsate slower (V 589 Mon) than do the objects that are already located closer to the ZAMS (HD 261711). This is evidence of sequential star formation, making the assignment of a single age to this and other young open clusters unjustified. In particular, we find that the duration of the star formation process in NGC 2264 has been ongoing for much longer than the cluster age of 1 to 5 million years reported in the literature [for example, (*18*, *19*)].

A clear relation between the seismic observables and evolutionary status for the pre-MS stars emerges, even though our sample is relatively heterogeneous owing to both the mixture of field

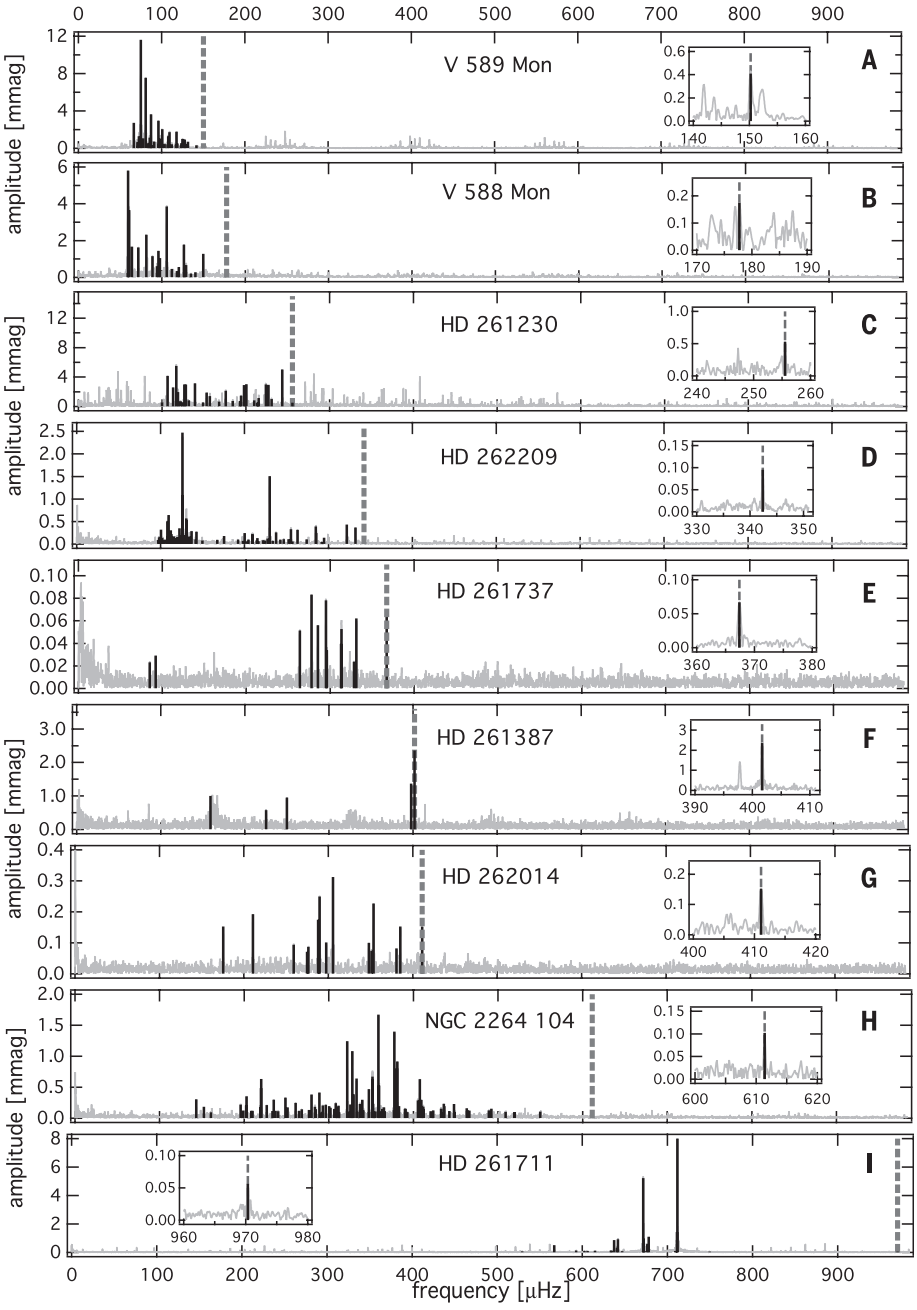

Fig. 3. NGC 2264 amplitude spectra. Sequence of amplitude spectra for a subset of nine pulsating pre-MS stars in the young cluster NGC 2264 from least evolved (V 589 Mon) to most evolved (HD 261711). In each panel, the *x* axis shows frequency in μHz, and the amplitudes on the *y* axes are given in millimagnitudes. The original amplitude spectra are shown in light gray, where all identified pulsation frequencies are marked with black solid lines. The location of the maximum pulsation frequency, f_{max}, for each star is marked with the dashed dark gray line. The small insets show the region immediately around f_{max} in order to illustrate its statistical significance.

and cluster stars of varying metallicity, as well as different precision for the available data sets. This relation is even clearer when we consider stars formed from the same birth environment, such as members of the young cluster NGC 2264. We have shown with this study that asteroseismology can discern different stages of evolution not only for dying intermediate-mass stars, as was recently found (*20*). Such observations can be similarly applied to unravel the star formation history of young stars and even deliver the relative ages of the various mass populations of pre-MS stars of young open clusters.

REFERENCES AND NOTES

1. S. W. Stahler, *Astrophys. J.* **274**, 822–829 (1983).
2. S. W. Stahler, *Astrophys. J.* **332**, 804–825 (1988).
3. F. Palla, S. W. Stahler, *Astrophys. J.* **360**, L47–50 (1990).
4. C. Hayashi, *Publ. Astron. Soc. Jpn.* **13**, 450–452 (1961).
5. L. G. Henyey, R. Lelevier, R. D. Levée, *Publ. Astron. Soc. Pac.* **67**, 154 (1955).
6. M. Suran, M. Goupil, A. Baglin, Y. Lebreton, C. Catala, *Astron. Astrophys.* **372**, 233–240 (2001).
7. K. Zwintz, *Astrophys. J.* **673**, 1088–1092 (2008).
8. K. Zwintz *et al.*, *Astrophys. J.* **729**, 20–33 (2011).
9. G. A. H. Walker *et al.*, *Publ. Astron. Soc. Pac.* **115**, 1023–1035 (2003).
10. A. Baglin, A., *The CoRoT Mission, Pre-Launch Status, Stellar Seismology and Planet Finding* ESA SP-1306, M. Fridlund, A. Baglin, J. Lochard, L. Conroy, Eds. (ESA Publications Division, Noordwijk, Netherlands, 2006).
11. G. H. Herbig, *Astrophys. J.* **4** (suppl.), 337–382 (1960).
12. D. B. Guenther *et al.*, *Astrophys. J.* **704**, 1710–1720 (2009).
13. M. Marconi, F. Palla, *Astrophys. J.* **507**, L141–L144 (1998).
14. S. W. Stahler, F. Palla, *The Formation of Stars* (Wiley-VCH, Weinheim, Germany, 2006).
15. E. Alecian *et al.*, *Mon. Not. R. Astron. Soc.* **429**, 1027–1038 (2013).
16. M. Casey, thesis, St. Mary's University, Canada (2011).
17. C. Aerts, J. Christensen-Dalsgaard, D. Kurtz, *Asteroseismology* (Springer, New York, 2010).
18. L. M. Rebull *et al.*, *Astron. J.* **123**, 1528–1547 (2002).
19. S. E. Dahm, T. Simon, *Astron. J.* **129**, 829–855 (2005).
20. T. R. Bedding *et al.*, *Nature* **471**, 608–611 (2011).

ACKNOWLEDGMENTS

Data obtained with the MOST satellite are available through the MOST Public Data Archive (http://most.astro.ubc.ca//archive.html), and data from CoRoT are available in the CoRoT Archive (http://idoc-corot.ias.u-psud.fr/index.jsp). Spectroscopic data can be obtained at the European Southern Observatory (ESO) archive (http://archive.eso.org) and the Canada-France-Hawaii Telescope (CFHT) archive (http://www3.cadc-ccda.hia-iha.nrc-cnrc.gc.ca/en/cfht). Data are also available from the public Web site: www.ster.kuleuven.be/~konstanze/science. We are grateful to the MOST and CoRoT teams for making this work possible. We thank N. Piskunov for his advice on the best usage of the SME software. The research leading to these results has received funding from the European Research Council (ERC) under the European Community's Seventh Framework Programme (FP7/2007–2013)/ERC grant agreement 227224 (PROSPERITY), from the Research Council of the KU Leuven under grant agreement GOA/2013/012, and from the Fund for Scientific Research of Flanders (FWO), Belgium, under grant agreement G.0B69.13. T.R. acknowledges partial financial support from the Presidium RAS Program "Nonstationary Phenomena in Objects of the Universe." D.G., J.M.M., A.F.J.M., and S.M.R. acknowledge the funding support of the Natural Sciences and Engineering Research Council (NSERC) of Canada. R.K. and W.W.W. are supported by the Austrian Fonds zur Förderung der wissenschaftlichen Forschung (P22691-N16) and by the Austrian Research Promotion Agency-ALR. E.P. and M.R. acknowledge financial support from the FP7 project "SPACEINN: Exploitation of Space Data for Innovative Helio- and Asteroseismology." E.M. is beneficiary of a postdoctoral grant from the Belgian Federal Science Policy Office cofunded by the Marie Curie Actions FP7-PEOPLE-COFUND2008 n246540 Mobility Grant from the European Commission. C.C. was supported by the Canadian Space Agency. E.M. is the beneficiary of a postdoctoral grant from the Belgian Federal Science Policy Office cofunded by the Marie Curie Actions FP7-PEOPLE-COFUND2008 n246540 Mobility Grant from the European Commission. Spectroscopic data were obtained with the 2.7-m telescope at McDonald Observatory, Texas; the 3.6m-telescope at La Silla Observatory under the ESO Large Programme LP185.D-0056; the CFHT (proposal CFHT2012AC003); the Cerro Tololo Inter-American Observatory 1.5-m telescope; and the Mercator Telescope (operated on the island of La Palma by the Flemish Community, at the Spanish Observatorio del Roque de los Muchachos of the Instituto de Astrofísica de Canarias) with the HERMES spectrograph, which is supported by the Funds for Scientific Research of Flanders (FWO), Belgium; the Research Council of KU Leuven, Belgium; the Fonds National Recherches Scientific (FNRS), Belgium; the Royal Observatory of Belgium, the Observatoire de Genève, Switzerland; and the Thüringer Landessternwarte Tautenburg, Germany.

SUPPLEMENTARY MATERIALS

www.sciencemag.org/content/345/6196/550/suppl/DC1
Materials and Methods
Figs. S1 to S6
Table S1
References (*21-68*)

19 March 2014; accepted 11 June 2014
Published online 3 July 2014;
10.1126/science.1253645

NOVAE

Fermi establishes classical novae as a distinct class of gamma-ray sources

The Fermi-LAT Collaboration*†

A classical nova results from runaway thermonuclear explosions on the surface of a white dwarf that accretes matter from a low-mass main-sequence stellar companion. In 2012 and 2013, three novae were detected in γ rays and stood in contrast to the first γ-ray–detected nova V407 Cygni 2010, which belongs to a rare class of symbiotic binary systems. Despite likely differences in the compositions and masses of their white dwarf progenitors, the three classical novae are similarly characterized as soft-spectrum transient γ-ray sources detected over 2- to 3-week durations. The γ-ray detections point to unexpected high-energy particle acceleration processes linked to the mass ejection from thermonuclear explosions in an unanticipated class of Galactic γ-ray sources.

The Fermi-LAT (Large Area Telescope) (*1*), launched in 2008, continuously scans the sky in γ rays, thus enabling searches for transient sources. When a nova explodes in a symbiotic binary system, the ejecta from the white dwarf surface expand within the circumstellar wind of the red giant companion, and high-energy particles can be accelerated in a blast wave driven in the high-density environment (*2*) so that variable γ-ray emission can be produced, as was detected at >100-MeV energies by the LAT in V407 Cygni 2010 (V407 Cyg) (*3*). In a classical nova, by contrast, the ejecta quickly expand beyond the confines of the compact binary into a much lower-density environment. High-energy particle acceleration could therefore be related to a bow shock driven by the ejecta in the interstellar medium or to turbulence and eventually weaker internal shocks formed in the inhomogeneous ejecta itself. The contribution of such expanding nova shells to cosmic-ray acceleration had been considered (*4*), but no predictions have so far been made for >100-MeV γ rays. The classical novae (or simply "novae" where appropriate) detected by the LAT with statistical significance of 12 to 20 σ (Table 1 and Fig. 1)—V959 Monocerotis 2012 (V959 Mon), V1324 Scorpii 2012 (V1324 Sco), and V339 Delphini 2013 (V339 Del)—were unanticipated. These observed γ rays have higher energies than nuclear line emission by radioactive decay at ~ MeV energies that remain undetected in individual novae (*5*) and ≲ 0.1-MeV emission detected in isolated cases (*6*).

V959 Mon was detected as a transient γ-ray source in June 2012 by the LAT while close (~20° separation) to the Sun (*7*) and then optically in August (*8*). Ultraviolet spectroscopy revealed an oxygen-neon nova (*9*), recognized as the class with the most massive white dwarfs (≳1.1 $M_\odot$) with massive (≳8 $M_\odot$) progenitors [e.g., (*10*)]. The expected peak visual magnitude of ~5 would have been observable with the naked eye ~50 days earlier, when the γ-ray transient was detected (*9*). V339 Del (*11*) was detected in August 2013 in a LAT-pointed observation triggered by its high optical brightness [4.3 magnitude at peak (*12*, *13*)]. Optical spectra of V339 Del suggest a carbon-oxygen nova (*14*), which are more common than the oxygen-neon types, with less massive white dwarfs evolved from ≲8 $M_\odot$ main-sequence progenitors. Optical brightening of V1324 Sco was detected in May 2012 (*15*) and found in LAT γ-ray data from June (*16*). Although the type for V1324 Sco is currently unclear, its optical spectroscopic evolution at early times (*15*) did not resemble oxygen-neon novae at similar stages. We take this to indicate that it is likely a carbon-oxygen type.

The LAT data (*13*) for the three classical novae are discussed together with an updated analysis of the originally detected symbiotic nova V407

*All authors with their affiliations appear at the end of this paper.
†Corresponding author. E-mail: teddy.cheung@nrl.navy.mil (C. C. Cheung); pierre.jean@irap.omp.eu (P. Jean); shore@df.unipi.it (S. N. Shore)

Table 1. Summary of the four novae. Tabulated are optical peak magnitudes and adopted distances from (*19*) for V407 Cyg, estimate of ~4- to 5-kpc V1324 Sco based on the maximum magnitude rate of decline relation (*17*) [notwithstanding the large uncertainties in this method (*29*)], (*9*) for V959 Mon (scaled from V1974 Cyg 1992), and (*30*) for V339 Del (scaled from OS Andromedae 1986), and observed dates of the optical peaks [unfiltered from (*3*), *V*-band, adopted, and visual magnitudes, respectively]. Positions in J2000.0 equinox (right ascension, RA; declination, Decl.), Galactic longitude (*l*) and latitude (*b*), 95% confidence localization error radius, and offset between the LAT and optical positions in units of degrees. Adopted start dates t_s (*13*) are given in Gregorian dates and modified Julian days (MJD). The γ-ray luminosities L_γ and total emitted energies were estimated with the average fluxes from the power-law fits of the >100-MeV LAT spectra integrated up to 10 GeV and durations from t_s up to the last >2 σ daily bin LAT detection. For V339 Del, the γ rays were detected for 25 days in 1-day bins (Fig. 2), but there was a hint of a detection 2 days earlier on the day of the optical peak in 0.5-day binned data (*13*), leading to a 27-day duration.

Nova	V407 Cyg 2010	V1324 Sco 2012	V959 Mon 2012	V339 Del 2013
Distance (kpc)	2.7	4.5	3.6	4.2
Peak magnitude	6.9	10.0	5*	4.3
Peak date	10.80 Mar 2010	19.96 Jun 2012	—	16.50 Aug 2013
Optical RA, Decl.	315.5409°, +45.7758°	267.7246°, −32.6224°	99.9108°, +5.8980°	305.8792°, +20.7681°
Optical *l*, *b*	86.9826°, −0.4820°	357.4255°, −2.8723°	206.3406°, +0.0754°	62.2003°, −9.4234°
LAT RA, Decl.	315.57°, +45.75°	267.72°, −32.69°	99.98°, +5.86°	305.91°, +20.78°
Optical-LAT offset	0.03°	0.07°	0.08°	0.03°
LAT error radius (95%)	0.08°	0.09°	0.18°	0.12°
t_s (date)	10 Mar 2010	15 Jun 2012	19 Jun 2012	16 Aug 2013
t_s (MJD)	55265	56093	56097	56520
Duration (days)	22	17	22	27
L_γ (10^{35} erg s^{-1})	3.2	8.6	3.7	2.6
Total energy (10^{41} erg)	6.1	13	7.1	6.0

*For V959 Mon, the optical peak magnitude of 9.4 (unfiltered) was observed ~50 days after the initial γ-ray detection, and we adopted an inferred peak of 5 magnitude (*9*).

Cyg (*3*). The γ-ray light curves of all four systems (Fig. 2) are similar, with 2- to 3-day-long peaks occurring 3 to 5 days after the initial LAT detections. The observed optical peak preceded the γ-ray peak by ~2 days in V1324 Sco (*13*, *17*) and ~6 days in V339 Del (*12*, *13*). Because the early optical light variations of the ejecta in novae are driven by line opacity changes in the ultraviolet during the expansion, the rise to peak optical brightness coincides with the maximum flux redistribution toward lower energies as the optically thick surface moves outward [see (*18*)]. The initial lack of detected γ rays could be because the ejecta are opaque and any >100-MeV emissions produced are absorbed by photon-atom interactions, with γ rays appearing only later when the density drops and the ejecta become transparent. The three novae were detected in γ rays during a time of high x-ray and ultraviolet/optical opacity. Coincidentally, the few days' delay of the γ-ray peak relative to the optical peak was also observed in V407 Cyg, but this may instead signal interactions with its red giant companion (below).

In compact classical nova binaries, typical companion separations are $a \sim 10^{11}$ cm [~100 times larger in symbiotic systems (*19*)], and expansion velocities v_{ej} at early times are many 100s to ≳1000 km s^{-1}. Thus, the ejecta reach the companion on a time scale of $t = 1000\ (a/10^{11}\ \text{cm})\ (v_{ej}/1000\ \text{km s}^{-1})^{-1}$ s (i.e., on the order of an hour or less). Modeling of the optical line profiles indicates that the spatial distribution of the ejected gas is bipolar rather than spherical in all cases, with greater extension perpendicular to the orbital plane in V959 Mon (*9*, *20*, *21*). Also, narrow absorption and emission line structures seen in optical and ultraviolet line profiles later in the expansion may be evidence of hydrodynamical instabilities and multiple ejections that may lead to the formation of strong turbulence and internal shocks within the ejecta after the ignition of the thermonuclear runaway (*22*). A clue to the physical process that causes the γ-ray emission mechanism may be the similarity of the high-energy spectral characteristics of V1324 Sco, V959 Mon, and V339 Del. Their >100-MeV spectra are all soft and can be fit with single power laws [the spectrum $N(E) \propto E^{-\Gamma}$, where N is the number of photons and E is energy] with photon indices Γ = 2.1 to 2.3, or exponentially cutoff power laws [the spectrum $N(E) \propto E^{-s}e^{-E/E_c}$, where E_c is the cutoff energy] [see (*13*), table S1, and fig. S1]. The exponentially cutoff power-law fits to the LAT data were preferred over the power-law fits at the 3.8 σ and 3.4 σ level for V959 Mon and V339 Del, respectively, but provided an insignificant improvement (2.0 σ) for V1324 Sco. Considering the uncertainties in the spectral fits, the three novae are similarly characterized by slopes s = 1.7 to 1.8, E_c ~1 to 4 GeV, and observed emission up to ~6 to 10 GeV. The total durations of the observed γ rays were also similar, being detected for 17 to 27 days at >2 σ statistical significances in daily bins (Fig. 2 and Table 1). Because the LAT-observed properties are similar, it is likely that the γ-ray emission of these classical novae has a similar origin, involving interactions of the accelerated high-energy protons (hadronic scenario) or electrons (leptonic scenario) within the ejecta.

In the hadronic scenario, high-energy protons that interact with nuclei produce neutral pions (π^0), which decay into two γ rays. For a representative hadronic model, we assume an exponentially cutoff power law distribution of

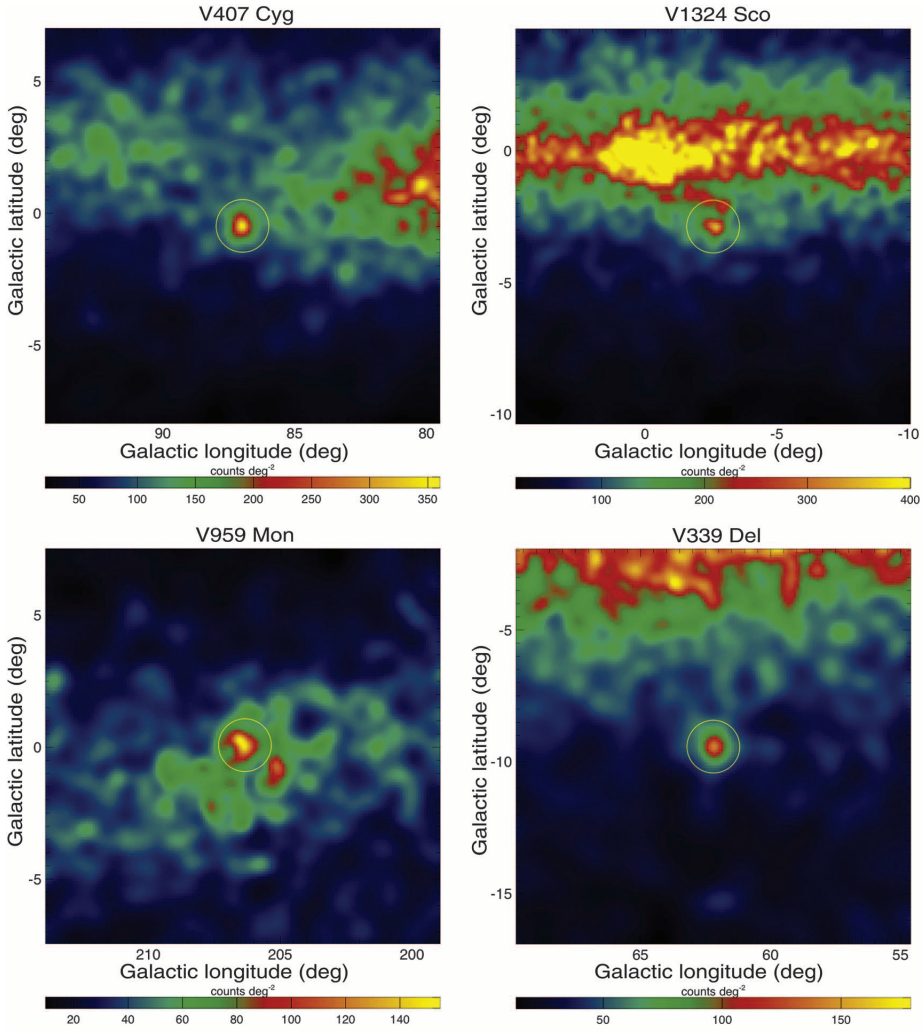

Fig. 1. Fermi-LAT >100-MeV γ-ray counts maps of the four novae in Galactic coordinates centered on the optical positions over the full 17- to 27-day durations. The maps used 0.1° by 0.1° pixels and were adaptively smoothed with a minimum number of 25 to 50 counts per kernel. Each nova (located at the centers of the yellow circles with 1° radius, which is the approximate LAT 95% containment at 1 GeV) is observed near the bright diffuse γ-ray emission in the Galactic plane, with V959 Mon in particular observed directly through the plane (0° latitude).

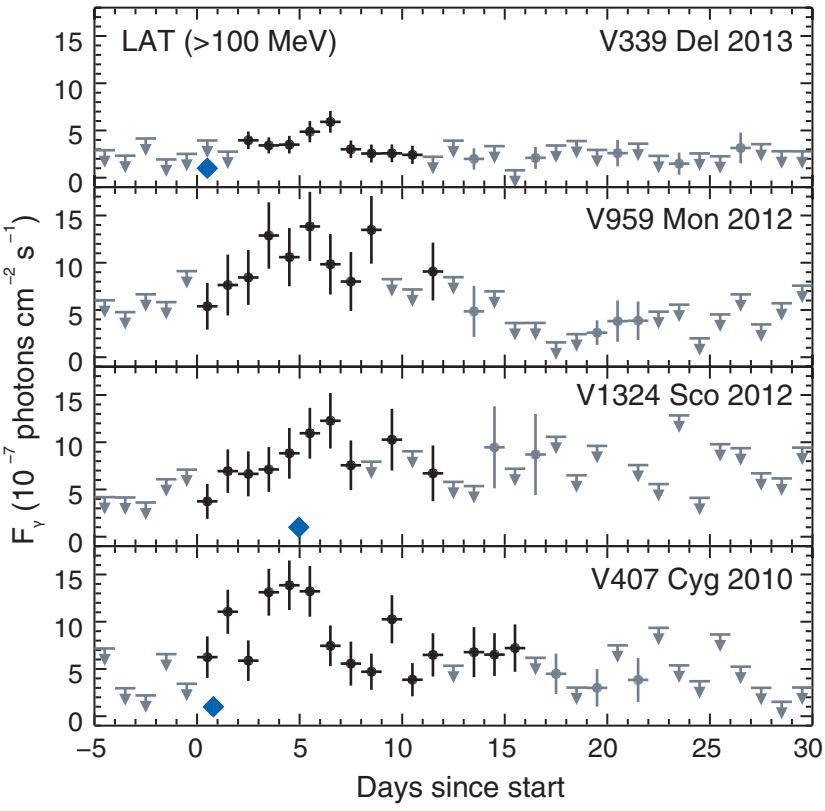

Fig. 2. Fermi-LAT 1-day binned light curves of the four γ-ray detected novae. Vertical bars indicate 1 σ uncertainties for data points with >3 σ (black) and 2 to 3 σ (gray) significances; otherwise, 2 σ upper limits are indicated with gray arrows. Start times t_s (from top to bottom panels) of 16 August 2013, 19 June 2012, 15 June 2012, and 10 March 2010 were defined as the day of the first γ-ray detection. In V339 Del, there was a 2.4 σ detection in 0.5-day binned data beginning 16.5 August (*13*), the epoch of the optical peak (blue diamond in each panel).

protons in the form $N_p\,(p_p) = N_{p,0}\,(p_p\,c)^{-S_p}\,e^{-W_p/E_{cp}}$ (proton/GeV), where p_p and W_p are the momentum and the kinetic energy of protons, respectively; $N_{p,0}$ the normalization; s_p the slope; and E_{cp} the cutoff energy. We fitted E_{cp} and s_p with the LAT spectra to obtain the best-fit π^0 models (Fig. 3). The lower limits to the cutoff energies (~3 to 30 GeV) suggest proton acceleration up to near-TeV energies. The slopes of the best-fit models of the proton spectrum have large statistical uncertainties (~0.8) but, interestingly, are compatible with a value of 2 expected in the first-order Fermi acceleration process. To match the observed γ-ray variability time scale in such a process, a magnetic field $B > 10^{-3}$ Gauss is required in a strong shock with $v_{ej} = 2000$ km s^{-1} to accelerate particles to >1 (10) GeV energies in ~0.2 (2) days. Formally, the updated best-fit proton spectrum for the symbiotic nova V407 Cyg (*3*) is parameterized by $s_p = 1.4^{+0.3}_{-0.4}$ GeV, but slopes of 2 to 2.2 are also viable at the 90% confidence level with $E_{cp} = 10^{+1.0}_{-0.7}$ GeV (*13*) (fig. S3). Lower-confidence fits were also obtained for V959 Mon and V339 Del but, conversely, with smaller slopes and lower cutoff energies (*13*) (fig. S3). Assuming that the γ-ray flux is due to the interactions of high-energy protons with the nuclei in the ejecta, the best-fit parameters allow us to estimate the total energy in high-energy protons of ~(3 to 17) × 10^{42} ergs and to derive conversion efficiencies (i.e., the ratio of the total energy in high-energy protons to the kinetic energy of the ejecta) ranging from ~0.1 to 3.7% for the classical novae and 6.6% for V407 Cyg.

In the leptonic case, accelerated electrons produce γ rays through a combination of inverse Compton scattering with low-energy photons and bremsstrahlung with atoms in the vicinity of the nova. For a leptonic model, we adopted a similar functional form for the distribution of the kinetic energy of high-energy electrons (W_e) in the form $N_e(W_e) = N_{e,0}\,W_e^{-s_e}\,e^{-W_e/E_{ce}}$ (electron/GeV) and fitted the normalization $N_{e,0}$, slope s_e, and cutoff energy E_{ce} to the LAT data for each nova (Fig. 3). The γ-ray luminosity of the calculated bremsstrahlung emission is <20% of the total γ-ray luminosity for all the novae (*13*). The best-fit parameters of the high-energy electron spectra for the three classical novae are similar within their confidence regions (*13*), with E_{ce} constrained to lie between 2 and 30 GeV and poorly constrained slopes. These models are statistically indistinguishable from the π^0 model. As in the hadronic model, the spectral parameters of the classical novae differ from those for V407 Cyg (mainly due to the lowest-energy ~200- to 300-MeV bin detected in its LAT spectrum), where the best-fit slope is negative (i.e., a positive index of the power law) and E_{ce} = 1.78 ± 0.05 GeV. The best-fit parameters for the leptonic scenario, where high-energy electrons interact primarily with the photons emitted by the nova photosphere (*23*), lead to total energies of ~(6 to 13) × 10^{41} ergs in high-energy electrons and conversion efficiencies of ~0.1 to 0.3% for the classical novae and 0.6% for the symbiotic system.

Detection of classical novae in γ rays was deemed unlikely in the past (*3*). The only nova previously detected in γ rays, the aforementioned V407 Cyg, was a rare symbiotic and likely recurrent [only 10 recurrent novae are known, of which 4 are symbiotic types (*24*)]. In the symbiotic novae, conditions are conducive for high-energy particle acceleration as the portion of the ejecta moving into the wind in the direction of the dense medium provided by the red giant companion decelerates within a few days. The γ rays peak early, when the efficiency for hadron and lepton acceleration is presumably favorable, with the red giant wind playing a key role in the γ-ray production (*2*, *23*). In contrast, the main-sequence star companions in the classical novae do not provide similarly dense target material; hence, it is likely that other dissipative processes are involved in particle acceleration and generation of the observed γ rays.

Because the γ-ray properties of the novae detected so far by the Fermi-LAT appear similar to one another, and their underlying properties are unremarkable, it appears that all novae can be considered to be candidate γ-ray emitters. Their detection by the LAT may imply close proximity and that other optical novae not yet detected with the LAT [e.g., (*25*)] are more distant and have fainter optical peaks [without considering extinction uncertainties (*26*)]. Indeed, all the LAT-detected novae have estimated distances of ≲4 to 5 kpc (Table 1). Despite systematic uncertainties in the adopted distances, it is interesting that the inferred mean γ-ray luminosities and total emitted energies of the novae span a small range ~(3 to 4) × 10^{35} ergs s^{-1} and ~(6 to 7) × 10^{41} ergs, respectively, except for the ~2 times

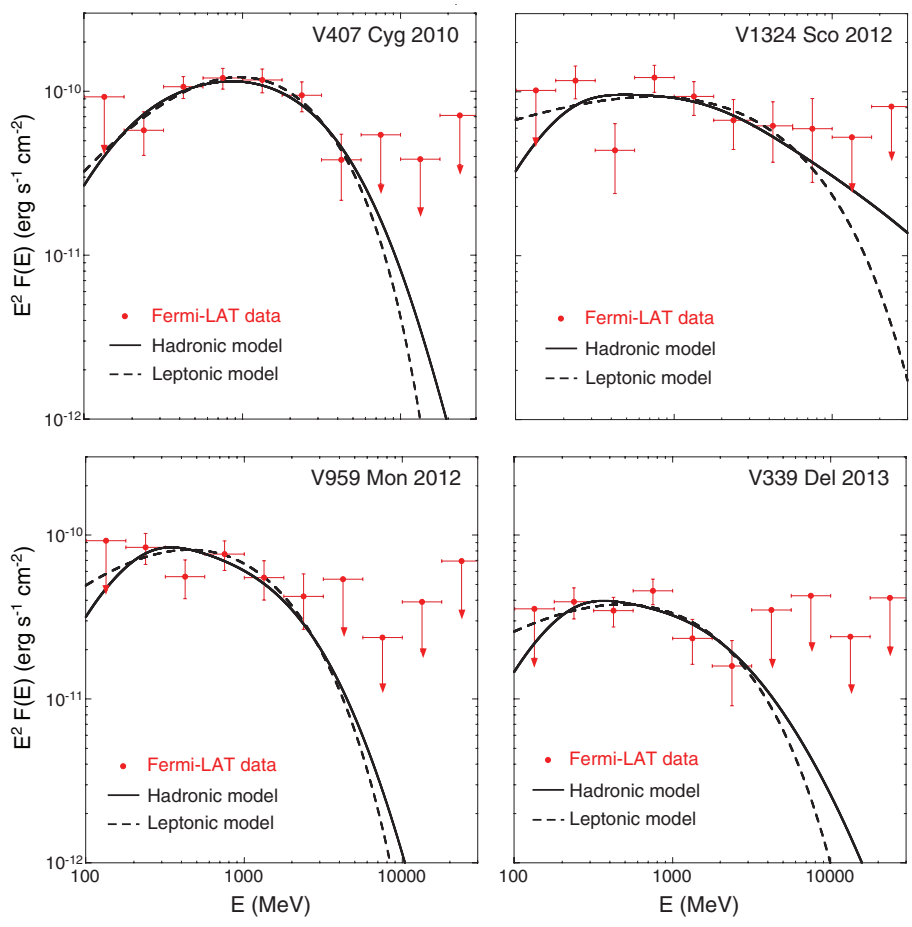

Fig. 3. Fermi-LAT >100-MeV average γ-ray spectra of the four novae over the full 17- to 27-day durations. Vertical bars indicate 1 σ uncertainties for data points with significances >2 σ otherwise, arrows indicate 2 σ limits. The best-fit hadronic and leptonic model curves are overlaid.

greater values for V1324 Sco, whose distance is highly uncertain.

The rate of novae in the Milky Way is highly uncertain, but considering a plausible range of ~20 to 50 per year (*27*) and reasonable spatial distributions in the Galactic bulge and disk (*28*), our estimate is 1 to 4 per year at ≲4- to 5-kpc distances. The γ-ray detection rate of novae averages roughly one per year over the time span of these observations (~5 years), consistent with the lower end of this extrapolation.

Although the γ-ray properties of the LAT-detected novae are similar, we emphasize the small and subtle differences that imply different emission mechanisms—e.g., the spectral shape of V407 Cyg compared with the three classical novae as well as the apparent higher energy extension of the V1324 Sco spectrum. Among the classical novae detected so far, they also appear different optically. The γ-ray emission mechanism and high-energy particle acceleration processes associated with the novae could depend on the particular system properties that remain to be investigated, such as the white dwarf mass, which determines the explosion energetics (ejected mass and expansion velocity), and the mass transfer dictated by the companion mass and separation.

REFERENCES AND NOTES

1. W. B. Atwood *et al.*, *Astrophys. J.* **697**, 1071–1102 (2009).
2. V. Tatischeff, M. Hernanz, *Astrophys. J.* **663**, L101–L104 (2007).
3. A. A. Abdo *et al.*, *Science* **329**, 817–821 (2010).
4. V. L. Ginzburg, S. I. Syrovatskii, *The Origin of Cosmic Rays* (Macmillan, New York, 1964), pp. 200–202.
5. M. Hernanz, in *Classical Novae*, M. F. Bode, A. Evans, Eds. (Cambridge Univ. Press, Cambridge, ed. 2, 2008) p. 252.
6. D. Takei *et al.*, *Astrophys. J.* **697**, L54–L57 (2009).
7. C. C. Cheung, E. Hays, T. Venters, D. Donato, R. H. D. Corbet, Fermi-LAT Collaboration, *The Astronomer's Telegram* **4224**, 1 (2012).
8. S. Fujikawa, International Astronomical Union Central Bureau for Astronomical Telegrams, reported by M. Soma, no. 3202 (2012).
9. S. N. Shore *et al.*, *Astron. Astrophys.* **553**, A123 (2013).
10. S. Starrfield, W. M. Sparks, J. W. Truran, *Astrophys. J.* **303**, L5 (1986).
11. K. Itagaki, International Astronomical Union Central Bureau for Astronomical Telegrams, reported by S. Nakano, no. 3628 (2013).
12. E. Hays, T. Cheung, S. Ciprini; Fermi-LAT collaboration, *The Astronomer's Telegram* **5302**, 1 (2013).
13. Supplementary materials are available on *Science* Online.
14. S. N. Shore, P. Skoda, P. Rutsch, *The Astronomer's Telegram* **5282**, 1 (2013).
15. R. M. Wagner *et al.*, *The Astronomer's Telegram* **4157**, 1 (2012).
16. C. C. Cheung, T. Glanzman, A. B. Hill, Fermi-LAT Collaboration, *The Astronomer's Telegram* **4284**, 1 (2012).
17. A. B. Hill, Fermi-LAT collaboration, in 4th Fermi Symposium, Monterey CA, eConf C121028, 112 (2012), 28 October to 2 November 2012.
18. S. N. Shore, *Bull. Astron. Soc. India* **40**, 185–191 (2012).
19. U. Munari, R. Margoni, R. Stagni, *Mon. Not. R. Astron. Soc.* **242**, 653 (1990).
20. V. A. R. M. Ribeiro, U. Munari, P. Valisa, *Astrophys. J.* **768**, 49 (2013).
21. G. H. Herbig, J. I. Smak, *Acta Astronomica.* **42**, 17–28 (1992).
22. J. Casanova, J. José, E. García-Berro, S. N. Shore, A. C. Calder, *Nature* **478**, 490–492 (2011).
23. P. Martin, G. Dubus, *Astron. Astrophys.* **551**, A37 (2013).
24. B. E. Schaefer, *Astrophys. J. Suppl. Ser.* **187**, 275–373 (2010).
25. C. C. Cheung, Fermi-LAT collaboration, in 4th Fermi Symposium, Monterey CA, eConf C121028, 106 (2012), 28 October to 2 November 2012.
26. K. Mukai, http://asd.gsfc.nasa.gov/Koji.Mukai/novae/novae.html, September 4, 2013 version.
27. A. W. Shafter, *Astrophys. J.* **487**, 226–236 (1997).
28. P. Jean, M. Hernanz, J. Gómez-Gomar, J. José, *Mon. Not. R. Astron. Soc.* **319**, 350–364 (2000).
29. M. M. Kasliwal *et al.*, *Astrophys. J.* **735**, 94 (2011).
30. S. N. Shore, *The Astronomer's Telegram* **5410**, 1 (2013).

ACKNOWLEDGMENTS

The Fermi-LAT Collaboration acknowledges support for LAT development, operation, and data analysis from NASA and the Department of Energy (United States), CEA/Irfu and IN2P3/CNRS (France), Agenzia Spaziale Italiana and INFN (Italy), MEXT, KEK, and JAXA (Japan), and the K. A. Wallenberg Foundation, the Swedish Research Council, and the National Space Board (Sweden). Science analysis support in the operations phase from INAF (Italy) and CNES (France) is also gratefully acknowledged. We acknowledge with thanks the variable star observations from the American Association of Variable Star Observers International Database contributed by observers worldwide and used in this research and the dedicated observers of the Astronomical Ring for Access to Spectroscopy (ARAS) group for their tireless and selfless efforts. C.C.C. was supported at the Naval Research Laboratory by a Karles' Fellowship and by NASA through DPR S-15633-Y and Guest Investigator programs 11-FERMI11-0030 and 12-FERMI12-0026. S.S. was supported by NASA and NSF grants to Arizona State University. The Fermi-LAT data reported in this paper are available from http://fermi.gsfc.nasa.gov/ssc/data/access.

The Fermi-LAT Collaboration

M. Ackermann,[1] M. Ajello,[2] A. Albert,[3] L. Baldini,[4] J. Ballet,[5] G. Barbiellini,[6,7] D. Bastieri,[8,9] R. Bellazzini,[4] E. Bissaldi,[10] R. D. Blandford,[3] E. D. Bloom,[3] E. Bottacini,[3] T. J. Brandt,[11] J. Bregeon,[12] P. Bruel,[13] R. Buehler,[1] S. Buson,[8,9] G. A. Caliandro,[3,14] R. A. Cameron,[3] M. Caragiulo,[15] P. A. Caraveo,[16] E. Cavazzuti,[17] E. Charles,[3] A. Chekhtman,[18‡] C. C. Cheung,[19†] J. Chiang,[3] G. Chiaro,[9] S. Ciprini,[17,20] R. Claus,[3] J. Cohen-Tanugi,[12] J. Conrad,[21,22,23,24] S. Corbel,[5,25] F. D'Ammando,[26,27] A. de Angelis,[28] P. R. den Hartog,[3] F. de Palma,[15] C. D. Dermer,[19] R. Desiante,[6,29] S. W. Digel,[3] L. Di Venere,[30] E. do Couto e Silva,[3] D. Donato,[31,32] P. S. Drell,[3] A. Drlica-Wagner,[33] C. Favuzzi,[30,15] E. C. Ferrara,[11] W. B. Focke,[3] A. Franckowiak,[3] L. Fuhrmann,[34] Y. Fukazawa,[35] P. Fusco,[30,15] F. Gargano,[15] D. Gasparrini,[17,20] S. Germani,[36,37] N. Giglietto,[30,15] F. Giordano,[30,15] M. Giroletti,[26] T. Glanzman,[3] G. Godfrey,[3] I. A. Grenier,[5] J. E. Grove,[19] S. Guiriec,[11,38] D. Hadasch,[39] A. K. Harding,[11] M. Hayashida,[40] E. Hays,[11] J. W. Hewitt,[41,31] A. B. Hill,[42,3,43] X. Hou,[44] P. Jean,[45,46†] T. Jogler,[3] G. Jóhannesson,[47] A. S. Johnson,[3] W. N. Johnson,[19] M. Kerr,[48] J. Knödlseder,[45,46] M. Kuss,[4] S. Larsson,[21,22,49] L. Latronico,[50] M. Lemoine-Goumard,[44,51] F. Longo,[6,7] F. Loparco,[30,15] B. Lott,[44] M. N. Lovellette,[19] P. Lubrano,[36,37] A. Manfreda,[4] P. Martin,[46] F. Massaro,[52] M. Mayer,[1] M. N. Mazziotta,[15] J. E. McEnery,[11,32] P. F. Michelson,[3] W. Mitthumsiri,[53,3] T. Mizuno,[54] M. E. Monzani,[3] A. Morselli,[55] I. V. Moskalenko,[3] S. Murgia,[56] R. Nemmen,[11,31,41] E. Nuss,[12] T. Ohsugi,[54] N. Omodei,[3] M. Orienti,[26] E. Orlando,[3] J. F. Ormes,[57] D. Paneque,[58,3] J. H. Panetta,[3] J. S. Perkins,[11] M. Pesce-Rollins,[4] F. Piron,[12] G. Pivato,[9] T. A. Porter,[3] S. Rainò,[30,15] R. Rando,[8,9] M. Razzano,[4,59] S. Razzaque,[60] A. Reimer,[39,3] O. Reimer,[39,3] T. Reposeur,[44] P. M. Saz Parkinson,[61,62] M. Schaal,[63‡] A. Schulz,[1] C. Sgrò,[4] E. J. Siskind,[64] G. Spandre,[4] P. Spinelli,[30,15] Ł. Stawarz,[65,66] D. J. Suson,[67] H. Takahashi,[35] T. Tanaka,[68] J. G. Thayer,[3] J. B. Thayer,[3] D. J. Thompson,[11] L. Tibaldo,[3] M. Tinivella,[4] D. F. Torres,[69,70] G. Tosti,[36,37] E. Troja,[11,32] Y. Uchiyama,[71] G. Vianello,[3] B. L. Winer,[72] M. T. Wolff,[19] D. L. Wood,[73‡] K. S. Wood,[19] M. Wood,[3] S. Charbonnel,[74] R. H. D. Corbet,[31,41] I. De Gennaro Aquino,[75,76] J. P. Edlin,[77] E. Mason,[78] G. J. Schwarz,[79] S. N. Shore,[4,75†] S. Starrfield,[80] F. Teyssier[81]

[1]Deutsches Elektronen Synchrotron DESY, D-15738 Zeuthen, Germany. [2]Department of Physics and Astronomy, Clemson University, Kinard Lab of Physics, Clemson, SC 29634-0978, USA. [3]W. W. Hansen

Experimental Physics Laboratory, Kavli Institute for Particle Astrophysics and Cosmology, Department of Physics and SLAC National Accelerator Laboratory, Stanford University, Stanford, CA 94305, USA. [4]Istituto Nazionale di Fisica Nucleare, Sezione di Pisa, I-56127 Pisa, Italy. [5]Laboratoire AIM, CEA-IRFU/CNRS/Université Paris Diderot, Service d'Astrophysique, CEA Saclay, 91191 Gif sur Yvette, France. [6]Istituto Nazionale di Fisica Nucleare, Sezione di Trieste, I-34127 Trieste, Italy. [7]Dipartimento di Fisica, Università di Trieste, I-34127 Trieste, Italy. [8]Istituto Nazionale di Fisica Nucleare, Sezione di Padova, I-35131 Padova, Italy. [9]Dipartimento di Fisica e Astronomia "G. Galilei", Università di Padova, I-35131 Padova, Italy. [10]Istituto Nazionale di Fisica Nucleare, Sezione di Trieste, and Università di Trieste, I-34127 Trieste, Italy. [11]NASA Goddard Space Flight Center, Greenbelt, MD 20771, USA. [12]Laboratoire Univers et Particules de Montpellier, Université Montpellier 2, CNRS/IN2P3, Montpellier, France. [13]Laboratoire Leprince-Ringuet, École polytechnique, CNRS/IN2P3, Palaiseau, France. [14]Consorzio Interuniversitario per la Fisica Spaziale (CIFS), I-10133 Torino, Italy. [15]Istituto Nazionale di Fisica Nucleare, Sezione di Bari, 70126 Bari, Italy. [16]INAF-Istituto di Astrofisica Spaziale e Fisica Cosmica, I-20133 Milano, Italy. [17]Agenzia Spaziale Italiana (ASI) Science Data Center, I-00133 Roma, Italy. [18]Center for Earth Observing and Space Research, College of Science, George Mason University, Fairfax, VA 22030, USA. [19]Space Science Division, Naval Research Laboratory, Washington, DC 20375-5352, USA. [20]Istituto Nazionale di Astrofisica, Osservatorio Astronomico di Roma, I-00040 Monte Porzio Catone (Roma), Italy. [21]Department of Physics, Stockholm University, AlbaNova, SE-106 91 Stockholm, Sweden. [22]The Oskar Klein Centre for Cosmoparticle Physics, AlbaNova, SE-106 91 Stockholm, Sweden. [23]Royal Swedish Academy of Sciences Research Fellow, funded by a grant from the K. A. Wallenberg Foundation. [24]The Royal Swedish Academy of Sciences, Box 50005, SE-104 05 Stockholm, Sweden. [25]Institut Universitaire de France, 75005 Paris, France. [26]INAF Istituto di Radioastronomia, 40129 Bologna, Italy. [27]Dipartimento di Astronomia, Università di Bologna, I-40127 Bologna, Italy. [28]Dipartimento di Fisica, Università di Udine and Istituto Nazionale di Fisica Nucleare, Sezione di Trieste, Gruppo Collegato di Udine, I-33100 Udine. [29]Università di Udine, I-33100 Udine, Italy. [30]Dipartimento di Fisica "M. Merlin" dell'Università e del Politecnico di Bari, I-70126 Bari, Italy. [31]Center for Research and Exploration in Space Science and Technology (CRESST) and NASA Goddard Space Flight Center, Greenbelt, MD 20771, USA. [32]Department of Physics and Department of Astronomy, University of Maryland, College Park, MD 20742, USA. [33]Fermilab, Batavia, IL 60510, USA. [34]Max-Planck-Institut für Radioastronomie, Auf dem Hügel 69, 53121 Bonn, Germany. [35]Department of Physical Sciences, Hiroshima University, Higashi-Hiroshima, Hiroshima 739-8526, Japan. [36]Istituto Nazionale di Fisica Nucleare, Sezione di Perugia, I-06123 Perugia, Italy. [37]Dipartimento di Fisica, Università degli Studi di Perugia, I-06123 Perugia, Italy. [38]NASA Postdoctoral Program Fellow, USA. [39]Institut für Astro- und Teilchenphysik and Institut für Theoretische Physik, Leopold-Franzens-Universität Innsbruck, A-6020 Innsbruck, Austria. [40]Institute for Cosmic-Ray Research, University of Tokyo, 5-1-5 Kashiwanoha, Kashiwa, Chiba, 277-8582, Japan. [41]Department of Physics and Center for Space Sciences and Technology, University of Maryland Baltimore County, Baltimore, MD 21250, USA. [42]School of Physics and Astronomy, University of Southampton, Highfield, Southampton SO17 1BJ, UK. [43]Funded by a Marie Curie IOF, FP7/2007-2013 grant agreement no. 275861. [44]Centre d'Études Nucléaires de Bordeaux Gradignan, IN2P3/CNRS, Université Bordeaux 1, BP120, F-33175 Gradignan Cedex, France. [45]CNRS, IRAP, F-31028 Toulouse cedex 4, France. [46]GAHEC, Université de Toulouse, UPS-OMP, IRAP, Toulouse, France. [47]Science Institute, University of Iceland, IS-107 Reykjavik, Iceland. [48]CSIRO Astronomy and Space Science, Australia Telescope National Facility, Epping NSW 1710, Australia. [49]Department of Astronomy, Stockholm University, SE-106 91 Stockholm, Sweden. [50]Istituto Nazionale di Fisica Nucleare, Sezione di Torino, I-10125 Torino, Italy. [51]Funded by contract ERC-StG-259391 from the European Community. [52]Department of Astronomy, Department of Physics, and Yale Center for Astronomy and Astrophysics, Yale University, New Haven, CT 06520–8120, USA. [53]Department of Physics, Faculty of Science, Mahidol University, Bangkok 10400, Thailand. [54]Hiroshima Astrophysical Science Center, Hiroshima University, Higashi-Hiroshima, Hiroshima 739-8526, Japan. [55]Istituto Nazionale di Fisica Nucleare, Sezione di Roma "Tor Vergata", I-00133 Roma, Italy. [56]Center for Cosmology, Physics and Astronomy Department, University of California, Irvine, CA 92697-2575, USA. [57]Department of Physics and Astronomy, University of Denver, Denver, CO 80208, USA. [58]Max-Planck-Institut für Physik, D-80805 München, Germany. [59]Funded by contract FIRB-2012-RBFR12PM1F from the Italian Ministry of Education, University and Research (MIUR). [60]Department of Physics, University of Johannesburg, P.O. Box 524, Auckland Park 2006, South Africa. [61]Santa Cruz Institute for Particle Physics, Department of Physics and Department of Astronomy and Astrophysics, University of California at Santa Cruz, Santa Cruz, CA 95064, USA. [62]Department of Physics, The University of Hong Kong, Pokfulam Road, Hong Kong, China. [63]National Research Council Research Associate, National Academy of Sciences, Washington, DC 20001, USA.. [64]NYCB Real-Time Computing Inc., Lattingtown, NY 11560-1025, USA. [65]Institute of Space and Astronautical Science, Japan Aerospace Exploration Agency, 3-1-1 Yoshinodai, Chuo-ku, Sagamihara, Kanagawa 252-5210, Japan. [66]Astronomical Observatory, Jagiellonian University, 30-244 Kraków, Poland. [67]Department of Chemistry and Physics, Purdue University Calumet, Hammond, IN 46323-2094, USA. [68]Department of Physics, Graduate School of Science, Kyoto University, Kyoto, Japan. [69]Institut de Ciències de l'Espai (IEEE-CSIC), Campus UAB, 08193 Barcelona, Spain. [70]Institució Catalana de Recerca i Estudis Avançats (ICREA), Barcelona, Spain. [71]3-34-1 Nishi-Ikebukuro, Toshima-ku, Tokyo 171-8501, Japan. [72]Department of Physics, Center for Cosmology and Astro-Particle Physics, The Ohio State University, Columbus, OH 43210, USA. [73]Praxis Inc., Alexandria, VA 22303, USA. [74]Durtal Observatory, 6 Rue des Glycines, F-49430 Durtal, France. [75]Dipartimento di Fisica "Enrico Fermi", Università di Pisa, Pisa I-56127, Italy. [76]Hamburger Sternwarte, Gojenbergsweg 112, 21029, Hamburg, Germany. [77]Ammon, ID 83401, USA. [78]INAF Osservatorio Astronomico di Trieste, Via G. B. Tiepolo 11, 34131 Trieste, Italy. [79]American Astronomical Society, 2000 Florida Ave NW, Washington, DC 20009–1231, USA. [80]School of Earth and Space Exploration, Arizona State University, P.O. Box 871404, Tempe, AZ 85287–1404, USA. [81]67 Rue Jacques Daviel, Rouen 76100, France. ‡Resident at Naval Research Laboratory, Washington, DC 20375, USA.

SUPPLEMENTARY MATERIALS

www.sciencemag.org/content/345/6196/554/suppl/DC1
Materials and Methods
Supplementary Text
Figs. S1 to S6
Tables S1 to S4
References (*31*–*48*)

26 March 2014; accepted 20 June 2014
10.1126/science.1253947

QUANTITATIVE SOCIAL SCIENCE

A network framework of cultural history

Maximilian Schich,[1,2,3]* Chaoming Song,[4] Yong-Yeol Ahn,[5] Alexander Mirsky,[2] Mauro Martino,[3] Albert-László Barabási,[3,6,7] Dirk Helbing[2]

The emergent processes driving cultural history are a product of complex interactions among large numbers of individuals, determined by difficult-to-quantify historical conditions. To characterize these processes, we have reconstructed aggregate intellectual mobility over two millennia through the birth and death locations of more than 150,000 notable individuals. The tools of network and complexity theory were then used to identify characteristic statistical patterns and determine the cultural and historical relevance of deviations. The resulting network of locations provides a macroscopic perspective of cultural history, which helps us to retrace cultural narratives of Europe and North America using large-scale visualization and quantitative dynamical tools and to derive historical trends of cultural centers beyond the scope of specific events or narrow time intervals.

Quantifying historical developments is crucial to understanding a large variety of complex processes from population dynamics to disease spreading, conflicts, and urban evolution. However, in historical research there is an inherent tension (*1*, *2*) between qualitative analyses of individual historical accounts and quantitative approaches aiming to measure and model more general patterns. We believe that these approaches are complementary: We need quantitative methods to identify statistical regularities, as well as qualitative approaches to explain the impact of local deviations from the uncovered general patterns. We have therefore developed a data-driven macroscopic perspective that offers a combination of both approaches.

We collected data from Freebase.com (FB) (*3*), the General Artist Lexicon (AKL) (*4*–*6*), and the Getty Union List of Artist Names (ULAN) (*7*), representing spatiotemporal birth and death information of notable individuals, spanning a time period of more than two millennia. The data sets are included in the supplementary materials (SM), accompanied by an explanation of their nature and data preparation (*8*) (tables S1 and S2). Potential sources of bias are addressed in the SM, including biographical, temporal, and spatial coverage; curated versus crowd-sourced data; increasing numbers of individuals who are still alive; place aggregation; location name changes and spelling variants; and effects of data set language. Most important, compared with contemporary worldwide migration flux (*9*), our data sets focus on birth-to-death migration within and out of Europe and North America (see fig. S1). Notability of individuals, simply defined as the curatorial decision of inclusion in the respective data set, differs slightly between the more

[1]School of Arts and Humanities, The University of Texas at Dallas, Richardson, TX 75080, USA. [2]Chair of Sociology, in particular of Modeling and Simulation (SOMS), Eidgenössische Technische Hochschule (ETH) Zurich, CH-8092 Zurich, Switzerland. [3]Center for Complex Network Research, Department of Physics, Biology and Computer Science, Northeastern University, Boston, MA 02115, USA. [4]Department of Physics, University of Miami Coral Gables, Coral Gables, FL 33146, USA. [5]School for Informatics and Computing, Indiana University Bloomington, Bloomington, IN 47405, USA. [6]Department of Medicine, Harvard Medical School, and Center for Cancer Systems Biology, Dana-Farber Cancer Institute, Boston, MA 02115, USA. [7]Center for Network Science, Central European University, Budapest 1052, Hungary.
***Corresponding author. E-mail: maximilian.schich@utdallas.edu**

current, partly crowd-sourced FB and the expert-curated AKL and ULAN.

There was sufficient data density for historical studies: In each data set, the number of notable individuals with birth and death locations provides substantially more data points over time than the commonly used estimates of the world population before the 20th century (Fig. 1A and fig. S2). Even though death locations are underreported (e.g., 153,000 out of 1.1 million in AKL), the data density was sufficient to construct heat maps or Lexis surfaces (*10*), as used in demography, to reveal death age (ir)regularities during more than five centuries, which enables us to highlight the impact of wars and varying longevity (compare Fig. 1B and fig. S3 for details).

We next added a spatial dimension by plotting the number of deaths versus births in each location (Fig. 1C and fig. S4). The plot distinguishes locations where notable people tended to be born (birth sources) from locations where they tended to die (death attractors). Both long-lived and short-lived death locations were observed, with the short-lived locations representing plane crash

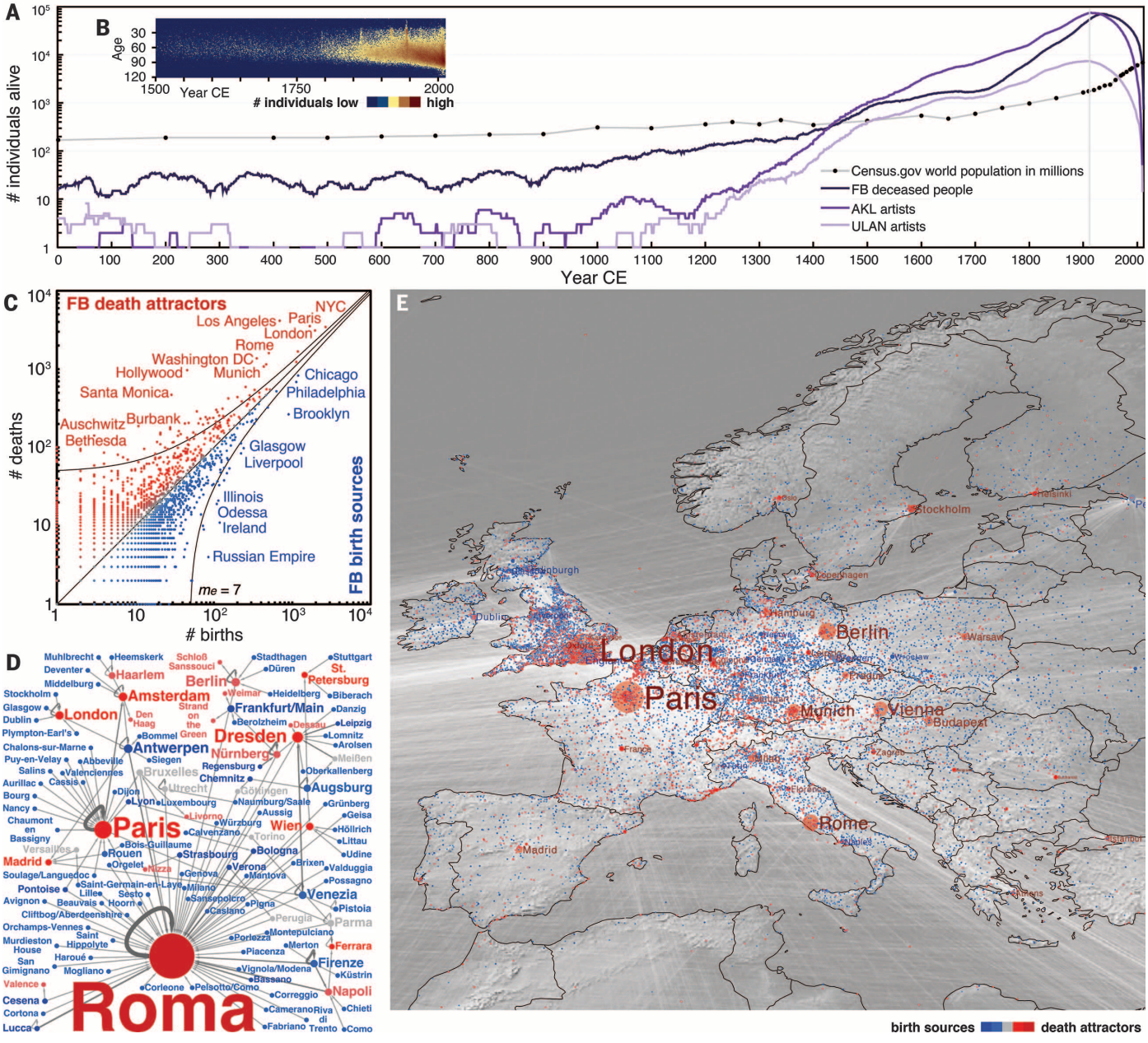

Fig. 1. Birth and death data of notable individuals reveal interactions between culturally relevant locations over two millennia. (**A**) Notable individuals with birth and death locations, alive in a given year from 1 to 2012 CE, for the FB, AKL, and ULAN databases shown together with the estimated world population (in millions, i.e., divided by 10^6 to compare the slope, compare fig. S2). As the data sets grow by orders of magnitude, fluctuations smooth out, allowing for quantification to complement qualitative inquiry. AKL and ULAN grow exponentially with the emancipation of artists around 1200. The decrease after the gray line is due to the fact that we only record individuals with known birth and death dates, and at recent times, more individuals are not yet dead or recorded (details on known biases are in the SM). (**B**) Demographic life table for FB indicating death age frequency from 1500 to 2012 CE (compare fig. S3 for detail). (**C**) Birth-death scatter plot for locations in FB, cumulated over all time with outliers colored as birth sources (blue) and death attractors (red) (see figs. S4 and S13 for dynamics, significance, and further data sets). (**D**) Illustration of birth-death flows of antiquarians in the 18th century, based on the Winckelmann Corpus (*11*), using the color scheme of the scatter plot above. (**E**) Migration in Europe based on FB, with node size corresponding to PageRank (compare figs. S5 to S7 for detail, further regions, and data sets).

sites, battlefields, or concentration camps. We found outliers, where the imbalance of births and deaths results in significant deviations from the diagonal (as defined in the SM under Birth-Death Imbalance). Indeed, highly significant outliers, like Hollywood, had more than 10 times as many deaths as births.

When individual birth and death locations are connected, the resulting network reveals a consistent pattern of cultural attraction and interaction in space. For example, several hundred antiquarians in the 18th century (with data derived from the Winckelmann Corpus) (*11*), died in a number of relevant cultural centers such as Rome, Paris, or Dresden, even though they had been born all over Europe (Fig. 1D; see SM).

We also constructed a worldwide historical migration network, connecting 37,062 locations via the birth-death data of 120,211 individuals in the FB data set from King David in 1069 BCE to Poppy Barlow in 2012 CE (see fig. S5). On a map of Europe (Fig. 1E), the distribution of colors reveals a differentiated landscape of sources (blue, more births) and attractors (red, more deaths). The sizes of nodes represent their importance, estimated by their PageRank, calculated from the underlying migration network (*12*). We chose PageRank, one of the most popular centrality measures, as it offers clear advantages over other centrality measures (compare SM under PageRank versus Eigenvector Centrality), as well as a simple analogy, where every death counts as a vote for the target location, in the same way that hyperlinks are considered as a vote for their target Web site. We find that the PageRank hierarchy intuitively reflects the hierarchy of urban population size (*13*). Yet, although PageRank correlated reasonably well with the number of births in locations ($r = 0.74$), and even better with the number of deaths ($r = 0.97$), it did not predict the imbalance of births and deaths ($r = 0.34$): Large attractive locations, such as London, Paris, or Rome were complemented by many small attractors, e.g., at the French Riviera or both sides of the Alps. Other highly ranked locations, such as Edinburgh or Dublin, were more fertile than deadly, as was most of rural Europe. Additional regions and data sets with similar conclusions are presented in figs. S5 to S7.

The numbers of notable individuals $N(t)$ and locations $S(t)$ grew exponentially over time (Fig. 2A and fig. S8). Yet, the difference in growth rates for individuals (r) and locations (s) implies an underlying Heaps' law (*14*) $S(t) \approx N(t)^{\alpha}$, where $\alpha = s/r \approx 0.9$. The sublinear exponent $\alpha < 1$ indicates that, in the long run, the growth of already existing attractive locations for notable individuals dominates over the emergence of new attractive locations.

The probability distributions of birth locations f_B and death locations f_D, or birth-to-death paths $f_{B \to D}$, follow Zipf's law (Fig. 2B and figs. S9 and S10) (*15*). The nature of the frequency distributions was highly consistent over several centuries, whereas the slopes for birth and death changed gradually over time (Fig. 2B and fig. S10, G to I). To our surprise, the slopes for births and deaths started to differ significantly from the 19th century onward in FB and even earlier for artists in AKL. The difference indicates that larger cultural centers attract a greater proportion of notable individuals, in line with recently discovered urban scaling laws (*16*, *17*). We used an established method to fit a power law to the data to obtain the scaling exponents (*18*). We further confirmed the significant difference between f_B and f_D, using a two-sample Kolmogorov-Smirnov (KS) test comparing birth and death distributions directly (see. fig. S10J).

The distribution of birth-to-death distances Δr changed very little during more than eight centuries (Fig. 2C and fig. S11). The median distance from birth to death has not even doubled between the 14th and the 21st centuries (214 km and 382 km, respectively), with a minimum of 135 km in the 17th century (see vertical lines in Fig. 2C). Only long-range mobility, captured by the tail of the probability distribution $P(\Delta r)$, changed because of the gradual colonization of the world and increasing traffic between the U.S. coasts. As such, these results are consistent with Ravenstein's laws of migration (*19*, *20*), formulated in the late 19th century, and other empirical observations of human mobility in geography, demography, and sociology, from Zipf's intercity movement of persons (*21*) to modern census statistics (*22*) and measurements based on tracking dollar bills or mobile phones (*23*, *24*). Our findings are nevertheless relevant, as (i) we can determine these patterns from a relatively small fraction of birth and death location pairs, and (ii) we demonstrate that the patterns hold for more than eight centuries on an international scale that is not divided by country boundaries.

Aside from these global patterns, we find considerable instabilities on a local level over the order of centuries. The death share, or the relative fraction of notable deaths in specific locations, was highly unstable over centuries (Fig. 2D and fig. S12). This local instability confirms recent expectations regarding the rise and fall of populations in top-ranked cities (*13*, *16*, *25*) but also points to substantial amounts of noise in the system (*26*).

Adding another aspect of local instability, the dynamics of birth-death imbalance for

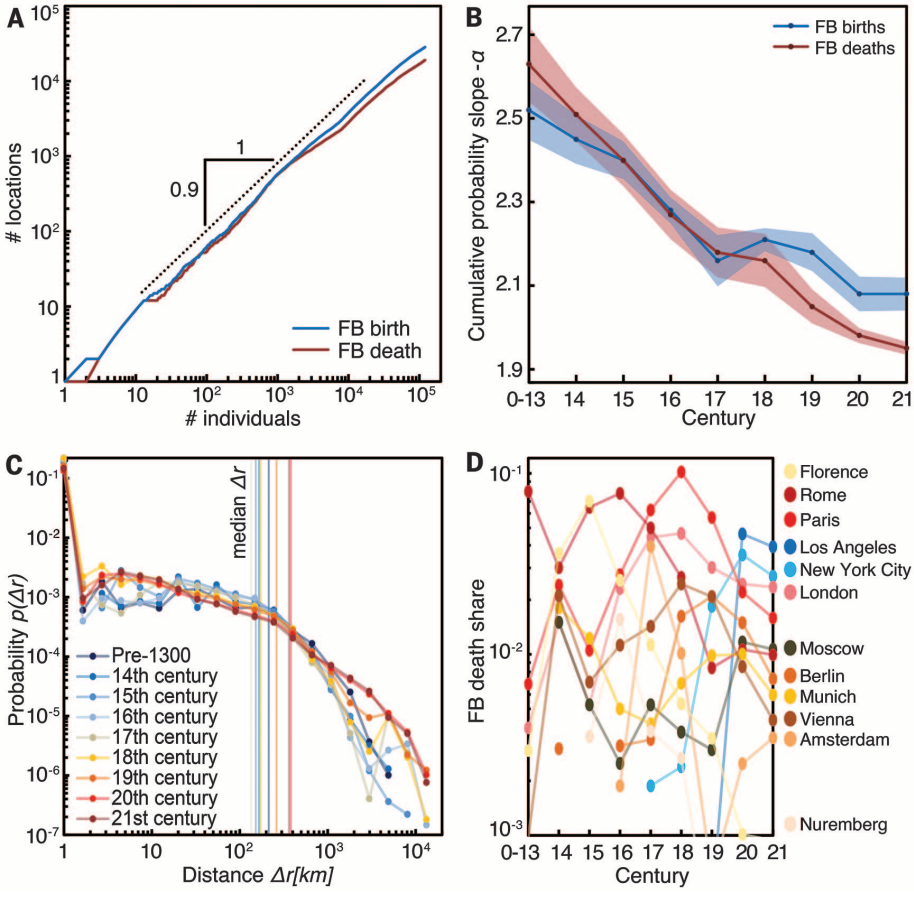

Fig. 2. Birth-death networks provide historical evidence for global patterns and local instabilities in human mobility dynamics. (**A**) The number $N(t)$ of individuals as a function of the number $S(t)$ of locations, where $\alpha = 0.9$ (compare fig. S8 for other data sets). (**B**) Cumulative probability distribution slopes for birth and death frequency in FB locations from before 1300 to 2012 CE. The shaded area indicates the uncertainty of the slope (*18*) (see fig. S10, G to J, for detail and other data sets). (**C**) The fat-tailed distribution of birth-to-death distances Δr in FB exhibits little change over time from before 1300 to 2012 CE (compare fig. S11). (**D**) The relative death share and, consequently, rank of major FB locations over centuries from before 1300 to 2012 CE (compare fig. S12).

individual locations over centuries are tracked in fig. S13, measured as multiples m_e of the square-root-deviation e from the perfectly balanced diagonal in Fig. 1C and fig. S4. In fact, individual locations fluctuate substantially in this respect, as in the case of New York City, which is now a clear death attractor but gave birth to more notable individuals than it attracted around 1920.

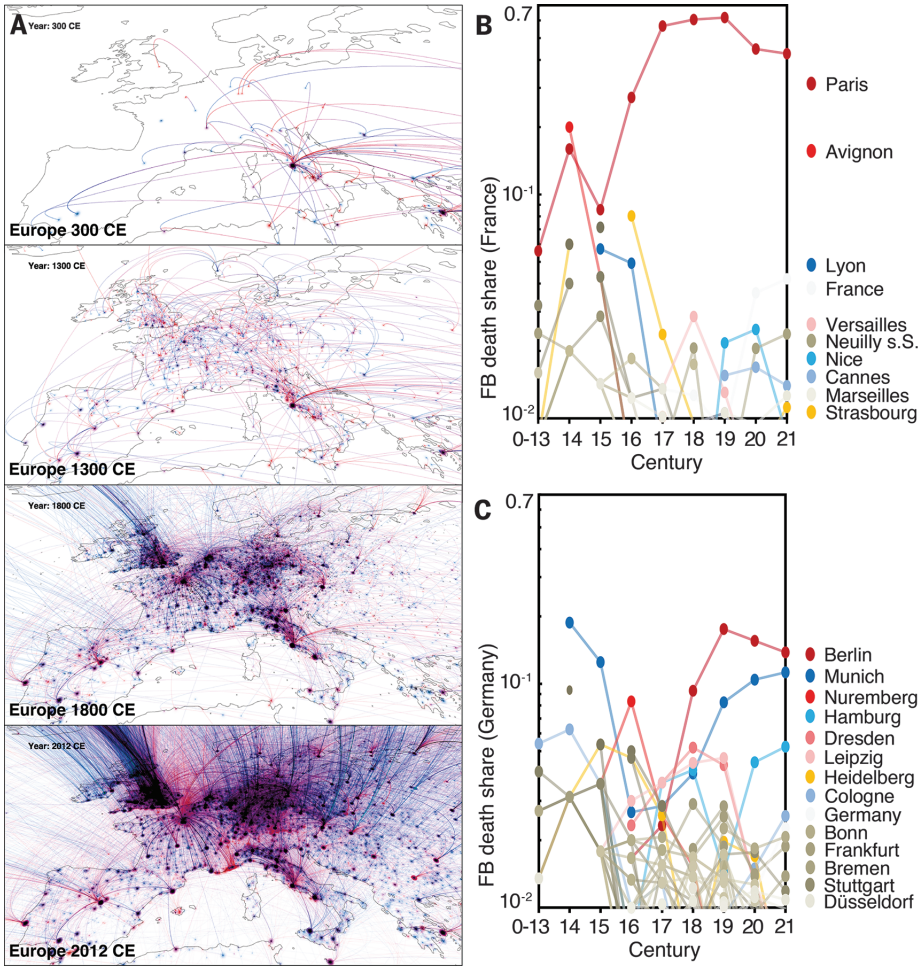

Fig. 3. The visualization of birth-death network dynamics offers a meta-narrative of cultural history. (**A**) A sequence of frames, based on movie S1, exemplifies the FB narrative for Europe from Roman times to the present. The dynamically applied color scheme (with black and white inverted in print) denotes birth-death imbalance (blue to red) (compare Fig. 1C). In the supplementary movie, individuals appear as particles, indicating collective directions of flow as they move toward their death locations. Throughout the movie, local cohesive dynamics emerge regionally in addition to the massive long-range interactions, first from and to Rome and eventually to emergent country capitals and economic centers, including those in the East. The final network state for locations in 2012—within what is now France and Germany—is the result of massive centralization toward Paris versus multicentric competition in Germany. (**B** and **C**) Death-share plots for locations from before 1300 to 2012 CE confirm that France is characterized by a winner-takes-all regime, where Paris takes in a substantial and almost constant share of notable individuals (*27*). Germany, in contrast, is characterized by a subcritical fit-gets-richer regime, where no center surpasses 19% in any given century.

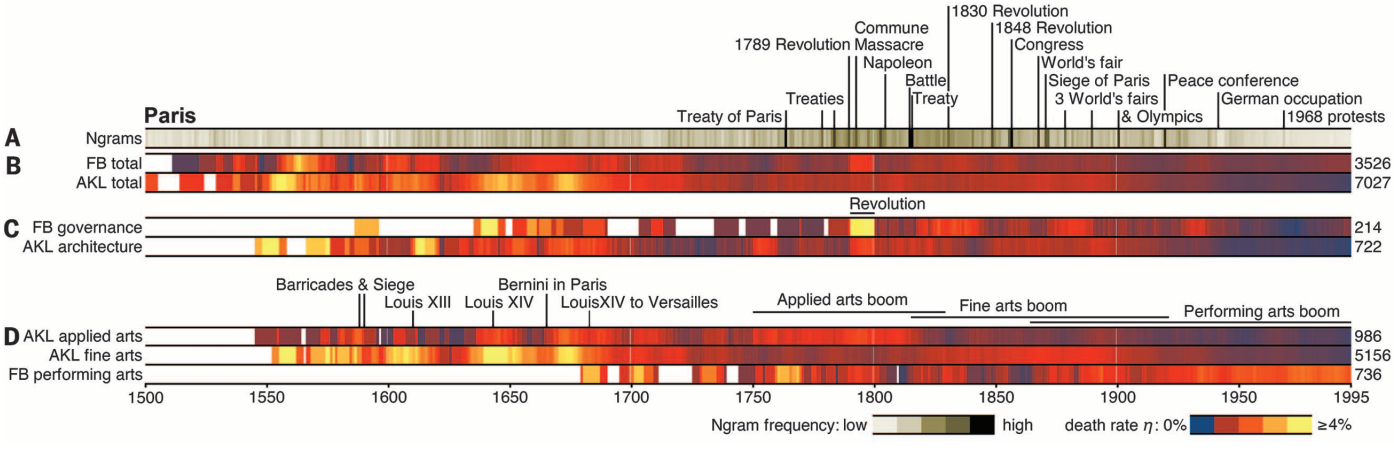

Fig. 4. Temporal death rate patterns in cultural centers reveal midterm trends that are hard to extract from other sources. (**A**) English Google Ngram trajectory for the pattern "Paris in {year}" from 1500 to 1995 CE. Dark spikes point to outstanding historical events in the city, labeled semi-automatically using Web searches, such as "Paris in 1763" returning "Treaty of Paris." (**B**) Paris death rate trajectories for FB total and AKL total indicate deviations from the nearly constant fitness $\eta_i^D(t)$ (compare fig. S16 and our model in the SM). Color indicates periods of accelerated (bright) versus slower growth (dark). The numbers at the ends of the trajectories indicate the respective number of individuals. (**C**) Trajectories for FB governance and AKL architecture positively correlate around the French Revolution from 1785 to 1805 (r = 0.89), whereas FB governance and artists in AKL fine arts slightly negatively correlate (r = −0.34). (**D**) Trajectories for AKL applied arts, AKL fine arts, and FB performing arts.

Next, we illustrate the qualitative relevance of our macroscopic perspective by delineating the meta-narratives of European and North American cultural history, based on birth-death data without additional source material (movies S1 and S2, Fig. 3A, and fig. S14). The sequence of images in Fig. 3A exemplifies the cultural narrative of Europe from 0 to 2012 CE, as presented in movie S1 based on FB: In the beginning, a pan-European elite defined Rome as the center of its empire via massive long-range interactions, followed by increasing point-to-point migration throughout Europe, where Rome remained a hub along with rising subcenters, such as Cordova and Paris. Starting in the 16th century, data density in Europe becomes sufficient to reveal regional clusters. In fact, it becomes evident that Europe is characterized by two radically different cultural regimes: A winner-takes-all regime, with massive centralization toward centers such as Paris, and a fit-gets-richer regime, where many subcenters compete with each other in federal clusters throughout Central Europe and Northern Italy (*27*) (see Fig. 3, B and C, and fig. S15).

After demonstrating the global quantitative and qualitative relevance of our macroscopic approach, we now focus on the dynamics of individual cultural centers, defined as locations with substantial amounts of notable deaths. We examined notable events identified from the Google Ngram English data set (*28*), a procedure that can and should be complemented with data sets in other languages to allow for comparison and eventually worldwide coverage (known biases are discussed in the SM). Recording the frequency of words and word combinations in an estimated 5% of all books ever published, the Google Ngram data were originally used to plot the pattern frequency against book publication dates (*29*). Here, instead, we obtained events by searching for the pattern "{location} in {year}," which allows us to map the "expression" of cultural centers over longer time periods, similar to a gene expression plot (*30*) (Fig. 4A). Particularly after 1750, dark spikes in the trajectory reveal outstanding historical events. Web searches even allow us to semiautomatically add event labels to these spikes. The resulting Ngram trajectories can be examined relative to total death rate trajectories (Fig. 4B and fig. S16), tracking deviations of locations from their nearly constant fitness $\eta_i^D(t)$ (compare fig. S17 and our model in the SM), and even relative to births and deaths within professional genres in FB, AKL, and ULAN (Fig. 4, C and D). By revealing such correlated changes and continuities, our approach allows for cross-fertilization of domain knowledge into other domains, periods, and geographic areas.

REFERENCES AND NOTES

1. R. L. Carneiro, *The Muse of History and the Science of Culture* (Springer, New York, 2000).
2. L. Spinney, *Nature* **488**, 24–26 (2012).
3. Freebase.com: A community-curated database of well-known people, places, and things (Google, Mountain View, CA, 2011); www.freebase.com.
4. A. Beyer, S. Bénédicte, W. Tegethoff, Eds., *Allgemeines Künstlerlexikon (AKL). Die Bildenden Künstler aller Zeiten und Völker* (De Gruyter, Berlin, 1991, rev. ed. 2010).
5. U. Thieme, F. Becker, Eds., *Allgemeines Lexikon der bildenden Künstler von der Antike bis zur Gegenwart* (Seemann, Leipzig, 1907, rev. ed. 1950).
6. H. Vollmer, Ed., *Allgemeines Lexikon der bildenden Künstler des XX. Jahrhunderts* (Seemann, Leipzig, 1953, rev. eds. 1962 and 1980).
7. Getty Vocabulary Program, *Union List of Artist Names* (The J. Paul Getty Trust, Los Angeles, 2010); www.getty.edu/research/tools/vocabularies/ulan/.
8. Materials and methods are available as supplementary materials on *Science* Online.
9. G. J. Abel, N. Sander, *Science* **343**, 1520–1522 (2014).
10. N. Keiding, *Philos. Trans. R. Soc.* **332**, 487–509 (1990).
11. Winckelmann-Gesellschaft Stendal, Eds., Corpus der antiken Denkmäler, die J.J. Winckelmann und seine Zeit kannten [database] (Biering & Brinkmann, München, 2000).
12. S. Brin, L. Page, *Comput. Netw. ISDN Syst.* **30**, 107–117 (1998).
13. M. Batty, *Nature* **444**, 592–596 (2006).
14. H. S. Heaps, *Information Retrieval: Computational and Theoretical Aspects* (Academic Press, Waltham, MA, 1978).
15. G. K. Zipf, *Human Behavior and the Principle of Least Effort: An Introduction to Human Ecology* (Addison-Wesley, Boston, 1949).
16. L. M. A. Bettencourt, J. Lobo, D. Helbing, C. Kühnert, G. B. West, *Proc. Natl. Acad. Sci. U.S.A.* **104**, 7301–7306 (2007).
17. L. M. A. Bettencourt, J. Lobo, D. Strumsky, G. B. West, *PLOS ONE* **5**, e13541 (2010).
18. A. Clauset, C. R. Shalizi, M. E. J. Newman, *SIAM Rev.* **51**, 661–703 (2009).
19. E. G. Ravenstein, *J. Stat. Soc. Lond.* **48**, 167–235 (1885).
20. E. G. Ravenstein, *J. R. Stat. Soc.* **52**, 241–305 (1889).
21. G. K. Zipf, *Am. Sociol. Rev.* **11**, 677–686 (1946).
22. P. Ren, *Lifetime Mobility in the United States: 2010* (U.S. Census Bureau, U.S. Department of Commerce, Washington, DC, 2011).
23. D. Brockmann, L. Hufnagel, T. Geisel, *Nature* **439**, 462–465 (2006).
24. C. Song, T. Koren, P. Wang, A.-L. Barabási, *Nat. Phys.* **6**, 818–823 (2010).
25. D. R. White, T. Laurent, N. Kejzar, in *Globalization as Evolutionary Process: Modeling Global Change*, G. Modelski, T. Devezas, W. R. Thompson, Eds. (Routledge, Milton Park, UK, 2007), pp. 190–225.
26. N. Blumm *et al.*, *Phys. Rev. Lett.* **109**, 128701 (2012).
27. G. Bianconi, A.-L. Barabási, *Phys. Rev. Lett.* **86**, 5632–5635 (2001).
28. Google Ngram English data set, version 20090715 (Google, Mountain View, 2009); http://storage.googleapis.com/books/ngrams/books/datasetsv2.html.
29. J.-B. Michel *et al.*, *Science* **331**, 176–182 (2011).
30. M. J. Hawrylycz *et al.*, *Nature* **489**, 391–399 (2012).

ACKNOWLEDGMENTS

We are grateful to Verlag Walther De Gruyter (AKL), The Getty Research Institute (ULAN), and Biering and Brinkmann (WCEN) for making data available to us and for allowing all data needed to replicate the conclusions of the paper to be available as SM. We furthermore thank our collaborators at BarabásiLab and ETH SOMS for discussions and comments on the manuscript. The work of M.S. was partially supported by German Research Foundation (DFG) grant (no. SCHI 1065/2-1) and The University of Texas at Dallas Arts and Technology (ATEC) Fellowship no. 1. D.H. is grateful for partial support by the European Research Council Advanced Investigator Grant "Momentum" (grant no. 324247).

SUPPLEMENTARY MATERIALS

www.sciencemag.org/content/345/6196/558/suppl/DC1
Materials and Methods
Figs. S1 to S17
Tables S1 and S2
References (*31*–*61*)
Movies S1 and S2
External Databases S1 to S4

6 May 2013; accepted 13 June 2014
10.1126/science.1240064

DINOSAUR EVOLUTION

Sustained miniaturization and anatomical innovation in the dinosaurian ancestors of birds

Michael S. Y. Lee,[1,2]* Andrea Cau,[3,4] Darren Naish,[5] Gareth J. Dyke[5,6]

Recent discoveries have highlighted the dramatic evolutionary transformation of massive, ground-dwelling theropod dinosaurs into light, volant birds. Here, we apply Bayesian approaches (originally developed for inferring geographic spread and rates of molecular evolution in viruses) in a different context: to infer size changes and rates of anatomical innovation (across up to 1549 skeletal characters) in fossils. These approaches identify two drivers underlying the dinosaur-bird transition. The theropod lineage directly ancestral to birds undergoes sustained miniaturization across 50 million years and at least 12 consecutive branches (internodes) and evolves skeletal adaptations four times faster than other dinosaurs. The distinct, prolonged phase of miniaturization along the bird stem would have facilitated the evolution of many novelties associated with small body size, such as reorientation of body mass, increased aerial ability, and paedomorphic skulls with reduced snouts but enlarged eyes and brains.

The evolution of birds from bipedal carnivorous dinosaurs is one of the most compelling examples of macroevolution (*1*–*7*). Numerous studies (*1*–*18*) have documented the cumulative evolution of avian characteristics along the ~160 million year (My) lineage leading from large Triassic theropods (oldest widely accepted records, *Herrerasaurus* and *Eodromaeus*, ~230 million years old) to modern birds (Neornithes; oldest widely accepted record, *Vegavis*, ~67 million years old). Nevertheless, there remain many intriguing questions regarding size and anatomical evolution along the bird stem lineage. Theropods were typically large to gigantic, but small body size characterized all taxa near the origin of forewing-powered flight in birds [Avialae *sensu* (*1*–*3*), Aves *sensu* (*15*)]. It has been both proposed (*4*–*8*) and contested (*9*–*11*) that sustained trends of size reduction occurred within theropod evolution. However, most

previous studies of size evolution along the bird stem lineage identified trends anecdotally and used undated cladograms or supertrees, along with parsimony-based character reconstructions [e.g., (*4*–*9*, *14*)] that ignore vital temporal (branch length) information, which potentially compromise accuracy (*19*). The only studies to use quantitative likelihood approaches in an explicitly temporal framework (*15*, *16*) focused on identifying individual branches undergoing fast changes [e.g., Coelurosauria and Paraves (*6*–*8*, *15*, *16*)] and thus did not evaluate directional trends (sustained miniaturization or gigantism) across consecutive branches. Furthermore, rates of anatomical innovation along the bird stem lineage remain underexplored. Most previous studies have evaluated evolutionary rates of a few continuous characters, such as limb proportions or body size (*6*, *11*, *15*, *16*, *19*). However, evolutionary innovation is arguably much better represented by the hundreds of discrete anatomical traits (from across the entire phenotype) that typically make up large phylogenetic data sets.

Here, we identify distinct evolutionary dynamics (sustained miniaturization and accelerated skeletal innovation) in the bird stem lineage, using the most character-rich anatomical data set for dinosaurs compiled to date (*20*) [data set 1, expanded from (*21*): 120 taxa, 1549 skeletal characters, including autapomorphies and invariant characters]. We also analyzed a second matrix (data set 2: 100 taxa, 421 characters) that uses a smaller number of characters but that has been iteratively scrutinized by numerous workers (*22*), based on (*8*, *23*). Stratigraphic age and femur length were recorded for all adequately known taxa (*20*). The femur is frequently preserved and scales more tightly with inferred body mass than any other measurement (*24*) [correlation coefficient (r) > 0.995], exhibiting homogenous allometry at least within nonavialan theropods (*6*). It is thus often used as a size proxy [e.g., (*9*, *11*, *15*, *24*)] and yields estimates highly consistent with volumetric (*14*) and composite (*16*) estimates. Accordingly, we use femur length as a size proxy up to Avialae [but not beyond (*6*): see supplementary materials (SM), part B]; use of multimeasurement proxies would greatly reduce taxon sampling.

[1]Earth Sciences Section, South Australian Museum, North Terrace, Adelaide 5000, Australia. [2]School of Earth and Environmental Sciences, University of Adelaide 5005, Australia. [3]Museo Geologico e Paleontologico "Giovanni Capellini," Via Zamboni 63, 40126 Bologna, Italy. [4]Dipartimento di Scienze Biologiche, Geologiche e Ambientali, Alma Mater Studiorum Università di Bologna, 40126 Bologna, Italy. [5]Ocean and Earth Science, University of Southampton, Southampton SO14 3ZH, UK. [6]MTA-DE Lendület Behavioural Ecology Research Group, Department of Evolutionary Zoology and Human Biology, University of Debrecen, 4032 Debrecen, Egyetem tér 1, Hungary.
***Corresponding author. E-mail: mike.lee@samuseum.sa.gov.au**

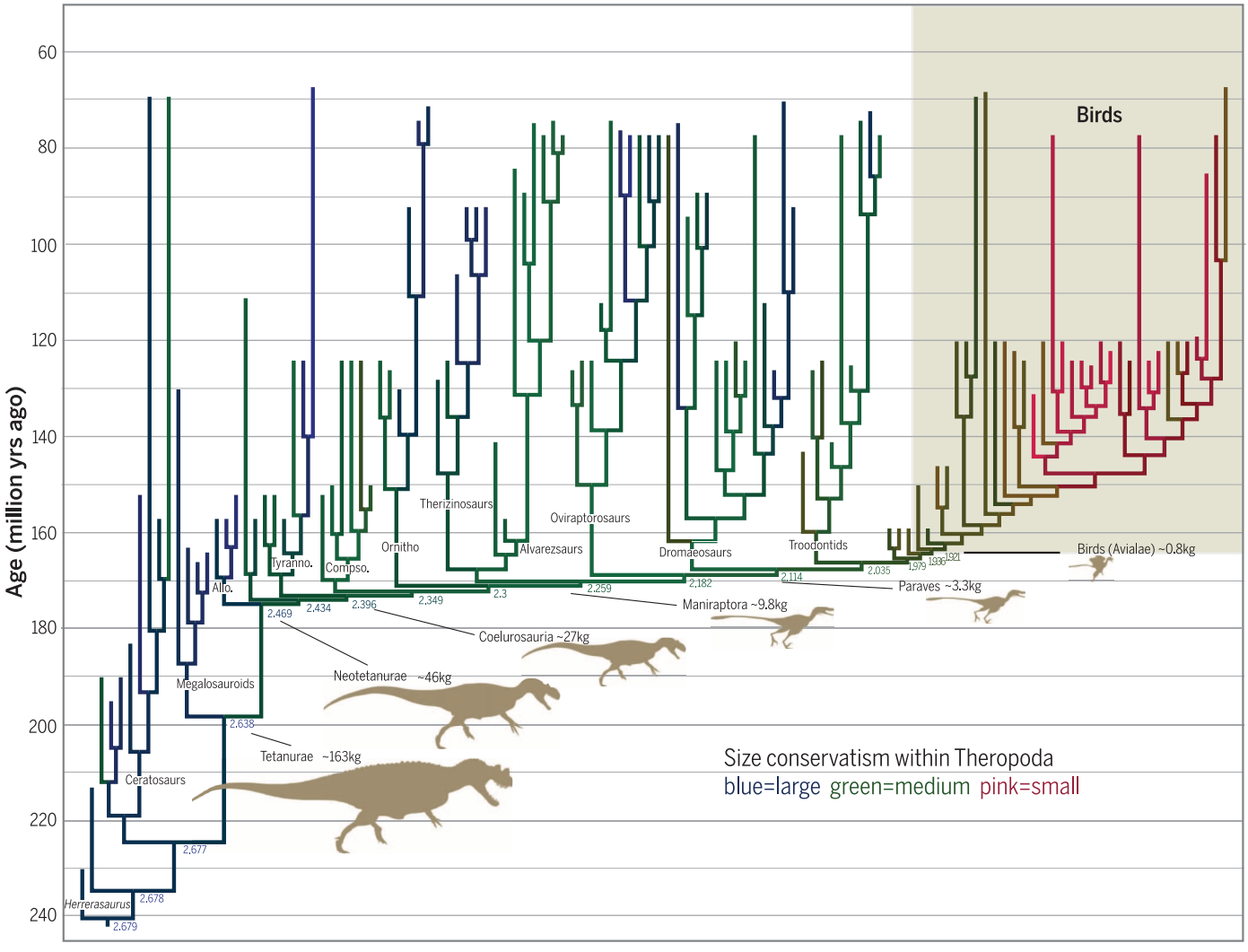

Fig. 1. Body size is highly conserved within theropod dinosaurs; birds and their closest relatives are consistently small. Bayesian maximum clade credibility consensus tree and size reconstructions from data set 1: Branches are colored according to inferred body size (indexed by $\log_{10}$ femur length), with ancestral values for nodes along the bird stem lineage shown. All taxon names and size values for all nodes and tips are in fig. S1; posterior probabilities of all clades are in fig. S2. Parsimony analysis reveals similar conservatism (fig. S8), as do Bayesian and parsimony analyses of data set 2 (*22*, *23*) (figs. S5 and S9). Abbreviations: Allo, Allosauroids; Tyranno, Tyrannosauroids; Compso, Compsognathids; Ornitho, Ornithomimosaurs.

The anatomical, stratigraphic, and size data were simultaneously analyzed using Bayesian inference: BEAST (*25*) modules originally developed for inferring patterns of DNA evolution and geographic spread in "real-time" virus samples were adapted to infer patterns of anatomical evolution and size changes in the "deep-time" fossil record. Bayesian Markov Chain Monte Carlo (MCMC) methods were thus used to reconstruct—with confidence intervals—phylogenetic relations, divergence dates, temporal duration of lineages, evolutionary rates across all 1549 (data set 1) or 421 (data set 2) morphological characters, as well as body size at every ancestral node. This approach explicitly considers the temporal (stratigraphic) distribution of taxa when estimating all these variables. Furthermore, all parameters were simultaneously estimated and thus jointly optimized. Such an approach has been argued to be better for finding global optima and estimating uncertainty (*25*, *26*) and thus preferable to the sequential inference typical of earlier approaches (*4*–*10*): inferring topology first, then sometimes inferring divergence dates, and then optimizing the trait of interest. A stochastic Markov model was applied to the discrete character data, with Bayes factors favoring inclusion of parameters for among-trait (gamma) and among-lineage (relaxed clock) rate variation. An undirected Brownian motion model was applied to the continuous (size) data. Tests for directionality using phylogenetic generalized least squares (PGLS) methods [as implemented in BayesTraits (*27*)] confirmed no significant trends toward size increase or decrease across Theropoda as a whole (*9*, *10*, *28*) (SM, part D, and fig. S7), whereas rate-heterogeneous diffusion models proved overparameterized (SM, part C). The significance and robustness of retrieved patterns was corroborated using both (i) simpler parsimony methods for inferring phylogeny and ancestral body sizes (which have been argued to entail fewer assumptions, but are consequently less powerful, and do not adequately measure uncertainty) and (ii) parametric simulations (SM, part E).

Body size, indexed by $\log_{10}$ femur length (FL_{10}), is highly phylogenetically conserved across theropods (Fig. 1 and fig. S1), and there is a prolonged, directional trend in size reduction that spans at least 50 million years and encompasses the entire bird stem lineage from the very base of Theropoda, with rapid decreases in 12 consecutive branches from Tetanurae onward (Fig. 2). The ancestral tetanuran is inferred to be ~198 million years old and ~163 kg, and size then decreases along subsequent nodes as follows; neotetanurans/avetheropods [~174 million years ago (Ma), ~46 kg], coelurosaurs (~173 Ma, ~27 kg), maniraptorans (~170 Ma, ~10 kg), paravians (~167.5 Ma, ~3 kg), and birds (~163 Ma, ~0.8 kg). A similar trend is found for data set 2: FL_{10} again continuously decreases across all bird stem nodes from Tetanurae onward, and there are similar estimated ancestral sizes and divergence dates for each of the above clades (fig. S5). Simulations demonstrate that this trend was sustained across more branches than expected, given a null model of nondirectionality across the entire tree ($P < 0.05$) (SM, part E).

This pervasive trend toward smaller body size along the avian stem lineage is retrieved because the oldest representatives of successively closer outgroups to birds tend to be progressively smaller. The oldest taxon in each outgroup clade tends to be relatively basal and exerts the strongest influence on the reconstructed body size in that part of the bird stem lineage, either because it is separated from the bird stem by chronologically short branch lengths (Bayesian Brownian motion model) or by few intervening nodes (parsimony reconstruction). In this and other studies (Fig. 1 and fig. S5) (*3*–*9*, *16*, *21*, *22*), major tetanuran clades branch off the bird stem lineage in this approximate order; megalosauroids, allosauroids, tyrannosauroids, ornithomimosaurs, alvarezsauroids, oviraptorosaurs, dromaeosaurids, and troodontids. Among the taxa sampled here, the oldest megalosauroid (*Afrovenator*) and allosauroid (*Sinraptor*) with preserved femora are inferred to be ~900 to 1600 kg; the oldest tyrannosauroid (*Guanlong*) and ornithomimosaur (*Harpymimus*) are ~100 kg; the oldest alvarezsauroid (*Haplocheirus*) is ~17 kg; the oldest oviraptorosaur (*Caudipteryx*) is ~5 kg; and the oldest troodontid (*Jinfengopteryx*) and other taxa near the base of birds (Avialae), such as *Archaeopteryx* and *Aurornis*, are consistently ~0.5 kg. Within most outgroup clades, there is concordance between phylogeny and stratigraphy (oldest taxa are generally basal) (Fig. 1); this increases confidence in the phylogenetic results as well as body size reconstructions. Both data sets reveal uncertainty in basal paravian relationships [e.g., (*21*)]; however, Bayesian MCMC methods, unlike other methods [e.g., (supertrees)], fully integrate over topological and other parameter uncertainty (*25*, *26*).

Our study quantifies rates of evolutionary innovation in dinosaurs using 1549 (data set 1) and 421 (data set 2) skeletal and other anatomical traits distributed across the entire body. A clear pattern emerges: Branches along the bird stem undergo substantially faster morphological evolution than those of the rest of the tree. In data set 1, every branch along the avian stem between Neotetanurae and birds (Fig. 3) evolves at least twice as fast as the average theropod "background" rate: Their average rate of change is 0.0319, which equates to 3.19% divergence per lineage per million years (range 1.96 to 5.33%), approximately four times as fast as the unweighted average branch rate across the entire tree (0.88% per lineage per million years). In both data sets, rates are fastest in the middle region of the bird stem lineage, between the most recent common ancestors of Neotetanurae and Paraves; these peak rates are consistent with

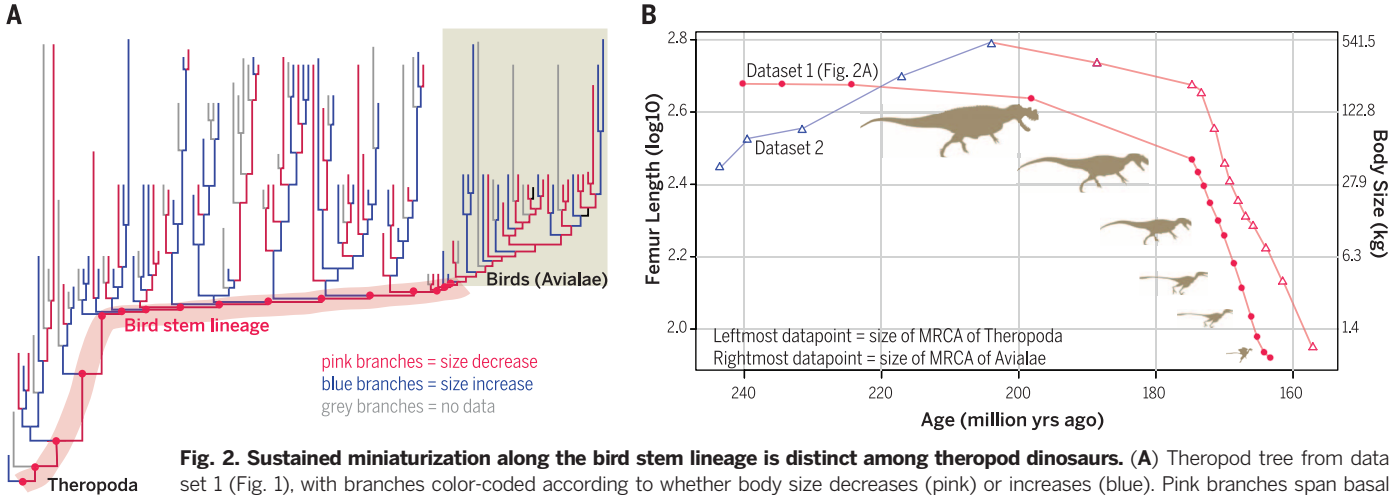

Fig. 2. Sustained miniaturization along the bird stem lineage is distinct among theropod dinosaurs. (**A**) Theropod tree from data set 1 (Fig. 1), with branches color-coded according to whether body size decreases (pink) or increases (blue). Pink branches span basal theropods to birds; in contrast, the rest of the tree shows no comparable "run" of decreases or increases. Parsimony analysis gives consistent results (fig. S8), as do Bayesian and parsimony analyses of data set 2 (*22*, *23*) (figs. S5 and S9). (**B**) Inferred evolution of body size along the bird stem lineage through time. Plot of body size versus age of successive nodes ("ancestors") along the bird stem lineage (from Fig. 1). Femur length is the left scale on *y* axis; inferred body size (*24*) is the right scale on *y* axis. Curves represent results from data sets 1 and 2; both indicate a sustained, unreversed size decrease commencing ~200 million years ago, with the next 12 or more consecutive nodes each smaller than the preceding.

the near-simultaneous stratigraphic appearance (~160 Ma) of several lineages in this part of the tree, notably Allosauroidea, Tyrannosauroidea, Compsognathidae, Alvarezsauroidea, and Paraves. The same patterns are found in data set 2 (fig. S6). The fast-evolving bird stem is not an artifact of internal node age constraints, as it persists in both data sets even if no age constraints (besides root age) are used (SM, part C). However, in such analyses, the peak rates "spread out" onto more basal branches of the bird stem lineage.

Rates of innovation along the bird stem are potentially inflated by oversampling of characters on this lineage (by avian-centric researchers). However, there are three reasons suggesting that the strong rate patterns found here are at least partly real. First, the primary data set (data set 1) attempted to avoid ascertainment bias by explicitly sampling characters across all branches of the theropod tree (including autapomorphies and invariant traits—not sampled in any previous studies). Second, data set 2 was largely constructed to infer relationships among alvarezsaurs (*23*) and thus likely oversampled characters (and overestimated rates) within this relatively minor "side" clade, yet nearly all the fastest branches in data set 2 are on the bird stem. Third, Bayesian approaches "dampen" perceived rate heterogeneity by smoothing these patterns when (co)sampling topologies and branch lengths and are thus more conservative in this respect than traditional sequential approaches. Ultimately, the potential effects of character oversampling will best be addressed by independent studies, each aiming to explicitly sample all characters—including autapomorphies and invariant characters—in similar fashion to the collection of molecular sequence data.

These results reconcile contradictory studies identifying presence (*4*–*8*) or absence (*9*–*11*) of a trend toward size reduction in theropods. Although there is no overall theropod-wide trend (fig. S7 and SM, part D), there is an exceptional trend within the single lineage that comprises much of the avian stem. This prolonged miniaturization is consistent with many aspects of bird origins. Many traits that evolve along the shrinking bird stem lineage are potentially related to developmental truncation, which often accompanies size reduction, regardless of which trait is under primary selection (*29*): short snouts, large brains and eyes (*12*), and smaller teeth with reduced serrations (*30*). Also, progressive elaboration of feathers along the bird stem, permitting more efficient insulation along with other functions, might have facilitated the evolution of smaller body sizes. Sauropodomorphs (the closest outgroup to theropods) and adequately known basal theropods were entirely or largely featherless; the most basal coelurosaurs had only simple hairlike filaments, whereas ornithomimosaurs and maniraptorans showed a range of more complex feather types (*13*, *17*–*19*, *21*, *22*). Finally, the evolution of many avian innovations along the bird stem would have been facilitated by smaller body size, including the reorganization of body mass balance, the increasingly horizontal (and biomechanically demanding) orientation of the femur, a stiffened tail, greater agility and cursoriality, and arboreal and/or aerial habits (*1*–*8*, *12*–*18*). Because size reduction, feather elaboration, paedomorphism, and other anatomical novelties permitted by small size all evolved in concert along the bird stem, identifying the primary driver of this sustained trend is probably

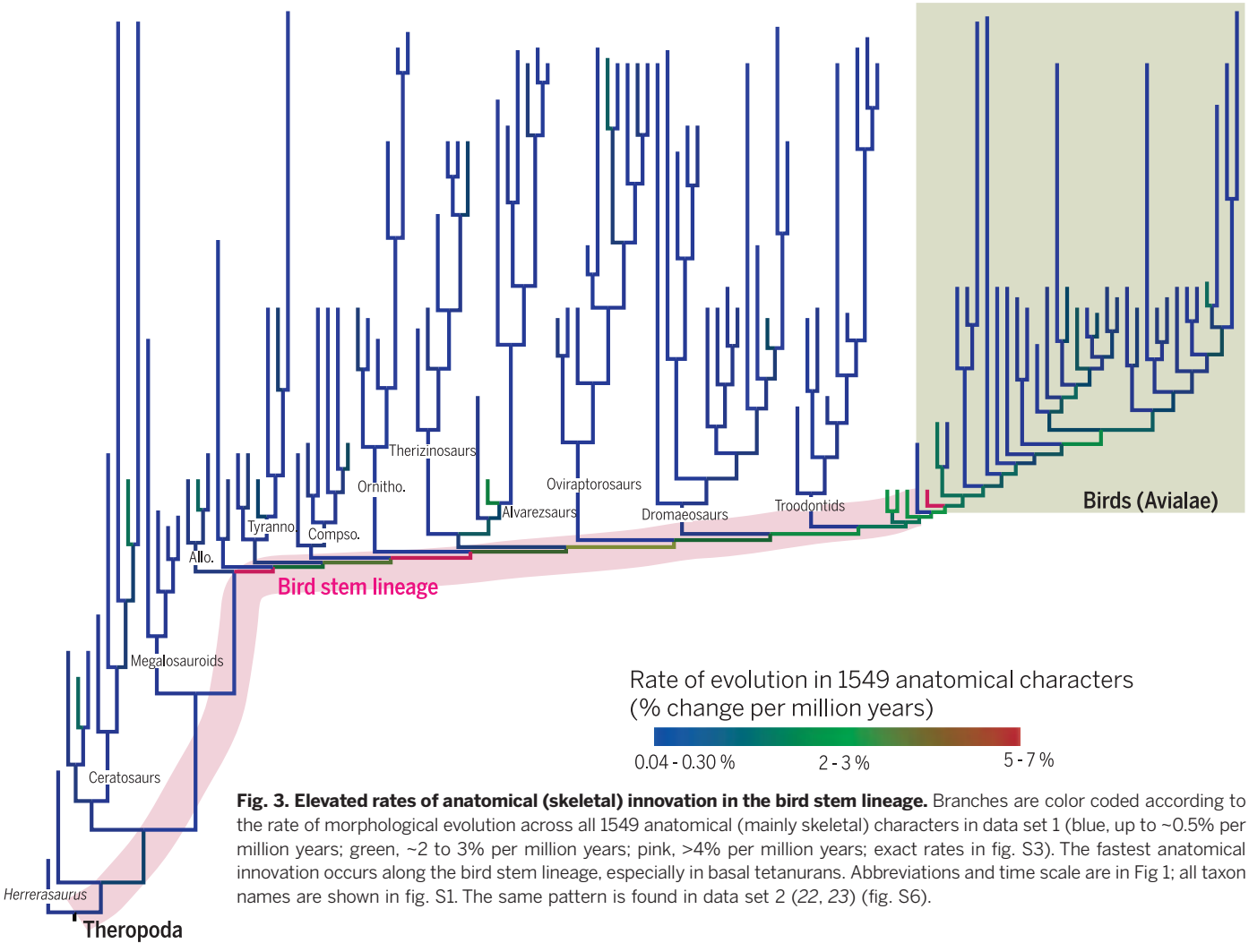

Fig. 3. Elevated rates of anatomical (skeletal) innovation in the bird stem lineage. Branches are color coded according to the rate of morphological evolution across all 1549 anatomical (mainly skeletal) characters in data set 1 (blue, up to ~0.5% per million years; green, ~2 to 3% per million years; pink, >4% per million years; exact rates in fig. S3). The fastest anatomical innovation occurs along the bird stem lineage, especially in basal tetanurans. Abbreviations and time scale are in Fig 1; all taxon names are shown in fig. S1. The same pattern is found in data set 2 (*22*, *23*) (fig. S6).

impossible. It is likely that all traits influenced and provided the context for the evolution of others (*31*).

REFERENCES AND NOTES

1. J. Gauthier, L. F. Gall, Eds., *New Perspectives on the Origin and Early Evolution of Birds* (Peabody Museum of Natural History, New Haven, CT, 2001).
2. G. Dyke, G. Kaiser, Eds., *Living Dinosaurs: the Evolutionary History of Modern Birds* (Wiley, Chichester, UK, 2011).
3. J. Gauthier, *Mem. Calif. Acad. Sci.* **8**, 1–55 (1986).
4. P. C. Sereno, *Annu. Rev. Earth Planet. Sci.* **25**, 435–489 (1997).
5. K. Padian, A. J. de Ricqlès, J. R. Horner, *Nature* **412**, 405–408 (2001).
6. T. A. Dececchi, H. C. E. Larsson, *Evolution* **67**, 2741–2752 (2013).
7. F. E. Novas, M. D. Ezcurra, F. L. Agnolín, D. Pol, R. Ortíz, *Rev. Mus. Argentino de Cienc. Nat. n.s.* **14**, 57–81 (2012).
8. A. H. Turner, D. Pol, J. A. Clarke, G. M. Erickson, M. A. Norell, *Science* **317**, 1378–1381 (2007).
9. M. T. Carrano, in *Amniote Paleobiology*, M. T. Carrano, T. J. Gaudin, R. W. Blob, J. R. Wible, Eds. (Univ. of Chicago Press, Chicago, 2006), chap. 8.
10. D. W. E. Hone, T. M. Keesey, D. Pisani, A. Purvis, *J. Evol. Biol.* **18**, 587–595 (2005).
11. R. B. Sookias, R. J. Butler, R. B. J. Benson, *Proc. Biol. Sci.* **279**, 2180–2187 (2012).
12. B.-A. S. Bhullar *et al.*, *Nature* **487**, 223–226 (2012).
13. A. M. Heers, K. P. Dial, *Trends Ecol. Evol.* **27**, 296–305 (2012).
14. V. Allen, K. T. Bates, Z. Li, J. R. Hutchinson, *Nature* **497**, 104–107 (2013).
15. M. N. Puttick, G. H. Thomas, M. J. Benton, *Evolution* **68**, 1497–1510 (2014).
16. R. B. J. Benson *et al.*, *PLOS Biol.* **12**, e1001853 (2014).
17. D. K. Zelenitsky *et al.*, *Science* **338**, 510–514 (2012).
18. X. Zheng *et al.*, *Science* **339**, 1309–1312 (2013).
19. R. B. J. Benson, J. N. Choiniere, *Proc. Biol. Sci.* **280**, 20131780 (2013).
20. Materials and methods are available as supplementary materials on *Science* Online. Data files are archived on Dryad Digital Repository (doi:10.5061/dryad.jm6pj).
21. P. Godefroit *et al.*, *Nature* **498**, 359–362 (2013).
22. X. Xu *et al.*, *Nature* **484**, 92–95 (2012).
23. J. N. Choiniere *et al.*, *Science* **327**, 571–574 (2010).
24. P. Christiansen, R. A. Farina, *Hist. Biol.* **16**, 85 (2004).
25. A. J. Drummond, M. A. Suchard, D. Xie, A. Rambaut, *Mol. Biol. Evol.* **29**, 1969–1973 (2012).
26. A. J. Drummond, S. Y. W. Ho, M. J. Phillips, A. Rambaut, *PLOS Biol.* **4**, e88 (2006).
27. M. Pagel, A. Meade, *BayesTraits: Software and Documentation* (2013); www.evolution.reading.ac.uk/BayesTraitsV2Beta.html.
28. L. E. Zanno, P. J. Makovicky, *Proc. Biol. Sci.* **280**, 20122526 (2013).
29. J. Hanken, D. B. Wake, *Annu. Rev. Ecol. Syst.* **24**, 501–519 (1993).
30. O. W. M. Rauhut, C. Foth, H. Tischlinger, M. A. Norell, *Proc. Natl. Acad. Sci. U.S.A.* **109**, 11746–11751 (2012).
31. T. S. Kemp, *Proc. Biol. Sci.* **274**, 1667–1673 (2007).

ACKNOWLEDGMENTS

We thank e-research SA for use of high-performance computing facilities, the Environment Institute (University of Adelaide) and Australian Research Council for funding, and the University of Bologna for logistic support. Author contributions. A.C., G.J.D., and D.N. collected phylogenetic and stratigraphic data; M.S.Y.L. analyzed data and assisted with data collection; all authors contributed to interpretation of results; M.S.Y.L. wrote and revised manuscript with input from all other authors. Data files are archived on Dryad Digital Repository (doi:10.5061/dryad.jm6pj).

SUPPLEMENTARY MATERIALS

www.sciencemag.org/content/345/6196/562/suppl/DC1
Materials and Methods
Figs. S1 to S9
References (*32*–*62*)

14 February 2014; accepted 20 June 2014
10.1126/science.1252243

MODELING DIGITS

Digit patterning is controlled by a Bmp-Sox9-Wnt Turing network modulated by morphogen gradients

J. Raspopovic,[1]* L. Marcon,[1]* L. Russo,[1] J. Sharpe[1,2]†

During limb development, digits emerge from the undifferentiated mesenchymal tissue that constitutes the limb bud. It has been proposed that this process is controlled by a self-organizing Turing mechanism, whereby diffusible molecules interact to produce a periodic pattern of digital and interdigital fates. However, the identities of the molecules remain unknown. By combining experiments and modeling, we reveal evidence that a Turing network implemented by Bmp, Sox9, and Wnt drives digit specification. We develop a realistic two-dimensional simulation of digit patterning and show that this network, when modulated by morphogen gradients, recapitulates the expression patterns of *Sox9* in the wild type and in perturbation experiments. Our systems biology approach reveals how a combination of growth, morphogen gradients, and a self-organizing Turing network can achieve robust and reproducible pattern formation.

Digits form in a periodic pattern that alternates digital and interdigital fates along the anterior-posterior (AP) axis of the limb bud. Traditionally, this pattern has been explained by a positional information model (*1*) based on an AP gradient of Sonic hedgehog (Shh) (*2*, *3*). However, embryonic and genetic manipulations (*4*, *5*) have shown that digit patterning is independent of Shh and may be instead controlled by a self-organizing mechanism. Over three decades ago, it was proposed that such a mechanism could be a Turing system (*6*, *7*), in which a diffusible activator and inhibitor (*8*) interact and self-organize to form the periodic digit pattern. Recent work has strengthened this hypothesis (*9*); however, two important questions remain to be addressed.

First, although a number of mathematical Turing models have been proposed to explain the periodic digit pattern (*10*, *11*), no computer simulation has been able to correctly reproduce the expression patterns of digit markers over time and space. Second, the diffusible molecules that implement the Turing network have not yet been identified. Transforming growth factor–β (TGF-β) molecules were proposed as activators in a Turing system (*12*, *13*), but the corresponding diffusible inhibitor could not be found. The galectins CG-1A and CG-8 have also been proposed as Turing molecules in the chick (*14*) but are not believed to play a similar role in mammals (*15*). More recently, bone morphogenetic proteins (BMPs) and their receptors have been proposed to form a Turing network (*10*), but this model assumed that the BMP receptors can diffuse through tissue, for which there is no evidence.

[1]Systems Biology Program, Centre for Genomic Regulation (CRG), and Universitat Pompeu Fabra (UPF), Dr. Aiguader 88, 08003 Barcelona, Spain. [2]Institució Catalana de Recerca i Estudis Avançats (ICREA), Passeig Lluís Companys 23, 08010 Barcelona, Spain.
*These authors contributed equally to this work. **†Corresponding author. E-mail: james.sharpe@crg.eu**

To identify the molecules that control digit specification, it is crucial to distinguish the genes involved in early digit patterning from downstream differentiation factors. We therefore analyzed the expression of the earliest known skeletal marker *Sox9* (*16*) and identified embryonic day 11.5 (E11.5) as the earliest stage that shows a periodic digital pattern (Fig. 1A). We also performed micromass cultures with E11.5 Sox9-EGFP (enhanced green fluorescent protein) limb autopods (*17*) and found that cells create a periodic Sox9 pattern by 15 hours, faster than previously reported (*18*), with dynamics reminiscent of a two-dimensional (2D) Turing simulation (Fig. 1B and movie S1). We observed that the periodic pattern formed even when the culture was initiated with $Sox9^-$ or $Sox9^+$ cells sorted by fluorescence-activated cell sorting (FACS) (Fig. 1, B and C, and movies S2 and S3), confirming that Sox9 is dynamically regulated by a self-organizing patterning mechanism.

When *Sox9* is knocked out, all the genes that reflect a digital or interdigital pattern (e.g., *Bmp2*, *Chordin*, *Noggin*) lose their normal periodic expression (*19*), suggesting that *Sox9* itself is part of the Turing network rather than a downstream differentiation marker. The two simplest Gierer-Meinhardt topologies (*8*), the activator-inhibitor and the substrate-depletion model (Fig. 1D), predict that the diffusible molecules of the Turing network should have periodic patterns that are either in-phase or out-of-phase, respectively. We therefore performed a microarray analysis to identify genes related to the major developmental signaling pathways that were differentially expressed between $Sox9^+$ and $Sox9^-$ FACS-sorted cells. On the basis of both the number of genes and fold-change magnitude, the pathways that were most strongly represented were WNT, BMP, and FGF (fibroblast growth factor) (fig. S1). We performed a second level of screening by whole-mount in situ hybridization (WMISH) to check which genes were genuinely expressed in-phase

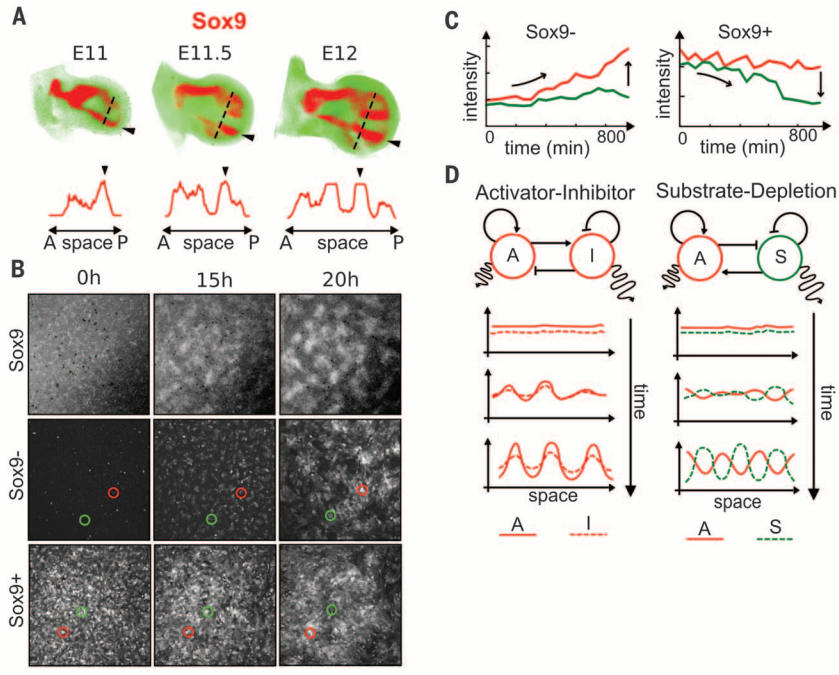

Fig. 1. The Sox9 periodic digit pattern. (**A**) Top: *Sox9* expression patterns (red) from E11 to E12 (limb shape in green). Bottom: Anterior-posterior (AP) profiles (dashed line above) highlight the progressive appearance of the *Sox9* periodic pattern, first visible at E11.5; arrowheads indicate digit 4. Limb orientation in all figures: distal to the right, posterior to the bottom. (**B**) First row: time course of micromass culture with Sox9-EGFP autopod cells; a periodic pattern emerges by 15 hours. Second and third rows: When cultures are initiated with $Sox9^{-}$ or $Sox9^{+}$ cells obtained by FACS sorting, they still form a periodic pattern by up-regulating or down-regulating Sox9 depending on the position (single cells highlighted by red and green circles). (**C**) Sox9-EGFP intensities of the tracked cells over time. (**D**) The two simplest models that can form a Turing pattern. In the Activator-Inhibitor model, an autocatalytic activator (A) promotes its own inhibitor (I), resulting in in-phase periodic patterns. In the Substrate-Depletion model, an activator (A) activates itself by depleting its own substrate (S), resulting in out-of-phase periodic patterns.

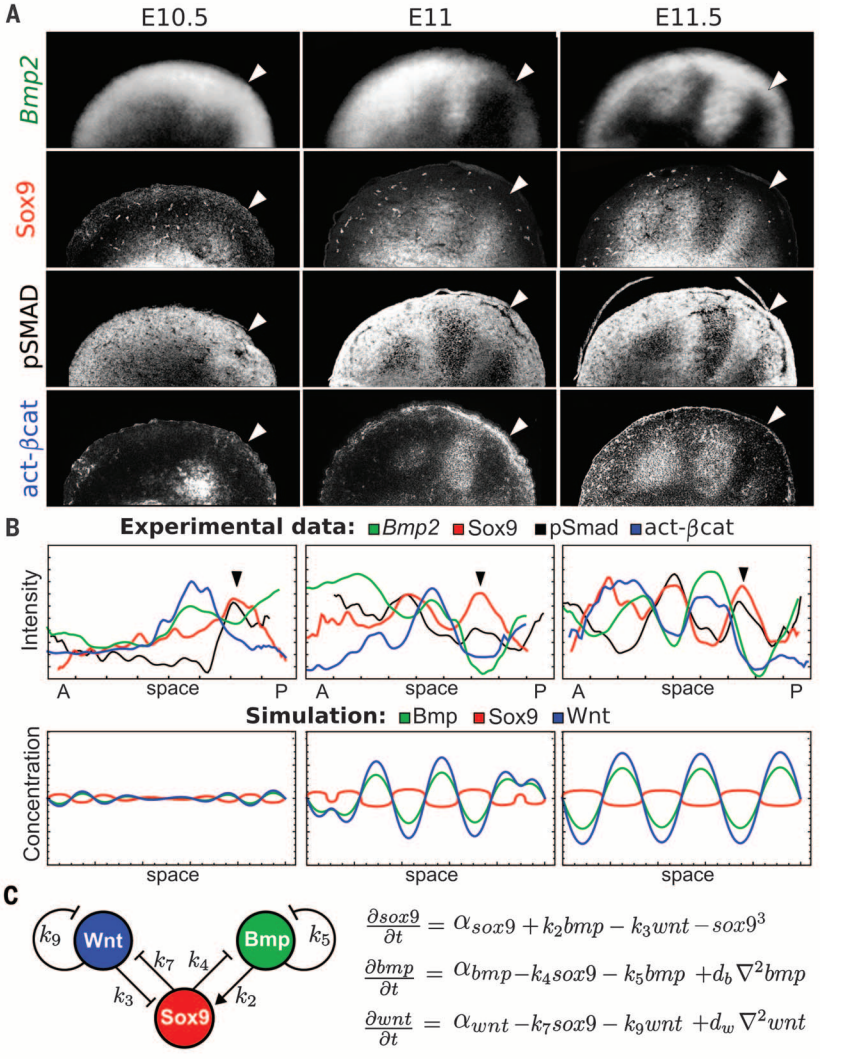

Fig. 2. Sox9 is out of phase with BMP and WNT. (**A**) Time course of *Bmp2* expression, Sox9-EGFP fluorescence (Sox9), BMP signaling (pSMAD), and WNT signaling activity (act-βcat). Digit 4 (white arrowhead) appears first (E10.5), followed by digit 3 and then 2 (see Sox9). *Bmp2* and act-βcat are out-of-phase with Sox9, whereas pSMAD is in-phase (see also fig. S2). (**B**) Top: Graphs show the progressive patterning along the AP axis measured from the images above. Black arrowheads point to digit 4. Bottom: A 1D simulation of the BSW model produces a Sox9 pattern that is out-of-phase with Bmp and Wnt, as shown in the experimental data above. (**C**) Network topology and equations of the BSW model.

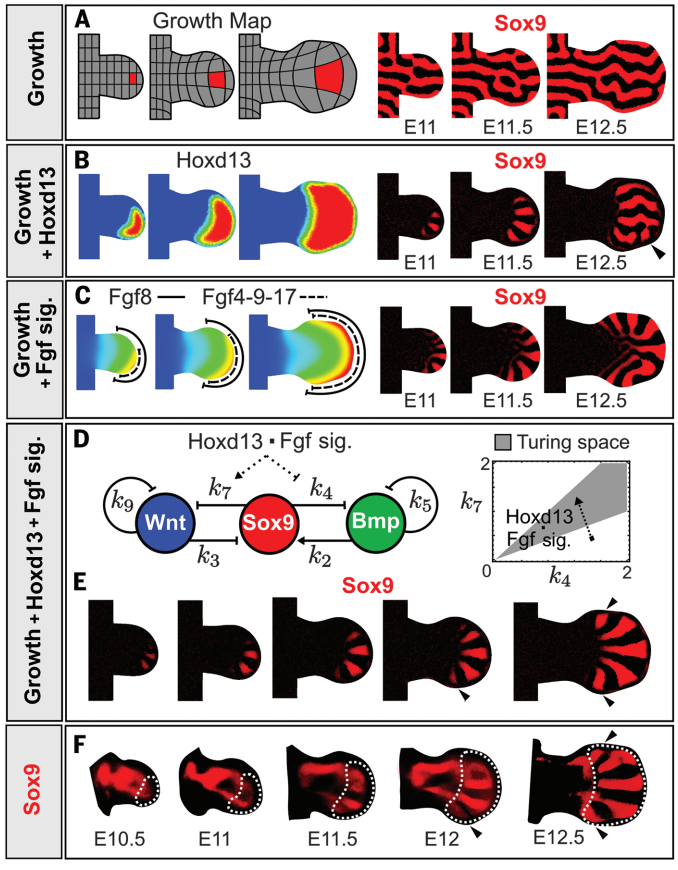

Fig. 3. Realistic computer simulation of digit patterning. (**A**) When the BSW model was simulated inside an experimental limb growth map (left), Sox9 (red) formed a pattern with randomly oriented stripes biased along the PD axis (right). (**B**) Experimental *Hoxd13* expression was mapped into the growing model (left, heat-color map: blue = 0 and red = 1). With the *Hoxd13* modulation, the model creates a digit-like pattern (right), which eventually shows digit bifurcation (arrowhead). (**C**) *Fgf* expression in the AER was mapped into the model (solid line for *Fgf8*, dashed line for *Fgf4-9-17*) and used to simulate an Fgf signaling gradient (left, heat-color map: blue = 0 and red = 1). With the Fgf modulation, the model predicted a radially oriented Sox9 pattern with bigger wavelength toward the distal tip (right). (**D**) When Fgf and Hoxd13 jointly modulate the parameters k4 and k7, the system shifts (dashed arrow) into the Turing space (gray region). (**E**) The simulated Sox9 pattern recapitulates the main features of (**F**) the experimental *Sox9* expression in the digits, outlined by the white dotted lines. Arrowheads mark the late appearance of digits 5 and 1.

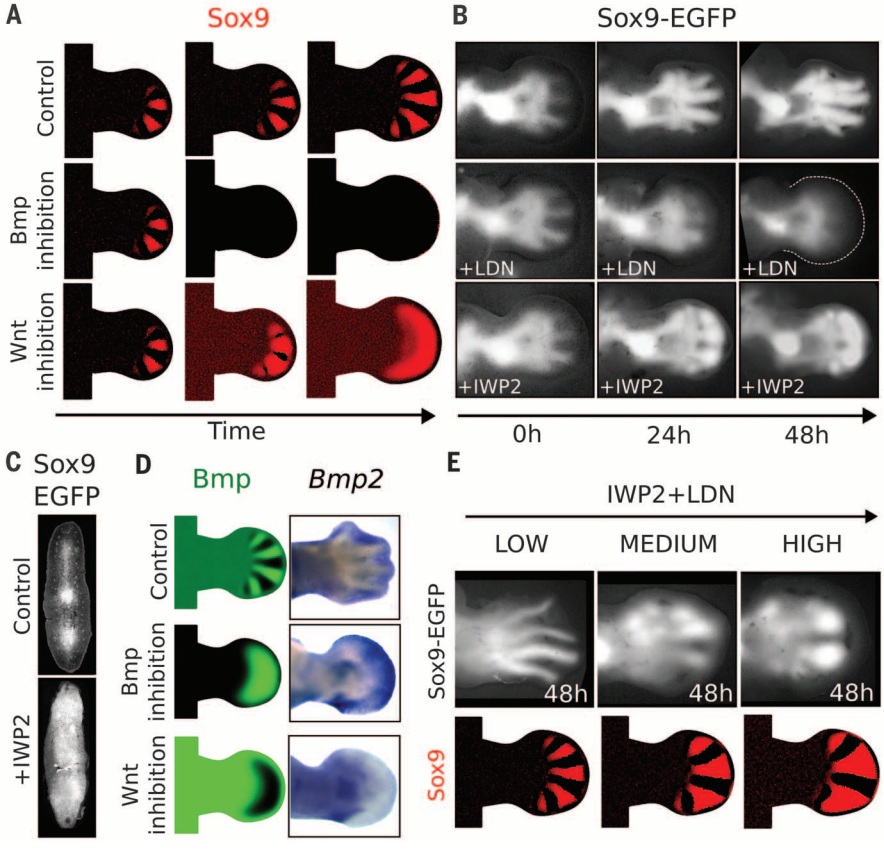

Fig. 4. Model predictions and experimental perturbations. (**A**) Sox9 patterns (red) predicted by the BSW model in different perturbations. Bmp inhibition causes loss of digital expression (second row), whereas Wnt inhibition predicts gradual loss of interdigits (third row). (**B**) Experimental manipulation of E11.5 limb buds in Sox9-EGFP limb culture confirmed the model predictions. Addition of the BMP signaling inhibitor LDN caused a loss of digital Sox9-EGFP (second row), whereas addition of the WNT inhibitor IWP2 caused the opposite result: Each digit expanded until complete fusion (third row). (**C**) Transverse sections show that WNT inhibition (+IWP2) induces expansion of Sox9-EGFP in the interdigital tissue (not only under the ectoderm). (**D**) The BSW model predicts that distal Bmp should be up-regulated and down-regulated in Bmp or Wnt signaling inhibition, respectively; the same behavior was observed for *Bmp2* expression in culture. (**E**) The model predicts progressively larger and fewer digits when both pathways are inhibited simultaneously (bottom row). Similar results are obtained by adding LDN and IWP2 simultaneously with progressively higher concentrations (low, medium, high) (upper row).

or out-of-phase with Sox9 (fig. S1). The analysis revealed in-phase and out-of-phase expression patterns for genes in the BMP and WNT pathways, but not for the FGF pathway. Specifically, *Bmp2* showed a pattern that is out-of phase with *Sox9* at all stages of digit patterning (Fig. 2A and fig. S1). None of the WNT ligands were differentially expressed, but target genes (e.g., *Axin2* and *Lef1*) were expressed in Sox9$^-$ cells at E12 (fig. S1). This is consistent with the observation that WNT ligands produced in the ectoderm repress *Sox9* and chondrogenesis (*20*, *21*). Indeed, knockout of β-catenin in the limb results in the expansion of *Sox9* toward the ectoderm, whereas β-catenin gain-of-function results in *Sox9* downregulation (*22*, *23*).

For a direct analysis of BMP, WNT, and FGF signaling activity, we performed immunohistochemistry for phosphorylated Smad1/5/8 (pSMAD), nonphosphorylated active β-catenin (act-βcat), and phosphorylated extracellular signal–regulated kinase (pERK) on serial cryosections of Sox9-EGFP limbs. This allowed us to correlate the activity of the three pathways with the spatial dynamics of digit patterning. We found that BMP signaling (pSMAD) is high in the digits and correlates with Sox9-EGFP (Fig. 2A and fig. S2), supporting the positive effect of BMP signaling on *Sox9* (*24*–*26*) and its importance for digit patterning (*27*). In contrast to pSMAD, WNT signaling (act-βcat) is high in the interdigital regions and has a pattern that is out-of-phase with Sox9 at all stages (Fig. 2A and fig. S2). This close spatial correspondence supports Wnt/β-catenin involvement in the Turing mechanism and is consistent with the repression of *Sox9* by Wnt/β-catenin (*21*, *22*). Finally, FGF signaling (pERK) shows no periodic pattern but only the expected proximodistal (PD) gradient, which is highest under the apical ectodermal ridge (AER) (fig. S2). Indeed, Fgf has previously been proposed as a modulator of the digit wavelength (*9*) rather than being part of the Turing network.

From the spatial relationships between these molecular patterns (Fig. 2B), we hypothesized that the Turing network that controls digit patterning is a three-node model implemented by Sox9, Bmp, and Wnt. Of the possible regulatory interactions between these three nodes, two are clear from the literature: the positive influence of BMP signaling on *Sox9* (*24*–*26*) and the inhibition of *Sox9* by WNT signaling (*21*–*23*). With these two interactions fixed, we performed a linear stability analysis for a three-component reaction-diffusion system (see supplementary text 2.2 and 2.3). Among all possible cases, we identified the topology shown in Fig. 2C (the Bmp-Sox9-Wnt, or BSW, model) as the simplest and most robust Turing network that can self-organize to produce a periodic pattern in which Sox9 is out-of-phase with both Bmp expression and Wnt signaling activity (Fig. 2B).

When simulated in 2D, the BSW model produces a pattern of randomly oriented stripes reminiscent of the pattern formed in micromass culture (fig. S3). The next challenge was to show that the model can reproduce the time course of *Sox9* expression in a realistic simulation of limb development. Because Turing patterns are influenced by growth and shape changes of the underlying tissue (*28*, *29*), we used a 2D growth model derived from clonal fate-mapping experiments (*30*). Within this tissue-movement map, the BSW network generated a stripy pattern that tended to orient along the PD axis (Fig. 3A, movie S4, and supplementary text 2.9.1). Next, because digit patterning appears to be relatively independent from the rest of the skeleton (*9*, *24*, *27*, *31*), we chose to modulate the BSW model to generate the Turing instability only in the digital region defined by *Hoxd13* expression (Fig. 3B, movie S5, and supplementary text 2.9.2). This naturally promoted the sequential appearance of PD-oriented stripes and greatly reduced the variability of the pattern across different simulation runs (supplementary text 2.9.2); however, digit bifurcations occurred after E12 (Fig. 3B). We previously showed that distal *Hox* genes and FGF signaling jointly modulate the wavelength (digit width) to specify digit number and avoid bifurcations (*9*). When we combined modulation by FGF signaling (Fig. 3C and movie S6) and *Hoxd13* (Fig. 3D), the model robustly produced Sox9 patterns that recapitulated the *Sox9* expression in wild-type limbs (Fig. 3, E and F; fig. S4; supplementary text 2.9.4 and 2.12; and movies S7 and S8).

Finally, we used E11.5 Sox9-EGFP limb cultures (fig. S5) to test predictions from the computer model and to verify the Turing network. Reducing Bmp signaling in the simulation (from E11.5 onward) predicted a loss of digital Sox9 expression (Fig. 4A and movie S9) similar to the result of inhibiting BMP signaling in limb culture (Fig. 4B). Conversely, reducing Wnt signaling in the model predicted that all digits should expand until they merge into a continuous domain of Sox9 expression (Fig. 4A and movie S10). The same dynamics were observed when WNT signaling was inhibited in vitro (Fig. 4B). Our results reveal that upon abrogation of Wnt/β-catenin signaling, Sox9 expands not only in the subectodermal mesenchyme (*23*) but also into the interdigital regions (Fig. 4C), proving that Wnt/β-catenin signaling is a necessary component of the periodic digital patterning process. The model also predicted that in all cases, Bmp expression should be opposite to that of Sox9, and we observed the same for *Bmp2* expression in the experiments (Fig. 4D). A further series of experiments, in which we implanted protein-soaked beads into the limb bud mesenchyme (fig. S6), also confirmed the predictions of the model and allowed us to hypothesize that the primary ligands are BMP2 and WNT3 (supplementary text 2.11.5 and movies S11 to S14).

Because inhibiting Bmp caused a loss of digits, whereas inhibiting Wnt caused a loss of interdigits, we explored whether the simultaneous inhibition of both pathways could balance out and instead cause an alteration of the pattern. The computer simulation predicted that a combination of both drugs would increase the digit period (the effective wavelength), resulting in an oligodactyly phenotype with fewer digits (Fig. 4E and supplementary text 2.11.4). Application of both drugs to the limb bud culture confirmed this prediction, showing that the digit period becomes larger as the concentrations of both drugs increase (Fig. 4E and fig. S7). This supports both our BSW model and the general concept of a Turing-type process, because the new pattern was not just a down-regulation or up-regulation of *Sox9* but a genuine rearrangement of the already initiated periodic digital pattern.

Our study reveals the main feedbacks involved in digit patterning; however, other regulatory pathways may be involved to confer extra redundancy or robustness to the system. We propose that Wnt/β-catenin is essential for digit patterning and in particular for repressing *Sox9* in the interdigital regions. This suggests a possible mechanistic link between molecular patterning and mesenchymal condensations, as Wnt/β-catenin signaling may prevent the formation of β-catenin–cadherin complexes, which otherwise promote tighter cell adhesion (*32*). Finally, our model suggests a correlation between three separate functions of FGF signaling: control of growth (*33*), promotion of distal PD markers as *Hoxd13* (*34*), and promotion of larger digit wavelength (*9*). Taken together, this suggests that any FGF-driven change in limb bud size would naturally be accompanied by a change in PD digit length (*Hoxd13* domain) and in AP digit width (Turing wavelength) (fig. S8 and supplementary text 2.9.4), thereby implementing a perfect strategy for scale invariance.

REFERENCES AND NOTES

1. D. Summerbell, J. H. Lewis, L. Wolpert, *Nature* **244**, 492–496 (1973).
2. R. D. Riddle, R. L. Johnson, E. Laufer, C. Tabin, *Cell* **75**, 1401–1416 (1993).
3. R. Zeller, J. López-Ríos, A. Zuniga, *Nat. Rev. Genet.* **10**, 845–858 (2009).
4. E. Zwilling, *Dev. Biol.* **9**, 20–37 (1964).
5. Y. Litingtung, R. D. Dahn, Y. Li, J. F. Fallon, C. Chiang, *Nature* **418**, 979–983 (2002).
6. A. M. Turing, *Bull. Math. Biol.* **52**, 153–197, 153–197 (1990).
7. S. A. Newman, H. L. Frisch, *Science* **205**, 662–668 (1979).
8. A. Gierer, H. Meinhardt, *Kybernetik* **12**, 30–39 (1972).
9. R. Sheth *et al.*, *Science* **338**, 1476–1480 (2012).
10. A. Badugu, C. Kraemer, P. Germann, D. Menshykau, D. Iber, *Sci. Rep.* **2**, 991 (2012).
11. H. G. Hentschel, T. Glimm, J. A. Glazier, S. A. Newman, *Proc. Biol. Sci.* **271**, 1713–1722 (2004).
12. C. M. Leonard *et al.*, *Dev. Biol.* **145**, 99–109 (1991).
13. T. Miura, K. Shiota, *Dev. Dyn.* **217**, 241–249 (2000).
14. R. Bhat *et al.*, *BMC Dev. Biol.* **11**, 6 (2011).
15. V. Georgiadis *et al.*, *Dev. Dyn.* **236**, 1014–1024 (2007).
16. E. Wright *et al.*, *Nat. Genet.* **9**, 15–20 (1995).
17. Y. Nakamura *et al.*, *Nat. Commun.* **2**, 251 (2011).
18. W. M. Kulyk, J. L. Franklin, L. M. Hoffman, *Exp. Cell Res.* **255**, 327–332 (2000).
19. H. Akiyama, M. C. Chaboissier, J. F. Martin, A. Schedl, B. de Crombrugghe, *Genes Dev.* **16**, 2813–2828 (2002).
20. K. Summerhurst, M. Stark, J. Sharpe, D. Davidson, P. Murphy, *GEP* **8**, 331–348 (2008).
21. D. ten Berge, S. A. Brugmann, J. A. Helms, R. Nusse, *Development* **135**, 3247–3257 (2008).
22. T. P. Hill, D. Später, M. M. Taketo, W. Birchmeier, C. Hartmann, *Dev. Cell* **8**, 727–738 (2005).
23. T. P. Hill, M. M. Taketo, W. Birchmeier, C. Hartmann, *Development* **133**, 1219–1229 (2006).
24. A. Bandyopadhyay *et al.*, *PLOS Genet.* **2**, e216 (2006).
25. Q. Pan *et al.*, *J. Cell. Physiol.* **217**, 228–241 (2008).
26. B. K. Zehentner, C. Dony, H. Burtscher, *J. Bone Miner. Res.* **14**, 1734–1741 (1999).

27. J. D. Bénazet *et al.*, *Development* **139**, 4250–4260 (2012).
28. E. J. Crampin, E. A. Gaffney, P. K. Maini, *Bull. Math. Biol.* **61**, 1093–1120 (1999).
29. T. Miura, K. Shiota, G. Morriss-Kay, P. K. Maini, *J. Theor. Biol.* **240**, 562–573 (2006).
30. L. Marcon, C. G. Arqués, M. S. Torres, J. Sharpe, *PLOS Comput. Biol.* **7**, e1001071 (2011).
31. C. Tickle, B. Alberts, L. Wolpert, J. Lee, *Nature* **296**, 564–566 (1982).
32. M. Bienz, *Curr. Biol.* **15**, R64–R67 (2005).
33. G. R. Martin, *Genes Dev.* **12**, 1571–1586 (1998).
34. N. Mercader *et al.*, *Development* **127**, 3961–3970 (2000).

ACKNOWLEDGMENTS

The Sox9-EGFP mouse line was kindly provided by H. Akiyama and P. Jay. The mRNA probe for Bmp2 was kindly provided by C. Pujades. We thank R. Zeller for the Smad4 mutant limbs; A. R. Moreno for in situs of Fgf4, 8 and Twist1; and D. Barcena for the help with the micromass cultures. J.S. was supported by CRG and ICREA, L.R. by Ministerio de Economía y Competitividad (MINECO) BFU2010-16428, and Centro de Excelencia Severo Ochoa, SEV-2012-0208, and L.M. by the CRG; J.R. was funded by a Ph.D. Fellowship from the Fundaçao para a Ciencia e Tecnologia. Confocal microscopy was done in the CRG Advanced Light Microscopy Unit, and FACS and microarrays in the CRG Core Facilities. The microarray data discussed in this publication are accessible through Gene Expression Omnibus series accession number GSE58158.

SUPPLEMENTARY MATERIALS

www.sciencemag.org/content/345/6196/566/suppl/DC1
Materials and Methods
Supplementary Text
Figs. S1 to S8
References (*35*–*87*)
Movies S1 to S14

10.1126/science.1252960

HIV LATENCY

Proliferation of cells with HIV integrated into cancer genes contributes to persistent infection

Thor A. Wagner,[1,2]* Sherry McLaughlin,[1,2]* Kavita Garg,[3] Charles Y. K. Cheung,[3] Brendan B. Larsen,[2] Sheila Styrchak,[1] Hannah C. Huang,[1] Paul T. Edlefsen,[2,3] James I. Mullins,[2]* Lisa M. Frenkel[1,2]*†

Antiretroviral treatment (ART) of HIV infection suppresses viral replication. Yet if ART is stopped, virus reemerges because of the persistence of infected cells. We evaluated the contribution of infected-cell proliferation and sites of proviral integration to HIV persistence. A total of 534 HIV integration sites (IS) and 63 adjacent HIV *env* sequences were derived from three study participants over 11.3 to 12.7 years of ART. Each participant had identical viral sequences integrated at the same position in multiple cells, demonstrating infected-cell proliferation. Integrations were overrepresented in genes associated with cancer and favored in 12 genes across multiple participants. Over time on ART, a greater proportion of persisting proviruses were in proliferating cells. HIV integration into specific genes may promote proliferation of HIV-infected cells, slowing viral decay during ART.

Despite suppression of viral replication during ART, HIV reservoirs, measured by the number of resting $CD4^+$ T cells with infectious virus induced in cell culture, decline slowly (*1*). The mechanisms hypothesized to allow infectious proviruses to persist include long-lived latently infected cells (*1*); low-level HIV replication (*2*), potentially due to insufficient intracellular drug concentrations (*3*–*5*); and the proliferation of HIV-infected cells (*2*, *6*–*10*). During ART, subpopulations of cells with identical HIV sequences comprise a progressively larger proportion of the persisting viral genomes (*8*), suggesting that proliferation of infected cells helps maintain the HIV reservoir. To further evaluate the contribution of infected-cell proliferation to HIV persistence, we developed a method [integration site loop amplification (ISLA)] to define sites of HIV integration in single cells and sequence up to 2.8 kb of the 3′ region of the viral genome adjacent to the integration site, allowing us to link specific viral variants to specific integration sites (fig. S1).

A total of 534 proviral integration sites were sequenced from three participants (B1, L1, and R1) at three time points each: after 1 to 2.3, 4.1 to 8.2, and 11.3 to 12.7 years of suppressive ART (Fig. 1, A to C). HIV integration at the same chromosomal site was found in multiple cells within each participant throughout follow-up, whereas no identical integration sites were shared by different participants, suggesting that HIV-infected cells proliferate, as reported (*2*, *6*–*8*).

The hypothesis was further investigated by comparisons of the viral genomes in 63 integration sites. When HIV C2V5 *env* sequences shared a specific integration site, the *env* sequences [~625 base pairs (bp)] were identical (n = 31 C2V5 *env* sequences from 13 integration sites, except for one pair of sequences with a 1-bp difference). In contrast, among proviruses integrated at different positions in the human genome (n = 45 unique integration sites), C2V5 *env* sequences were distinct except for three groups from participant B1 (fig. S2) (13 out of 13 versus 3 out of 45; $P < 0.0001$). Sequences of the entire *C2env-nef-3′*LTR (long terminal repeat) region (~2.8 kb) from these three groups of proviruses had 2 to 39 nucleotide differences, indicating that many were distinct viruses (fig. S2). In comparison, eight pairs of *C2env-nef-3′*LTR sequences with identical integration sites differed by 0 to 2 bases (mean 0.9), an error rate consistent with misincorporations during the ISLA protocol. Phylogenetic analyses of 396 additional HIV *env* sequences (*8*), together with those from the ISLA method, revealed multiple additional identical viral sequences (*8*), strongly suggesting that multiple HIV-infected clonal cell populations persist during ART (Fig. 2 and figs. S2 and S3).

Three approaches were used to explore whether the distribution of HIV integration sites observed was random or shaped by selective forces. Specifically, we examined the distribution of HIV integrations in genes associated with cancer, regulation of cell proliferation, or cell survival.

First, proviral integration sites were examined for overrepresentation in cancer-associated genes from five combined sources (n = 1332 unique genes) (*11*–*15*). Across the three participants, 12.5% (36 out of 288) of the unique genes from all proviral integrations were annotated as associated with cancer (*11*–*15*), compared with only 5.19% (1332 out of 25,660) of the human genes in the human genome ($P < 0.0001$). In addition, unique integrations in proliferating HIV-infected cells (defined as identical integration sites derived from ≥2 separate cells) (table S1, A to C) were also increased in cancer-associated genes (6 out of 34, 17.65% versus 1332 out of 25,660, 5.2%; $P = 0.0076$), which suggests that HIV integration could disrupt the regulation of these genes, as is known to occur during tumor induction by nonacute oncogenic retroviruses (*16*).

Second, given that HIV integrates preferentially into actively transcribed genes, especially those activated upon HIV infection (*17*–*19*), we compared our participants' integration sites to the >44,000 integration sites mapped in acutely infected $CD4^+$ T cells (Jurkat cells). The majority of our participants' proviruses were integrated within genes (425 out of 534, 79.6%) (Fig. 1, A to C), particularly within introns (337 out of 425, 79.1%), as previously observed (*9*, *17*, *20*). The frequency of unique proviral integration sites in cancer-associated genes (12.70%) was similar to those mapped in the acutely infected Jurkat cells (11.14%) (*21*). However, our participants' integration sites in proliferating cells were enriched for cancer-associated genes over samples of the same size from the Jurkat cell data set ($P = 0.0486$). In the Jurkat cell data set, 11.14% of integrations were found in cancer genes, compared with 15.97% in our participants ($P = 0.0828$).

[1]Seattle Children's Research Institute, 1900 9th Avenue, Seattle, WA 98101, USA. [2]University of Washington, Seattle, WA, USA. [3]Fred Hutchinson Cancer Research Center, Seattle, WA, USA.
*These authors contributed equally to this work. †Corresponding author. E-mail: lfrenkel@uw.edu

Importantly, the frequency of proliferating cells significantly increased through time on ART (Fig. 1, D to F), both when considering all integration sites ($P = 0.0013$) and when considering only unique integration sites ($P = 0.0048$) (Fig. 1, D to F). However, unique integrations into cancer genes did not increase over time. These findings suggest that HIV integrates preferentially into cancer-associated and other genes that

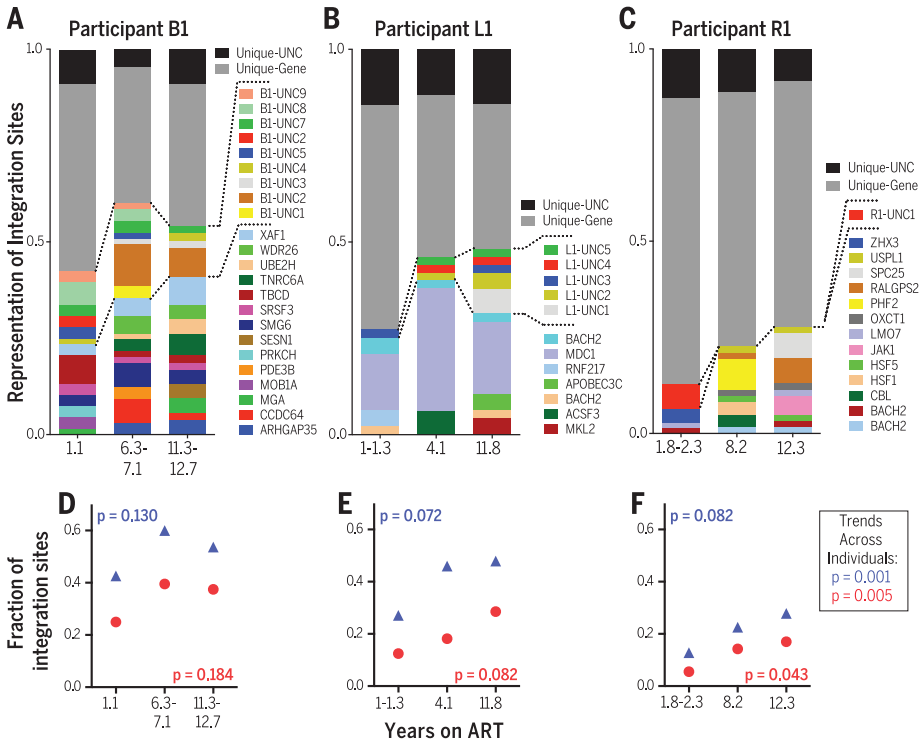

Fig. 1. Representation of HIV integration sites sampled through time. (**A** to **C**) show the scaled representation of each gene with integration sites mapped for the three participants at three intervals (times in years given along the *x* axis) after initiation of suppressive ART. Integration sites were detected in all chromosomes of all participants, except for chromosome 18 in participant B1, and chromosome 20 and the Y chromosome in L1, the only male studied. The gray and black regions at the top of each column indicate the proportion of uncharacterized noncoding regions (UNC, black) and genes (gray) that had only one integration site found at any time point. The other colors represent each of the genes (intragenic regions) and uncharacterized noncoding regions that were found to have virus integrated at the same position in multiple cells. (**D** to **F**) show the proportion of all HIV-infected cells found to be demonstrably proliferating (blue triangles), defined by ≥2 cells with identical integration sites (from any time point), and the proportion of unique integration sites with evidence of proliferation (red dots). Data are plotted by time (*x* axis) after initiation of suppressive ART. The *P* values shown report the significance of the upward trends of these values through time using nonparametric Cochrane-Armitage tests (*45*).

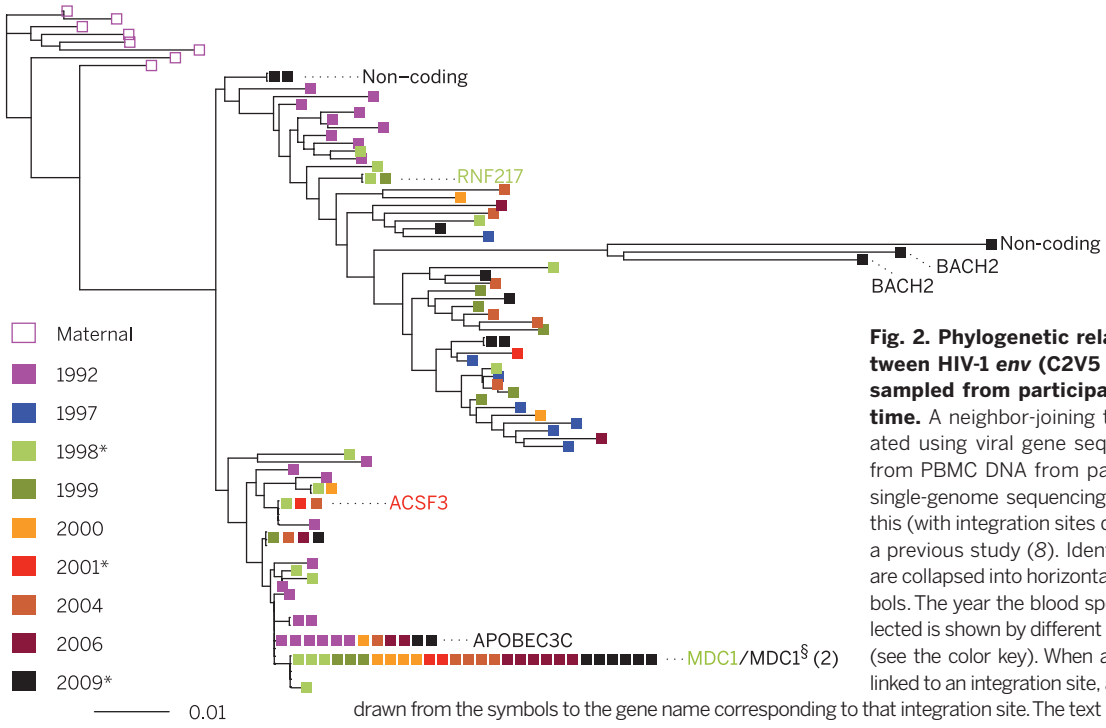

Fig. 2. Phylogenetic relationships between HIV-1 *env* (C2V5 region) genes sampled from participant L1 through time. A neighbor-joining tree was generated using viral gene sequences derived from PBMC DNA from participant L1 by single-genome sequencing, including from this (with integration sites determined) and a previous study (*8*). Identical sequences are collapsed into horizontal strings of symbols. The year the blood specimen was collected is shown by different colored symbols (see the color key). When an *env* gene was linked to an integration site, a dotted line was drawn from the symbols to the gene name corresponding to that integration site. The text color of the gene name indicates the year that the specimen was collected with a specific integration site, using the same color key. Participant L1 was perinatally infected with HIV-1, and viral sequences from his mother are shown with open boxes. The horizontal scale indicates a 1% difference between sequences. Asterisks after the year indicate cancer-associated genes time points that integration sites were determined, and § indicates genes with GO terms from the list of hallmarks of cancer (*25*). Three proviruses (indicated in the figure) were found to be defective as a result of hypermutation (assessed using the tool at www.hiv.lanl.gov/content/sequence/HYPERMUT/hypermut.html), resulting in the introduction of stop codons into the *env* genes of all three sequences.

promote cell proliferation in a manner distinct from homoeostatic proliferation (*7*, *22*). The increasing overrepresentation of proliferating cells containing proviruses suggests that HIV integration plays a mechanistic role in infected cell survival during ART.

Our third approach examined gene ontology in order to associate integration sites with biological processes (GO terms). The unique HIV integrations in our participants were enriched in genes controlling cell proliferation (table S2) and were overrepresented in hallmark cancer GO terms (*23*–*25*) when compared with integrations from the Jurkat cell data set (51.29% versus 41.96%; $P = 0.0001$). Integrations in proliferating cells were also highly enriched in the 10 hallmarks of cancer gene categories considered together compared with the Jurkat cell dataset ($P < 0.0001$). Among the 43 hallmark GO terms, significant enrichment was observed for three terms linked to the regulation of cell proliferation or survival (each $P < 0.0001$), including negative regulation of cell cycle (GO:0045786), cell adhesion (GO:0007162), and DNA repair (GO:0006281). This suggests that HIV integration may promote proliferation and persistence of infected cells.

Three genes have been favored for HIV integration in cell lines: *CREBBP*, *FBX11*, and *DNMT1* (*18*). We detected HIV integrated into the cancer gene *CREBBP* in participants B1 and R1 after 7 and 8.2 years of ART, respectively, indicating that some sites of preferential integration may affect cell survival. However, because we detected only a single integrant in each participant, our findings do not reveal whether integration into *CREBBP* potentiated cell proliferation. Interestingly, among the 288 unique virus integration sites detected within genes, 12 (*ANKRD13C*, *BACH2*, *C2CD3*, *CREBBP*, *HNRNPUL1*, *IKZF3*, *KCTD13*, *MAPK1*, *OXCT1*, *STAT5B*, *ST8SIA4*, and *TRAPPC10*) had proviruses in two of our three participants (table S1), an unusually high number ($P = 0.0264$), suggesting that these regions favor HIV integration and/or survival.

A comparison of our results to published studies of integration sites detected during ART (*9*, *10*, *26*, *27*) revealed a striking persistence of cells with HIV integrated into *basic leucine zipper transcription factor 2* (*BACH2*), a transcription regulator with numerous biological functions—including tumor suppressor functions in B cells (*28*), regulating immune activation (*29*), maintaining naïve T cells, and regulating generation of effector-memory T cells (*30*)—and it is the target of *Menin* binding for regulation of CD4 T cell senescence and cytokine homeostasis (*31*). HIV integrations were mapped to seven positions in *BACH2* in participant L1 and 2 positions in participant R1 (Fig. 3). Despite uneven sampling of HIV integration sites during ART, proviruses were detected in the *BACH2* gene of 7 of 28 individuals previously reported; at 0 out of 74 sites in 16 individuals (*26*, *33*), 37 out of 442 sites in 2 of 3 individuals (*9*), 1 out of 63 sites in 1 of 8 individuals (*27*), and 4 out of 23 sites in peripheral blood mononuclear cells (PBMCs) from 1 person (*10*). All of these integrations occurred in intron 5, just upstream from the start codon of *BACH2*, and all in the same transcriptional orientation as the gene (Fig. 3). In contrast, among the >44,000 integration sites in the Jurkat cell data set (*21*), only one integration into intron 5 of *BACH2* was found (Fig. 3), and none among the integration sites evaluated in other studies of various cultured cells (*17*, *19*, *34*). The finding of disproportionate integrations into this intron of *BACH2* in proliferating and persisting cells strongly suggest that this event favors cell survival; HIV integration just upstream of the start of the coding sequence could lead to promoter insertion–mediated activation (*16*) and thus dysregulation of the *BACH2* gene. Indeed, another *BACH2* intron is a target for integration by murine leukemia viruses found in B cell lymphomas of mice (*32*).

The most extreme case of proliferation (31% of infected cells in participant L1) was found with provirus integrated into *MDC1* (*mediator of DNA damage checkpoint 1*), corresponding to cell expansion by a factor of ~4×10^8 in vivo. However, our study design likely underestimates the occurrence of HIV integration into genes that favor cell proliferation. First, sampling of integration sites was limited, and examination of phylogenetic trees suggests additional proliferating cell populations for which integration sites were not derived (Fig. 2 and figs. S2 and S3). Second, ~20% of the integration sites were outside of gene coding regions, and these regions were not assessed for associations with cancer or cell survival, although many were noted within proliferating cells (Fig. 1). Third, cancer databases often omit genes associated infrequently with cancers, and given the rapid rate that new cancer genes are reported (*12*), some recently described cancer genes have not yet been added to these databases. For example, *BACH2*, despite being regarded as a tumor suppressor in B cells (*28*) and a cellular oncogene in mice (*32*), has not yet been classified as a cancer

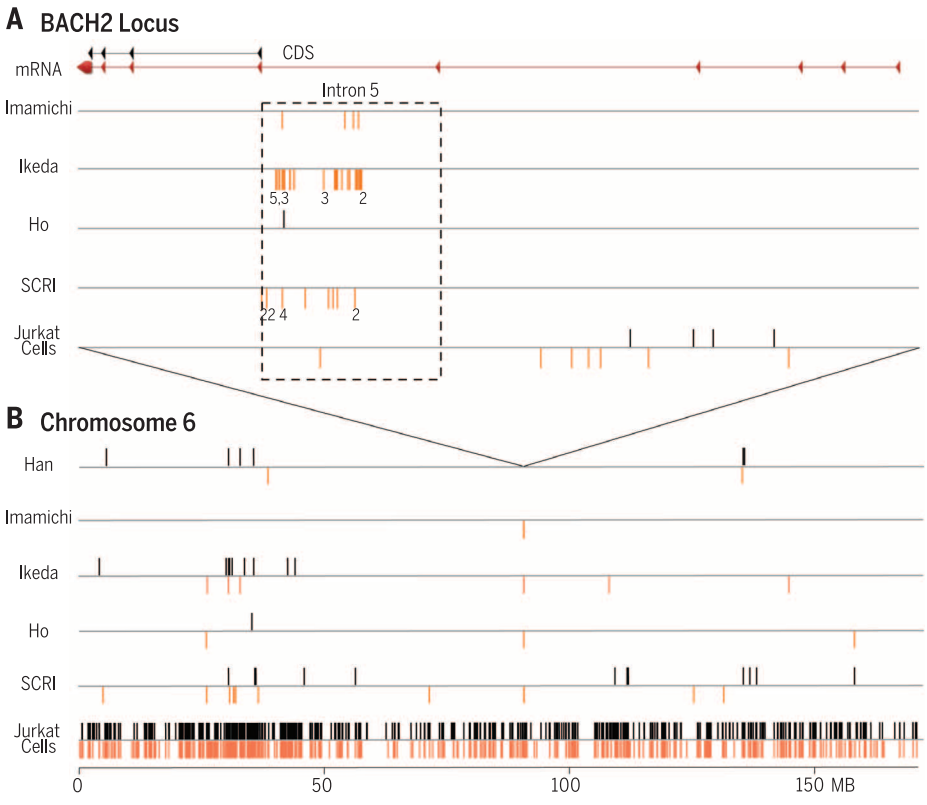

Fig. 3. HIV-1 integration sites in chromosome 6, including the BACH2 locus. (**B**) (bottom) shows the integration sites mapped in the human chromosome 6 in this (SCRI, Seattle Children's Research Institute) and other studies of individuals sampled while on suppressive ART, including from Han *et al*. (*26*), Imamichi *et al*. (*10*), Ikeda *et al*. (*9*), and Ho *et al*. (*27*). Data taken from the Wang *et al*. (*21*) study of virus integrations found 72 hours after infection of Jurkat cells are also shown. The vertical lines represent an integration site over the 172-MB chromosome. Vertical black lines above the horizontal line from each study represent virus integration in the same orientation (5′ to 3′) as the chromosome. Vertical orange lines below the horizontal indicate virus integrations in the opposite orientation. (**A**) shows an enlargement of the region of chromosome 6 encoding the BACH2 gene. The exons corresponding to a common mRNA transcript are shown on the red line with red arrowheads. The coding sequences (CDS) of the gene are shown with black arrowheads. The position of intron 5 is enclosed in the alignment below in a broken-line box.

gene. Also, mutations in *IZKF3*, which also had HIV integrations detected in two of our three participants, was recently associated with a form of acute lymphoblastic leukemia (*35*). Fourth, as somatic mutations that "drive" cancers are estimated to only convey a 0.4% growth advantage (*36*), HIV integration into genes with subtle enhancement of cell proliferation may be difficult to detect as clonal due to our limited sampling.

HIV-infected cells that express viral proteins are likely to be eliminated by immune surveillance, or virus replication may lead to cell lysis. Whether the proliferating and persisting HIV-infected cells that we describe harbor replication-competent virus is critical to defining their role in perpetuating the infectious virus reservoir. Undoubtedly, some clonal populations persist due to defects in expression of the proviral genome (*9*, *10*, *37*). Although we did not evaluate viral sequences for replication competency, lethally hypermutated viral genomes were linked to three integration sites (Fig. 2). However, cells producing viremias with identical *env* sequences have been shown to harbor replication-competent virus (*38*). Also, approximately 12% of proviruses refractory to in vitro induction were found to have intact genomes and may be infectious (*27*). Although transcriptional interference was not detected in the aforementioned noninduced viral transcripts (*26*, *27*), others have observed that the site of integration may cause transcriptional interference (*34*, *39*–*43*).

In conclusion, HIV integration into genes associated with cancer or cell cycle regulation appears to confer a survival advantage that allows these cells to persist during suppressive ART, with cell proliferation appearing to serve as an important mechanism of HIV persistence. To be defined are the mechanisms contributing to cell proliferation, the role of proliferating cells in perpetuating the infectious virus reservoir, and whether therapies that target HIV-infected proliferating cells, specific genes, or their products may contribute to a curative strategy for HIV infection.

REFERENCES AND NOTES

1. J. D. Siliciano *et al.*, *Nat. Med.* **9**, 727–728 (2003).
2. N. H. Tobin *et al.*, *J. Virol.* **79**, 9625–9634 (2005).
3. A. Sigal *et al.*, *Nature* **477**, 95–98 (2011).
4. S. Letendre *et al.*, *Arch. Neurol.* **65**, 65–70 (2008).
5. C. V. Fletcher *et al.*, *Proc. Natl. Acad. Sci. U.S.A.* **111**, 2307–2312 (2014).
6. J. R. Bailey *et al.*, *J. Virol.* **80**, 6441–6457 (2006).
7. N. Chomont *et al.*, *Nat. Med.* **15**, 893–900 (2009).
8. T. A. Wagner *et al.*, *J. Virol.* **87**, 1770–1778 (2013).
9. T. Ikeda, J. Shibata, K. Yoshimura, A. Koito, S. Matsushita, *J. Infect. Dis.* **195**, 716–725 (2007).
10. H. Imamichi *et al.*, *AIDS* 1 (2014).
11. S. A. Forbes *et al.*, *Nucleic Acids Res.* **39** (Database), D945–D950 (2011).
12. M. S. Lawrence *et al.*, *Nature* **505**, 495–501 (2014).
13. M. Zhao, J. Sun, Z. Zhao, *Nucleic Acids Res.* **41** (D1), D970–D976 (2013).
14. C. Kandoth *et al.*, *Nature* **502**, 333–339 (2013).
15. B. Vogelstein *et al.*, *Science* **339**, 1546–1558 (2013).
16. H. Fan, C. Johnson, *Viruses* **3**, 398–422 (2011).
17. A. R. Schröder *et al.*, *Cell* **110**, 521–529 (2002).
18. F. Bushman *et al.*, *Nat. Rev. Microbiol.* **3**, 848–858 (2005).
19. R. S. Mitchell *et al.*, *PLOS Biol.* **2**, e234 (2004).
20. M. J. Soto, A. Peña, F. G. Vallejo, *AIDS Res. Hum. Retroviruses* **27**, 547–555 (2011).
21. G. P. Wang, A. Ciuffi, J. Leipzig, C. C. Berry, F. D. Bushman, *Genome Res.* **17**, 1186–1194 (2007).
22. D. Persaud *et al.*, *J. Virol.* **78**, 968–979 (2004).
23. D. Hanahan, R. A. Weinberg, *Cell* **100**, 57–70 (2000).
24. D. Hanahan, R. A. Weinberg, *Cell* **144**, 646–674 (2011).
25. C. L. Plaisier, M. Pan, N. S. Baliga, *Genome Res.* **22**, 2302–2314 (2012).
26. Y. Han *et al.*, *J. Virol.* **78**, 6122–6133 (2004).
27. Y. C. Ho *et al.*, *Cell* **155**, 540–551 (2013).
28. S. Swaminathan *et al.*, *Nat. Med.* **19**, 1014–1022 (2013).
29. R. Roychoudhuri *et al.*, *Nature* **498**, 506–510 (2013).
30. S. Tsukumo *et al.*, *Proc. Natl. Acad. Sci. U.S.A.* **110**, 10735–10740 (2013).
31. M. Kuwahara *et al.*, *Nat. Commun.* **5**, 3555 (2014).
32. J. Liu *et al.*, *BMC Mol. Biol.* **10**, 2 (2009).
33. Y. Han, M. Wind-Rotolo, H. C. Yang, J. D. Siliciano, R. F. Siliciano, *Nat. Rev. Microbiol.* **5**, 95–106 (2007).
34. M. K. Lewinski *et al.*, *J. Virol.* **79**, 6610–6619 (2005).
35. L. Holmfeldt *et al.*, *Nat. Genet.* **45**, 242–252 (2013).
36. I. Bozic *et al.*, *Proc. Natl. Acad. Sci. U.S.A.* **107**, 18545–18550 (2010).
37. L. Josefsson *et al.*, *PLOS Pathog.* **9**, e1003432 (2013).
38. J. A. Anderson *et al.*, *J. Virol.* **85**, 5220–5223 (2011).
39. H. P. Mok, S. Javed, A. Lever, *Gene Ther.* **14**, 741–751 (2007).
40. K. Imai, H. Togami, T. Okamoto, *J. Biol. Chem.* **285**, 16538–16545 (2010).
41. J. Friedman *et al.*, *J. Virol.* **85**, 9078–9089 (2011).
42. P. G. Eipers, J. F. Salazar-Gonzalez, C. D. Morrow, *Virology* **410**, 151–160 (2011).
43. S. Sherrill-Mix *et al.*, *Retrovirology* **10**, 90 (2013).
44. L. M. Frenkel *et al.*, *J. Virol.* **77**, 5721–5730 (2003).
45. P. Armitage, *Biometrics* **11**, 375–386 (1955).

ACKNOWLEDGMENTS

We wish to express gratitude to the study participants who donated their time and provided specimens, and to N. H. Tobin, A. J. Melvin, and K. M. Mohan for their contributions to this study. Additionally, we thank Y. C. Ho, R. and J. Siliciano, H. Imamichi and C. Lane, and N. Malani and F. Bushman for providing their HIV integration site data. HIV *env* sequences generated from specific integration sites were deposited in GenBank under accession numbers (KM025062 to KM025124 and KM201287 to KM201295). Additional HIV *env* sequences were deposited in GenBank under accession numbers AY075701 to AY077450 (*44*), AY483287 to AY484389 (*2*), and KC314011 to KC315287 (*8*). Sequences of HIV-3′-LTR and adjacent chromosome integration sites are available in table S3. Other data are tabulated in the main paper and in the supplementary materials. Integration site sequences and HIV sequence alignments are available for download at http://mullinslab.microbiol.washington.edu/publications/supplemental.html. These studies were funded by R01AI091550 (L.M.F.), K23AI077357 (T.A.W.), R01 AI111806 (J.I.M.), the Molecular Profiling and Computational Biology Core of the University of Washington's Center for AIDS Research (P30 AI027757), and the Canadian Institutes of Health (HIV/AIDS Research Initiative award 201311CVI-322424-244686) (C.Y.K.C.). We wish to thank A. Embry and D. Lawrence at the National Institutes of Health for their support. The authors report no conflicts of interest related to this research.

SUPPLEMENTARY MATERIALS

www.sciencemag.org/content/345/6196/570/suppl/DC1
Materials and Methods
Figs. S1 to S3
Tables S1 to S3
References (*46*–*59*)

20 May 2014; accepted 27 June 2014
Published online 10 July 2014;
10.1126/science.1256304

COINFECTION

Helminth infection reactivates latent γ-herpesvirus via cytokine competition at a viral promoter

T. A. Reese,[1] B. S. Wakeman,[2] H. S. Choi,[3]* M. M. Hufford,[4]* S. C. Huang,[1] X. Zhang,[1] M. D. Buck,[1] A. Jezewski,[1] A. Kambal,[1] C. Y. Liu,[1] G. Goel,[5] P. J. Murray,[6] R. J. Xavier,[5]† M. H. Kaplan,[4]† R. Renne,[3]† S. H. Speck,[2]† M. N. Artyomov,[1] E. J. Pearce,[1] H. W. Virgin[1]‡

Mammals are coinfected by multiple pathogens that interact through unknown mechanisms. We found that helminth infection, characterized by the induction of the cytokine interleukin-4 (IL-4) and the activation of the transcription factor Stat6, reactivated murine γ-herpesvirus infection in vivo. IL-4 promoted viral replication and blocked the antiviral effects of interferon-γ (IFNγ) by inducing Stat6 binding to the promoter for an important viral transcriptional transactivator. IL-4 also reactivated human Kaposi's sarcoma–associated herpesvirus from latency in cultured cells. Exogenous IL-4 plus blockade of IFNγ reactivated latent murine γ-herpesvirus infection in vivo, suggesting a "two-signal" model for viral reactivation. Thus, chronic herpesvirus infection, a component of the mammalian virome, is regulated by the counterpoised actions of multiple cytokines on viral promoters that have evolved to sense host immune status.

Mammals are populated by many chronic viruses, termed the virome, which can regulate host physiology and disease susceptibility (*1*). For example, more than 90% of humans are latently infected with herpesviruses that, after clearance of acute infection, produce little infectious virus and often cause no overt disease. Like the human γ-herpesviruses Epstein-Barr virus (EBV) and Kaposi's sarcoma–associated herpesvirus (KSHV), murine γ-erpesvirus-68 (MHV68) establishes lifelong latency. Studies in this model system showed that the cytokine

[1]Department of Pathology and Immunology, Washington University School of Medicine, St. Louis, MO 63110, USA. [2]Emory University Vaccine Center, Atlanta, GA 30322, USA. [3]Department of Molecular Genetics and Microbiology, University of Florida, Gainesville, FL 32610, USA. [4]Departments of Pediatrics and Microbiology and Immunology, Indiana University School of Medicine, Indianapolis, IN 46202, USA. [5]Center for Computational and Integrative Biology and Gastrointestinal Unit, Massachusetts General Hospital, Harvard Medical School, Boston, MA 02114, USA. [6]Departments of Infectious Diseases and Immunology, St. Jude Children's Research Hospital, Memphis, TN 38105, USA.
*These authors contributed equally to this work. †These authors contributed equally to this work. ‡**Corresponding author. E-mail: virgin@wustl.edu**

interferon-γ (IFNγ) inhibits MHV68 replication and reactivation from macrophages, a major cellular site for latency (*2*–*5*); controls persistent replication in vivo (*6*); and is present at low amounts during latency (*7*).

Many people around the world are coinfected with herpesviruses and intestinal helminths. Although herpesviruses can modulate immunity to harm or benefit the host (*7*–*11*), the effects of helminth coinfection on chronic herpesvirus infection are unexplored. Intestinal helminths generate strong T helper 2 (T_H2)–driven cytokine responses, which counter the biological effects of IFNγ and drive the activation of macrophages with an M2 (immunoregulatory) rather than M1 (proinflammatory) phenotype (*12*). Parasitic worms may influence control of pathogens—including *Mycobacterium tuberculosis*, HIV, and *Plasmodium* species in humans—but there are few studies elucidating the mechanisms behind this immunomodulation (*13*). Thus, we considered the hypothesis that parasite infection would induce MHV68 reactivation in vivo.

We examined the effects of acute infection with *Heligmosomoides polygyrus* or *Schistosomiasis mansoni* (*Sm*) egg administration on MHV68

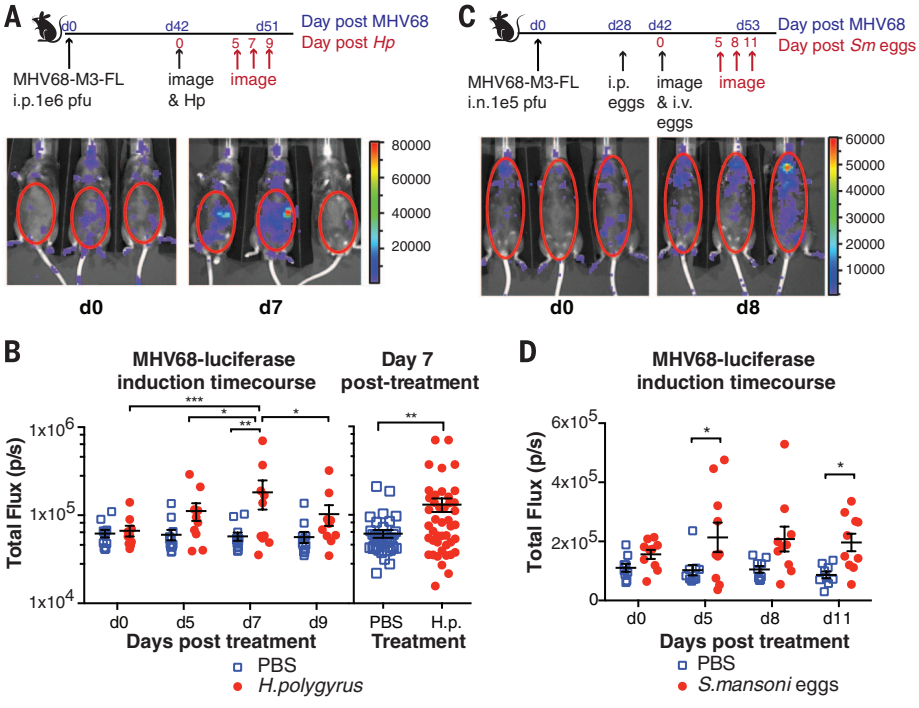

Fig. 1. Challenge with *H. polygyrus* and *S. mansoni* eggs reactivates MHV68. (**A**) C57BL6/J mice were infected intraperitoneally (i.p.) with MHV68-M3-FL and challenged with *H. polygyrus* 42 days later. Mice were imaged before *H. polygyrus* infection (day 0, d0) and 5, 7, and 9 days after. Three representative mice imaged on days 0 and 7 are shown. (**B**) Total flux (photons per second, p/s) was quantitated for mice in two independent experiments for the timecourse after infection with *H. polygyrus*. Data from four independent experiments at day 7 after *H. polygyrus* (H.p.) infection are also shown. (**C**) C57BL/6J mice were infected intranasally (i.n.) with MHV68-M3-FL. The diagram indicates the timecourse of the experiment and challenge with *Sm* eggs or phosphate-buffered saline (PBS) as a control. Mice were injected with D-Luciferin and imaged before intravenous (i.v.) challenge with *Sm* eggs (day 0). They were subsequently imaged 5, 8, and 11 days after challenge with *Sm* eggs. Three representative mice imaged on days 0 and 8 are shown. (**D**) Total flux was quantitated from mice in two independent experiments after *Sm* egg challenge. Symbols represent individual mice, and the mean and standard error are indicated. *$P < 0.05$, **$P < 0.01$, ***$P < 0.001$ by two-way repeated measures analysis of variance (ANOVA) with Tukey's and Bonferroni's post-test.

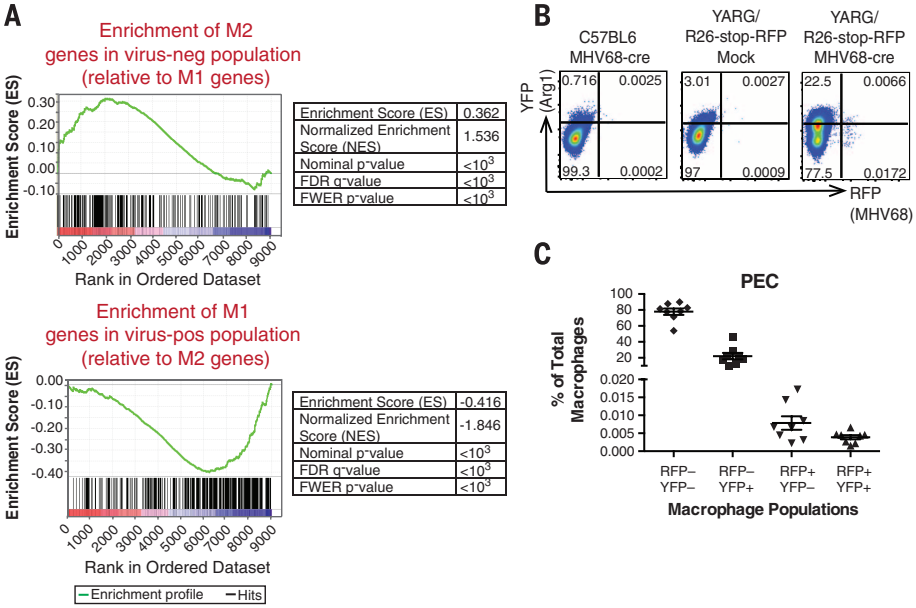

Fig. 2. IL-4 and IFNγ signatures identified in different macrophage populations during MHV68 infection. (**A**) GSEA of virus-positive and -negative cells sorted from the peritoneum of MHV68-infected mice compared to BMDMs stimulated with IL-4 or IFNγ/LPS. (**B**) C57BL/6J mice or YARG/R26-stop-RFP mice were either mock infected or infected with MHV68-cre. CD11b+F4/80+ cells were gated and examined for RFP and YFP expression. Representative plots from two independent experiments, with three to five mice per experiment, are shown. (**C**) Quantitation of fluorescence-activated cell sorting (FACS) analysis in (B), with each symbol representing a single mouse. PEC, peritoneal exudate cells.

reactivation from latency using a MHV68 virus expressing luciferase under the control of a lytic viral promoter upon reactivation from latency in vivo (MHV68-M3-FL) (*14*). Both acute *H. polygyrus* infection and *Sm* egg challenge reactivated MHV68 infection (Fig. 1, A to D). Mice latently infected for more than 100 days also showed increased luciferase expression after *Sm* egg challenge (fig. S1). By contrast, infection with the systemic bacteria *Listeria monocytogenes* did not stimulate viral reactivation (fig. S2). Thus, responses to either a nematode parasite or trematode eggs induced herpesvirus reactivation, suggesting a role for T_H2 cytokines in viral reactivation.

To determine whether T_H2 cytokines affect latently infected macrophages, we compared host gene expression patterns in virally infected and uninfected macrophages during chronic infection. We engineered MHV68 to express cre-recombinase (MHV68-cre) from a locus permitting heterologous gene expression without altering viral replication or reactivation (*15*) (fig. S3). Reporter mice in which fluorescent protein expression is induced by cre recombination [Rosa26-floxed stop-eYFP or tandem dimer (td)RFP (eYFP, enhanced yellow fluorescent protein; RFP, red fluorescent protein) (*16*)] were infected with MHV68-cre. Virus-positive and -negative cells sorted from latently infected mice (fig. S3G) were subjected to RNAseq analysis. Transcription in these cells was compared to that in bone marrow–derived macrophages (BMDMs) stimulated with interleukin-4 (IL-4) (M2) or IFNγ plus lipopolysaccharide (LPS) (M1) compared to untreated BMDMs (M0). Gene set enrichment analysis (GSEA) revealed that genes up-regulated in M1 BMDMs were enriched in

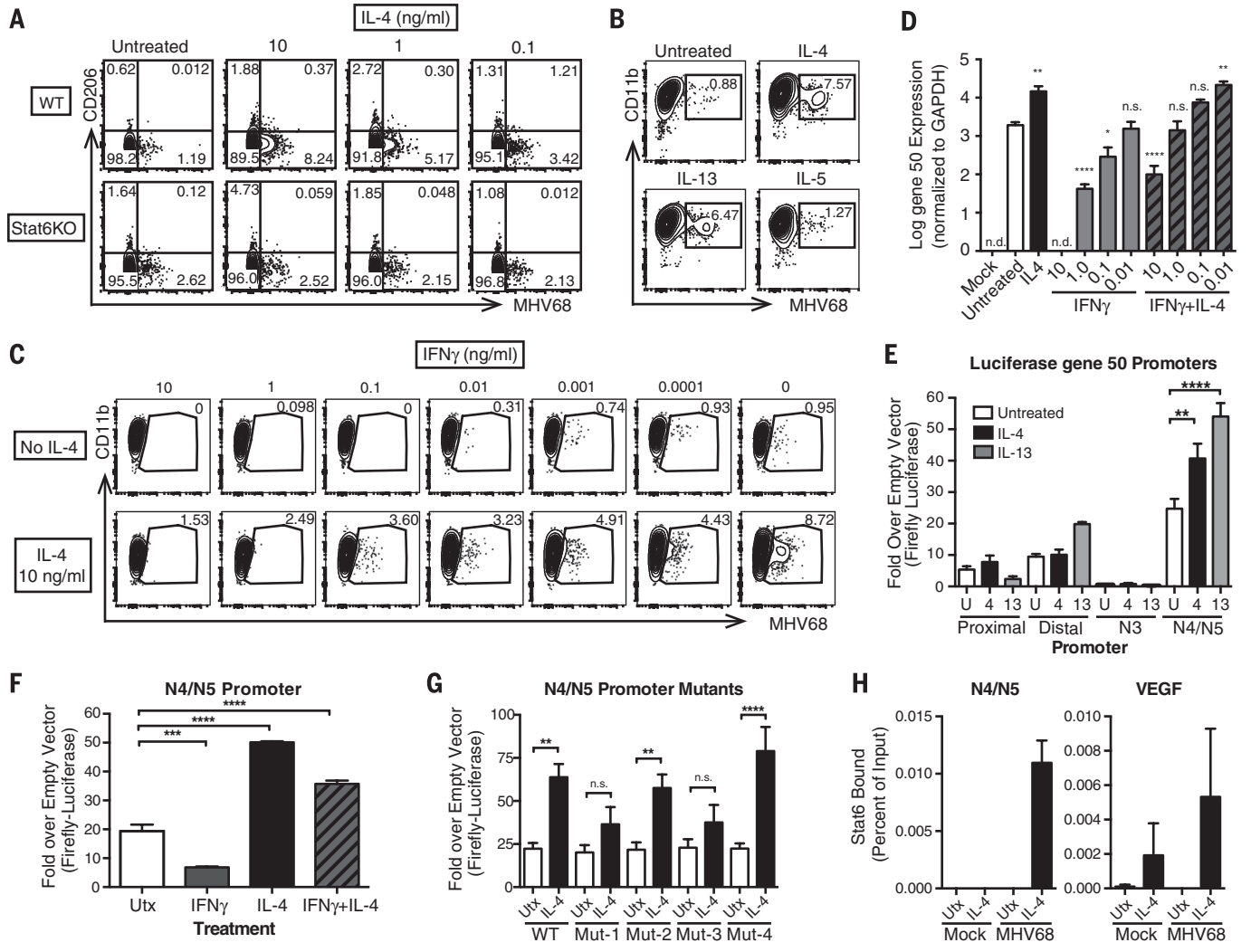

Fig. 3. IL-4 promotes viral replication and antagonizes IFNγ suppression of viral replication through direct binding to a viral promoter. (**A**) BMDMs were untreated or treated with the indicated doses of IL-4 and infected with MHV68. Twenty-four hours after infection, cells were analyzed for expression of MHV68 lytic viral proteins and CD206 expression. Data from three independent experiments are shown. WT, wild-type. (**B**) Pretreatment of BMDMs with IL-4, IL-13, or IL-5 before infection with MHV68 and FACS analysis. (**C**) BMDMs were pretreated with varying doses of IFNγ ± 10 ng/ml of IL-4. At 24 hours after infection, cells were analyzed for expression of lytic viral proteins. Data from three independent experiments are shown. (**D**) *Gene 50* expression was analyzed by reverse transcription polymerase chain reaction (RT-PCR) in BMDMs pretreated with IL-4 and/or IFNγ. Expression was normalized to *Gapdh* (glyceraldehyde phosphate dehydrogenase). Data from four independent experiments are shown. (**E**) RAW264.7 cells were transfected with vectors expressing luciferase under control of four different *gene 50* promoters (*23*, *24*). Cells were then treated with or without IL-4 or IL-13 for 24 hours, lysed, and assayed for luciferase activity. (**F**) Cells were transfected with the N4/N5 promoter luciferase construct and treated with IL-4, IFNγ, or both. (**G**) N4/N5 luciferase mutants were transfected into RAW264.7 cells and assayed for sensitivity to IL-4. (**H**) RAW264.7 cells were infected with MHV68 at multiplicity of infection = 5 and treated with IL-4 for 8 hours. After ChIP with Stat6 antibody, quantitative PCR (qPCR) was performed for the N4/N5 promoter region or vascular endothelial growth factor (VEGF). Percentage of input after normalizing to immunoglobulin G control was calculated for both N4/N5 and VEGF. One experiment representative of four independent experiments is shown. Error bars indicate SEM. n.d. not detected; n.s. not significant. **P* < 0.05, ***P* < 0.01, ****P* < 0.001, *****P* < 0.0001 by *t* test or one-way ANOVA with Sidak's multiple comparisons test.

virus-positive macrophages, whereas genes upregulated in M2 BMDMs were enriched in virus-negative cells (Fig. 2A and table S1). This was consistent with the role of IFNγ, which drives M1 macrophage polarization, in inhibiting MHV68 replication and reactivation (*3*, *4*). We therefore tested whether latent MHV68 infection was restricted to M1-type macrophages by infecting tdRFP mice carrying the Arginase-1 (Arg1)–YFP reporter (YARG, a marker for macrophages stimulated with T_H2 cytokines) (*17*) with MHV68-cre. Surprisingly, virus-positive macrophages were either positive or negative for *Arg1* (Fig. 2, B and C), suggesting that despite the role for IFNγ in controlling chronic MHV68 infection, at least some virus-infected cells were exposed to cytokines that drive *Arg-1* expression in vivo.

Along with the observation that T_H2 cytokine-inducing parasites promote reactivation from latency, the presence of an IL-4 signature in some virus-infected macrophages suggests a role for IL-4 in viral infection. We tested this by determining the effect of IL-4 on MHV68 replication in BMDMs. Treatment with IL-4 increased *Arg1* expression (fig. S4A), consistent with M2 polarization (*18*). As expected, few infected BMDMs expressed lytic viral antigens upon MHV68 infection (*19*). However, IL-4 pretreatment increased the number of BMDMs expressing viral proteins and enhanced viral replication (Fig. 3A and fig. S4, B to D); it also increased infection of transformed RAW264.7 macrophages (fig. S4E). Treatment with IL-4 after MHV68 infection increased viral replication (fig. S4F), indicating that IL-4 acts on replication rather than by increasing the number of infected cells. Enhancement of replication was dependent on the T_H2-associated transcription factor Stat6 (Fig. 3A) and occurred with IL-13 stimulation, another T_H2-associated cytokine that uses the IL-4 receptor α chain and signals via Stat6 (Fig. 3B and fig. S4, D and G). The T_H2 cytokine IL-5, which does not signal through Stat6, did not promote MHV68 replication (Fig. 3B).

After treatment with IL-4, the majority of infected cells did not express the M2 markers CD206 or *Arg1* (Fig. 3A and fig. S4A), suggesting that not all IL-4-induced changes in macrophage differentiation are required for enhanced MHV68 replication (*20*). Etomoxir blocks IL-4–induced changes in fatty acid oxidation (*21*) and upregulation of CD206 (fig. S5A) but did not block enhancement of MHV68 replication by IL-4 (fig. S5B). Moreover, IL-4 enhanced replication in the absence of peroxisome proliferator–activated receptor γ (PPARγ) or ARG1, key proteins involved in M2 macrophage function, or inducible nitric oxide synthase, an essential protein in M1 macrophage function (fig. S5, C to G) (*20*). Importantly, IL-4 antagonized IFNγ-mediated suppression of viral replication (Fig. 3C) (*3*). Because Stat6 antagonizes Stat1 (*22*), we tested whether IL-4 promoted virus replication in the absence of Stat1.

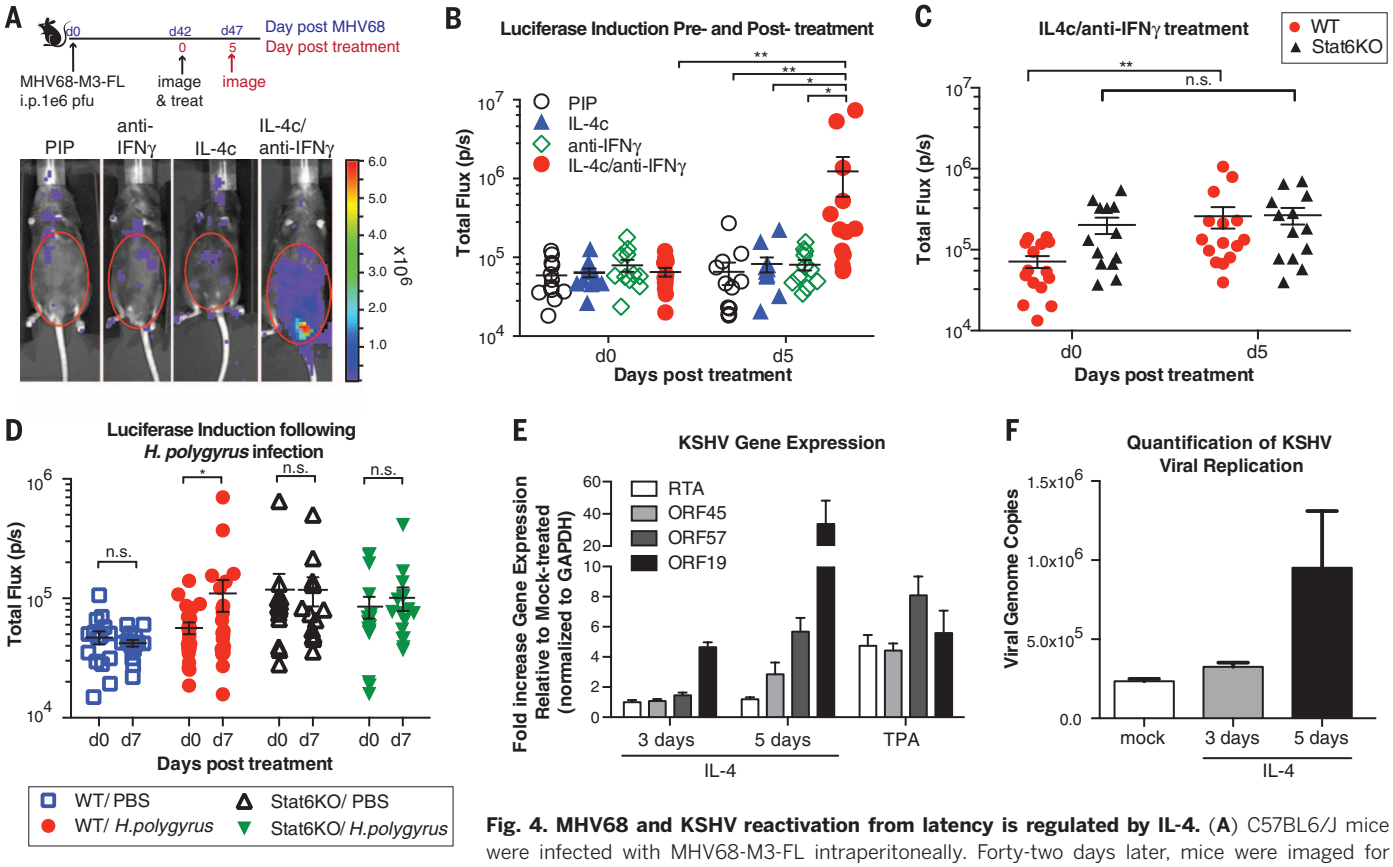

Fig. 4. MHV68 and KSHV reactivation from latency is regulated by IL-4. (**A**) C57BL6/J mice were infected with MHV68-M3-FL intraperitoneally. Forty-two days later, mice were imaged for luciferase expression (d0) and then received isotype control (PIP), anti-IFNγ (H22), IL-4c, or both anti-IFNγ and IL-4c. On day 44, mice received a second dose of IL-4c or PBS. Mice were imaged 5 days after the first treatment, and total flux from the abdominal region was quantitated. Data from four representative mice are shown. (**B**) Quantitation of total flux from three individual experiments described in (A) is shown. Each symbol represents an individual mouse. Bars denote means; and error bars represent standard errors. (**C**) WT or Stat6KO mice were treated as in (A) with anti-IFNγ/IL-4c and imaged 5 days later. Bars denote the means of individual mice (symbols); error bars represent standard errors. (**D**) The experimental set-up was the same as that of Fig. 1A. Latently infected WT and Stat6KO mice infected with MHV68-M3-FL were infected with *H. polygyrus* or treated with PBS on day 42, and reactivation was quantitated by luciferase induction 7 days later. (**E**) BCBL-1 cells were treated with IL-4 for 3 or 5 days or 12-*O*-tetradecanoylphorbol-13-acetate (TPA) for 48 hours, and viral gene expression was analyzed. The fold increase in gene expression over mock after normalization of GAPDH is shown. Data are from three independent experiments. (**F**) Supernatants from cells treated in (E) were collected, and virus was isolated by centrifugation. Viral genome copy number was assayed by qPCR using serial diluted LANA expression plasmid as a standard curve. One experiment representative of two independent experiments is shown. For luciferase experiments: $*P < 0.05$, $**P < 0.01$. n.s., not significant by two-way repeated measures ANOVA with Tukey's and Bonferroni's post-test. Error bars indicate SEM.

IL-4 increased virus replication in Stat1-deficient BMDMs (fig. S6).

Previously, we found that IFNγ-mediated suppression of viral replication was associated with inhibition of promoters driving expression of the essential viral latent-to-lytic switch gene (*gene 50*) (*3*, *23*). IL-4 antagonizes IFNγ-mediated suppression of *gene 50* transcription (Fig. 3D). This effect was specific to the viral promoter because IL-4 did not block IFNγ-mediated induction of *Nos2*, and IFNγ did not inhibit IL-4–mediated induction of *Arg1* and *Relma/Fizz1* (fig. S7). Furthermore, IL-4 and IL-13 transactivated the *gene 50* N4/N5 promoter (Fig. 3E) (*24*), and IL-4 antagonized IFNγ-mediated suppression of the N4/N5 promoter (Fig. 3F). The effect of IL-4 on the N4/N5 promoter was diminished by mutation of two of four putative Stat-binding sites in the promoter (Fig. 3G and fig. S8). Further, chromatin immunoprecipitation (ChIP) experiments revealed that Stat6 bound to the N4/N5 promoter after IL-4 treatment of MHV68-infected cells (Fig. 3H). Taken together, these data suggest that activated Stat6 induced by IL-4/IL-13 promotes viral replication by binding to and acting on a viral promoter to induce expression of *gene 50*.

These counterbalancing effects of IFNγ and IL-4 on virus replication and viral promoter activity suggest a potential mechanism by which IL-4–inducing pathogens such as helminths promote reactivation. Therefore, we treated mice infected with MHV68-M3-FL virus with a blocking antibody to IFNγ (anti-IFNγ) (clone H22) (*25*), an isotype control antibody (clone PIP), long-lasting IL-4 complexes (IL-4c) (*26*), or a combination of anti-IFNγ and IL-4c. No reactivation was observed after treatment with anti-IFNγ, IL-4c, or PIP alone, indicating that a single signal was insufficient to reactivate virus in vivo. However, robust reactivation was observed in mice that received a combination of IL-4c and anti-IFNγ (Fig. 4, A and B, and fig. S9A). We next assayed reactivation using an independent assay (*27*, *28*). Little or no preformed virus was detectable in tissues after treatment with PIP, IL-4c, or anti-IFNγ alone (*27*), whereas treatment with IL-4c plus anti-IFNγ increased infectious virus (fig. S9, B and C). Together, these data support a "two-signal" mechanism by which coinfections could induce reactivation via induction of IL-4 and inhibition of T_H1 responses (*12*).

Increased reactivation after treatment with both IL-4c/anti-IFNγ required Stat6 (Fig. 4C). We did not test the role of Stat1 or the IFNγ receptor because both are required to establish latency (*6*). To assess whether the effects of helminth infection on MHV68 reactivation also required Stat6, we challenged MHV68-infected Stat6KO mice with *H. polygyrus*. We found that helminth infection did not reactivate MHV68 from latency in Stat6KO mice, further supporting a two-signal model for control of γ-herpesvirus reactivation in vivo (Fig. 4D).

Our results suggested a possible role for IL-4 in human γ-herpesvirus reactivation. We therefore tested whether IL-4 could reactivate the human γ-herpesvirus KSHV in the BCBL-1 human B cell lymphoma cell line. We found that treatment with IL-4 increased immediate early (RTA, ORF45, and ORF57) and late (ORF19) viral transcripts (*29*) (Fig. 4E). RTA is the homolog in KSHV of MHV68 *gene 50*, and ORF45 and ORF57 are both transactivators, indicating a common role of IL-4 in regulating important viral transcriptional transactivators. Furthermore, IL-4 treatment of cells increased virus production (Fig. 4F), indicating that IL-4 is capable of inducing reactivation of KSHV.

A notable aspect of herpesvirus infection is its permanence despite ongoing immunity combined with the capacity to reactivate and spread to new hosts. This work illuminates one potential mechanism by which a γ-herpesvirus exhibits these two apparently disparate functions. Our data suggest that the virus evolved cytokine-responsive promoters to remain latent under some conditions (IFNγ-dominant) and reactivate under other conditions (IL-4–dominant). In this setting, coinfection may govern the outcome of reactivation by changing the balance in IL-4 and IFNγ, thus raising a potential issue with herpesvirus reactivation and proposed live helminth therapies (*12*). Additionally, our data illustrate one potential mechanism by which helminths and other type 2 immune response–inducing parasites influence host control of another pathogen through M2 macrophage polarization (*13*). The fact that viral promoters for an essential gene are responsive to host cytokines implies that the viral genome evolved to sense the infection status of the host. We speculate that a similar mechanism for IL-4–induced reactivation of KSHV could also be true. Although not extensively studied, seroprevalence to KSHV is associated with hookworm and other parasitic infections in Uganda (*30*). Intriguingly, certain Burkitt's lymphoma cell lines are reported to express EBV transcripts in response to IL-4 (*31*).

Although mouse studies are done in specific pathogen-free animals, our data suggest that there is added complexity when multiple pathogens infect the same host, particularly in situations where one pathogen has the capacity to respond to specific immune signals generated to another pathogen to regulate chronic infection. Previously, we showed that herpesvirus infection, a component of the mammalian virome (*1*), enhances resistance to some pathogens (*7*). Here, we demonstrate the opposite effect: that coinfection regulates herpesvirus reactivation. These studies emphasize that the spectrum of immunity to chronic infection is a dynamic equilibrium regulated by coinfections, in part through highly evolved pathogen genomes with the capacity to sense host cytokines.

REFERENCES AND NOTES

1. H. W. Virgin, *Cell* **157**, 142–150 (2014).
2. E. Flaño, S. M. Husain, J. T. Sample, D. L. Woodland, M. A. Blackman, *J. Immunol.* **165**, 1074–1081 (2000).
3. M. M. Goodwin, S. Canny, A. Steed, H. W. Virgin, *J. Virol.* **84**, 3711–3717 (2010).
4. A. Steed, T. Buch, A. Waisman, H. W. Virgin IV, *J. Virol.* **81**, 6134–6140 (2007).
5. K. E. Weck, S. S. Kim, I. V. Virgin HW, S. H. Speck, *J. Virol.* **73**, 3273–3283 (1999).
6. S. A. Tibbetts, L. F. van Dyk, S. H. Speck, H. W. Virgin IV, *J. Virol.* **76**, 7125–7132 (2002).
7. E. S. Barton *et al.*, *Nature* **447**, 326–329 (2007).
8. Y. Nguyen, B. A. McGuffie, V. E. Anderson, J. B. Weinberg, *Virology* **380**, 182–190 (2008).
9. F. Saito *et al.*, *Inflammation* **36**, 1295–1303 (2013).
10. J. W. Peacock, S. F. Elsawa, C. C. Petty, W. F. Hickey, K. L. Bost, *Eur. J. Immunol.* **33**, 1849–1858 (2003).
11. H. W. Virgin, E. J. Wherry, R. Ahmed, *Cell* **138**, 30–50 (2009).
12. H. J. McSorley, J. P. Hewitson, R. M. Maizels, *Int. J. Parasitol.* **43**, 301–310 (2013).
13. P. Salgame, G. S. Yap, W. C. Gause, *Nat. Immunol.* **14**, 1118–1126 (2013).
14. S. Hwang *et al.*, *J. Virol.* **82**, 12498–12509 (2008).
15. J. M. Moser, J. W. Upton, R. D. Allen III, C. B. Wilson, S. H. Speck, *J. Virol.* **79**, 9480–9491 (2005).
16. H. Luche, O. Weber, T. Nageswara Rao, C. Blum, H. J. Fehling, *Eur. J. Immunol.* **37**, 43–53 (2007).
17. T. A. Reese *et al.*, *Nature* **447**, 92–96 (2007).
18. P. Loke *et al.*, *BMC Immunol.* **3**, 7 (2002).
19. M. M. Goodwin *et al.*, *J. Virol.* **84**, 12039–12047 (2010).
20. S. Gordon, F. O. Martinez, *Immunity* **32**, 593–604 (2010).
21. D. Vats *et al.*, *Cell Metab.* **4**, 13–24 (2006).
22. Y. Ohmori, T. A. Hamilton, *J. Biol. Chem.* **275**, 38095–38103 (2000).
23. K. S. Gray, R. D. Allen III, M. L. Farrell, J. C. Forrest, S. H. Speck, *J. Virol.* **83**, 314–328 (2009).
24. B. S. Wakeman *et al.*, *J. Virol.* **88**, 5474–5490 (2014).
25. J. T. Harty, R. D. Schreiber, M. J. Bevan, *Proc. Natl. Acad. Sci. U.S.A.* **89**, 11612–11616 (1992).
26. S. J. Jenkins *et al.*, *Science* **332**, 1284–1288 (2011).
27. K. E. Weck, M. L. Barkon, L. I. Yoo, S. H. Speck, H. W. Virgin IV, *J. Virol.* **70**, 6775–6780 (1996).
28. See supplementary materials and methods on *Science* Online.
29. H. Nakamura *et al.*, *J. Virol.* **77**, 4205–4220 (2003).
30. K. Wakeham *et al.*, *Infect. Agent. Cancer* **6**, 15 (2011).
31. L. L. Kis *et al.*, *Blood* **117**, 165–174 (2011).

ACKNOWLEDGMENTS

T.A.R. was supported by a Damon Runyon Postdoctoral Fellowship. This work was supported by grants U54 AI057160 and AI084887 and Crohn's and Colitis Foundation grant 274415 to H.W.V., grants AI032573 and CA164062 to E.J.P., grant CA119917 to R.R., and grant CA52004 to S.H.S. We thank R. Schreiber and K. Sheehan for supplying anti-IFNγ and PIP, G. Randolph and E. Gautier for PPARγ f/f x LyzMcre mice and helpful discussion, J. Urban for help setting up the *H. polygyrus* system, D. Kreamalmeyer for animal care and breeding, members of the Virgin lab for manuscript review and discussion, the Genome Technology Access Center at Washington University for sequencing, and the Flow Cytometry Core at Washington University for assistance with sorting. The data presented in this manuscript are tabulated in the main paper and in the supplementary materials. The GEO accession numbers for RNAseq data on virus-infected cells and for the BMDMs are GSE58116 and GSE21895, respectively. T.A.R. designed the project, performed experiments, and wrote the paper. H.W.V. assisted with project design and paper writing. B.S.W. and S.H.S. defined promoters and performed promoter assays. X.Z. created and characterized MHV68-cre virus and performed limiting dilution PCR and Western blots. H.S.C. and R.R. performed KSHV experiments. M.M.H. and M.H.K. performed ChIP experiments. S.C.H. and E.J.P. helped design helminth experiments and supplied reagents. M.D.B. did RT-PCR for *gene 50* and host genes. A.J. did flow cytometry with IL-4 in RAW264.7 cells. A.K. did Western blots. C.Y.L. did plaque assays. G.G. and R.J.X. did initial bioinformatic analysis of gene expression by array, later replaced with RNASeq. P.J.M. provided arginase mice. M.N.A. analyzed sequencing data.

SUPPLEMENTARY MATERIALS

www.sciencemag.org/content/345/6196/573/suppl/DC1
Materials and Methods
Figs. S1 to S9
Table S1
References (*32*–*53*)

8 April 2014; accepted 16 June 2014
Published online 26 June 2014;
10.1126/science.1254517

COINFECTION

Virus-helminth coinfection reveals a microbiota-independent mechanism of immunomodulation

Lisa C. Osborne,[1,2] Laurel A. Monticelli,[1,2] Timothy J. Nice,[3] Tara E. Sutherland,[4] Mark C. Siracusa,[1,2]* Matthew R. Hepworth,[1,2,5] Vesselin T. Tomov,[5] Dmytro Kobuley,[1,2] Sara V. Tran,[1,2] Kyle Bittinger,[1] Aubrey G. Bailey,[1] Alice L. Laughlin,[1] Jean-Luc Boucher,[6] E. John Wherry,[2] Frederic D. Bushman,[1] Judith E. Allen,[4] Herbert W. Virgin,[3] David Artis[1,2,7]†

The mammalian intestine is colonized by beneficial commensal bacteria and is a site of infection by pathogens, including helminth parasites. Helminths induce potent immunomodulatory effects, but whether these effects are mediated by direct regulation of host immunity or indirectly through eliciting changes in the microbiota is unknown. We tested this in the context of virus-helminth coinfection. Helminth coinfection resulted in impaired antiviral immunity and was associated with changes in the microbiota and STAT6-dependent helminth-induced alternative activation of macrophages. Notably, helminth-induced impairment of antiviral immunity was evident in germ-free mice, but neutralization of Ym1, a chitinase-like molecule that is associated with alternatively activated macrophages, could partially restore antiviral immunity. These data indicate that helminth-induced immunomodulation occurs independently of changes in the microbiota but is dependent on Ym1.

The microbiota of the mammalian gastrointestinal (GI) tract is composed of trillions of beneficial commensal bacteria that promote nutrient metabolism and regulate multiple physiological processes (*1*, *2*). The GI tract is also a common site of infection by pathogenic viruses, bacteria, protozoa, and helminths. The dynamic cross-regulation that exists between the host, the microbiota, and enteric pathogens regulates intestinal homeostasis (*3*–*9*), indicating that these are highly coevolved relationships. Signals derived from commensal bacteria and helminth parasites can influence the mammalian immune response (*1*, *2*, *10*–*12*), and helminth infection can elicit alterations in the composition of commensal bacteria that have been associated with limiting inflammation in multiple tissues (*13*–*16*). Despite speculation regarding whether helminth-induced immunomodulation is mediated through direct effects on the mammalian immune system or indirectly via changes in the microbiota (*14*, *17*, *18*), this fundamental question has not been addressed. Given the impact of helminth-elicited immunomodulation both as a risk factor for bacterial, viral, and protozoan coinfection (*19*–*22*) and as a potential therapeutic strategy for multiple inflammatory diseases including asthma, multiple sclerosis, and inflammatory bowel disease (*23*, *24*),

[1]Department of Microbiology, Perelman School of Medicine, University of Pennsylvania, Philadelphia, PA 19104, USA. [2]Institute for Immunology, Perelman School of Medicine, University of Pennsylvania, Philadelphia, PA 19104, USA. [3]Department of Pathology and Immunology, Washington University School of Medicine, St. Louis, MO 63110, USA. [4]Institute of Immunology and Infection Research, Centre for Immunity, Infection and Evolution, School of Biological Sciences, University of Edinburgh, Edinburgh EH9 3JT, UK. [5]Department of Medicine, Division of Gastroenterology, Perelman School of Medicine, University of Pennsylvania, Philadelphia, PA 19104, USA. [6]Laboratoire de Chimie et Biochimie Pharmacologiques et Toxicologiques, Université Paris Descartes, Paris, France. [7]Department of Pathobiology, School of Veterinary Medicine, University of Pennsylvania, Philadelphia, PA 19104, USA. *Present address: Department of Medicine, Rutgers New Jersey Medical School, Newark, NJ 07103, USA. †Corresponding author. E-mail: dartis@mail.med.upenn.edu

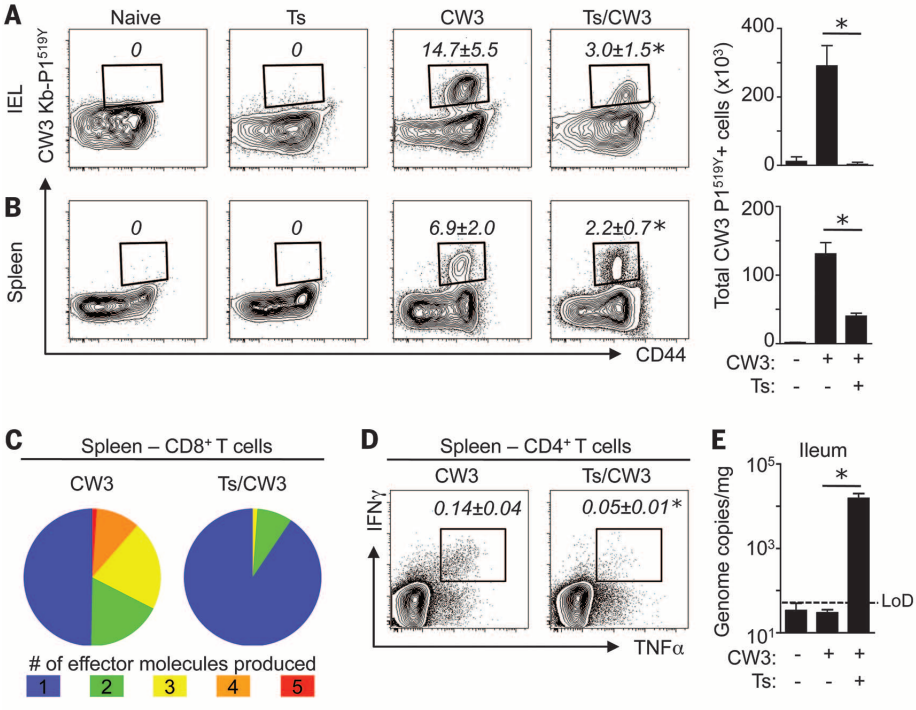

Fig. 1. Helminth coinfection impairs immunity to enteric viral infection. C57BL/6 mice were either left naïve or infected with 500 *Trichinella spiralis* (Ts) larvae per os (po). At day 12 post-*Trichinella* infection, mice were infected with 10^6 plaque-forming units (pfu) MNV CW3 (po) and killed at day 8 post-CW3 infection. (**A** and **B**) Flow cytometric detection of antigen-specific MNV CW3 $P1^{519Y}$ tetramer$^+$ CD8$^+$ T cells in naïve, *Trichinella* (Ts)–infected, CW3-infected, or Ts/CW3–coinfected mice in the (A) small intestine intraepithelial lymphocytes (IEL) and (B) spleen. Numbers in flow plots represent mean frequencies ± SEM of CW3 Kb-$P1^{519Y}$ tetramer$^+$ cells within the CD8$^+$ lymphocyte gate of each group. Error bars in bar graphs indicate SEM. (**C**) Splenocytes from CW3 and Ts/CW3 mice were stimulated with MNV CW3 $P1^{519Y}$ peptide and assayed for production of IFN-γ, TNF-α, chemokine (C-C motif) ligand 3, CD107a, and granzyme B. Pie charts show fractions of peptide-responsive CD8$^+$ T cells producing any combination of these effector molecules. (**D**) Splenocytes from mono- and coinfected mice were stimulated with a pool of MHCII IA^b–restricted MNV-specific peptides and assayed for production of IFN-γ and TNF-α. Numbers in flow plots represent mean frequencies ± SEM of dual-producing IFN-γ$^+$ TNF-α$^+$ cells within the CD4$^+$ CD44^{hi} lymphocyte gate of each group. (**E**) MNV genome copies in ileal tissue were quantified by real-time polymerase chain reaction (RT-PCR). All data are representative of two to four independent experiments with a minimum of three to five mice per group. Statistics compared monoinfected versus coinfected groups by using the Student's *t* test. *$P < 0.05$. LoD, limit of detection.

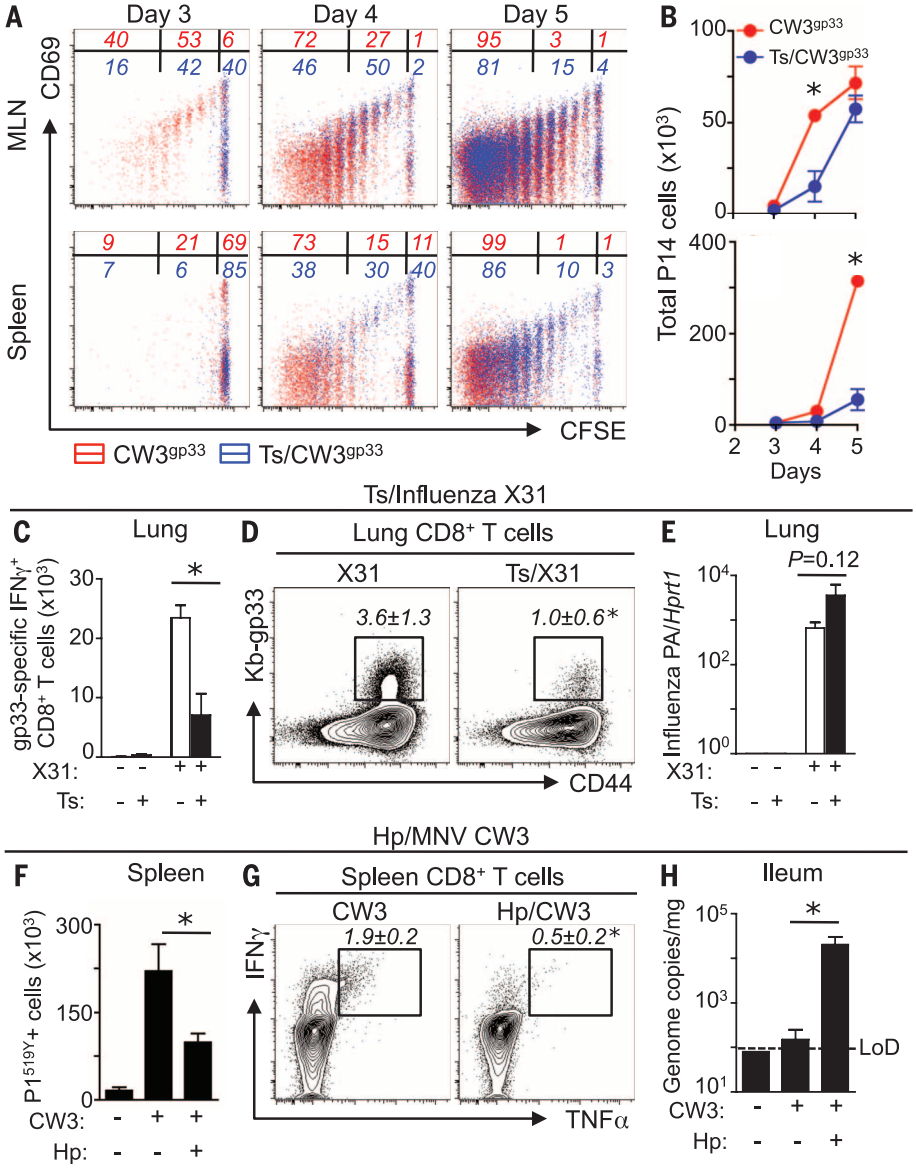

Fig. 2. Impaired virus-specific CD8$^+$ T cell activation and proliferation in the presence of helminth coinfection. (**A**) Carboxyfluorescein diacetate succinimidyl ester (CFSE) dilution and CD69 expression of adoptively transferred gp33-specific P14 CD8$^+$ T cells isolated from the MLNs and spleen of MNV CW3^{gp33} mono- and Ts/MNV CW3^{gp33}–coinfected mice. Red, monoinfected; blue, coinfected. Numbers in flow plots represent frequencies of cells in divisions 0, 1 to 5, or 6+ (right to left). (**B**) Quantification of total P14 cells in the MLNs (top row) and spleen (bottom row) in mono- and coinfected mice. (**C** to **E**) C57BL/6 mice were infected with 500 Ts larvae po. At day 12 post-Ts infection, mice were infected with 10^5 median tissue culture infectious dose influenza X31^{gp33} intranasally (in) and killed at day 7 post-X31 infection. (C) Lung lymphocytes from influenza X31^{gp33} monoinfected (X31) and coinfected (Ts/X31) mice were stimulated with gp33 peptide and assayed for production of IFN-γ. Total gp33-specific IFN-γ$^+$ CD8$^+$ T cells in the lung are shown. (D) Frequency of gp33-specific CD8$^+$ T cells in the lungs. Numbers in flow plots represent mean frequencies ± SEM of Kb-gp33 tetramer$^+$ cells within the CD8$^+$ lymphocyte gate of each group. (E) Quantification of influenza PA gene in lung tissue, normalized to *Hprt1*. (**F** to **H**) C57BL/6 mice were infected with 200 Hp larvae po. At day 12 post-Hp infection, mice were infected with 10^6 pfu MNV CW3 po and killed at day 7 post-CW3 infection. (F) Total splenic Kb-P1^{519Y} tetramer$^+$ CD8$^+$ T cells from CW3 monoinfected and Hp/CW3–coinfected mice. (G) Splenocytes were stimulated with P1^{519Y} peptide and assayed for production of IFN-γ and TNF-α. Numbers in flow plots represent mean frequencies ± SEM of dual-producing IFN-γ$^+$ TNF-α$^+$ cells within the CD8$^+$ CD44^{hi} lymphocyte gate of each group. (H) MNV genome copies in ileal tissue were quantified by RT-PCR. All data are representative of two independent experiments with a minimum of three to five mice per group. Bar graphs represent means ± SEM. Statistics compare monoinfected versus coinfected groups by using a two-way analysis of variance (ANOVA) with Bonferroni's post-testing [(B), (C), and (E)] or the Student's *t* test [(D) and (F) to (H)]. *$P < 0.05$.

it is critical to define the regulatory mechanisms by which helminth parasites can influence innate and adaptive immunity.

To test whether helminth infection elicits immunomodulation through direct effects on the mammalian immune system or via alterations in the microbiota, we developed a model of enteric coinfection using the helminth parasite *Trichinella spiralis* (Ts), which inhabits the small intestine for about 2 to 3 weeks before progressing to a persistent extraintestinal phase, and a murine norovirus (MNV CW3) that acutely infects the ileum. As expected, *Trichinella* infection induced type 2 immune responses (fig. S1). In the presence of the microbiota, *Trichinella*-MNV coinfection (fig. S2A) was associated with decreased frequencies and numbers of MNV-specific CD8$^+$ T cells within the small intestine, Peyer's patches, and spleen compared with monoinfected controls (Fig. 1, A and B, and fig. S2, B and C). Further, MNV-specific CD8$^+$ T cells isolated from helminth-coinfected mice exhibited diminished polyfunctional effector function as compared with monoinfected controls (Fig. 1C). Analysis of MNV-specific CD4$^+$ T cells using major histocompatibility complex II (MHCII) IA^b tetramers specific for an epitope (P1496) within the MNV capsid (table S1) identified that helminth-coinfected mice also had fewer antigen-specific CD4$^+$ T cells (fig. S2D) and impaired accumulation of virus-specific CD4$^+$ T cells expressing both interferon-γ (IFN-γ) and tumor necrosis factor–α (TNF-α) compared to monoinfected controls (Fig. 1D). Notably, the defective T cell responses were associated with elevated viral loads in intestinal tissue of *Trichinella*/MNV CW3–infected mice compared to monoinfected controls (Fig. 1E).

We generated a recombinant gp33-expressing strain of MNV CW3 (CW3^{gp33}) to track the activation and early proliferation of MNV-specific CD8$^+$ T cells in vivo. Adoptively transferred congenic gp33-specific P14 CD8$^+$ T cells accumulated and exhibited polyfunctional effector function in the intestine and spleen after MNV infection (fig. S3). Spatial and kinetic analysis of gp33-specific P14 CD8$^+$ T cell activation and proliferation revealed that helminth coinfection resulted in delayed virus-specific CD8$^+$ T cell proliferation and activation (Fig. 2A), as well as reduced or delayed accumulation of virus-specific T cells in the draining mesenteric lymph nodes (MLNs) and spleen (Fig. 2B). Similar to oral infection, systemic viral infection stimulated robust antiviral P14 CD8$^+$ T cell proliferation in monoinfected mice, which was dampened in helminth-coinfected mice (fig. S4), suggesting that helminth infection can impair systemic antiviral immune responses to MNV independent of inflammatory or tissue-repair processes operating in the intestine.

The immunomodulatory effects of *Trichinella* infection on antiviral immunity were long lived (fig. S5); able to influence established infection with MNV CR6, a related strain that persists in the colon of immune-competent mice (fig. S6); and evident in the lung after respiratory influenza infection (Fig. 2, C to E), indicating that helminth-elicited immunomodulation is operational at

extraintestinal tissues and can influence immunity to multiple viral pathogens. Further, the immunomodulatory effects of helminth infection on antiviral immunity were not restricted to *Trichinella* and were also evident after infection with *Heligmosomoides polygyrus bakeri* (Hp) (Fig. 2, F to H).

Despite ongoing clinical trials testing the potential efficacy of helminth immunotherapy to treat inflammatory diseases and the detrimental effects of helminth coinfection on protective immune responses to other human pathogens (*19*, *21*, *23*, *24*), the mechanisms underlying helminth-elicited immunomodulation remain poorly understood. Helminth infections can induce shifts in the composition of commensal bacterial communities, and these alterations have been proposed to play a role in modulating the host immune response (*13*–*18*). Further, commensal bacteria–derived signals can modulate lymphocyte responses to infection (*3*, *4*, *9*), including antiviral immunity (*25*–*27*). To test whether *Trichinella* infection altered the composition of the intestinal microbiota, we performed sequencing and phylogenetic analysis of bacterial 16*S* ribosomal RNA (rRNA) genes of small intestine and colon luminal contents. These analyses revealed alterations in commensal bacterial communities in both the small and the large intestine after *Trichinella* infection (Fig. 3, A to D). Notable changes included a reduction in the relative abundance of the *Turicibacteraceae* family and an increase in the relative abundance of *Lactobacillacaeae* in the small intestine (Fig. 3C) and increased colonic representation of *Clostridiales* (Fig. 3D).

To test whether these alterations contributed to helminth-induced immunomodulation, we compared the influence of helminth coinfection on antiviral immunity in the presence or absence of the microbiota using germ-free (GF) mice. Establishment of *Trichinella* in the intestine and peripheral tissues and induction of helminth-induced T helper 2 (T_H2) cell responses were similar in conventional (CNV) and GF mice (fig. S7). The diminished antiviral responses seen in helminth-coinfected mice were evident in both CNV and GF mice (Fig. 3, E to G). These data indicate that helminth-elicited immunomodulation of antiviral immunity can occur independently of changes in the microbiota and suggest that coevolution may have resulted in mechanisms that allow helminths to directly regulate host immune responses.

Helminth infection elicits the induction of type 2 cytokines and is associated with signal transducer and activator of transcription 6 (STAT6)–dependent alternative activation of macrophages (AAMacs), but these responses are not typically associated with protective antiviral immune responses. Therefore, we tested whether STAT6-dependent differentiation of AAMacs may underlie the dysregulated antiviral immune response in the context of helminth coinfection. Ex vivo analysis revealed a significant population expansion of macrophages ($CD11b^+$ $CD11c^-$ cells) in the MLNs of *Trichinella*-infected mice that was unaltered by MNV infection (Fig. 4A). Up-regulation of known AAMac-associated genes, including arginase-1 (*Arg1*), RELMα (*Retnla*), and Ym1 (*Chi3l3*), was detected in the ileum of wild-type (WT) but not STAT6- or

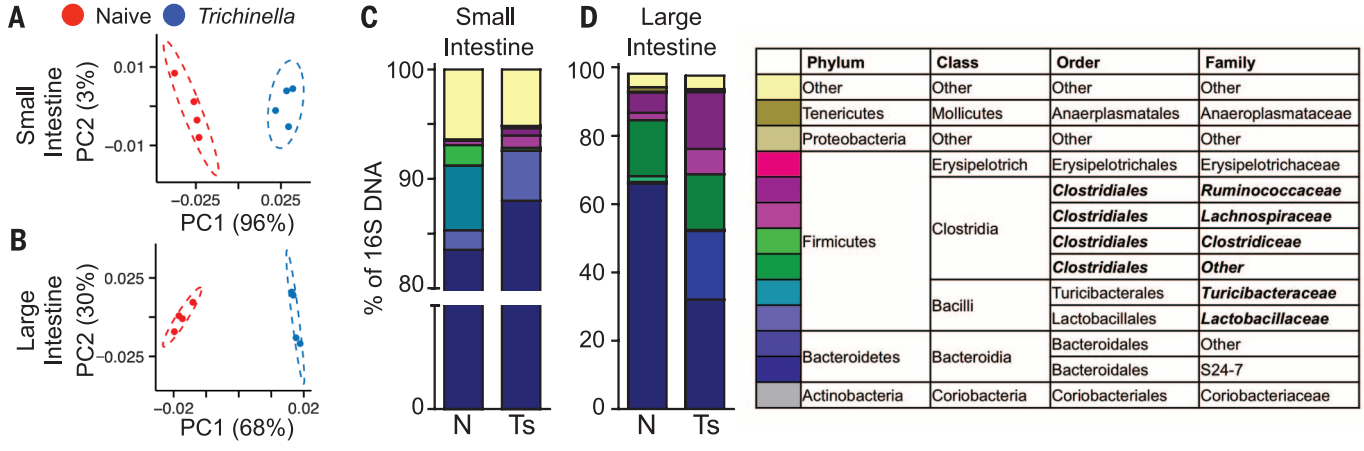

	Phylum	Class	Order	Family
	Other	Other	Other	Other
	Tenericutes	Mollicutes	Anaerplasmatales	Anaeroplasmataceae
	Proteobacteria	Other	Other	Other
	Firmicutes	Erysipelotrich	Erysipelotrichales	Erysipelotrichaceae
		Clostridia	***Clostridiales***	***Ruminococcaceae***
			Clostridiales	***Lachnospiraceae***
			Clostridiales	***Clostridiceae***
			Clostridiales	***Other***
		Bacilli	Turicibacterales	***Turicibacteraceae***
			Lactobacillales	***Lactobacillaceae***
	Bacteroidetes	Bacteroidia	Bacteroidales	Other
			Bacteroidales	S24-7
	Actinobacteria	Coriobacteria	Coriobacteriales	Coriobacteriaceae

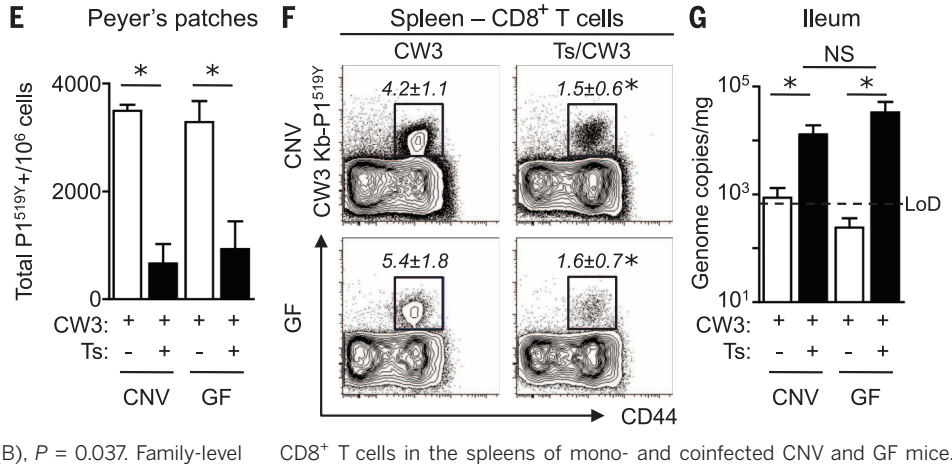

Fig. 3. Helminth-induced immunomodulation of antiviral immunity is independent of changes in the microbiota. (**A** to **D**) Luminal contents of the small and large intestines isolated from naïve or day 12 Ts-infected C57/BL6 mice were subjected to 16*S* sequencing by using Illumina MiSeq. Principal coordinate (PC) analysis of bacterial populations in the small intestine (A) and the large intestine (B) of naïve and Ts-infected mice. Axes represent weighted UniFrac distances between naïve and *Trichinella*-infected groups and are annotated, with the percentage of total variation explained. Statistical analyses were performed on groups of four mice, using PERMANOVA to test for differences in community composition according to weighted UniFrac centroid position. For (A), $P = 0.034$; (B), $P = 0.037$. Family-level phylogenetic analysis of bacterial sequences in the small (C) and the large (D) intestine of naïve and Ts-infected mice. In the legend on right, bold italicized taxa exhibited differences in relative abundance between naïve and Ts-infected mice. (**E** to **G**) Naïve and Ts-infected CNV or GF C57BL/6 mice were infected with MNV CW3 and killed at day 7 post-CW3. (E) MNV CW3 $P1^{519Y}$–specific $CD8^+$ T cells in the Peyer's patches of mono- and coinfected CNV and GF mice. (F) Frequency of MNV CW3 $P1^{519Y}$–specific $CD8^+$ T cells in the spleens of mono- and coinfected CNV and GF mice. Numbers in flow plots represent mean frequencies ± SEM of CW3 Kb-$P1^{519Y}$ $tetramer^+$ cells within the $CD8^+$ lymphocyte gate of each group. (G) MNV genome copies in ileal tissue were quantified by RT-PCR. Data in (E) to (G) are representative of three independent experiments with a minimum of three to five mice per group. Statistical analyses in (E) to (G) were performed by using two-way ANOVA with Bonferroni's post-testing. *$P < 0.05$. NS, not significant.

interleukin-4Rα (IL-4Rα)–deficient mice (Fig. 4B and fig. S8A), indicating that AAMac responses were evident in coinfected mice at the site of MNV CW3 infection. Critically, deletion of STAT6 was sufficient to restore MNV CW3^{gp33}–induced CD8$^+$ T cell proliferation (Fig. 4C), and mice lacking STAT6 or IL-4Rα exhibited reduced viral loads compared with coinfected WT controls after MNV infection (Fig. 4D and fig. S8B). Further, delivery of IL-4/anti-IL-4 complexes was sufficient to induce expression of AAMac-associated genes and impair antiviral immunity in vivo compared with control-treated mice (fig. S9). Collectively, these data suggest that AAMacs may limit the induction of host-protective antiviral immune responses in a type 2 cytokine- and STAT6-dependent manner.

Because MNV has tropism for macrophages (*28*), we tested the ability of bone marrow–derived macrophages (BM-Macs) to control viral replication. After recombinant IL-4 (rIL-4) treatment, BM-IL4 Macs undergo STAT6-dependent alternative activation, and BM-IL4 Macs infected with MNV CW3^{gp33} exhibited STAT6-dependent increases in viral burdens compared with control BM-Macs (fig. S10). Furthermore, although MNV CW3^{gp33}-infected control BM-Macs could elicit robust CD8$^+$ T cell proliferation in vitro, BM-IL4 Macs demonstrated STAT6-dependent inhibition of MNV-specific CD8$^+$ T cell proliferation (fig. S11A). To test whether AAMacs could modulate early antiviral immune responses in vivo, control BM-Macs or BM-IL4 Macs were adoptively transferred into mice along with MNV CW3^{gp33}. Mice receiving BM-IL4 Macs exhibited fewer antiviral CD8$^+$ T cells and increased viral burdens (fig. S11, B and C). Together, these data indicate that helminth-elicited STAT6-dependent induction of AAMacs can limit innate and adaptive immune responses to enteric viral infection.

AAMac effector molecules arginase-1, RELMα, and Ym1 have been implicated in regulating immunity and inflammation (*29*–*31*). However, antiviral CD8$^+$ T cell activation remained impaired in helminth-coinfected mice after inhibition of arginase-1 (fig. S12A) or deletion of RELMα (fig. S12B), indicating that these factors are dispensable for helminth-induced impairment of antiviral immunity. The chitinase-like molecule

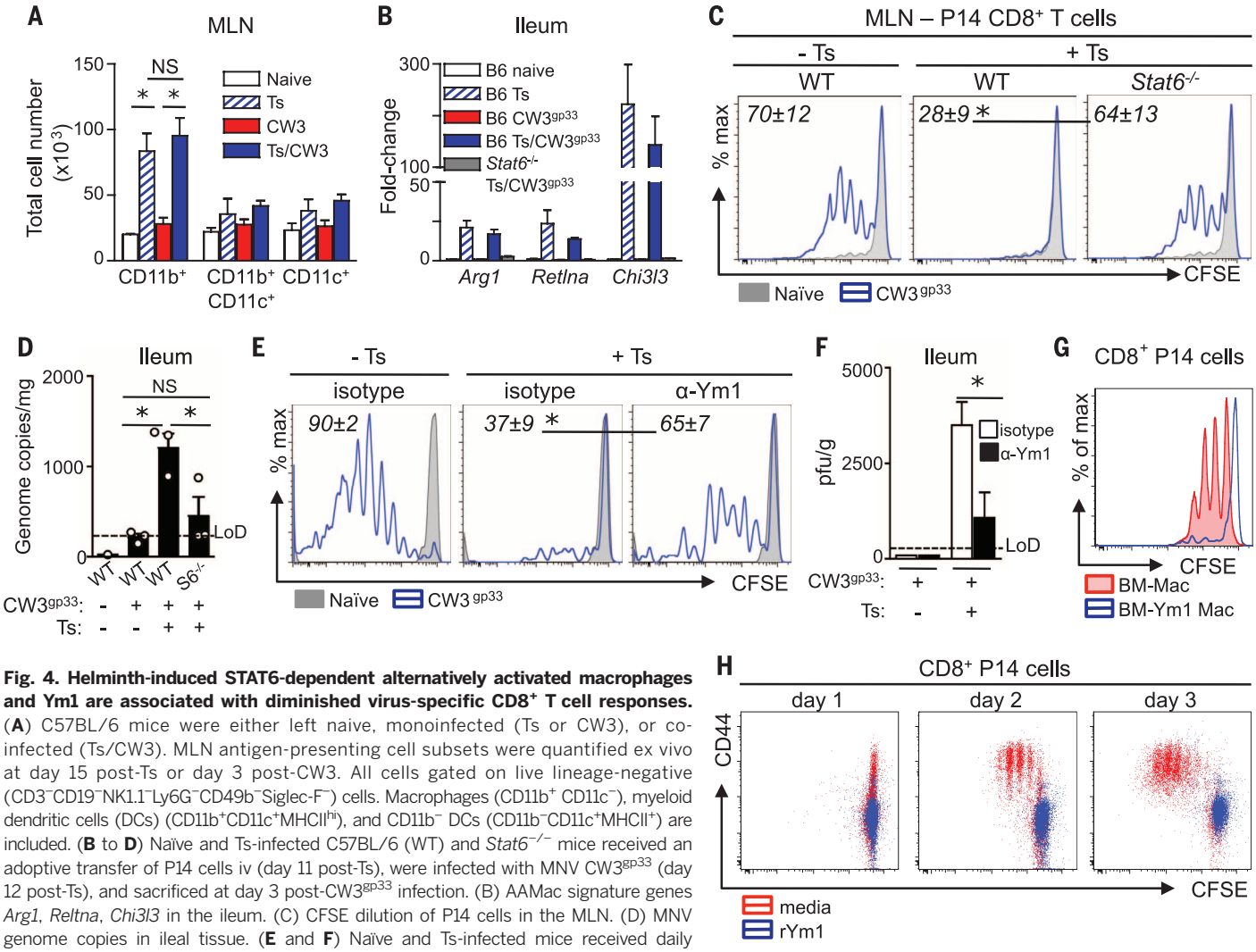

Fig. 4. Helminth-induced STAT6-dependent alternatively activated macrophages and Ym1 are associated with diminished virus-specific CD8$^+$ T cell responses. (**A**) C57BL/6 mice were either left naive, monoinfected (Ts or CW3), or coinfected (Ts/CW3). MLN antigen-presenting cell subsets were quantified ex vivo at day 15 post-Ts or day 3 post-CW3. All cells gated on live lineage-negative (CD3$^-$CD19$^-$NK1.1$^-$Ly6G$^-$CD49b$^-$Siglec-F$^-$) cells. Macrophages (CD11b$^+$ CD11c$^-$), myeloid dendritic cells (DCs) (CD11b$^+$CD11c$^+$MHCII^{hi}), and CD11b$^-$ DCs (CD11b$^-$CD11c$^+$MHCII$^+$) are included. (**B** to **D**) Naïve and Ts-infected C57BL/6 (WT) and *Stat6*$^{-/-}$ mice received an adoptive transfer of P14 cells iv (day 11 post-Ts), were infected with MNV CW3^{gp33} (day 12 post-Ts), and sacrificed at day 3 post-CW3^{gp33} infection. (B) AAMac signature genes *Arg1*, *Reltna*, *Chi3l3* in the ileum. (C) CFSE dilution of P14 cells in the MLN. (D) MNV genome copies in ileal tissue. (**E** and **F**) Naïve and Ts-infected mice received daily treatments of 300 μg of isotype mAb or anti-Ym1 starting at day 11 post-Ts infection and were MNV CW3^{gp33}–infected at day 12 post-Ts infection. (E) CFSE dilution of adoptively transferred P14 CD8$^+$ T cells in the MLN at day 3 post-CW3^{gp33} infection. (F) Viral load in the ileum as determined by plaque assay at day 7 post-CW3^{gp33} infection. (**G**) BM-Macs were infected with CW3^{gp33} and cultured with CFSE-labeled P14 CD8$^+$ T cells in the presence (blue trace) or absence (red fill) of rYm1 for 3 days. (**H**) Purified CFSE-labeled P14 CD8$^+$ T cells were stimulated with plate-bound αCD3 and soluble αCD28 in the presence (red) or absence (blue) of rYm1. Data in (A) to (F) are representative of one to three independent experiments with a minimum of three to five mice per group. Graphs represent means ± SEM. In (C) and (E), gray solid histogram, naïve mice; blue trace, CW3^{gp33}-infected. Numbers in flow plots represent mean frequencies ± SEM of CFSE-dividing P14 cells of each group. Data in (G) and (H) are representative of at least two independent experiments with technical replicates. Statistical analysis was performed by using two-way ANOVA with Bonferroni post-testing [(A) and (F)], Student's *t* test [(C) and (E)], or one-way ANOVA with Tukey's post-test (D). *P <0.05.

Ym1 is one of the most highly expressed AAMac effector molecules in multiple settings of acute and chronic type 2 cytokine-associated inflammation (*32*–*36*). Although Ym1 has been implicated in promoting chemoattraction and inflammation (*37*, *38*), the biological functions of this molecule are not well understood (*39*). To test whether Ym1 contributes to helminth-induced immunomodulation, virus-helminth–coinfected mice were treated with an isotype control monoclonal antibody (mAb) or a mAb against Ym1 (anti-YM1). Neutralization of Ym1 in coinfected animals significantly enhanced virus-specific $CD8^+$ T cell proliferation (Fig. 4E), the polyfunctional capacity of antiviral $CD8^+$ T cells, and the number of virus-specific $CD4^+$ T cells expressing effector cytokines (fig. S13). Anti-Ym1 treatment of coinfected mice was associated with enhanced control of viral replication (Fig. 4F). Further, although $CW3^{gp33}$-infected BM-Macs stimulated robust P14 $CD8^+$ T cell proliferation, this was inhibited by addition of recombinant Ym1 (rYm1) (Fig. 4G). rYM1 was also sufficient to inhibit T cell receptor–driven activation and proliferation of purified $CD8^+$ T cells (Fig. 4H). Taken together, these findings reveal a role for helminth-induced AAMacs and Ym1 in immunomodulation of protective immune responses to concomitant viral infection.

These data identify that helminth coinfection can inhibit antiviral immunity via a pathway of innate immunomodulation. This was independent of changes in the microbiota but associated with induction of potent AAMac responses and Ym1-dependent inhibition of antiviral T cell responses (fig. S14). Therefore, although helminth parasites and commensal bacteria colonize the same niche within the intestine, coevolution of helminths with their mammalian hosts may have resulted in mechanisms that allow direct regulation of the host innate immune system and antiviral immunity independently of changes in the microbiota. These findings, coupled with a report by Reese *et al.* (*40*) identifying a critical role for helminth-induced IL-4/IL-13 and STAT6 activity in reactivation of latent γ-herpesvirus infection in macrophages, indicate a conserved mechanism of innate immunomodulation in the context of virus-helminth coinfection. The identification of an immunomodulatory role for the AAMac-Ym1 pathway could have implications for the development of helminth-based therapies for multiple chronic inflammatory diseases as well as improved vaccination strategies in helminth-infected individuals.

REFERENCES AND NOTES

1. A. J. Macpherson, N. L. Harris, *Nat. Rev. Immunol.* **4**, 478–485 (2004).
2. L. V. Hooper, D. R. Littman, A. J. Macpherson, *Science* **336**, 1268–1273 (2012).
3. A. Benson, R. Pifer, C. L. Behrendt, L. V. Hooper, F. Yarovinsky, *Cell Host Microbe* **6**, 187–196 (2009).
4. J. A. Hall *et al.*, *Immunity* **29**, 637–649 (2008).
5. S. Vaishnava, C. L. Behrendt, A. S. Ismail, L. Eckmann, L. V. Hooper, *Proc. Natl. Acad. Sci. U.S.A.* **105**, 20858–20863 (2008).
6. K. Atarashi *et al.*, *Science* **331**, 337–341 (2011).
7. K. S. Hayes *et al.*, *Science* **328**, 1391–1394 (2010).
8. M. Raetz *et al.*, *Nat. Immunol.* **14**, 136–142 (2013).
9. I. I. Ivanov *et al.*, *Cell* **139**, 485–498 (2009).
10. D. R. Littman, E. G. Pamer, *Cell Host Microbe* **10**, 311–323 (2011).
11. J. E. Allen, R. M. Maizels, *Nat. Rev. Immunol.* **11**, 375–388 (2011).
12. D. E. Elliott, J. V. Weinstock, *Ann. N. Y. Acad. Sci.* **1247**, 83–96 (2012).
13. S. Rausch *et al.*, *PLOS ONE* **8**, e74026 (2013).
14. S. T. Walk, A. M. Blum, S. A. Ewing, J. V. Weinstock, V. B. Young, *Inflamm. Bowel Dis.* **16**, 1841–1849 (2010).
15. M. J. Broadhurst *et al.*, *PLOS Pathog.* **8**, e1003000 (2012).
16. R. W. Li *et al.*., *Infect. Immun.* **80**, 2150–2157 (2012).
17. A. J. Bancroft, K. S. Hayes, R. K. Grencis, *Trends Parasitol.* **28**, 93–98 (2012).
18. J. M. Leung, P. Loke, *Int. J. Parasitol.* **43**, 253–257 (2013).
19. E. Stelekati, E. J. Wherry, *Cell Host Microbe* **12**, 458–469 (2012).
20. P. Salgame, G. S. Yap, W. C. Gause, *Nat. Immunol.* **14**, 1118–1126 (2013).
21. S. Metenou, S. Babu, T. B. Nutman, *Curr Opin HIV AIDS* **7**, 231–238 (2012).
22. J. A. Potian *et al.*, *J. Exp. Med.* **208**, 1863–1874 (2011).
23. M. J. Wolff, M. J. Broadhurst, P. Loke, *Trends Parasitol.* **28**, 187–194 (2012).
24. H. J. McSorley, R. M. Maizels, *Clin. Microbiol. Rev.* **25**, 585–608 (2012).
25. T. Ichinohe *et al.*, *Proc. Natl. Acad. Sci. U.S.A.* **108**, 5354–5359 (2011).
26. M. C. Abt *et al.*, *Immunity* **37**, 158–170 (2012).
27. S. C. Ganal *et al.*, *Immunity* **37**, 171–186 (2012).
28. C. E. Wobus *et al.*, *PLOS Biol.* **2**, e432 (2004).
29. J. T. Pesce *et al.*, *PLOS Pathog.* **5**, e1000371 (2009).
30. J. T. Pesce *et al.*, *PLOS Pathog.* **5**, e1000393 (2009).
31. M. G. Nair *et al.*, *J. Exp. Med.* **206**, 937–952 (2009).
32. P. Loke *et al.*, *BMC Immunol.* **3**, 7 (2002).
33. J. Zhao *et al.*, *Parasitol. Res.* **112**, 2689–2695 (2013).
34. M. G. Nair *et al.*, *Infect. Immun.* **73**, 385–394 (2005).
35. A. Q. Ford *et al.*, *BMC Immunol.* **13**, 6 (2012).
36. N. C. Chang *et al.*, *J. Biol. Chem.* **276**, 17497–17506 (2001).
37. M. Owhashi, H. Arita, N. Hayai, *J. Biol. Chem.* **275**, 1279–1286 (2000).
38. M. Arora *et al.*, *Proc. Natl. Acad. Sci. U.S.A.* **103**, 7777–7782 (2006).
39. T. E. Sutherland, R. M. Maizels, J. E. Allen, *Clin. Exp. Allergy* **39**, 943–955 (2009).
40. T. A. Reese *et al.*, *Science* **345**, 573 (2014).

ACKNOWLEDGMENTS

We thank members of the Artis laboratory for discussions and critical reading of the manuscript; F. Finkelman for providing anti–IL-4 clone 1D11.2; the NIH Tetramer Core Facility (contract HHSN272201300006C) for providing MHCII IA^b tetramers; the University of Pennsylvania Matthew J. Ryan Veterinary Hospital Pathology Lab, the NIH/National Institute of Diabetes and Digestive and Kidney Diseases Center for Molecular Studies in Digestive and Liver Diseases (P30-DK050306), and its core facilities (Molecular Pathology and Imaging, Molecular Biology, Cell Culture, and Transgenic and Chimeric Mouse); the Penn Center for AIDS Research (P30-AI045008) for assistance and support; and the Abramson Cancer Center Flow Cytometry and Cell Sorting Resource Laboratory for technical advice and support. The ACC Flow Cytometry and Cell Sorting Shared Resource is partially supported by a National Cancer Institute Comprehensive Cancer Center Support grant (2-P30 CA016520). The data tabulated in this paper are reported in the main paper and in the supplementary materials. Illumina MiSeq data can be found in the National Center for Biotechnology Information Sequence Read Archive with accession number SRP043964. Research in the Artis lab is supported by the NIH (AI061570, AI074878, AI087990, AI095466, AI095608, AI097333, AI106697, and AI102942 to D.A.; T32-AI007532 to L.A.M.; and F32-AI085828 to M.C.S.), the Crohn's and Colitis Foundation of America (D.A. and M.R.H.), the Burroughs Wellcome Fund Investigator in Pathogenesis of Infectious Disease Award (D.A.), and the Edmond J. Safra Foundation/Cancer Research Institute Irvington Fellowship (L.C.O.). E.J.W. and V.T.T. are supported by NIH grants AI083022, AI082630, and K08-DK097301. T.E.S. and J.E.A. were supported by the Medical Research Council UK (MR/J001929/1). T.J.N. was supported by NIH training grant 5T32A100716334 and postdoctoral fellowships from the Cancer Research Institute and American Cancer Society. H.W.V. was supported by grant R01 AI 084887, the Crohn's and Colitis Genetics Initiative grant 274415, and the Broad Foundation grant IBD-0357. Washington University and H.W.V. receive income based on licenses for MNV technology. The authors declare no other potential conflicts of interest.

SUPPLEMENTARY MATERIALS

www.sciencemag.org/content/345/6196/578/suppl/DC1
Materials and Methods
Supplementary Text
Figs. S1 to S14
Table S1
References (*41*–*57*)

4 June 2014; accepted 8 July 2014
Published online 17 July 2014;
10.1126/science.1256942

Multimode Plate Reader

The new EnSight Multimode Plate Reader is the first plate reader on the market to offer both labeled and label-free detection, together with well-imaging technology (which facilitates cell imaging), on a single benchtop system. This unique combination allows researchers to run their assays on the same platform—generating more predictive results earlier in the drug discovery process. The EnSight system enables researchers to generate more reliable readouts and obtain an expanded set of data from their samples. They can also use the EnSight system's variety of technology modes to perform confirmatory assays, helping to ensure that results are not biased to the detection technologies used for their sampling. The EnSight system offers cell imaging capabilities that allow researchers to quickly visualize cells and generate per-cell data. When using primary/stem cells, this per-cell data is a more physiologically relevant model than the per-well data generated by traditional multimode detection technologies.

PerkinElmer
For info: 877-754-6973
www.perkinelmer.com/ensight

Serum Replacement

Animal component free and chemically defined, Cell-Ess serum replacement is used in place of fetal bovine serum (FBS) as a cell culture media supplement. Unlike FBS, Cell-Ess does not contain variable levels of growth factors, hormones and plating factors that signal cells to behave in non-normal ways. Cell-Ess delivers only critical factors enabling greater experimental control and analysis of cell behavior for cell lines and primary cells.

Cell-Ess
For info: 866-413-6248
www.cell-ess.com

Embryoid Body Formation Kit

The Cultrex Embryoid Body (EB) Formation Kit is a tool for generating consistent, reproducible, and identically sized embryoid bodies. It has been qualified to form EBs from human embryonic stem cells and induced pluripotent stem cells (hESCs and iPSCs). The kit includes ROCK Inhibitor Y-27632, which significantly increases survival of PSCs in single cell culture, a specialized EB Formation Matrix to stimulate cell aggregation and development of EB, and a 96-well EB Formation Plate, that allows for control of the EB size and shape. No transfer step is required for formation or differentiation, which allows for high throughput work. This is the only commercially available kit for formation and differentiation of size-consistent embryoid bodies.

Trevigen
For info: 301-216-2800
www.trevigen.com

Neural Cell Models

An extensive range of induced pluripotent stem cell (iPSC)-derived neural cells including normal and Alzheimer's disease neural progenitor cells, and cerebral cortical neurons is now available. These neural cells are derived using integration-free, fully defined neural induction conditions and are capable of generating a spectrum of cortical neurons that are electrically active and have the ability to form functional synapses and circuits in vitro. Cerebral cortical neurons are implicated in numerous neurological diseases including Alzheimer's disease, autism, epilepsy, and stroke. A complete suite of cell reprogramming and neural differentiation services is also offered to meet the needs of neural cell researchers. For cell reprogramming simply provide patient/donor skin fibroblasts, blood cells, or iPS cells and AMSBIO will take care of the rest. Additionally, ongoing support is provided after the neural progenitor cells and/or functional neurons are delivered to facilitate the adaptation of the neural cells in experimental systems.

AMS Biotechnology
For info: +44-(0)-1235-828200
www.amsbio.com

Virus-Free iPSCs

The Simplicon RNA Reprogramming Technology uses synthetic self-replicating RNA to create large numbers of human induced pluripotent stem cells (iPSCs) using a single transfection step. This efficient reprogramming of somatic cells is accomplished without viral intermediates or host genome integration, offering a more defined and safer system for iPSC generation. The Simplicon RNA Reprogramming Technology uses a single synthetic, polycistronic self-replicating RNA strand engineered to mimic cellular RNA. The RNA strand contains the four reprogramming factors, OCT-4, KLF-4, SOX-2, and GLIS1, and enables the creation of integration- and virus-free iPSCs using only one transfection step. Once the cells are generated, the RNA and reprogramming factors can easily be eliminated from the cell culture medium in a controlled manner.

EMD Millipore
For info: 800-645-5476
www.emdmillipore.com/simplicon

Inverted Microscope

The Leica DMi1 enables cell biologists to check and document cell and tissue cultures within seconds. Its ease-of-use and efficient operation make it an excellent choice for routine laboratory work as well as for training. Combining high performance and affordability, the Leica DMi1 is equipped with LED illumination that provides constant color temperature with up to 20 years life-time. The convenient two-hour auto-off function helps reduce energy costs. For the finest visualization of cells cultured in a variety of containers, phase contrast is available in addition to brightfield illumination. The 40–50 mm or 80 mm working distance means that a wide variety of culture containers like flasks, dishes, or multiwell plates can be used on the fixed stage. An optional object guide with different kinds of holding frames is available to securely and reliably hold and move laboratory vessels during observation and documentation.

Leica Microsystems
For info: +49-64-4129-2201
www.leica-microsystems.com

Electronically submit your new product description or product literature information! Go to www.sciencemag.org/products/newproducts.dtl for more information.

Newly offered instrumentation, apparatus, and laboratory materials of interest to researchers in all disciplines in academic, industrial, and governmental organizations are featured in this space. Emphasis is given to purpose, chief characteristics, and availability of products and materials. Endorsement by *Science* or AAAS of any products or materials mentioned is not implied. Additional information may be obtained from the manufacturer or supplier.

Downloaded from www.sciencemag.org on August 11, 2014

By **Carrie Arnold**

The stressed-out postdoc

After he defended his dissertation and moved to a new lab for his postdoc, Ian Street hoped his battles with anxiety and depression were over. He was happy about his successful defense, and a change of scenery seemed just what he needed. But a breakup with his girlfriend and the pressures of being a new postdoc brought back familiar feelings of sadness, isolation, and worry. When he was a graduate student, Street had access to an array of resources, from on-campus counseling to support groups. As a postdoc, however, he was no longer a tuition-paying student, so he was cut off from those sources of support.

There is no rigorous estimate of the incidence and extent of mental health issues in postdocs. There is little doubt, however, that being a postdoc is stressful. Most postdocs work extremely hard, often for long hours and at low pay. Because of their commitment to work—and because they tend to work in labs far from home—they often are isolated from close friends and family. Furthermore, there aren't enough jobs, and they may feel stuck. "I'm kind of freaking out," says Cleyde Helena, a neuroendocrinology postdoc at Florida State University in Tallahassee. "I always wanted a tenure-track position, but with my CV and current abilities, I don't think I can get it," she says. "I could do another postdoc, but that takes time. I'm 37."

"If you love to dance ... make time to dance every day."

Not long after starting his postdoc, Street found that his creativity and motivation were shot. His productivity suffered, and his feelings of inadequacy grew worse. He worked longer hours to try and keep up. "My brain wasn't working right; it kept getting in my way," he says. "Soon, my biggest aspiration was just to survive."

Like other high achievers, postdocs find it hard to seek help. "People are afraid to admit they can't hack it," Street says. Jennifer Cohen, a current AAAS Science and Technology Policy Fellow (AAAS is the publisher of *Science*), says that many postdocs avoid on-campus help even when it's available because they worry their research advisers or other members of the lab will find out they are struggling.

Former postdoc Mahadeo Sukhai, vice president of the board of directors of the National Postdoctoral Association, says that some foreign populations are especially opposed to help. "I'm from the South Asian diaspora, and I can tell you that if you have a conversation with someone from this diaspora about a mental health issue, it's probably not going to go very well." That's bad because foreign postdocs "tend to be much further from home, and ... have to deal with these issues far from their normal supports," says Jennifer Oh, director of postdoctoral scholar affairs at the University of California, San Diego.

What can be done? Institutions need to find ways to provide appropriate support services to all postdocs, including those with fellowships. Advisers should be attentive to changes in behavior such as mood swings, working at night, isolation, and emotional outbursts. Christian Gloria of Hawaii Pacific University, Kaneohe, first author of an article in the journal *Stress and Health* that studied a population of postdocs, says that advisers can offer significant support by reinforcing positive emotions.

Postdocs should be reassured that their problems need not threaten their careers. They can help themselves by seeking support (including professional help), employing "adaptive" coping strategies (such as planning and positive reframing), and avoiding "maladaptive" ones (including denial, self-distraction, and substance abuse).

Along with medication and therapy, Street began to view his life as an experiment. He started running. He started a gratitude journal and amassed a collection of life hacks to improve his productivity. He blogged about his experiences and discovered that others were experiencing the same thing. "I thought I was the only one," he says.

Finally, it can help to get out of the lab more and do things you enjoy. "It's easy to forget there's life outside the lab," Cohen says. "So if you love to dance ... make time to dance every day. It will keep you sane when everything else gets crazy." ■

Carrie Arnold is a freelance science writer living in Virginia.

ILLUSTRATION: ROBERT NEUBECKER

Downloaded from www.sciencemag.org on August 11, 2014

Published by AAAS